

Transactions of the ASME

Experimental Investigation of Critical Design Factors for Vane-Type Cyclones	<i>A. B. Walker and W. H. Cole</i>	1715
Estimation of Temperature Patterns in Multiply-Shielded Systems	<i>J. G. Bartas and E. Mayer</i>	1722
Heat Transfer by Radiation From Flames	<i>R. A. Sherman</i>	1727
Rate of Temperature Change of Simple Shapes	<i>Victor Paschke and J. W. Hlinks</i>	1742
Pressure Drop for Parallel Flow Through Rod Bundles	<i>B. W. Le Tourneau, R. E. Grimble, and J. E. Zerbe</i>	1751
Resistance Coefficients for Laminar and Turbulent Flow Through One-Half-Inch Valves and Fittings	<i>C. P. Kittredge and D. S. Rowley</i>	1759
Losses in Pipe and Fittings	<i>R. J. S. Pigott</i>	1767
Compensation of Steady-State Flow Forces in Spool-Type Hydraulic Valves	<i>R. N. Clark</i>	1784
Skewed Boundary-Layer Flow Near the End Walls of a Compressor Cascade	<i>R. W. Moore, Jr., and D. L. Richardson</i>	1789
An Investigation of the End-Wall Boundary Layer of a Turbine-Nozzle Cascade	<i>J. R. Turner</i>	1801
Jet-Pump Theory and Performance With Fluids of High Viscosity	<i>R. G. Cunningham</i>	1807
An Experimental Study of Centrifugal-Pump Impellers	<i>A. J. Acosta and R. D. Bowerman</i>	1821
Computer Representations of Engineering Systems Involving Fluid Transients	<i>F. D. Ezekiel and H. M. Paynter</i>	1840
Method for Presenting the Response of Temperature-Measuring Systems	<i>Robert Looney</i>	1851
Responses of Temperature-Sensing-Element Analogs	<i>G. A. Coon</i>	1857
Signal Stabilization of a Control System	<i>Rufus Oldenburger</i>	1869
Design Basis for Cascade-Type Positional Servomechanisms	<i>Sidney Lees and T. C. Blaschke</i>	1873
The Phase-Space Method for Analysis of Nonlinear Control Systems	<i>Y. H. Ku</i>	1897
Influence of Repeated Bending Loads on Biaxial Residual Stresses in Shot-Peened Plates	<i>T. M. Elsesser</i>	1904
The Flow and Fracture of Nodular Cast Iron	<i>W. R. Clough and M. E. Shank</i>	1911
Creep Characteristics of Type 347 Stainless Steel at 1050 and 1100 F in Tension and Compression	<i>M. J. Manjoine</i>	1921
Design and Development of a Two-Cycle Turbocharged Diesel Engine	<i>P. J. Lonzecky</i>	1929
Future Developments of the High-Speed Diesel Engine	<i>Ernest Chatterton</i>	1941
Analysis of a Process-Fluid-Flow Network by Electrical Analogy	<i>C. F. Koyan and J. A. Balmford</i>	1957
Electrical Effects Accompanying the Stick-Slip Phenomenon of Sliding of Metals on Plastics and Lubricated Surfaces	<i>G. W. Sohl, J. Gaynor, and S. M. Skinner</i>	1963

TRANSACTIONS OF THE AMERICAN SOCIETY OF MECHANICAL ENGINEERS

VOLUME 79

NOVEMBER 1957

NUMBER 8

Transactions

of The American Society of Mechanical Engineers

Published on the tenth of every month, except March, June, September, and December

OFFICERS OF THE SOCIETY:

W. F. RYAN, *President*

JOSEPH L. KOPP, *Treasurer*

C. E. DAVIES, *Secretary*

EDGAR J. KATZ, *Asst. Treasurer*

O. B. SCHIER, *2nd, Deputy Secretary*

COMMITTEE ON PUBLICATIONS:

W. E. REASER, *Chairman*

KERR ATKINSON

D. G. A. SKROTEKI

JOHN DE S. COUTINHO

HENDLEY N. BLACKMON

H. N. WEINBERG } *Junior Advisory Members*
J. N. VIEHMANE }

GEORGE A. STETSON, *Editor Emeritus*

LEO BLODGETT, *Consulting Editor*

J. J. JAKLITICH, JR., *Editor*

J. A. NORTH, *Production*

REGIONAL ADVISORY BOARD OF THE PUBLICATIONS COMMITTEE:

ROY L. PARSHALL—I
GLENN R. FRYLING—II
F. J. HEINZE—III
FRANCIS C. SMITH—IV

H. M. CATHER—V
C. R. EARLE—VI
M. B. HOOAN—VII
LENN HELANDER—VIII

Published monthly by The American Society of Mechanical Engineers. Publication office at 20th and Northampton Streets, Easton, Pa. The editorial department is located at the headquarters of the Society, 29 West Thirty-Ninth Street, New York 18, N. Y. Cable address, "Mechanics," New York. Price \$1.50 a copy, \$12.00 annually for Transactions and the *Journal of Applied Mechanics*; to members, \$1.00 a copy, \$6.00 annually. Add \$1.50 for postage to all countries outside the United States, Canada, and Pan American Union. Changes of address must be received at Society headquarters seven weeks before they are to be effective on the mailing list. Please send old as well as new address.... By-Law: The Society shall not be responsible for statements or opinions advanced in papers or... printed in its publications (B13, Par. 4).... Entered as second-class matter March 2, 1928, at the Post Office at Easton, Pa., under the Act of August 24, 1912.... Copyrighted, 1957, by The American Society of Mechanical Engineers. Reprints from this publication may be made on condition that full credit be given the Transactions of the ASME and the author, and that date of publication be stated.

Experimental Investigation of Critical Design Factors for Vane-Type Cyclones

By A. B. WALKER¹ AND W. H. COLE,² BOUND BROOK, N. J.

Many of the so-called high-efficiency mechanical collectors in use today are of the multiple-tube vane type. A basic investigation has been made on the effects of tube size, inlet-vane design, and utilization of outlet-tube vanes on the performance of this type collector. The critical nature of these factors and methods for obtaining higher efficiency and gas flow is demonstrated. A comparison between predicted field results from laboratory tests and actual field results is presented, and the accuracy of specific laboratory techniques in predicting field performance indicated.

INTRODUCTION

THERE has been a considerable amount of work published on the performance and design factors of dust-collecting cyclones, notably that of Ter Linden (1)³ and First (2). However, this information has been confined to tangential-entry cyclones. Many of the so-called high-efficiency mechanical collectors in use today are of the multiple-tube vane type where the incoming dust-laden gas is given a rotating motion in each cyclone by passage through a series of turning vanes usually located in an annular space between the gas-inlet and gas-outlet tubes, rather than by a simple tangential entry into the cylindrical portion of the cyclone. The trend in size of these multiple-tube collectors has been toward the smaller diameters in order to take advantage of the possibilities of increased centrifugal force on the entrained dust particles by reduced radius of rotation. This approach in increasing the performance of multiple-tube cyclonic collectors is limited by practical considerations such as tube plugging.

Questions immediately arise as to other means of increasing performance without resorting to smaller tubes. As an initial attempt toward answering these questions, basic studies were made in the laboratory to determine the effects on over-all performance of inlet-vane blade shape, number of inlet-vane blades, tube size, and the use and configuration of outlet-tube vanes for the conversion and recovery of energy normally lost in the outlet tube. Figs. 1(a) and 1(b) schematically depict the type of tubes tested in this work.

The initial studies have shown some design factors to be critical in the performance of vane-type cyclones. These factors indicate possibilities for improved efficiency without resorting to unusually small tubes and even indicate the possibilities of high efficiency in large tubes in the range of 16 to 24 in. diam where plugging and other operating difficulties are greatly reduced. They are:

¹ Chief, New Products Section, Research-Cottrell, Inc.

² Physicist, New Products Section, Research-Cottrell, Inc.

³ Numbers in parentheses refer to the Bibliography at the end of the paper.

Contributed by the Committee on Air Pollution Controls and presented at a joint session with the Fuels Division at the Annual Meeting, New York, N. Y., November 25-30, 1956, of THE AMERICAN SOCIETY OF MECHANICAL ENGINEERS.

NOTE: Statements and opinions advanced in papers are to be understood as individual expressions of their authors and not those of the Society. Manuscript received at ASME Headquarters, October 11, 1956. Paper No. 56-A-199.

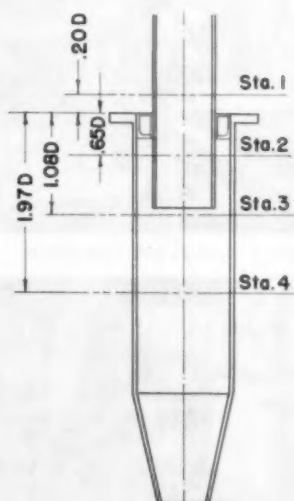


FIG. 1(a) SCHEMATIC DIAGRAM OF TUBE TYPES STUDIED SHOWING TUBE PROPORTIONS

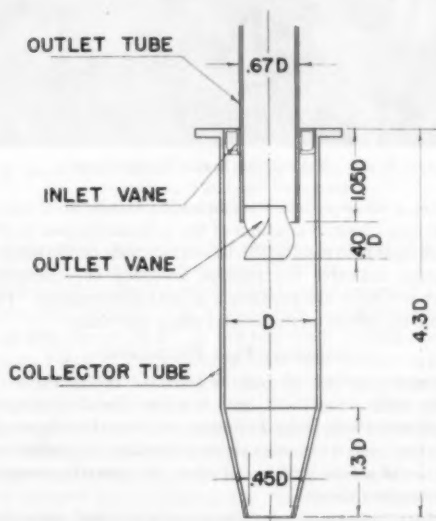


FIG. 1(b) LOCATION OF INTERNAL-VELOCITY TRAVERSE PLANES

1 Inlet-vane design, both with respect to blade shape and blade number.

2 Utilization of outlet-tube vanes, both for recovery of kinetic energy normally dissipated in turbulence and the reduction of entry and exit losses in the gas-outlet tube.

Concurrently with the laboratory work on the various design

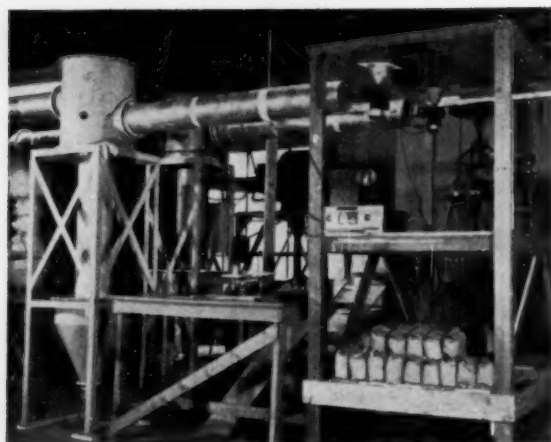


FIG. 2 LABORATORY TEST UNITS

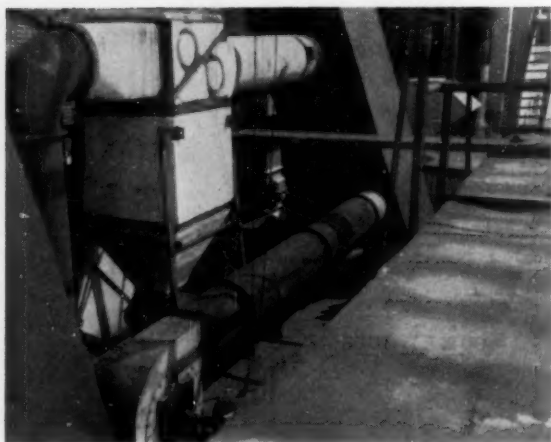


FIG. 3 NINE-TUBE FIELD PILOT PLANT

parameters, a series of field tests on multiple-tube units was conducted on some design variations of the collectors shown in Fig. 1. A comparison of field results with laboratory tests on the same tube configuration indicates the relative accuracy of utilization of laboratory results in the prediction of field performance. Figs. 2 and 3 show the laboratory and pilot-plant test units.

LABORATORY TEST TECHNIQUES

Comparative testing of various collector configurations and correlation with actual field tests required the development of test techniques which yielded reliable and reproducible results in the laboratory, and which also yielded a method of predicting the performance of a field unit based upon the operating conditions at the particular field site.

Of primary importance was the preparation and dispersion of the test aerosols and the particle size of these aerosols. Redispersed fly ash was used as the test aerosol. Characteristics of the test dusts are shown in Table 1. The test dusts were divided into batches of about 300 lb, quartered according to standard methods (3), and then bagged into 13 and 26-lb lots depending upon the size unit under test. A representative sample from each batch was quartered and analyzed for particle size in order to maintain continuous control of dust size. Prior to each test, the dust was rough-screened to remove large agglomerates or

TABLE 1 CHARACTERISTICS OF FLY-ASH TEST DUSTS
(Cumulative percentages by weight as determined by sieve plus sedimentation methods)

Batch no.	Particle diameter in microns							Specific gravity
	+297	-297	-149	-74	-44	-20	-10	
A.....	0.4	99.6	98.5	94.7	87.0	69.6	49.8	2.48
B.....	0.3	99.7	98.5	94.7	85.2	69.9	51.7	2.71
C.....	0.4	99.6	97.9	92.8	82.8	67.4	48.9	2.63
D.....	0.5	99.5	97.6	91.5	81.2	65.7	47.1	2.57
E.....	0.3	99.7	98.6	95.0	86.3	69.5	50.7	2.52

foreign matter and preheated at least 1 hr at 350 F to eliminate moisture, minimize further agglomeration, and improve the uniformity of the feed. The dust feed was accomplished by introducing the ash from a mechanically agitated hopper into the impeller of a small ventilating blower of approximately 140 cfm capacity. Silverman and Billings described this dispersion method in a recent paper (4). The outlet of the blower was directed into a collector-inlet flue of sufficient length to insure dispersion of the dust. Feed rate was maintained within an accuracy of ± 20 per cent by adjustment of a machined peripheral slot and was adjusted to yield a uniform inlet concentration of 3 grains per cu ft at 80 F.

Upon completion of the feed, the inlet flue, inlet and outlet headers, inlet tube, and hopper were manually rapped and cleaned, and the dust accumulations at each point measured. Collection efficiency was calculated from the ratio of the hopper collection to the total dust feed minus inlet-flue accumulation.

The method of size analysis utilized was sedimentation in methyl alcohol by a modification of the Cummings' method (5) after prior screen analysis of the +44-micron fraction. Later observations made on methods of analysis indicate that sedimentation of the total sample may have advantages over sieve plus sedimentation methods, particularly where the samples contain a substantial portion of large, low-density, fragile material. In sedimentation of the total sample, the effective particle-size distribution obtained seems more accurate for prediction of mechanical collector performance than methods based upon actual physical size, since the mechanisms of particle collection and size analysis both depend on the terminal settling velocities of the particles. This method also eliminates errors due to attrition of fragile materials in the sieving process. Thus, when obtaining laboratory performance prediction information using test dusts which are known to be fragile and of low density, size-analysis methods based on terminal settling velocity should be preferred over those based on measurement of actual physical size.

The test dusts used were all relatively fine fly ash having a large percentage of spherical particles. The error introduced by utilization of sieves on the +44-micron sizes was therefore minimized.

Flow measurements were made with orifice plates calibrated with standard pitot transverse utilizing methods outlined in The American Society of Mechanical Engineers Power Test Codes (6). Collector pressure drops were measured with side-wall taps located up and downstream of the collector in flue sections of equal cross section.

These test methods gave reproducible results over long periods of time and allowed direct comparisons to be made between various collector designs, without the necessity for any assumptions on particle-size distribution and specific gravity. The homogeneity of the fly ash from the principal source of test dust, as indicated in Table 1, also simplified comparison and correlation of results.

CRITICAL NATURE OF COLLECTOR INLET-BLADE PROFILE

Directly comparative tests were run in the laboratory on the

collector shown in Fig. 1(a) with test dust A and an eight-blade inlet vane utilizing two inlet-blade profiles. These collectors were identical in every detail except for the profile of the blade and the depth of the ring required to mount the two blade types. Fig. 4 shows the blade profiles. Fig. 5 demonstrates the marked improvement in collector performance due to the change in blade design. It is significant that a major improvement in performance results from a seemingly minor change in vane shape, indicating the basic importance of this factor in mechanical collector performance.

In addition to the actual comparative performance tests, studies on internal flow patterns in the two designs were made utilizing an Airfoil Pitometer (7). Initial measurements at the stations designated 1, 2, 3, and 4, as shown in Fig. 1(a) indicated distinctly asymmetrical flow at all stations when the inlet to the tube was enclosed in the test header shown photographically in Fig. 2. The blocking effect of the gas-outlet tube in single-tube collectors with side inlets is the predominant factor in this asymmetrical flow for removing the header and drawing the gas in axially resulted in a symmetrical pattern at all stations. The simplification of velocity measurements where the flow is symmetrical plus the consideration that, in actual multiple-tube installations the gas entry to each tube from a common large inlet header would be

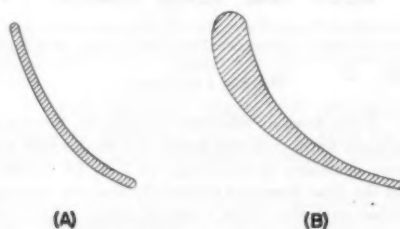


FIG. 4 INLET-VANE BLADE PROFILES

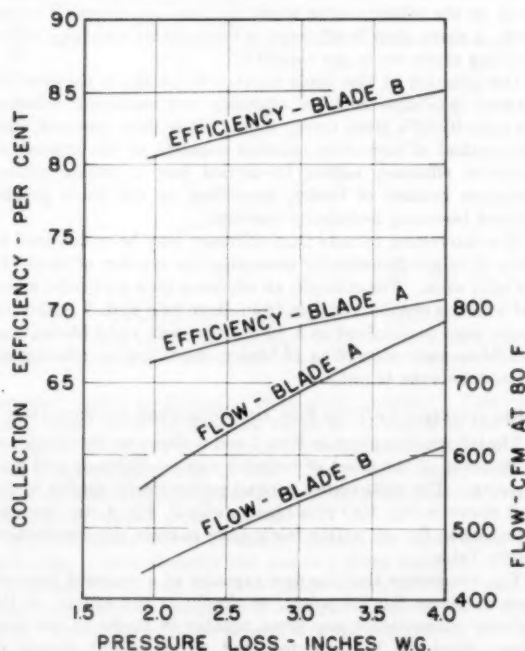


FIG. 5 EFFECT OF INLET-VANE BLADE SHAPE ON COLLECTOR PERFORMANCE CHARACTERISTICS; TEST DUST A

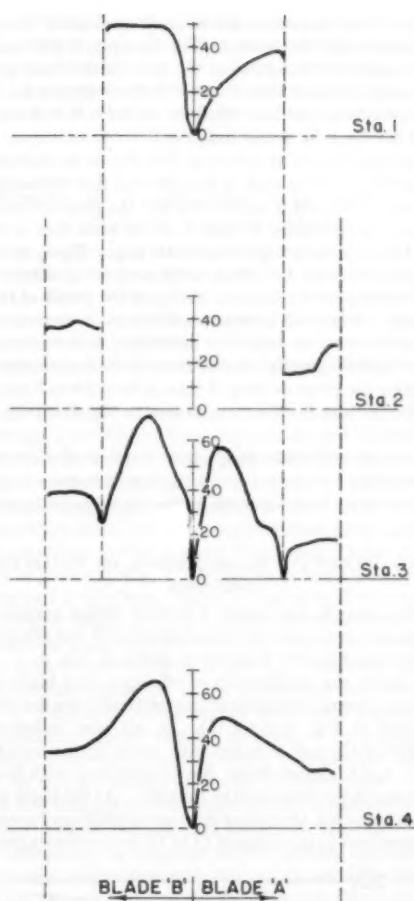


FIG. 6 EFFECT OF INLET-VANE BLADE SHAPE ON INTERNAL TANGENTIAL VELOCITY PATTERNS
(Velocities expressed in feet per second.)

essentially axial, resulted in the decision to adopt this mode of operation for the internal flow measurements.

The internal tangential velocity patterns obtained at a constant average inlet velocity of 27.2 fps, which corresponds to a total flow of 500 cfm at 80 F, on the two blade profiles studied are shown on Fig. 6. The local tangential velocities are expressed in feet per second at actual test temperature and represent the average of traverses on several radii. The accuracy of the absolute magnitude of the velocities in the region below the mouth of the outlet tube is open to some question since a calculation of the total downward flow, based on axial components of the same vector utilized in calculating the tangential components presented, exceeds the total upward flow at stations 3 and 4. This effect is probably due to the influence of strong radial components in this region on the accuracy of the Airfoil Pitometer. This condition does not exist in the collector-tube annulus or the outlet tube as the total flow, as calculated by integration of the internal axial velocities, agrees closely with the total system flow. Thus, the absolute magnitudes of tangential velocities in the annulus and the outlet tube may be utilized without excessive error; however, the flow patterns at stations 3 and 4 may be utilized only on a qualitative comparative basis.

In spite of this limitation, the over-all qualitative comparison of the two blade profiles is clear. For example, it will be noticed that the tangential velocities in the tube with blade profile B are substantially higher than those with blade profile A. It is to be expected, then, that the efficiency of tube B will be higher than that of tube A for a constant inlet flow.

In examining Fig. 5, at a flow of 570 cfm or an inlet velocity approximately equal to that of the internal flow measurements, the efficiency of tube B is 84 per cent and the pressure loss 3.4 in. water gage; the efficiency of tube A at the same flow is 66.5 per cent and the pressure loss is 2.0 in. water gage. Thus, an increase in collection efficiency from 66.5 to 84 per cent is obtained on a relatively fine material merely by changing the profile of the inlet-vane blades. While this increase in efficiency is accompanied by an increase in pressure drop, it is important to note that the increase in efficiency greatly exceeds that which is obtained merely by increasing the pressure drop of tube A from 2.0 to 3.4 in. water gage. This increase in efficiency, as seen in Fig. 5, is from 66.5 to 69.5 per cent.

Future studies of blade design may result in the desired tangential velocity increases without a significant increase in pressure loss. The current work has been limited to a relatively few blade profiles.

EFFECT OF INLET-VANE BLADE NUMBER ON COLLECTOR PERFORMANCE

An initial step in the study of further design criteria for an optimum inlet vane was the determination of the effect on performance of the number of blades of profile B, Fig. 4.

Fig. 7 shows the relationship of efficiency and blade number obtained on several collectors of geometrically similar design to those shown in Fig. 1(a) or (b). In all size collectors, and irrespective of the use of outlet-tube vanes in the outlet tubes, there is a rapid, almost linear rise in efficiency with increasing blade number in the range of 0 to 7 blades. As the blade numbers are further increased, the rate of increase in efficiency becomes less. At blade numbers in the range of 14 to 18 the increase is practically

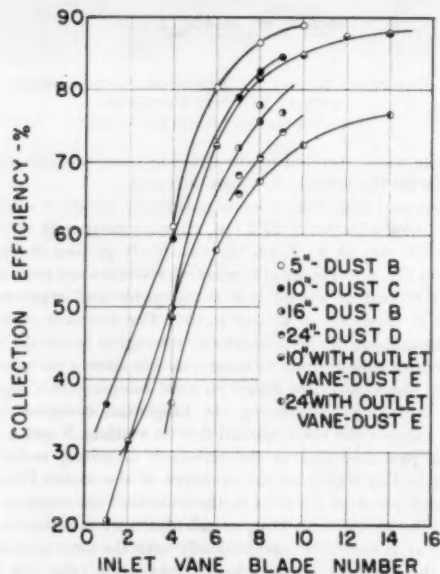


FIG. 7 EFFECT OF INLET-VANE BLADE NUMBER ON EFFICIENCY OF SEVERAL GEOMETRICALLY SIMILAR COLLECTORS AT A CONSTANT PRESSURE DROP OF 3.0-IN. WATER GAGE (Dust identification per Table 1.)

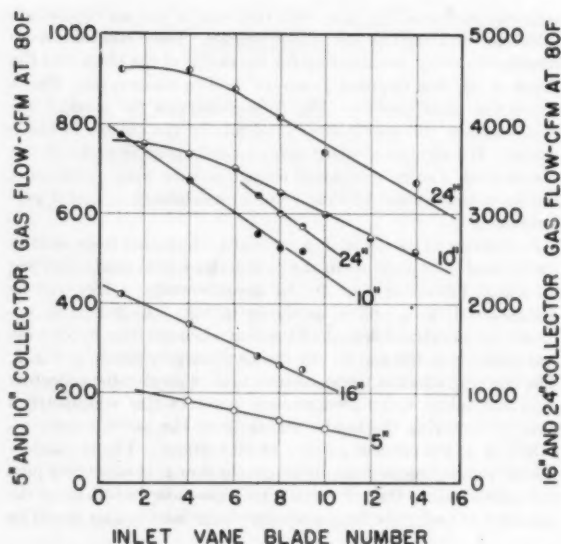


FIG. 8 EFFECT OF INLET-VANE BLADE NUMBER ON COLLECTOR GAS-FLOW CAPACITY AT A CONSTANT PRESSURE DROP OF 3.0-IN. WATER GAGE

(See Fig. 7 for legend.)

negligible. Thus, from an efficiency standpoint, there is a critical minimum blade number in the range of 7 blades and a region of performance flexibility in the range of 7 to 14 blades. Fig. 8 shows that the flow decreases essentially linearly with increasing blade number over the whole range studied. (An exception to this is the nonlinearity, in the range below 4 blades, of the units with outlet-tube vanes. This will be discussed in a later section.) Thus, as the primary vane blade numbers are decreased below seven, a sharp drop in efficiency is encountered without a corresponding sharp rise in gas capacity.

The selection of the blade number is usually a compromise between maximum collector efficiency and maximum collector gas capacity at a given energy input. It is clear, however, that this method of increasing collector capacity at the expense of collection efficiency cannot be carried past a certain critical minimum number of blades, depending on the blade profile, without becoming technically unsound.

It is interesting to note that efficiency may be maintained in tubes of larger diameter by increasing the number of blades in the inlet vane. For example, an efficiency on a particular material which is obtained with a 10-in.-diam tube with 7 inlet-vane blades may be obtained in a 16-in. tube with eight blades, and in a 24-in. tube with 10 to 14 blades, depending on whether an outlet-tube vane is utilized.

RELATIONSHIP OF TUBE SIZE AND COLLECTOR PERFORMANCE

The information given in Figs. 7 and 8 allows an interpretation to be made of the effect of collector size on efficiency and flow capacity. The units tested were all geometrically similar to the unit shown in Fig. 1(a) with blade profile B, Fig. 4, and were all tested using fly ash within fairly close particle size-distribution limits, Table 1.

Fig. 9 indicates that the flow capacity at a constant pressure drop varies as the 1.9 power, or closely as the square, of the collector diameter for any given number of blades in the inlet vane. First (2) has reported that no significant change in pressure drop exists in geometrically similar tangential-entry cyclones over a three-fold change in size if the cyclones are

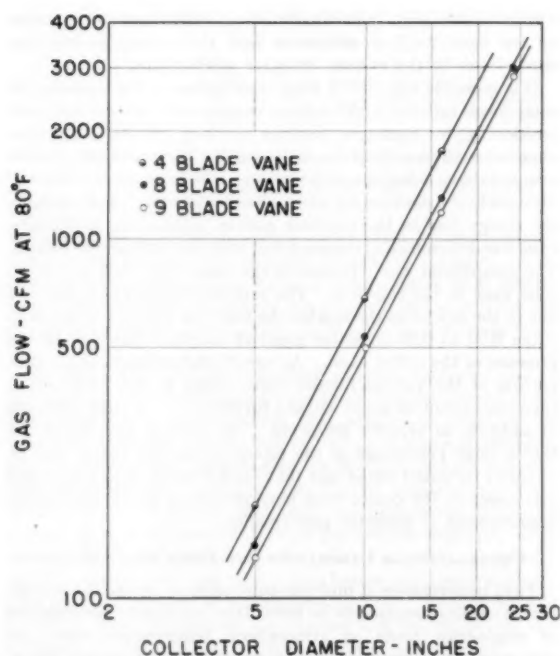


FIG. 9 EFFECT OF COLLECTOR SIZE ON GAS-FLOW CAPACITY OF GEOMETRICALLY SIMILAR COLLECTORS AT CONSTANT PRESSURE DROP

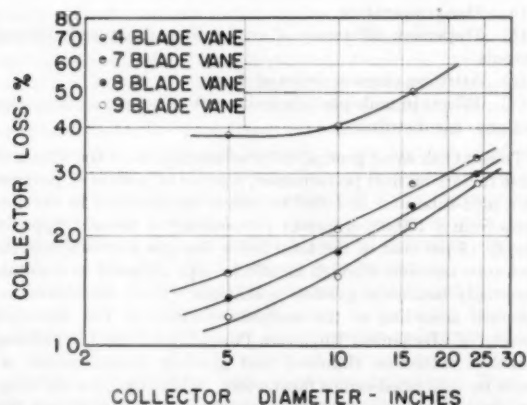


FIG. 10 EFFECT OF COLLECTOR SIZE ON COLLECTOR DUST LOSS OF GEOMETRICALLY SIMILAR COLLECTORS AT CONSTANT PRESSURE DROP

operated under conditions of equal entry velocity. This condition exists when the flow rate varies as the square of the tube diameter. Shepherd and Lapple (8) report the same condition over a seven-fold change in size. The present results confirm the square-law variation of gas flow with collector diameter within the accuracy of the measurements.

Fig. 10 shows the relationship, plotted on logarithmic coordinates, of tube diameter and loss on a given material. These curves are based upon the information shown in Fig. 7, and in some cases involve interpolation or slight extrapolation of these data. From Fig. 10 it can be seen that the relationship between loss and diameter in the range studied can be approximated as a power of the tube diameter, particularly in the larger sizes. The value of the exponent is dependent on blade number, ranging from

0.24 to 0.61 from four-blade to nine-blade vanes in a particular collector design on a particular material. Further, it seems plausible that the value of the exponent also will be dependent upon the dust-size distribution. Anderson (9) has indicated that the relationship between collector diameter and collector loss in tangential-entry cyclones is linear when using relatively coarse cement dust.

EFFECTIVENESS OF OUTLET-TUBE VANES FOR INCREASING COLLECTOR GAS-FLOW CAPACITY

The high proportion of the total energy loss in the cyclone which can be attributed to loss in the gas-outlet tube has been demonstrated by Barth (10). The possibilities of reduced energy consumption, or increased flow capacity for a given energy input without appreciable reduction in efficiency by utilizing outlet-tube vanes, have been demonstrated also by Schiele (11) and Ter Linden (1).

Several outlet-tube vane designs were evaluated experimentally and a design, consisting of three helically-shaped blades critically positioned at the mouth of the gas-outlet tube and joined together at its axis, was selected for quantitative evaluation.

Gas-flow and efficiency measurements were made on both the 10-in. and 24-in.-diam. tubes with and without outlet-tube vanes. Results are shown in Figs. 7 and 8 for a range of inlet-vane blade numbers of profile B, Fig. 4. Increases in flow up to 40 per cent were obtained in the 10-in. tube with negligible effect on efficiency in the practical design range above seven inlet-vane blades. The increasing effectiveness of the outlet-tube vane with increasing inlet-vane blade number may be explained on the basis that one of the fundamental principles of the outlet-tube vanes is the conversion of rotational kinetic energy into static pressure. The higher rotational kinetic energies resulting in the configurations with higher inlet-vane blade numbers increase the theoretical amount of kinetic energy available for conversion. Thus, it might be said that outlet-tube-vanes become increasingly effective in collector designs yielding high tangential velocity.

It is interesting to consider the theoretical possibilities of kinetic-energy conversion with the actual effectiveness of the outlet-tube vane studied. Both the literature cited and the fact of a critical outlet-tube-vane position suggest that other effects exist aside from the recovery of rotational kinetic energy in the form of static pressure. An attempt was made to determine how much of the static-pressure gain can be accounted for by the

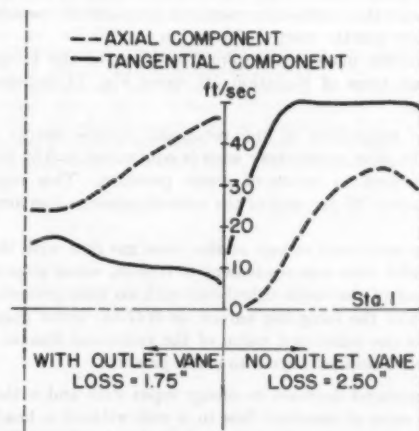


FIG. 11 EFFECT OF OUTLET VANES ON TANGENTIAL AND AXIAL-VELOCITY PROFILES IN OUTLET TUBE AT CONSTANT FLOW (Velocities expressed in feet per second.)

removal of the rotational kinetic energy and how much is due to any additional effects. The method employed was to compare the measured change in collector pressure loss at a constant gas flow due to the outlet-tube vane with the corresponding change in the total kinetic energy of the gas. Detailed velocity traverses were obtained at a constant total-gas flow through the collector with the airfoil pitometer in the outlet tube with and without the outlet-tube vane. Again, the measurements were obtained without a header arrangement in order to obtain symmetry of flow and simplify the measurements. The gas entered the inlet tube axially and was discharged through the outlet tube into a straight flue section where the total collector static-pressure loss was measured with side-wall taps. The tangential and axial-velocity components based on internal-velocity traverses made in the outlet tube with and without the outlet-tube vane system are shown in Fig. 11. Since the velocity profiles were quite similar on any radius in a single plane of the outlet tube, the analysis was based on the velocity profile along a typical radius.

The total kinetic energy of the gas in the outlet tube in each case (with and without the outlet-tube vane at constant total flow) is the sum of the energy in the axial and tangential direction since essentially no radial component was detected by measurement. Thus, the total kinetic energy per unit volume, passing a plane in the outlet tube, is given by

$$KE = \frac{1}{2}\rho \left[\frac{\int_0^r v_a^3 x dx}{\int_0^r v_a x dx} + \frac{\int_0^r v_t^3 x dx}{\int_0^r v_t x dx} \right] \dots \dots [1]$$

where

KE = average kinetic energy per unit volume of gas passing plane in exit tube

ρ = density of gas

x = distance from outlet-tube axis

v_a = axial-velocity component = $f(x)$

v_t = tangential-velocity component = $g(x)$

r = radius of outlet tube

Although the axial-velocity profile is radically altered by the recovery vane as shown in Fig. 11, calculations based upon a graphical evaluation of the integrals in Equation [1] utilizing the velocity profiles shown in Fig. 11 indicate that there is a negligible change in the magnitude of the kinetic energy of the axial flow as a result of the redistribution of the axial-velocity profile. Thus the comparison of the total kinetic energy of the gas with and without the outlet-tube vane can be made by consideration of only the kinetic energy of rotation.

Calculations made by graphical solution of the integrals in the second term of Equation [1] using Fig. 11 indicated the following:

1 The magnitude of the rotational kinetic energy in the outlet tube with no recovery vane is equivalent to 0.52 in. water gage expressed in terms of static pressure. This represents approximately 20 per cent of the over-all pressure loss across the collector.

2 The rotational energy at the same gas flow with the vane in the outlet tube was equivalent to 0.05-in. water gage or only 10 per cent of the value calculated with no vane present. The difference of the foregoing values, or 0.47-in. water gage, thus represents the calculated value of the rotational kinetic energy in the outlet tube converted to static pressure.

The measured decrease in energy input with and without the recovery vane at constant flow in a unit without a header was 0.75-in. water gage or 30 per cent of the total collector drop with no vane present. The fact that the measured decrease was greater than the calculated value of rotational kinetic energy of

0.47-in. water gage, particularly since losses must be incurred by the vane itself, is indicative that the outlet-tube vane reduces losses in the system by other mechanisms.

It is probable that one of these mechanisms is the reduction of entry losses into the outlet tube as evidenced by the critical axial positioning, for optimum pressure recovery, of the outlet-tube vane below the mouth of the outlet tube. There was also experimental evidence that the outlet-tube vane reduces the exit losses of the outlet tube discharging into the header plenum. For example, the energy loss in the collector system without an outlet-tube vane was determined at constant flow with and without the header. The comparison was repeated at the same flow with an outlet-tube vane in the collector. The results indicated that the loss due to the header in the single-tube unit was reduced 50 per cent (from 0.50 to 0.25-in. water gage) at constant flow due to the presence of the outlet vane. An exact interpretation of the proportion of the various factors contributing to the total outlet-tube loss cannot be made without further study of static pressure in addition to velocity gradients. The current indications are that a large percentage of the rotational kinetic energy can be removed by outlet vanes and that further study of entrance and exit losses in the outlet tube may provide a means for further improvement of collector performance.

CORRELATION OF LABORATORY AND FIELD PERFORMANCE

Field performance of multiple-tube units at elevated temperature is usually assumed to be lower than laboratory performance of single-tube units at atmospheric temperature when the collectors are compared on the basis of equal energy input. This discrepancy may be attributed to the influence of several factors:

- (a) Gas temperature.
- (b) Dispersion differences of artificially and naturally formed aerosols.
- (c) Attrition characteristics of dust.
- (d) Effects in multiple-tube units such as hopper recirculation and poor gas distribution.

To establish some general order of magnitude of the effects of these factors on field performance, a series of tests is in progress on a nine-tube unit installed to collect the material in the flue gases from a 100,000-lb-per-hr pulverized-fuel boiler. Approximately 15 per cent of the total boiler flue gas is drawn into the nine-tube test unit through an offtake pipe designed to maintain essentially isokinetic gas-flow conditions. Field efficiencies are obtained according to the methods outlined in The American Society of Mechanical Engineers Power Test Code (6) utilizing alundum extraction thimbles, and gas-flow measurements are made by calibrated-orifice flowmeters. Collector pressure drops are obtained using wall taps in flues of equal cross-sectional area entering and leaving the test collector. Inlet-thimble samples are analyzed for specific gravity and particle-size distribution by the previously described sedimentation method for particle-size analysis.

Some representative results obtained to date on two nine-tube designs compared with single-tube results from laboratory tests are shown in Table 2. Field efficiencies for these cases are seen to be 2 and 6.5 points lower than predicted on the basis of single-tube laboratory tests. Anderson (12) has shown the effects of gas temperature on efficiency at constant collector pressure drop to be negligible in the range of 80 to 500 F. Thus, these differences must be attributed to the dispersion and attrition characteristics of the dusts and to adverse effects associated with multiple-tube arrangements, such as recirculating hopper flow or poor gas distribution to the individual collector tubes. The latter factor in turn may be related to the influence of the header

TABLE 2 A COMPARISON OF LABORATORY EXPECTED AND ACTUAL MULTIPLE-TUBE FIELD RESULTS

Collector design	Pressure drop, in. wg	Per cent material under 10 microns diam	Specific gravity	Operating temp., deg F		—Expected—		—Actual—	
				Laboratory	Field	Efficiency, per cent	Flow/tube,* cfm @ 80 F	Efficiency, per cent	Flow/tube,* cfm @ 80 F
A	3.0	34	2.19	80	370	86.5	495	84.5	550
B	3.0	38	2.21	80	370	86.5	670	80.0	700

* Corrected to 80 F by $V = k \sqrt{(Th)}$.

design and stacking arrangements of the tubes. Unfortunately, field results on single-tube efficiency are not yet available. Such data when completed will be valuable in identifying what proportion of the efficiency discrepancy can be attributed to multiplicity effects and what proportion, if any, to individual dust characteristics.

Gas flow in the multiple-tube units in these tests are 5 and 11 per cent higher per tube than for the single-tube laboratory units. Preliminary flow measurements with single-tube units in the field indicate that the higher flow per tube is due to a multiplicity effect, as the gas flow for a single-tube field unit compares closely with the single-tube laboratory results after temperature corrections are made. This is in agreement with Anderson's (12) results on the effect of gas temperature on gas-volume capacity. It is probable that the multiplicity effect, in turn, is due to a greater relative pressure loss per tube in the header portion of a single-tube unit as compared to a multiple-tube unit. Further work is required, however, before conclusions can be made on the influence of header design on multiple-tube performance.

CONCLUSION

The critical nature of the inlet-vane design and the improvements evident from the initial studies indicate possibilities for increase of cyclone collector efficiencies by means other than the customary reduction of the collector-tube diameter. As theoretical considerations indicate, the effects of higher tangential velocities predominate in increasing the separating forces on suspended dusts, for these forces vary directly as the square of the tangential velocity and inversely as the first power of the radius of rotation. Thus, if tangential velocities can be increased in tubes of larger diameter, the possibilities of equal or improved performance are promising. The current work on inlet-vane design indicates that increased tangential velocities can be obtained at relatively small increases in energy input.

The recovery of rotational kinetic energy in the outlet tube and the reduction of entry and exit losses in the outlet tube, by utilization of outlet-tube vanes, provides a means for overcoming the effect on over-all performance of the increased energy requirements of obtaining high tangential velocities. Thus a new approach involving increased energy input in the collector inlet vane to obtain high tangential velocities for high separating forces, plus the utilization of energy-recovery and loss-reduction

devices in the outlet tube after dust separation is complete, offers promise of improvement of performance, and flexibility, of cyclonic mechanical collectors.

ACKNOWLEDGMENTS

Acknowledgment is made to the following who contributed to the work: Dr. H. J. White, Research-Cottrell, Inc.; Dr. L. Silverman of Harvard University, School of Public Health; P. X. Gallagher, Princeton University; J. A. Armstrong, W. A. Baxter, and J. H. Brummer of the New Products Section Staff, Research-Cottrell, Inc.; M. Gallo, Secretary; and Johns-Manville Corporation, Manville, N. J., for co-operation in conduction of field tests.

BIBLIOGRAPHY

- 1 "Investigations Into Cyclone Dust Collectors," by A. J. Ter Linden, Proceedings of The Institution of Mechanical Engineers, vol. 160, 1949, p. 128.
- 2 "Cyclone Dust Collector Design," by M. W. First, ASME Paper No. 49-A-127, unpublished.
- 3 "Scott's Standard Methods of Chemical Analysis," edited by N. H. Furman, D. Van Nostrand Company, Inc., New York, N. Y., fifth edition, vol. 2, 1939, pp. 1308-1310.
- 4 "Methods of Generating Solid Aerosols," by Leslie Silverman and C. E. Billings, *Journal of the Air Pollution Control Association* vol. 6, August, 1956, pp. 80-81.
- 5 "Micromeritics," by J. M. Dallavalle, Pitman Publishing Corporation, New York, N. Y., second edition, 1948, pp. 85-86.
- 6 "Test Code for Dust-Separating Apparatus," PTC 21-1941, THE AMERICAN SOCIETY OF MECHANICAL ENGINEERS, New York, N. Y., December, 1941.
- 7 "Airfoil Pitometer for Simultaneous Measurement of Static Pressure, Velocity, and Flow Direction," by M. W. First and Leslie Silverman, *Industrial and Engineering Chemistry*, vol. 42, February, 1950, pp. 301-308.
- 8 "Flow Pattern and Pressure Drop in Cyclone Dust Collectors," by C. B. Shepherd and C. E. Lapple, *Industrial and Engineering Chemistry*, vol. 31, August, 1939, p. 972.
- 9 "Effect of Tube Diameter in Cyclonic Dust Collectors," by E. Anderson, *Chemical and Metallurgical Engineering*, vol. 40, October, 1933, pp. 525-526.
- 10 "Druckverluste und Abscheideleistungen von Zyklonabscheidern," by W. Barth, *VDI-Tagungsheft* 3, 1954.
- 11 "Möglichkeiten zur Wiedergewinnung der Drallenergie von Zyklonabscheidern," by O. Schiele, *VDI-Tagungsheft* 3, 1954.
- 12 "Effect of Gas Temperature on Multiclone Gas Volume and Capacity and Collection Efficiency," by Evald Anderson, Western Precipitation Corporation Report, July 9, 1941 (not published).

Estimation of Temperature Patterns in Multiply-Shielded Systems

By J. G. BARTAS¹ AND E. MAYER²

The method of difference equations is applied to the problem of estimating temperature patterns in multiply-shielded systems. Results are obtained in terms of elementary functions which can be evaluated readily. The equations are employed to examine the effect of shield curvature, end radiation, and gas radiation on the temperature recorded by a shielded thermocouple for a variety of operating conditions. Calculations indicate that whereas shield curvature and gas radiation may be neglected in a well-designed shielded thermocouple, end radiation can result in a substantial error in the thermocouple-temperature measurement.

NOMENCLATURE

The following nomenclature is used in the paper:

- A, B, C, D = constants
 E = end radiation factor
 F = intrashield radiation factor
 G = gas-shield radiation factor
 h = heat-transfer coefficient, (Btu/hr-sq ft-deg R)
 k = integer (1, 2, . . . n)
 n = number of probe elements
 T = temperature, deg R
 $\Delta T = T_o - T_i$, deg R
 ϵ = emissivity
 σ = Boltzmann constant, (Btu/hr-sq ft-deg R⁴)
- Subscripts**
 c = convection
 g = gas
 i = innermost
 o = outermost
 r = radiation
 w = wall

1, 2, . . . k , . . . n = index refers to shield element

Other symbols are defined as they are introduced in the text.

INTRODUCTION

A schematic diagram of a multiply-shielded system is shown in Fig. 1. The shield system is assumed to be located in a flowing gas stream of temperature T_g , which is, in turn, contained in a duct with a wall temperature T_w .

The temperature of the central body T_i , in the absence of any shielding, may be computed by solving a heat-balance equation which considers radiant-heat exchange with the duct wall, convection and radiation to and/or from the gas stream, and any

heat generated or absorbed by the shield. Conduction is neglected since this effect usually can be made negligible by suitable insulation of the supports. An additional heat-balance equation is written for each added shield. The system of equations describing the shield array shown in Fig. 1 contains n unknown temperatures among the n algebraic relations. This system of equations may be solved in a number of ways.

The use of difference equations in the analysis of multiply-shielded systems appears to have been neglected in the engineering literature. This mathematical procedure, however, yields equations in terms of elementary functions which are readily evaluated. Hence, this paper is primarily intended to present an engineering method for estimating rapidly the temperatures in configurations with thermal-radiation shields.

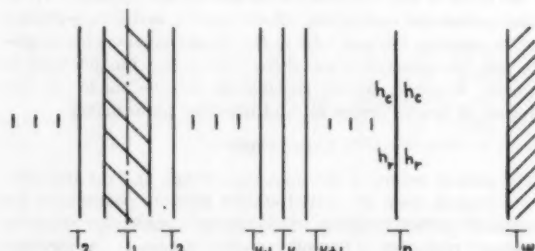


FIG. 1 SCHEMATIC DIAGRAM OF A SIMPLE SHIELD SYSTEM

ASSUMPTIONS

The following assumptions are made:

- 1 The convection coefficient h_c is constant within the shield system.
- 2 The linearized radiation coefficient h_r is constant within the shield system.
- 3 The stream temperature T_g is uniform.
- 4 The wall temperature T_w of the duct enclosing the shield system is uniform.
- 5 The temperature of each shield T_k is uniform.
- 6 Conduction losses are negligible.

The linearized radiation coefficient h_r is generally computed as

$$h_r = 4\sigma\epsilon\bar{T}^3$$

where \bar{T} is an "average" temperature in the shield system. The calculation of the convective heat-transfer coefficient h_c and the "effective" gas stream temperature T_g has been amply discussed in many references (1, 5)³ and is not included here.

A SIMPLE SHIELD SYSTEM

The following analysis of a simple shield system illustrates the general analytical procedure and, furthermore, leads to results closely approximating those of more complex systems described in the next section.

Consider a shield system consisting of a set of plane parallel shields arranged about a central body as shown in Fig. 1. As-

³ Numbers in parentheses refer to Bibliography at end of paper.

¹ Senior Heat Transfer Engineer, Aircraft Accessory Turbine Department, General Electric Company, West Lynn, Mass. Assoc. Mem. ASME.

² Senior Physicist, ARDE Associates, Newark, N. J. Contributed by the Heat Transfer Division and presented at a joint session with the Fuels Division and the Research Committees on Furnace Performance Factors and Heat Conduction Charts at the Annual Meeting, New York, N. Y., November 25-30, 1956, of THE AMERICAN SOCIETY OF MECHANICAL ENGINEERS.

NOTE: Statements and opinions advanced in papers are to be understood as individual expressions of their authors and not those of the Society. Manuscript received at ASME Headquarters, July 31, 1956. Paper No. 56-A-130.

sume that the external radiation and convection heat-transfer coefficients are equal to the internal radiation and convection heat-transfer coefficients, respectively. Also, assume that end radiation to and from the shield assembly is negligible, and there is no interchange of radiation between the shield system and the gas stream.

With reference to Fig. 1 the foregoing assumptions lead to the following heat-balance equation, per unit shield surface area, for the shield element with index k

$$2h_c(T_g - T_k) + h_r(T_{k-1} - T_k) + h_r(T_{k+1} - T_k) = 0 \quad 1 < k < n \dots [1]$$

It is convenient to employ the temperature-difference identity

$$\Delta T \equiv T_g - T$$

in terms of which the heat-balance equation becomes

$$\Delta T_{k+1} - 2A\Delta T_k + \Delta T_{k-1} = 0 \quad 1 < k < n \dots [2]$$

where

$$A = \frac{h_c + h_r}{h_r}$$

Equation [2] is a homogeneous linear difference equation of the second order with constant coefficients. The solutions of difference equations of this type, where A is a real constant, are well known. For the case where $A > 1$ the general solution is of the form⁴

$$\Delta T_k = C_1 e^{\alpha k} + C_2 e^{-\alpha k} \dots [3]$$

where α is defined by $\cosh \alpha = A$, and C_1 and C_2 are constants which are determined by the boundary conditions.

The boundary conditions are given by the heat-balance equations written for the central body ($k = 1$) and the outermost shield ($k = n$). These equations are

$$h_c(T_g - T_1) + h_r(T_{n+1} - T_1) = 0 \quad k = 1 \dots [4]$$

$$2h_c(T_g - T_n) + h_r(T_{n-1} - T_n) + h_r(T_{n+1} - T_n) = 0 \quad k = n \dots [5]$$

In terms of the temperature difference ΔT the boundary conditions become

$$A\Delta T_1 - \Delta T_2 = 0 \dots [6]$$

$$2A\Delta T_n - \Delta T_{n-1} = \Delta T_{n+1} \dots [7]$$

The constants C_1 and C_2 are determined by substitution of Equation [3] into the boundary conditions, Equations [6] and [7], which yield

$$C_1 = \frac{e^{-\alpha}}{e^{\alpha n} + e^{-\alpha n}} \Delta T_w \dots [8]$$

$$C_2 = \frac{e^{\alpha}}{e^{\alpha n} + e^{-\alpha n}} \Delta T_w \dots [9]$$

Inserting these results into Equation [3] and simplifying, we arrive at a simple expression for the temperature of any element in the simple shield system

$$\frac{\Delta T_k}{\Delta T_w} = \frac{\cosh(k-1)\alpha}{\cosh n\alpha} \quad k = 1, 2, \dots n \dots [10]$$

The temperature difference at the central body ($T_g - T_1$) may be computed readily from the relation obtained by setting $k = 1$ in Equation [10]

⁴ Reference (2), p. 241.

$$\frac{T_g - T_1}{T_g - T_w} = \frac{1}{\cosh n\alpha} \dots [11]$$

Equation [11] is convenient for estimating the number of radiation shields necessary to suppress lateral radiant-heat transfer in a multiply-shielded system to a desired level. Equation [11] is plotted in Fig. 2, where curves of $(\Delta T_1)/(\Delta T_w)$ versus n for h_c/h_r values of $1/2$, 1, and 2 are shown. Note that Equation [11] is valid for gas temperatures either greater or less than the wall temperature.

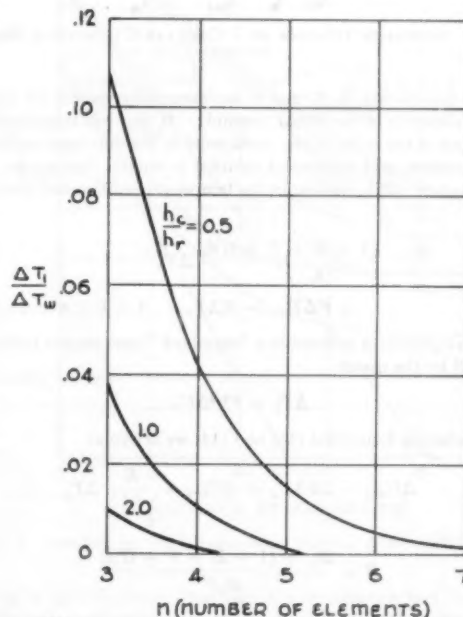


FIG. 2 $(\Delta T_1)/(\Delta T_w)$ VERSUS n FOR h_c/h_r RATIOS OF 0.5, 1.0, AND 2.0

THE GENERAL SOLUTION

The method of determining the temperature pattern in a shield system subject to more general boundary conditions is analogous to the method outlined in the foregoing. A schematic diagram of a circular cylindrical multiply-shielded system is shown in Fig. 3. The heat-balance equation for the k th element, including end radiation effects, is

$$(2h_c + Gh_r)(T_g - T_k) + Fh_r(T_{k-1} - T_k) + h_r(T_{k+1} - T_k) + Eh_r(T_w - T_k) = 0 \quad 1 < k < n \dots [12]$$

The parameter G is a measure of the amount of net radiation between the gas and the k th shield in relation to the lateral radiation between the shields. It includes end radiation to and from the gas, as well as any radiant heat exchange with the gas flowing between the shields.

The radiant-interchange configuration factor F is the fraction of radiant energy leaving the surface of the k th element, which is intercepted by the surface of the $(k-1)$ th element. For circular cylindrical shields

$$F = \frac{R_{k-1}}{R_k}$$

where R is the shield radius (4).

The factor E is a measure of the amount of end radiation between the wall and the k th element. Values for E also may be computed with the aid of reference (4).

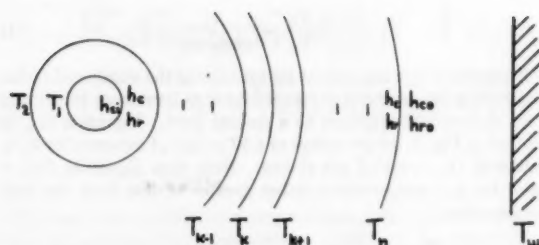


FIG. 3 SCHEMATIC DIAGRAM OF A CIRCULAR CYLINDRICAL SHIELD SYSTEM

The parameters E , F , and G are assumed constant for all internal elements of the shield assembly. If they are considered as functions of the index k , the coefficients in the difference equation are variables, and no general solution is usually obtainable.

Equation [12] is written in the temperature-difference notation as

$$\Delta T_{k+1} - \frac{2h_c + (1 + E + F + G)h_r}{h_r} \Delta T_k + F \Delta T_{k-1} = E \Delta T_w \quad 1 < k < n \dots [13]$$

This equation is reduced to a "standard" form similar to Equation [2] by the use of

$$\Delta T_k = F^{k/2} \Delta U_k \dots [14]$$

Combining Equations [13] and [14] we arrive at

$$\Delta U_{k+1} - 2B \Delta U_k + \Delta U_{k-1} = \frac{E}{F^{k/2}} \Delta T_w \dots [15]$$

where $B = \frac{2h_c + (1 + E + F + G)h_r}{2h_r F^{1/2}}$

Equation [15] is a nonhomogeneous linear equation of the second order with constant coefficients.

The general solution of a nonhomogeneous equation of the form of Equation [15] may be expressed as the sum

$$\Delta U_k = \Delta U_k^{(H)} + \Delta U_k^{(P)} \dots [16]$$

where $\Delta U_k^{(H)}$ is the general solution of the homogeneous equation

$$\Delta U_{k+1} - 2B \Delta U_k + \Delta U_{k-1} = 0$$

and $\Delta U_k^{(P)}$ is any particular solution of Equation [15].

The general solution of the homogeneous equation is (cf. Equations [2] and [3]).

$$\Delta U_k^{(H)} = D_1 e^{\beta k} + D_2 e^{-\beta k} \dots [17]$$

where $B = \cosh \beta$

The particular solution can be derived by the method of undetermined coefficients. It may be verified that a particular solution is

$$\Delta U_k^{(P)} = \frac{-E \Delta T_w}{F^{k/2} (2BF^{1/2} - 1 - F)} \dots [18]$$

by substituting this expression in Equation [15].

The general equation for ΔT_k is therefore

$$\Delta T_k = F^{k/2} [D_1 e^{\beta k} + D_2 e^{-\beta k}] - \frac{E \Delta T_w}{2BF^{1/2} - 1 - F} \quad 1 < k < n \dots [19]$$

The two boundary conditions for the shield system shown in Fig. 3, including end radiation effects, are

$$(h_c + h_{ci} + G_r h_r)(T_g - T_k) + h_r(T_{k+1} - T_k) + E_r h_r(T_w - T_k) = 0 \quad k = 1 \dots [20]$$

$$(h_c + h_{co} + G_r h_r)(T_g - T_k) + F h_r(T_{k-1} - T_k) + h_{ro}(T_w - T_k) + E_r h_{ro}(T_w - T_k) = 0 \quad k = n \dots [21]$$

In the temperature-difference notation the boundary conditions are written as

$$J_1 F^{1/2} \Delta T_1 - \Delta T_2 = E_r \Delta T_w \dots [22]$$

$$J_n F^{1/2} \Delta T_n - F \Delta T_{n-1} = (1 + E_r) \frac{h_{ro}}{h_r} \Delta T_w \dots [23]$$

where

$$J_1 = \frac{h_c + h_{ci} + (1 + E_r + G_r)h_r}{F^{1/2} h_r}$$

$$J_n = \frac{h_c + h_{co} + (F + G_r)h_r + (1 + E_r)h_{ro}}{F^{1/2} h_r}$$

The constants D_1 and D_2 in Equation [19] are evaluated with the aid of the boundary condition Equations [22] and [23]. After some algebraic manipulation the final equation for $(\Delta T_k)/(\Delta T_w)$ is

$$\frac{\Delta T_k}{\Delta T_w} = F^{k/2} \left\{ \frac{\phi_1 \psi_1 + \phi_2 \psi_2}{(J_1 J_n - 1) \sinh(n-1)\beta - (J_1 + J_n - 2B) \sinh(n-2)\beta} - \frac{E}{2BF^{1/2} - 1 - F} \right\} \dots [24]$$

where

$$\psi_1 = J_n \sinh(n-k)\beta - \sinh(n-k-1)\beta$$

$$\psi_2 = J_1 \sinh(k-1)\beta - \sinh(k-2)\beta$$

$$\phi_1 = \frac{E_r}{F} + \frac{(J_1 F^{1/2} - 1)E}{F(2BF^{1/2} - 1 - F)}$$

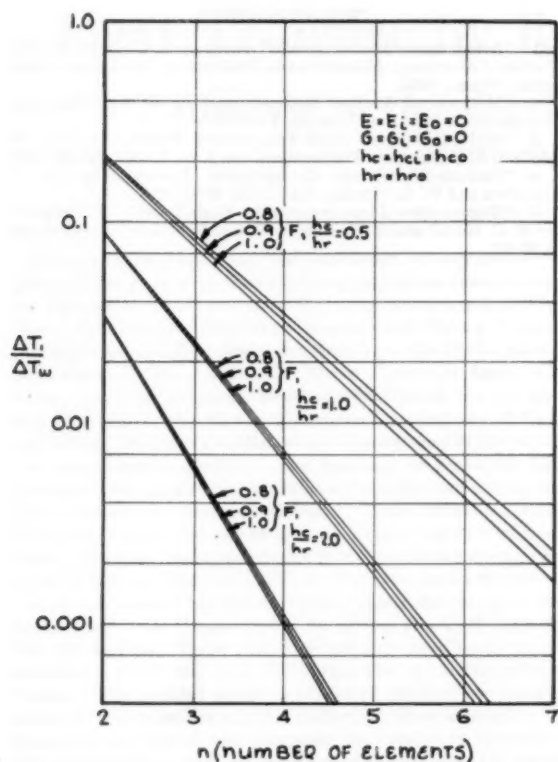
$$\phi_2 = \frac{(1 + E_r)h_{ro}}{F^{n/2} h_r} + \frac{(J_n F^{1/2} - F)E}{F^{n/2} (2BF^{1/2} - 1 - F)}$$

The refinements of Equation [24] are inconsistent with the crude initial assumptions. However, the equation may be used to determine the relative importance of several parameters which have been assumed to influence the temperature pattern of the shield system.

EFFECT OF SHIELD CURVATURE IN THERMOCOUPLE APPLICATIONS

The first of these parameters to be considered is shield curvature. The ratio $(\Delta T_1)/(\Delta T_w)$ is plotted as a function of the number of probe elements in Fig. 4 for several values of h_c/h_r with the configuration factor F taken as 1.0, 0.9, and 0.8. The innermost probe element ($k = 1$) has been selected for comparison since this element is of most interest in shielded-thermocouple applications where curvature effects may be important.

It is seen in Fig. 4 that the influence of sharply curved and/or widely spaced curved shields on the temperature of the innermost element of a shielded-thermocouple system is secondary in relation to the influence of the number of shields and to variations in convective and radiant heat transfer. Furthermore, the factor F is close to unity for typical shielded-thermocouple geometries (3). These assemblies therefore may be analyzed as parallel shield

FIG. 4 EFFECT OF SHIELD-CURVATURE FACTOR F ON $(\Delta T_1)/(\Delta T_w)$

assemblies, with only higher-order errors incurred due to neglecting the effect of shield curvature.

END RADIATION

A shielded thermocouple is also a convenient model to use in estimating the contribution of end radiation to variations in the temperature patterns of a shield system. The ratio $(\Delta T_1)/(\Delta T_w)$ is plotted against the number of thermocouple elements n in Fig. 5 for end radiation coefficient (E) values of 0.00, 0.01, and 0.02. The end-radiation factor E is of the order of 0.01 to 0.02 for typical shielded assemblies (3).

It can be seen in Fig. 5 that end radiation becomes the dominating influence as the number of shields increases. This is due to the fact that end radiation depends very little on the number of shields and becomes completely independent of the number of shields once lateral radiation is suppressed. For example, if $h_c/h_r = 2.0$ and $E = 0.02$, the ratio $(\Delta T_1)/(\Delta T_w)$ is dependent on the number of shields as given in Table 1.

TABLE 1

Number of shields ($n - 1$)	$\frac{\Delta T_1}{\Delta T_w}$
1	0.0390
2	0.0094
3	0.0043
4	0.0034
5	0.0033
∞	0.00327

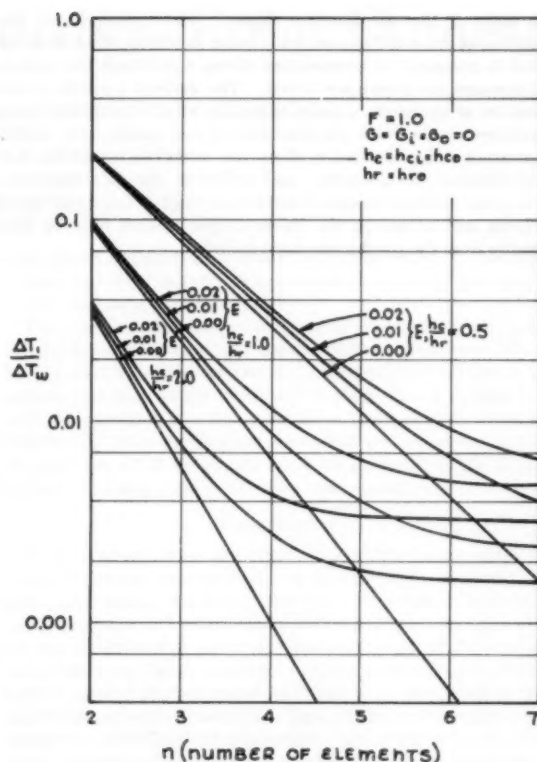
FIG. 5 EFFECT OF END-RADIATION FACTOR E ON $(\Delta T_1)/(\Delta T_w)$

Fig. 5 quantitatively illustrates the well-known fact that end radiation should not be ignored if a high degree of accuracy in thermocouple temperature measurements is required.

GAS RADIATION

It is not feasible to plot the effect of varying G for a thermocouple since the curves for various values of G tend to overlap. This effect is illustrated by Table 2.

TABLE 2

Number of shields ($n - 1$)	$\frac{(\Delta T_1)/(\Delta T_w)}{\text{Value of } G}$	
	0.00	0.01
1	0.0948	0.0941
2	0.0271	0.0269
3	0.0089	0.0089
4	0.00406	0.00406

CONDITIONS: $h_c = h_{ci} = h_{co} = h_r = h_{ro}$
 $E = E_i = E_o = 0.01$
 $F = 1.0$

As the number of shields increases the temperature of the probe approaches the gas temperature and no appreciable radiant energy is exchanged between the thermocouple and the gas stream.

CONCLUSIONS

The foregoing analysis presents an engineering method for estimating rapidly the temperatures in a system which contains

an array of thermal-radiation shields. The application of the calculus of finite differences leads to an equation which may be used to compute the temperature of *any* shield once the system parameters have been evaluated. The method applied to the problem of temperature measurement by shielded thermocouples produces results which are qualitatively well known; e.g., shield curvature and gas-radiation effects are secondary quantities in a well-shielded thermocouple; end radiation may be important. The quantitative influence of convection, radiation, the number of shields, and so on, on the thermocouple reading may be seen readily from the graphs which are included.

BIBLIOGRAPHY

- 1 "Aerodynamic Measurements," edited by R. C. Dean, Jr., Gas Turbine Laboratory, Massachusetts Institute of Technology, Cambridge, Mass., 1953.
- 2 "Methods of Applied Mathematics," by F. B. Hildebrand, Prentice-Hall, Inc., New York, N. Y., 1952.
- 3 "Multiply-Shielded High-Temperature Probes," by E. M. Moffatt, SAE Quarterly Transactions, vol. 6, no. 4, 1952, pp. 567-580.
- 4 "Radiant-Interchange Configuration Factors," by D. C. Hamilton and W. R. Morgan, NACA TN 2836, 1952.
- 5 "Temperature Measurements in High-Velocity Airstreams," by H. C. Hottel and A. Kalitinsky, Trans. ASME, vol. 67, 1945, pp. A-25-32.

Heat Transfer by Radiation From Flames

A Summary of the Work of the International Flame Research Foundation

By R. A. SHERMAN,¹ COLUMBUS, OHIO

A unique example of international co-operation is given in the program of research on radiation from flames in industrial furnaces that is being conducted at the Royal Netherlands Blast Furnace and Steel Works. Financial support and direction came first from the Netherlands, France, and Great Britain. These countries have now been joined by Belgium, Sweden, the United States, and the High Authority of the European Community of Coal and Steel. This paper outlines the organization of the work, the experimental facilities, the methods of research, and presents the outstanding results on the effect of the variables studied on flame radiation. These variables have been the type of fuel oils or coke-oven gas, the rate of heat input, the type and rate of supply of atomizing agent, the type of burner, the excess of air, the type and amount of carbureting agent for gas, and the temperature of the combustion air. Of these several variables, the C/H ratio of the oil and gas fuels and the mixing conditions most markedly affect the emissivity and the radiation of the flames. The results point to the need for further knowledge of the relation of the radiating characteristics of flames to the rate of heat transfer to "work" in furnaces. The research has now been extended to include the use of pulverized coal.

INTRODUCTION

IN recognition of the need for greater knowledge of the transfer of heat by radiation from flames in industrial furnaces, Prof. J. E. de Graaf, then director of research, The Royal Netherlands Blast Furnace and Steel Works, initiated, shortly after World War II, an experimental program of research to fill this need. A tunnel furnace fired with a flame one fourth the linear dimensions of an open-hearth flame was built at the IJmuiden, Holland, plant by Professor de Graaf and experimental work was started. Within a short time, word of the research reached France and England where it aroused considerable industrial interest, and arrangements were soon made whereby the industries of those countries were enabled to contribute both to the financial support and to the planning and execution of the experiments and to the analysis and publication of the results.

As early as 1951, interest from the United States was demonstrated, and in 1952, under the leadership of Prof. Hoyt C. Hottel of the Massachusetts Institute of Technology, an American committee was formed for co-operation in the research. This committee has since been active in financial support of the program and in reviewing the results of the work, Sweden and Belgium

¹ Technical Director, Battelle Memorial Institute. Fellow ASME. Contributed by the Heat Transfer Division and presented at a joint session with the Fuels Division and the Research Committees on Furnace Performance Factors and Heat Conduction Charts at the Annual Meeting, New York, N. Y., November 25-30, 1956, of THE AMERICAN SOCIETY OF MECHANICAL ENGINEERS.

NOTE: Statements and opinions advanced in papers are to be understood as individual expressions of their authors and not those of the Society. Manuscript received at ASME Headquarters, August 9, 1956. Paper No. 56-A-111.

have joined and the High Authority of the European Community of Coal and Steel in 1955 made a major financial contribution to the support of the work.

The story of this unique example of international co-operation—unique because it was the result of spontaneous activity on the part of scientists and engineers without governmental action—has been widely publicized in England and France, but, with the exception of a few notes and a brief paper by Professor Thring (1),² no comprehensive account of the objectives, method of operation, or of the results has been published in the United States. This paper aims to furnish this account.

ORGANIZATION

In November, 1955, the International Joint Committee for Flame Radiation, prior to that time a rather informal and loosely knit organization, was formalized by its registration in Holland as the International Flame Research Foundation. Its objectives are the attainment of knowledge and experience on the combustion of gaseous, liquid, and solid fuel, in particular as the combustion aims at the heating of materials, and the placing of that knowledge and experience at the disposal of others for further development and industrial application. The Foundation is of the not-for-profit type and is required by its charter to apply its income and property solely toward the promotion of its stated objectives.

The president of the Foundation, who had been from the beginning the chairman of the Joint Committee, is the eminent Prof. G. M. Ribaud, noted French physicist, who recently retired as director of research for the gas industry of France.

The general superintendent of the research program is Prof. M. W. Thring, formerly Head of Physics Department, British Iron and Steel Research Association, and since 1953, Head of Fuel Technology, Sheffield University.

The governing body of the Foundation is the Joint Committee made up of two or more representatives of each national committee. The present membership of the Joint Committee is as follows:

Belgium: P. Coheur, Professor, National Metallurgical Research Center, Liège; G. A. Homès, Professor of Metallurgy, Universities of Mons and Brussels.

France: Raymond Chéradame, Director General, Research Center, Coal Industry of France, Paris and Verneuil; Henri Malcor, President, French Institute for Iron and Steel Research, Paris.

Great Britain: O. A. Saunders, Professor, Imperial College of Science and Technology, London; D. T. A. Townend, Director General, British Coal Utilization Research Association, Leatherhead.

Netherlands: J. E. de Graaf, Professor, Technological University, Delft, and Technical Advisor, Royal Netherlands Blast Furnace and Steel Works, IJmuiden; J. O. Hinze, Professor, Technological University, Delft.

Sweden: O. G. Hammar, Professor, University of Göteborg.

² Numbers in parentheses refer to Bibliography at end of paper

America: F. S. Bloom, President, Bloom Engineering Company, Pittsburgh, Pennsylvania; E. G. Chilton, Research Department, Shell Oil Company, Emeryville, Calif.; Ralph A. Sherman, Technical Director, Battelle Memorial Institute, Columbus, Ohio; (alternate: Bertrand A. Landry, Paris Branch, Battelle Memorial Institute).

In addition, Professor Ribaud, Professor Thring, and G. W. van Stein Callanfels, General Secretary, are members of the Joint Committee.

The Joint Committee holds meetings several times a year to decide on general policies. A Technical Advisory Committee, and special committees on Aerodynamics, on Pulverized Fuel, on Burners, on Furnaces, on Instruments, on Editing, and on Finances, bring to the planning and analysis of the work the best available talent for each phase.

The National Committees are autonomous and can obtain their financial support and can select their membership in any way that each group may decide proper. The financial contribution from each country may be suggested by the Joint Committee but the final decision is made for itself by each National Committee.

Although the original conception of the work was in a steel company and the experimental furnace was intended to have a reasonable similarity to an open-hearth steel furnace, the research is of such a basic nature that interest and support have come not only from the steel industry, but also from other sources including the boiler and fuel-equipment manufacturers, the glass industry, the cement industry, and from the coal, petroleum, and gas industries.

The execution of the work at IJmuiden is in the charge of a Principal Investigator who was first British, then French, and is now again British. The Joint Committee for some time also has paid for the services of another investigator, presently British, to work with Professor Hammar in Sweden on the fitting out of a new experimental furnace with cold walls at Göteborg. For the main experiments at IJmuiden, in which 30 to 40 men have been required for several weeks, investigators are furnished from co-operating companies in the several countries. Normally, their salaries and traveling expenses are borne by their employers; thus, there are, in addition to the cash contributions, substantial contributions "in kind."

Several companies and associations in England, France, and Holland have carried on research on flame radiation independently to supplement or to complement the work at IJmuiden. Much of the information so obtained has been made available to the Joint Committee or published separately in the literature.

As described later, the expenditures in the past three years for new facilities and equipment have been heavy, but the \$56,000 costs in 1955 are expected to be the last major expenditures of a capital nature. The total cost of the experimental furnaces and equipment now available at IJmuiden was approximately \$200,000. The operating costs in 1955 paid by the Joint Committee were approximately \$64,000, and the contributions in kind amounted to about \$25,000.

EXPERIMENTAL FACILITIES

The original experimental furnace and testing facilities installed by the Royal Netherlands Steel Works were used from the start of the work through 1953 for a series of seven sets of formal tests and much supplementary investigation. Since then, a new furnace for the gas and oil studies, housed in a permanent special building 65 × 79 ft, has been available. The building also provides rooms for gas analysis, instruments, fuel pumps, and supplies. In an attached, partly enclosed structure is a plant for the preparation of pulverized coal, and at one side is an air preheater.

Fig. 1 is a view of the laboratory. Fig. 2 shows the building plan.

Fig. 3 shows a plan and elevation of the gas or oil furnace which is of the same size and shape as the original furnace. It is essentially square in transverse vertical section, $6\frac{1}{2} \times 6\frac{1}{2}$ ft, and about 20 ft long from the burner to the furnace exit. The furnace is lined with a high-grade sillimanite refractory enclosed with insulating refractory and jacketed in a steel casing.

The gas or oil burners are installed on the center axis of the furnace at the nose of the "dog house." Secondary air is normally admitted at low velocity through ports in the walls at either side of the burner; mixing is by diffusion. Air also can be admitted around the burner if desired.

Fig. 4 shows plan and vertical sections of the second recently completed furnace designed especially for burning pulverized coal. It is of similar construction but is only 4 ft 11 in. × 5 ft 2 in. in transverse vertical section and is $34\frac{1}{2}$ ft long. Doors are provided on one side at the bottom for removal of ash. This furnace can be equipped with internal water cooling for the purpose of increasing the thermal load thereby simulating a steam boiler.

Air for combustion is supplied by blowers. The air preheater, fired with blast-furnace gas, can heat the air to 1380 F. All rates of flow of fuel and air are closely controllable and are measured and recorded. Fig. 5 is a view of the instrument room showing the many recorders.



FIG. 1 VIEW OF THE LABORATORY

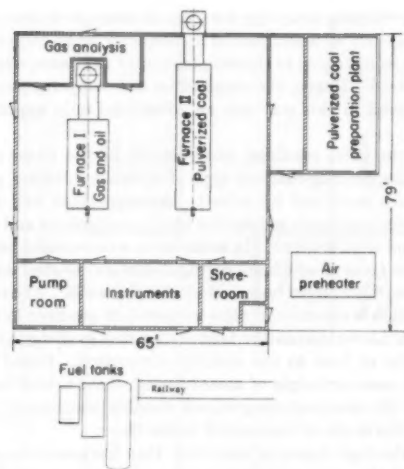


FIG. 2 PLAN OF LABORATORY

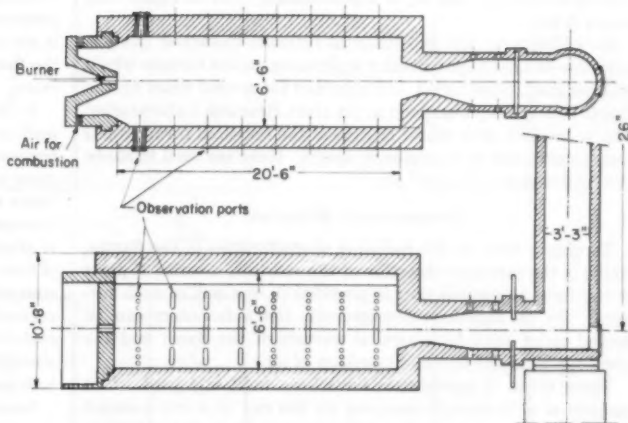


FIG. 3 PLAN AND SECTIONAL ELEVATION OF GAS OR OIL FURNACE

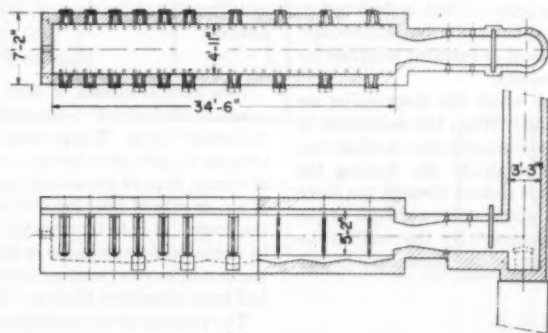


FIG. 4 PLAN AND SECTIONAL ELEVATION OF PULVERIZED-COAL FURNACE



FIG. 5 INSTRUMENT ROOM OF IJMUIDEN LABORATORY

The range of heat input to the oil and gas-fired furnace has been 4 to 10 million Btu per hr, or approximately 4600 to 11,500 Btu per cu ft-hr.

In addition to the experimental furnaces described there is available at IJmuiden a smaller scale water-cooled furnace which was designed, constructed, and operated for several years by the Royal Dutch Shell Company at its Delft Research Laboratories. Also a one-fifth scale model of each of the fuel-fired furnaces has been constructed of transparent plastic; these are used to study mixing patterns of fuel and air.

EXPERIMENTAL METHODS

To obtain data on the radiating characteristics of the flames, which is the principal objective of the research, a series of ports in the form of vertical slots is provided in one wall of each furnace. By an ingenious arrangement, the radiometers can be moved up or down for a vertical traverse of the flame and the ports can be closed to avoid inleakage of air.

Three types of radiometers have been built and used. One consists of a thermopile mounted on the end of a water-cooled tube which contains a series of diaphragms to limit the field of view of the thermopile. The second type uses a fixed-focus rhodium-plated mirror to reflect the radiation onto a thermopile. A third type is based on this same principle but is designed to measure radiation from two sources simultaneously. Electrically heated, tube or sphere furnaces are used at frequent intervals for purposes of calibration of the radiometers.

In the wall opposite that through which the thermopiles are inserted is a vertical water-cooled slot. When the radiometer is sighted through the flame at this low-temperature surface, the radiation from the flame alone is received. By turning the radiometer through a small angle, it is sighted through the flame onto the opposite refractory wall in which a thermocouple at the inner surfaces measures the temperature. By the method developed by Schmidt (2), the emissivity of the flame may be calculated as follows

$$e = \frac{R_1 - R_2 + R_3}{R_3}$$

where e is the emissivity of the flame, R_1 is the radiation measured from the flame alone, R_2 is that from the flame and hot refractory wall, and R_3 is the radiation of the wall alone as calculated from the observed temperature, assuming an emissivity of the wall of unity. This is a simple arithmetical relation inasmuch as

$$R_1 = \sigma e T_f^4$$

$$R_2 = \sigma e T_f^4 + (1 - e) R_3$$

and

$$R_3 = \sigma T_w^4$$

where σ is the Stefan-Boltzmann constant and T_f and T_w are the absolute temperatures of the flame and wall, respectively.

Then

$$\frac{\sigma e T_f^4 - \sigma e T_f^4 - (1 - e) \sigma T_w^4 + \sigma T_w^4}{\sigma T_w^4}$$

becomes

$$\frac{\sigma T_w^4 - \sigma T_w^4 + e \sigma T_w^4}{\sigma T_w^4}$$

which reduces to e . Having derived e , one obviously can derive a flame temperature as

$$T_f = \sqrt[4]{\left(\frac{R_1}{\sigma e}\right)}$$

This derivation assumes that the factor $(1 - e)$ is equal to the

transmissivity. This is true only for gray flames. It is true for nongray flames, such as nonluminous flames, only when the temperature of the wall is equal to the temperature of the flame, which is not usually true. Hence, the emissivities and temperatures of the flames derived in this way can be considered only approximate.

In addition to these readings, observations of the flame are made with a disappearing-filament type of optical pyrometer, gas temperatures are measured by velocity thermocouples, and the gases are sampled and analyzed for the usual constituents and for water vapor and solid content. In some tests, water-cooled heat-flow meters, the faces of which are corrugated stainless-steel disks of about 1 1/2 in. diam, have been installed in the walls. The rate of heat absorption is measured by the temperature gradient in the steel disk. Air blown across the face of the disk is designed to prevent transfer of heat to the disk by convection. Based on essentially the same principle of measurement of the rate of heat absorption by the temperature gradient, another instrument has been used for the study of convection in the flame.

Because of the high degree of ingenuity that has gone into the development of the various instruments used in this work, it is regretted that, in the interest of brevity, descriptions must be omitted. The reader who is interested is referred to the British and French publications of the work that are cited in the references.

PLAN OF EXPERIMENTS

Two general classes of tests have been made: (a) "Performance" or "industrial" tests, and (b) "combustion mechanism" or "scientific" tests. The purpose of the performance tests is to determine the effects of certain variables, such as type of fuel, type of burner, type of atomizing agent, degree of mixing of air, excess of air, or rate of heat input upon the radiating characteristics of the flame. It is to be expected that the results of such tests can be immediately applicable in industrial furnaces. Seven series of performance tests, each series consisting of many separate tests, had been completed through 1955.

The purpose of the combustion-mechanism tests is to examine a few flames in considerable detail. For example, the rate of mixing and the appearance and disappearance of carbon in the flame are studied both longitudinally and laterally and, by measuring the radiation of small elements of the flames, an attempt is made to relate the carbon content and the radiating characteristics of the flame. Only two series of these tests have been made.

The factorial method of planning the experiments has been used in all series of tests. Thus, in a series of tests of five variables, 32 separate tests were so selected as to give all combinations of high and low values of each variable from which not only the effect of the high and low levels could be obtained but also the interaction of the several variables.

The data have been analyzed statistically and the confidence level of each derived data point has been calculated. As the tests were run through two shifts, with the third shift being used to make necessary adjustments to equipment, the tests have been so planned as to enable a calculation of the effects, if any, of the three teams of men used to obtain the data.

Variables Investigated. Table 1 summarizes the variables that have been investigated in the seven series of performance tests and the two series of combustion-mechanism tests that had been made up to the end of 1955. A total of ten variables has been studied. In some series, only one variable was studied at several different values or levels; in the first series, the effects of five different variables were determined. Those factors that were used as variables in each series are designated by a heavy border around the applicable blocks.

As one of the most important factors that govern the radiation

TABLE 1 CONDITIONS AND VARIABLES OF TESTS THROUGH 1955

VARIABLES	Performance Tests						Combustion-Mechanism Tests		
	1 ² 4.5	2 ⁶ 7	3 ⁸ 9	4 ⁸ 9	5 ⁸ 9	6 ¹⁰	7 ¹⁰	1 ¹¹	2 ¹²
Fuel	(a) Heavy fuel oil (b) Creosote-pitch	Heavy fuel oil	Coke-oven gas and fuel oil	Coke-oven gas and fuel oil	Coke-oven gas, fuel oil, and creosote-pitch	(a) Heavy fuel oil (b) Light fuel oil (c) Creosote oil	(a) Heavy fuel oil (b) Coke-oven gas	Heavy fuel oil	(a) Coke-oven gas (b) Coke-oven gas + propane (c) Light fuel oil (d) Heavy fuel oil
Rate of heat input, million Btu/hr	(a) 7.6 (b) 10.6	(a) 5.5 (b) 9.9	(a) 6.8 (b) 10.4	8.7	8.7	7.1	4.4	7.6	6.0
Atomizing agent	(a) Steam (b) Air	(a) Steam (b) Air	Steam	Steam	Steam	(a) Steam (b) Air	-	(a) Steam (b) Air	Air
Rate of supply of atomizing agent, lb/lb fuel	Steam, 0.35 to 0.55 Air, 0.53 to 0.81	(a) 0.2 (b) 0.5	-	-	-	-	-	Steam, 0.3 Air, 0.5	Light oil: (a) 0.46 (b) 0.73 Heavy oil: (c) 0.44
Thrust on burner, lb	-	-	(a) 1.3 (b) 2.5 (c) 2.6 (d) 5.0	3.3	3.56	(a) 2.2 (b) 4.4, air at side of furnace (c) 4.4, air around burner	(a) 2.2 (b) 3.3	-	(a) 2.6 (b) 4.8
Type of burner	-	Five types of burners	-	-	-	-	-	-	-
Excess of air at furnace exit, per cent	(a) 58 (b) 70	20	(a) 0 (b) 40	8 to 10	9 to 11	-	(a) 10 (b) 40	Steam, 15 Air, 65	0 to 16
Carburizing agent	-	-	Heavy fuel oil	Heavy fuel oil	(a) Heavy fuel oil (b) Creosote-pitch	-	-	-	-
Amount of carburant, per cent	-	-	(a) 0 (b) 15.0	(a) 0 (d) 60 (b) 20 (e) 80 (c) 40 (f) 100	(a) 0 (b) 33.3 (c) 66.7 (d) 100.0	-	-	-	-
Temperature of combustion air, F	-	-	-	-	-	-	(a) 212 (b) 1200	-	-

* Reference to publication giving results of tests.

□ Blocks with heavy borders indicate variables of test series.

TABLE 2 CHARACTERISTICS OF FUELS

	Residual oil			Light fuel oil	Creosote pitch	Creosote oil	Coke-oven gas, vol per cent
	1	2	3				
Density, 60 F.....	0.952	0.982	0.981	0.826	1.150	0.998	
Saybolt universal viscosity, 100 F, sec.....	1750	960	1130	34	1120*	37	
Conradson carbon, %.....	8.1	13.85	22.7	...	CO ₂2.1 C ₆ H ₆2.0 O ₂0.3 CO.....8.2 H ₂49.5 CH ₄26.8 Na.....11.1 Total 100.0
Asphaltenes, %.....	3.25	7.60	19.5	...	
Initial boiling point, deg F.....	385	360	417	
Boiling point for 70%, deg F.....	968	530	511	
Final boiling point, deg F.....	575	615	
Composition, %:							
Carbon.....	84.6	86.8	85.0	89.8	88.0	
Hydrogen.....	11.5	10.2	13.4	5.7	8.3	
Oxygen.....	1.0	0.5	2.2	
Sulphur.....	3.5	1.9	0.9	0.8	0.01	
High heat value, Btu/lb.....	18675	18270	16490	484 ^b	
Ratio: C/H.....	7.35	8.5	6.3	15.8	10.6	2.18

* At 122 F.

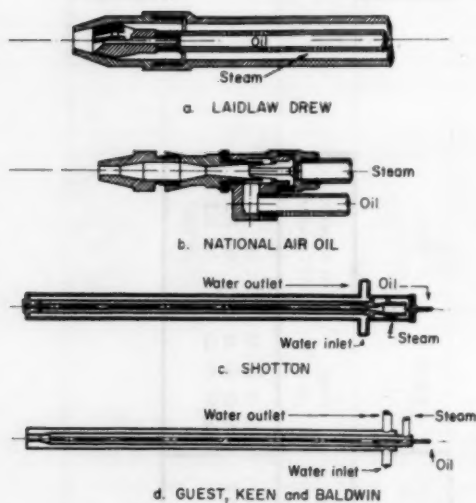
^b Btu/cu ft.

FIG. 6 FOUR OIL BURNERS USED IN PERFORMANCE TEST 2

from the flame, the type of fuel has been subject to intensive investigation, both as single fuels of different types and as mixtures.

Characteristics of Fuels Used. Table 2 presents data on the characteristics of the fuels that have been used in the tests.

Although complete data are not given for all fuels on the same basis, the data do give a picture of the class of the fuels. The oils are from the Middle East fields. Shipments obtained varied somewhat in viscosity, in Conradson carbon, and in C/H ratio. The light fuel oil would be classed in the United States as a No. 2 oil.

The creosote pitch was stated to be a blend of the creosote-oil fraction of coal tar boiling between 535 and 680 F and the pitch, the residue above the latter temperature. The ratios used have been 50-50 and 40 per cent creosote oil and 60 per cent pitch. The creosote oil used alone was, from its boiling range, a slightly lighter fraction than that said to have been used in the blend.

The coke-oven gas was that from the ovens at the steel plant used for the production of blast-furnace coke.

Burners Used. Fig. 6 shows four of the burners used in the series

of tests of burners. They include external mixing and internal mixing both at the front and the back.

The oil was supplied to the burners at pressures slightly above those of the atomizing agent. Air or steam was supplied at a pressure of 10 to 100 psi as required by the amount of atomizing agent used. Early in the work, the amount of atomizing agent was expressed as the ratio of the weight of the agent to that of the fuel. Because one of the most important effects of the rate of supply of atomizing agent appeared to be that on the rate of mixing of the fuel and air, in test series 3 and following, the thrust of the burner when feeding fuel and atomizing agent was measured. Fig. 7 shows the arrangement by which the thrust was measured. The burner was suspended by three wires and a wire attached to the lower part of the burner passed over the pulley to support a pan on which weights were placed to balance the thrust. It was possible to measure the thrust within 20 g in a total of 1000 g, or 2 per cent. The thrust is taken as a measure of the momentum of the jet, a most important factor in the mixing of the fuel and air.

Fig. 8 shows the type of burner used for gas alone or for gas with oil. The raw gas issued from the row of ports around the central oil-burner nozzle. A special replaceable plate was made for the gas ports to facilitate changing the thrust while maintaining the same delivery of gas. Air or oxygen could be supplied through the outer row of ports.

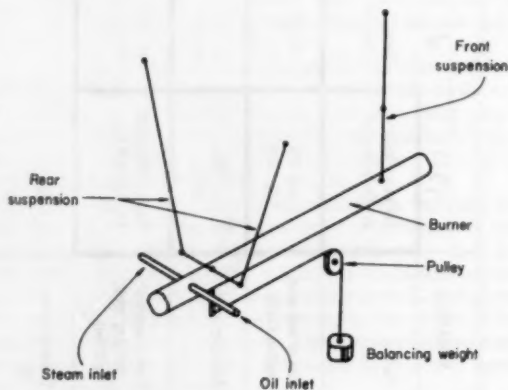


FIG. 7 SETUP FOR MEASURING THRUST OF BURNERS

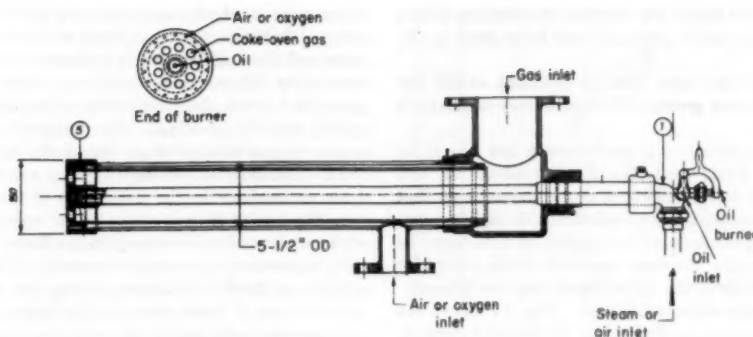


FIG. 8 BURNER USED FOR GAS OR FOR GAS AND LIQUID FUELS

HIGH LIGHTS OF RESULTS OBTAINED

Because of the large number of data obtained from the research over the years, no attempt will be made in this paper to present more than certain high lights. The interested reader can consult the published British and French papers for the details.

Effect of Type of Fuel on Radiation From Flame. Fig. 9 shows data obtained from the first series of tests that prove the important effect that the type of fuel can have on the radiation from the flame. The ordinate is the radiation in Btu per sq ft-hr from the flame alone; that is, with a cold back wall. The shapes of the curves for the flames of residual oil and the creosote-pitch blend are similar, reaching a maximum at about 5 ft from the burner. Under the method of calculation from the raw data, the effects of other variables are eliminated. At the maximum, the radiation from the creosote pitch, which had about three times the Conradson carbon, six times the asphaltene content, and about twice the C/H ratio of the residual oil, was about 20 per cent higher than that from the residual oil. Although, at the last point of measurement, at about 14 ft from the burner, the radiation was the same for the two fuels, yet the total radiation from the creosote-pitch blend was greater than that from the residual-oil flame.

Figs. 10 and 11 show the radiation from flames of coke-oven gas alone, of coke-oven gas carbureted with varying percentages of residual oil, and of the creosote-pitch blend. The percentages of each fuel are calculated on the basis of the heat value that each contributes to the total. The coke-oven gas burned with an essentially nonluminous flame and its radiation was that only of the CO_2 and H_2O content. The radiation increased substantially

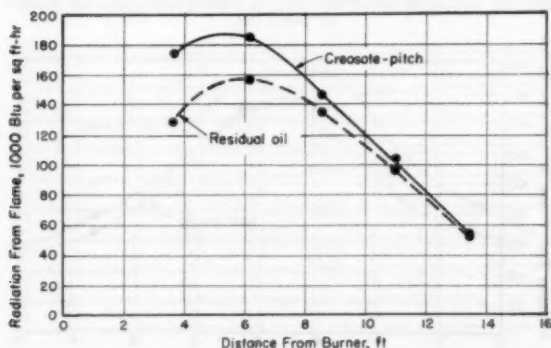


FIG. 9 RADIATION FROM FLAMES OF RESIDUAL OIL AND BLEND OF 40 PER CENT CREOSOTE OIL, 60 PER CENT PITCH—PERFORMANCE TEST NO. 1

uniformly along the length of the flame as mixing and combustion progressed.

Fig. 10 shows that a substantial increase in radiation from the flame is obtained by the addition of 20 per cent of oil and that further increases in carbureting oil continue to increase the radiation. Both Figs. 10 and 11 show that, as compared with 100 per cent liquid fuel, one third to 40 per cent of the heat value of residual oil can be replaced by a weakly radiating coke-oven gas without a great decrease in radiation from the flames. With a

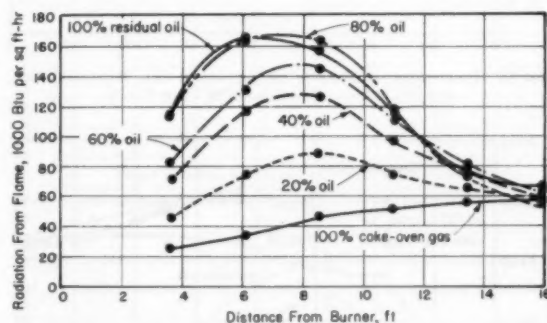


FIG. 10 RADIATION FROM FLAME OF COKE-OVEN GAS CARBURETED WITH VARYING PERCENTAGES OF RESIDUAL OIL—PERFORMANCE TEST NO. 4

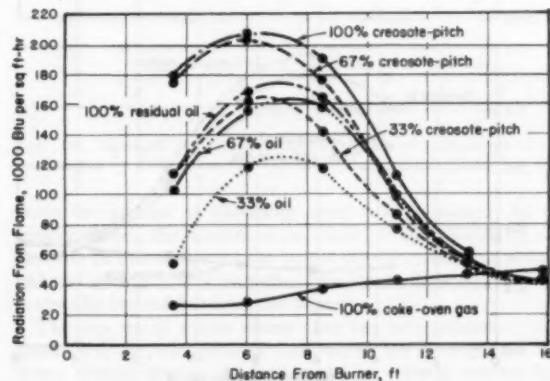


FIG. 11 RADIATION FROM FLAME OF COKE-OVEN GAS CARBURETED WITH RESIDUAL OIL AND BLEND OF CREOSOTE AND PITCH—PERFORMANCE TEST NO. 5

larger furnace and thicker flame, the decrease in radiation with a given replacement of fuel oil by gas would not be as great as observed here.

Both Figs. 10 and 11 also show that the radiation at the last point of measurement is not greatly different for any of the fuels or blends.

Fig. 12 presents data obtained in performance test No. 6 for three widely different liquid fuels, No. 2 oil, residual oil, and creosote oil. Although its viscosity was about the same as that of the No. 2 oil, the creosote oil gave a substantially higher radiation than did the light petroleum oil and higher, in fact, than did the residual oil. Yet again, the close approach of the values for radiation of the three fuels at the tail of the flames can be seen.

Emissivities and Temperatures of Flames. Fig. 13 shows the emissivities and temperatures, as derived by the Schmidt method, for four of the flames whose radiation was shown in Fig. 11. The temperatures of the creosote-pitch, residual-oil, and oil-carbureted

flames were closely the same after the second position of measurement. Their emissivities differed more than did their temperatures and these differences in emissivity were thus the principal reasons for differences in radiation evident in Fig. 11. As the carbon is burned, the emissivities approach those for flames containing only CO_2 and H_2O . The temperature of the flame of the coke-oven gas is surprisingly low in the early part of the flame and its emissivity surprisingly high for a completely nonluminous flame particularly in the latter part of the flame. Calculation, from the data of Hottel, et al., on the emissivity of CO_2 and H_2O , whose contents for the coke-oven gas flame were 7.7 and 20.0 per cent, respectively, gives an emissivity of 0.21 at the final temperature of 2500 F indicated in Fig. 13 as compared with the derived value of 0.345 shown in the figure. If the true temperature were actually higher, as suspected, the emissivity would be somewhat lower than 0.21.

The Schmidt method of derivation of emissivity and temperature of the flame is strictly applicable only to gray flames, and nonluminous gas flames are not gray. This problem undoubtedly will have further attention in the experimental research at IJmuiden.

Further, in regard to the temperature shown in Fig. 13, it is to be realized that, derived as they were, they are averaged radiant temperatures across the width of the flame. The temperature of the flame obviously varied across the furnace, and maximum temperatures higher than 2800+ F shown for the creosote pitch, for example, occurred in the furnace.

Fig. 14 presents a curve taken from a recent paper by Riviere (10). This curve shows the relation of the emissivity of the flame

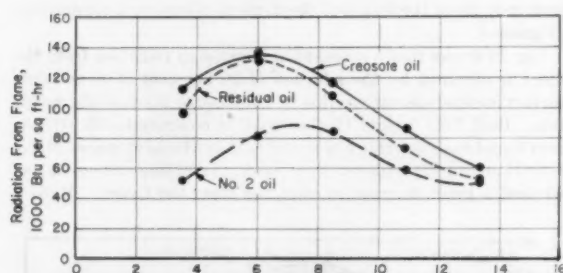


FIG. 12 RADIATION OF FLAMES OF CREOSOTE OIL, RESIDUAL OIL, AND NO. 2 OIL—PERFORMANCE TEST NO. 6

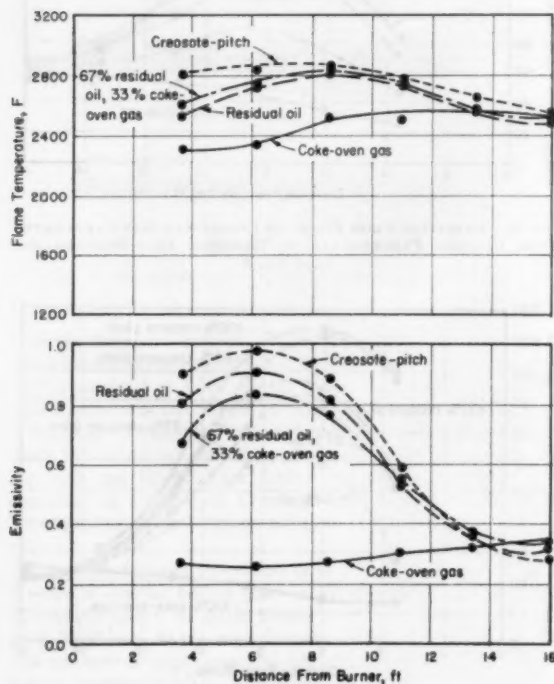


FIG. 13 TEMPERATURE AND EMISSIVITY, DERIVED BY SCHMIDT METHOD, OF FLAMES OF COKE-OVEN GAS, RESIDUAL OIL, CREOSOTE PITCH, AND GAS CARBURETED WITH OIL—PERFORMANCE TEST NO. 5

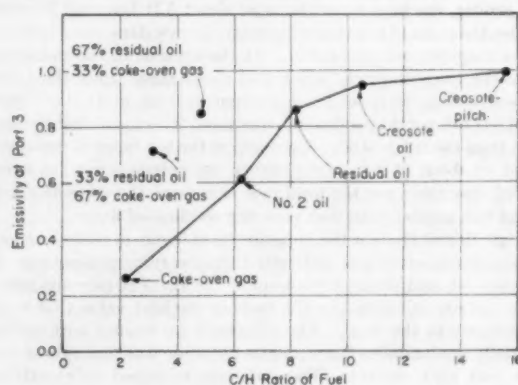


FIG. 14 RELATION OF EMISSIVITY OF FLAME AND THE C/H RATIO IN THE FUEL

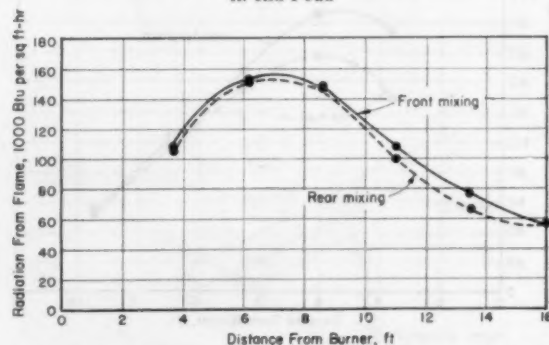


FIG. 15 RADIATION OF OIL FLAMES OF FRONT-MIXING AND REAR-MIXING BURNERS—PERFORMANCE TEST NO. 2

at Port 3, which is essentially the maximum, for coke-oven gas and four liquid fuels to the C/H ratio of the fuels. The data come from performance tests Nos. 3 to 6. For these individual fuels, including even the blend of creosote and pitch, a good relationship of the maximum emissivity to the C/H ratio is shown. However, the two points for the 67-33 per cent and 33-67 per cent residual oil and coke-oven gas fuels added to the Rivière's figure in the upper left show that the relation does not hold for such mixed fuel.

Effect of Burner Design. Among the five burners used in performance test No. 2, no outstanding differences in flame radiation were found. A definite difference in the burners was that of the point of admission of the atomizing agent into the oil stream, that is, at the back end or at the front or nozzle end.

Fig. 15 shows the radiation from the flame along the length of the flame for the National Air-Oil, front-mixing, and the Shotton, rear-mixing, burners. The differences between the two types are seen to be slight.

Effect of Type of Atomizing Agent. Fig. 16 presents the radiation along the flame when using air or steam as the atomizing agent in the burner. The greater radiation from the flame when air is used is marked. This greater radiation must have resulted from a greater emissivity of the flame when using air inasmuch as the temperature of the flame was similar for air and steam, as shown by measurements presented in the detailed reports of the tests. The same relation of higher emissivity and radiation for air than for steam has been found in all subsequent tests where the type of atomizing agent has been a variable.

Effect of Amount of Atomizing Agent. Fig. 17 shows the effect on the radiation from the flame of the rate of supply of atomizing agent; the curves apply both to air and to steam. The effect is small in the early part of the flame but increases to a substantially greater radiation as the amount of atomizing agent is decreased. This results principally from the increased emissivity of the flame with lower amounts of steam or air. The underlying reason is undoubtedly connected with the less rapid mixing of the combustion air by the reduced momentum of the jet when less atomizing agent is used.

Fig. 18 presents further data on the effect of amount of atomizing agent and on the method of admission of the combustion air. Data are given for three fuels as obtained in performance test No. 6 and reported by Rivière (10).

The rate of supply of atomizing agent is here expressed as the thrust on the burner. Comparison of the two lower sets of curves at 2.2 lb and 4.4 lb of thrust, when the combustion air was admitted at low velocity on either side of the furnace, as normally used in the tests, shows that the radiation from the flame of the No. 2 oil was greatly reduced over the entire length of the flame

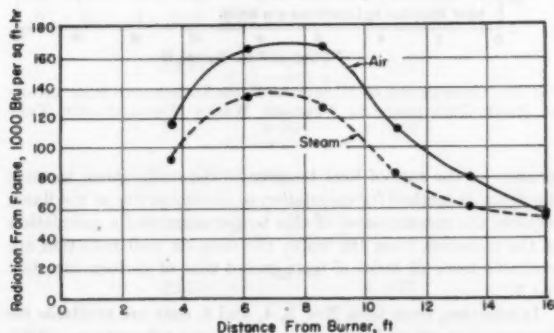


FIG. 16 RADIATION OF OIL FLAMES WHEN USING AIR AND STEAM AS ATOMIZING AGENT—PERFORMANCE TEST NO. 2

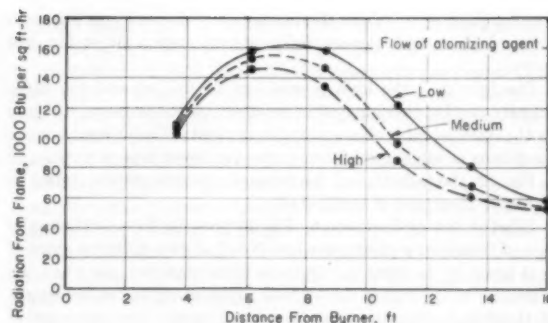


FIG. 17 RADIATION OF OIL FLAMES WITH VARYING AMOUNTS OF ATOMIZING AGENT—PERFORMANCE TEST NO. 2

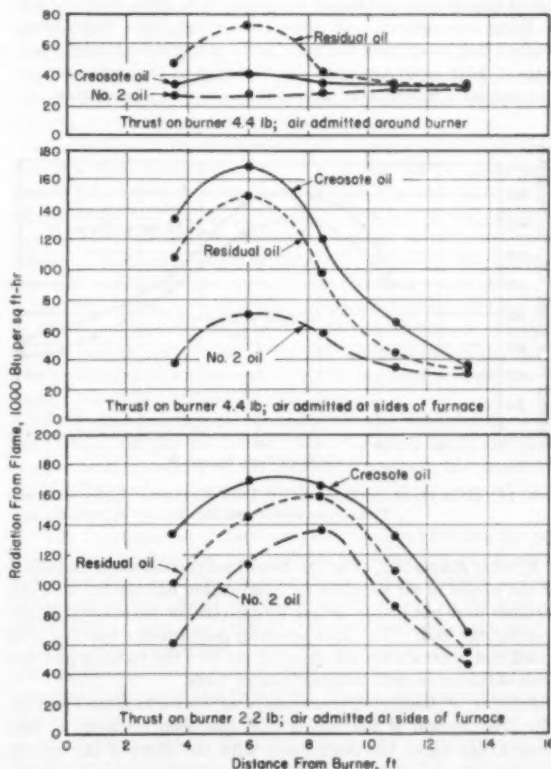


FIG. 18 EFFECT OF MIXING CONDITIONS ON RADIATION FROM FLAMES OF THREE LIQUID FUELS—PERFORMANCE TEST NO. 6

when the amount of atomizing agent was increased. At the greater thrust, the maximum radiation for the residual oil and creosote oil moved toward the burner but the maximum was not reduced greatly. The radiation from these fuels was reduced materially beyond 8 ft from the burner.

The top set of curves shows that the combination of high thrust and the admission of combustion air through the dog house directly around the burner at high velocity resulted in a flame of No. 2 oil with radiating characteristics similar to those shown in Figs. 10 and 11 for coke-oven gas. The creosote oil was only slightly more radiant. The residual oil still displayed the

familiar peak at 6 ft from the burner but this peak was less than half as high as with the admission of combustion air at low velocity.

The fact that the high momentum of the jet and the high-velocity combustion air had more effect on the creosote oil than on the residual oil is of considerable interest. Under less extreme conditions of mixing as shown in the two lower sets of curves and in Fig. 12, the radiation of the flame of creosote oil was shown to be higher than that of residual oil.

Effect of Rate of Heat Input. Fig. 19 presents data on the radiation of flames in performance test No. 2 at two different rates of heat input to the furnace. Quite as to be expected, the radiation is greater at the higher rate of heat input along the entire length of the flame although it is less marked at the first observation port. The detailed data show that the emissivity of the flames at the peak of their radiation did not differ much with rates of heat input in this test; hence, the greater radiation at that point resulted largely from the higher temperature of the flame as the rate of firing was greater. In general, however, later experiments showed that away from the peak, as even at the peak when small rates of heat input are used, the variation of the emissivity accounted for a substantial part of the variation in radiation.

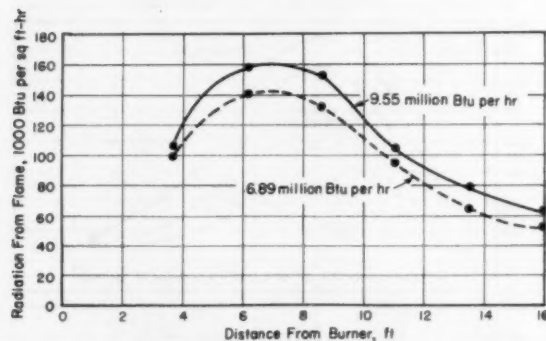


FIG. 19 RADIATION OF FLAMES AT TWO RATES OF HEAT INPUT—PERFORMANCE TEST NO. 2

Effect of Excess Air. Fig. 20 shows that the radiation decreased as the excess of air supplied for combustion increased. The differences were not great; 58 per cent excess for the low and 70 per cent for the high. The data are from performance test No. 1 in which full control over inleakage of air into the furnace had not been obtained as was possible in later tests.

Relation of Radiant Characteristics of Flame to Heat Transfer. The presentation of the results that has been made up to this point in the paper has dealt solely with the effect of the several variables on the rate of radiation and the temperature and emissivity of the flame at various points along the length of the flame. The ultimate objective of a search for knowledge on radiation from flames obviously must go beyond the establishment of these relations and must include the establishment of an understanding of the effect of the variables on the rate of heat transfer to work in the furnace. This work might be steel as in an open hearth, billets as in a reheating furnace, water-filled or oil-filled tubes as in a steam generator or an oil still, cement in a kiln, or glass in a glass tank.

In the experimental furnace for gas and oil at IJmuiden, the only load comprises the heat absorbed by water-cooled ports and probes, and the radiation from the outer walls of the furnace. Because this load on the furnace remains substantially constant in all tests, the inside temperature of the walls furnishes a certain

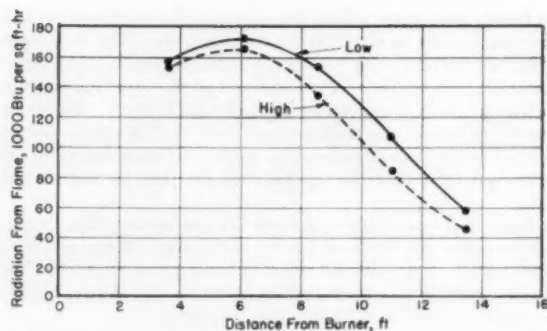


FIG. 20 RADIATION OF OIL FLAMES WITH VARYING AMOUNTS OF EXCESS AIR—PERFORMANCE TEST NO. 1

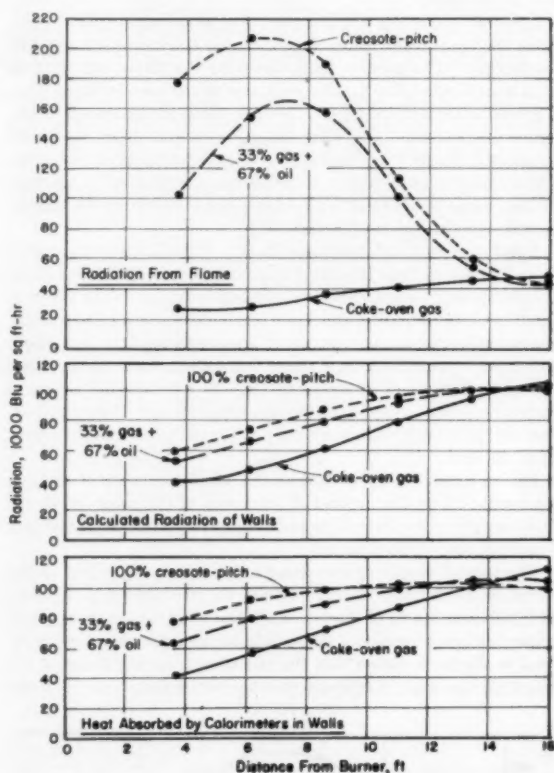


FIG. 21 COMPARISON OF RADIATION FROM FLAMES AND INDICATIONS OF HEAT DELIVERED TO FURNACE WALLS—PERFORMANCE TEST NO. 5

measure of the rate of heat transfer to the wall. Also, because the Schmidt method for calculation of the emissivity of the flame requires the measurement of this temperature and a calculation of the radiation from the walls, the data on wall radiation are available from all series of tests except that of performance test No. 1.

In addition, from tests Nos. 3, 4, and 5, data are available for the heat absorption of the calorimeters, or heat flowmeters, which have been described briefly; thus, another measure of the heat delivered by the flame is available.

Fig. 21 presents in the top section the radiation from the flames of three fuels differing substantially in their radiant characteristics. These already have been shown in Fig. 11. In the middle section are given the data for the radiation of the walls, and in the bottom section those for the heat absorbed by the calorimeters. The similar shape of the wall radiation and calorimeter curves is evident. The values are also of similar order, but the calorimeter values are somewhat the greater.

Two points are striking in a comparison of the radiation of the flame with either of the measures of heat delivered to the furnace walls. The first is that, although the flame-radiation curves differ widely for the three fuels, the heat delivered to the walls obviously differs much less among the fuels. The second is that, although the peak of flame radiation occurs at 6 to 7 ft from the burners, with the liquid fuels, there is no similar peak in the rate of heat delivery to the walls. The curves rise substantially uniformly along the length of the furnace for all three fuels.

The explanation for the latter fact is undoubtedly (a) that longitudinal radiation from the flame to the walls and from the walls in one part to the walls in other parts tends toward uniformity of the wall temperature, and, (b) that the flame is a cone and not a cylinder. Furthermore, convection undoubtedly plays a considerable part in fixing the wall temperature. Near the burner, heat is transferred from the walls to the combustion air that enters at the front and flows between the walls and the expanding jet of flame. In the rear part of the furnace, where the mixing and combustion are nearing completion and the flame sweeps the walls, the transfer of heat by convection from the high-temperature gases must add materially to the transfer of heat by radiation.

To arrive at some numerical measure of the relative total rate of transfer of heat from the flame, the areas under the curves of radiation from the flame of Fig. 21 have been measured by a planimeter. Similarly, the areas under the curves of the radiation of the walls and of those of the calorimeter measurements have been measured. It is recognized that this integration for the radiation of the flames is in error because the diameter of the flames and thus the area of each unit of length is not constant along the length of the flame. However, lacking data on the contour and area of the flames, they are all treated as cylinders.

The results of the integrations follow:

Radiation From Flame

$$\text{Ratio: } \frac{\text{Creosote pitch}}{\text{Coke-oven gas}} = 3.60$$

$$\text{Ratio: } \frac{\text{Gas oil}}{\text{Coke-oven gas}} = 2.88$$

Wall Radiation From Wall Temperatures

$$\text{Ratio: } \frac{\text{Creosote pitch}}{\text{Coke-oven gas}} = 1.24$$

$$\text{Ratio: } \frac{\text{Gas oil}}{\text{Coke-oven gas}} = 1.19$$

Wall Radiation From Calorimeters

$$\text{Ratio: } \frac{\text{Creosote pitch}}{\text{Coke-oven gas}} = 1.23$$

$$\text{Ratio: } \frac{\text{Gas oil}}{\text{Coke-oven gas}} = 1.17$$

These calculations show that, whereas the flame-radiation data indicate that the creosote-pitch and gas-oil flames had potential radiating powers 3.6 and 2.88 times, respectively, that of the coke-

oven gas flame, the data on the heat absorbed at the walls indicate that with the creosote-pitch and oil-gas flames this was only 24 to 19 per cent more than that with the coke-oven gas flame. This calculation, it is again emphasized, does not allow for the difference in area of the flame along the length of the furnace. However, it does suggest that convection must have played an important part in the transfer of heat in the furnace.

Although these integrations have been carried out only on these three flames, inspection of all the published data from the IJmuiden tests clearly indicates that although an increase in measured radiation from the flames is always reflected in an increased transfer to the walls, the increase to the walls is less than proportional to that from the flames.

The conclusion to be drawn from these comparisons is that, because a given increase in radiation of the flame does not give a corresponding increase in the transfer to the work, further research on all the factors affecting both radiation and convection in furnaces is of great importance. Also, these results emphasize the important contribution that will be made to the knowledge of heat transfer by radiation when work in the form of water tubes or other materials is placed in the IJmuiden furnace to obtain definite and unquestioned information on the useful rate of heat transfer in various parts of the furnace.

Effect of Preheating Combustion Air. The statistical analysis of the data from performance test No. 7 has not yet been completed. However, Rivière has presented the high lights of the effects of the four variables studied in this test series. Because the preheat of the air for combustion was the variable studied in this series that had not been investigated previously, the following relevant conclusions are quoted from Rivière's paper (10):

"An increase in the temperature of the combustion air from 212 to 1200 F changed only slightly the initial conditions of mixing of the fuel and air, but slowed up the mixing at the end of the flame. The result was an increase of about 10 per cent in the distance required to obtain a stoichiometric mixture.

"For residual-oil flames, the change in the temperature of the air modified neither the content of carbon particles in the flame nor the total emissivity of the flame. In contrast, the emissivity of the coke-oven gas flames decreased by five to ten per cent when the air temperature was increased.

"The temperatures of the flames and of the walls were the two dependent variables the most greatly influenced by the increase in the temperature of the combustion air. Thus, the temperature of the gas on the axis of the flame was increased on the average 260 F with an increase of 990 F in the temperature of the air."

Combustion-Mechanism Tests. As previously stated, the purpose of the combustion-mechanism tests had been to study the process of mixing in the flame, the process of combustion, with particular reference to the content of free carbon in the gas, and to relate these data to the temperature, the radiation, and the emissivity of the flames. In the first series of tests, the difficult procedure for the quantitative determination of the carbon in the gas was not developed with complete success but it was for the second series. No attempt will be made in this paper to summarize the results of these two tests. References (11) and (12) give analyses of the principal findings.

SUMMARY

The international co-operation in industrial research on heat transfer by radiation from flames that is being carried out by the International Flame Research Foundation at IJmuiden and at co-operating laboratories has produced and is producing much valuable information on an incompletely understood subject. The present paper has touched on the high lights of the methods of research and the instrumentation that has been developed.

The effects of the characteristics of the fuels used, the types of burners, the rate of firing, the type of atomizing agent, the method of mixing of combustion air, the amount of excess air, and the temperature of the combustion air have been touched upon. The need for further information on the relation between the radiating power of flames and the heat transferred to the work has been emphasized. It is hoped that an interest has been stimulated to study the detailed reports and to follow the future work.

ACKNOWLEDGMENTS

Emphasis is again to be placed on the fact that the data presented in this paper, with little attempt at original interpretation by the author, have resulted from a vast amount of planning, arduous work in experimentation, and detailed analysis of the data by many European scientists and engineers.

Particular thanks are owing to Prof. J. E. de Graaf, IJmuiden, to Monsieur Michel Rivière, French Institute for Iron and Steel Research, Paris, and for several years Principal Investigator at IJmuiden, to Dr. Marcel Michaud of Air Liquide, Paris, and Secretary of the French Committee, and to Prof. M. W. Thring, Sheffield, who carefully reviewed the original draft of this paper and made many valuable suggestions for its improvement.

Acknowledgment is also made to those members of the American Committee who made helpful suggestions on the original draft, and to the group at Battelle, H. R. Hazard, W. R. Keagy, Jr., W. T. Reid, H. W. Russell, and C. E. Sims, who closely followed the research and who critically reviewed the paper.

BIBLIOGRAPHY

- 1 "Flame Radiation Research," by M. W. Thring, *Industrial Heating*, vol. 19, 1952, pp. 1602-1612, 1724, 1726.
- 2 "Study of the Radiation of the Bunsen Flame," by H. Schmidt, *Annalen der Physik*, vol. 29, 1909, pp. 971-1028.
- 3 "Reports of the 1949 Trials at IJmuiden," eleven papers, *Journal of the Institute of Fuel* (London), vol. 24, November, 1951, and vol. 25, January, 1952.
- 4 Ten of papers of reference (3), in somewhat more complete form, and two additional papers, *Chaleur et Industrie* (Paris), vol. 27, January, February, March, July, August, September, November, 1951; vol. 28, January, June, July, November, 1952.
- 5 "The Results of the Industrial Trials at IJmuiden," by M. Rivière (in French), presented at First Symposium on Flame Radiation, Paris, France, June 23, 1953, conducted by French Committee on Flame Radiation.
- 6 "Results of the Burner Trials at IJmuiden," nine papers, *Journal of the Institute of Fuel* (London), vol. 26, October, 1953.
- 7 The same papers of reference (6), "Liquid Fuel Flames with Injection Burners" (in French), 94 pages, published May, 1954, by French Committee on Flame Radiation, Paris, France.
- 8 "The Radiation From Turbulent Jet Diffusion Flames of Liquid Fuel/Coke-Oven Gas Mixture," three papers, *Journal of the Institute of Fuel* (London), vol. 32, January, 1956, pp. 23-44.
- 9 The same papers of reference (8), "Coke-Oven-Gas and Liquid-Fuel Flames" (in French), 51 pages, published December, 1955, by French Committee on Flame Radiation, Paris, France.
- 10 "Results of Sixth and Seventh Performance Tests," by M. Rivière (in French), presented at Second Symposium on Flame Radiation, Paris, France, December, 1955, conducted by French Committee on Flame Radiation.
- 11 "The Results of Combustion Mechanism Trials in a Diffusion Flame," by M. Leveque, C. Levy, G. Loovet, and M. Michaud (in French), presented at First Symposium on Flame Radiation, Paris, France, June 23, 1953, conducted by French Committee on Flame Radiation.
- 12 "Results of the Second Series of Combustion-Mechanism Tests," by M. Rivière (in French), presented at the Second Symposium on Flame Radiation, Paris, France, December 6, 1955, conducted by French Committee on Flame Radiation.

Appendix

THE AMERICAN FLAME RADIATION COMMITTEE

Chairman, Prof. H. C. Hottel, Massachusetts Institute of Tech-

nology, Cambridge, Mass.; Secretary, F. S. Bloom, Bloom Engineering Co., Pittsburgh, Pa.; Treasurer, J. B. Wagstaff, U. S. Steel Corporation, Monroeville, Pa.

Contributing Companies and Their Representatives

Armco Steel Corporation, Dr. Charles R. Taylor, K. C. McCutcheon; Battelle Memorial Institute, Ralph A. Sherman; Bethlehem Steel Company, Dr. J. E. Eberhardt; Bloom Engineering Company, Inc., Fred S. Bloom; Corning Glass Company, Thomas W. Rochester, Jr.; Inland Steel Company, Frank W. Luerssen; Linde Air Products Company, J. H. Zimmerman; Petro-Chemical Development Company, John W. Throckmorton; Pittsburgh Plate Glass Company, F. R. Hohmann; Richfield Oil Corporation, C. A. Day; Shell Development Company, Dr. Ernest G. Chilton; Sinclair Refining Company, O. F. Campbell; United States Steel Corporation, J. B. Wagstaff; Algoma Steel Corporation, Ltd., A. Dunakowski; Esso Research and Engineering Company, W. T. Knox.

Associate Members

R. C. Corey, U. S. Bureau of Mines; Prof. R. V. Dunkle, University of California; Prof. E. R. G. Eckert, University of Minnesota; Prof. G. A. Hawkins, Purdue University; Prof. H. C. Hottel, Massachusetts Institute of Technology; Dr. S. S. Penner, California Institute of Technology; Dr. Kurt Wohl, University of Delaware; Prof. W. J. Wohlenberg,³ Yale University.

Discussion

J. H. CHESTERS.⁴ The value of IJmuiden lies not so much in the direct application of results to practice as in the stimulation it provides to study one's own particular combustion equipment—with us the open-hearth furnace. In so doing one starts with the advantage of using instruments that have been specifically developed for this type of work, and that only require strengthening to be capable of operating under steel-plant conditions. As will be seen from the forthcoming Special Report No. 59 of the Iron and Steel Institute, attempts are being made in Great Britain to make IJmuiden-type measurements (including flame temperature by the Schmidt method) on actual furnaces, but it may be a long while before it is possible to recommend changes on this basis, since the effect of other factors, e.g., the contribution of convection, are still unknown.

Meantime, spurred on by the work at IJmuiden, we have investigated our oil-burning systems to great advantage. Our first discovery was that pressure drops throughout the system were excessive and that the use of pressure gages on the control panel to control oil and steam flows (still quite common practice), can be most misleading. By fitting larger steam pipes and substantial simplification (and incidentally, therefore, cheapening) of atomizers, ample steam has been made available at the burner tip without the necessity of increasing boiler pressure.

Trials made on a burner rig have enabled the relationship between oil and steam pressure and flow to be evaluated for different types of nozzles and momentum-conversion efficiencies, as determined at IJmuiden, to be found for actual steel-plant burners. This has led not only to the use of more efficient types but has put us in a position to predict in advance the correct nozzle size for substantially increased oil and steam flows. The anomaly in all this work still lies, as the author rightly indicates, in the convection factor. Our own guess would be that in an

³ Deceased.

⁴ Assistant Director of Research, The United Steel Cos. Ltd., Research and Development Department, Swinden Laboratories, Moorgate, Rotherham, England.

open-hearth furnace convection is responsible for, say, 10 per cent of the heat transfer. It is, however, conceivable that whereas doubling the steam flow, as the IJmuiden results suggest, may lower radiation, it may simultaneously double the convection element and thus increase production to the extent observed.

The higher radiation levels obtained at IJmuiden when using compressed-air atomization also have led to arrangements being made for comparative trials in steelworks of air versus steam atomization—trials that would probably never have been arranged without the incentive of greater radiation offered by the IJmuiden data.

The justification for what some people still consider to be the large amount of money being spent at IJmuiden by this uniquely organized team is easy when it is realized that an annual operating cost of about £30,000 only represents a saving in a steelworks making 1,000,000 tons of steel a year of 0.6 gal. of oil per ton of product—a small figure compared with that already achieved in one of our open-hearth shops.

J. E. DE GRAAF.⁵ This paper gives an admirable account of the main lines of the research on flames and their properties by the International Flame Research Foundation. The discussion by a co-worker of this Foundation can thus only be limited to details.

The author correctly states that gas could replace about a third of the calorific input of an oil flame when the radiation of the flame is considered. When convective transfer is considered, the same or a slightly more favorable conclusion can be drawn. It is, however, necessary to warn against a thoughtless application as the results may depend on the way the oil is replaced by gas. "The measurements reported were obtained with a gas flame forming an envelope around the oil flame. It thus replaced probably parts of the oil flame which, because of rapid mixing with the surrounding air, showed little soot formation and contributed only in a small way to the radiation of the flame as a whole. If, e.g., the gas flame were inside the oil flame or if the oil were atomized by gas, the results might be different. This will be investigated in the near future."

It might be of interest to mention that the experiments described in Fig. 18 were undertaken because, at least from a certain angle, one could expect that a decrease in difference of velocity between jet and combustion air would decrease the rate of mixing. Although this factor by itself will be there, it is obviously overpowered by another factor which increases strongly the rate of mixing. Such a factor might be the strong turbulence in the fast-moving air, or the higher oxygen pressure in the air envelope, compared with the normal condition with a dilution of about 50 per cent waste gas (recirculation). It will be necessary to analyze the aerodynamics of two concentric jets in connection with the experiments on pulverized coal, which have been started.

With regard to the question of convection, it is interesting to note that some of the investigations described in the paper were repeated on a 200-ton OH furnace by J. M. van Langen, research physicist at K.N.H.S., IJmuiden. He could confirm the influences on radiation as discussed by the author, including the decrease of specific radiation when the amount of atomizing agent was increased. Experiments on the rate of steel production, however, showed a reverse effect in that the rate of production increased when the amount of atomizing agent was increased for a constant oil consumption per hour. This shows that in this case radiation was not the only effective means of heat transfer; in fact, it points definitely toward an influence of convection because an increase of amount of atomizing agent increased the velocity of the flame gases. This is in keeping with the general

experience that furnace charging should be done so as to avoid a "smooth" surface of the scrap heaps.

M. A. MAYERS.⁶ We owe the author a debt of gratitude for his description of the work being done at IJmuiden. As he points out, the products of this research have been available heretofore only in the foreign literature.

The author's own competence in the field of radiation makes it possible for him to present the leading results of the International Flame Research Foundation in clear summary form. We can hope that this may be only the first of a series of "Progress Reports" by which the author may keep American engineers abreast of this highly significant work.

Many of us are awaiting the results of tests by the Foundation in their pulverized-fuel furnace. It may be expected that this work will provide a long-needed continuation of the author's measurements at Battelle.⁷ In this connection it seems strange that none of the American boiler manufacturers, whose employees include a major fraction of American talent in the application of pulverized-coal flames, is included among the list of companies contributing to the American Flame Radiation Committee.

MICHEL RIVIERE.⁸ This remarkable description of the work done by the International Flame Research Foundation on heat transfer by radiation from flames does not need in itself any comment. However, the writer would like to sum up the results obtained in the light of the industrial applications already achieved.

It should be emphasized here that the Joint Committee has always taken the policy that the work done in IJmuiden should be of general interest to all the contributing industries so that each of them could get something out of the results obtained. Therefore no specific problem of any one industry is taken into the general program of the Foundation. All the development work has to be done by the industries interested and, although it is sometimes impossible to know whether any given improvement originated from the IJmuiden work or from the industry itself, the considerable interest which comes out of this co-operative research has had a stimulating effect on the development of combustion and heat-transfer studies in many European industries.

But interest is not enough to make productive research, and IJmuiden has helped industry in getting the proper instruments necessary for this research. Most of instruments designed for the research of the Foundation have been or are used—and some of them on a large scale—on production furnaces. The most spectacular example is probably the heat-transfer study done recently on petroleum-refining furnaces by means of a "heat-flow meter" designed at IJmuiden, a study which has led to find out means of improving the production of these furnaces by over 10 per cent and reducing the fuel consumption by 17 per cent. Some of the instruments designed by the International Foundation are now being commercialized (for instance, a high-velocity pyrometer for gas-temperature measurements in the range 1800–3000 F, and a portable gas-sampling apparatus). A piece of equipment designed to measure flame monochromatic emissivities at IJmuiden is now being used (in a commercial type) to measure the emissivity of the outgoing gases of steelmaking converters; when the oxidation of the charge is achieved, a sharp change of emissivity occurs, which gives an accurate signal of the time to pour out the steel.

⁵ Chief Mechanical Engineer, Burns and Roe, Inc., New York, N. Y. Mem. ASME.

⁷ "Burning Characteristics of Pulverized Coals and the Radiation From Their Flames," by R. A. Sherman, *Trans. ASME*, vol. 56, 1934, pp. 401–409.

⁸ Institut de Recherches de la Sidérurgie, St. Germain-en-Laye, France.

⁶ Professor, Technological University, Delft, Holland.

The greatest influence of this co-operative research is certainly the increase of productivity achieved on production furnaces in several industries during recent years. The main lines along which these improvements have been obtained are:

An increase of jet momentum (or burner thrust)—which IJmuiden has shown does increase combustion rates, but reduces radiation from the flame (mainly by a reduction of flame emissivity)—has been investigated on many production furnaces and is not always favorable to better production. It improves the melting rates in the open-hearth furnaces, but it not favorable to quick refining periods. An increase of momentum can increase the rate of production in cement kilns, but in glass tanks working at too high values of burner thrust has been found to be detrimental to good production.

A change from steam atomization of oil to air atomization—which increases the radiation of the IJmuiden flames—has led to cheaper production in the open hearth.

The differences observed in the properties of flame produced by different oil burners were found very small on the IJmuiden furnace. This fact has led to simplifying the design of fluid-atomized oil burners, giving better efficiencies (smaller amount of atomizing agent to produce a given momentum). These burners, which need very small maintenance, are now in common use in open hearths, glass tanks, cement kilns, and so on.

Another aspect of the help brought by IJmuiden to the industry is to establish the validity of model work. Owing to the difficulty of measuring flow patterns and concentration distribution in actual production furnaces it is difficult to "calibrate" the models used in these studies. The Joint Committee has done a great deal of work on this subject and it has been possible to prove that cold model measurements enable prediction of the concentration patterns (of fuel and air) in actual furnaces within ± 15 per cent.

Direct applications of results obtained by this international research, use of new instruments and methods by industry, and also training of industrial engineers have largely contributed to increased productivity in European furnace practice in recent

years. Development of this research and further applications to industrial furnaces are still needed and it is our hope that the already important collaboration with American industries can be increased in the coming years.

M. W. THRING.⁹ The writer is happy that such a careful study of our IJmuiden researches has been prepared. It may be of interest to comment on our future program and on the suggestions made by the author. The writer foresees certain future capital items, particularly gas producers for oil and coal, but on the whole we should be able to carry out our major program without further heavy capital expenditure; although in this connection one must admit that the furnaces we have are not suitable in shape for the study of wide-angle liquid-fuel pressure-jet flames.

The author raises the point of applicability of the Schmidt method to our flames. We have checked this carefully and in the regions where the flame is luminous we do not appear to get a significant error from the fact that our background temperature differs from the mean radiant temperature of the flame, but the writer agrees that in the nonluminous tail of the flame there must be an appreciable error. In the luminous region the non-uniformity of temperature through the flame obscures the errors due to the inequality of flame and background temperature. Unfortunately, there is no really good substitute for the Schmidt method and to improve the latter by using a variable-temperature black-body furnace behind the flame would complicate the work very severely.

Another point on which the writer would like to comment is the author's method of comparing flame and wall radiation. The writer agrees fully that the narrow-angle peak-radiation readings show a much bigger difference, say, in going from oil to coke-oven gas, than do the wall radiation or calorimeter readings. However, he believes this can be explained almost entirely by the fact that the flame is conical and not cylindrical so that the part

⁹ Professor of Fuel Technology and Chemical Engineering, University of Sheffield, Sheffield, England.

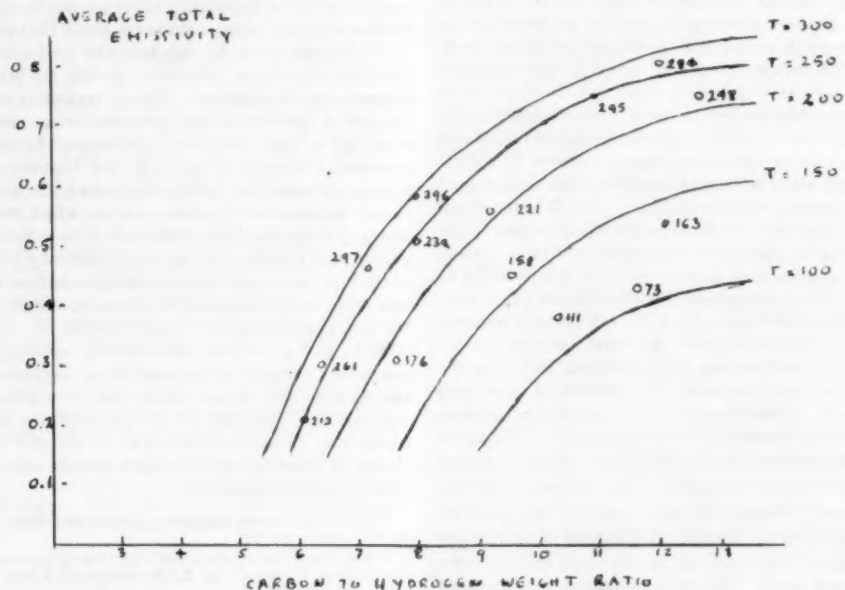


FIG. 22 OBSERVATIONS ON SMALL EXPERIMENTAL FURNACE WITH AIR-ATOMIZED TURBULENT JET-DIFFUSION FLAME (Mean emissivity in the tail of the flame as a function of carbon-hydrogen ratio of fuel with average boiling point of fuel as parameter.)

of the flame which radiates so much more when measured over a fixed angle actually occupies a very small part of the furnace. This is why the wall radiation rises as one goes along the furnace so that, if it were possible to do a complete radiation balance, one would find the comparisons of Figs. 21(a) and (b) to be fully consistent with each other without bringing in convection. The calorimeters provide a measure of the heat flow to the surroundings which would agree closely with that of any other calorimeter flush with the wall. It is true that if one greatly increased the wall cooling as we are doing in the Gothenburg furnace which is entirely water-cooled, or in the pulverized-coal furnace into which water-cooled tubes can be inserted, then the flame will be chilled by the heat loss and radiate differently, but this is a separate control variable and not lack of an essential measurement. The main point is that all the flames are similar at the tail which is the main source of heat to the walls because it fills the furnace but that in a real furnace it is often the level of the peak radiation from the early part of the flame which decides whether one has a keen flame or not.

The author mentions smaller furnaces and the writer would like to state that we have two 18-in-square hot models of the IJmuiden furnace at Sheffield University on which we have studied a wider range of liquid fuels than it has been possible to study at IJmuiden. One set of results is shown in Fig. 22 of this discussion.

Next year we hope to study at IJmuiden low-volatile coal in the pulverized-coal furnace among other variables, to follow up this year's trial. A trial on high-efficiency burners and the use of carbon black in oil, a variable suggested by the American Committee, is now under way.

It is a great satisfaction that we are able to make progress by unofficial international co-operation on a problem that is too costly for the industry of any one country, and we welcome all the help and discussion that we have received and we hope to receive from the United States.

AUTHOR'S CLOSURE

The comments of the several discussers are appreciated.

None of them raises any special issues concerning points covered in the paper and thus does not require a specific reply.

The fact that all but one of the written discussions came from abroad is of interest. One might conclude that this demonstrates a lack of interest on the part of American fuel consumers in the subject. The existence of the American Committee proves that this is not wholly true, but in consideration of the amount of fuel consumed in this country, it is clear that the support of the International Flame Research Foundation should be greater than it is relative to the support abroad. Mr. Mayers has raised an interesting point in calling attention to the lack of support by the boiler manufacturers of the United States. The performance of a boiler in regard to circulation, to furnace slagging, and to the formation of bonded deposits in superheaters and boiler passes is affected greatly by furnace temperatures and hence by radiation from flames. A better understanding of this action might point the way to an alleviation of some of these difficulties.

The examples of savings of fuel and of increased output from furnaces cited by Dr. Chesters, Professor de Graaf, and M. Rivière as stemming from the results of the IJmuiden research should arouse more interest in the program than do the technical data presented in the paper.

Although not presented as written discussions, the author had had two letters from abroad citing omissions in the paper which he takes this occasion to correct.

Mr. E. Schneider of the High Authority of the European Community of Coal and Steel has called attention to the fact that the IJmuiden research is not a unique example of international co-operation as experimental research on the Low Shaft Blast Furnace has been under way at Liège with international industrial support for several years.

Prof. G. M. H. Burnay, Director of the Thermodynamics Laboratory of the University of Liège has pointed out that he has constructed a furnace similar to the IJmuiden furnace near Ougrée and that experimental research is under way. He proposed to investigate in detail the applicability of the Schmidt method for the determination of flame emissivities and temperatures about which the author has raised some question.

Rate of Temperature Change of Simple Shapes

BY VICTOR PASCHKIS¹ AND J. W. HLINKA,² NEW YORK, N. Y.

Charts have been prepared showing rates of temperature change in simple shapes plotted against temperature. Additional curves show time values, so that one graph yields any of the three relationships: Rate-temperature, rate-time, temperature-time. Samples of the charts are shown, examples of use are given, and limits of the graphs are tabulated. Methods used in establishing the charts are given.

NOMENCLATURE

The following abbreviations are used; typical dimensions are added in parentheses. However any consistent units may be used.

- c = specific heat (Btu/lb, F)
- h = boundary conductance (Btu/sq ft, hr, F)
- k = thermal conductivity (Btu/ft, hr, F)
- L = critical dimension of body (see below) (ft)
- t = temperature (F); subscripts used:
 - a —ambient, after step change
 - i —initial value, constant through body; before step change
 - n —at point having distance x/L from center
- x = distance of any given point from center of body (ft)
- α = thermal diffusivity, $\alpha = k/c\rho$ (sq ft/hr)
- ρ = density (lb/cu ft)
- τ = time (hr)

The critical dimension is the half thickness in the case of the slab, and the radius in case of cylinder and sphere

$$N_{FO} = \alpha\tau/L^2 \text{ Fourier number} \dots\dots\dots [1]$$

$$\theta = \frac{t_n - t_a}{t_i - t_a} \text{ dimensionless temperature} \dots\dots\dots [2]$$

The subscript n is used to indicate the dimensionless position at which the dimensionless temperature is taken

$$m = k/hL \text{ relative boundary resistance}^3 \dots\dots\dots [3]$$

$$n = x/L \text{ relative position} \dots\dots\dots [4]$$

$$\partial\theta/\partial N_{FO} \text{ rate of temperature change in dimensionless terms}$$

INTRODUCTION

The rate of temperature change in an object is important in

¹ Technical Director, Heat and Mass Flow Analyzer Laboratory, Columbia University. Mem. ASME.

² Research Engineer, Heat and Mass Flow Analyzer Laboratory, Columbia University.

³ In convection terms this unit would be described as the inverse of the Nusselt number.

Contributed by the Research Committee on Heat Conduction Charts and presented at a joint session with the Heat Transfer and Fuels Divisions and the Research Committee on Furnace Performance Factors at the Annual Meeting, New York, N. Y., November 25-30, 1956, of THE AMERICAN SOCIETY OF MECHANICAL ENGINEERS.

NOTE: Statements and opinions advanced in papers are to be understood as individual expressions of their authors and not those of the Society. Manuscript received at ASME Headquarters, August 7, 1956. Paper No. 56-A-118.

many operations; rates are important in connection with thermal stresses, they are critical for the hardness of metals obtained in heat-treating, they influence the optical properties of glass, they may be significant in the course of chemical reactions. This list, of course, is not meant to be complete but merely illustrative of cases where the rates of temperature change are important.

The rate of temperature change is dependent on both time of heating or cooling and location within the body. Sometimes the question may arise, what is the rate at a certain time after start of heating or cooling; but probably more often it is desired to know the rate at any point in the body at the moment when this point is at a certain critical temperature. Calculation of the rates, even for the simplest shapes is a time consuming matter, and therefore charts have been developed to determine such rates for the three simple shapes: The slab, cylinder, and sphere. In each case the shape is originally at constant temperature throughout and the ambient in which the shape finds itself undergoes a step change of temperature.

In the present paper, samples of these charts are presented, the arrangement of the charts is reviewed, and a list of the available charts for this problem is given. The development of these charts is part of an ASME sponsored project to set up a number of charts in the field of heat transfer. Suggestions for other problems for which charts would be desirable are invited. Correspondence should be addressed to the senior author.

OLD CHARTS

A large number of charts have been published from which the temperatures within a body of one of the three simple shapes (slab without end effects; long cylinder; sphere) can be read if the body is initially at constant temperature throughout, and at time zero the temperature of the ambient undergoes a step change (1-4).⁴ Probably the most complete presentation was made by Heisler (5). Lacking other curves, rates of temperature change had heretofore to be found by determining the slope of the time-temperature curves at the temperature in question. This was inaccurate because of the scales used in presenting the time-temperature relationships.

Rates as function of time for the problem just mentioned have been published (6) by the authors' laboratory. This publication suffers from two limitations: (a) Instead of giving the rates at the surface, rates are shown for a point close to, but below the surface; and (b) the rates are plotted against time, while in many instances it is desired to know the rates as function of the temperature prevailing at the point. An answer to the latter question required—prior to the availability of the present charts—the determination of the time elapsed after the step change of the ambient temperature to reach the desired temperature value at the given point in the body; this time can be found, for example, from the Heisler charts (5). And then the rates at this temperature can be found by going to the rate-time charts (6). The new charts to be discussed eliminate the necessity for this dual approach, for they yield the time-temperature function, time-rate function, and the temperature-rate functions.

⁴ Numbers in parentheses refer to the Bibliography at the end of the paper.

DIMENSIONLESS UNITS

All charts—those mentioned before and those discussed in this paper—are presented in dimensionless units. This manner of presentation makes the charts as general as possible.

SAMPLE CHART

A total of 11 charts is used to represent the results, all of which are plotted in the same way. Fig. 1 is a sample chart.

- (a) The abscissas are dimensionless temperatures, θ .
- (b) The ordinates are dimensionless temperature rates, $\partial\theta/\partial N_{Fo}$.
- (c) One family of curves is presented for various values of the dimensionless boundary resistance, m .
- (d) Another family of curves is presented for various values of the dimensionless time or Fourier number, N_{Fo} .

At time $\tau = 0$, temperature $t_a = t_s$, and hence $\theta = 1$. As time progresses, θ decreases, approaching zero as time approaches infinity. The rate curves start from zero at $\theta = 1$ (except at the surface: See the following section), increase first steeply, reach a maximum, and then decrease to zero again at $\theta = 0$. The rates for any value of θ and for any condition (shape; position) are higher, the lower the value of m is.

Since the lower part of the graph is difficult to read, an insert is added which is an enlargement of this region.

It will be noted from Fig. 1 that a second set of curves is plotted in the main graph over the same abscissa axis; this second set gives dimensionless times N_{Fo} . In this way one graph permits reading of the following relationships: Rate-temperature, rate-time, temperature-time.

All rates are negative because the numerator in the expression for θ becomes smaller as time progresses, both in heating and in cooling. Absolute rates are, of course, positive in heating, negative in cooling.

The sample chart, Fig. 1, holds for the mid-point ($n = 0.5$) of a slab being cooled, and a few examples will show its utilization.

Example 1. A steel slab, 3 in. thick, but long and wide enough to disregard end effects, is originally at a uniform temperature of 1600 F. It is cooled in a cooling medium of 100 F, with a boundary conductance of 3000 Btu/sq ft, hr, F. What is the rate of cooling at a point 0.75 in. below the surface, when this point is at 1300 F? At what time is this temperature reached? The properties of the steel are chosen as follows:

$$\begin{aligned} c &= 0.15 \text{ Btu/lb F} \\ k &= 18 \text{ Btu/ft, hr, F} \\ \rho &= 485 \text{ lb/cu ft} \end{aligned}$$

Hence

$$\begin{aligned} \alpha &= 18/(0.15 \times 485) = 0.248 \text{ sq ft/hr} \\ L &= 3/2 \text{ in.} = 0.125 \text{ ft} \\ x/L &= 0.75/1.5 = 0.5 \\ \alpha/L^2 &= 15.9 \text{ 1/hr} \\ m &= 18/0.125 \times 3000 = 0.048 \\ \theta &= (1300 - 100)/(1600 - 100) = 0.80 \end{aligned}$$

Locate on the abscissa axis, Fig. 1, the value $\theta = 0.80$. Since no curve is available for $m = 0.048$, read the values

$$\begin{aligned} \text{at } m &= 0.04 & \partial\theta/\partial N_{Fo} &= -2.50 \\ \text{at } m &= 0.05 & \partial\theta/\partial N_{Fo} &= -2.44 \end{aligned}$$

and by linear interpolation

$$\text{for } m = 0.048 \quad \partial\theta/\partial N_{Fo} = -2.45$$

In order to find the actual rate, multiply the dimensionless rate by $(t_s - t_a)$ and by α/L^2 . Hence, in the present example

$$(t_s - t_a) = 1500$$

$$\alpha/L^2 = 15.9$$

Therefore the rate is

$$\frac{\partial(t_s - t_a)}{\partial \tau} = (-2.45)(+1500)(15.9) = -58,400 \text{ F/hr}$$

At the intersection of a vertical line erected at $\theta = 0.80$ with the (estimated) position of $m = 0.048$ there is a line of $N_{Fo} = 0.091$ (this line may be visually interpolated). Hence

$$\tau = N_{Fo}/(\alpha/L^2) = 0.091/15.9 = 0.00572 \text{ hr}$$

Example 2. A piece of ceramic 0.5 in. thick is initially at a uniform room temperature of 70 F and is heated in such a manner that heat is received only by one side while the other can be considered for purposes of calculation to be completely insulated. The ceramic is brought suddenly into an ambient of 2070 F. What is the rate of temperature increase at a point 0.25 in. below the surface, when this point reaches a temperature of 900 F? At what time do this rate and temperature occur? The boundary conductance from the surface to the surrounding of the ceramic is 25 Btu/sq ft, hr, F.

Assume the properties of the ceramic as follows

$$\begin{aligned} c &= 0.25 \text{ Btu/lb, F} \\ k &= 0.15 \text{ Btu/ft, hr, F} \\ \rho &= 30 \text{ lb/cu ft} \end{aligned}$$

Hence

$$\alpha = 0.15/(0.25 \times 30) = 0.02 \text{ sq ft/hr}$$

Since heating is only from one side, the critical thickness equals the total thickness of the body: $L = 0.5 \text{ in.} = 0.0417 \text{ ft}$

$$\begin{aligned} \alpha/L^2 &= 0.02/0.0417^2 = 11.5 \text{ 1/hr} \\ m &= 0.15/25 \times 0.0417 = 0.144 \\ \theta &= (900 - 2070)/(70 - 2070) = 0.585 \end{aligned}$$

By following the same procedure as in example 1 one finds the dimensionless rate

$$\partial\theta/\partial N_{Fo} = -1.12$$

Hence the actual rate, by multiplying with $(70 - 2070)$ and by 11.50 is

$$\partial\theta/\partial N_{Fo} = +25,800 \text{ F/hr}$$

At the intersection of the vertical line erected at $\theta = 0.585$ with the (estimated) position of $m = 0.144$ there is an interpolated line, $N_{Fo} = 0.265$ from which the actual heating time may be obtained. Hence

$$\tau = N_{Fo}/(\alpha/L^2) = \frac{0.265}{11.5} = 0.023 \text{ hr}$$

RATES AT SURFACE

It has been mentioned before that the course of the rate curves at all points in all shapes is essentially similar, except at the surface. Since the ambient undergoes a step change in temperature, the rate at the surface at the moment when the step change occurs is infinite. Just before the step change of the ambient, a constant initial temperature exists, and the rate of temperature change is, of course, zero; at the instant of change a discontinuity occurs, but as the value of θ drops below 1, the dimensionless rate becomes finite and rapidly decreases. For any given value of θ , the rates are higher, the lower the m value is.

Fig. 2 may serve as example for one of the surface-rate charts.

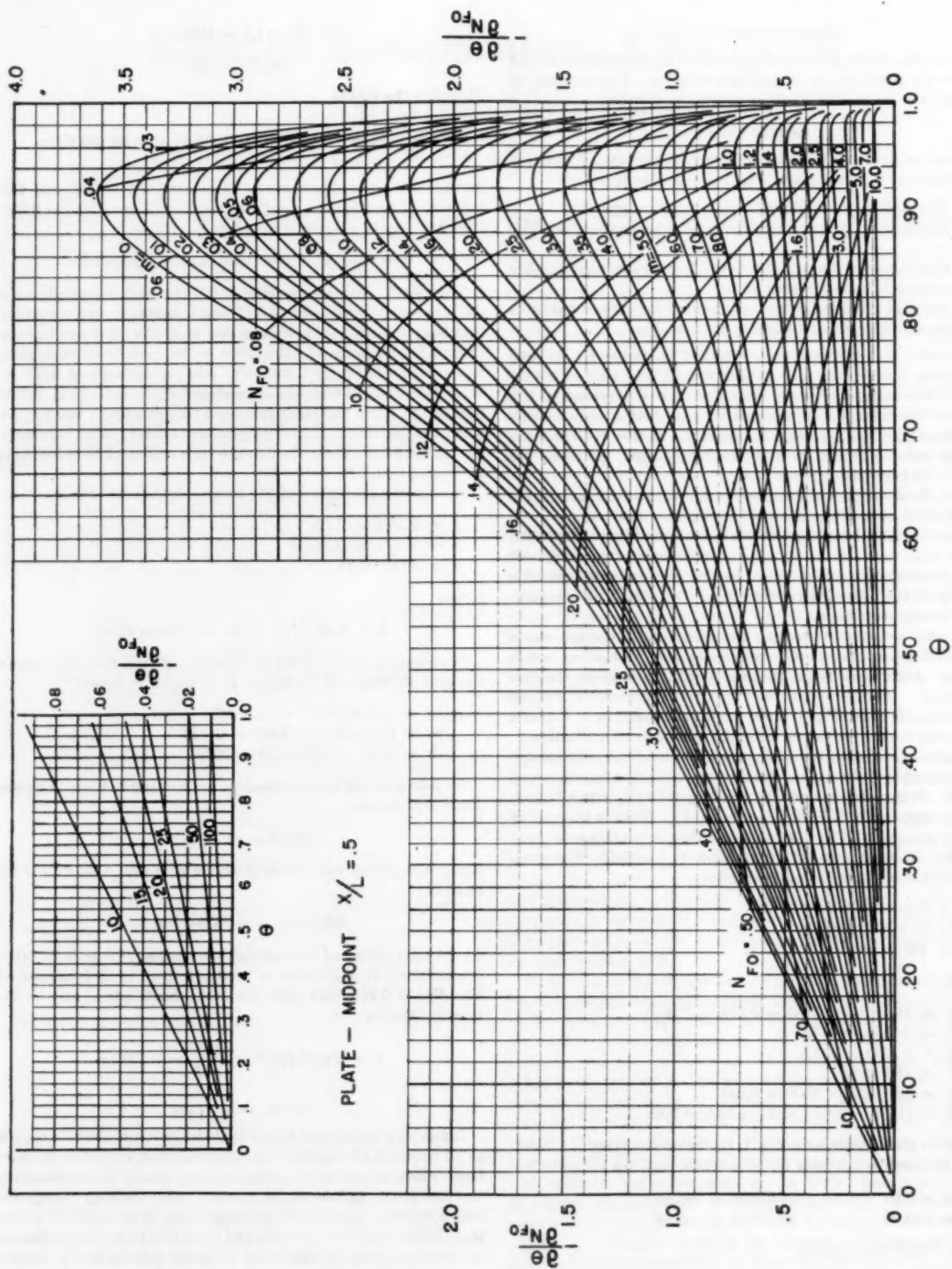


FIG. 1 RATE OF TEMPERATURE CHANGE AND TIME PLOTTED AGAINST TEMPERATURE. PLANE AT $1/4$ OF TOTAL THICKNESS BELOW SURFACE. PLATE HEATED OR COOLED FROM BOTH SIDES

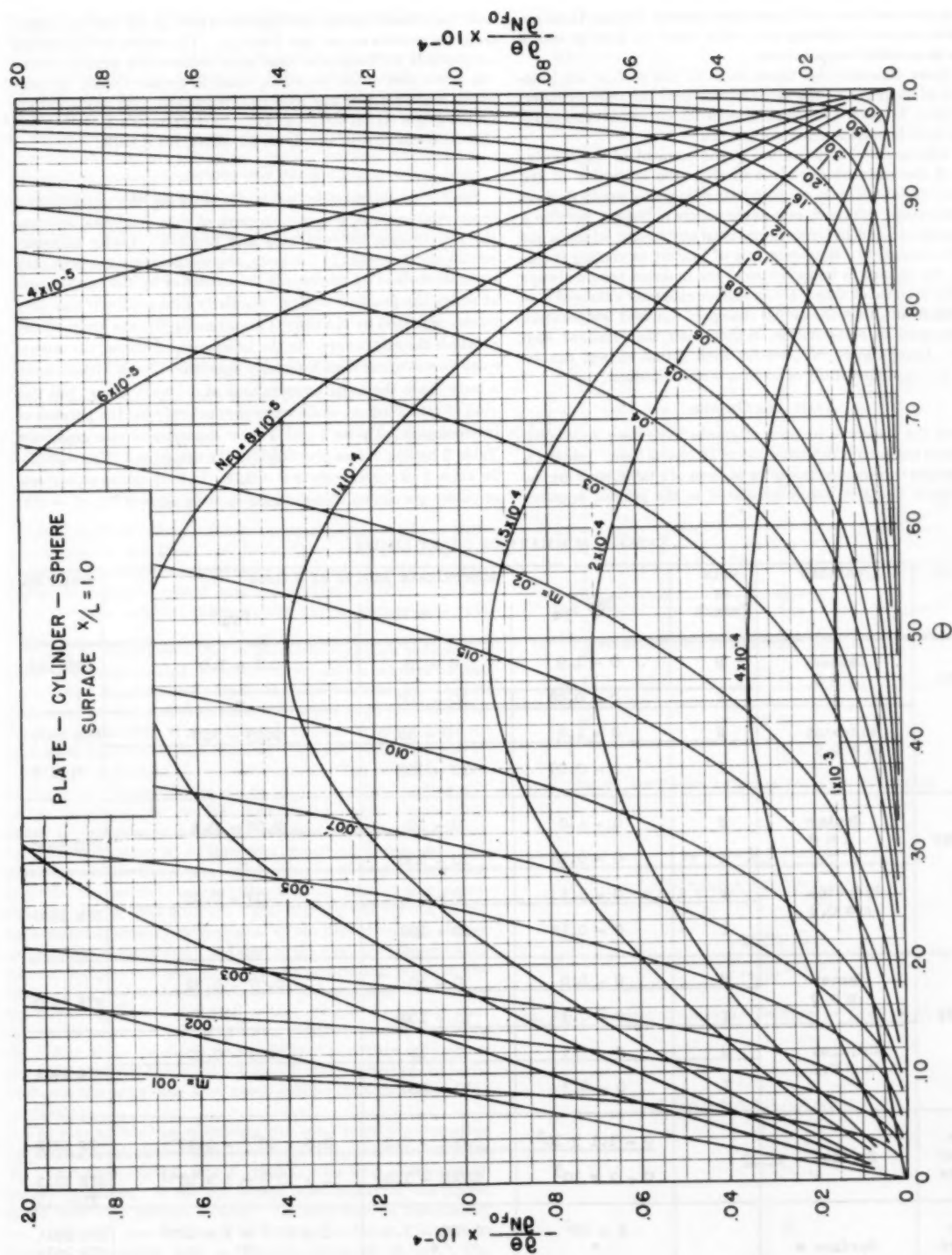


FIG. 2 RATE OF TEMPERATURE CHANGE AND TIME PLOTTED AGAINST TEMPERATURE. FOR THE SURFACE OF A PLATE, CYLINDER, OR SPHERE, HEATED OR COOLED FROM BOTH SIDES

The temperature lines are of particular interest because there are no charts available showing very early times to heat or cool a surface to specified temperatures.

For short dimensionless times, rates at the surface are independent of shape; i.e., the same curves hold for slab, cylinder, and sphere; however as time progresses the curves deviate as indicated later in the tabulation of graphs.

The infinite rate at the surface at the moment of the step increase of the ambient can serve to show the limitation of the concept; an infinite rate of temperature increase would destroy most materials; but such rate never occurs in nature, because a step change in ambient temperature is an abstraction which is not actually obtainable. Whatever way of heating or cooling is employed, the change in temperature of the ambient occurs always in a finite interval of time. If the surface rate near values of $\theta = 1.0$ is important, then the actual change of ambient temperature must be used in computation, rather than the idealized step change. Computation of rates for such actual change can be carried out mathematically or by means of computers.

AVAILABLE GRAPHS

Within the project, a number of graphs have been developed. Space does not permit reproduction of all charts here. Instead a list of graphs is presented hereafter in form of a table, showing the approximate limits of values presented in the graphs, together

with the number under which prints of each graph can be ordered from the authors at cost (see Table 1). The charts for the surface supplement each other so that each consecutive number shows the lower part of the preceding chart in greater detail; because of the scale, rates of say 1000 cannot be read with any accuracy on the graph (HTR 1912) for a maximum rate of 1.1×10^5 ; but the value can be read simply on the chart, HTR 1913.

RATE GRADIENTS

Similar to temperature gradients, showing the temperature-space relationships, one can conceive of rate gradients, showing the relationship between rate and position. Under transient conditions at a point in the body, the temperature gradient may be characterized by the time of occurrence or by the temperature at which the gradient occurs. Similarly rate gradients also may be characterized by the time of occurrence or by the temperature at which the rate occurs. In the latter case, of course, the several rates do not occur simultaneously since the different positions in a body reach the same temperatures at different times; but this kind of rate gradient could serve conveniently for the purpose of interpolation. Tables 2 and 3 show examples of rate gradients, Table 2 having values identified by the same time ($N_{Fo} = 0.25$). In Table 3 all curves refer to $\theta = 0.75$. In both tables several sets of values are shown, one each for $m = 0$; $m = 0.01$; $m = 0.1$;

TABLE 1 SUMMARY OF CHART LIMITS

Shape	Position	Main or Insert	Approximate Limits of Values			Graph No.
			$\partial\theta/\partial N_{Fo}$	m	N_{Fo}	
Plate	Center $n = 0$	M	0 - 1.9	0 - 10	0.1 - 1.0	HTR 1906
		I	0 - 0.09	10 - 100	-	
	Midpoint $n = 0.5$	M	0 - 4.0	0 - 10	0.03 - 1.0	HTR 1907
		I	0 - 0.09	10 - 100	-	Fig. I
Cylinder	Center $n = 0$	M	0 - 4.0	0 - 10	0.08 - 0.6	HTR 1908
		I	0 - 0.18	10 - 100	-	
	Midpoint $n = 0.5$	M	0 - 5.5	0 - 10	0.03 - 0.40	HTR 1909
		I	0 - 0.18	10 - 100	-	
Sphere	Center $n = 0$	M	0 - 6.0	0 - 10	0.07 - 0.32	HTR 1910
		I	0 - 0.3	10 - 100	-	
	Midpoint $n = 0.5$	M	0 - 7.5	0 - 10	0.03 - 0.30	HTR 1911
		I	0 - 0.3	10 - 100	-	
Plate Cylinder Sphere	Surface		$0 - 1.1 \times 10^5$	0.001 - 0.2	$1.5 \times 10^{-6} - 1 \times 10^{-4}$	HTR 1912
			$0 - 2 \times 10^3$	0.001 - 1.0	$4 \times 10^{-5} - 1 \times 10^{-3}$	HTR 1913 Fig. II
Plate Cylinder Sphere	Surface *		2×10^2	0.001 - 1.0	$4 \times 10^{-4} - 1 \times 10^{-2}$	HTR 1914
		"	"	"	"	HTR 1915
		"	"	"	"	HTR 1916

* Here the plate, cylinder, and sphere values deviate, and separate charts are presented.

$m = 1.0$. In order to make comparison more meaningful, both tables are for a plate.

Fig. 3, finally, gives one comparison of the steepness of the rate gradients for different shapes. It holds for $\theta = 0.75$ (same as Table 3) and shows the rate gradients for plate, cylinder, and sphere for $m = 1.0$ (solid lines) and $m = 0$ (broken lines). The difference between the shapes decreases with increasing value of m . Obviously the gradient is steepest near the surface; interpolation here is often most difficult, and possibly additional curves might be desirable for the three shapes, holding for a value of $n = 0.9$.

TABLE 2 RATE GRADIENTS IN PLATE FOR EQUAL TIME

m	$\frac{\partial \theta}{\partial N Fo} = f(m); N Fo = 0.25$		
	$x/L = 0$	$x/L = 0.5$	$x/L = 1.0$
0	0.166	1.22	0
0.01	0.165	1.22	0.0284
0.1	0.149	1.21	0.221
1.0	0.60	0.625	0.540

TABLE 3 RATE GRADIENTS IN PLATE FOR EQUAL TEMPERATURES θ

m	$\frac{\partial \theta}{\partial N Fo} = f(m); \theta = 0.75$		
	$x/L = 0$	$x/L = 0.5$	$x/L = 1.0$
0	1.775	2.52	0
0.01	1.75	2.425	1.275×10^{-4}
0.1	1.476	1.84	128
1.0	0.555	0.56	1.3

METHOD OF COMPUTATION

Points Inside the Body. Rates for points inside the body were determined on the Heat and Mass Flow Analyzer, using the electric-analogy method previously described (7). It does not appear necessary to repeat here the method in detail; but one point deserves mention; namely, the way to measure the rate itself.

It may be remembered that in the electric-analogy method the body to be investigated is broken down into a number of discrete lumps (in the present study 15 lumps were used). Within each lump a resistance represents the resistance to heat flow (inverse of conductivity \times shape factor), and an electric capacitance represents the heat storage capacity: Specific heat \times volume \times density. One element of such electric computing circuit is shown in Fig. 4(a). Computations can be made either for "heating up" or for "cooling." In the first case the uncharged circuit is exposed at time zero to a constant voltage; in the latter case the fully charged circuit is, at time zero, grounded at one end. Results—as also do the charts—apply equally to heating and cooling. In the present computations cooling (discharging a pre-charged circuit) was selected. The current flowing out of the capacitance is directly proportional to the rate of voltage change at this point in the circuit; and this, in the analogy, represents the rate of temperature change at the corresponding point in the body. Every current measurement causes a voltage drop across the measuring device; and such voltage drop, in the present case, represents an error. By using a very small measuring resistance (R_e in Fig. 4b) in the circuit (so small that the voltage drop across the measuring resistance did not exceed 0.02 per cent of the nodal voltage), the error was kept much smaller than the instrument readability.

The rate as function of voltage was established by measuring two voltages simultaneously, one at point V_e , the other at point V_o . Of course, both V_e and V_o change with time as the capacitance discharges. If an $x-y$ plotter were available, the curves could have been plotted directly. Lacking such an instrument, the voltage V_o was measured by means of a Leeds & Northrup Speedomax recorder with a full-scale range of 10 mv. The voltage V_e which is much higher (30-100 volts) necessitated the use of an amplifier.

Surface. Rates at the surface cannot be determined ac-

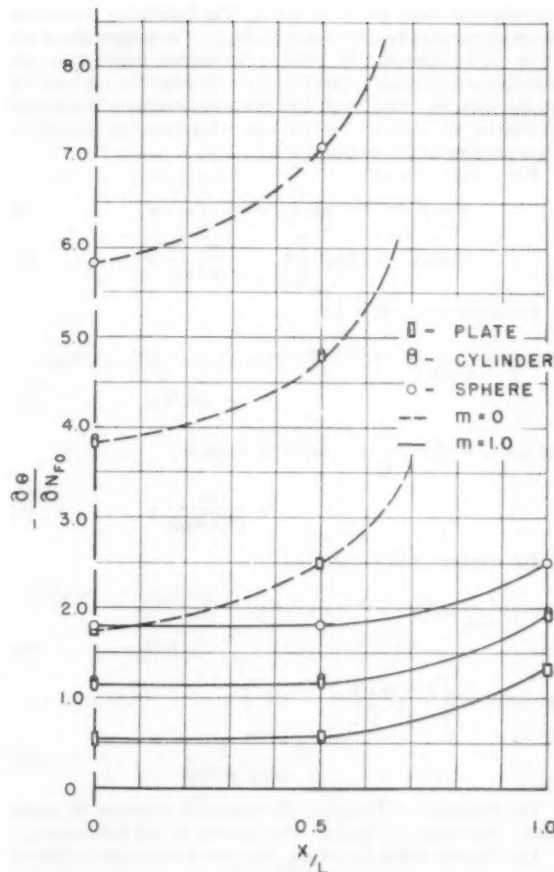


FIG. 3 INFLUENCE OF SHAPE ON RATE GRADIENTS

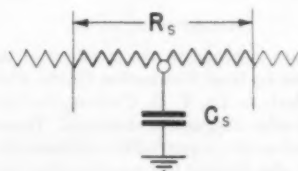


FIG. 4(a) TYPICAL ELEMENTAL SECTION OF COMPUTING CIRCUIT

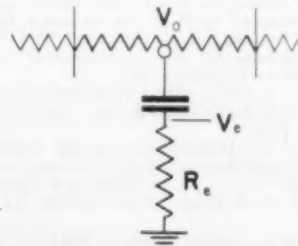


FIG. 4(b) ELEMENT WITH RATE MEASURING RESISTOR R_e

curately with finite spatial elements. The inaccuracy is worse at the start but rapidly decreases with time. The magnitude of the error can be decreased by using in the surface region finer and finer lumps and would vanish entirely with infinitely fine lumping at the surface. Since such fine lumping presents experimental difficulties, the surface rates were computed, based on the following equations for low values of N_{FO} :

For a plate, $x/L = 1.0$

$$\theta = e^{(1/m)^2 N_{FO}} \operatorname{erfc}(1/m) \sqrt{(N_{FO})} + \dots \dots \dots [5]$$

$$\partial\theta/\partial N_{FO} = (1/m)^2 \left[\theta - \frac{m}{\sqrt{(\pi N_{FO})}} + \dots \right] \dots \dots [6]$$

For a cylinder, $x/L = 1.0$

$$\theta = \frac{1}{1-3m/8} \{ e^{(1/m-3/8)^2 N_{FO}} \operatorname{erfc}[(1/m-3/8) \sqrt{(N_{FO})}] - 3m/8 + \dots \} \dots \dots [7]$$

$$\partial\theta/\partial N_{FO} = (1/m)^2 \left[(1-3m/8)^2 \theta + 3m/8 - \frac{m}{\sqrt{(\pi N_{FO})}} + \dots \right] \dots \dots [8]$$

For a sphere, $x/L = 1.0$

$$\theta = \frac{1}{1-m} \{ e^{(1/m-1)^2 N_{FO}} \operatorname{erfc}(1/m-1) \sqrt{(N_{FO})} - m + \dots \} \dots \dots [9]$$

$$\partial\theta/\partial N_{FO} = \left(\frac{1-m}{m^2} \right) \left[(1-m)\theta + m - \frac{m}{1-m} \frac{1}{\sqrt{(\pi N_{FO})}} + \dots \right] \dots \dots [10]$$

The derivation of Equation [5] is given in reference (8) (page 252). Equations [6] to [10] were derived in this laboratory.

The Fourier series describing the time-temperature relations are well known [e.g., Jakob (9)]. Differentiation of these series gives the rates. For high values of N_{FO} it is sufficient to use but the first term; hence evaluation of the rates is simple. This method was used for the three shapes at $x/L = 0.5$ and $x/L = 0$.

ACKNOWLEDGMENTS

The authors are indebted to the members of the ASME Research Committee on Heat Conduction Charts which guides this project, particularly to Dr. T. H. Chilton, the former chairman and Dr. A. C. Mueller, the present chairman. Thanks are also due to Dr. H. G. Landau who suggested the mathematical solution for the surface and who derived the equations for the cylinder and sphere.

BIBLIOGRAPHY

- 1 "Charts for Estimating Temperature Distributions in Heating or Cooling Solid Shapes," by H. P. Gurney and J. Lurie, *Industrial and Engineering Chemistry*, vol. 15, 1923, pp. 1170-1172.
- 2 "Die Grundgesetze des Wärmeüberganges," by H. Groeber, Julius Springer, Berlin, Germany, 1921.
- 3 H. Hottel as quoted in "Heat Transmission," by W. H. McAdams, McGraw-Hill Book Company, Inc., New York, N. Y., third edition, 1954, pp. 36-38.
- 4 "Tafeln über die Abkühlungsvorgänge Einfach Körper," by H. Bachmann, Julius Springer, Berlin, Germany, 1938.
- 5 "Temperature Charts for Induction and Constant-Temperature Heating," by M. P. Heisler, *Trans. ASME*, vol. 69, 1947, pp. 227-236.
- 6 "Establishing of Cooling Curves of Welds by Means of Electrical Analogy," by V. Paschakis, *Welding Journal*, Welding Research Supplement, vol. 22, 1943, pp. 462s-483s.

7(a) "A Method for Determining Unsteady-State Heat Transfer by Means of an Electrical Analogy," by V. Paschakis and H. D. Baker, *Trans. ASME*, vol. 64, 1942, pp. 105-112.

7(b) "Heat and Mass Flow Analyzer," by V. Paschakis, *Scientific Monthly*, vol. 73, no. 2, 1951, pp. 81-88.

8 "Conduction of Heat in Solids," by H. J. Carslaw and J. C. Jaeger, University Press, Oxford, England, 1950.

9 "Heat Transfer," by M. Jakob, John Wiley & Sons, Inc., New York, N. Y., vol. 1, 1949.

Discussion

M. P. HEISLER.⁵ As the authors correctly point out, rates of temperature change are important in many industrial operations. The method of plotting used in this paper has a distinct advantage over the method previously used by the senior author in that it greatly broadens the areas in which the chart can be applied usefully.

It may be appropriate to call attention to a number of minor errors in context and in the equations. The authors' statement that an infinite rate of temperature increase would destroy most materials is questionable. The implication here is that an infinite rate would set up such large internal thermal stresses that material failure inevitably would follow. Thermal stresses are not induced by temperature rates per se but by internal temperature differences. An object whose temperature increases uniformly at an infinite rate will have no thermal stresses. Rupture cannot occur unless internal temperature differences are large enough to bring the material fibers beyond their ultimate strength.

Familiar examples in which temperature rates do not destroy materials occur daily in quenching operations and in pressing heated platens against cooler objects. For all practical purposes the temperature rates involved here are infinite, yet failure does not occur simply because sufficiently large temperature differences are not involved.

The inclusion of $-m$ and $+m$ in Equations [9] and [10] is incorrect. Equation [10] also appears to have additional inaccuracies. It should be written

$$\frac{\partial\theta}{\partial N_{FO}} = \left(\frac{1-m}{m^2} \right) [\theta - m/(1-m) \sqrt{(\pi N_{FO})} +]$$

That this is true can be seen immediately by comparing Equations [5] and [9], which differ only in that Equation [9] uses $[(1/m) - 1]$ whereas Equation [5] uses $1/m$. Hence their derivatives with respect to N_{FO} should differ only in these terms.

P. J. SCHNEIDER.⁶ The authors of this paper, together with the ASME Research Committee on Heat Conduction Charts, have recognized the need for providing temperature-rate curves for workers in this field who have long since lost their enthusiasm in appealing to the slowly converging series solutions. Regarding suggestions for additional charts, the writer inquires as to whether consideration has been given to the semi-infinite solid $x > 0$. This shape is not only technically important in itself but it provides a close approximation to the plane plate for the early period of heating or cooling. The semi-infinite solid can be treated analytically for all values of τ since the solution for θ is in closed form. From Reference (8)⁷ the temperature solution expressed in the authors' nomenclature is

$$\theta = \operatorname{erf}(n/2 \sqrt{N_{FO}}) + e^{(n+N_{FO}/m)/m} \operatorname{erfc}[n/2 \sqrt{N_{FO}} + \sqrt{(N_{FO})/m}] \dots \dots [11]$$

⁵ Atomic International, Canoga Park, Calif. Mem. ASME.

⁶ Heat Transfer Laboratory, University of Minnesota, Minneapolis, Minn.

⁷ Page 53.

Differentiation with respect to N_{FO} gives

$$N_{FO}(\partial\theta/\partial N_{FO}) = \left\{ \xi \operatorname{erfc} [(N_{NU}/2 + \xi)/\sqrt{\xi}] - (\xi - N_{NU}/2)e^{-(N_{NU}/2 + \xi)^2/\xi} / \sqrt{\pi\xi} \right\} e^{(N_{NU} + \xi)} - N_{NU}e^{-N_{NU}/4\xi} / 2\sqrt{\pi\xi} \dots [12]$$

with the dimensionless abbreviations (x measured from the surface)

$$N_{NU} = hx/k, \quad \xi = h^2\alpha\tau/k^2 \dots [13]$$

The surface temperature ($n = 0$) is given by Equation [11], herewith, as

$$\theta_0 = e^\xi \operatorname{erfc} \sqrt{\xi} \dots [14]$$

and the heating or cooling rate is taken from Equation [12] as

$$N_{FO}(\partial\theta/\partial N_{FO})_0 = \xi e^\xi \operatorname{erfc} \sqrt{\xi} - \sqrt{(\xi/\pi)} \dots [15]$$

Similar results for the temperature gradient are given by

$$\sqrt{(N_{FO})}(\partial\theta/\partial n) = \left\{ \sqrt{(\xi)} \operatorname{erfc} [(N_{NU}/2 + \xi)/\sqrt{\xi}] - e^{-(N_{NU}/2 + \xi)^2/\xi} / \sqrt{\pi} \right\} e^{(N_{NU} + \xi)} + e^{-N_{NU}/4\xi} / \sqrt{\pi} \dots [16]$$

and

$$\sqrt{(N_{FO})}(\partial\theta/\partial n)_0 = \sqrt{(\xi)}e^\xi \operatorname{erfc} \sqrt{\xi} \dots [17]$$

Some calculated values are given in Table 4, and the surface heating or cooling rate is shown in Fig. 5 of this discussion.

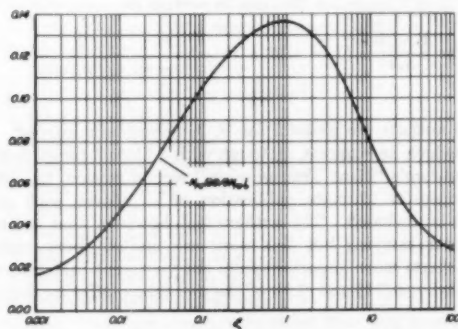


FIG. 5

TABLE 4

ξ	θ_0	$N_{FO}(\partial\theta/\partial N_{FO})_0$	$\sqrt{(N_{FO})}(\partial\theta/\partial n)_0$
0.001	0.96530	-0.01688	0.03053
0.01	0.89646	-0.04745	0.08965
0.1	0.72358	-0.10605	0.22882
1	0.42758	-0.13661	0.42758
10	0.17048	-0.07928	0.53912
100	0.05614	-0.02780	0.56141

The result obtained by substituting Equation [14] in [15] is equivalent to Equation [6] of the paper, derived for small N_{FO} . This follows from the fact that in the early period of heating or cooling the plate behaves as a semi-infinite solid. Thus, while Equation [6] holds for the plate with small N_{FO} , it holds for all N_{FO} when referred to the semi-infinite solid $x > 0$. The writer feels that Equations [12] and [16] plotted with N_{NU} as the independent variable and ξ a parameter would serve as a useful supplement to the valuable charts already prepared in the Heat and Mass Flow Analyzer Laboratory.

AUTHORS' CLOSURE

Mr. Heisler is correct in stating that an infinite rate of tem-

perature change would not necessarily destroy the material at hand.

The authors cannot agree with Mr. Heisler's statement regarding Equations [9] and [10]. Derivations of the equations for a sphere follow:

The differential equation for a sphere having temperature dependence on r and τ only is

$$\frac{\partial^2\theta}{\partial r^2} + \frac{2}{r} \frac{\partial\theta}{\partial r} = \frac{1}{\alpha} \frac{\partial\theta}{\partial \tau} \quad 0 \leq r < a \dots [18]$$

$$\theta(r, 0) = 1 \dots [19]$$

$$-k \frac{\partial\theta}{\partial r} = h\theta \quad \text{at } r = a \dots [20]$$

with

$$\lambda = \frac{N_{FO}}{m^2}$$

and

$$\epsilon = \frac{n}{m}$$

Equation [18] becomes

$$\frac{\partial^2\theta}{\partial \epsilon^2} + \frac{2}{\epsilon} \frac{\partial\theta}{\partial \epsilon} = \frac{\partial\theta}{\partial \lambda} \quad 0 \leq \epsilon < \frac{1}{m} \dots [21]$$

with conditions

$$\theta(\epsilon, 0) = 1 \dots [22]$$

$$\frac{\partial\theta}{\partial \epsilon} = -\theta \quad \text{at } \epsilon = \frac{1}{m} \dots [23]$$

Let

$$y = \mathcal{L}(\theta) = \int_0^\infty e^{-\epsilon\lambda} \theta(\epsilon, \lambda) d\lambda \dots [24]$$

and

$$\mathcal{L}\left(\frac{\partial\theta}{\partial \lambda}\right) = sy - 1 \dots [25]$$

then

$$\frac{d^2y}{d\epsilon^2} + \frac{2}{\epsilon} \frac{dy}{d\epsilon} = sy - 1 \dots [26]$$

with

$$\frac{dy}{d\epsilon} = -y \quad \text{at } \epsilon = \frac{1}{m} \dots [27]$$

and

$$\frac{dy}{d\epsilon} = 0 \quad \text{at } \epsilon = 0$$

The general solution to [9] is

$$y = \frac{1}{s} + \frac{1}{\epsilon} (A \sinh \epsilon\sqrt{s} + B \cosh \epsilon\sqrt{s}) \dots [28]$$

for finiteness at $\epsilon = 0$

$$B = 0$$

Then

$$\frac{A}{\epsilon^2} (\epsilon \sqrt{s} \cosh \epsilon \sqrt{s} - \sinh \epsilon \sqrt{s}) = -\left(\frac{1}{s} + \frac{A \sinh \epsilon \sqrt{s}}{\epsilon}\right) \dots [29]$$

at $\epsilon = \frac{1}{m}$ Equation [29] becomes

$$A \left[\frac{\sqrt{s}}{m} \cosh \frac{\sqrt{s}}{m} + \left(\frac{1}{m} - 1\right) \sinh \frac{\sqrt{s}}{m} \right] = -\frac{1}{m^2 s} \dots [30]$$

Substitution for A and B in Equation [28] yields the particular solution

$$y = \frac{1}{s} \left\{ 1 - \frac{\sinh \epsilon \sqrt{s}}{m^2 \epsilon \left[\frac{\sqrt{s}}{m} \cosh \frac{\sqrt{s}}{m} + \left(\frac{1}{m} - 1\right) \sinh \frac{\sqrt{s}}{m} \right]} \right\} \dots [31]$$

Replacing the hyperbolic functions by exponentials and subsequent expansion yields

$$y = \frac{1}{s} - \frac{1}{s} \left[\frac{e^{-\sqrt{s}(\frac{1}{m}-1)} - e^{-\sqrt{s}(\frac{1}{m}+1)}}{m\epsilon(\sqrt{s}+1-m)} \right] \\ \left[1 - \frac{\sqrt{s}-1+m}{\sqrt{s}+1-m} e^{-2\frac{\sqrt{s}}{m}} + \left(\frac{\sqrt{s}-1+m}{\sqrt{s}+1-m}\right)^2 e^{-4\frac{\sqrt{s}}{m}} - \dots \right] \dots [32]$$

Using the inverse transform definition

$$\mathcal{L}^{-1} \left(\frac{1}{s} \right) = 1$$

and

$$\mathcal{L}^{-1} \left[\frac{e^{-\sqrt{s}z}}{s(\sqrt{s}+1-m)} \right] = \frac{1}{1-m} \left\{ \operatorname{erfc} \frac{z}{2\sqrt{\lambda}} - e^{(1-m)z+(1-m)^2\lambda} \operatorname{erfc} \left[\frac{z}{2\sqrt{\lambda}} + (1-m)\sqrt{\lambda} \right] \right\}$$

at $\epsilon = \frac{1}{m}$ in [32]; then

$$\theta = 1 - \frac{1}{1-m} \left\{ 1 - e^{(1-m)^2\lambda} \operatorname{erfc} (1-m)\sqrt{\lambda} \right. \\ \left. - 2 \operatorname{erfc} \frac{1}{m\sqrt{\lambda}} + 2e^{2\left(\frac{1-m}{m}\right)^2 + (1-m)^2\lambda} \right. \\ \left. \operatorname{erfc} \left(\frac{1}{m\sqrt{\lambda}} + (1-m)\sqrt{\lambda} \right) + \dots \right\} \dots [33]$$

Neglecting terms and rearranging, the surface temperature becomes

$$\theta = \frac{1}{1-m} \left\{ e^{(1-m)^2\lambda} \operatorname{erfc} (1-m)\sqrt{\lambda} - m + \dots \right\} \dots [34]$$

or

$$\theta = \frac{1}{1-m} \left\{ e^{\left(\frac{1-m}{m}\right)^2 N_{FO}} \operatorname{erfc} \left(\frac{1-m}{m} \right) \sqrt{N_{FO}} - m + \dots \right\} \dots [35]$$

The rate of temperature

$$\frac{d\theta}{dN_{FO}} = \frac{1}{1-m} \left\{ \left(\frac{1-m}{m} \right)^2 e^{\left(\frac{1-m}{m}\right)^2 N_{FO}} \operatorname{erfc} \left(\frac{1-m}{m} \right) \sqrt{N_{FO}} \right. \\ \left. - \frac{(1-m)}{m\sqrt{(\pi N_{FO})}} + \dots \right\} \dots [36]$$

In terms of θ Equation [36] can be written as

$$\frac{d\theta}{dN_{FO}} = \frac{1-m}{m^2} \left[(1-m)\theta + m - \frac{m}{1-m} \frac{1}{\sqrt{(\pi N_{FO})}} + \dots \right] \dots [37]$$

The authors are grateful for P. J. Schneider's interest. The curve which he suggests, although with a limited range, is shown in McAdam's "Heat Transmission," second edition, fig. 13. In the hoped-for ultimate publication of all charts, such graphs should be included. The authors feel, however, that as long as funds for carrying out this work are limited there might be other charts more important from the viewpoint that evaluation of Equations [11] and [12], of the discussion, offer no great difficulties.

Pressure Drop for Parallel Flow Through Rod Bundles¹

By B. W. LE TOURNEAU,² R. E. GRIMBLE,³ AND J. E. ZERBE,⁴ PITTSBURGH, PA.

Friction factors for flow parallel to a rod bundle have been determined experimentally in a Reynolds-number range from approximately 5000 to 100,000. Three rod arrays were used; namely, a 1.20 pitch-to-rod diameter ratio on a square lattice, and a 1.12 pitch-to-rod diameter ratio on both square and equilateral triangular lattices. Entrance plus exit-loss coefficients, and joint loss coefficients between axially aligned rod bundles also were measured experimentally for tube-sheet end connections. For the square arrays, the effect of tube-sheet flow area on these loss coefficients was investigated. Results are presented in graphical form.

NOMENCLATURE

The following nomenclature is used in the paper (consistent units):

- A_f = flow area among rods
- D = rod diameter
- D_h = hydraulic equivalent diameter among rods
- f = friction factor
- g = acceleration of gravity
- K_{e+e} = entrance plus exit-loss coefficient
- K_j = joint-loss coefficient
- L = length of a rod bundle
- n = number of rod bundles in series
- p = pitch of rod array
- ΔP = pressure drop
- Q = volumetric flow rate
- Re = Reynolds number = $D_h V \rho / \mu$
- S = dimensionless pitch = p/D
- V = average velocity among rods
- β = area ratio, flow area in tube sheet/flow area among rods
- ϵ = absolute roughness
- ρ = fluid density
- μ = fluid viscosity

INTRODUCTION

Turbulent flow outside of and parallel to the axis of a tube bundle is of frequent occurrence in certain types of commercial heat exchangers, and the same type of flow occurs in nuclear reactors when rod bundles are utilized as fuel elements. Very few pressure-drop data specifically applicable to such a geometry are available in the literature. Usually, frictional losses are

calculated, as recommended by McAdams (1),⁵ by calculating a hydraulic equivalent diameter for the rod bundle and using it as a round tube diameter in a conventional friction-factor correlation such as given by Moody (2) and others. Some specific work on flow parallel to rod bundles has been done recently by Miller, Byrnes, and Benforado (3), and by Dingee, Bell, Chastain, and Fawcett (4), incidental to heat-transfer experiments.

The present experiments were conducted in order to determine whether frictional losses calculated by the method suggested by McAdams were sufficiently accurate for design use, and to determine form-loss coefficients for tube-sheet end connections of various flow areas.

DESCRIPTION OF APPARATUS

The specimen rod bundles used in these experiments were of two types, illustrated in Figs. 1 and 2. Fig. 1 shows a typical square-lattice rod bundle, consisting of 64 aluminum rods held together with $1/16$ -in-thick aluminum tube sheets at the ends. The rods were on a 0.375-in-square pitch, and the tube sheets had 49 holes and 28 half-holes, sharp edged, on the same 0.375-in-square pitch centered over the flow channels among the rods. The rods and tube sheets were joined mechanically and were interchangeable. Two sets of rods, 0.312 and 0.333 in. diam finished by centerless grinding, were available, as were five sets of tube sheets having holes 0.218, 0.248, 0.272, 0.286, and 0.300 in. diam, so that the area ratio, tube-sheet flow area to flow area among the rods, could be varied over a fairly wide range for each of the two dimensionless pitches (pitch-to-rod diameter ratios) of 1.12 and 1.20. The assembled rod bundles were 3.00 in. square (8×8 rods) and were 5 in. or 24 in. long, the former for form-loss-coefficient tests and the latter for friction-factor tests.

The triangular pitch bundles consisted of 19 Zircaloy rods held together with $1/16$ -in-thick Zircaloy tube sheets. The rods were 0.50 in. diam on a 0.56-in. equilateral-triangular pitch, for a 1.12 dimensionless pitch. The tube sheets had 36 sharp-edged holes 0.22 in. diam centered over the flow channels among the rods. Rods and tube sheets were joined by welding. The assembled rod bundles were hexagonal, 2.54 in. across flats, and were $10\frac{1}{4}$ in. or $24\frac{1}{2}$ in. long, the former for form-loss coefficient tests and the latter for friction-factor tests.

The rod bundles fitted snugly into one of two test sections, one for the square-pitch rod bundles and one for the triangular-pitch bundles. The test sections were installed in a hydraulic test loop constructed of standard 3-in. copper pipe and shown in Fig. 3. The loop circulating pump was rated 300 gpm at 140-ft head. Flow rate was varied by means of a bypass valve and a throttle valve and was measured by reading the pressure drop across either of two calibrated orifice plates with a mercury manometer. Loop heaters, thermostatically controlled, were provided, and temperature of the circulating water was read on a bimetallic dial thermometer. Static pressure taps, suitably located for measuring over-all pressure drop across the rod bundles, were provided in each test section, and the pressure drop was read on a well-type manometer, with either mercury or carbon tetrachloride as a fluid depending on the magnitude of the pressure differential.

⁵ Numbers in parentheses refer to the Bibliography at the end of the paper.

¹ This work was done under U. S. Atomic Energy Commission Contract AT-11-1-GEN-14.

² Engineer, Thermal and Hydraulic Section, Bettis Atomic Power Division, Westinghouse Electric Corporation. Assoc. Mem. ASME.

³ Supervising Engineer, Bettis Atomic Power Division, Westinghouse Electric Corporation.

⁴ Section Manager, Bettis Atomic Power Division, Westinghouse Electric Corporation. Assoc. Mem. ASME.

Contributed by the Hydraulic Division and presented at the Annual Meeting, New York, N. Y., November 25-30, 1956, of THE AMERICAN SOCIETY OF MECHANICAL ENGINEERS.

NOTE: Statements and opinions advanced in papers are to be understood as individual expressions of their authors and not those of the Society. Manuscript received at ASME Headquarters, April 4, 1956. Paper No. 56-A-134.

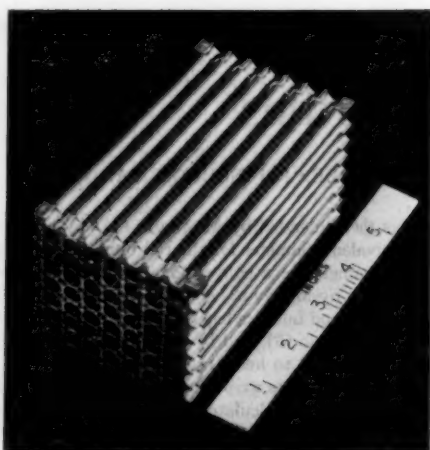


FIG. 1 TYPICAL SQUARE-PITCH ROD BUNDLE

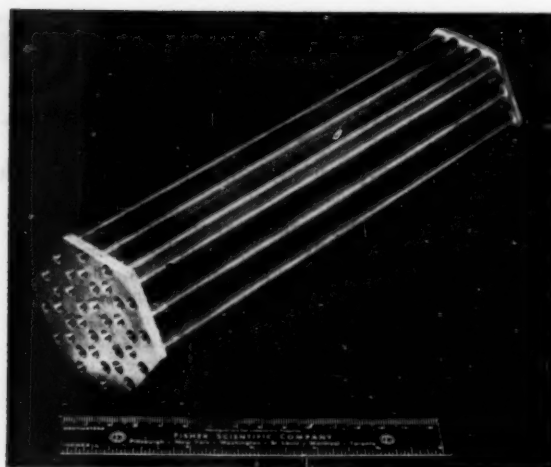


FIG. 2 TYPICAL TRIANGULAR-PITCH ROD BUNDLE

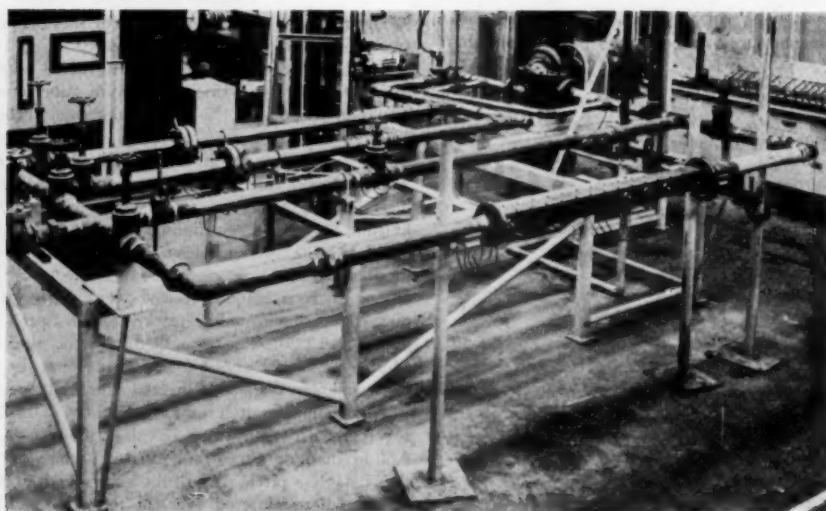


FIG. 3 BETTIS 3-IN. HYDRAULIC TEST LOOP

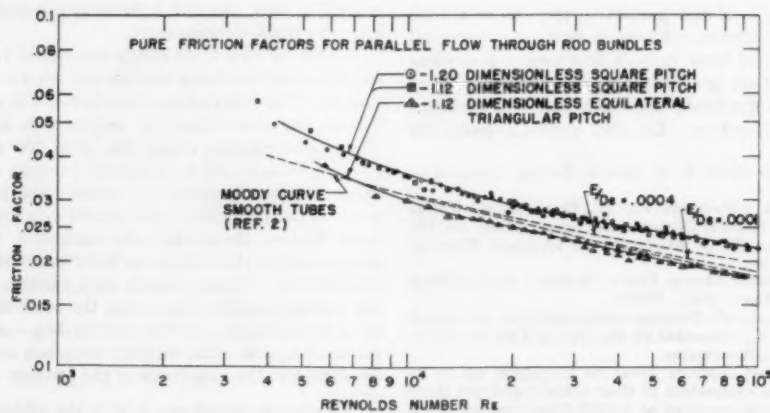


FIG. 4

METHOD OF TEST

Friction-factor tests were run for each of the three rod arrays: 1.12 and 1.20 dimensionless square pitch and 1.12 dimensionless equilateral triangular pitch. Form-loss coefficient tests were run for six combinations of rod and tube-sheet hole diameters for the square arrays and for one such combination for the triangular array. Table 1 summarizes the exact configurations used.

For the friction-factor experimental determination, a single long rod bundle was inserted in the appropriate test section. The pressure drop across an interior length of the rod bundle was measured by using static-pressure taps in the test section wall located a minimum of 3 in. into the rod bundle from the tube sheets. In the case of the square-pitch rod bundles, additional experiments were made by measuring the over-all pressure drops (including tube sheets) across a long and a short rod bundle, which otherwise were identical geometrically, and considering the difference between the two pressure drops as a pure frictional drop in the differential length of rod bundle. Excellent agreement was obtained between these two methods.

The entrance plus exit-loss-coefficient experiments were made by measuring the over-all pressure drop across a single short subassembly. The joint-loss-coefficient tests were made by aligning axially three or four identical rod bundles and measuring the over-all pressure drop across the series of rod bundles. Spacings of zero and $1/16$ in. between adjacent bundles were investigated.

Each geometrical configuration was tested at various flow rates up to the maximum available and at temperatures from 80 to 150 F in order to secure a wide range of turbulent Reynolds numbers from approximately 5000 to 100,000. All tests were made under isothermal conditions.

For measurements of over-all pressure drop across one or more rod bundles, static taps 6 in. or more upstream and downstream from the bundles were used. It was shown in every case that neglecting frictional losses in the test sections between pressure taps and rod bundles introduced negligible error.

CALCULATIONS

The over-all pressure drop across one or more rod bundles in parallel flow may be expressed by

$$\frac{\Delta P}{\rho} = \frac{V^2}{2g} \left[\frac{nL}{D_e} + K_{e,s} + (n-1)K_j \right] \quad [1]$$

wherein the pressure drop in feet of fluid flowing is expressed as a number of velocity heads in the rod bundle (as measured away from the end connections). This equation may be used to compute pressure drop if the experimental friction factors and form-loss coefficients are known; it is here used conversely to determine the experimental friction factors and loss coefficients from measured pressure drops.

When less than one entire rod bundle is used, as in the friction-factor experiments, only the frictional term is applicable since there are no end connections to require form-loss coefficients, and the friction factor may be computed by

$$f = \frac{2g\Delta P D_e}{\rho V^2 L} \quad [2]$$

The friction factors for each of the three rod arrays were computed from experimental pressure drops by Equation [2], and a curve of friction factor versus Reynolds number plotted for each array. These curves were used in the calculation of the form-loss coefficients.

The entrance plus exit-loss coefficients $K_{e,s}$ were computed from the experimental over-all pressure-drop data across a single

TABLE 1 GEOMETRICAL CONFIGURATIONS FOR FORM LOSS TESTS

Lattice type	Pitch, in.	Rod diam, in.	Dimensionless pitch	Tube-sheet hole diam, in.	Area ratio, β
Square.....	0.375	0.312	1.20	0.300	1.09
Square.....	0.375	0.312	1.20	0.286	0.99
Square.....	0.375	0.312	1.20	0.272	0.89
Square.....	0.375	0.312	1.20	0.218	0.57
Square.....	0.375	0.333	1.12	0.248	0.89
Square.....	0.375	0.333	1.12	0.218	0.69
Equilateral triangular ..	0.56	0.50	1.12	0.220	0.78

rod bundle by using the following equation, which is the solution of Equation [1] with $n = 1$ for $K_{e,s}$, and an appropriate friction-factor curve

$$K_{e,s} = \frac{2g\Delta P}{\rho V^2} - \frac{fL}{D_e} \quad [3]$$

The joint loss coefficients K_j were computed from the experimental over-all pressure-drop data across three or four rod bundles in series, using the following equation, which is the solution of Equation [1] with $n > 1$ for K_j , and appropriate friction-factor and entrance plus exit-loss-coefficient curves

$$K_j = \frac{1}{n-1} \left(\frac{2g\Delta P}{\rho V^2} - \frac{n f L}{D_e} - K_{e,s} \right) \quad [4]$$

Entrance plus exit-loss coefficients computed from Equation [3] were plotted versus Reynolds number for each of the seven configurations in Table 1. Computed joint losses also were plotted against Reynolds number for each of the seven configurations.

Reynolds numbers were based on the average velocity and the hydraulic equivalent diameter among the rods, away from the end connections

$$Re = \frac{D_e V \rho}{\mu} \quad [5]$$

The hydraulic equivalent diameter used in the foregoing calculations was based on an infinite rod array, neglecting the test-section wall. Thus, for square arrays

$$D_e = \frac{4p^2}{\pi D} - D$$

and for the equilateral triangular array

$$D_e = \left(\frac{2\sqrt{3}}{\pi} \right) \frac{p^2}{D} - D$$

DISCUSSION OF RESULTS

Friction Factors (also see authors' closure). Experimentally determined pure friction factors for parallel flow through rod bundles are presented in Fig. 4 and are compared with the friction-factor curves for smooth tubes from reference (2).

From Fig. 4 it is seen that the experimental friction factors for 1.12 equilateral triangular pitch rods lie approximately 2 to 5 per cent below the Moody curve for smooth tubes and that the experimental friction factors for both the 1.12 and 1.20 dimensionless square-pitch rods lie approximately 12 to 25 per cent above the Moody curve for smooth tubes, depending on the Reynolds number. It is believed that the portions of the experimental curves above $Re = 15,000$, where the slope of the experimental curves is less than that of the Moody curve for smooth tubes,

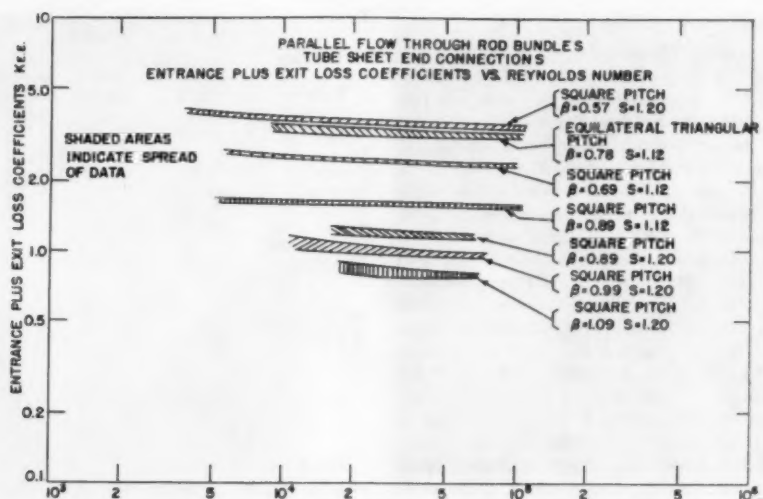


Fig. 5

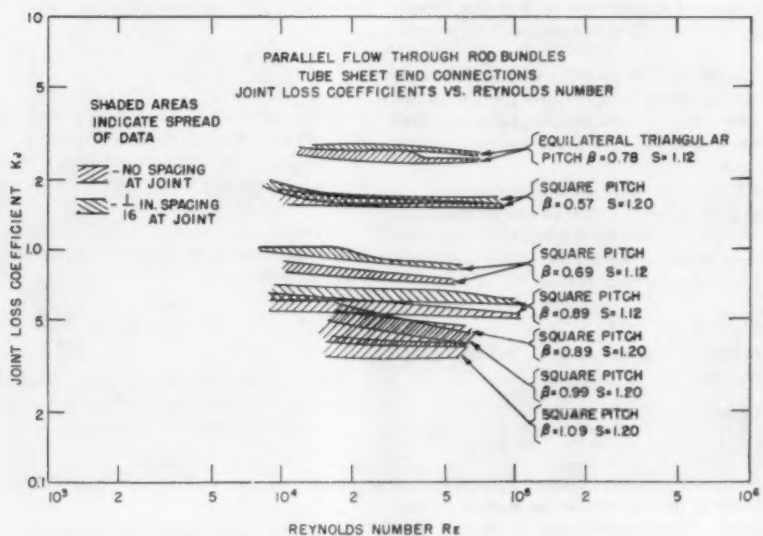


Fig. 6

show the influence of relative roughness. The slopes would coincide approximately with tube data if the triangular-pitch rods were assumed to have a relative roughness of 0.0001 and the square-pitch rods a relative roughness of 0.0004. Although the roughness of the rods was not measured, these values seem reasonable for machined surfaces and equivalent diameter of about $1/4$ in.

With these corrections regarding roughness, the data can be correlated within experimental error by the relations $f_{rod} = 1.12 f_{tube}$ for square pitch, and $f_{rod} = 0.95 f_{tube}$ for equilateral triangular pitch over the dimensionless pitch range tested, at Reynolds numbers from 10,000 to 100,000, where f_{tube} is taken from the Moody curves (2) which are plotted from the equation of Colebrook and White (5)

$$\frac{1}{\sqrt{f}} = 1.74 - 2 \log_{10} \left(\frac{2\epsilon}{D_*} + \frac{18.7}{Re\sqrt{f}} \right)$$

The differences between rod and tube-friction factors may be explained partially by errors in flow area and equivalent-diameter measurements, but these errors are not large enough to explain the entire differences. It may be that the semiempirical concept of hydraulic equivalent diameter for noncircular flow cross sections (which assumes that the pressure drop is proportional to the wetted perimeter per unit flow cross-sectional area) is not exactly correct for a flow cross section so different from a round tube as the region outside rods. The error introduced here may also be opposite in direction between square and triangular pitch rods.

Form-Loss Coefficients. The experimental results for entrance plus exit-loss coefficients as functions of Reynolds number are presented in Fig. 5 and the results for joint loss coefficients in Fig. 6 for each of the configurations tested. In these graphs, the width of the shaded region indicates the experimental scatter of the data. Since these coefficients are calculated as relatively small differences, the accuracy is not as high as in the frictional

data. No attempt was made to separate entrance and exit losses. All of the form-loss coefficients showed a very slight decrease with increasing Reynolds number, as might be expected.

In Fig. 7 a cross plot of entrance plus exit-loss coefficients as a function of area ratio β (tube-sheet flow area/flow area among the rods) is presented, and in Fig. 8 a similar cross plot of joint loss coefficients versus area ratio β , both at $Re = 50,000$. Reasonable curves were obtained, showing a fairly sharp increase in loss coefficients as the area ratio β was decreased. The loss coefficients based on the velocity in the tube sheets, $K\beta^2$, also increase with decreasing area ratio β , but of course much less sharply.

It should be noted that the area ratio β does not fully describe the end-connection flow geometry for round-hole tube sheets, but it is felt that over the limited range of these experiments it does as well as or better than any other single parameter. To describe completely the end-connection flow geometry for entrance-plus-exit and joint-loss purposes it is necessary to specify three geometrical dimensionless ratios, such as the area ratio β , the dimensionless pitch S , and a ratio involving the tube-sheet thickness. The tube-sheet thickness was not under investigation in these experiments, and it can be seen from Figs. 7 and 8 that the two dimensionless pitches tested lie on the same loss-coefficient versus area-ratio curves within experimental error. Therefore it is concluded that, within the limited dimensionless pitch range of these experiments, the area ratio β is an adequate parameter for end-connection flow geometry.

The joint-loss coefficients were slightly higher with a $1/16$ -in. spacing allowed at the joints between rod bundles than with the rod bundles pressed tightly together. This, of course, would be expected and it is apparent that as spacing is increased, the joint-loss coefficients must approach the entrance plus exit-loss coefficients as a limit.

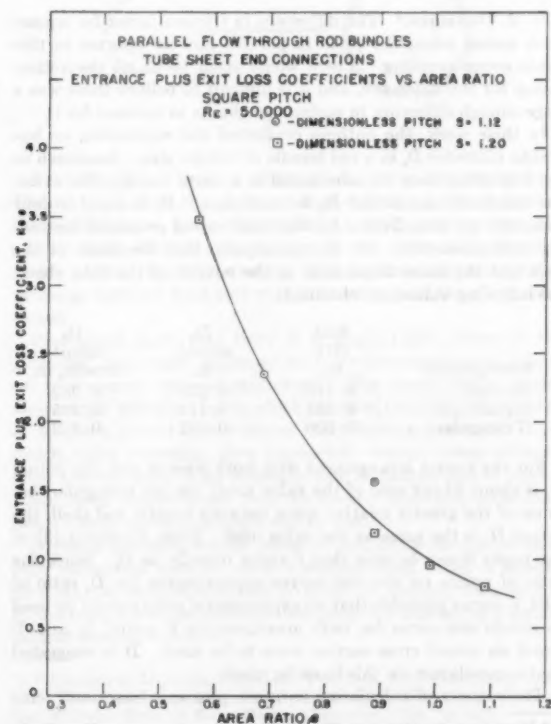


Fig. 7

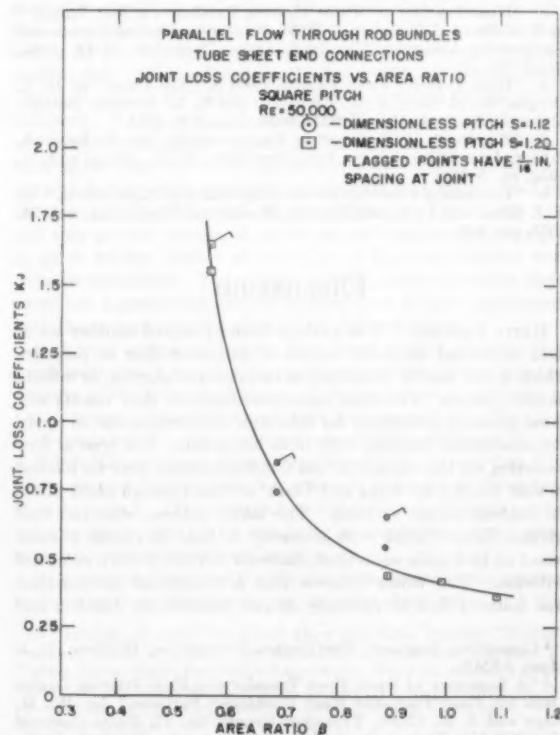


Fig. 8

The form-loss coefficients measured in these experiments are rather complex combinations of contraction, expansion, and turning losses (and perhaps others). For instance, the water on entering a rod bundle must first undergo contraction into a multi-tubular system (the tube-sheet holes), then a further contraction at the larger area ratios at the junction of the tube sheet and the rods, followed immediately by an expansion to the cross-shaped area among the rods and then followed by a change in velocity profile. No attempt has been made to predict these coefficients for comparison with the experimental data, since their complex nature would make agreement accidental. However, the fact that the loss coefficients for the triangular-pitch array were larger than for the square-pitch arrays of equal area ratio is partially explained by the larger turning losses caused by the larger pitch-to-tube sheet hole diameter ratio with the triangular configuration than for the same area ratio in a square configuration.

It should be noted that the form-loss coefficients as defined by Equation [1] include entrance effects on the friction factor and were defined such that the length L for frictional calculations was the entire length of the rod bundle including tube sheets. This was done for convenience in design calculations making use of the experimental data.

Discussion of Errors. The 95 per cent confidence limit on the measured friction factors has been estimated as follows (6). The friction factor is calculated from the equation

$$f = \frac{\frac{\Delta P}{L}}{\frac{\rho}{2g} \left(\frac{V}{D_s} \right)^2} = \frac{2\Delta P g A_f^2 D_s}{Q^2 \rho L}$$

Negligible error in L is assumed. The 95 per cent confidence limit on $\Delta P/\rho Q^2$ is estimated from the scatter in the experimental data as approximately ± 3 per cent (somewhat higher at the lowest flow rates). The 95 per cent confidence limits on the flow area and the equivalent diameter are estimated at 3 per cent and 2 per cent, respectively.

The 95 per cent confidence limit on friction factor is then given approximately by

$$\frac{\Delta f}{f} = \left\{ \left[\frac{\Delta \left(\frac{\Delta P}{\rho Q^2} \right)}{\frac{\Delta P}{\rho Q^2}} \right]^2 + \left(\frac{2\Delta A_f}{A_f} \right)^2 + \left(\frac{\Delta D_e}{D_e} \right)^2 \right\}^{1/2}$$

$$= [(0.03)^2 + (2 \times 0.03)^2 + (0.02)^2]^{1/2} = 7 \text{ per cent}$$

so that the observed spread between the square and triangular arrays is significant.

ACKNOWLEDGMENTS

The authors wish to express their gratitude to the Westinghouse Electric Corporation and to the United States Atomic Energy Commission for granting permission to publish this work. The authors would like to thank many members of the Bettis Atomic Power Division for assistance in these experiments and are especially indebted to Mr. S. W. Cota and Mr. C. F. McCullough for their untiring assistance in the laboratory.

BIBLIOGRAPHY

- 1 "Heat Transmission," by W. H. McAdams, McGraw-Hill Book Company, Inc., New York, N. Y., third edition, 1954, p. 162.
- 2 "Friction Factors for Pipe Flow," by L. F. Moody, *Trans. ASME*, vol. 66, 1944, pp. 671-684.
- 3 "Heat Transfer to Water Flowing Parallel to a Rod Bundle," by P. Miller, J. J. Brynes, and D. M. Benforado, Nuclear Science and Engineering Congress, Cleveland, Ohio, December 12-16, 1955, Paper No. 47.
- 4 "Heat Transfer From Parallel Rods in Axial Flow," by D. A. Dingee, W. H. Bell, J. W. Chastain, and S. L. Fawcett, Battelle Memorial Institute Report BMI-1026, August 9, 1955.
- 5 "Handbook of Engineering Fundamentals," by O. Eshbach, Editor, John Wiley & Sons, Inc., New York, N. Y., second edition, 1952, pp. 6-47.
- 6 "Describing Uncertainties in Single-Sample Experiments," by S. J. Kline and F. A. McClintock, *Mechanical Engineering*, vol. 75, 1953, pp. 3-8.

Discussion

DAVID ARONSON.^{*} The authors have presented another set of data concerned with the nature of turbulent flow in passages which is not readily described as circular, rectangular, or infinite parallel planes. The close agreement between their results and those obtained previously for tube flow encourages one to apply the established formulas with little hesitation. The type of flow occurring on the outside of rod bundles perhaps may be likened to that studied by Kays and Clark⁷ of flow through plain plate-fin heat-exchanger surfaces. The latter authors observed that friction factor varied with geometry so that Reynolds number based on hydraulic equivalent diameter did not prove a complete criterion. The writer believes that a theoretical investigation was made of flow in variously shaped conduits by Lemlich and

Seth of the University of Cincinnati. The authors may be interested in obtaining a copy of the paper prepared by Mr. Seth under Professor Lemlich's guidance.

The authors have given us a very clear picture of the nature of their tests and yet were this paper presented at a different stage of our technical advance there would be a number of questions asked which now might seem unwarranted. Presumably the tests are part of a program to investigate core elements for a nuclear reactor. Hence the use of tube sheets with holes between the rods, but no holes to communicate with the inside of rods, seems to be a reasonable arrangement. If the information is not classified, could the authors give some indication as to why flow parallel to tubes is preferred to flow across the tubes?

Mention is made of a contraction of the flow after the fluid leaves the holes in the tube sheets. Is this contraction due to the fact that the holes are blocked partially by the rods?

With regard to the entrance-plus-exit-loss coefficients and the joint-loss coefficients, the values are given as a function of the velocity in the space between rods. Conventionally this expression of an entrance and exit loss is related to flow through tubes having a flow area smaller than the outer passages. In the present instance, the restriction to flow results from the limited area for flow presented by the holes in the tube sheet. For the purpose of calculating performance of other arrangements it might be helpful were the authors to express the end losses as functions of the velocities in the tube-sheet holes as well as of velocities in the bundle itself.

For the presentation of the flow-friction characteristics of flow in the bundle itself the authors have done well in their presentation of the data and in setting a confidence limit on their measured values. This seems to be an excellent way of expressing the reliability of the test.

W. J. DANZIGER.⁸ The difference in friction factor for square pitch versus triangular pitch in parallel flow as reported in this paper seems puzzling. There would seem to be no theoretical reason for the difference, and it is difficult to believe there was a large enough difference in surface roughness to account for it.

In their work, the authors evaluated the equivalent, or hydraulic diameter D_e , in a rod bundle of infinite size. Inasmuch as the wall effect may be substantial in a small bundle, the writer has calculated the actual D_e for each case. D_e is equal to four times the net area divided by the total wetted perimeter (including shell perimeter). On the assumption that the inside of the shell had the same dimensions as the outside of the tube sheet, the following values are obtained:

Arrangement	Rod OD, in.	D_e actual, in.	D_e infinite bundle, in.
Square.....	0.312	0.220	0.262
Square.....	0.333	0.174	0.205
Triangular.....	0.500	0.192	0.192

For the square arrangement with both sizes of rod, the actual D_e is about 84 per cent of the value used; for the triangular, because of the greater relative space between bundle and shell, the actual D_e is the same as the value used. From Equation [2] of the paper it can be seen that f varies directly as D_e . Since the ratio of points on the two curves approximates the D_e ratio of 0.84, it seems probable that all experimental points could be used to obtain one curve for both arrangements if actual D_e and V based on actual cross section were to be used. It is suggested that a correlation on this basis be tried.

The manner of calculating entrance plus exit losses and joint

^{*} Consulting Engineer, Worthington Corporation, Harrison, N. J. Mem. ASME.

⁷ "A Summary of Basic Heat Transfer and Flow Friction Design Data for Plain Plate-Fin Heat Exchanger Surfaces," by W. M. Kays and S. H. Clark, Technical Report No. 17, Navy Contract N6-ONR-251, Task Order 6, Stanford University, Stanford, Calif., August 15, 1953.

⁸ Heat Transfer Division, The M. W. Kellogg Company, New York, N. Y.

losses, involving pitch-diameter ratio, pitch arrangement, and ratio of hole area to bundle cross-section area, all to get a factor to use with bundle velocity, is rather complicated. In all arrangements of holes and rods used, the hole area was reduced at least slightly by the ends of the rods. If correlation of these pressure-drop data could be obtained as a function of velocity through the minimum hole cross-sectional area at the rods, a considerable simplification would result. It is suggested that this approach be investigated.

H. P. EICHENBERGER.⁹ The subject paper is both useful and interesting. Its use is obvious. It might be well worth while to consider the fluid-flow phenomena in greater detail.

The hydraulic diameter is so defined that the dimensionless pressure drop per unit length (darcy friction factor) is the same in two tubes of arbitrary cross section if the average shear stress is the same. The same statement can be expressed as follows: The average dimensionless shear stress $\tau/\rho V^2$ is proportional to the darcy friction factor f . In general $\tau/\rho V^2 = f(\text{Re, roughness, geometry})$.

The tests of this paper seem to indicate that the average shear stress $\tau/\rho V^2$ depends on the geometry to some extent, if the Reynolds number Re , is defined on the basis of the hydraulic diameter. This is not surprising since there are two reasons for the change of this dimensionless shear stress:

1 When changing from a circular to another cross section with the same hydraulic diameter, one would expect that the dimensionless shear stress is decreased because the effective Re is increased. This is best illustrated by a form whose wall is a circle with small sharp waves, Fig. 9.

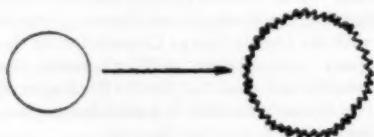


FIG. 9

2 An increase in shear stress is caused by secondary flow. There is flow from the places of high-velocity gradient toward the middle of the duct. For instance, a flow is set up from the middle of the sides of a square toward the center and from the center toward the four corners. This increases the momentum exchange between fluid and wall and counteracts the effect mentioned.

Since tests show that there is in general little effect of the geometry, one could conclude that the afore-mentioned effects are of the same order of magnitude. This needs further study. However, if this is so, forms which promote secondary flows, such as a square, should have a higher darcy friction factor and those which make secondary flow impossible, though being different from a circle, such as an infinitely long rectangle, should have a lower darcy friction factor than the circle of some Reynolds number. This is actually brought out by test.¹⁰

In these comparisons the effect of roughness should be carefully taken into account, since a surface finish which is smooth for a circular cross section may be rough for another cross section of the same hydraulic diameter and same Re because of a locally thinner laminar sublayer.

⁹ Accessories Division, Thompson Products, Inc., Cleveland, Ohio.

¹⁰ "Hütte" des Ingenieurs Taschenbuch, 27 Edition, I volume, Verlag: Wilhelm Ernst & Sohn, Berlin, Germany, 1941, p. 475.

AUTHORS' CLOSURE

The authors are grateful for the valuable comments and suggestions of Messrs. Aronson, Danziger, and Eichenberger.

The fact that the observed differences in friction factor between the square-pitch and equilateral triangular-pitch rod bundles are fictitious, as pointed out by Mr. Danziger, is entirely correct. The apparent differences are due to the fact that our calculated friction factors, as presented in Fig. 4, were based on the hydraulic equivalent diameter of an infinite rod array, rather than the true equivalent diameter of the finite rod bundle including the test section walls. At the time the paper was written, it was not realized that the two equivalent diameters were so different for our square-pitch bundles. While this discrepancy was independently discovered by the authors prior to the presentation of the paper, the authors are grateful to Mr. Danziger and also to Mr. F. C. Gilman of the Worthington Corporation for pointing it out to them.

The experimental friction factors and Reynolds numbers for the square-pitch bundles have been recalculated by using the actual equivalent diameter of the finite rod bundles and plotted in Fig. 10. It is noted that the resulting friction factor versus Reynolds number curve for the square-pitch bundles is in excellent agreement with the curve given in Fig. 4 for the triangular-pitch bundles (for which the two equivalent diameters were equal). Therefore, our revised correlation for the experimental parallel-flow rod friction factor data is $f_{\text{rod}} = 0.95 f_{\text{tube}}$ for both square and equilateral triangular-pitch rod bundles, over the dimensionless pitch and Reynolds number range tested, where f_{tube} is taken from the Moody curves (2) and the friction factor for the rod bundles is based on the actual equivalent diameter.

However, the authors remain in agreement with Messrs. Aronson and Eichenberger that friction factors may vary with geometry as well as with Reynolds number and relative roughness. In this connection, the authors would like to make reference to the excellent theoretical analysis of pressure drop in parallel-flow rod bundles recently completed by Deissler and Taylor.¹¹ Using the assumption that expressions for the eddy diffusivity of momentum previously verified for flow in tubes apply in general along lines normal to a wall, Deissler and Taylor have shown that the conventionally defined friction factors for parallel flow through an infinite rod bundle may be expected to decrease considerably as the dimensionless pitch approaches 1.0, and they present calculated curves for both square and triangular-pitch friction factors as functions of Reynolds number and dimensionless pitch. The authors were pleased to note that their corrected experimental friction factors were in good agreement with those given theoretically by Deissler and Taylor.

It is true, as pointed out by Mr. Aronson, that the form-loss coefficients would be more conventionally defined if based on the velocity in the tube sheet holes. It should be noted that this is not necessarily the smaller area since in one case $\beta > 1$. The loss coefficients based on the tube sheet hole velocity would be $K\beta^2$, and if $K\beta^2$ is plotted versus β from Figs. 7 and 8, it is found that $K\beta^2$ also increases slightly with decreasing β , although of course less sharply than K . The authors based their loss coefficients on the velocity among the rods for simplicity in calculating over-all pressure drop through a series of bundles.

In answer to a question by Mr. Aronson, there is a contraction in most cases as the flow leaves the tube sheet holes, and this

¹¹ "Analysis of Axial Turbulent Flow and Heat Transfer Through Banks of Rods or Tubes," by Robert G. Deissler and Maynard F. Taylor, Lewis Flight Propulsion Laboratory, National Advisory Committee for Aeronautics, Cleveland, Ohio. (To be published in the proceedings of the AEC Reactor Heat Transfer Conference, held November 1 and 2, 1956, in New York, N. Y.).

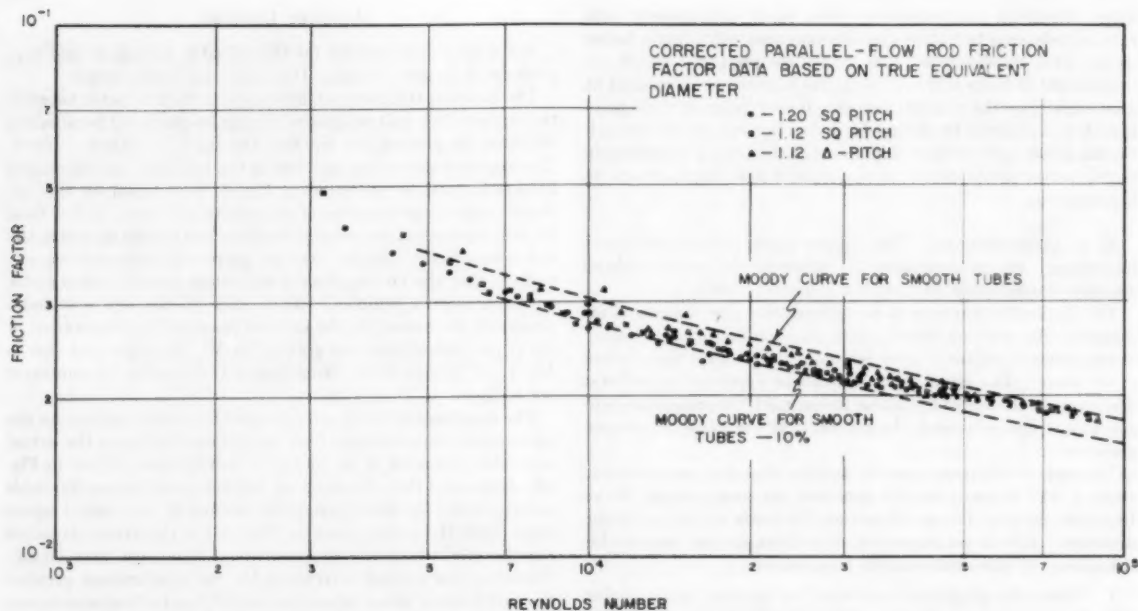


FIG. 10

contraction is due to the fact that the holes are partially blocked by the rods. If the form loss coefficients are based on the minimum flow area at this contraction, as suggested by Mr. Danziger, curves corresponding to Figs. 7 and 8 are obtained which have a slope between the slopes of K and $K\beta^2$, when all three are plotted against β .

In answer to another question by Mr. Aronson, rod bundles of the general type investigated (though not of the same dimen-

sions) were chosen as the fuel elements for the blanket region of the Pressurized Water Reactor (PWR) core which is being built at Bettis Plant by the Westinghouse Electric Corporation under a contract with the Atomic Energy Commission for the Duquesne Light Company power station at Shippingport, Pennsylvania. Parametric studies indicated that, for the PWR core, flow parallel to the rod fuel elements resulted in a more favorable thermal and hydraulic design than flow across the rods.

Resistance Coefficients for Laminar and Turbulent Flow Through One-Half-Inch Valves and Fittings

By C. P. KITTREDGE¹ AND D. S. ROWLEY²

Apparatus and test procedures to determine resistance coefficients for laminar and turbulent flow through 1/2-in. I.P.S. valves, fittings, and fabricated bends are described. Resistance coefficients are given as functions of Reynolds number. Results of the investigation are discussed briefly.

NOMENCLATURE

The following nomenclature is used in the paper:

- A = constant, dimensionless; area, sq ft
- C = constant, dimensionless
- C_D = drag coefficient, dimensionless
- C_f = friction coefficient, dimensionless
- $D = C_D A (\rho V^2) / 2$ = drag force on submerged body, lb
- d = internal diameter, in. or ft
- f = friction factor for straight pipe, dimensionless
- g = acceleration due to gravity, ft/sec²
- $h = K(V^2/2g) =$ head loss caused by fitting, based on no-length concept, ft of fluid
- $h_f = f(L/d)(V^2/2g) =$ head loss caused by pipe friction, ft of fluid
- K = resistance coefficient, dimensionless
- L = length of pipe, ft
- m = exponent, dimensionless
- n = exponent, dimensionless
- R = radius of bend, in.
- $Re = Vd/\nu =$ Reynolds number, dimensionless
- V = average velocity in pipe, fps; approach velocity for submerged body, fps
- ν = kinematic viscosity of fluid, ft²/sec
- ρ = mass density of fluid, (lb)(sec)²/ft⁴
- ϕ = function of

INTRODUCTION

Relatively little information has been published on the resistance offered to laminar flow through valves and fittings. Karr and Schutz (1)³ tested globe and angle valves over the range of Reynolds number approximately 1 to 10³ and compared their findings with those of earlier investigators. Their paper contains

¹ Associate Professor of Mechanical Engineering, Princeton University, Princeton, N. J. Mem. ASME.

² Research Department, The Carter Oil Company, Tulsa, Okla.; formerly, Assistant in Research, Mechanical Engineering Department, Princeton University. Assoc. Mem. ASME.

³ The no-length concept considers only the excess loss produced by a fitting over and above that due to a piece of straight pipe of length equal to the center-line length of the fitting.

⁴ Numbers in parentheses refer to the Bibliography at the end of the paper.

Contributed by the Hydraulic Division and presented at the Annual Meeting, New York, N. Y., November 25-30, 1956, of THE AMERICAN SOCIETY OF MECHANICAL ENGINEERS.

NOTE: Statements and opinions advanced in papers are to be understood as individual expressions of their authors and not those of the Society. Manuscript received at ASME Headquarters, August 6, Paper No. 56-A-190.

a bibliography which has not been duplicated here. Beck and Miller (2) and Beck (3, 4, 5) reported tests on a variety of valves, fittings, and bends over the range of Reynolds number approximately 30 to 1000. Beck⁴ reported a few losses for bends at low Reynolds numbers which were less than the losses caused by equal lengths of straight pipe. This unexplained anomaly together with the general paucity of information for the laminar flow state prompted the program of research herein described.

A typical arrangement of the apparatus used is shown in Fig. 1. The basic equipment was assembled by R. R. John (6) who tested several 1/2-in. I.P.S. valves and fittings over the range of Reynolds number approximately 1000 to 30,000 with kerosene as the working fluid. The apparatus was improved (7) and the range of Reynolds number extended down to about 20 by using SAE 10 oil. The resistance coefficients for turbulent flow were in satisfactory

⁵ Reference (4), p. 371 and fig. 6, p. 372.

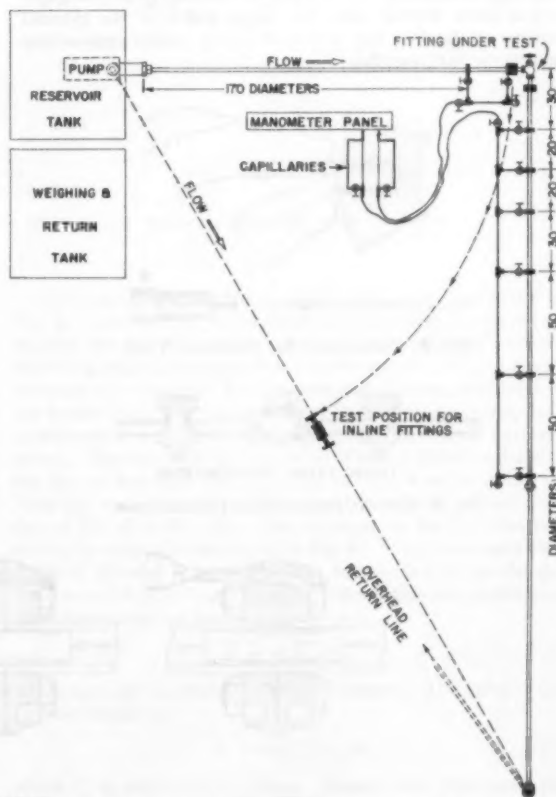


FIG. 1 PLAN VIEW OF TEST APPARATUS SHOWING TANGENTS ARRANGED FOR RIGHT-ANGLE FITTING

agreement with published values for similar fittings. The general trends of the coefficients for laminar flow were in accord with the trends of drag coefficients for submerged bodies.

DESCRIPTION OF APPARATUS

About 100 gal of the working fluid were stored in a steel tank immediately above the pump, Fig. 1. Any desired portion of the discharge from the pump could be directed through straightening vanes and a bellmouth nozzle into the pipe under test. The remainder of the flow was bypassed to the reservoir tank. The test pipe was $1/2$ -in. I.P.S. drawn brass. About 170 diameters were used for a calming length between the bellmouth and the upstream piezometer tap. The maximum available test reach between upstream and downstream piezometer taps was from 230 to 375 diameters depending upon the arrangement. It terminated in a tee in which a thermometer was inserted. The fluid was returned through a vertical loop to a swing spout which deflected it either to the reservoir tank or to an elevated weighing tank. Flow from the weighing tank to the reservoir tank was by gravity.

The average diameter of the $1/2$ -in. I.P.S. brass pipe was 0.6274 in. as calculated from the weight of water required to fill it. This pipe was used with all valves and fittings except the long-radius fabricated bends. The latter were made on a draw bench from seamless brass tubing and required special tangents, similar in most respects to those shown in Fig. 1. The average internal diameter of the bend tangents was 0.7073 in. as calculated from the weight of carbon tetrachloride required to fill them. It was important to determine these diameters accurately because pipe-friction losses depend upon the fourth power of the internal diameter for laminar flow and upon higher powers approaching the fifth for turbulent flow.

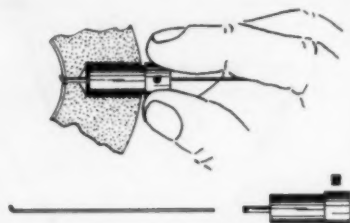


FIG. 2 PIEZOMETER TAP ROUNDING TOOL



FIG. 3 TYPICAL FITTING TEST INSTALLATION

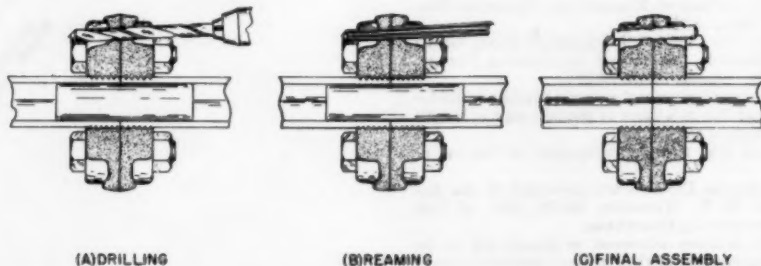


FIG. 4 FITTING NIPPLE TO TANGENT JOINT

The piezometer taps were drilled and reamed to a $1/16$ -in. diameter. The inside edge of each tap was rounded on a $1/16$ -in. radius as shown in Fig. 2.

Brass nipples of the same internal diameter as the pipe were screwed into the valves and fittings to the full depth of the female thread. A flange was screwed on the outer end of each nipple and the assembly faced off. The center-line length of each fitting with attached nipples was about 15 diameters. A typical fitting inserted between the test-pipe flanges is shown in Fig. 3. Mandrels were used to insure accurate internal alignment between the pipes and fitting nipples as shown in Fig. 4. Each joint was aligned with two taper pins and made up with a thin paper gasket having a hole slightly larger than the pipe.

Three manometers were provided; namely, a mercury differential, an inverted U-tube with variable air pressure over the working fluid, and a water differential. A capillary with bypass was installed in each lead from the manifolds to damp pressure oscillations as necessary. The time required to obtain true steady-state levels of the manometer columns approached one hour for each pressure measurement at the lowest Reynolds numbers, even though the capillaries were not used. In spite of this, the manometers were satisfactory for testing the valves and fittings for which the disturbances seldom extended beyond 100 diameters downstream. The disturbance caused by a long-radius bend could be detected more than 200 diameters downstream for laminar flow. This made it almost impossible to separate the small loss caused by the bend from the loss due to the straight pipe. The manometers were replaced by a 0-25 psi Dynisco strain-gage differential-pressure cell which eliminated the waiting time and improved the accuracy. A Leeds and Northrup portable precision potentiometer was used to measure the potential drop across the strain-gage bridge in the cell. The cell was calibrated in place with two Ashcroft dead-weight gage testers.

The accuracy of the weighing scale was verified with known weights. All thermometers were calibrated for full and partial immersion conditions. Specific weights were determined by weighing one-liter samples of fluids on a precision balance. Kinematic viscosities were measured with a calibrated modified Ostwald viscosimeter. The viscosity of a control sample was verified by an independent agency.

RESULTS

A number of runs were made on the $1/2$ -in. I.P.S. brass pipe with a piece of flanged straight pipe installed in place of a fitting. The friction factors obtained are shown in Fig. 5, and the agreement with the formulations of Poiseuille and Blasius provided a check on the apparatus and procedures. Similar tests for the long-radius bend tangents, also shown in Fig. 5, attested to the accuracy of the pressure cell and potentiometer.

The disturbance caused by a valve or fitting at $R > 2000$ could seldom be detected at any of the downstream pressure taps.

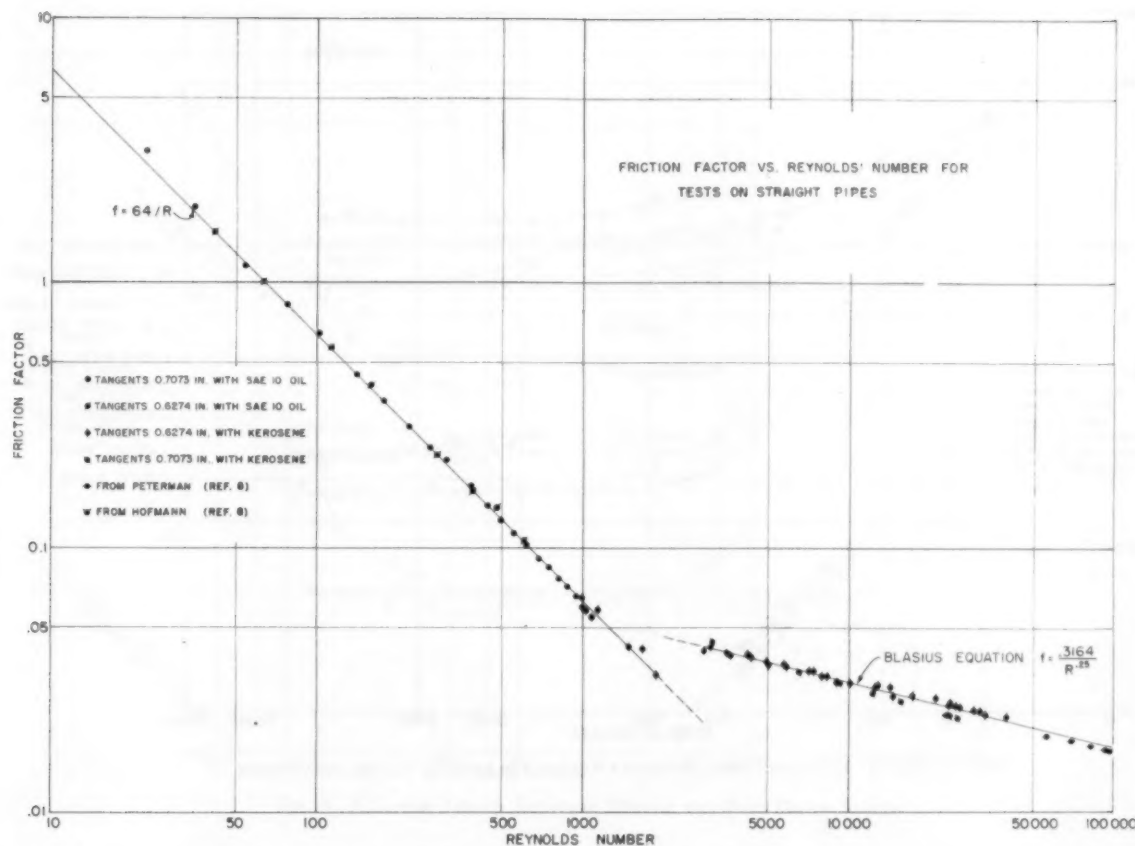


FIG. 5 FRICTION FACTOR VERSUS REYNOLDS NUMBER FOR TESTS ON STRAIGHT PIPES

Thus the long downstream test section made possible a direct determination of the straight-pipe loss for all such runs. Straight-pipe losses were calculated for all runs at $R < 2000$ using $f = 64/R$.

Resistance coefficients (K -factors) for all of the valves and fittings tested are shown in Figs. 6, 7, and 8. The lower critical Reynolds number is about 2000 for a straight pipe, but this does not necessarily apply to the reach immediately downstream from a fitting where additional disturbances are present. The resistance coefficients shown in Fig. 6 do not change appreciably with decreasing Reynolds number until an apparent critical value less than $R = 1000$ is reached. Below this apparent critical Reynolds number, the values of K increase approximately according to the equation

$$K = A/R^n \dots \dots \dots [1]$$

where A and n are constants. The globe valve with composition disk is an example for which $A = 203$, $n = 0.5$, and the apparent critical Reynolds number is about 350.

Resistance coefficients for all fabricated bends tested are given in Fig. 7. No consistent trend of K as a function of R/d is apparent for the four bends tested. The curve for the 90-deg elbow has been shown in Fig. 7 for comparison. There appears to be little difference between it and the bends at Reynolds numbers less than 2000.

Resistance coefficients for all check valves tested are shown in Fig. 8. Since part of the momentum of the flow is required to displace the movable element, a check valve produces variable throttling unless the momentum is sufficient to hold the valve in the wide-open position. For the tests with kerosene, the point at the lowest Reynolds number shown for each valve corresponds approximately to the lowest velocity at which flow could be maintained. The two working fluids were of nearly the same density, but the oil was more than 20 times as viscous as the kerosene. Thus the momentum of the kerosene at $R = 1000$ was less than that of the oil at $R = 50$. This accounts for the fact that two curves for each valve are shown in Fig. 8. Many more tests with fluids of different viscosities would be required to fix the dependence of K on ρV^2 , but a possible formulation can be obtained from the assumption that

$$K = \phi(R, \nu/\nu_r) \dots \dots \dots [2]$$

where ν_r is any convenient reference viscosity. The form of the function might be

$$K = C(R)^m (\nu/\nu_r)^n \dots \dots \dots [3]$$

where C , m , and n are constants. Enough data were available for the swing-check valve with composition disk to determine tentative values of the constants in Equation [3]. The straight lines in Fig. 8 for the partially open condition of this valve have

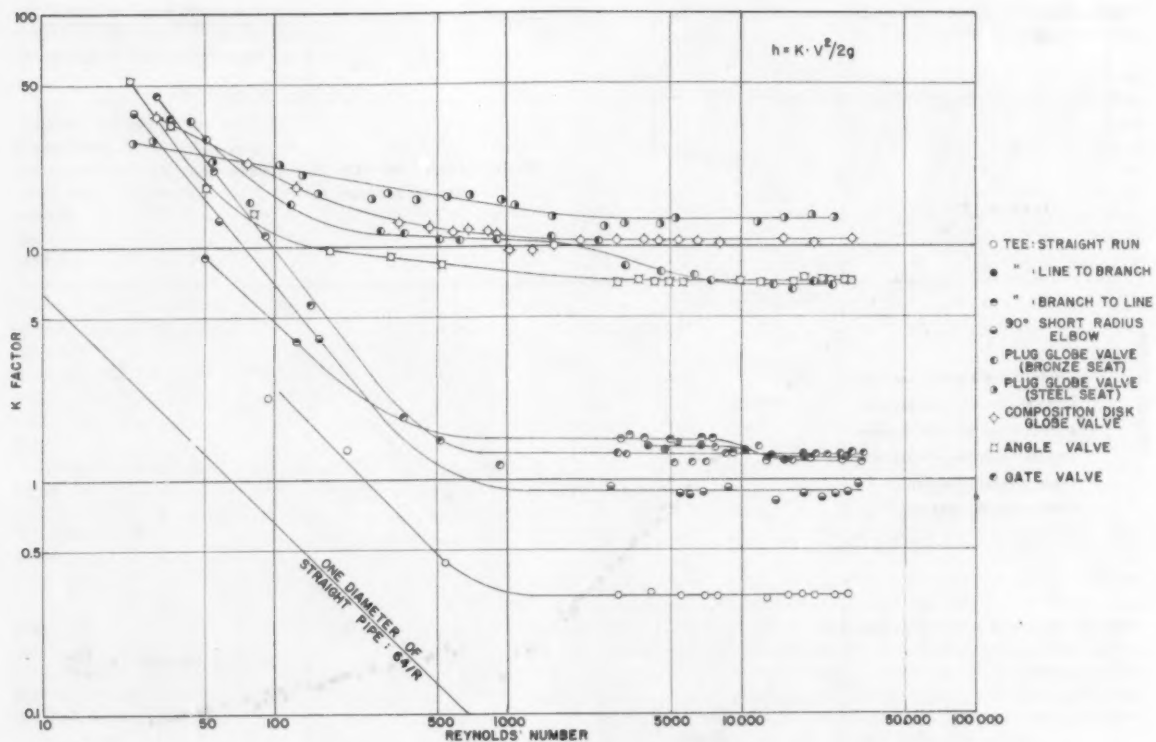


FIG. 6 K-FACTOR VERSUS REYNOLDS NUMBER FOR SEVERAL VALVES AND FITTINGS

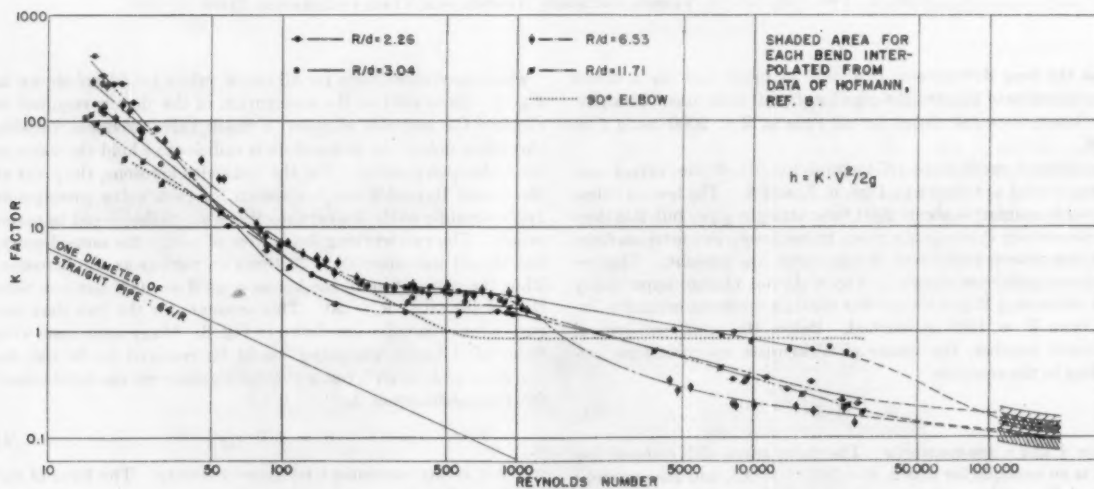


FIG. 7 K-FACTOR VERSUS REYNOLDS NUMBER FOR FOUR SMOOTH-WALLED BENDS

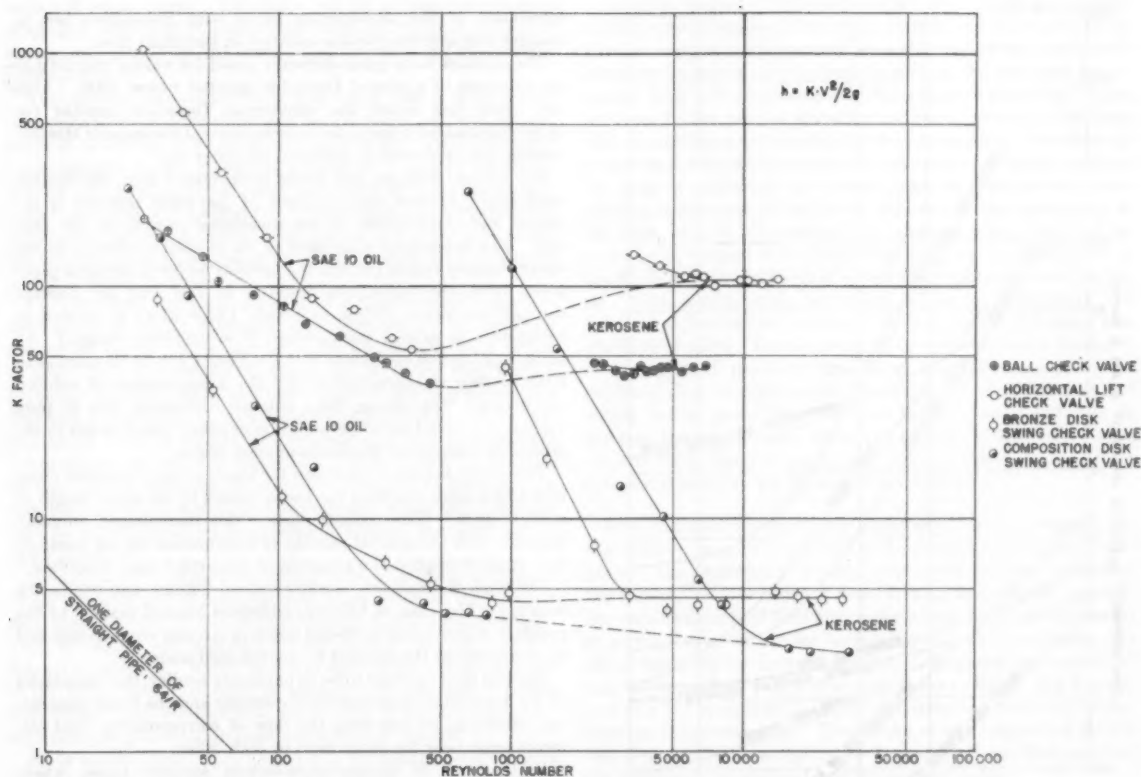


FIG. 8 K-FACTOR VERSUS REYNOLDS NUMBER FOR FOUR CHECK VALVES

been drawn for $C = (2.928)(10)^n$, $m = -1.635$, and $n = -1.644$. The reference viscosity was that of pure water at 60 F for which $\nu_r = 1.130$ centistokes = 0.00001216 sq ft/sec.

The Naval Boiler and Turbine Laboratory, Philadelphia, Pa., made available the data for many of the tests reported by Beck. In order to compare this work with the tests reported here, Beck's computations were revised to eliminate the loss due to a length of straight pipe equal to the center-line length of each valve and fitting. This revealed many apparently negative values of K at low Reynolds numbers together with generally decreasing values of K as R decreased. Lack of agreement between the results of the two investigations made any graphical comparison impractical.

The difficulty inherent in determining accurate values for resistance coefficients at low Reynolds numbers can be illustrated by the results of a typical run. For example, oil flowing through the $R/d = 2.62$ bend at $V = 0.1612$ fps caused an over-all loss of head of 0.628 ft of oil in the test reach $L = 348.9d$. The corresponding velocity head was $V^2/2g = 0.000404$ ft of oil and $R = 17.27$. The lost head in the tangents was 0.460 ft of oil and in a piece of straight pipe equal to the center-line length of the bend would have been 0.062 ft of oil. Thus the excess head loss caused by the bend was 0.106 ft of oil and the corresponding value of $K = 262$.

The general upward trend of K with decreasing R below the apparent critical Reynolds number is consistent with the behavior of drag coefficients as shown in Fig. 9. The resistance to flow past a submerged body, such as a sphere or cylinder, is caused largely by the wake unless the Reynolds number is very

small. Such a wake is analogous to the secondary flow produced by a valve or fitting in the reach of pipe immediately downstream. It should not be inferred that Fig. 9 represents an attempt to correlate the resistance coefficients for any valve or fitting with the drag coefficients for any submerged body. The presentation shows only the fact that a general increase in the values of resistance coefficients with decreasing Reynolds numbers is to be expected.

ACKNOWLEDGMENTS

The authors take this opportunity to thank the Cities Service Oil Company, the De Laval Steam Turbine Company, and the Walworth Company for contributions of equipment and material. The project was made possible by appropriations from the general and special funds of the Department of Mechanical Engineering, Princeton University.

BIBLIOGRAPHY

- 1 "Pressure Drop Tests on Globe and Angle Valves With Oil and Water Flow," by Milton Karr and L. W. Schutz, *Journal of the American Society of Naval Engineers*, vol. 52, May, 1940, pp. 239-256.
- 2 "Pressure Losses in Marine Fuel Oil Systems," by Cyrus Beck and H. M. Miller, *Journal of the American Society of Naval Engineers*, vol. 56, February, 1944, pp. 62-83.
- 3 "Laminar Flow Friction Losses Through Fittings, Bends, and Valves," by Cyrus Beck, *Journal of the American Society of Naval Engineers*, vol. 56, May, 1944, pp. 235-271.
- 4 "Laminar Flow Pressure Losses in 90-Degree Constant Circular Cross-Section Bends," by Cyrus Beck, *Journal of the American Society of Naval Engineers*, vol. 56, August, 1944, pp. 366-388.
- 5 "Comparison of 3 1/4-Inch I.P.S. and 6-Inch I.P.S. Valves and

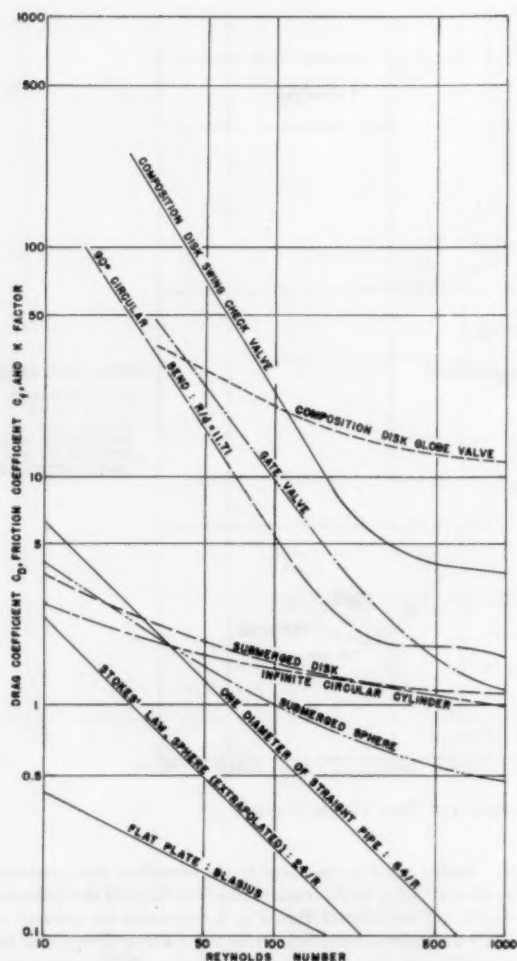


FIG. 9 COMPARISON IN LAMINAR FLOW RANGE OF SEVERAL DIMENSIONLESS RESISTANCE COEFFICIENTS: C_D , C_F , AND K

Fittings in Laminar Flow," by Cyrus Beck, *Journal of the American Society of Naval Engineers*, vol. 56, August, 1944, pp. 389-395.

6 "Investigation of the Resistance Coefficients of a Series of One-Half Inch Pipe Fittings," by R. R. John, unpublished thesis submitted in partial fulfillment of the requirements for the degree of BS in Engineering, Princeton University, Princeton, N. J., 1951.

7 "Resistance Coefficients in Laminar and Turbulent Flow for Pipe Fittings," by D. S. Rowley, unpublished thesis, submitted in partial fulfillment of the requirements for the degree of BS in Engineering, Princeton University, Princeton, N. J., 1952.

8 "Loss in 90-Degree Pipe Bends of Constant Circular Cross Section," by Albert Hofmann, authorized translation of *Mitteilungen des Hydraulischen Instituts der Technischen Hochschule München*, Heft 3, 1929, pp. 29-41, published by ASME, 1935.

Discussion

CYRUS BECK.⁶ The work reported by the authors is a welcome addition to the relatively small body of information on flow losses through valves, fittings, and bends. The methods of measurement of pressure drops, pipe dimensions, flow rate, and fluid constants appear satisfactory in view of the substantial

⁶ Naval Air Development Center, Johnsville, Pa.

correlation of the pipe-friction factor with Poiseuille's law in laminar flow and the Blasius equation in turbulent flow.

The authors have quite correctly noted for valves and fittings the existence of a critical Reynolds number below 1000. This the writer has called the convergent Reynolds number (or Reynolds-number region) for reasons beyond the scope of this discussion but explained in authors' reference (3).⁷

For valves, fittings, and bends in turbulent flow, the friction coefficient's relative independence of Reynolds number is expected and attributable to the turbulence normal to the pipe flow. The substantial constancy of the friction coefficient in the upper laminar region (unlike the friction factor in straight pipe) arises from the turbulence induced in the fluid by passage through the valve, fitting, or bend. (This effect is utilized in rotameters to extend the constant flow-coefficient range.) An increasing friction coefficient with decreasing Reynolds number in laminar flow is characterized by the disappearance of induced turbulence. The change from induced turbulence flow to pure viscous flow acted on by deformation or other forces occurs in the critical or convergent Reynolds-number region.

The writer has reported losses for bends at low Reynolds numbers which were less than the losses caused by an equal length of straight pipe.⁸ The authors state, "this unexplained anomaly together with the general paucity of information for the laminar-flow state prompted the program of research herein described."

Although the authors consider valves, fittings, and bends, the writer, for the sake of brevity, addresses himself mainly to the problem of flow losses in 90-deg bends of circular cross section and in particular to the alluded to unexplained anomaly.

For two fluid motions to be dynamically similar, the boundaries of the flows must be geometrically similar and the forces generating, directing, or retarding the flow of corresponding fluid elements must bear the same ratio to each other.

In the case of circular-cross-section straight pipes, where roughness is not a factor, the geometrical-similarity condition is immediately satisfied. A fluid element in the flow of a viscous, incompressible fluid in a straight pipe is subjected to the interaction of inertia, viscous, and pressure forces, designated F_i , F_v , and F_p . The plot of any two independent force ratios yields a unique curve. As shown in authors' reference (4)⁹

$$F_i/F_v = R \quad \text{and} \quad F_p/F_i = P$$

where

R = Reynolds number, dimensionless

P = friction coefficient, dimensionless

It is well known, of course, that the friction factor in straight-pipe flow is a function of Reynolds number.

When a viscous fluid is forced around a 90-deg bend, a new influence begins to operate on each fluid element. The fluid is now subjected to a centrifugal force F_c which is responsible for its curvilinear motion. Four forces operate on the fluid, F_i , F_v , F_p , F_c . Any three independent force ratios define the fluid-motion characteristics. From authors' reference (4)¹⁰

$$F_i/F_c = R/d$$

where

R = bend radius of curvature

d = inside pipe diameter

It is apparent that corresponding to each R/d a different P

⁷ Reference (3) of the paper, p. 348.

⁸ Reference (4) of the paper, p. 371 and fig. 6, p. 372.

⁹ Ibid., pp. 374, 375.

¹⁰ Ibid., pp. 376, 377.

versus R curve exists. This gives rise to a family of friction-coefficient versus Reynolds-number curves. Such a system of curves was found by the writer and is presented in authors' reference (4).¹¹

The pressure losses characterizing a valve, fitting, or bend may be computed in terms of equivalent length in diameters of straight pipe or a friction (or resistance) coefficient. An alternative representation is the no-length equivalent length or no-length friction (or resistance) coefficient employed by the authors and, in fact, most other investigators. The pressure loss corresponding to the physical length of the valve, fitting, or bend is subtracted. The writer questions the validity of such a subtraction in general and in bends in particular.

Consider fluid flowing in a length of straight pipe in a manner determined by inertia, viscous, and pressure forces; the fluid now encounters a bend and a new force, the centrifugal force, begins to play a role in determining the character of the flow regime. Dynamic similarity does not exist between the straight-section flow and the bend flow. Any meaning attached to a simple subtraction of losses is arbitrary since clearly defined and different forces control the two flow situations. It would be as reasonable, for comparison purposes, to subtract losses in two straight-pipe flow regimes at the same Reynolds number where only one happens to be influenced by compressibility forces characterized by Mach number.

When losses due to a valve, fitting, or bend are large compared to an equal length of straight pipe, subtraction of the pressure drop corresponding to the physical length makes little difference. This, of course, will generally be the case at high laminar-flow Reynolds numbers. Where new and distinct fluid forces operate in the valve, fitting, or bend of a magnitude comparable to the fluid forces in the straight pipe, application of the no-length concept does not yield the simplest correlation of results.

As is known, fluid, upon entering a horizontal bend (from a straight pipe), divides itself symmetrically into two mirror-image spirals corresponding to the upper and lower semicircles of the circular cross section of the bend. (This can be easily observed by introducing a dark fluid filament in laminar flow of a transparent liquid in a glass bend.) The velocity distribution is no longer a paraboloid of revolution symmetrical about the longitudinal axis. There is a redistribution of the originally straight streamlines into spiraling unbroken ones in the bend giving rise, conceivably, to reduced, unsymmetrical velocity gradients. The writer offers as a hypothesis that the reduction in the rate of deformation corresponds to lower viscous stresses resulting in less transformation of mechanical energy into heat than occurs in an equal length of straight pipe. Such a phenomenon would explain the equivalent length of a bend at low Reynolds numbers being less than the physical length. Verification of the hypothesis would require rather careful measurements in controlled flow through bends.

The writer can suggest no reason for the discrepancies between the results of the authors and his own. Their statement, "No consistent trend for K as a function of R/d is apparent for the four bends tested," leaves the situation unresolved in a manner quite unrelated to the anomaly attributed to the writer. It may be that in the laminar Reynolds-number region investigated, the bends tested do not reveal clearly separate curves but a family of curves would certainly be expected in some range of Reynolds numbers.

Viewing the matter in the limited perspective possible, it appears that some important factor in the situation is being unwittingly omitted. It is hoped other interested investigators may supply additional data and perhaps the harmonizing element in a puzzling problem.

¹¹ Reference (4) of the paper, fig. 8.

A. R. C. MARKL.¹² The authors are to be highly commended for their presentation of the results of flow tests extending to extremely low Reynolds numbers for which up-to-date information is extremely scarce, particularly in view of the fact that Beck's results were not corroborated. The consistency of the results obtained in the present investigation gives evidence of extreme care in organizing and conducting the experiments. For the very reason that the information produced appears so highly reliable, the writer would like to ask that the paper be amplified by a more detailed description of the parts subjected to test, preferably in the form of fully dimensioned drawings showing details of all contours in contact with the flowing medium, the bend radii of the 90-deg elbow, the fit-up of the screwed ends of the tees, and so on. This would prove invaluable to future researchers. A measure of the surface roughness in both pipe and fittings also would be of value. Furthermore, if the pressure drop of the valve or fitting itself could be dissociated from that caused in the following pipe, in other words if readings also were taken at the fitting outlet, presentation of this information would help in deriving the fitting losses where two or more fittings follow each other in such close succession that the pipe losses resulting from flow disturbance by the fitting are not realized.

R. J. S. PIGOTT.¹³ First, this writer would like to congratulate the authors on a valuable and well-executed experimental program. The consistency of the points shows the high quality of the testing. This writer has been working for some 50 years on the various aspects of fluid flow, mainly because he was interested in getting better means for reasonably accurate calculation. In all of this work we have been greatly hampered by the lack of rational formulas for pipe flow, and losses in bends and fittings, and this has been largely owing to incomplete data and faulty location of pressure taps. This situation was aggravated by the fact that, with the exception of Freeman, no one had specified the roughness, or explored into the viscous region.

The present paper furnishes a quantity of data connecting up the viscous and turbulent regions and, since the work was on $1/8$ -in. material, gives us an anchor point for one end of the size range. The writer has had this paper too short a time to make any detailed comparisons with other work, but inspection discloses some features of interest.

1 The writer, in the paper given at the same session, has continued the connection of elbow and bend roughness, as well as Reynolds number, with f , the pipe-friction factor. In the course of this study (recent test data, as well as much of the older data) it became evident that both f and k remained at the flat constant value to much lower values of Reynolds number than indicated by the Colebrook transition equation.¹⁴ These tests on $1/8$ -in. fittings show a very short transition region—in some cases, none. They therefore tend to support the view expressed in the writer's paper, that the Colebrook equation does not represent the variation of f in the transition region correctly.

2 In the case of the tubing bends, the various r/d tests do not show a consistent position relative to the r/d , but cross and recross the cast-elbow relatively rough threads right through the values for the smooth tubing bends. Probably this indicates that, in the viscous region, neither roughness nor R has effect and a single line also might be suitable for all r/d -values. We need more tests, on other sizes, to settle such a point.

The writer would suggest that cross sections of the valves and fittings, or at least the flow passage, be added. The resistance of valves of the same size has been found to vary $2^{1/2}:1$ depending

¹² Research Consultant, Tube Turns, Louisville, Ky.

¹³ Retired, Pittsburgh, Pa. Fellow ASME.

¹⁴ "Friction Factors for Pipe Flow," by L. F. Moody, *Trans. ASME*, vol. 66, 1944, pp. 671-684.

on the passage fairing. Cast elbows always have a passage much larger than the pipe ID, and that introduces trouble; what size is it? It also would be highly desirable if the authors could give, if possible, the absolute roughness of the cast fittings, valves, and drawn tubing, including the bends. It is now clearly evident we must have roughness measurement if we are to spot the test values in correct relation. In these tests, for example, the plug globe valve was tested with steel and bronze seats; if there were no difference in the flow configuration, there would be no difference in the test values in the turbulent region.

AUTHORS' CLOSURE

The authors wish to thank Messrs. Beck, Markl, and Pigott for their discussions.

Mr. Beck suggests that there may be cases where the losses due to the secondary flow downstream from a bend or elbow may be less than for the same flow in a straight pipe. The usual experience is that any secondary flow is associated with an increase in the conversion of mechanical energy to heat and such was the case for the bends and elbow tested. Much more information is needed, particularly on larger sizes of pipe, to determine if scale effects are present. Mr. Beck has raised an interesting point that Reynolds number and geometrical ratios may be insufficient to describe completely the flow around bends under all circumstances.

Mr. Markl and Mr. Pigott have asked for considerable information which the authors are unable to supply. It has not been possible to obtain drawings of the flow passages in the various valves and fittings. The fittings were all sand castings and therefore quite rough. Fig. 5 shows that the roughness of the

straight pipe was less than the thickness of the laminar boundary layer for the range of Reynolds numbers covered by the investigation.

The tee tested on straight run had the branch closed by a pipe plug. The tee tested from branch to line and from line to branch was fitted with 4-in. nipples all around, the unused nipple being capped at the outer end in each case. The 90-deg elbow appeared to have a radius of about $\frac{1}{4}$ inch. This had little significance because the inside diameter of the elbow was about the same as the outside diameter of the pipe. Thus, to some degree, the flow suffered a sudden expansion into an enlarged chamber followed by a sudden contraction on leaving. Fig. 7 shows that this produces about the same loss as a smooth bend in the laminar flow state.

Mr. Markl has asked for information for use in computing the loss caused by a series of closely spaced fittings. The only reliable way to determine such an over-all loss is to test the fittings in the series arrangement. Each fitting is likely to influence the flow in subsequent fittings and the losses probably will depend on the space between fittings.

Mr. Pigott has inferred that the results of the tests can be used to disprove the Colebrook formula. Such is not the case. The Colebrook formula applies only to the losses caused by fluid friction in rough pipes from which fitting losses are excluded. Neither condition was fulfilled in the tests reported. The authors agree with Mr. Pigott that like fittings should produce equal losses. The two plug globe valves tested were of quite different internal construction so that the flow passages around the plugs could not be considered comparable.

Losses in Pipe and Fittings

By R. J. S. PIGOTT,¹ PITTSBURGH, PA.

NOMENCLATURE

The following nomenclature is used in the paper:

- R = Reynolds number, general: $\frac{d\rho v}{\mu}$
 R_c = Reynolds number at which f becomes constant
 R_s = Reynolds number at which constant f -lines intersect the von Karman smooth-turbulent line
 f = friction factor in $\Delta p = \frac{0.000108 f \rho v^3}{d}$
 f' = friction factor as generally used in the von Karman equations
 f_c = constant value of f after R_c is exceeded
 ϵ = absolute roughness, in.; total height of projection, not rms
 $\frac{\epsilon}{d}$ = relative roughness, number
 k_1 = true bend loss, fraction of velocity head, number
 k_2 = loss due to roughness, fraction of velocity head, number
 k = total bend loss, $k_1 + k_2$; excludes pipe loss of bend

1—PIPE AND TUBE

The examination of recent test data on pipes, elbows, and bends, prompts another attempt at putting loss values in better condition, and on a more nearly rational basis. The writer's paper of 1933 (1)² was, so far as he can find, the first introduction of roughness as a systematic factor in the f versus R plot; but the method of plotting with arbitrary numbered lines covering a small range of relative roughness in each line was not too satisfactory. Later the same year, the von Prandtl and von Karman smooth-turbulent and rough-turbulent equations became available, as well as Nikuradse's test work substantiating them. Finally the Colebrook equation furnished Prof. L. F. Moody with enough new material to produce his valuable 1944 paper (2). This paper presented the von Karman relation, showing the smooth-pipe line to be a continuous curve, and the values of f becoming finally constant; the Colebrook transition relation furnished a plausible junction between the two regions.

Two conditions of the 1944 chart must be kept in mind:

1 The locus of the R_c values for each roughness, at which viscosity effects vanish and f becomes constant, is not from test data but from the points at which the Colebrook values approach the constant values of f within $1/2$ per cent.

2 The Colebrook equation is a convenient means of getting mutually consistent transition lines, but there is no inherent proof that it is correct. Experimental material available since 1944 justifies a re-examination of this situation. During the past 10 years a number of engineers, who are chiefly concerned

with pipe flow, have remarked to the author that the Colebrook curves are too high for large steel pipe.

Nikuradse's experiments on approximately 1 to 4-in. pipe, and Hofmann's on 1.70-in. pipe and bends, started with drawn brass pipe and fine-machined cast bends. These were roughened with classified sand and lacquer. The roughness measurement was based on the maximum grain diameter, and the type of roughness produced was not exactly like cast pipe. Sand-casting surfaces are substantially the negative of the sand cores, with relatively sharp peaks and rounded valleys; whereas the artificially sand-roughened pipes show rounded peaks. Further, foundry sand is not classified, and the grain size varies over a range. We know from the experiments of Freeman, Hopf, Fromm, Fritsch, and Stanton, that the character of the roughness, as well as the absolute height, affects the friction factor.

Nikuradse found the results shown in Fig. 1. Starting with smooth pipe, he varied roughness from $\epsilon/d = 0.000985$ to 0.0333. The considerable drop in f , below the final constant value, between the viscous and fully turbulent flow has not been duplicated by other investigators; however, traces of this drop show in a few of the various tests, but generally the falling f with increase of R , as indicated by the Moody-Colebrook curves, is found.

An extensive investigation by R. V. Smith, J. S. Miller, and J. W. Ferguson, Bureau of Mines, sponsored by the American Gas Association (3), has provided new and authoritative data. One of the difficulties of earlier tests is that the range of Reynolds number has been too small, either to reach full turbulence, or down to the viscous region. But these tests were carried up to $R = 20,000,000$ in 8-in. pipe, and correspondingly for the smaller sizes, so that rough turbulence is fully developed and locatable. The test covered 2 to 8-in. seamless steel, 3 and 8-in. welded pipe; sixteen groups of tests in all, in three of which the Nikuradse shape of f -curve was indicated. In addition, 3-in. stainless-steel tube was superfinished to $\epsilon/d = 0.0000022$ -in. rms by profilometer. This is the first time a smooth pipe has been prepared for flow tests to a known roughness, measured by modern instruments. Fig. 2 shows the values obtained for 2 and 4-in. seamless, and 3-in. stainless. In each of these plots the ϵ/d -values are given for those groups which the investigators thought most authoritative, together with the corresponding Moody chart lines. Fig. 3 shows the 6 and 8-in. seamless, and 8-in. welded groups; Fig. 4 shows the 3-in. seamless and welded. Filtration to eliminate dust and moisture separation for water or hydrocarbon condensates was employed in many tests; the moisture separation was not always complete. It may be noted that the Nikuradse type of f -curve appears in one test each, 3-in., 4-in., and 6-in. sizes. The other thirteen groups show the more usual continuously falling curve, lying roughly halfway between Nikuradse and Colebrook values; errors of up to 20 per cent are thus possible by the Colebrook curves. Another condition predicted by Nikuradse was supported—that all pipes, of any roughness, as R decreased finally join the smooth-turbulent line, and then behave as hydraulically smooth pipe. In these tests, the 2-in. seamless pipe, $\epsilon/d = 0.000282$ in., was carried to low enough R to join that line. Since all the tests were carried well above the point of constant f , we can get the value of R_c in modern steel pipe for a range of sizes.

In view of the extent and accuracy, Freeman's tests (4) were

¹ Retired. Fellow ASME.

² Numbers in parentheses refer to the Bibliography at the end of the paper.

Contributed by the Hydraulic Division and presented at the Annual Meeting, New York, N. Y., November 25–30, 1956, of THE AMERICAN SOCIETY OF MECHANICAL ENGINEERS.

NOTE: Statements and opinions advanced in papers are to be understood as individual expressions of their authors and not those of the Society. Manuscript received at ASME Headquarters, May 18, 1956. Paper No. 56—A-63.

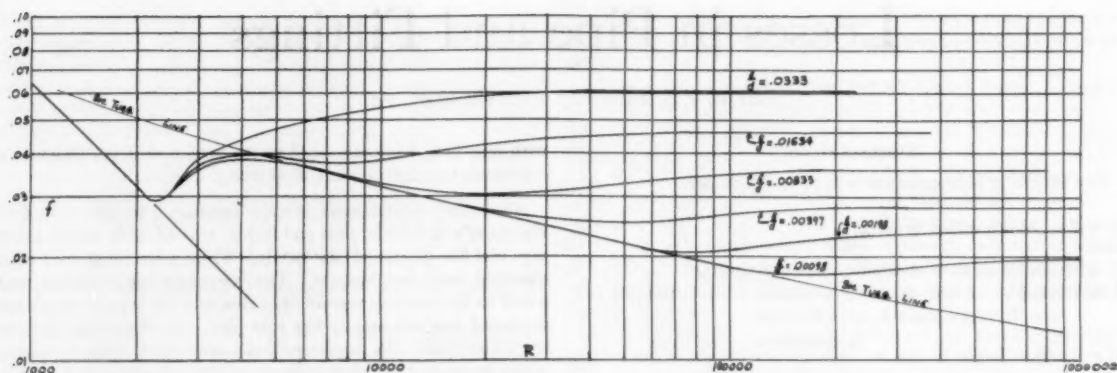


FIG. 1 NIKURADSE'S TESTS ON SAND-ROUGHENED PIPE

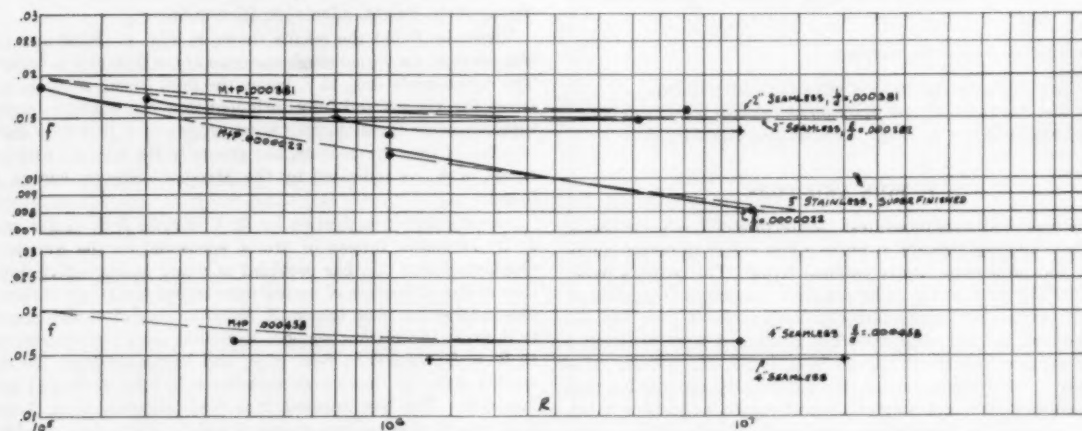


FIG. 2 BUREAU OF MINES-A.G.A. TESTS, 2-IN. AND 4-IN. SEAMLESS STEEL, 3-IN. HONED STAINLESS

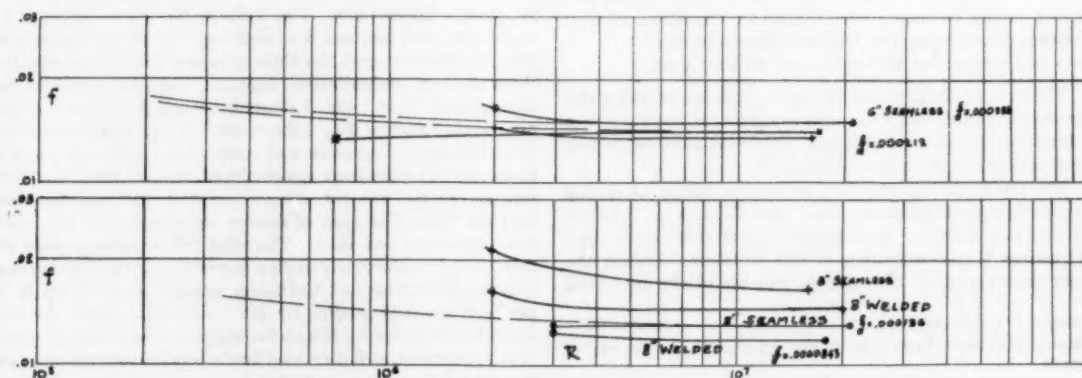


FIG. 3 BUREAU OF MINES-A.G.A. TESTS, 6-IN. AND 8-IN. SEAMLESS STEEL, 8-IN. WELDED STEEL

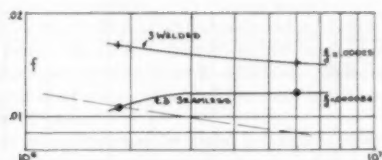


FIG. 4 BUREAU OF MINES-A.G.A. TESTS, 3-IN. SEAMLESS STEEL AND 3-IN. WELDED STEEL

re-examined. He used brass pipe, $1/4$ to 4 in., wrought-iron pipe $1/4$ to 8 in., asphalted cast iron 4 and 8 in., and a series of elbows, tees, $2 1/2$ to 8 in., as well as other fittings. All were tested clean, quite a number rusted, and a few with artificial roughening. All of the brass-pipe tests lie on the von Karman smooth-turbulent line. The 5, 6, and 8-in. wrought-iron pipes were tested quite near to R , and show that this material was noticeably rougher than our present-day steel pipe. Several of the smaller sizes were tested in the viscous region, and give another line for checking the work. The viscous-region results gave a line, $f = 66.5/R$, instead of the well-substantiated $f = 64/R$, indicating a systematic error of 3.9 per cent. The volume measurements and the manometers appear to be beyond criticism, but the piezometers are not. The screwed-type piezometers were machined to the nominal standard inside diameter, not necessarily matching the actual upstream diameter of the pipe. The piezometer holes appear large, and the method of assuring proper edges is not given. But more important, as Mr. Freeman himself discusses, the wrought-iron pipe was contracted at the ends by the operation of threading, sometimes as much as 0.10 in. Such a contraction, $2d$ upstream from the piezometer holes for the smaller pipe, $1/2d$ for the 8 in., could easily produce errors of several per cent in static reading. This type of piezometer was used for all wrought-iron pipe except $1/4$ in. The 1, 3, and 4-in. brass also used them, but brass cuts so freely there was no contraction.

While the amount of correction cannot now be determined, it is interesting to note that a 2 per cent correction would put the $1/4$ to 2-in. wrought iron on the smooth-turbulent line. In these sizes, the contraction was $2d$ ahead of the piezometer holes. Sizes 4, 5, 6, and 8 in. had progressively shorter distances from contraction to piezometer holes, down to $1/2d$, consequently more disturbance, and requiring a larger correction, up to perhaps 5 per cent. With tentative correction, Freeman's tests afford further support to Nikuradse's prediction mentioned previously.

In Figs. 5, 6, and 7, a few tests by other investigators are shown. Davis' test on 2-in. wrought iron was made about the same time as Schoder's 6-in. wrought iron—1908-1909. Both show values lower than Freeman's and both tend to join the smooth-turbulent line sooner. Tests by J. E. Busher on 2, 4, 6, and 8-in. steel pipe, incidental to tests on welding elbows and bends, have quite flat coefficient curves. The Bureau of Mines tests, Figs. 2, 3, and 4, are similar. We might infer that modern steel pipe not only has a different roughness from the wrought-iron pipe of earlier tests but also a different kind of roughness. Freeman describes the roughness of his wrought-iron pipe as slag nodules and patches of scale about 0.02 in. in height—an irregular and more or less discontinuous type; whereas modern steel pipe has no slag, little or no scale patches, a continuous and relatively uniform surface.

Since the test data showing the value of R , are very limited, tests on other forms of conduit might be usable for this purpose. Venturi meters use approach and diffuser cones, connected by a straight throat, but their losses occur in the same way as straight pipe. More than 30 years ago, Prof. W. S. Pardos showed that the venturi discharge coefficient could be calculated from pipe-friction factors, and that the coefficient of discharge becomes constant at a value of R determined by the relative roughness only. Venturi meters are generally made with cast-iron or cast-steel cones, so that the relative roughness is quite well defined.

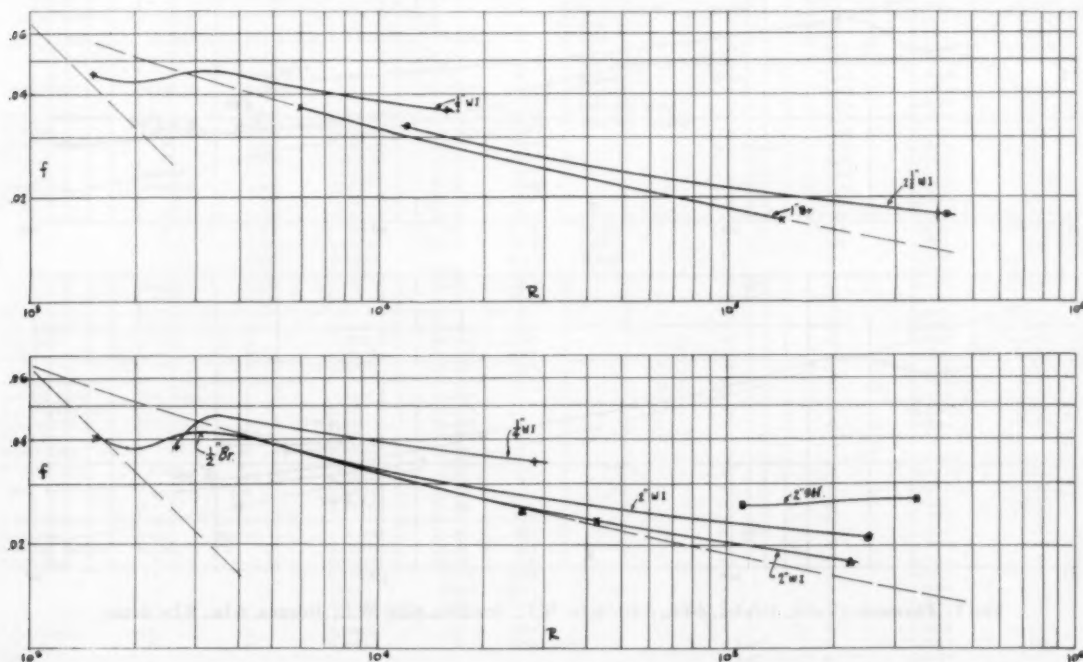


FIG. 5 FREEMAN, $1/4$ -IN., $1/2$ -IN., 2-IN., $2 1/2$ -IN. W.I.; $1/4$ -IN., 1-IN. BRASS; DAVIS, 2-IN. W.I.; BUSHER, 2-IN. STEEL

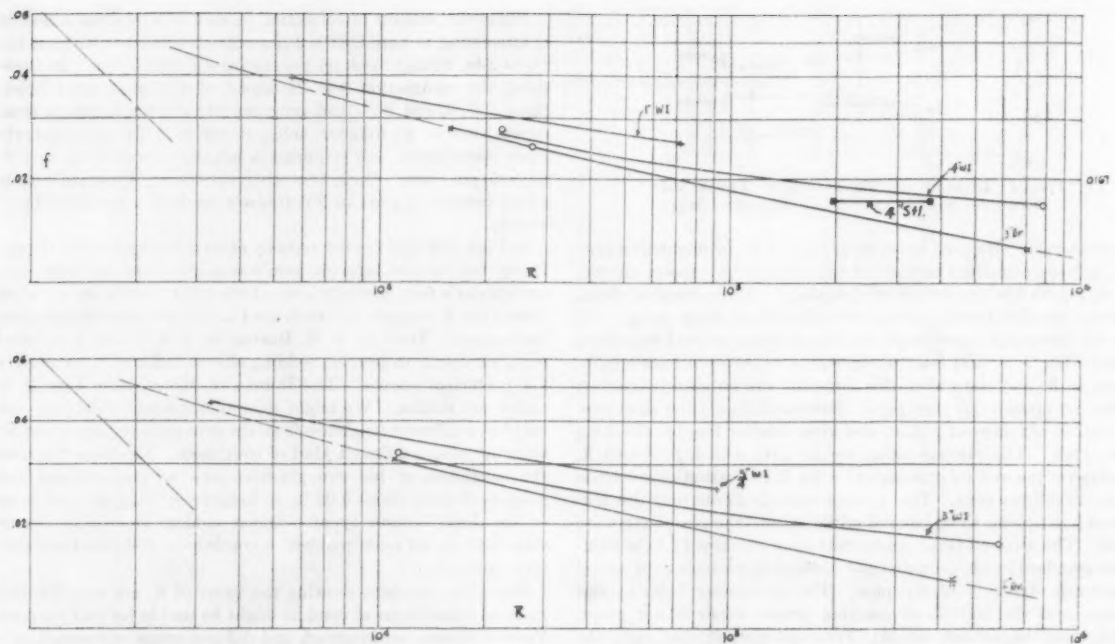


FIG. 6 FREEMAN, $\frac{1}{4}$ -IN., 1-IN., 3-IN. 4-IN. W.I., 2-IN., 3-IN. BRASS; BUSHES, 4-IN. STEEL

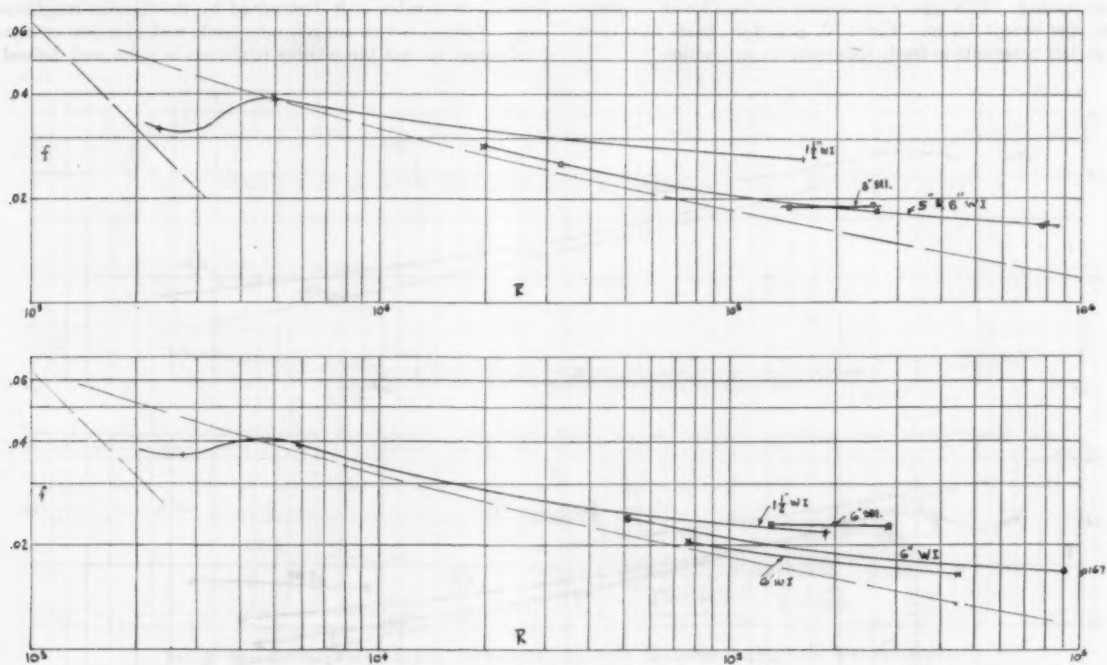


FIG. 7 FREEMAN, $1\frac{1}{4}$ -IN., $1\frac{1}{2}$ -IN., 5-IN., 6-IN., 8-IN. W.I.; SCHODER, 6-IN. W.I.; BUSHES, 6-IN., 8-IN. STEEL

Fig. 63 of the 1937 ASME Fluid Meters Report shows the values of R at which the coefficient, and consequently f , becomes constant for sizes from 1 in. ($\epsilon/d = 0.0102$) to 200 in. ($\epsilon/d = 0.00005$). These values are represented by $R = 380d/\epsilon$. This chart is based on hundreds of accurate tests, and has been in successful use for more than 20 years.

Another group that may be useful is that of elbows and bends. Since most of the tests thereon show a variation of k , the bend-loss factor, at the lower Reynolds numbers, the k varies with f in this region, then the value of R at which k becomes constant should be R_r . Some 35 test groups from Freeman 2 1/2 to 8 in., Hofman 1.70 in., and Schoder 6 and 8 in., have been assembled, recalculated to the basis eliminating pipe friction from k where necessary, and shown in Table 1 for pipe and venturi, Table 2 for elbows and bends. There is new material by J. E. Busher, 2 to 8 in., and the Naval Boiler and Turbine Laboratory, 1 1/2 to 6 in. The scatter is indeed rather wide, but examination of Figs. 9 and 10 indicates some useful general relations. Fig. 9 is a plot of R , versus ϵ/d for pipe and venturi tubes; Fig. 10 that for elbows and bends. On these two plots have been drawn the R_r line from Professor Moody's 1944 chart, and also the locus of the intersections of f , and the smooth-turbulent line. This latter line is the lowest point that could be reached by R_r .

It is at once apparent that none of the data exceeds about 1600 (d/ϵ), which is less than half the Colebrook-Moody line at 3500 (d/ϵ). The venturi data lie at 380 (d/ϵ), close to the average of all points, about 400 (d/ϵ). Of the modern test data by the Bureau of Mines-A.G.A., and Busher, four points lie above, ten below, and two about on the average line. The tests by the Naval Boiler and Turbine Laboratory are on cast-brass or bronze fittings. Since these are cast with much finer facing sand than cast iron, the roughness has been taken at one-half that of cast iron, in the lack of any actual measurement. These tests lie closely on the over-all average, 400 (d/ϵ). It is interesting to find that the average for elbows and bends is the same as for straight pipe and venturi-meter tubes.

TABLE 1 STRAIGHT PIPE AND VENTURI TUBES

Investigator	Material	Diameter inches	ϵ/d	R_r Millions	f_r
Smith, Miller and Ferguson	Steel	1.964	0.000188	1.5	.01352
	seamless	1.964	0.000282	0.5	.01487
Bureau of Mines-A.G.A.	"	1.964	0.000381	0.4	.01562
	welded	3.094	0.000383	3.5	.01170
Actual I.D.	seamless	4.041	0.000270	<1.0	.01452
1955	"	4.041	0.000358	<0.36	.01637
	"	6.079	0.000286	5.0	.01461
	"	6.079	0.00017	6.0	.01322
	"	6.079	0.000212	<0.7	.01388
	"	8.019	0.00045		.01623
	welded	8.019	0.000136	<3.0	.01272
	"	8.159	0.000281	5.0	.01435
	"	8.159	0.000380	7.0	.01160
J.E. Busher	Steel	2	0.0032	<0.110	.0266
Tube Turns	welded	4	0.0009	<0.215	.0192
1945	"	6	0.00176	<0.131	.0227
	"	8	0.00062	<0.147	.0175
Venturi Tubes	Cast Iron	1	0.0102	0.038	
W.S. Pardee and E.S. Smith	"	2	0.0051	0.078	
Fluid Meters Report 1937	"	4	0.0026	0.150	
A.S.M.E.	"	8	0.0013	0.300	
	"	16	0.00064	0.600	
	"	30	0.00034	1.125	
	"	60	0.00017	2.25	
	"	100	0.000102	3.75	
	"	200	0.000051	7.50	
Nikuradse	Brass	Approx.	0.000985	0.89	.0197
Sand and Lacquer	Rghnd.	1	0.00198	0.56	.0237
Roughening	"	4	0.00397	0.35	.0276
	"	"	0.00834	0.178	.0355
	"	"	0.0163	0.089	.0457
	"	"	0.0333	0.037	.0603
E.W. Schoder	W.I.	6	0.00036	1.5	.0164
A.S.C.E.	C.I.	8	0.0016	1.0	.0220
1909					

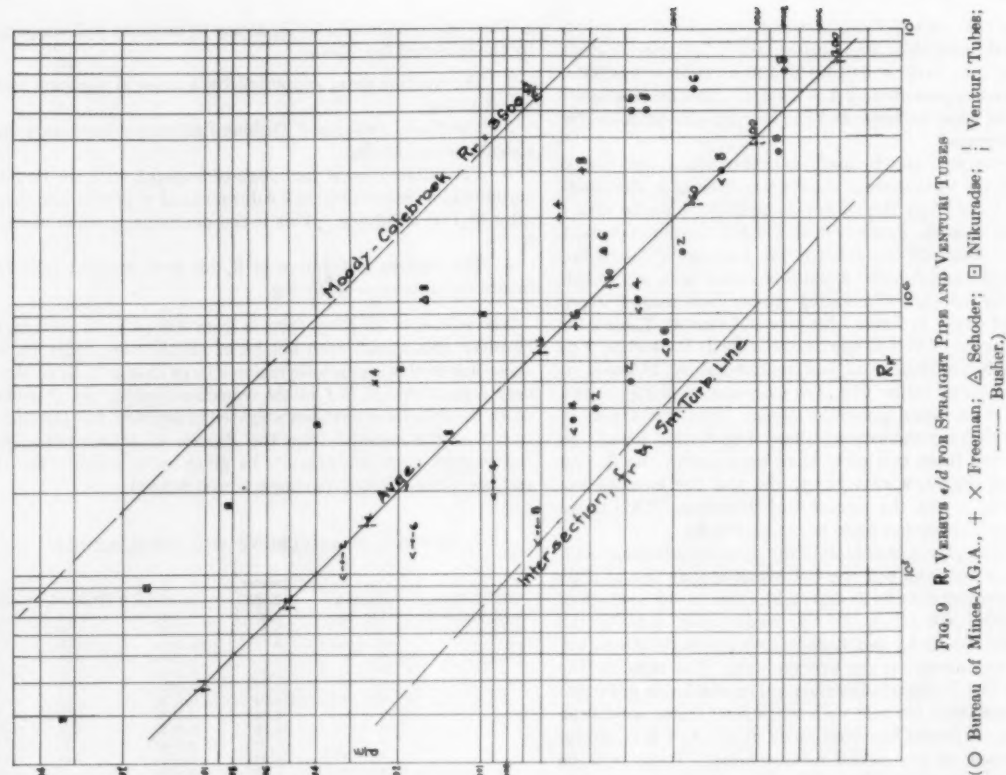
The Cd/ϵ relationship for R_r seems to be quite well supported by the following four facts:

- 1 The venturi data, supported by a mass of accurate tests, are at 45 deg.
- 2 The Naval Boiler and Turbine Laboratory tests, very consistent, are at 45 deg.
- 3 The intersection of the rough-turbulent f_r with the smooth-turbulent line is at a slope of 0.9 down to $\epsilon/d = 0.0006$, and thereafter at 1.00 or 45 deg. This is the minimum possible value of R_r .
- 4 The highest test values of R_r for both straight pipe and bends are quite close to 45 deg.

The scatter of all these tests is from 120 (d/ϵ) to 1500 (d/ϵ); however, this spread need not be at all alarming, since we observe that in this asymptotic region a large change in R_r produces only a small change in f in the transition region. In these two plots, the data have not been weighted in any way, but the author feels that the material from the Bureau of Mines-A.G.A. and the venturi data could safely be given more weight than the rest, since the relative roughness is well defined.

TABLE 2 CAST ELBOWS AND STEEL BENDS

Investigator	Material	Diameter inches	ϵ/d	R_r Millions	f_r
Naval Boiler & Turbine Lab.	Cast. Br.	1.5	0.0034	<0.21	1.06
	"	2.5	0.0021	<0.35	1.05
1955	"	4	0.0013	0.60	1.14
Elbows	"	6	0.00085	1.01	1.15
	"	1.80	0.0029	<0.23	1.80
	"	2.77	0.0019	0.43	1.44
	"	4.34	0.0012	0.56	1.10
	"	6.35	0.0008	1.23	0.84
	"	1.90	0.0029	0.21	2.78
	"	2.77	0.0019	0.40	2.17
	"	4.34	0.0012	0.64	1.85
	"	6.35	0.0008	1.01	1.59
	"	1.5	0.0034	0.22	0.64
	"	2.5	0.0021	0.28	0.66
	"	4	0.0013	0.64	0.66
	"	6	0.00085	1.10	0.61
J. E. Busher	Steel	2	0.0058	0.160	1.5
Tube Turns	"	4	0.0031	0.249	1.5
1945	"	6	0.0023	0.211	1.5
	"	8	0.0019	0.181	1.5
Hofmann	Brass	1.69	0.00044		1.0
1925	"	1.69	0.00044	0.19	2.0
Machined Brass	"	1.69	0.00044	0.18	4.0
Sand and Lacquer	"	1.69	0.00044	0.18	6.0
	Br. Rghnd.	1.69	0.00044	0.18	10.0
	"	1.68	0.0019	0.10	1.0
	"	1.68	0.0019	0.13	2.0
	"	1.68	0.0019	0.135	4.0
	"	1.68	0.0019	0.135	6.0
	"	1.68	0.0019	0.14	10.0
Freeman	C.I.	2.5	0.0041	<0.15	0.59
1892	"	2.5	0.0041	0.12	1.70
Elbows	"	3	0.0034	<0.10	0.56
	"	3	0.0034	<0.15	1.67
	" 45°	3	0.0034	<0.03	0.63
	" 180°	3	0.0034	0.15	0.61
	"	4	0.0026	<0.25	0.57
	"	4	0.0026	0.05	0.57
	"	4	0.0026	<0.35	1.72
	"	4	0.0026	<0.06	1.72
	"	4	0.0026	0.11	0.64
	"	4	0.0026	<0.05	1.30
	"	4	0.0026	<0.05	2.14
	"	4	0.0026	0.30	4.56
	"	4	0.0026	<0.06	0.53
Freeman	C.I.	4	0.0026	<0.05	4.56
	"	6	0.0017	0.30	0.57
	"	6	0.0017	<0.10	0.57
	"	6	0.0017	<0.10	1.66
	"	6	0.0017	<0.05	1.66
	" 45°	6	0.0017	0.25	0.56
	"	8	0.0013	0.80	0.62
	"	8	0.0013	0.45	0.62
	"	8	0.0013	<0.05	2.01
	"	8	0.0013	0.11	1.03
	"	8	0.0013	0.18	1.03
	"	8	0.0013	0.33	2.78
	"	8	0.0013	0.27	2.78
	" 180°	8	0.0013	0.27	1.03
	" 180°	8	0.0013	0.27	2.78

FIG. 9 R_r VERSUS f/d FOR STRAIGHT PIPES AND VENTURI TUBES

(○ Bureau of Mines-A.G.A., + × Freeman; △ Schoder; □ Nikuradse; | Venturi Tubes;
— Interaction, for a 5-in. Tube.)

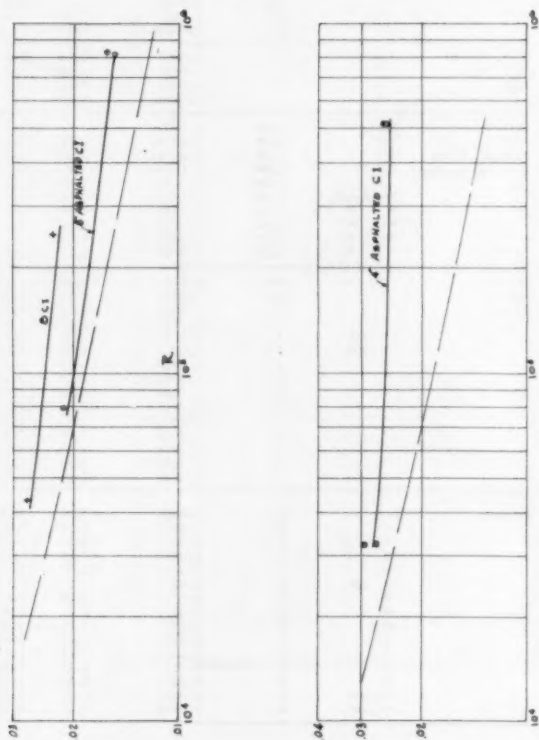
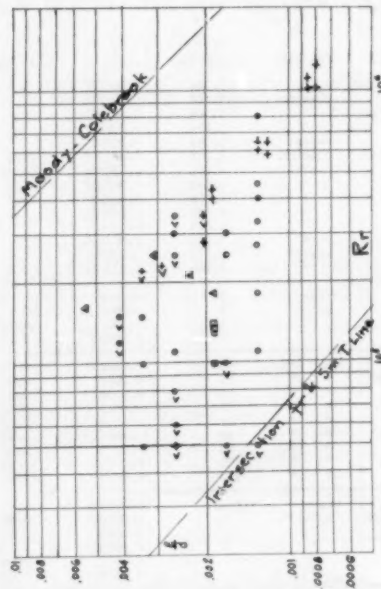


FIG. 8 FREEMAN 4-IN. AND 8-IN. ASPHALTED C.I.: SCHODER 8-IN. C.I.

FIG. 10 R_r VERSUS f/d FOR ELBOWS AND BENDS

(○ Freeman; + Naval Boiler and Turbine Laboratory; △ Busher;
□ Hofmann.)

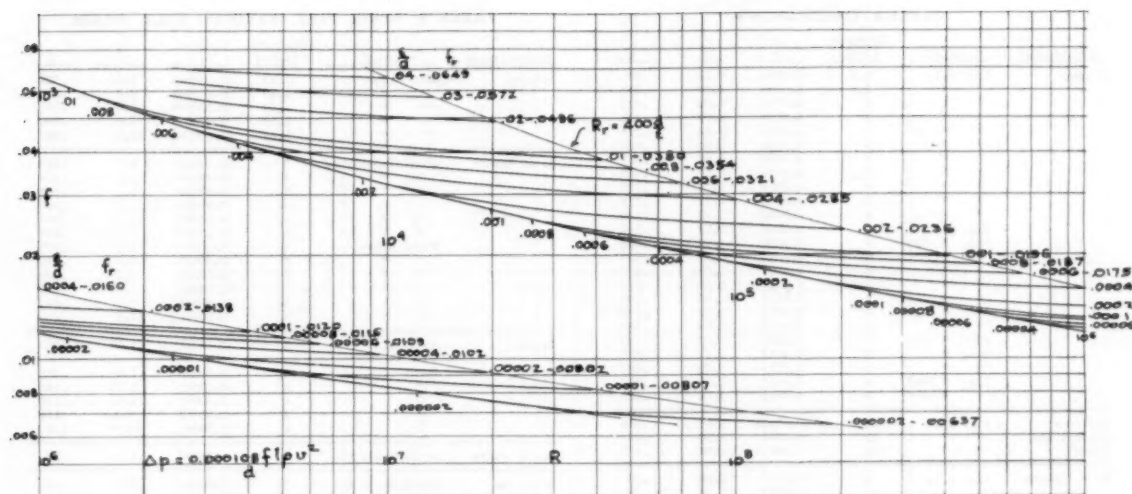
FIG. 11 FRICTION FACTOR f VERSUS REYNOLDS NUMBER R

Fig. 11 shows the revised f versus R plot, using the von Karman smooth-turbulent line and rough-turbulent values, the same as Moody, but with $R_c = 400 (d/\epsilon)$. This chart gives f -values lower than the Colebrook equation used in the Moody chart; the maximum difference, 5.4 per cent, occurs around $R = 30,000$, $\epsilon/d = 0.001$. These differences decrease toward zero as the smooth-turbulent line or R_c is approached. Even the maximum difference is less than the spread from varying roughness in the same pipe, or between different investigators on smooth pipe. The range of the transition region has been considerably reduced by the reduction of R_c ; since the values of f may follow these curves as a maximum, remain flat, or dip down as in Nikuradse's tests, a reduction of the range in which this uncertainty may occur is certainly advantageous.

It is now quite evident that ϵ/d alone is not enough to define relative roughness completely. Hopf, Fromm, and Fritzsche in their investigations, differentiated roughness between "wavy" and "rough." This thought might be generalized as follows:

- (a) Those rugosities that are sharp enough to produce *vena contracta* effects and
- (b) those that do not.

The surface of riveted pipe, especially with flow against the laps, should behave like (a); tar and asphalt coatings, wire reinforcing submerged in rubber hose, and corrugated pipe, should act like (b). Sand-cast material may lie between, because while the rugosities generally are sharp, they are so close together that *vena contracta* effects could not develop fully.

Another characteristic having a bearing might be described as "continuous" or "discontinuous." Freeman's wrought-iron pipe showed "patches" of scale and slag lumps; probably the same condition applies to the other earlier investigators' pipe. Our modern steel pipe shows a fairly uniform continuous roughness, very little scale, no slag. Riveted pipe, both straight and spiral, sheet air duct, and tuberculated steel or cast iron have discontinuous roughness. Sand castings, even with the usual unclassified sand, show relatively uniform and continuous roughness.

For the proper understanding of what roughness really is we need to have tests conducted on pipes of controlled roughness in all types, and measured by modern instruments. The profilometer, in its present form, is useful mostly for smooth materials

from drawn tubing up to steel pipe, but lacks the range for rougher material. F. F. Versaw, of the Gulf Research & Development Company, developed an air gage in connection with metal-cutting research, in which the range can be adjusted for any roughness, from drawn brass through cast iron. It is probable that we shall require these instruments to be curve-drawing, since this is about the best way to get a reliable measure of uniformity, continuity, and sharpness.

It will be noted from the test data that while the f -curves may rise continuously with decreasing R , they may also lie flat, or dip down as in Nikuradse's work. At present we are unable to predict which curve will occur; nor are we likely to do so until we have real characteristic data on types of roughness.

The maximum differences of Fig. 11 f -values from the Moody chart are about as follows:

	Per cent
1 Water, 2-in. steel or C.I.	-4 to -5
4-12-in. steel,	-3
6-12-in. C.I.	-2
2 Steam, 2-6-in. steel	-2
12-in. steel	0
3 Natural gas, 3-12-in. steel	0

As R increases toward R_c , these differences decrease toward zero, as the values for f , are the same in both charts.

The main reason why actual results sometimes vary from those calculated by the charts, is not so much due to inaccuracy of the charts as to our failure to get the actual roughness. This may change as much as 15 per cent in relatively short periods of time, as plainly shown in the Bureau of Mines-A.G.A. tests.

2—ELBOW AND BEND LOSSES

The curves for k , total bend loss, in the author's 1950 paper (6) can now be reconsidered, as we have enough new data on modern steel pipe to give a better picture of the pipe-bend situation. All of the data used in the 1950 study were relatively old, nearly all prior to 1910. Now we have tests by Busher, Crane, Taylor, Beij, and Vogel on present-day pipe, quite noticeably different from the wrought iron used at the time of the earlier investigations. Some of the old work has been recalculated, in those cases where k for cast fittings was determined by subtracting the loss for the equivalent length of wrought-iron pipe from the

TABLE 3 CAST ELBOWS

Investigator	Material	Diameter Inches	$\frac{r}{d}$	$\frac{E}{d}$	k
Freeman	Std. C.I.	2.5	0.0041	0.59	.69
		2.5	0.0041	1.70	.299
		3	0.0034	0.56	.776
		3	0.0034	1.67	.208
		4	0.0034	0.62	.294
		4	0.0034	0.61	.683
		4	0.0026	0.57	.587
		4	0.0026	0.57	.708
		4	0.0026	1.72	.150
		4	0.0026	1.72	.215
	Flg. " 45°	4	0.0026	1.30	.176
		4	0.0026	2.14	.154
		4	0.0026	4.56	.090
		6	0.0017	0.57	.530
		6	0.0017	1.66	.186
		6	0.0017	0.57	.550
		6	0.0017	1.66	.155
		6	0.0017	0.56	.258
		6	0.0013	0.62	.380
		6	0.0013	1.03	.239
Williams	Flg. C.I.	12	0.00085	1.08	.386
		12	0.00085	1.90	.23
		12	0.00085	2.00	.17
		12	0.00085	2.00	.17
E. W. Schoder	Flg. C.I.	6	0.0017	0.60	.50
		6	0.0017	1.34	.26
		6	0.0017	1.76	.22
		6	0.0017	1.90	.16
		6	0.0017	2.16	.13
		6	0.0017	3.00	.12
		6	0.0017	4.00	.12
		6	0.0017	4.00	.12
Vogel	Flg. C.I.	8	0.0013	0.70	.39
		8	0.0013	0.70	.39
Davis	Std. C.I.	2	0.0051	0.728	.593
		2	0.0051	1.15	.337
		2	0.0051	2.50	.209
Crane Co.	Flg. C.I.	2	0.0051	1.0	.427
		2	0.0051	1.0	.376
		2	0.0051	1.8	.275
		2	0.0051	0.60	.667
Naval Boiler & Turbine Lab.	Cast Br.	1.5	0.0034	1.06	.33
		2.5	0.0021	1.05	.29
		4	0.0013	1.14	.20
		6	0.00065	1.23	.23
		1.80	0.0029	1.80	.46
		2.77	0.0019	1.44	.31
		4.34	0.0012	1.10	.27
		6.35	0.0008	0.94	.45
		1.80	0.0029	2.78	.41
		2.77	0.0019	2.17	.27
		4.34	0.0012	1.85	.20
		6.35	0.0008	1.59	.37
		1.5	0.0034	0.64	.59
		2.5	0.0021	0.66	.57
		4	0.0013	0.66	.53
		6	0.00085	0.61	.63
Hofmann	Cast Br.	1.69	0.0058	1.0	.313
		1.69	0.0058	2.0	.304
		1.69	0.0058	4.0	.236
		1.69	0.0058	6.0	.161
Hofmann	Sand Coated	1.69	0.0058	10.0	.131
		1.69	0.0058	10.0	.131
		1.69	0.0058	10.0	.131
		1.69	0.0058	10.0	.131

TABLE 4 STEEL PIPE, WELDING ELLS, BRASS

Investigator	Material	Diameter Inches	$\frac{r}{d}$	$\frac{E}{d}$	k
Hofmann	Mch. Brass	1.69	0.000046	1.0	.221
		1.69	0.000046	2.0	.139
		1.69	0.000046	4.0	.101
		1.69	0.000046	6.0	.080
		1.69	0.000046	10.0	.097
J. E. Basher	Steel Tube Turns	2	0.00090	1.5	.220
		4	0.00045	1.5	.233
		6	0.00030	1.5	.228
		8	0.00023	1.5	.246
		4	0.00045	1.0	.384
		4	0.00045	1.5	.249
	Steel Pipe	4	0.00045	2.0	.149
		4	0.00045	3.0	.122
		4	0.00045	4.0	.096
		4	0.00045	5.0	.102
		4	0.00045	7.5	.119
		4	0.00045	10.0	.130
Yarnell	Celluloid	6	0.00001	1.5	.15
		6	0.00001	1.5	.15
H. Beij	Steel	4	0.00015	1.5	.215
		4	0.00045	3.37	.145
		4	0.00045	4.07	.178
		4	0.00045	5.00	.174
		4	0.00045	9.85	1.65
Taylor Forge	Steel Weld. Ell	3	0.00060	1.5	.12
		3	0.00060	1.5	.12
Crane Co.	Steel Weld. Ell	2	0.00090	1.5	.421
		2	0.00090	1.5	.215
Saph and Schoder	Brass 180°	2	0.000029	3.64	.147
		2	0.000029	4.33	.148
		2	0.000029	4.76	.132
		2	0.000029	5.77	.163
		2	0.000029	7.63	.132
		2	0.000029	9.58	.132

tion, all of the test material on wrought bends was old, and only on wrought-iron pipe. The k -values seemed unaccountably high in the low r/d -range. Drawn brass and large air duct, as would be expected, gave the low values, and cast iron the highest. Since steel pipe is between those groups in roughness, it would be expected that the k -values also should lie between those of the smoothest and roughest groups. But in the lowest r/d -range, many tests showed as high as cast iron. In most cases, the tests had actually been run on cast-iron fittings up to r/d of 2.5, along with wrought-iron pipe for the larger radii. Short-radius steel bends such as welding elbows were not yet developed. But the recent data in general show the same relatively high values of k as the early tests. There appears to be a logical reason for this behavior. All steel fittings and bends are worked to shape hot. In the case of pipe bends, a filling material such as sand is generally used to prevent buckling and ellipsing as much as possible. The inner side of the bend wrinkles and the filler does not eliminate this completely. At the heat of bending, and high stresses involved, the sand filler indents into the outer side of the bend, thus moving the relative roughness up toward that of cast iron. The smaller the value of r/d , the more severe the stresses will be, and the greater the indentation. In the case of welding elbows, these are made by different processes, and as the interior of the pipe is exposed to the atmosphere, scale can form and be indented into the pipe wall by whatever inside support devices are used.

Nonferrous tubing, such as brass, is usually bent cold; while sand is used for larger sizes, the smaller sizes, 1-in. OD and less, are often bent with helical steel spring-wire coils to preserve circularity. Either of these methods can produce indentation. A further effect is the coarsening of grain which takes place from cold-stretching the outer wall; this effect can easily be seen, and roughens the surface. Inner-wall wrinkling also can occur. Support for the idea of roughening by the processes of bending is given by Hofmann's work on brass. His bends were not formed by bending but machined in split castings. They therefore had the same roughness for all r/d -values. His loss factors are lower in the range $r/d = 1$ to 3 than those of any other investigator.

over-all loss as measured. This procedure gives a value of k which may be as much as 15 per cent too high for long-radius fittings, when cast-iron pipe is the line material. It may very well be that using the losses for straight pipe subtraction for steel bends may have given rise to the very dubious rise in loss for $r/d > 4$ reported by many of the investigators.

The hypotheses presented in the author's 1950 paper (6) was that the over-all loss in a bend is composed of the following:

- 1 Equivalent straight pipe loss.
- 2 True bend loss, unaffected by R or e/d ; this would be the loss in a perfectly smooth conduit.
- 3 An additional loss varying with both R and e/d , and consequently with f .

The new data, and some of the old, are given in Table 3 for cast fittings, and in Table 4 for welding elbows, and steel or brass bends. Fig. 12 through 16 give the plotted data; solid-line curves are the revised calculated values. In the 1950 formula-

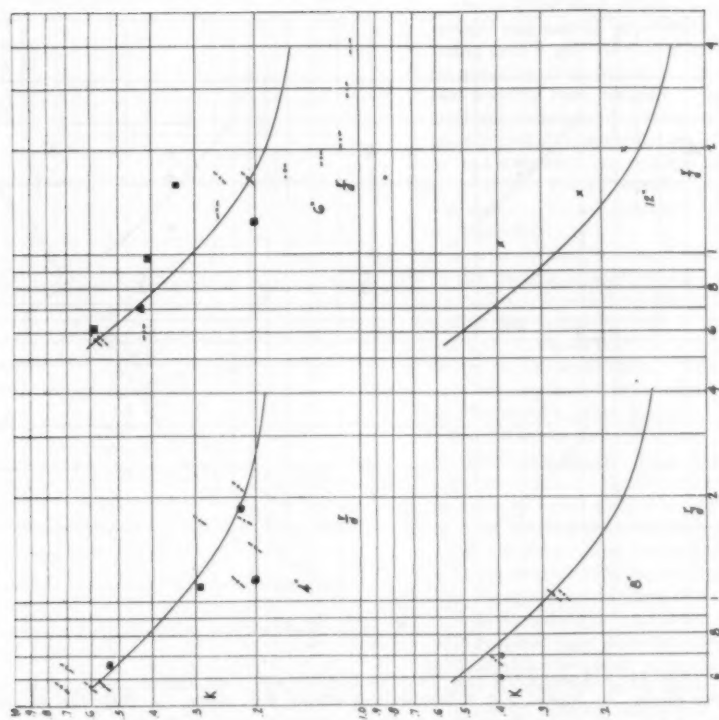


FIG. 13 k VERSUS r/d FOR 4-IN. THROUGH 12-IN. CAST ELBOWS; SEE FIG. 12

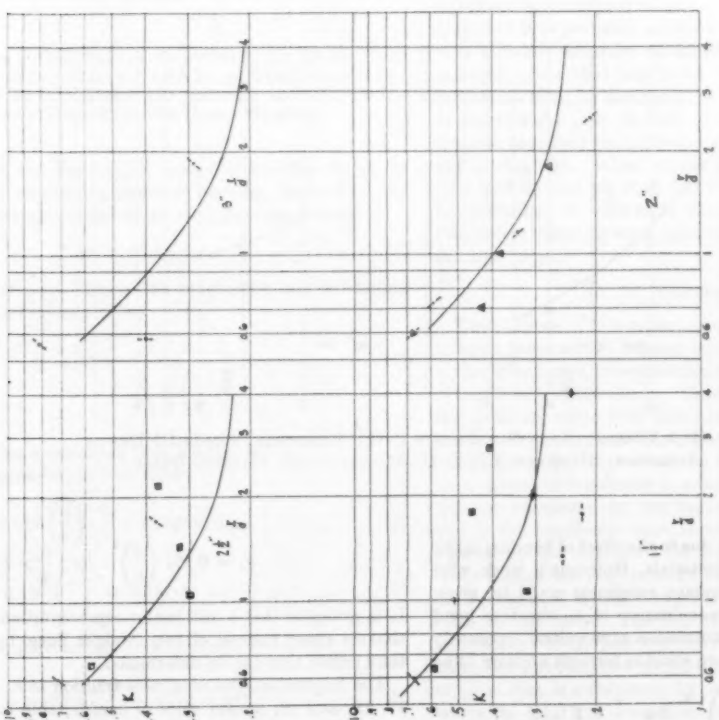
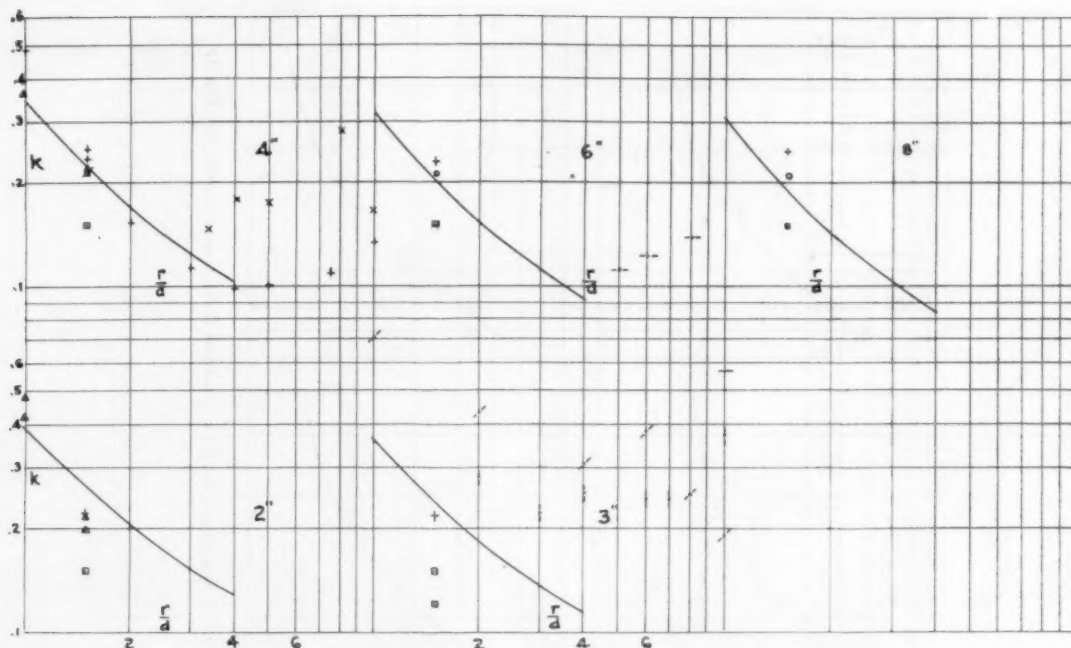
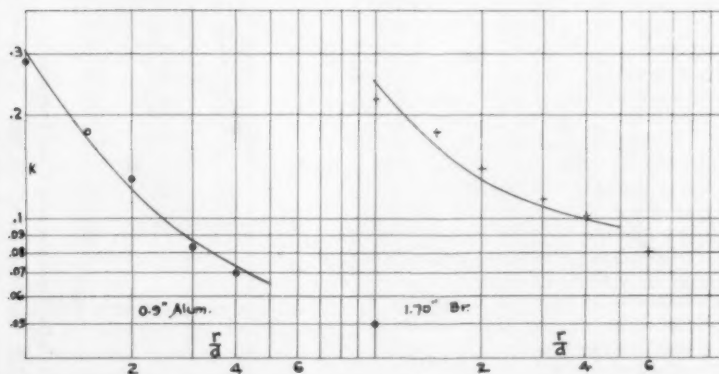


FIG. 12 k VERSUS r/d FOR $1\frac{1}{4}$ -IN. THROUGH 3-IN. CAST ELBOWS
(O Vogel, 8 in.; + Hofmann, 1.70-in. ID; Δ Crane, 2 and 6-in. flgd.; ∇ Crane, 2-in. sed.; \square N.B.T.L., $1\frac{1}{4}$, $2\frac{1}{4}$, 4, 6-in. brass; — Freeman, 2, $2\frac{1}{4}$, 3, 4, 6, 8-in. sed. and flgd.; — Davis, 2 in.; --- Schoder, 6 in.)

(O Vogel, 8 in.; + Hofmann, 1.70-in. ID: Δ Crane, 2 and 6-in. fldg.; ∇ Crane, 2-in. seed.; \square N.B.T.L., 1 1/4, 2 1/4, 4, 6-in. brass; \diagup Freeman, 2, 2 1/4, 3, 4, 6, 8-in. seed. and fldg.; \diagdown Davis, 2 in.; — — — Schoder, 6 in.)

FIG. 14 k VERSUS r/d FOR WELDING ELBOWS AND PIPE BENDS

(○ Vogel, 6, 8, 10-in. welding elbows; + Busher, 2, 4, 6, 8-in. welding elbows, 4-in. bends; × Beij, 4-in. bends; △ Crane, 2-in. welding elbow; ▽ Yarnell, 6 in.; □ Taylor Forge, 2-in. to 10-in. welding elbows; / Brightmore, 3 in.; | Balch, 3 in.; --- Schoder, 6 in.)

FIG. 15 k VERSUS r/d FOR NONFERROUS TUBE; BRIDGEMAN, 0.90-IN-ID DRAWN ALUMINUM; HOFMANN, 1.70-IN-ID MACHINED AND POLISHED BRASS

In view of the high values of k due to the effect of bending in the case of steel and nonferrous materials, Hofmann's work with smooth bends of definitely constant roughness could be given more weight. This meant a re-evaluation of k_1 , the true bend loss fraction of k . The 1950 formulation gave values apparently too high below $r/d = 1$. A more suitable formula appears to be

$$k_1 = 0.157 \left(\frac{d}{r} \right)^{1.78} \quad \text{for } \frac{r}{d} < 1 \dots \dots \dots [1]$$

$$k_1 = 0.157 \left(\frac{d}{r} \right)^2 \quad \text{for } \frac{r}{d} > 1 \dots \dots \dots [2]$$

It is probable that a still better representation might be a continuous curve instead of two straight lines, but we need more tests before that can be determined.

The fraction k_2 , the roughness fraction of k , is shown in Figs. 17, 18, and 19, and in spite of considerable scatter, does show reasonable consistency. The points for steel pipe and drawn

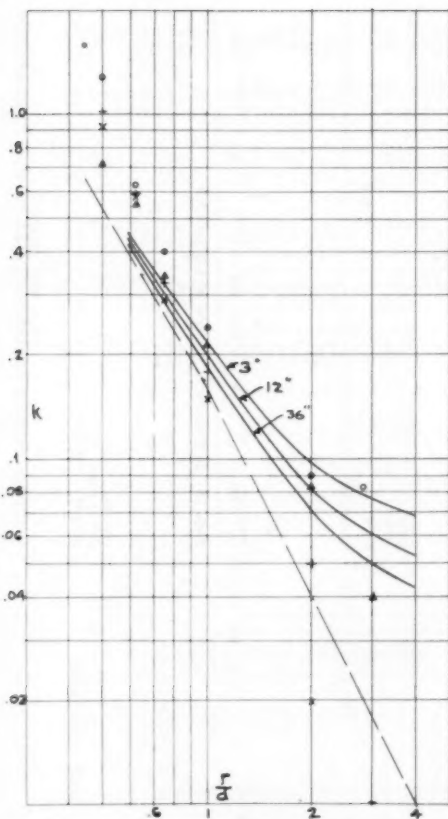


FIG. 16 k VERSUS r/d FOR SQUARE SHEET-STEEL AIR DUCT; O. E. PARKER, 12 IN. \times 12 IN.; MADISON, 12 1/4 IN. \times 12 1/4 IN. AND 33 IN.; BROWN, 12 IN. \times 12 IN.; BUSEY AND CARRIER, 12 IN. \times 12 IN., BUSEY AND CARRIER, ROUND DUCT, ALL SIZES

tubing are above the line but, if corrected for the change in ϵ/d and f due to roughening effect of bending, lie well on the line. For cast fittings and square air duct, k_1 is represented by

$$k_1 = 43.8f^{1.5} \quad [3]$$

For steel and nonferrous tubing, the roughening due to bending appears to be well represented by

$$k_2 = 43.8f^{1.5} \left(\frac{2}{\sqrt{r/d}} \right) \quad [4]$$

The total bend loss k excluding pipe friction is then:

For cast fittings and square air duct

$$k = 0.157 \left(\frac{d}{r} \right)^{1.75} + 43.8f^{1.5} \quad \text{for } \frac{r}{d} < 1 \quad [5]$$

$$k = 0.157 \left(\frac{d}{r} \right)^2 + 43.8f^{1.5} \quad \text{for } \frac{r}{d} > 1 \quad [6]$$

For steel and nonferrous pipe (not made for $r/d < 1$)

$$k = 0.157 \left(\frac{d}{r} \right)^2 + 97.6f^{1.5} \sqrt{\left(\frac{d}{r} \right)} \quad [7]$$

Fig. 20 gives the k versus r/d curves for cast iron, cast brass, or bronze, and smooth sheet-steel, square air ducts. Since finer facing sand is generally used for nonferrous materials, they will be smoother than cast iron. A roughness of one half that of cast iron has been assigned. Fig. 21 gives the same curves for steel and drawn nonferrous tubing. There is little doubt that glass is probably somewhat smoother than brass, and aluminum or lead somewhat less smooth, but the test data are too scanty to prove it. For all practical purposes, the single set of curves will suffice. Table 5 gives the values from which Figs. 20 and 21 were plotted.

Round air duct, although made of the same smooth sheet as square duct, is usually provided with mitered elbows: 2-45 deg joints for $r/d = 0.6$ to 2.0; 3-30 deg joints for $r/d = 3.0$; 4-22.5 deg joints for $r/d = 4$. Kirschbach and Schubart's work (7, 8) shows that the losses are rather closely twice those for the smooth square duct. The actual wall material is the same as for square duct, but the additional loss is caused by the joints and the sharp angular change at each joint.

Fig. 20 shows that r/d -values above 4 do not provide any appreciable gain for less than 36-in. cast-iron pipe, but a small gain for air duct. Fig. 21 looks as if there is some gain still to be made at larger radii, but this is deceptive. The roughening effect of bending about vanishes at $r/d = 4$, and the curves beyond that point are as flat as in Fig. 20.

In the author's 1950 paper (6) the use of equivalent pipe length was recommended in place of k and the velocity head. Table 6 gives the values in equivalent pipe length, for cast-iron fittings with cast-iron pipe, cast-iron fittings with steel pipe, cast-bronze fittings with brass pipe, and square air duct. Table 7 gives the values for steel and brass bends.

For some time the author has had doubts that the customary method of using k as a total loss without including an imaginary quantity of equivalent pipe friction has any real value. This expedient was adopted to save work in figuring the total line drop, but it is probably merely a slovenly way of doing the job. It is certainly incorrect to assign a so-called pipe friction to a cast-iron elbow that was based on steel pipe; and there is no theoretical basis for assuming the flow in the bend is the same as in the straight pipe, in fact we know it is not. The velocity traverse may be symmetrical entering a bend, but it certainly is not coming out. When we get better information on bends, it may well be that we shall find it better to treat the imaginary "pipe-friction" as part of k_2 , and treat each elbow or bend as a complete entity, figuring pipe friction on the real amount of straight pipe.

CONCLUSION

The purpose of this paper, as of that in 1950, is simply to attempt a more nearly rational and consistent method of computing pipeline losses, to replace the usual guessing at k , with a range of 2 or 3 to 1 in the choice. Since we are now dealing in quite a few practical cases with much higher velocities than formerly, it becomes much more important that we calculate losses more accurately. In many cases the friction loss in a pipeline may be a means of regulating a process. In one case such as this, the loss calculated by the values published by manufacturers and in the handbooks gave results nearly four times those calculated by the author's 1950 data. This difference would entirely change the requirements for the pumping system. A test on a completed layout showed the 1950 formulation to be quite close to the facts. The manufacturers' data admittedly had included 35 to 50 per cent above test results, and many of the handbook data are also placed well on the "safe" side. This kind of estimating is satisfactory for, say, a line from boiler to turbine, where the total line loss is a small fraction of the operating pres-

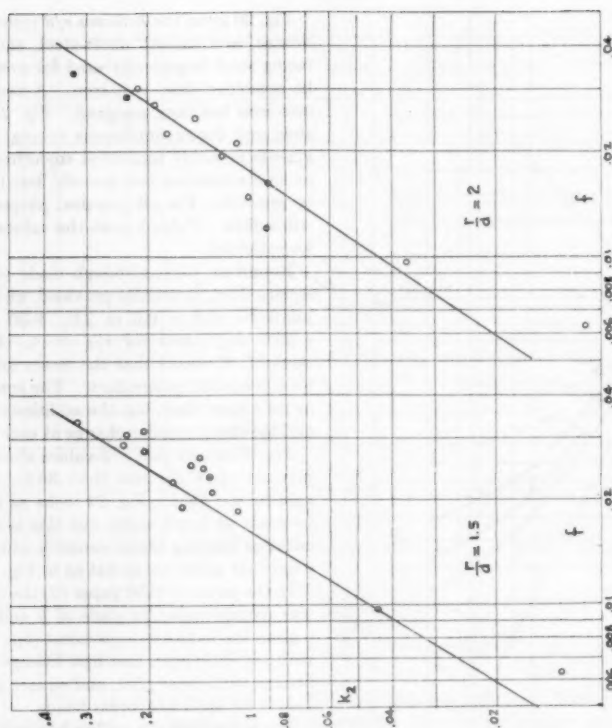
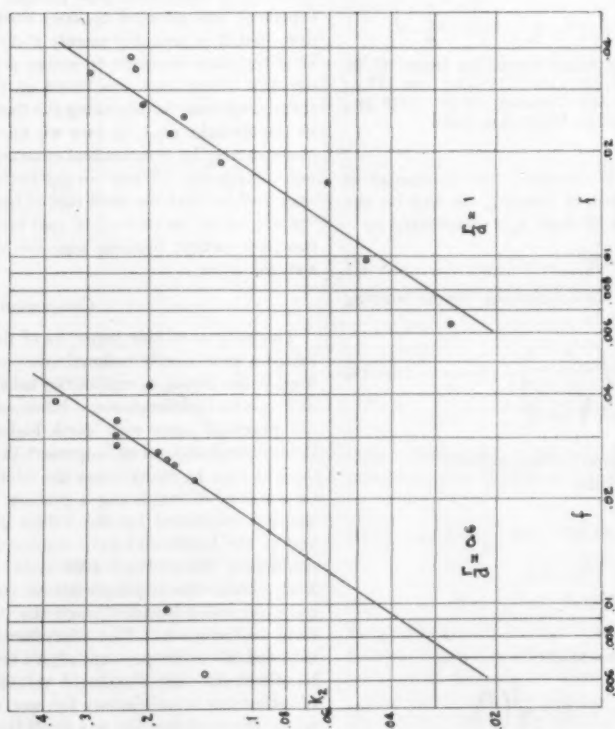
FIG. 18 k_2 VERSUS f , FOR $r/d = 1.5$ AND 2.0FIG. 17 k_2 VERSUS f , FOR $r/d = 0.6$ AND 1.0

TABLE 6 LOSS IN EQUIVALENT PIPE LENGTH CAST ELBOWS
AND AIR DUCT

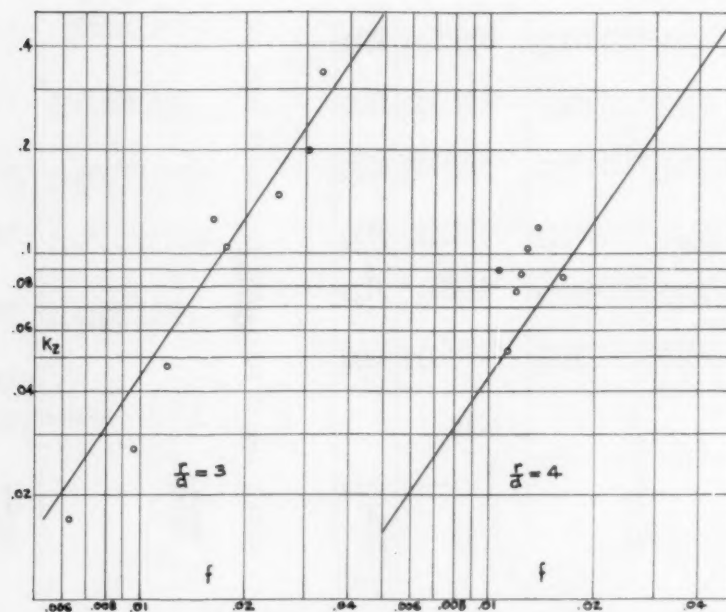
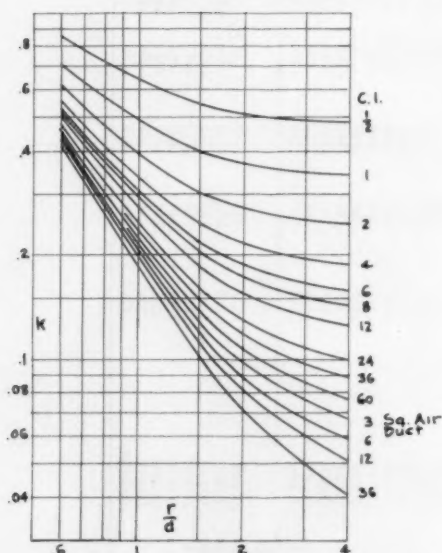
Material	Size	$\bar{F} = 0.6$	$\bar{w} = 1$	$\bar{w} = 1.5$	$\bar{w} = 2$	$\bar{w} = 3$	$\bar{w} = 4$
C.G. Fittings	1/2	73	54	46	44	42	41
C.G. Pipe	1	355	308	267	260	276	274
	2	337	284	246	249	258	254
	3	318	267	230	233	242	238
	6	11.8	6.78	4.75	4.76	5.07	5.06
	8	16.4	9.20	6.44	5.48	4.79	4.54
	12	26.4	14.4	9.79	6.15	7.03	6.61
	16	34.8	20.6	13.6	15.9	13.3	12.3
	24	36	21.8	14.5	17.2	14.5	13.4
	60	170.0	84.4	51.5	39.9	32.0	28.6
C.G. Fittings	1/2	1.66	1.22	1.05	1.05	1.05	.94
Steel Pipe	1	5.54	3.53	2.73	2.45	2.27	2.12
	2	5.54	3.53	2.73	2.45	2.27	2.12
	3	5.54	3.53	2.73	2.45	2.27	2.12
	4	11.6	6.92	5.12	4.48	4.04	3.87
	6	18.0	10.4	7.40	6.35	5.63	5.36
	8	24.5	13.8	9.63	8.16	7.16	6.78
	12	34.3	19.3	13.1	11.7	10.1	9.46
	16	42.7	24.4	16.6	14.6	12.6	11.7
	24	99.7	61.4	26.8	21.6	18.0	16.7
	36	137.0	84.6	40.6	32.1	26.4	24.2
C.G. Fittings	1/2	.50	.66	.57	.54	.52	.51
Cast Br. Pipe	1	1.89	1.27	1.07	1.07	1.07	1.06
C.G. Fittings	1/2	2.98	2.08	1.77	1.77	1.79	1.76
Cast Br. Pipe	1	3.90	2.68	2.27	2.07	2.00	1.93
C.G. Fittings	1	4.92	3.42	2.92	2.62	2.56	2.50
Cast Br. Pipe	1	4.92	3.42	2.92	2.62	2.56	2.50
	2	9.86	5.86	4.44	3.79	3.42	3.28
	3	14.8	8.84	6.08	5.19	4.61	4.38
	4	19.8	11.8	8.16	6.92	6.15	5.86
	6	29.8	17.8	12.1	10.4	9.20	8.71
	12	63.6	33.1	21.4	17.2	13.4	13.1
Square	3	9.20	4.46	2.66	2.01	1.59	1.41
Cast Iron	12	28.4	14.3	8.71	6.54	5.13	4.62
Cast Iron	16	44.4	20.7	11.6	8.40	6.2	5.46
	36	136.0	70.9	38.2	26.6	18.7	15.4

TABLE 7 LOSS IN EQUIVALENT PIPE LENGTH STEEL AND BRASS BENDS

Material	Size	$\bar{\epsilon} = 1$	$\epsilon = 1.5$	$\epsilon = 2$	$\epsilon = 3$	$\epsilon = 4$
Steel Pipe	1 1/2	1.05	7.21	6.50	4.6	3.9
	1	1.76	1.21	.96	.73	.62
	1-1/3	2.72	1.84	1.45	1.04	.91
	2	3.50	2.34	1.84	1.37	1.14
	3	5.28	3.45	2.67	1.98	1.63
	4	6.96	4.56	3.56	2.63	2.19
	6	10.46	6.82	5.16	3.77	3.03
	8	14.4	8.96	6.73	4.84	3.93
	12	22.0	13.5	10.0	7.17	5.74
	24	44.6	26.6	19.4	13.5	10.8
	36	69.5	40.9	29.4	20.5	16.1
Brass Pivots and Pipes	1 D.	.36	.23	.18	.13	.10
	1/4	.60	.49	.37	.26	.21
	1/2	1.75	1.04	.76	.52	.42
	3/4	2.04	1.21	.87	.60	.46
	1	4.28	2.46	1.76	1.20	.93
	1 1/4	5.56	3.16	2.26	1.56	1.21
	1 1/2	11.4	7.65	5.30	3.45	2.65
	2	28.7	15.6	10.6	6.2	5.24

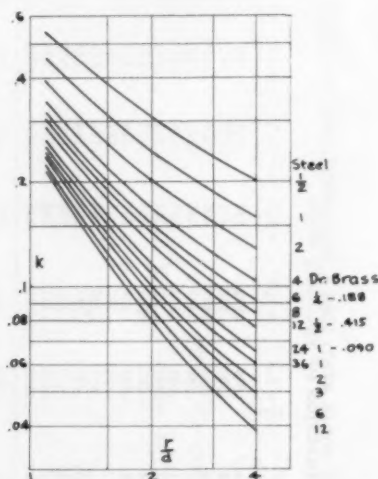
TABLE 5. CALCULATED TOTAL BEND LOSS k , EXCLUDING PIPE FRICTION; FRACTION OF VELOCITY HEAD

Material	Size	$\frac{d}{D}$	$\Gamma = 0,6$	$\Gamma = 3,0$	$\Gamma = 1,5$	$\Gamma = 2,0$	$\Gamma = 3,0$	$\Gamma = 4,0$
S.S.	1/2	.0204	.659	.632	.545	.514	.493	.485
	3/4	.0136	.767	.540	.453	.422	.401	.393
	1	.0102	.714	.487	.400	.369	.348	.340
	1-1/2	.0068	.654	.427	.340	.309	.288	.280
	2	.0051	.619	.392	.305	.274	.253	.245
	2-1/2	.0041	.598	.371	.284	.253	.224	.216
	3	.0034	.562	.355	.268	.237	.216	.208
	3-1/2	.0026	.531	.334	.247	.216	.195	.187
	4	.0017	.502	.305	.218	.187	.166	.158
	4-1/2	.0013	.517	.290	.203	.172	.151	.143
	12	.00095	.499	.272	.183	.154	.133	.125
	24	.00043	.473	.246	.159	.128	.107	.099
Air Duct	36	.00028	.462	.235	.148	.117	.098	.088
	60	.00017	.451	.224	.137	.106	.085	.076
	3	.0010	.442	.215	.128	.097	.076	.068
	4	.00080	.433	.206	.119	.088	.067	.059
Square	12	.00050	.428	.199	.112	.081	.060	.051
	36	.000293	.416	.189	.102	.071	.050	.041
Air Duct	3	.0001	.884	.430	.256	.194	.152	.136
	6	.000050	.866	.412	.238	.176	.134	.118
	12	.000025	.852	.398	.224	.162	.120	.102
	36	.0000083	.832	.378	.204	.142	.100	.082
Steel	1/2	.0012	.541	.383	.311	.240	.202	.202
	1	.0017	.453	.312	.248	.189	.158	.158
	1-1/2	.0012	.415	.281	.222	.167	.139	.137
	2	.00090	.391	.261	.205	.153	.127	.127
	3	.00060	.359	.235	.182	.135	.111	.111
	4	.00045	.341	.220	.169	.124	.102	.102
	4-1/2	.00030	.317	.201	.152	.111	.090	.090
	6	.00023	.303	.189	.142	.102	.083	.083
	8	.00015	.287	.176	.131	.093	.075	.075
	12	.000075	.265	.158	.115	.080	.064	.064
	24	.000030	.255	.150	.108	.075	.059	.059
	36	.000010	.223	.116	.079	.050	.038	.038
O.D.	1/4	.00030	.317	.201	.152	.111	.090	.090
	1/2	.00014	.295	.174	.130	.092	.074	.074
	1	.000063	.261	.155	.113	.078	.062	.062
	1-1/2	.000037	.257	.152	.110	.076	.060	.060
	2	.000029	.243	.140	.100	.068	.053	.053
	3	.000020	.235	.134	.094	.063	.049	.049
Drawn Brass	6	.000010	.223	.124	.086	.056	.043	.043
	12	.0000050	.213	.116	.079	.050	.038	.038

FIG. 19 K_2 VERSUS f , FOR $r/d = 3.0$ AND 4.0 FIG. 20 K VERSUS r/d , FOR CAST-IRON, CAST-BRASS, AND SQUARE AIR DUCT

sure, but it is not of much use for close design of a gas-distributing system, or for a closed-system process in which the line loss constitutes practically the whole load.

It would appear that if a real knowledge of bend losses is to be attained, we must consider a comprehensive research to get modern and more accurate data on the whole range of roughness and bend radius, using suitable instruments to measure and classify roughness. Such a program would cost more than any one or two companies, for example, would care to undertake. It would therefore have to be a joint affair, like the ASME

FIG. 21 K VERSUS r/d , FOR STEEL AND OTHER WROUGHT BENDS

Fluid Meters Committee's work on orifices, or the earlier work on properties of steam. This broad interest type of work is often handled by more than one national society, jointly. In the present subject, the American Gas Association, the American Petroleum Institute, and the American Water Works Association would be as much interested as THE AMERICAN SOCIETY OF MECHANICAL ENGINEERS. If enough engineers are interested, we can get it done.

BIBLIOGRAPHY

- 1 "The Flow of Fluids in Closed Conduits," by R. J. S. Pigott, *Mechanical Engineering*, vol. 55, 1933, pp. 497-501, 515.
- 2 "Friction Factors for Pipe Flow," by L. F. Moody, *Trans. ASME*, vol. 66, 1944, pp. 671-684.

3 "Flow of Natural Gas Through Experimental Pipe-Lines and Transmission Lines," by R. V. Smith, J. S. Miller, and J. W. Ferguson, Bureau of Mines-A.G.A.—not yet issued.

4 "Experiments Upon the Flow of Water in Pipes and Pipe-Fittings," by J. R. Freeman, ASME, New York, N. Y., 1941.

5 Private reports, by J. E. Busher, Tube Turns, 1945.

6 "Pressure Losses in Tubing, Pipe, and Fittings," by R. J. S. Pigott, Trans. ASME, vol. 72, 1950, pp. 679-688.

7 "Loss of Energy in Mitre Bends," by Hans Kirschbach, Transactions of the Munich Hydraulic Institute, Technical University Bulletin 3, vol. 3, 1929; ASME, New York, N. Y., 1935, pp. 43-64.

8 "Energy Loss in Smooth- and Rough-Surfaced Bends and Curves in Pipe-Lines," by Werner Schubart, Transactions of the Munich Hydraulic Institute, Technical University Bulletin 3, vol. 3, 1929; ASME, New York, N. Y., pp. 81-99.

9 "Loss in 90° Pipe Bends of Constant Circular Cross-Section," by Albert Hofmann, Transactions of the Munich Hydraulic Institute, Technical University Bulletin 3, vol. 3, 1929; ASME, New York, N. Y., pp. 29-41.

Appendix

MEASUREMENT OF ϵ ABSOLUTE ROUGHNESS, AND k THE BEND LOSS

Prior to the work of Freeman, experimenters did not give any definite measurement of absolute roughness, in most cases it was not even estimated. Freeman measured the roughness due to scale and slag patches with a steel rule, admittedly not very precise. Hofmann examined sections of his smooth brass, and sand-roughened surfaces under a microscope, and obtained statistical-type measurements that should be accurate to perhaps 0.001 in. Nikuradse measured his sand-grain size by using two plates above and below a single-grain layer; this method gives chiefly a maximum grain size, not an average. But in addition, he measured a suitable size sample of grains individually by microscope, likewise the condition of the pipe wall after application of sand with lacquer, and his results should easily be within 0.001 in. All of these methods measured ϵ as total free height of the roughnesses. Not until the work of Smith, Miller, and Ferguson for the Bureau of Mines-A.G.A. program was any really satisfactory method employed. They used the profilometer, which up to the present is the most satisfactory device for measuring small roughnesses. The instrument gives the root-mean-square value of the rugosity, which ought to be close to the effective roughness, although as yet we have no real assurance that this is the value that we need.

The early investigators generally measured the loss of elbows or bends close to the entry and exit; by the time Freeman made his experiments, it was known that this procedure could lead to errors. Since that time it has been quite clearly shown that, provided there is no prior unusual disturbance of the flow, (such as an elbow or valve), the upstream-pressure measurement may be safely made close to the bend, say 3 to 5 diameters, but downstream the flow does not become fully normal for some 50 diameters, and it is unsatisfactory to take the downstream pressure any closer. Consequently, the losses for these two lengths of straight pipe are included with the real loss of the bend, and must be known and subtracted from the test measurement to get the bend loss. Further, it had become customary, and is still customary, to calculate an imaginary straight pipe loss for the actual length of the bend and subtract this from the total bend loss as measured. The purpose was originally to allow calculation of the total pipe loss including elbows and bends, as if this were completely separate, and then add the loss for elbows and bends, as $k \times (\text{velocity head})$. On account of its general use this method has been retained in the present paper, and k as therein employed consists of k_1 the true bend loss of a dead smooth pipe, plus k_2 the loss due to Reynolds number and relative roughness; to get the total real loss of the bend, the pipe-friction loss for the length of the bend must be added.

As noted in the body of the paper, there is no justification for assuming a separate pipe friction for the bend, and it would be not only sounder, but more accurate to treat the imaginary pipe loss as what it is, a part of k_2 .

Discussion

A. R. C. MARKL.² Any attempt to organize and rationalize available data in an engineering domain which has not yet fully surrendered to mathematical analysis will always be welcomed by practicing engineers, and this is all the more true if the author is known as a pioneer and authority of long standing on the subject.

The writer will restrict his comments to the proposed formulas for the bend-loss coefficient k , specifically Equation [7]. Its proposed breakdown into two components, one representing the bend loss proper and the second accounting for the resultant flow disturbance in the following pipe appears logical. It is the writer's thought that the formula provides a good scaffolding from which a rational theory eventually can be built up. Ultimately it may be found to afford a means of evaluating pressure drop in a compact system in which successive fittings closely follow each other so that the pipe-loss component k_2 will not be fully realized; it is often such systems which are critical from a standpoint of pressure drop.

The question remains, however, whether the parameters and factors used in the formula properly reflect available experimental evidence. This is not readily answered because, as the author himself observes, bend-loss coefficients listed in literature vary considerably. Figures given in handbooks are often much in error on the high side, in part because they are based on old data obtained with screwed cast fittings which not only involve greater roughness but also pockets at the ends, in part because of a desire to provide conservative information. Some manufacturers, including the writer's company, purposely list higher values in their literature than were obtained in their own tests; this is intended to compensate for some of the factors which often are overlooked in pressure-drop calculations, such as the effect of welding rings, icicles where no rings are used, mismatch between pipe lengths, roughening due to scale deposits, corrosion, minor pressure pulsations, and so on. The writer believes that, wherever design constants are to be derived from test data obtained under ideal laboratory conditions, some form of correction is necessary to prevent the user from arriving at underestimates which can prove costly to correct; or else values should be given separately for ideal and average-to-poor field conditions.

Considering the contradictory data, the author has done a remarkable job. The only criticism the writer has to offer is related to his intentional disregard of the upward trend of the k -value beyond $r/d = 5 \pm 1.5$. To the writer's knowledge, every single investigation covering a sufficient range of bend radii has revealed this trend and it just cannot be discounted as fortuitous. Fig. 22 of this discussion shows it very clearly for modern investigations of broad scope; and the same tendency is found to be present in similarly extensive older investigations, specifically those conducted by Brightmore, by Davis, and by Balch shortly after the turn of the century, although they all show higher values as would be expected for the type of material then available. This phenomenon is also evident in the results of recent tests reported by Kittridge,⁴ which relate to carefully assembled screwed fittings; over the turbulent range covered

² Research Consultant, Tube Turns, Louisville, Ky.

⁴ "Resistance Coefficients for Laminar and Turbulent Flow Through One-Half-Inch Valves and Fittings," by C. P. Kittridge and D. S. Rowley, published in this issue, pp. 1759-1766.

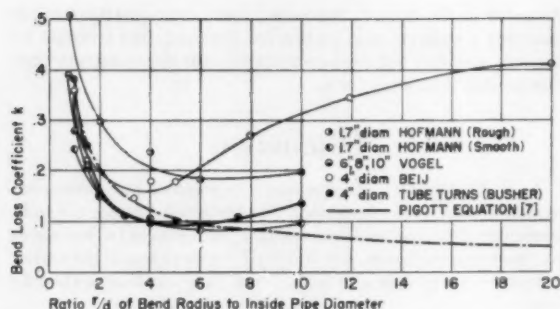


FIG. 22 PLOT OF BEND-LOSS COEFFICIENT VERSUS BEND RADIUS-TO-DIAMETER RATIO

(between Reynolds numbers from approximately 4000 to 25,000), the k -values obtained for $r/d = 6.53$ consistently remained lower than those for $r/d = 2.26$ and $r/d = 11.71$.

Tests of the writer's company as reported by Busher are given particular emphasis in Fig. 22, first because the writer personally knows how, and with what care, they were conducted and evaluated, and then because charts in the author's paper include both the pipe-friction coefficient f and the bend-loss coefficient k for these tests, so that a direct comparison between them and the author's formula can be made. These tests are plotted as solid points connected by a solid line; a plot of Equation [7], with $f = 0.0174$ as read for 4-in. steel from Fig. 6, is shown by the dash-dot line. The two curves coincide at $r/d = 1$ and $r/d = 6$; between these points Equation [7] overpredicts the pressure drop, and beyond the second point it increasingly underpredicts the pressure drop as r/d gets larger.

R. E. TEMPLETON.¹ The purpose of the paper was to arouse interest in obtaining a more nearly rational and consistent method of computing pipeline losses. The main point of interest was concerned with nonviscous flow with Reynolds numbers in the turbulent-flow region.

The writer concurs with the author that the Colebrook-Moody line at $3500 d/\epsilon$ appears to be too high. Information available seems to substantiate the results presented in the paper. However, the important fact to be noted is that maximum percentage deviation of the friction factor that resulted from this difference was only about 5 per cent. The 5 per cent deviation occurred in small sizes of pipe with water as the flowing medium. In larger sizes with water and in a range of sizes with such mediums as steam and natural gas the deviation was much less.

Rather than discuss the broad field of fittings, the author has focused his attention on just one area; that of losses in bends, which includes those of elbows. In order that some of the inherent problems of flow through bends might be better understood, four aspects of this problem will be included in this discussion.

1 As mentioned by the author, the flow through a bend is not the same as that through straight pipe. The flow pattern of a liquid in a bend includes a secondary pattern superimposed upon the main motion through the pipe. This secondary motion is similar to two parallel opposite rotating flows at right angles to the axis of the pipe. This particular motion is due to the centrifugal force of the flowing medium and the frictional resistance of the pipe itself.

2 The next factor to be considered is that of the laminar layer that exists with all flowing mediums in pipelines. The higher the

velocity of the flowing medium, the thinner will be this laminar layer. In the situation where the laminar layer is thicker than the roughness layer, the effect of the wall friction would be similar to that of a smooth pipe, even though the wall of the pipe itself is not necessarily smooth. With increased velocity, the roughness may protrude through the decreased laminar layer and cause increased pressure loss. Therefore, when the quantity flowing through a given pipe is below the average capacity of that pipe, the laminar layer may be relatively thick and the effect of friction reduced. At the other extreme, if the quantity flowing is greater than the average capacity of the pipe, then the laminar layer may be extremely thin and the full effect of the roughness obtained. The important point here is that the thickness of this layer at any given time is not known; therefore it becomes difficult to list one constant k -value for a bend fitting without prior knowledge of what the friction factor of the bend is with the quantity flowing.

The present practice of some manufacturers is to list bend losses in terms of equivalent length of straight pipe. This equivalent length is determined by dividing the bend coefficient by the friction factor of the straight portion of pipe. For the purpose of tabulating one equivalent length for a bend of a given r/d -value, the manufacturer must select an average friction factor which may or may not agree with that of the actual conditions in a given problem.

3 Another consideration is that of the upstream and downstream flow conditions. The locations of valves and fittings upstream or downstream from the bend or elbow under consideration have a definite effect on the total pressure loss for the particular fitting. The manufacturer, of necessity, must base his data on a more or less uniform turbulent condition. The inclusion of valves or fittings in a line induces a nonuniform turbulence into the system. Depending on the location, the system may not return to the uniform turbulent state before reaching the particular fitting under consideration. Information concerning the combined effect of the relative locations of valves and fittings on total pressure loss is scarce.

4 The final consideration is that of the type of fitting used. Care must be exercised in using data presented by manufacturers. There is a considerable difference between fittings that are threaded, flanged, or welded. In threaded fittings, a change in diameter always exists at the threaded connection, resulting in higher friction losses. Manufacturers' data have shown flanged elbows with approximately 25 per cent less resistance to flow than threaded elbows.

Figs. 20 and 21 summarize the author's work on bends. These curves show the k versus r/d relationships for many different sizes of pipe from r/d values of 0.6 to 4. The author concludes that the roughening effect of bending about vanishes at an $r/d = 4$. Data published in the National Bureau of Standards by K. H. Beij² and several other investigators on bend coefficients versus r/d showed that an r/d value between 4 and 6 was the minimum value of k . At an r/d -value greater than 6, the bend coefficient increased. Their data included r/d values up to 20. Two conclusions can be drawn from this information; (a) the optimum design on the basis of minimum pressure loss occurs at an r/d -value between 4 and 6; and (b) further investigation is necessary to resolve the apparent differences between the results presented by the author and those mentioned in the foregoing for r/d -values greater than 4.

Some thought should be given also to the consideration of the practical significance of the results. One of the most important factors in the design of a system, where the line-friction pressure

¹ Design Engineer, M. W. Kellogg Company, New York, N. Y.

² "Pressure Losses for Fluid Flow in 90° Pipe Bends," by K. H. Beij, *Journal of Research of the National Bureau of Standards*, vol. 21, July, 1933, pp. 1-18 (Research Paper 1110).

drop is the major portion of the design loss for that system, is that of the final piping layout. Typical examples are the suction lines to a compressor or a gas-distributing system as mentioned by the author. In the average design engineering concern, the pipe system must be sized before the final layout is established. The designer, therefore, must attempt to determine how each line in the system will be run and what fittings such as valves, elbows, tees, and so on, will be included. Because of the many difficulties involved in pipe arrangement, extra fittings many times must be added, which can create a greater error than a 5 per cent deviation in the equivalent length of one particular fitting. In many cases the designer must be satisfied with the right order of magnitude of line plus equivalent length for purposes of figuring the total pressure drop. In certain cases where it is important that the line drop control the flow distribution, then redesign may be necessary on the basis of the final layout. Design in this manner is costly.

Another consideration is that of the previous history of any particular piece of pipe or fitting. Previous use or, in the case of new pipe, the amount of exposure to the elements of nature before installation could change the pipe condition radically from that assumed in the design.

The useful life of the pipe and fittings is another important practical consideration. After a period of several years of operation, especially with corrosive material, there will be a reduction in cross-sectional area and an increase in the wall roughness. Final design of any piping system must take this factor into account.

The degree of accuracy of data used by a designer should be at a maximum in order that he might have the best information available. However, if some of the factors mentioned in the foregoing exist in a given problem, extreme accuracy in the friction factor without corresponding accuracy in the other factors is meaningless. The writer concurs with the author that a real knowledge of bend losses must be attained, but also there should be a comprehensive research on the whole range of roughnesses and bend radii. The study should not be limited to bends alone, but should encompass such items as different types of valves, tees, reducers, and enlargements. Study also should be made on the cumulative effects of pipe, valves, and fittings on each other. The results of such a study would be invaluable to the designer.

AUTHOR'S CLOSURE

The author is happy to find that two experienced engineers raise questions on the deliberate rejection of increase in the value of k above $r/d = 4$. The reasons for this apparently arbitrary position are as follows:

1 It is clear that as r/d increases toward infinity, the value of k must at some time become zero. When $r/d = \infty$, the pipe is straight, there can be no bend loss, and no loss due to disturbance of flow: k will therefore be zero.

2 Mr. Markl gives, in Fig. 22, curves of four sets of tests, which were included in the author's study. It will be noted that the tests by Beij and by Busher on the same size and roughness of pipe do not agree; the spread is quite wide at the higher values of r/d . Referring now to Fig. 14 of the author's 1950 ASME paper, 12 sets of tests show only a rise in k for half, and these tests present multiple maxima and minima. The remaining half do not show a rise. The location of the hills and valleys show no consistency whatever.

3 The data by O. C. Bridgeman (Fig. 14, 1950) was taken

during the war, at the Bureau of Standards, on aluminum tubing and gasoline. The program was undertaken for the air force by the Co-Operative Research Committee, (joint SAE-API), and some 28 progress reports were issued at various stages; unfortunately these reports were not finally collated and published, so that most interested engineers have not seen or studied the results. The work covered more test points than any investigation other than Freeman or Bureau of Mines-AGA; there is no question of the quality. In these tests, in five sizes of tubing, no increase of k with r/d was found. Further, if we use Hofmann's test points instead of the range he plotted, no appreciable rise is found.

4 The restrictions in space usually occurring in buildings—columns, equipment, and so on—much reduce our practical interest in r/d values over 4, and substantially the lowest k -values will be reached without any increase of r/d above 4.

Mr. Markl points out the need for correction of the author's values for design conditions; this is certainly true, and the values obtained from tests on substantially ideal materials and conditions will be the lowest ordinarily obtaining. But the author has always preferred to establish a base on test data, than apply correction in known amount.

Mr. Markl confirms my statement that both manufacturers and hand-book authors include a safety-factor applied to the basic values; this varies from 35 per cent to over 100 per cent, and the amount is generally not indicated. This puts the designer in a dubious position: He does not know what safety factor is already applied before he adds his own. Mr. Markl compares Formula [7] with the Busher test, but it is seen that the formula line lies between Busher and Beij, up to $r/d = 6$. There is nothing to be gained by making r/d larger than 4 and the formula was based only on data up to this value; it does not appear that deviation of the formula above this value is of any importance.

In general the author concurs with Mr. Templeton's four points, but some qualifying statements are perhaps desirable. In point 2, the association of k_f with f should cover the conditions, at least until we get more test data to refine formulation. In any attempt to establish a method for rational selection of k , taking care of all variations that can occur would make formulation both complex and difficult; at this time, the writer feels that such a step is not feasible. Freeman's tests, the only ones in which consistent attempt was made to pin down proximity effects, showed no clear trend between close and widely spaced fittings. It seems quite probable, although certainly not provable now, that the lower loss for the first fitting will show up as an increased loss for the following fitting due to more distorted entry flow, for conditions of close spacing. Point 4, Freeman's data, showed no consistent difference between flanged and screwed fittings; the author offered a possible explanation in his 1950 paper. If the manufacturers have found a difference, it would be very desirable to publish the complete test data, so it could be studied: In the present doubtful condition of the known data, a mere statement of a k -value does not carry enough weight.

The author wishes to thank Mr. Markl and Mr. Templeton for adding their thinking to this situation; we need not only more test facts, but more thinking about those we have. In cases like the present one, with insufficient and badly scattering data, we are forced to make guesses; if the ideas of a two-part k and roughening of wrought bends in the making get further support in the future, the guesses may have been lucky.

Compensation of Steady-State Flow Forces in Spool-Type Hydraulic Valves

By R. N. CLARK,¹ SEATTLE, WASH.

Three heretofore unreported schemes for reducing the steady-state flow forces in spool-type hydraulic valves are described. Experimental data are presented which compare the steady-state flow-force characteristics of valves using each of these schemes to the characteristics of uncompensated valves.

INTRODUCTION

IT HAS been known for years that certain forces act on the moving member of a hydraulic valve and that these forces are somehow dependent on the flow rate of the fluid passing through the valve. Until recently there has been little engineering incentive to investigate the exact nature of these flow forces because most hydraulic-valve actuators were high-powered or self-locking so that the force generated within the valve was negligible as compared with the available actuating force.

With the advent of high-performance hydraulic servomechanisms in which valve actuators are severely limited in force and power capacity, it became necessary to establish the origin of the flow forces. It was shown² that in spool-type valves with square-edged lands, and in other types of sliding valves, a steady-state force approximately proportional to the flow rate through the valve is generated within the metering chamber and acts upon the moving member in a direction that tends to close the valve. It was further shown³ that some valve designs would produce a transient-flow force on the moving member proportional to the rate of change of flow rate, and that this force could be either an opening or a closing force depending upon the design of the valve. These flow forces are additional to the friction, inertial, and other mechanical forces which are present on the moving members of valves.

It was shown³ that the transient flow force usually could be controlled by careful valve designs and should be a closing force in order to obtain dynamic stability. No further detailed consideration of the transient flow force is given here.

Several schemes have been presented^{4,5} for compensating or reducing the steady-state flow force. This is desirable from the standpoint of the force and power requirements of the valve actuator. During the course of some development work on electrohydraulic and boost servovalves at the author's facility, three

¹ Formerly Research Engineer, Aeronautical Division, Minneapolis-Honeywell Regulator Company, Minneapolis, Minn.; at present, Assistant Professor of Electrical Engineering, University of Washington.

² "Contributions to Hydraulic Control—1 Steady-State Axial Forces on Control-Valve Pistons," by S.-Y. Lee and J. F. Blackburn, Trans. ASME, vol. 74, 1952, p. 1005.

³ "Contributions to Hydraulic Control—2 Transient Flow Forces and Valve Instability," by S.-Y. Lee and J. F. Blackburn, Trans. ASME, vol. 74, 1952, p. 1013.

⁴ "Contributions to Hydraulic Control—6 New Valve Configurations for High-Performance Hydraulic and Pneumatic Systems," by S.-Y. Lee, Trans. ASME, vol. 76, 1954, p. 905.

Contributed by the Hydraulic Division and presented at the Annual Meeting, New York, N. Y., November 25-30, 1956, of THE AMERICAN SOCIETY OF MECHANICAL ENGINEERS.

NOTE: Statements and opinions advanced in papers are to be understood as individual expressions of their authors and not those of the Society. Manuscript received at ASME Headquarters, July 31, 1956. Paper No. 56-A-121.

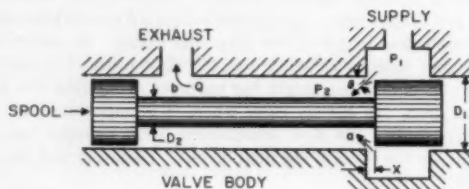


FIG. 1 FULL ANNULAR, SQUARE-EDGED ORIFICE

additional schemes for steady-state flow-force compensation have been investigated, and these are reported here.

UNCOMPENSATED VALVE

One metering orifice of a conventional square-edged spool valve is shown in Fig. 1. The steady-state flow-force characteristics for this type of valve have been developed elsewhere.² Within the assumptions stated in that paper, the steady-state flow force on the spool in Fig. 1 is

$$F_0 = KQ\sqrt{(P_0)} \cos \theta \dots \dots \dots [1]$$

where F_0 is the force (tending to close the valve) in pounds, Q is the flow rate in cubic inches per second, P_0 is the pressure drop across the orifice in pounds per square inch ($P_1 - P_2$ in Fig. 1), θ is the discharge angle of the vena contracta, and K is a constant dependent on the density of the fluid. For a square-edged orifice, such as that in Fig. 1, with zero radial clearance and, when the spool displacement X is small compared with the dimensions of the valve body upstream of the orifice, θ is about 69 deg. A typical value for K is 0.0126. Substituting these numbers in Equation [1] yields

$$(\text{Single orifice}) \quad F_0 = 0.0045 Q\sqrt{P_0} \dots \dots \dots [2]$$

Using Equation [2], the flow-force equation for a conventional four-way valve may be derived. In a four-way valve there are two orifices in series so that twice the force of a single orifice is developed on the spool

$$(\text{Four-way valve}) \quad F_0 = 0.0064 Q\sqrt{P_0} \dots \dots \dots [3]$$

where F_0 is the force on the spool in pounds and P_0 is the pressure drop across the valve in pounds per square inch.

Equations [2] and [3] are plotted in Fig. 2 to provide a quantitative reference for evaluating the compensation schemes described later. Both curves in Fig. 2 are for constant pressure drops, P_0 and P_0 , as indicated. The steady-state flow forces on uncompensated valves are sometimes called Bernoulli forces and this name is used hereinafter.

COMPENSATION SCHEMES

Radial-Hole Orifices. From Equation [1] it is apparent that if θ can be made 90 deg the flow force will be zero. This is accomplished, to an approximate degree, with a metering orifice like that shown in Fig. 3. Two small holes are drilled through the sleeve diametrically opposite one another so that no net lateral force will exist on the spool when the orifice is closed. As the small holes are uncovered by sliding the spool from the

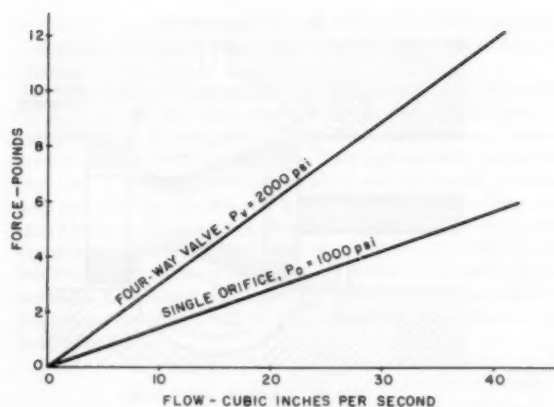


FIG. 2 FLOW-FORCE CURVES FOR UNCOMPENSATED ORIFICE AND FOUR-WAY VALVE

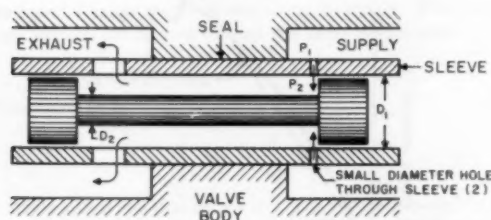


FIG. 3 METERING ORIFICE FORMED BY SMALL RADIAL HOLES

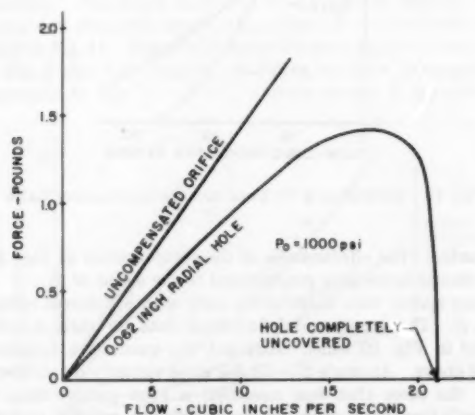


FIG. 4 FLOW-FORCE CHARACTERISTIC FOR ORIFICE SHOWN IN FIG. 3

closed position toward the right, the angle of discharge θ for very small openings will be about 69 deg, because the displacement is small compared with the diameter of the radial holes. However, as the holes are further uncovered, the discharge angle θ is influenced by the slender upstream passageways and increases until the holes are completely uncovered. At this point the stream is directed into the chamber at 90 deg, and the force developed on the spool is zero. Fig. 4 shows the experimental flow-force data that were taken using 0.062-in. radial holes drilled into a sleeve with 0.500 in. ID.

It is apparent from Fig. 4 that the orifice illustrated in Fig. 3 does not offer much advantage over an uncompensated orifice. Although some compensation is realized below 15 cu in. per sec,

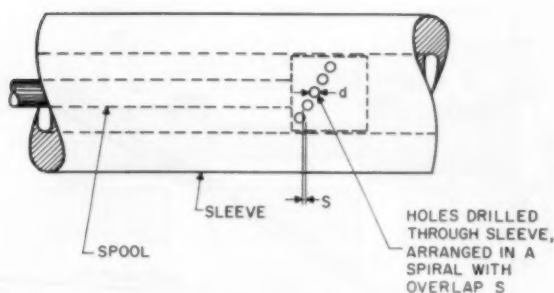


FIG. 5 SPACING OF RADIAL HOLES WITH OVERLAP

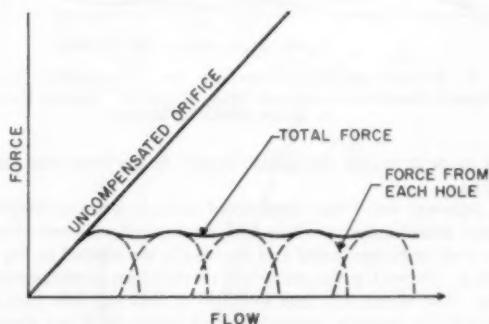


FIG. 6 SUMMATION OF FLOW-FORCES FROM EACH RADIAL HOLE

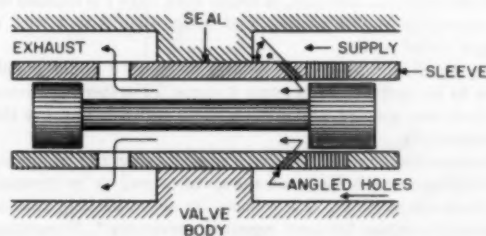


FIG. 7 FIRST ONE OR TWO RADIAL HOLES AT AN ANGLE

the abrupt reversal of the force gradient that occurs at about 18 cu in. per sec could be troublesome in a dynamic sense. To overcome these difficulties, each of the radial holes shown in Fig. 3 is replaced by a series of smaller holes arranged in a spiral around the sleeve so that one begins to open before its neighbor is completely uncovered. This arrangement is illustrated in Fig. 5. The force contribution from each hole will overlap that of its neighbor with the resultant characteristic indicated in Fig. 6.

The diameter of the radial holes is chosen on the basis of the required sensitivity of the valve (orifice area opened per inch of displacement). More than one set of spirals may be used to increase the sensitivity of the valve. The overlap s is usually chosen to satisfy a specified orifice area versus displacement characteristic. If $s = 0.18d$ this characteristic will be approximately linear, except for small displacements from the closed position where only part of the first hole is uncovered.

A further refinement on the radial-hole orifice is the placing of the first one or two holes in the spiral at an angle, as shown in Fig. 7 so that the jet streams from these holes will impinge on the face of the spool causing an opening reaction force. This reaction

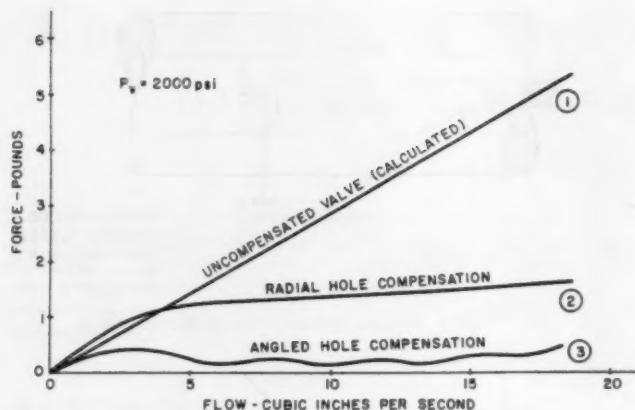


FIG. 8 FLOW-FORCE CHARACTERISTIC OF A FOUR-WAY VALVE. CURVE 2: RADIAL HOLE COMPENSATION ONLY. CURVE 3: RADIAL HOLES WITH ONE AT AN ANGLE OF 30 DEG

force tends to reduce the initial "hump" in the flow-force curve (Fig. 6).

A four-way valve was constructed using a series of 0.028-in. radially drilled holes as orifices with a square-edged spool. Flow-force tests were conducted and the results are plotted in Fig. 8, curve 2. Curve 1 is the calculated curve for an uncompensated valve. The sleeve was then modified so that one hole (and its diametrically opposite partner) at each return land was slanted at an angle of 30 deg (α in Fig. 7). The results of the modification are apparent in curve 3 of Fig. 8. A reduction in the flow force, at maximum flow rate, of better than 10 to 1 is realized with the radial-plus-angled porting, and better than 3 to 1 with the straight radial porting.

The initial hump and unevenness of curve 3 could possibly prove to be undesirable in some systems. Further experiments with hole size, spacing, and angle α could probably improve these characteristics.

Recirculation Lands. Flow-force compensation can be obtained by utilizing reaction forces on the spool as well as by increasing the discharge angle θ . One scheme for accomplishing reaction-force compensation has been reported previously.³ Experiments at the author's facility showed that while this scheme would compensate the steady-state flow forces satisfactorily, the transient flow force that is inherent in that type orifice caused valve instability. Compensation of the undesired transient flow force by providing conventional square-edged lands with the proper damping length³ resulted in an excessively long valve package. In order to utilize the reaction force for steady-state compensation and at the same time realize positive damping, the scheme illustrated in Fig. 9 was devised. Here the fluid that is metered across the orifice is directed in a curved path and circulated through a cavity in the land. The entrance angle in the curved exhaust chamber is made 69 deg to coincide with the angle of the vena contracta of the metered jet and thus provide efficient direction of the exhaust fluid. A turbine-like reaction force is generated on the spool as the fluid leaves the cavity at angle β .

An exact calculation of this reaction force is virtually impossible owing to the complex flow pattern that exists in the flow chamber. However, one may reason qualitatively that the reaction force will be small when the flow is small because the velocity of the circulating fluid will be low, and some fluid will probably leave the chamber without circulating. At high flow rates, however, the velocity of the circulating fluid will be high, and a steady stream will circulate and discharge turbine fashion from

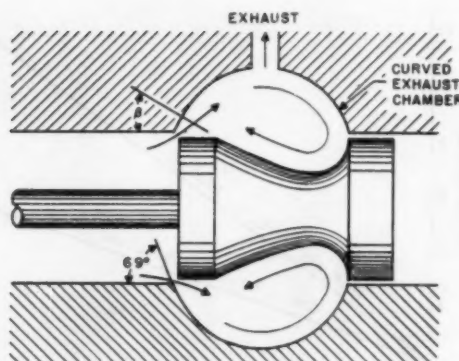


FIG. 9 RECIRCULATION LAND

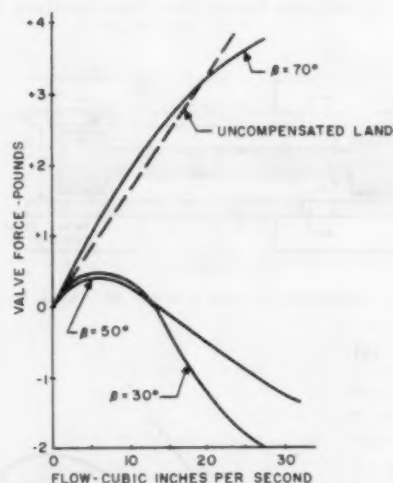


FIG. 10 FLOW-FORCE CURVES FOR RECIRCULATION LAND

the cavity. The effectiveness of the compensation at high flow rates should be roughly proportional to the cosine of β .

Three spools were constructed, each with a different exhaust angle β . The experimental flow-force data for these spools is plotted in Fig. 10 which bears out the qualitative hypothesis stated above. An angle $\beta = 70$ deg gives virtually no compensation; the force that was measured is even greater than the Bernoulli force from an uncompensated orifice, which is probably due to the effects of radial clearance and imperfect metering edges.³ For $\beta = 50$ deg and $\beta = 30$ deg, the valve is overcompensated. The reaction force becomes great enough at a flow rate of about 13 cu in. per sec to overcome the Bernoulli force, so the net force on the spool is zero; and at higher flow rates it tends to open the valve. From Fig. 10 it appears that an angle $\beta = 55$ deg would probably give the most desirable form of compensation. However, the overcompensated land is useful when incorporated in a four-way valve with conventional lands so that the net result is a satisfactorily compensated valve. The initial hump in the curves for $\beta = 50$ deg and $\beta = 30$ deg could be reduced by closer machining tolerances on the radial clearance and metering edges.

No oscillatory valve instability was encountered with the recirculation lands that were tested, indicating that the damping for this type of orifice is positive. Inasmuch as the compensation is

accomplished in the land, a four-way valve that utilizes this form of compensation need be no larger than a conventional uncompensated valve.

Pressure-Drop Compensation. In the derivation of Equation [1], it is assumed that the velocity of the flow at point *b*, Fig. 1, is negligible as compared with that at the orifice. As a practical matter, this is not always the case. In a high-capacity valve, the flow rate is often high enough to cause an appreciable pressure drop between the points *a* and *b*, Fig. 1. As a result, a force will exist on the spool, assuming that both lands have the same area exposed to the fluid. This force will tend to open the valve if the flow is in the direction indicated in Fig. 1 and it will tend to close the valve if oppositely directed. For turbulent flow, the pressure drop along the shank will be proportional to the square of the fluid velocity

$$F_p = K_1 A V^2 \dots \dots \dots [4]$$

where *A* is the wetted area of the land ($\pi/4(D_1^2 - D_2^2)$) and is also the cross-sectional area of the flow space; K_1 is a constant depending on the geometry of the flow space, surface roughness, etc.; and *V* is the fluid velocity along the shank. Flow rate and fluid velocity are related through the cross-section area

$$Q = VA \dots \dots \dots [5]$$

Combining Equations [4] and [5] gives

$$F_p = \frac{K_1}{A} Q^2 \dots \dots \dots [6]$$

A single orifice like that shown in Fig. 5 was constructed to check Equation [6]. Three spools were fabricated to fit this valve, each with a different shank diameter (D_2 in Fig. 1) but otherwise identical. The shank diameters were chosen so that the wetted areas *A* of the lands were in the ratios 1:2:4, as indicated in the table in Fig. 11. The total force on the spool should be that shown in Fig. 6 plus F_p . Experimental data on these three spools are presented in Fig. 11. Each of these curves is approximately

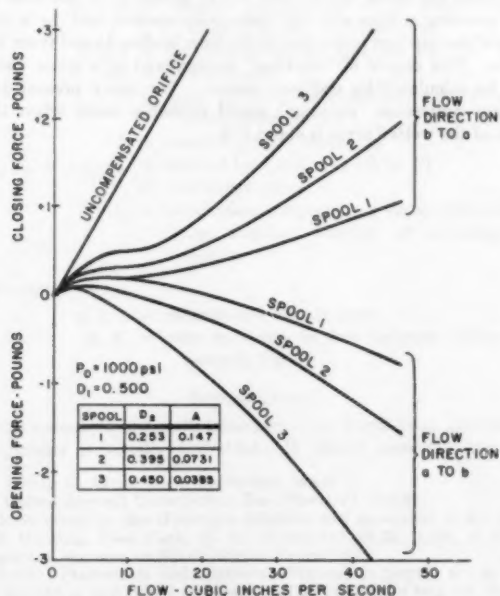


FIG. 11 FLOW-FORCE CHARACTERISTICS WITH PRESSURE DROP ALONG SHANK

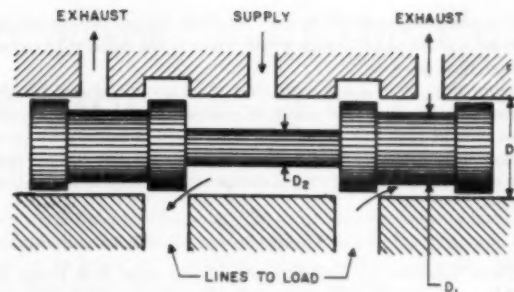


FIG. 12 FOUR-WAY VALVE WITH PRESSURE DROP COMPENSATION

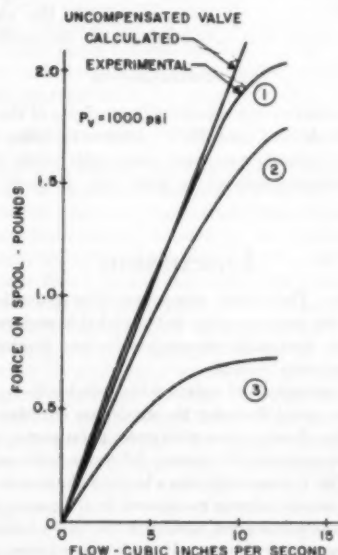


FIG. 13 FLOW-FORCE CURVES FOR THE VALVE IN FIG. 12

parabolic, as would be expected from Equation [6], for flow rates above 16 cu. in. per sec. Below this flow rate the component of force of Fig. 6 is predominant.

Pressure-drop compensation was attempted on a conventional four-way valve using full annular emission, as shown in Fig. 12, by making the shank diameter at the return side of the valve larger than that at the pressure side. Again, three different combinations of shank diameters were used to provide wetted areas in the ratios 1:2:4, as indicated in the following table:

Curve (Fig. 13)	D_1 , in.	D_2 , in.	A_1/A_2
1	0.152	0.152	1
2	0.206	0.152	2
3	0.229	0.152	4

$$A_1 = \frac{\pi}{4} (D_1^2 - D_2^2) \quad A_2 = \frac{\pi}{4} (D_1^2 - D_2^2) \quad D = 0.250$$

Experimental results are presented in Fig. 13. Curve 1 is the uncompensated case and the force curve is very close to that expected from theory. Curve 2, for a difference in area of 2:1, shows a slight amount of compensation; while curve 3, for a difference in areas of 4:1, gives about a two-to-one reduction in force over the uncompensated configuration. A possibility exists for increasing the ratio of the areas beyond 4:1 to achieve more than a

two-to-one compensation factor. In most valves this would introduce a problem of "choking" the valve in the exhaust chamber at high flow rates.

From Fig. 13 it is apparent that the force developed by the pressure drop along the shank is comparable to the Bernoulli force only at high flow rates. For this reason pressure-drop compensation is probably best utilized in high-capacity valves that also employ some other forms of compensation, such as radial-hole orifices.

CONCLUSIONS

Three schemes for reducing the steady-state flow forces in spool-type hydraulic valves are presented, along with experimental results on valves utilizing these schemes. The practical results that are obtained from these methods will vary widely depending on how they are incorporated into the valve design. Considerable design flexibility is inherent in the methods.

ACKNOWLEDGMENTS

The work reported represents the joint efforts of the author and Messrs. R. E. Michel and F. W. Ainsworth, who, with many others at the author's company, have contributed helpful suggestions. Acknowledgment is gratefully given to these contributors.

Discussion

S.-Y. LEE.³ The three valve-flow force-reduction schemes presented in the paper appear to be workable and very interesting. It is felt that each scheme has its own limitations which should be evaluated carefully.

The basic limitations of valves with radial-hole-type ports are (a) for a given spool diameter the maximum effective port width is much smaller than a valve with rectangular ports; (b) linearity at small valve openings is poorer; (c) valve with angular holes as shown in Fig. 7 apparently has a larger leakage rate.

As for the second scheme mentioned in the paper the machining of an accurately shaped cavity on the valve body could present some practical problems. It is also questioned whether the over-all length of the complete four-way valve using this compensation scheme turns out to be much shorter than the force-reduction scheme used in footnote 2 of the paper.

³ Massachusetts Institute of Technology, Cambridge, Mass.

The scheme as shown in Fig. 12 appears to be the simplest of all even though theoretically it is not possible to get perfect compensation due to the fact that the steady-state flow force varies linearly with the flow rate while the force used to compensate it varies with the square of the flow rate. Another difficulty is the "choking" effect as pointed out by the author when one attempts to increase the ratio of the areas beyond 4:1.

AUTHOR'S CLOSURE

Dr. Lee has pointed out some practical considerations of the compensation schemes discussed in the paper.

It is true, as Dr. Lee points out, that a valve using the radial hole porting scheme will have less sensitivity than one having the more conventional metering orifices. In our work with manually operated valves having a fairly long rated stroke this characteristic proved to be desirable. In a valve actuated by a magnetic device, however, this characteristic could prove to be a limitation.

Circular ports do produce a nonlinear displacement-area relationship in the null region, but again, in our system this was not a detrimental factor. In general, linearity in a valve is not necessarily desirable from any other standpoint than that of simplification of the dynamic analysis of the hydraulic system. In some manually operated systems, in fact, a nonlinear displacement-area characteristic is most desirable in that it gives the operator a proper "feel" for his system.

Experimental models of valves using the angled hole scheme did not show greater leakage to be an inherent characteristic. When the valve is closed, all the holes are covered by the land, and there is no reason for the leakage to be excessive. Fig. 7 shows the valve in a partially open state.

We attempted to incorporate the scheme described in reference² in a single spool four-way valve. If a two-spool valve were to be used as in footnote 2, the combined lengths of both spools could possibly be made comparable to a single-spool valve utilizing the recirculation land scheme.

The degree of "choking" encountered with the pressure drop compensation scheme depends not only on the ratio A_2/A_1 , but also upon the ratios A_0/A_R and A_0/A_1 where A_0 is the area of the metering orifices with the valve fully opened, and A_R is the area of the smallest restriction in the lines leading to and from the valve. The degree of "choking" encountered in a given valve can be calculated by ordinary means. For many present-day designs noticeable "choking" would probably occur when the ratio of the wetted areas is about 1:4.

Skewed Boundary-Layer Flow Near the End Walls of a Compressor Cascade

By R. W. MOORE, JR.,¹ AND D. L. RICHARDSON²

Turbulent end-wall boundary layers with considerable skewness are caused by the relative motion of adjacent blade rows in an axial compressor. Flow conditions similar to those near the hub of an axial-compressor rotor were produced in a stationary cascade of blades, and the results of extensive measurements of boundary-layer flow between the blades are presented. An estimate based on the data of the values of terms in the momentum integral equation in the free-stream direction shows the importance of the crossflow in determining boundary-layer growth. A qualitative description of end-wall flow is given.

NOMENCLATURE

The following nomenclature is used in the paper:

- A to L = points in flow between blades in cascade, Fig. 8
 C = air velocity relative to stationary hub
 C_p = cascade static pressure-rise coefficient,
 $C_p = (p_2 - p_1)/(p_0 - p_1)$
 H = shape factor defined by Equation [9]
 p = static pressure
 p_0 = stagnation pressure
 q = dynamic head $q = p_0 - p$
 S = air-velocity vector relative to blade within boundary layer
 U = free-stream velocity just outside of boundary layer
 u, v, w = velocity components in boundary layer along x, y , and z -coordinates
 x, y, z = curvilinear co-ordinates (see Fig. 2)
 $r\Omega$ = wheel speed
 β = angle between free-stream air velocity and axial direction
 δ = boundary-layer thickness
 $\delta^*, \theta^*, \delta^{**}, \theta^*, \theta_{**}$ = defined by Equations [3] to [7]
 τ_w = wall shear stress
 Ω_y = y -direction component of vector representing angular velocity of co-ordinate system

Subscripts

- x, y, z = refer to co-ordinate axes
 E, K = refer to points in flow between blades in cascade, Fig. 8

INTRODUCTION

The casing (or end-wall) boundary layer found in an axial-flow compressor is usually turbulent. It differs from the two-di-

mensional flat-plate boundary layer in that the velocity vectors representing the flow vary not only in magnitude but also in direction in going from the free stream toward the wall. Such boundary layers are referred to as being skewed.

Compressor performance can be influenced strongly by the behavior of the end-wall boundary layer. Since the flow in this region is very complex, an experimental study was carried out for a special, but typical case.³ A flow field similar to one that might exist in the region between the blades of an axial-compressor rotor hub was investigated. The results, mostly of a qualitative nature, are reported in this paper.

FLOW ENTERING A ROTOR IN HUB REGION

Before considering the end-wall flow through an axial-compressor blade row, it is necessary to establish the nature of the entering flow. The relative motion of adjacent rows results in an end-wall boundary layer which, relative to the downstream blade row, is generally skewed and has high kinetic energy as it enters the downstream row. As an illustration, the particular case of flow in the hub region will be used. The top portion of Fig. 1 shows a unidirectional boundary layer at the exit of a stator which has a large defect in energy adjacent to the wall. By following the rule for addition of vectors (i.e., the relative velocity plus wheel speed equals the absolute velocity), one can obtain the velocity relative to the rotor blades. Note that the velocity vectors relative to the rotor blades are all approximately the same length, but are skewed in direction. The velocity varies from U , directed at the free-stream flow angle, to the wheel speed $r\Omega$, directed tangentially at the wall. The same description can be applied to the flow leaving the rotor and entering a stator, the important aspect being the relative motion of adjacent blade rows. In general, the velocity vectors at the exit of the upstream blade row will not be unidirectional as in the foregoing case, but will be skewed in some manner. Clearance between the tips of the blades and the wall and any motion of the casing relative to the blades strongly influences the wall boundary layer, so the configurations of the boundaries in two successive blade rows must be specified for any particular problem.

STUDY OF END-WALL FLOW THROUGH BLADE ROW

General Approach and Some Assumptions. The discussion will be limited to an incompressible fluid. We consider the flow relative to the blades and refer to the flow outside the boundary layer as the free stream. The change in radius, measured from the rotational axis of a machine to a free streamline, is assumed small so that the stagnation pressure based on the relative velocity, $p + \rho U^2/2$, will be constant along a free streamline. The region of shear flow near the casing is considered a boundary layer with small thickness that is turbulent.

It is convenient to think in terms of a curvilinear co-ordinate system as in Fig. 2. The x -axis is in the direction of the free stream just outside the boundary layer, the y -axis is perpendicular to the end wall or casing, and the z -axis is perpendicular to the x and y -axes forming a right-hand, orthogonal system.

³ The study was conducted in the Gas Turbine Laboratory of the Massachusetts Institute of Technology.

¹ Arthur D. Little, Inc., Cambridge, Mass.

² United Aircraft Corporation, East Hartford, Conn.

Contributed by the Hydraulic Division and presented at the Annual Meeting, New York, N. Y., November 25-30, 1956, of THE AMERICAN SOCIETY OF MECHANICAL ENGINEERS.

NOTE: Statements and opinions advanced in papers are to be understood as individual expressions of their authors and not those of the Society. Manuscript received at ASME Headquarters, July 31, 1956. Paper No. 56-A-131.

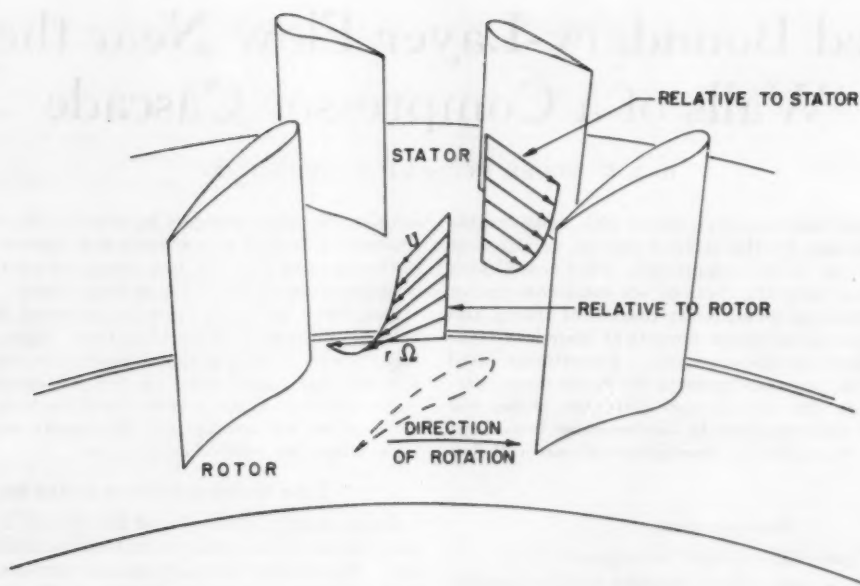


FIG. 1 VELOCITY PROFILES IN HUB REGION OF AN AXIAL-FLOW COMPRESSOR

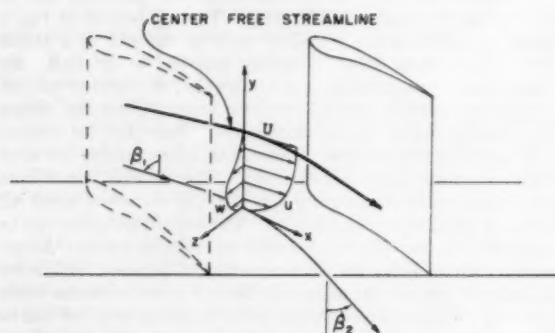


FIG. 2 BOUNDARY-LAYER FLOW BETWEEN TWO BLADES

The velocity of the free stream just outside the boundary layer is U , and the velocity components in the boundary layer along the x , y , and z -axes are u , v , and w , respectively. The component u is often called the "main-flow" velocity, and w the "crossflow" velocity.

The primary concern here is with the boundary-layer flow so the free stream, as determined by the blades, is considered to be specified; that is, the velocity, static pressure, and curvature at each point of every free streamline are assumed to be known. For thin boundary layers, $\partial p / \partial y \approx 0$, and the pressure through the boundary layer is determined by the free stream.

A complete description of the flow would contain the velocity and flow direction at all points within the boundary layer in a region between two blades such as the one in Fig. 2. This information also could be expressed in terms of the boundary-layer flow along several different x -axes, each for a different free streamline. In this study, most of the attention was focused on the free-streamline axis which leaves the blade row approximately halfway between the two blades, Fig. 2.

Momentum Integral Equations. The momentum integral equations for the turbulent boundary layer with crossflow were

developed by Mager⁴ for a free-streamline co-ordinate system rotating about an arbitrary axis in space. The equations when limited to apply only along the x -axis by setting $z = 0$ are

$$\frac{\partial \theta_s}{\partial x} + \frac{1}{q} \frac{\partial q}{\partial x} \left(\frac{\delta_s^*}{2} + \theta_s \right) + \frac{\partial \theta_{ss}}{\partial z} - 4 \frac{\Omega_y}{U} \theta_{ss} = \frac{\tau_{sx}}{2q} \dots [1]$$

$$\begin{aligned} \frac{\partial \theta_s}{\partial z} + \frac{\partial (\delta_s^* - \theta_{ss})}{\partial x} + \frac{1}{2q} \frac{\partial q}{\partial z} (\theta_s - \theta_{ss} - \delta_s^*) \\ + \frac{1}{q} \frac{\partial q}{\partial x} (\delta_s^* - \theta_{ss}) - \frac{2\Omega_y}{U} (\theta_s + \theta_{ss}) = - \frac{\tau_{sz}}{2q} \dots [2] \end{aligned}$$

The terms involving Ω_y are extremely small and are not considered further.

The definitions of the integral quantities are

$$\delta_s^* \equiv \frac{1}{U} \int_0^s (U - u) dy \dots [3]$$

$$\theta_s \equiv \frac{1}{U^2} \int_0^s (U - u) u dy \dots [4]$$

$$\delta_s^* \equiv \frac{1}{U} \int_0^s w dy \dots [5]$$

$$\theta_s \equiv \frac{1}{U^2} \int_0^s w^2 dy \dots [6]$$

$$\theta_{ss} \equiv \frac{1}{U^2} \int_0^s (U - u) w dy \dots [7]$$

The excessive number of variables renders the equations insoluble except for cases where several simplifying assumptions can be introduced. Mager,⁴ in treating the flow in a 90-deg bend, was able to simplify the equations sufficiently to solve them

⁴ "Generalization of Boundary-Layer Momentum-Integral Equations to Three-Dimensional Flows Including Those of Rotating Systems," by Arthur Mager, NACA TN 2310, March, 1951.

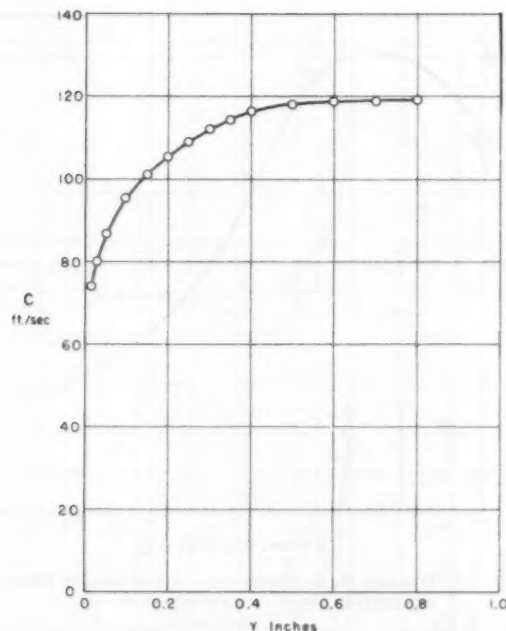


Fig. 3 Distribution of Inlet Velocity Relative to Stationary Hub

approximately and get results that compared favorably with experimental measurements. He showed that the term $\partial\theta_{xx}/\partial z$ in Equation [1] was small compared to the other terms, indicating that the effect of the crossflow on the main flow was negligible. Equation [1] then became independent of the crossflow and could be solved independently of Equation [2]. The values of θ_x computed from Equation [1] were then used in a solution of Equation [2]. Early in the present study, it became apparent that this rather important simplification was not valid for the case being considered (see Discussion, Magnitudes of Terms in the x -Momentum Integral Equation), and attempts to find other simplifications which would enable some sort of solution of the equations were unsuccessful. As a result, this investigation is primarily experimental. However, the authors have found it very helpful to use the momentum integral equations as a basis for discussing the data.

Experimental Procedure. Observation of the behavior of the wall boundary layer in an actual machine is quite difficult for several reasons. Measurements relative to the blades at inlet, between the blades, and at outlet from the blades are necessary. In a rotor, such measurements involve considerable mechanical complication. In a stator following a rotor, fluctuations of the flow with time are present. In addition, the dimensions of the flow passage between blades in a machine are generally too small to permit accurate measurements. To avoid these difficulties, a cascade was constructed to simulate the flow near the hub of an axial-compressor rotor. A brief description of the cascade is given in the Appendix. The inlet conditions to the cascade

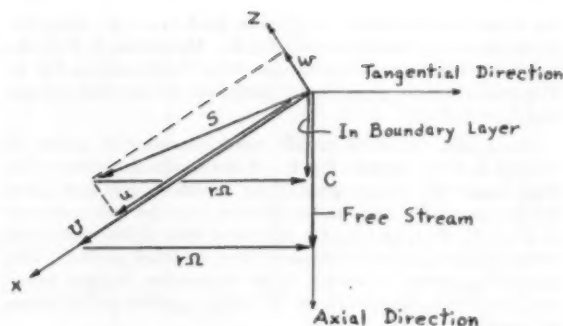


Fig. 4 Velocity Triangles

were patterned after the entry conditions to the rotor, in a single-stage, axial-flow, research compressor. The inlet-velocity profile relative to the stationary hub was measured and plotted versus y , the distance from the hub, as in Fig. 3. In the case of an axial-entry rotor, this velocity profile is not skewed, but is in the axial direction. The flow in the streamline co-ordinate system relative to the moving blades was obtained by subtracting the wheel-speed vector from the air-velocity vector relative to the hub at each value of y . The relative velocity S , was reduced to its components u and w as shown in Fig. 4. The resulting inlet profiles relative to the moving rotor blades are plotted in Fig. 5, along with the profiles produced in the stationary cascade.

The cascade airfoils had the following:

Circular-arc camber lines.

NACA Four-Digit Series thickness distribution with 9 per cent maximum thickness.

Chord = 2.8 in.

Camber angle = 35 deg

The cascade was set with the following:

Stagger angle = 34.3 deg (measured from a perpendicular to plane of cascade)

Gap-chord ratio = 0.828

The free-stream flow entered the cascade at $\beta_1 = 52$ deg and left at $\beta_2 = 22.5$ deg (angles measured as shown in Fig. 2). The resulting distribution of static pressure at the wall is shown in

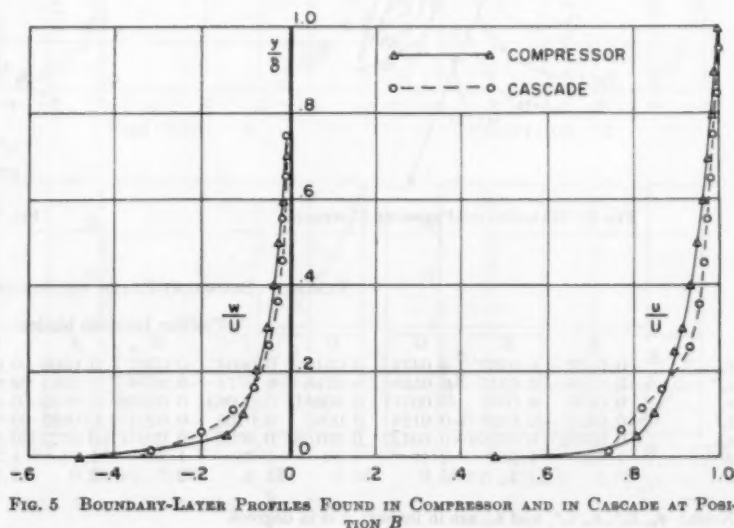


Fig. 5 Boundary-Layer Profiles Found in Compressor and in Cascade at Position B

Fig. 6 and the distribution of dynamic head, $(p_0 - p)$, along the center free streamline is shown in Fig. 7. The points, B, E, G, H, I, and K refer to measuring stations along the streamline, Fig. 8. The over-all static pressure-rise coefficient for the free stream was $C_p = 0.337$.⁵

The u and w -velocity profiles were measured⁶ at points A through L of the cascade, Fig. 8, and the results are presented in Figs. 9 and 10. The progress of the boundary-layer flow along the free-streamline axis can be observed from the measurements at B, E, G, H, I, and K, Fig. 9. Some idea of flow variations across the passage can be obtained from the other profiles. The integral quantities appearing in the momentum integral equations have been calculated from the velocity profiles and are given in Table 1.

The bottom wall of the cascade was coated with a mixture of kerosene and carbon black before one of the runs. When the flow was turned on, traces were made on the coating that are roughly indicative of the flow direction adjacent to the wall. Fig. 11 is a photograph of the resulting traces.

The static pressure distribution around the blades was measured at several distances y from the end wall. The axial and tangential components of the pressure force on the blade were computed and are plotted versus y in Fig. 12. The forces are nondimensionalized with the value at $y = 1.5$ in., which was taken to be the free-stream condition.

⁵ This value differs from the value predicted by two-dimensional theory because the cascade did not behave uniformly. One of the five blade passages was badly stalled over its entire span.

⁶ Measuring techniques are described in the Appendix.

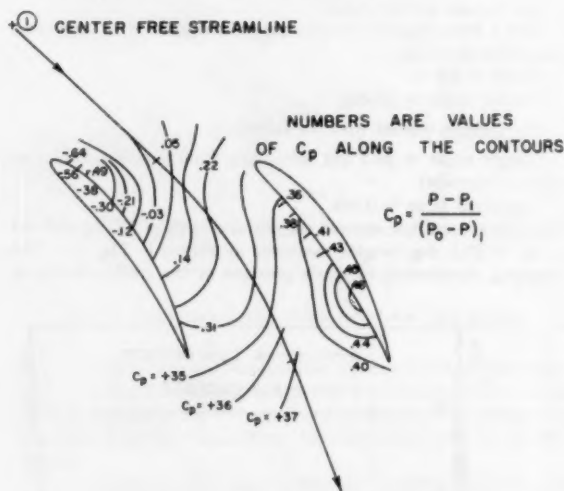


FIG. 6 WALL-STATIC-PRESSURE CONTOURS

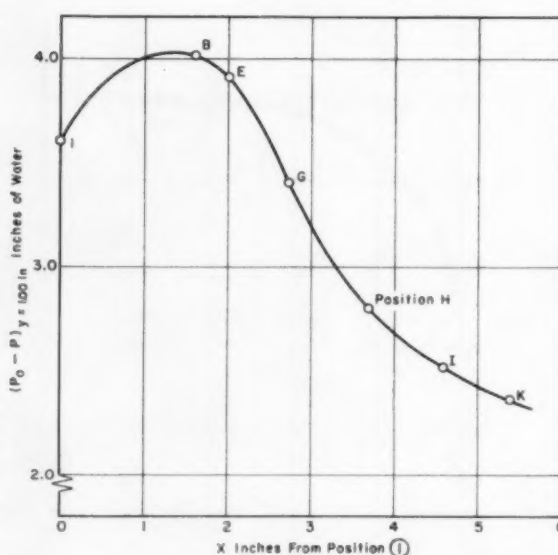


FIG. 7 DYNAMIC HEAD DISTRIBUTION ALONG CENTER FREE STREAMLINE OUTSIDE OF BOUNDARY LAYER

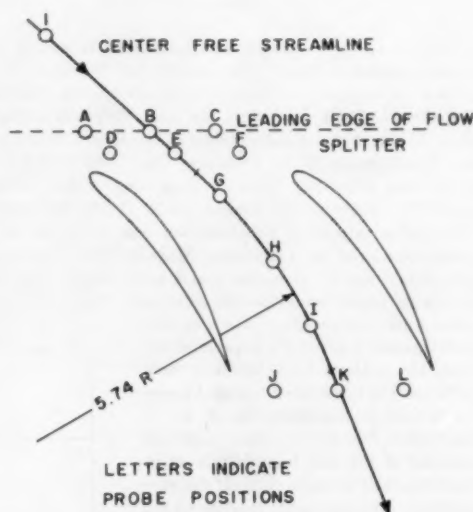


FIG. 8 LOCATION OF PROBE POSITIONS

TABLE 1 BOUNDARY-LAYER QUANTITIES

	Position between blades											
	B	E	G	H	I	K	A	C	D	F	J	L
θ_s	0.0523	0.0437	0.0474	0.0518	0.0604	0.0761	0.0506	0.0522	0.0347	0.0532	0.159	0.0426
δ_s^*	0.0598	0.0545	0.0558	0.0718	0.0771	0.1034	0.0564	0.0670	0.0406	0.0697	0.253	0.0596
δ_s	0.0139	0.0037	0.00311	0.00081	0.00063	0.00659	0.0180	0.00944	0.00374	0.00280	0.00205	0.00083
δ_s^*	-0.0434	-0.0308	-0.0124	0.0063	0.0105	0.0294	-0.0682	-0.0448	-0.0362	-0.0348	0.0284	0.0108
θ_{ss}	-0.00702	-0.00366	-0.00122	0.00168	0.0029	0.00941	-0.0123	-0.00715	-0.00278	-0.00558	0.01162	0.00219
H	1.14	1.25	1.18	1.39	1.28	1.36	1.11	1.28	1.17	1.31	1.59	1.40
β	53.5	51.5	45.0	36.5	31.5	22.5	62.0	52.0	60.0	51.0	25.0	29.0

NOTE: θ_s , δ_s^* , δ_s , θ_{ss} , and β are in inches; β is in degrees.

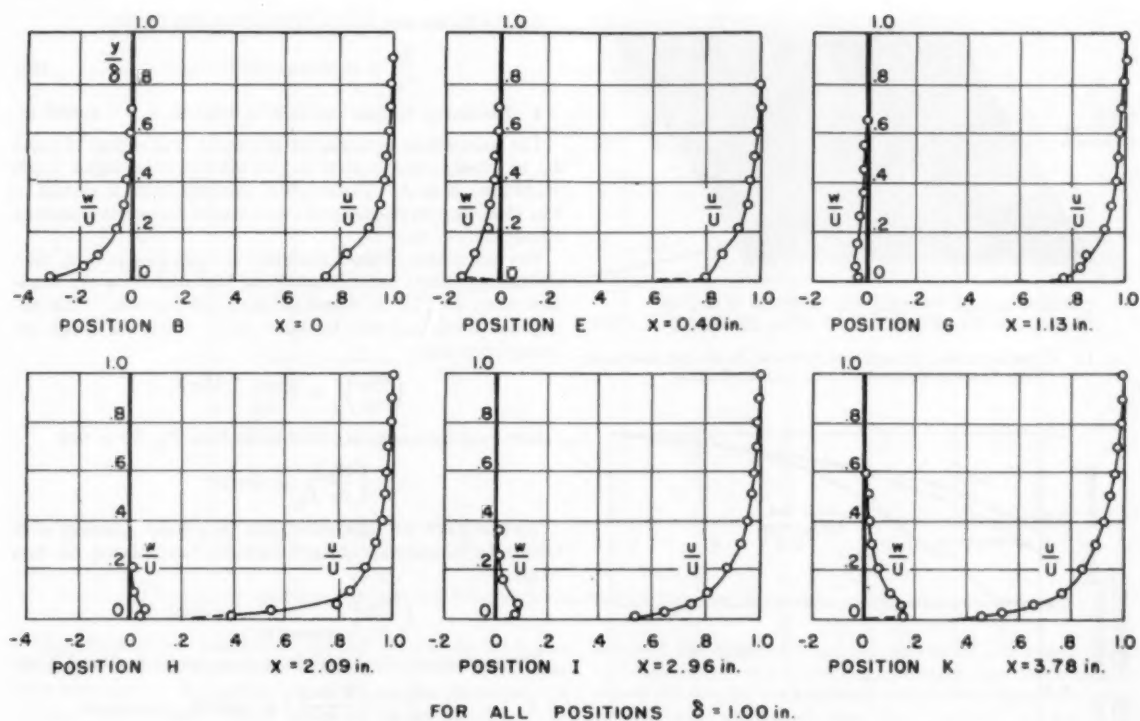


FIG. 9 BOUNDARY-LAYER PROFILES ALONG CENTER FREE STREAMLINE

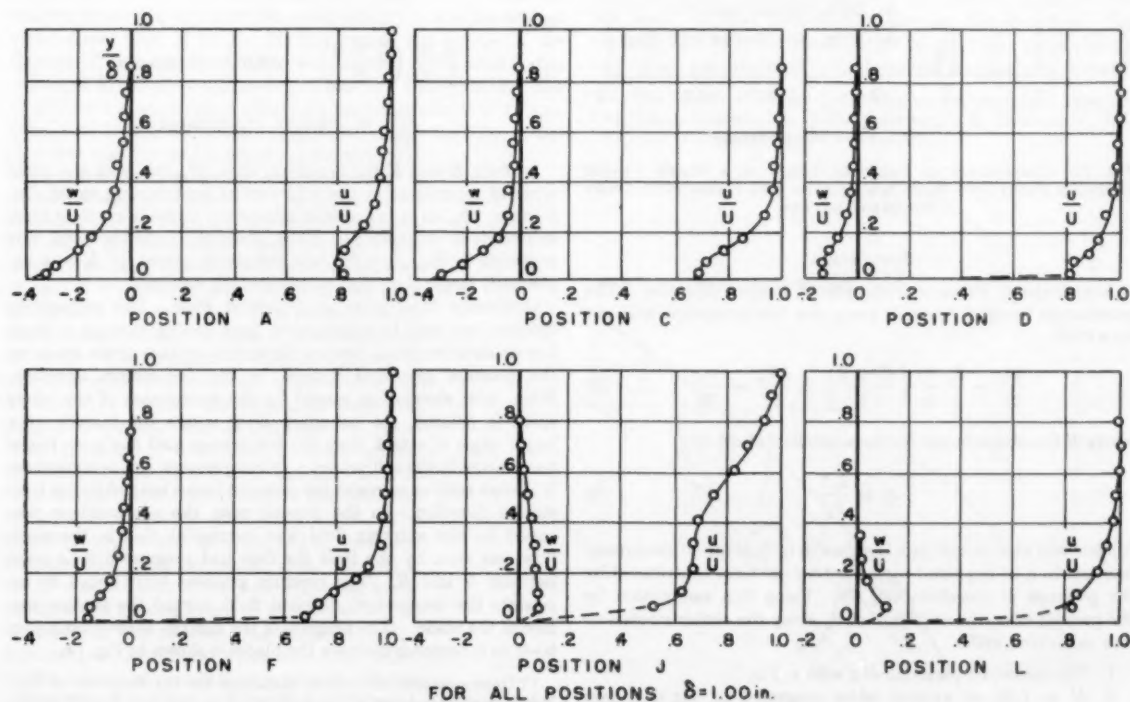


FIG. 10 BOUNDARY-LAYER PROFILES



FIG. 11 CARBON-BLACK TRACES ON BOTTOM WALL OF CASCADE WITH SKEWED INLET-WALL BOUNDARY LAYER

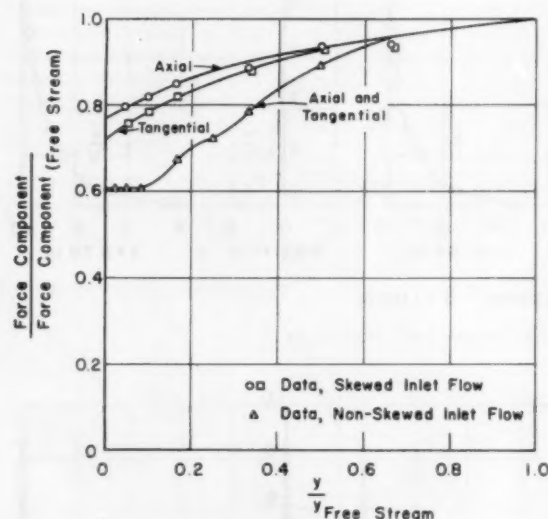


FIG. 12 COMPONENTS OF PRESSURE FORCE ON A BLADE VERSUS DISTANCE FROM END WALL FOR SKEWED AND NONSKEWED INLET BOUNDARY LAYERS

DISCUSSION

Magnitudes of Terms in x -Momentum Integral Equation. The momentum integral equation along the free-streamline axis can be written

$$\frac{\partial \theta_s}{\partial x} + \frac{\theta_s}{q} \frac{\partial q}{\partial x} \left(\frac{H+2}{2} \right) + \frac{\partial \theta_{ss}}{\partial x} = \frac{\tau_{0s}}{2q} \quad [8]$$

where H is a shape factor for the u -profile defined by

$$H \equiv \frac{\delta_s^*}{\theta_s} \quad [9]$$

Mager⁴ was able to calculate the growth of θ_s along a free-streamline axis in a 90-deg bend by neglecting the term contributed by the presence of crossflow, $\partial \theta_{ss}/\partial x$. Using this assumption for the present case, the variation of θ_s along the center streamline was calculated with:

1 The measured variation of q with x , Fig. 7.

2 $H = 1.30$, an average value suggested by the data (see Table 1).

3 The Squire and Young formula⁷ for skin friction

$$\frac{2q}{\tau_{0s}} = [5.89 \log_{10} (4.075 Re_s)]^2 \quad [10]$$

4 The initial θ_x from the data at point E , $\theta_{xE} = 0.0437$ in.

The calculations were started at point E and carried to point K ; no attempt was made to include the high shear region which exists from B to E . The result of the calculation is plotted in Fig. 13 along with the measured variation of θ_x along the assumed streamline.

The calculation predicts considerably more growth in θ_s than the measurements indicate, implying that neglecting the crossflow term, $\partial \theta_{ss}/\partial x$, in Equation [8] is not justified. This implication is strengthened by other data. Using the rough approximation that

$$\left(\frac{\partial \theta_{ss}}{\partial x} \right)_E \approx \frac{(\theta_{ss})_E - (\theta_{ss})_C}{x_E - x_C}$$

(where subscripts refer to points in the flow, Fig. 8) we find

$$\left(\frac{\partial \theta_{ss}}{\partial x} \right)_E \approx +0.007$$

We can make the same calculation for a point upstream of K (about 0.3 in. upstream along the axis) by interpolating the data to give

$$\left(\frac{\partial \theta_{ss}}{\partial x} \right)_{\text{upstream of } K} \approx +0.006$$

The pressure-gradient and shear-stress terms at E and K are

$$\text{at } E \quad \frac{\theta_s}{q} \frac{\partial q}{\partial x} \left(\frac{H+2}{2} \right) \approx -0.008 \quad (\text{measured})$$

$$\frac{\tau_{0s}}{2q} \approx 0.0017 \quad (\text{calculated})$$

at K

$$\frac{\theta_s}{q} \frac{\partial q}{\partial x} \left(\frac{H+2}{2} \right) \approx -0.015 \quad (\text{measured})$$

$$\frac{\tau_{0s}}{2q} \approx +0.0015 \quad (\text{calculated})$$

At both E and K the crossflow term, $\partial \theta_{ss}/\partial x$, is of the same order of magnitude as the other terms contributing to $\partial \theta_s/\partial x$. Further, $\partial \theta_{ss}/\partial x$ is opposite in sign to the pressure-gradient term and tends to decrease θ_s . Thus, when the crossflow term was neglected in Equation [8], the calculated growth of θ_s was appreciably larger than that which actually occurred.

Qualitative Description of End-Wall Flow. The momentum deficient end-wall boundary-layer fluid flowing through a blade row tends to be forced toward the suction surface of the blade by the pressure gradients normal to the free-stream direction. When inlet skewing as caused by the subtraction of the wheel speed is present, the boundary layer enters the cascade at a larger angle of attack than the free stream and has some initial momentum in the x -direction. In compressors, this x -momentum is always such as to resist the pressure forces normal to the free-stream direction. In the present case, the x -momentum possessed by the entering fluid was overcome; that is, the crossflow was zero, by the time the flow had progressed to a point between G and H . The pressure gradient then began to accelerate the momentum deficient fluid toward the suction surface of the blade. The progress of the initially skewed boundary layer as it proceeds between the blades is shown in Fig. 14.

⁷ "Determination of General Relations for the Behavior of Turbulent Boundary-Layers," by A. E. von Doenhoff and Neal Tetervin, NACA Report 772, 1943.

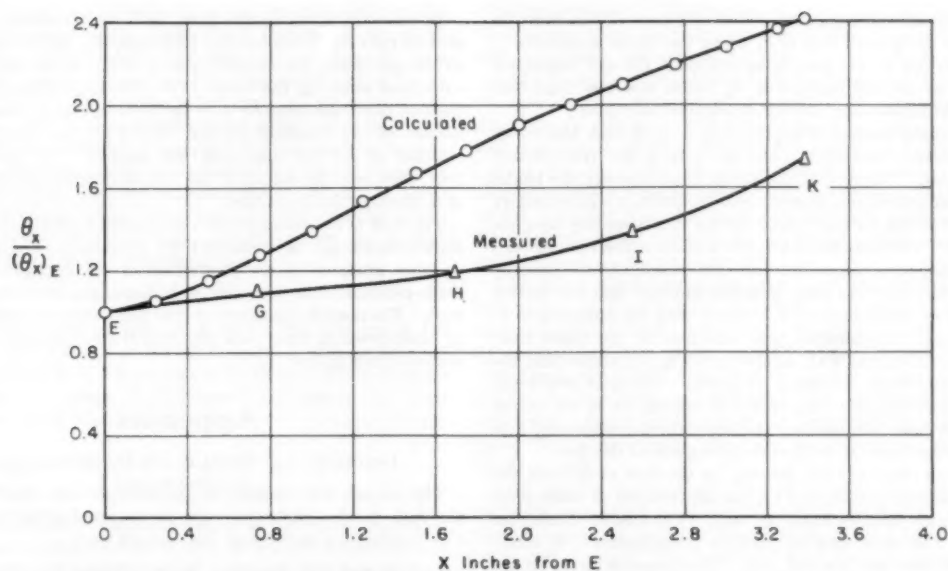


FIG. 13 GROWTH OF θ_x ALONG CENTER STREAMLINE OF CASCADE, MEASURED AND CALCULATED

The effects of the crossflow on the main flow along the center streamline can be ascertained by examining the data. The fluid flowing on to the leading edge of the splitter plate (point *B* in Fig. 8) had a high velocity and was directed parallel to the plane of the cascade. This simulated the flow on to the rotor hub where the velocity adjacent to the hub is $r\Omega$ directed tangentially. The velocity at the wall was immediately reduced to zero and the velocities near the wall were decreased quickly in a region of high shear stress from *B* to *E*. In this region, the x -velocity deficiency $U - u$ increased in the $-x$ -direction as indicated by the values of δ_x^* at *D* and *B* and at *E* and *C*. This probably was caused by a more adverse x pressure gradient from *C* to *F* than from *A* to *D* (see wall pressure distribution, Fig. 6). The crossflow was negative and increased in magnitude in the $-x$ -direction as shown by the values of δ_x^* at *D* and *B* and at *E* and *C*. The result was a transport of x -momentum toward the pressure surface of the blade under conditions such that the region along the center streamline between *B* and *E* experienced a net influx of x -momentum due to the crossflow. This influx of x -momentum was sufficient to cause θ_x to decrease from *B* to *E*. The momentum integral equation in the x -direction expresses this interaction quantitatively. Under the conditions described, $\partial\theta_{xx}/\partial x$ is positive and, as indicated by Equation [1], tends to decrease θ_x . This general scheme persisted from *E* to *G* but the transport of x -momentum by the crossflow was not sufficient to overcome the pressure gradient. The quantity $\partial\theta_{xx}/\partial x$ was positive and θ_x increased with distance along the x -axis. Near the exit at *K*, $U - u$ increased in the x -direction and w was positive and getting larger in the x -direction so that $\partial\theta_{xx}/\partial x$ was positive. As at the inlet, the rate of growth of θ_x was less than that which would occur if no crossflow were present. In the region from *G* to *K*, no measurements were taken at points away from the center free stream-

line and the magnitude and the sign of $\partial\theta_{xx}/\partial x$ is not known.

Certain effects of inlet skewing can be inferred from a comparison of the present work to some results from tests on a similar cascade with nonskewed inlet flow described by Roche and Thomas.⁸ In both cases $\partial\theta_{xx}/\partial x$ was positive and of appreciable magnitude at the exit plane of the cascade but the over-all growth of θ_x along the center streamline in the nonskewed cascade was the same as that computed neglecting the crossflow. This suggests that $\partial\theta_{xx}/\partial x$ was negative in the entry region of the nonskewed cascade, so that the crossflow augmented the growth

⁸ "The Effects of Slotted Blade Tips on the Secondary Flow in a Compressor Cascade," by R. F. Roche and L. R. Thomas, Jr., MIT Gas Turbine Laboratory, SM thesis, 1954.

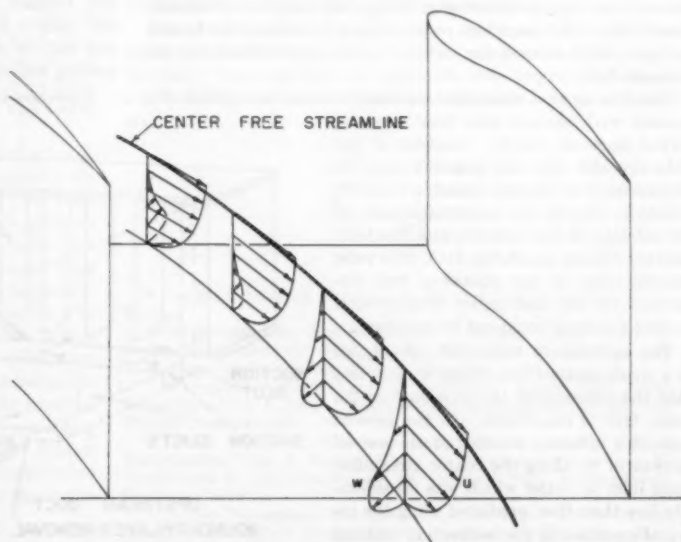


FIG. 14 SKEWED BOUNDARY-LAYER FLOW BETWEEN TWO BLADES IN A CASCADE

of θ_s . It appears then, that the effect of a skewed inlet flow was to decrease the growth rate of θ_s along the center streamline in the inlet portion of the cascade as well as in the exit region, resulting in an over-all increase in θ_s which was less than that which would have occurred with nonskewed inlet flow.

The foregoing discussion applies only to flow near the center free streamline; conditions near the blades are considerably more complex. The flow in the corner regions where the blades meet the end wall cannot properly be described as a wall boundary layer which is thin for the properties of a thin boundary layer are not present. The carbon-black traces indicate a flow of blade-surface boundary layer toward the end wall adjacent to the pressure surface of the blade and away from the end wall near the suction surface. The v -component of velocity can be appreciable in these regions. Furthermore, the variation of the blade force with distance from the wall, as shown in Fig. 12, shows that the thin boundary-layer condition of $\partial p / \partial y \approx 0$ does not exist. It is apparent that any description of conditions in the corner region must take into account the truly three-dimensional (appreciable velocities in three directions) aspects of the flow.

An over-all effect of inlet skewing on the flow away from the center streamline is indicated by the distribution of blade-pressure force with distance from the wall. The cascade blades for this study had been used in previous investigations⁸ of three-dimensional flow near the end wall. The pressure forces on the blades had been measured with an inlet boundary layer which was not skewed, and these results also are presented in Fig. 12. The blade forces are considerably higher near the end wall when the inlet boundary layer is skewed as in the present case. The fact is not surprising when one considers that the skewed inlet flow is characterized by large velocities at high angles of attack on the blades near the end wall.

CONCLUSIONS

The relative motion between adjacent blade rows causes the wall boundary layer to be energized and skewed, relative to the downstream blade row, by the vector subtraction of the wheel speed. A boundary layer leaving one blade row with large velocity deficiency is energized and gets a "fresh start" as it enters the next row, a very helpful situation in a machine with continuously rising static pressure along the flow path. The skewed inlet flow in compressors always has some initial momentum in the z -direction which resists the acceleration of the boundary-layer fluid toward the suction surface of the blade by the pressure field.

The flow along a streamline centered between two blades of a cascade with skewed inlet flow was observed in some detail. Analysis of the data revealed that the crossflow term in the momentum integral equation in the z -direction, $\partial \theta_{ss} / \partial z$, was appreciable and, so, the solution of the equation with this term omitted did not match the data. No valid simplification of the equations was discovered for the case under consideration so that solutions could not be obtained.

The appreciable magnitude of $\partial \theta_{ss} / \partial z$ is a mathematical expression of the fact that the influence of the crossflow on the main flow is important. In the present case, this influence resulted in an over-all growth of θ_s along the center streamline from inlet to outlet which was considerably less than that predicted using the integral equation in the x -direction without the crossflow term.

In contrast, some results from tests on a cascade with non-skewed inlet flow revealed that although $\partial \theta_{ss} / \partial z$ was appreciable at the exit plane, the over-all growth of θ_s was the same as that calculated omitting the term. The primary difference between the two cases was inferred to be in the inlet region, where the influence of the crossflow on the main flow was determined by whether or not the inlet flow was skewed. The skewed inlet flow, then, was the source of the reduction in the over-all growth of θ_s through the blade row.

The flow in the corners where the blades meet the wall is truly three-dimensional as evidenced by carbon-black traces. The pressure gradient in the y -direction is not negligible and the blade-pressure force decreases with decreasing distance from the wall. The cascade with skewed inlet flow exhibited less reduction of blade-pressure force near the wall than a cascade with non-skewed entering flow.

Appendix

DESCRIPTION OF CASCADE AND INSTRUMENTATION

The cascade was designed to approximate flow conditions near the hub in the blade passages of an axial-compressor rotor. The outstanding features of this cascade were:

1 The end-wall boundary layer entering the plane of the cascade was highly skewed, the flow at the wall being at a high angle of incidence.

2 The effects on the inlet flow of a moving end wall ahead of the blade row were simulated by use of a splitter plate and a suction slot.

The arrangement is sketched in Fig. 15. The boundary layer produced by the ducting from the fan supplying the main flow was removed at some distance upstream of the cascade. A high-velocity air jet, injected below and at an angle with the main flow, produced the high-velocity crossflow close to the wall. The lower crossflow velocities away from the wall were obtained by causing a slight curvature in the main flow upstream of the cascade. This curvature was induced by suction and blowing on the supply duct. A sharp-leading-edge "flow splitter" was used as the end wall on the blades and a suction slot was placed just beneath the flow splitter. The flow splitter and suction slot made it possible to have high velocities just upstream of the end wall on the blade row, thereby simulating the effects of a moving wall upstream of the blades.

Traverses in the y -direction were made with two probes on a

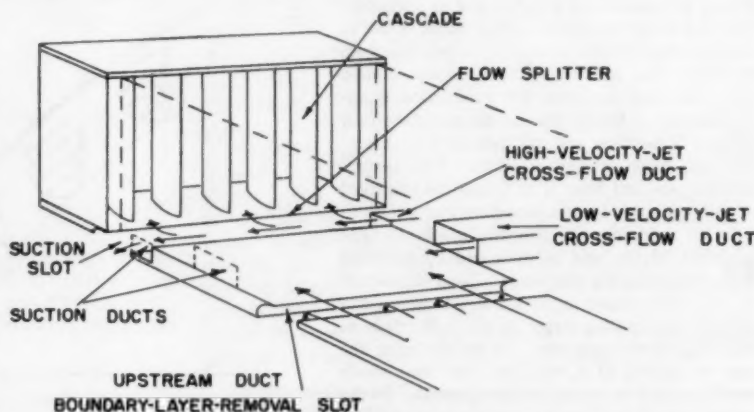


FIG. 15 SKEWED INLET-BOUNDARY-LAYER CASCADE

rig equipped with a micrometer for measuring distance from the wall and a protractor for measuring flow direction. A three-hole cobra probe of 0.014-in-ID tubes was used to measure total pressure and angle. Static pressure was measured with an 0.125-in-OD sphere static probe set at the angle found with the cobra probe. Velocities at all measuring positions were calculated from the difference between measured total and static pressures. To measure pressures, probes were attached to a system consisting of a pressure transducer and a galvanometer. Pressure distribution on the blade surfaces was measured with the aid of two blades equipped with static taps, one tapped on the suction surface and the other on the pressure side.

ACKNOWLEDGMENTS

The work reported in this paper was performed under the sponsorship of the Office of Naval Research. The authors are indebted to Profs. E. S. Taylor and R. C. Dean of Massachusetts Institute of Technology Gas Turbine Laboratory for their encouragement and guidance.

Discussion

R. E. KRONAUER.⁹ The authors are to be complimented on a clear and accurate presentation of a complex flow problem and on the experimental simulation of rotor flow in a stationary cascade. As the authors have remarked, the inlet skewing or energizing of the boundary layer permits the layer to maintain a healthy profile in the presence of the adverse pressure rise. From the practical engineering standpoint this is the most significant result of inlet skewing, and one which undoubtedly has permitted the design of axial compressors without detailed consideration of end-wall boundary layers.

However, the techniques of compressor design are now at the point where it seems both feasible and profitable to include a detailed look at end-wall flow. The existence of this paper attests to this view. Most previous attempts to analyze the secondary flow of end-wall boundary layers in airfoil cascades have neglected the action of viscosity in the cascade itself. In the case of the conventional cascade-inlet flow this has led to an anomalous situation wherein some of the boundary-layer fluid is expected to enter a region in which the static pressure is higher than its total pressure and no viscosity is present to assist it. Despite this, useful results regarding the secondary turning have been obtained. In the case of the skewed inlet flow the energizing of the boundary layer removes the anomaly, but in doing so introduces high local shear stress at the cascade end wall and places the inviscid assumption in new doubt.

The data presented here give a clear picture of what actually happens in a characteristic situation. The entrance region is the place where the high shear is principally found. The large turning of the skewed fluid by the transverse pressure gradient in the passage soon reduces the transverse shear and, in the case presented, actually causes it to reverse sign. At the same time the longitudinal pressure gradient decelerates the boundary-layer fluid and reduces the longitudinal shear. Thus, only in the inlet region is there a significant entropy increase due to high relative velocity of the entering boundary layer. It would seem possible that some of this might be eliminated by causing the blades of one row to overhang slightly the casing of the previous row. In any event, confidence in the validity of neglecting viscosity for the motion of the bulk of boundary-layer fluid is bolstered by this work. The effects of viscosity can be included by examining a viscous sublayer, much thinner than the entire end-wall boundary layer.

⁹ Assistant Professor, Harvard University, Cambridge, Mass.

ARTUR MAGER.¹⁰ The continued interest in the behavior of three-dimensional boundary layers as related to turbomachinery, and particularly the various experimental attempts to check the validity of the approximations and simplifications of the analysis, are very much appreciated by the writer. Step by step, we are continuously gaining a better understanding of the phenomena and this should reflect in improved theories, as well as in improved designs. The present investigation is very valuable, since it provides some fundamental information on the behavior of the turbulent boundary layer and especially on the shape of the velocity profiles under conditions similar to those encountered at the hub of a compressor rotor.

The writer is in complete agreement with the authors as to the importance of the crosswise variation of crossflow. In fact a re-examination of both, the reference cited by the authors, as well as a somewhat later issued report,¹¹ where the procedure was formalized, will surely reveal that the neglect of this term occurs only in the zero-order approximation, but not in the first-order equations. Particular attention has been called to the importance of this variation in one of the examples in the paper published in 1954.¹²

Still, in the special case here examined, the approximate methods, suggested in the work cited, for dealing with the three-dimensional turbulent boundary layer, would probably not work well, if at all. The reason for this failure is not the neglect of the crosswise variation of crossflow in the zero-order terms, but rather, the very special way in which this three-dimensional flow starts. One should remember that the authors have simulated, very skillfully, a case of a two-dimensional boundary layer which, after it has grown appreciably, is suddenly perturbed laterally. Because of this, the so introduced crosswise viscous effects have, in effect, a different characteristic length than the originally unperturbed, two-dimensional layer. A sort of sublayer thus develops, starting from the point where the lateral perturbation is applied. This case has been investigated for the laminar boundary layer by the writer¹³ and also thoroughly discussed by Moore.¹⁴ The investigation of the laminar boundary layer¹³ has indicated that in the presence of small pressure gradients, and with abruptly turning streamlines, the "sublayer" thus created is very thin and that an excellent solution for the crossflow-velocity profile may be obtained by considering the "outer flow" in the boundary layer as nonviscous.

The measurements reported here enable us to determine whether a similar assumption for the turbulent boundary layer is valid. The unperturbed (without any pressure gradient) zero-order equations (in the authors' notation and co-ordinates) are

$$u^0 \frac{\partial u^0}{\partial x} + v^0 \frac{\partial u^0}{\partial y} = 0$$

$$\frac{\partial u^0}{\partial x} + \frac{\partial v^0}{\partial y} = 0$$

¹⁰ Research Scientist, Marquardt Aircraft Company, Van Nuys, Calif.

¹¹ "Incompressible, Non-Meridional Boundary Layer Flow on Bodies of Revolution," by A. Mager, NAVORD Report No. 3386, U. S. Naval Ordnance Test Station, Inyokern, 1954.

¹² "Three-Dimensional Laminar Boundary Layer With Small Cross-Flow," by A. Mager, *Journal of the Aeronautical Sciences*, vol. 21, 1954, pp. 835-845.

¹³ "Thick Laminar Boundary Layer Under Sudden Lateral Perturbation," by A. Mager, 50 Jahre Grenzschichtforschung, H. Görtler and W. Tollmien, editors, Fr. Vieweg & Sohn, Braunschweig, Germany, 1955.

¹⁴ "Three-Dimensional Boundary Layer Theory," by F. Moore, *Advances in Applied Mechanics*, vol. 4, Academic Press Inc., New York, N. Y., 1956.

while the first-order equation for the "skewed" velocity is

$$u^0 \frac{\partial w}{\partial x} + v^0 \frac{\partial w}{\partial y} = c(u^{02} - U^{02})$$

where $c = d\alpha/dx$ is the curvature of the free streamline and α is the turning angle. Eliminating velocity v^0 one obtains

$$\left(u^0 \frac{\partial u^0}{\partial y}\right) \frac{\partial w}{\partial x} - \left(u^0 \frac{\partial u^0}{\partial x}\right) \frac{\partial w}{\partial y} = c(u^{02} - U^{02}) \frac{\partial u^0}{\partial y}$$

whose solution for w as a function of (y/δ) is given by

$$\frac{w}{U^0} = \frac{w}{U^0} \Big|_{\text{initial}} + \alpha \left(\frac{u^0}{U^0} - \frac{U^0}{u^0} \right)$$

This solution has the characteristic deficiency in that it does not satisfy the proper boundary condition at $y = 0$. But in the outer portion of the turbulent boundary layer u^0 is only slightly different from U^0 so that one also may write

$$\frac{w}{U^0} \approx \frac{w}{U^0} \Big|_{\text{initial}} - 2\alpha \left(1 - \frac{u^0}{U^0} \right)$$

In other words, in this approximation, the shape of the skewed velocity in the outer portion of the boundary layer should depend chiefly on the amount the primary velocity is short of unity. The examination of Fig. 9 indicates that such a dependence seems to be in agreement with the experimental measurements. The scale and sign of this distribution is governed by the turning of the free streamline. Since the largest values of the w -velocity are obtained near the surface, one may check the validity of the foregoing expression for w/U^0 by inquiring at what turning (from point B) the skewed velocity for $0.1 \leq y/\delta \leq 0.2$ vanishes. Taking $u^0/U^0 = (y/\delta)^{1/4}$ and the initial values of w/U^0 from Fig. 5, one finds that the foregoing expression indicates the vanishing of w for $\beta = 41.2$ and $\beta = 42.3$ at $y/\delta = 0.1$ and $y/\delta = 0.2$, respectively. According to Table 1 these values occur between positions G and H , and again the examination of Fig. 9 reveals that indeed the w -velocity changes sign in passing from G to H .

Consequently we may conclude that the experiments reported by the authors indicate that a very fine approximation for the w -velocity in the turbulent boundary layer is obtained from the nonviscous "outer-flow" solution. The growth of the three-dimensional "sublayer" in the turbulent layer, even when the free-streamline turning is not too abrupt, appears to be very small, at least in the case investigated. All this is very fortunate indeed, since the simplicity of the expression for w/U^0 should permit its use even in very preliminary engineering computations.

G. L. MELLOR.¹⁴ The paper is clearly a concise nugget of information, which, because of the difficulties of the experiment, has long been wanting.

The realization that the entrance flow to a compressor rotor or stator is generally characterized by rather high relative velocities at the walls instead of a typical boundary layer with a normal zero bounding velocity is apparently a new idea. Perhaps the importance of the authors' investigations may be underscored by some simple mathematical considerations.

Past investigations have shown, in connection with radial-equilibrium studies, that (see Fig. 16, herewith) two-dimensional

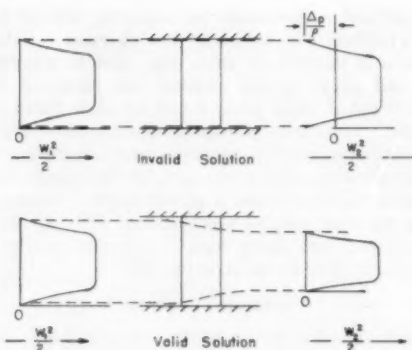


FIG. 16

inviscid solutions of the flow through a cascade gave negative kinetic energies at the exit

$$\frac{W_2^2}{2} = \frac{W_1^2}{2} - \frac{\Delta p}{\rho}$$

in cases where the entering flow was bounded by low velocities $W_1^2/2 < \Delta p/\rho$ near the walls. This, of course, gives the impossible result that these velocities are imaginary $-W_2^2 = iW_2^2$, which was sometimes physically interpreted as backflow. But it seems a bit risky to make such an interpretation, based on mathematical solution, which would give negative velocities for legitimate backflows and which states no information concerning imaginary velocities except that they are imaginary.

Now the correct analysis is simplicity itself, for it says that the only possible (steady-flow) inviscid solution is that there can be no pressure rise or decrease in kinetic energy. Since the flow is turned into the axial direction, it must in fact separate from the solid walls and form its own (free-stream) boundaries to maintain a constant flow area. Despite its triviality, this solution must be recognized as the only valid inviscid solution.

It is, of course, the engineer's job to decide the extent to which idealizations apply to real cases. Viscous shear forces are present in a real fluid flow. In a straight diffuser, for example, which has the same trivial inviscid solution, with an entering boundary layer, the flow path is made long enough so that these shear forces are responsible for the diffusion that does take place. However, in a cascade the diffusion rate is much higher relative to the shear forces and the inviscid solution which says that the flow must separate from the wall may not be far wrong.

With this experience in mind, it perhaps does not stretch the imagination too much to state that real compressors would not work at all if it were not for the fact that high tangential velocities at the blade extremities are inherent in the physical arrangement of a given cascade moving relative to its neighbors. Therefore the kinetic energy is not low near the walls. A collapsing axial velocity is avoided if the blade can reorient the high tangential velocities in an axial direction. The transition from position B to position G in the authors' Fig. 9 is testimony that the blades aided by the secondary-flow mechanism do accomplish this reorientation.

A continuation of this type of work with an eye toward more efficient turning at the blade extremities may possibly result in higher stage-work capacities, as well as higher efficiencies. Twisted blade tips, for example, are the result of the negative conclusion that a blade geometry which is good design in the main flow section is probably not good design in the boundary layer. If we hypothesize a simple arrangement of repeating symmetric stages where the flow has settled down to an equilibrium velocity

¹⁴ Research Assistant, Gas Turbine Laboratory, Massachusetts Institute of Technology, Cambridge, Mass.

distribution (analogous to the simple fully developed pipe flow) the velocity diagram would tell us how to twist the blades' extremities if we know the axial-velocity distribution. Experimentally the blades could first be designed conventionally, the velocity distribution measured, and the blade tips twisted to accept this flow. Hopefully, the axial boundary layer would be reduced by the elimination of some of the losses, after which a second measurement would tell us how to twist the tips again. By this process, we could iterate experimentally to the optimum blade extremity design.

Obviously, the problem has been very much simplified and the experimental work would be expensive, thus pointing up the need for a theoretical analysis which would at least serve as a guide and a basis for an intelligent absorption and application of empirical information. It is expected that this problem will be studied by future researchers and there is no doubt that they will have been guided considerably by the work of Moore and Richardson.

E. A. PINSLEY.¹⁸ The general case of the three-dimensional boundary layer has received relatively little attention in comparison to the efforts expended toward the solution of the two-dimensional boundary-layer problem. This is unfortunate, considering that the boundary layers most often encountered in practice are three dimensional. The amount of experimental research in the field of three-dimensional boundary layers is especially meager although not surprising, considering the complex nature of these flows. The authors are to be commended for their welcome contribution to the available data.

The basic simplification afforded by the concept of the boundary layer is that changes in any physical quantity due to viscous action are limited to a region close to the surface. When conditions of symmetry exist, such as in the case of two-dimensional or axisymmetric boundary layers, or even in the case of yawed infinite cylinders, it is possible to simplify the problem further by the choice of a co-ordinate system which eliminates gradients along one co-ordinate axis. In the present investigation, it was not possible to employ this simplification and a free-streamline co-ordinate system was chosen in order to reduce the data according to the three-dimensional momentum-integral relationships developed by Mager. The use of the momentum-integral technique is, of course, entirely valid. However, the integrations, implicit in the definitions given by Equations [3] to [7], do not allow us to distinguish between effects due to viscous action and those which would occur in an inviscid flow having the same initial shear-flow pattern and geometrical boundary conditions. In these experiments, the pressure gradient required to turn the free-stream flow was sufficiently large to cause a considerable overturning in the low-velocity boundary region. Or, equivalently, the reorientation of the inlet vorticity due to the curvature of the flow was sufficient to generate a sizable secondary flow. It is significant that a secondary flow having a distribution qualitatively similar to the cross-flow distribution presented in Fig. 9 would have occurred in a completely inviscid flow. This suggests that an analysis of three-dimensional boundary layers should in some manner account for the presence of secondary flows by considering the difference between the actual flow and an equivalent inviscid flow. One possible approach would be to compute the behavior of the term, $\partial\theta_{\infty}/\partial z$, in the inviscid flow and apply the results directly to the momentum-integral solution of the real flow given in Equation [8].

Methods for the computation of inviscid-flow patterns have been developed by several investigators (e.g., Hawthorne,¹⁷

Kronauer,¹⁸ Smith¹⁹). These methods are generally quite tedious to employ. However, it would be instructive to apply this approximate technique using the present data. A second approach would be to compare the measured velocity components with the inviscid-velocity components directly within the various definitions of displacement and momentum thickness. Such redefined thicknesses would then be representative of the effects of viscosity in the same sense as the displacement and momentum thickness of a two-dimensional boundary layer are representative of the modification of the external flow by shear stresses. With sufficient data, it might be possible to formulate the auxiliary empiricisms required for the development of a complete solution whenever a momentum-integral method is employed. To be of practical value, the auxiliary empirical relationships must be relatively independent of the geometry of the inviscid-flow pattern.

L. H. SMITH, JR.²⁰ The importance of the flow in the hub and casing regions of a turbomachine has long been known. That many investigators have grappled with the problem is evident from the large amount of existing literature on secondary flow; but it is equally evident, at least to those of us who have had the opportunity to study the details of the flow in multistage compressors, that the literature is inadequate. The reason for this inadequacy, it would seem, is that the physical and mathematical models upon which the analyses are based do not portray adequately the state of affairs that actually exists in a multistage turbomachine. The models are too simple. It is easy to understand the reasons why the simplifications were made; it was felt that the simple models were close enough to the real thing to be qualitatively instructive, and besides, the simple problems themselves were difficult enough.

The present paper is to be applauded because it represents a recognition of one of the very important facets of the multistage wall-boundary-layer problem—the skewness of the approach flow. But the authors found that their step toward realism came at a price; it was no longer possible to write the streamline momentum-integral equation so as to contain derivatives with respect to one variable only. Such complications are to be expected as more realistic models are studied.

The reason for the skewness, as the authors nicely point out, is the relative motion between adjacent blade rows. But this relative motion can give rise to two additional important phenomena as well as the skewness: (a) Fluid in the boundary layer, under certain circumstances, can have a higher total pressure than the free-stream fluid, and (b) for heavily loaded blade rows with separated wakes the flow can be quite unsteady. The first of these can completely change the nature of the flow near the wall and the second can limit steady-state analyses to qualitative rather than quantitative usefulness. It is hoped that the present paper will encourage other investigators to tackle realistically the wall-boundary-layer problem, and at least to obtain accurate experimental measurements even when no neat mathematical approach appears forthcoming.

F. S. WEINIG.²¹ When reading this paper, one has immediately the satisfying feeling that finally there are at least real measurements which tell of what is going on in the wall boundary layer of a cascade which rotates or of which at least the inlet conditions

¹⁸ "Secondary Flows in Fluid Dynamics," by R. E. Kronauer, Pratt & Whitney Research Report No. 132, Gordon McKay Laboratory, Harvard University, April, 1951.

¹⁹ "Secondary Flow in Axial-Flow Turbomachinery," by L. H. Smith, Jr., Trans. ASME, vol. 77, 1955, pp. 1065-1076.

²⁰ Technical Engineer, Aircraft Gas Turbine Division, General Electric Company, Cincinnati, Ohio. Assoc. Mem. ASME.

²¹ Aerodynamics Consultant, Aircraft Gas Turbine Division, General Electric Company, Cincinnati, Ohio. Mem. ASME.

¹⁷ Research Dept., United Aircraft Corp., East Hartford, Conn.
¹⁸ "Secondary Circulation in Fluid Flow," by W. R. Hawthorne, Gas Turbine Laboratory, Massachusetts Institute of Technology, Cambridge, Mass., May, 1950.

imitate what is going on before the inlet of such a rotating cascade. The authors certainly have to be favorably commended on this.

Aside from the skewness of the boundary layer, the pressure distribution in the free flow of the channel is decisive for the resulting secondary flow. It may be mentioned that this pressure distribution is, for most practical purposes, sufficiently equal to the one of the corresponding two-dimensional cascade flow. If $\chi(z) = \varphi + i\psi$ is the complex potential of this flow then

$$\log \frac{d\chi/dz}{W_{ref}} = \log \frac{w}{w_{ref}} - i(\nu - \nu_{ref})$$

The lines of constant pressure are identical with the lines of constant velocity w (compare Fig. 6) and the lines of pressure gradient are identical with the lines of constant flow direction ν .

If the flow would be laminar, one would expect paint traces to follow such isoclines $\nu = \text{const}$. In turbulent flow the paint traces will follow rather a direction resulting from the pressure-gradient lines and the direction of the adjacent free-stream lines, and with appropriate proportionality factors for $\text{grad } u$ and $(\rho/2)u^2$ one may easily obtain a good approximation for the expected paint pattern (comparison of Figs. 6 and 11).

The approach to the secondary flow is being attempted in different ways. One is under assumption of an inlet flow which by whatever reasons is rotational or nonpotential, but that the further flow might be treated as nonviscous. Another is the approach used here by taking in account viscosity and expansion of the momentum equation to skewed or skewing boundary layer. One disadvantage of the latter approach seems to be the difficulty in applying it to the whole channel wall; e.g., to the corner between walls and blades. Aside from that, the complexity of more than one simultaneous differential equation may appear insignificant. There may be found a way of iterative process by which the modern powerful computing machines may solve these Equations [1] and [2] without neglecting major terms than those introduced by the approximate Equation [10] for shear stress and the use of a constant form factor H .

At first sight the writer has the impression that the suppression of terms which are small of second order θ_{xx} and θ_x or the convenient suppression of the term $(\Omega_x/u)\theta_x$, which may be considered to be rather a term small only of first order, are not the main reasons for the differences between predicted and measured θ_x (Fig. 13).

It is supposed that some combined approach by first neglecting viscosity and the following improvement by boundary-layer theory may greatly improve the theory of the skewed boundary-layer flow. But it is just the nonviscous treatment which for larger deflections is quite weak, since always some kind of linear-

ization is attempted, which for this really nonlinear problem itself is quite doubtful, even if the attempted linearizations would be true linearizations; that means if they would take into account all the first-order terms and would not neglect for convenience one or more of them.

In some respect these so-called linearizations represent for larger deflections only convenient suppressions of some degree of freedom and should be appraised only as such. In the case of the quasi-two-dimensional bend flow with shearing inlet conditions, this suppression of a degree of freedom consists in confining the distortion of vortex lines to the stream surfaces dictated by the individual laminae of nondisturbed flow.

One of the results is the creation of secondary vorticity. But with it a reduction of the primary vorticity is involved, e.g., in a 1:2 radius-ratio 90-deg circular bend by 60 per cent. The consequences of this have not yet been investigated to the writer's knowledge. It is supposed that with this under certain considerations an increase of boundary-layer momentum thickness could be involved and—consistent with assumed nonviscosity—a finite velocity would be created on the side walls, which in real flow would mean additional shear stress. It is believed that more thought must be given to such consequences before real valid conclusions can be drawn.

AUTHORS' CLOSURE

The authors are very grateful for the able comments of the discussers which form an important part of this paper. Several of the ideas brought forth suggest directions for future work. The general conclusion seems to be that the analytical treatment of problems of this sort should begin with the calculation of the inviscid flow pattern with the given inlet conditions and solid boundaries. Messrs. Kronauer, Mager, Pinsley, and Weinig all point this out and Mr. Mager's calculation offers proof that, for the present case at least, this approach is valuable. The redefinition of displacement and momentum thicknesses using the inviscid solution velocities rather than the free stream velocity as a reference, as suggested by Mr. Pinsley, might be the key to establishing empirical rules which would enable one to superpose the effects of viscosity on the inviscid solution.

In the opinion of the authors, future studies of the flow near the end wall should include the effects of skewed inlet flow which, in compressors, seems to be of basic importance. As suggested by Mr. Mellor, the final evaluation of the design of the blade tips and roots should be done in an actual compressor. For preliminary testing of a large variety of designs, cascades of the type used for the present work might be suitable. In addition, the effects of tip clearance and shrouding can only be realistically determined when the inlet flow is skewed in the characteristic manner.

An Investigation of the End-Wall Boundary Layer of a Turbine-Nozzle Cascade¹

By J. R. TURNER,² PHILLIPSBURG, N. J.

As a part of a research program aimed at an explanation of the low efficiencies measured near the casings of turbines, an experimental investigation of the flow through a rectilinear cascade of turbine nozzles was conducted to study the effects of the end-wall boundary layer on the flow pattern through the nozzles. Secondary flows in the boundary-layer fluid produce an accumulation of low-energy fluid in the cascade exit plane that is considerably different from the flow field of the two-dimensional wakes. To describe the effects of the secondary flows, detailed data are included showing blade-pressure-distribution variations through the end-wall boundary layer, flow directions, and total and static pressure at cascade discharge, both with and without an inlet boundary layer on the end wall. From these data, qualitative conclusions have been drawn concerning the nature and origin of these low-energy accumulations. The most significant of these conclusions are (a) that the end-wall boundary-layer behavior inside the nozzle passage is essentially independent of the boundary layer entering the cascade; (b) the low-energy fluid which appears in the suction-surface end-wall corner at cascade discharge has its origin only in the end-wall and suction-surface boundary layers.

NOMENCLATURE

The following nomenclature is used in the paper:

- x, y, z = cascade co-ordinates (see Fig. 2)
 p = local static pressure, lb_f/ft²
 p_{atm} = barometric pressure, lb_f/ft²
 p_{∞} = static pressure in uniform flow upstream of cascade, lb_f/ft²
 p_0 = local stagnation pressure, lb_f/ft²
 μ = viscosity of air, ft-sec/lb_m
 ρ = density of air, lb_m/ft³
 V = velocity, fps
 V_s = characteristic cascade downstream velocity

$$V_s = \left[\frac{2g_0}{\rho} (p_{02} - p_{atm})_{\max} \right]^{1/2}, \text{ fps}$$

$$g_0 = 32.2 \text{ lb}_m/\text{lb}_f\text{ft}/\text{sec}^2$$

¹ Research carried out by author as a Research Assistant at Massachusetts Institute of Technology Gas Turbine Laboratory, Cambridge, Mass. Extracted from M.I.T. Gas Turbine Laboratory Report No. 30, "An Investigation of the End-Wall Boundary Layer of a Turbine-Nozzle Cascade," June, 1955.

² Research Engineer, Ingersoll-Rand Company; formerly, Aerodynamics Engineer, Missile Development Division, North American Aviation, Inc., Downey, Calif.

Contributed by the Hydraulic Division and presented at the Annual Meeting, New York, N. Y., November 25-30, 1956, of THE AMERICAN SOCIETY OF MECHANICAL ENGINEERS.

NOTE: Statements and opinions advanced in papers are to be understood as individual expressions of their authors and not those of the Society. Manuscript received at ASME Headquarters, July 31, 1956. Paper No. 56-A-132.

$$C_p = \frac{p - p_{\infty}}{\frac{1}{2} \rho V_{\infty}^2} = \frac{p - p_{\infty}}{(p_{02} - p_{atm})_{\max}}$$

$$P_0 = \frac{p_0 - p_{atm}}{(p_{02} - p_{atm})_{\max}}$$

d_t = throat diameter of nozzle passage

δ = boundary-layer thickness, in.

δ^* = boundary-layer displacement thickness, in.

θ = boundary-layer momentum thickness, in.

H = boundary-layer shape factor, $H = \delta^*/\theta$

Subscripts

1 = properties in cascade-entry plane

2 = properties in cascade-exit plane

INTRODUCTION

Detailed measurements of the flows in steam or gas turbines invariably show regions of low efficiency near the inner and outer casings. Presumably this effect is due to the presence of boundary layers on these casing walls. As a part of a research program in the M.I.T. Gas Turbine Laboratory aimed at understanding, predicting, and controlling this phenomenon in turbines, an experimental investigation of the flow through a rectilinear cascade of turbine nozzles was conducted to study the effects of the casing, or end-wall, boundary layer on the flow pattern through the nozzles.

When fluid is turned in a cascade, the pressure field of the main stream is imposed on the boundary-layer fluid flowing over the end wall of the cascade. Owing to an unbalance between the imposed pressure gradients and the centrifugal force of the low-velocity, boundary-layer fluid, a component of acceleration is produced in the boundary-layer fluid normal to the main stream direction and toward the suction surface of the passage. This motion is usually termed "secondary flow." Transport of the boundary-layer fluid by secondary motion produces behind the cascade a three-dimensional flow field considerably different from the flow field of the two-dimensional wakes. The three-dimensional flow field produced at the exit of a rectilinear cascade of turbine nozzles by these secondary flows is investigated here.³

In spite of the large three-dimensional low-energy accumulations and exit-flow angle gradients caused by these boundary-layer flows, mass-averaged nozzle efficiencies may be of the order of 98 and 99 per cent.⁴ This indicates that the nozzle efficiency is not a sufficiently sensitive index of blade performance to register end-wall effects. The importance of nozzle secondary flows to over-all turbine efficiency lies more in their influence on the angle gradients and energy distribution of the flow leaving the nozzle than in their effect on nozzle efficiency itself, since nonuniformity in this nozzle-exit flow influences the efficiency of the following rotor buckets. Therefore this investigation has been concerned

³ The two-dimensional characteristics of the turbine-nozzle passage used for this investigation have been studied by C. Faulders; see "An Interferometric Study of the Boundary Layer on a Turbine-Nozzle Blade," by C. R. Faulders, Trans. ASME, vol. 76, 1954, p. 61.

⁴ "Secondary Flows and Boundary Layer Accumulations in Turbine Nozzles," by H. Rohlik, et al., NACA Report 1618, 1954.

primarily with obtaining a qualitative description of boundary-layer behavior in the nozzle passage and its effect on the nozzle-exit flow. No attempt has been made as yet to relate this information to actual turbine performance or to design procedures.

For this study, a rectilinear cascade has some advantages over an annular cascade. The spanwise (radial) pressure gradients established in an annular cascade by the swirl velocity cause low-energy fluid at the outer casing to flow radially inward along the span of the blades toward the inner shroud. The low-energy fluid therefore appears at the passage discharge in the suction-surface, inner-shroud corner, or scattered along the suction surface. In a rectilinear cascade, however, there is no spanwise pressure gradient due to swirl velocity to distort or displace the accumulation of low-energy fluid. The low-energy fluid then forms in the suction-surface end-wall corner at the cascade exit plane.

APPARATUS

The rectilinear turbine-nozzle cascade used in these tests is of 16-in. span and 22-in. width and consists of 11 blades. The nozzle sections are of commercial design, scaled to 1.875 times normal size. The diagram of these sections in cascade (Fig. 1) shows axial entry, a pitch of 2.156 in., and a throat diameter of 0.486 in.; the gaging angle

$$\text{arc sin } \frac{\text{throat diameter}}{\text{pitch}}$$

is then 13 deg. The nozzle-area ratio is 4.25 to 1.

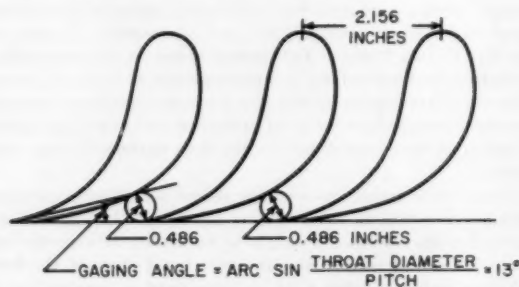


FIG. 1 TURBINE-NOZZLE SECTIONS IN CASCADE

Testing was done in a low-speed wind tunnel, with an approach velocity of approximately 23 fps and an exit velocity of approximately 100 fps. The cascade discharged into the test cell; the flow is unrestricted downstream of the cascade except on the top end wall, which extended 8 in. downstream. It was found that the mixing of the exit stream at the edges of the cascade did not affect passages buried in the center of the cascade.

Total-pressure and flow-angle measurements were made with a five-tube probe. This probe was mounted in a traversing rig which provided for measurement of flow angles in spanwise and transverse planes (see Fig. 2 for definition of cascade co-ordinates). All pressure data were recorded through electromechanical pressure transducers. The transducer systems used upstream and downstream would detect pressure differences of 6.7 per cent of upstream dynamic pressure and 0.6 per cent of downstream dynamic pressure.

All data were taken at a Reynolds number of 25,200.^{*} The boundary layer at the cascade inlet was approximately 2 in. thick, with displacement thickness $\delta^* = 0.37$ in. and shape factor $H = 1.4$. Tests also were run with this inlet boundary layer com-

^{*} $\text{Rey} = \frac{\rho V_\infty d}{\mu}$ (see nomenclature).

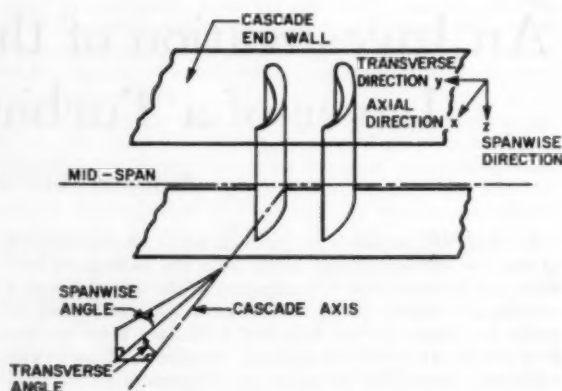


FIG. 2 DEFINITION OF CASCADE CO-ORDINATES

pletely removed to determine the effect of an inlet boundary layer on the nozzle secondary-flow pattern.

EXPERIMENTAL RESULTS AND CONCLUSIONS

From a correlation of static-pressure distributions, total-pressure contours and flow-angle measurements at the cascade exit, and flow traces etched in carbon black on the passage surfaces, a picture of the flow field in the cascade may be formed and qualitative conclusions drawn concerning the origin of the low-energy accumulations.

Static-Pressure Distributions. Static pressures were measured on the blade surface, at blade midspan, and at several spanwise stations near the blade extremity well inside the end-wall boundary layer, Fig. 3(a). These measurements show that the pressure distribution around the nozzle section does not vary appreciably from one spanwise station to another.

Points on the pressure-distribution curves may be related to passage geometry through Fig. 3(b). The pressure on the blade-pressure surface decreases to the 27 per cent point due to passage convergence; it then increases as the passage starts to turn and the fluid decelerates at the outside of the passage. Beyond the 40 per cent point, the pressure decreases to the trailing edge due to passage convergence. On the suction surface, the pressure decreases to a point beyond the throat and then rises to the trailing edge. The nozzle throat is located at 60 per cent of the suction surface. At the throat, the pressure on the suction surface has nearly the same value as the pressure far downstream. Further pressure decrease occurs to a point of minimum pressure at about 70 per cent of the surface. Beyond this point, the blade continues to curve to its trailing edge and the resulting area increase causes deceleration and a pressure rise.

There is evidence that the fluid does not flow continuously to the trailing edge along the blade-suction surface but separates downstream of the throat. The positive pressure gradient past the 70 per cent surface co-ordinate indicates that the blade-surface boundary layer may separate. If the flow separates from the suction surface, the design velocity distribution is not realized and the suction-side pressure then does not continue to increase to the trailing edge to match the pressure on the pressure side. The pressure difference between suction and pressure surfaces at the trailing edge may be due to such a flow separation.

Fig. 3(c) shows the transverse variation in static pressure across the cascade exit, measured at the end wall. This pressure distribution shows clearly the difference in pressure between the suction and pressure sides of the passage noted previously. On the suction side of the passage the curve shows a constant pressure through a small distance near the suction surface of the

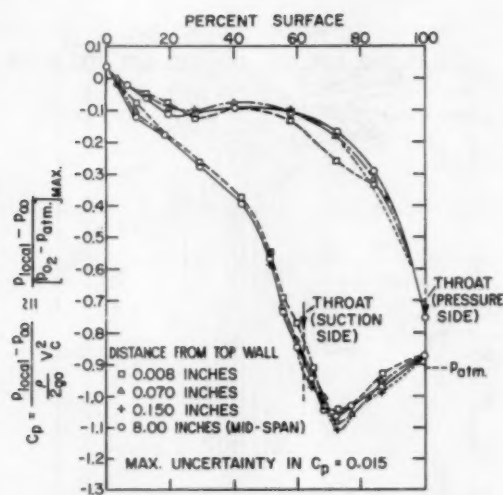


FIG. 3(a) BLADE PRESSURE DISTRIBUTION

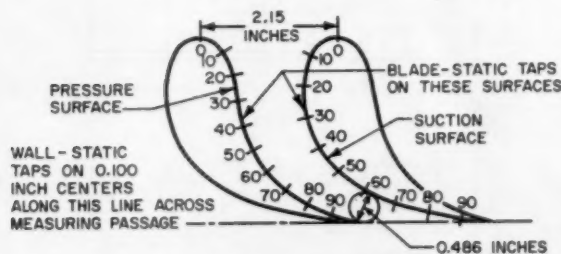


FIG. 3(b) PER CENT SURFACE CO-ORDINATES OF NOZZLE SECTION

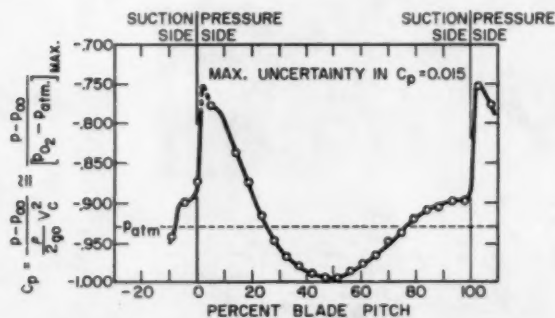


FIG. 3(c) EXIT-PLANE STATIC PRESSURE DISTRIBUTION

blade. This is further indication of a separated region on the suction surface.

Total-Pressure Distribution. To describe the exit flow, contours of constant total pressure in the exit plane of the cascade have been plotted in Fig. 4(a). Numbers on the contours represent local normalized total pressure

$$P_t = \frac{P_t - P_{t00}}{(P_{t02} - P_{t01m})_{\max}}$$

These contours approximate contours of constant total-pressure loss through the cascade. Strictly, it is possible to plot contours

of constant total-pressure loss only if each point in the exit plane can be identified with a point on the same streamline at the entry plane. Because of the complicated secondary flows, it is difficult to trace the path of a streamline. However, for these tests the upstream dynamic pressure was only 5 per cent of $(p_{02} - p_{01m})_{\max}$, so that the normalized upstream total pressure P_{t0} can vary only between 1.0 and 0.95. Therefore the passage loss is very nearly $P_{t0-2} = 1.0 - P_{t0}$, at least for values of P_{t0} considerably less than 0.95. Contours of constant P_{t0} may be interpreted approximately as contours of constant passage loss.

The large accumulation of low-energy fluid shown by the contours to be in the end-wall suction-surface corner of the passage is commonly observed in turning passages. Following along a spanwise line near the suction surface, downward from the end wall, there is first an increase in total pressure, followed by a decrease to a pocket of low-energy fluid, then an increasing total pressure to the region where the total pressure is influenced only by the blade wakes and no longer by the end wall. This peculiar pattern at exit is produced by the flow in the end-wall boundary layer inside the passage, which sweeps low-energy fluid across the passage toward the blade-suction surface. On reaching the suction surface inside the passage, this low-energy fluid apparently rolls up into a vortexlike flow and is subsequently deflected slightly in the spanwise direction, giving the exit-plane contours described in Fig. 4(a).

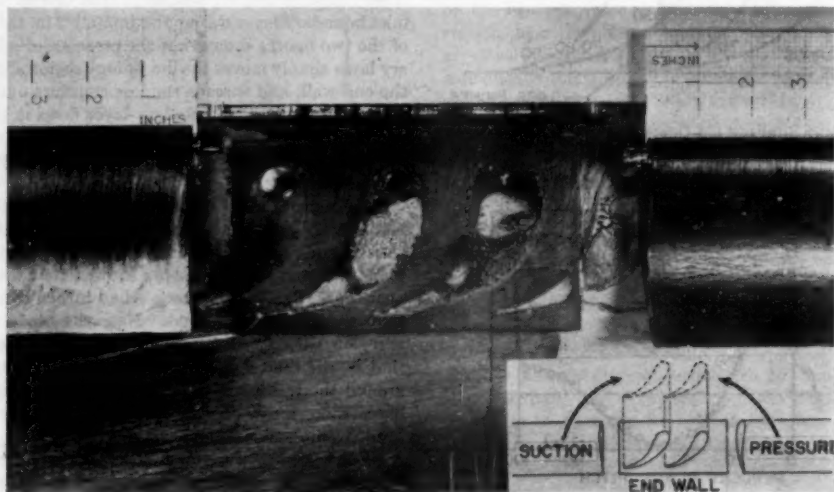
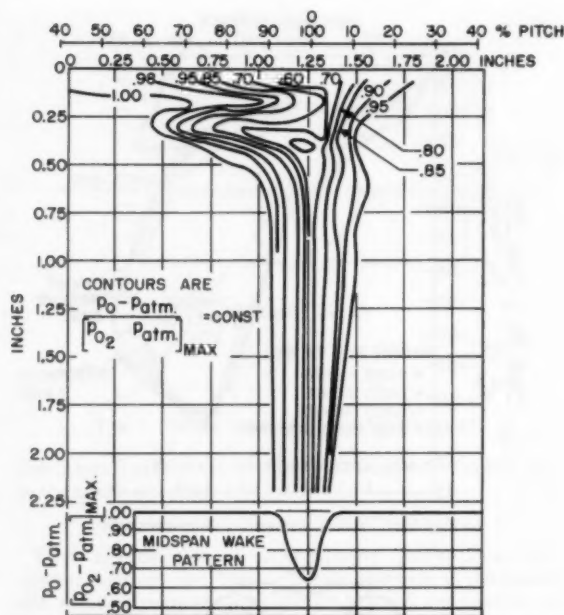
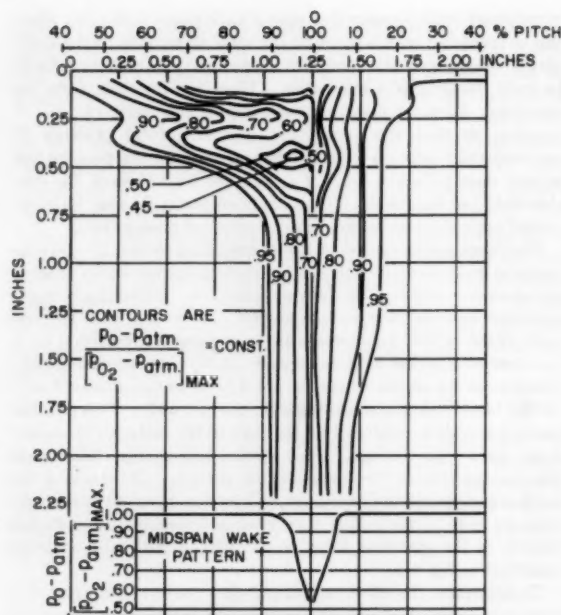
To determine the effect on this exit-flow pattern of the end-wall boundary-layer thickness at the cascade entry plane, measurements were made with the entering boundary layer completely removed just upstream of the cascade. The resulting exit-plane total-pressure contours are shown in Fig. 4(b).⁶ The pattern of these contours is quite similar to that of Fig. 4(a), in which the inlet boundary layer was approximately 2 in. thick. Comparison of the two figures shows that the presence of a large inlet boundary layer simply moves the low-energy region slightly farther from the end wall, and spreads the loss contours over a larger area in the exit plane.⁷ The boundary-layer flows in the passage which produce the low-energy accumulation in the suction corner at exit therefore exist independent of the boundary-layer fluid entering the cascade.

Simultaneously with the exit-plane total-pressure measurements of Fig. 4(a), measurements of fluid turning angle through the cascade were made. In the center of the passage in the exit plane the angle measurements showed that the low-energy fluid near the end wall of the cascade had turned through larger angles than the main-stream fluid. Near the blade trailing edge was a region with turning angle lower than main-stream turning; that is, the fluid coming off the pressure surface tended to flow around the trailing edge. This effect occurred along the entire blade span, but with lowest turning angles near the end wall, in the trailing-edge region.

Flow Visualization. A mixture of carbon black and oil was painted on the nozzle-passage surfaces to obtain a picture of the boundary-layer flows inside the passage. Fig. 5 is a photograph of the flow traces etched in the carbon black on the pressure and suction surfaces of a nozzle section and on the end wall. The photograph shows the cascade end wall as it would be seen from inside the blade row looking along the blades. The blade-suction surface is on the left and the pressure surface on the right.

⁶ The cases investigated are two extremes; the inlet boundary layer of Fig. 4(a) was approximately 2 in. thick, or 50 per cent of the blade chord, and thus larger than normally would be encountered in a machine.

⁷ Similar effects of inlet boundary layer on size and position of loss region were found by Stanitz in a 90-deg accelerating bend: "An Experimental Investigation of Secondary Flow in an Accelerating Rectangular Elbow With 90° of Turning," by J. Stanitz and W. Osburn, NACA TN 3015, October, 1953.



On the end wall at the cascade inlet the air velocities are not high enough to etch the carbon black. As the flow is accelerated through the passage, the streamline traces become visible and show a strong flow in the boundary layer, across the passage from the pressure side to the suction side. These traces appear to terminate at the blade-suction surface, indicating that the boundary-layer fluid leaves the end wall abruptly. This fluid then rolls up into the vortexlike flow which is observed in the exit-plane total-pressure contours, as discussed previously.

Estimates of the exit flow angle from the end-wall traces show a turning angle of approximately 85 to 87 deg in the boundary

layer near the center of the blade pitch. At the trailing edge, the traces show that the fluid has a tendency to flow around the trailing edge from the pressure side to the suction side of the blade. The static-pressure distributions have shown that a higher pressure exists on the pressure surface than on the suction surface at the trailing edge, which produces this flow. The fluid moves around the trailing edge until it is deflected by fluid coming from the suction side of the adjacent passage, forming the "tails" seen trailing from the blades in the photograph.

The traces on the blade pressure surface indicate a rather uniform and parallel flow. The spanwise lines seen on the center

portion of the blade are due to running of the carbon-black mixture under the force of gravity; the flow velocities there were not large enough to sweep the mixture along in the direction of the flow. The pressure-surface traces show no evidence of flow of the pressure-surface boundary layer toward the end wall. It appears, therefore, that the low-energy fluid which is shown by the total pressure contours to be accumulated in the suction-surface end-wall corner at exit has its origin only in the end-wall and suction-surface boundary layers.

The suction-surface traces show an uninterrupted flow, outside of the end-wall boundary layer, to the region of the trailing edge where there is a discontinuity in the flow. There is evidence that the flow is separated from the blade surface in this region, as has been pointed out previously in considering other data. The spanwise sweep of the lines near the trailing edge again may be due to running of the mixture under the force of gravity, in a separated region.

On the suction surface within $1/2$ in. of the blade tip there are two light streaks in the carbon black which stand out quite clearly. These streaks were caused by scouring of the carbon black by relatively high-velocity fluid passing close to the blade surface [note shape and position of the 0.50 contour of Fig. 4(a)]. These streaks describe the path of the end-wall boundary-layer fluid which has rolled up at the suction surface into a vortexlike flow inside the passage, and show the spanwise deflection of the roll-up as it flows to the passage exit. Between the blade end and these streaks is a small region which shows a strong spanwise component of velocity away from the end wall. This flow corresponds to the clockwise rotation (viewed looking upstream) of the boundary-layer roll-up in the end-wall suction-surface corner.

SUMMARY OF RESULTS AND CONCLUSIONS

1 There are strong secondary flows in the end-wall boundary layer of a turbine-nozzle passage which carry low-energy fluid to the suction side of the passage.

2 The low energy of the fluid accumulated in the end-wall suction-surface corner of the nozzle passage at exit is due to frictional dissipation on the end wall and suction surface inside the nozzle passage. The end-wall boundary layer remains thin throughout the passage and is continually being swept to the blade-suction surface by secondary flows. This requires new boundary-layer growth from free-stream fluid. The large shear stresses associated with thin boundary layers may cause high rates of dissipation on the end wall.

3 The secondary flows in the end-wall boundary layer inside the nozzle passage exist independent of the inlet boundary layer and are essentially unchanged even when the inlet boundary layer is completely removed.

4 There is no appreciable difference between the blade-surface pressure distribution at midspan and at the blade end inside the end-wall boundary layer. The blade force does not change, therefore, in the region of the end wall.

5 A roll-up of the end-wall boundary layer into a vortexlike flow was indicated by the total-pressure distribution at cascade exit and by flow traces on the blade surface. The streak on the rear suction surface of the blade observed here and in actual turbines was associated with this flow.

6 For the nozzle profile tested the flow was separated from the suction surface near the trailing edge, except in a region very near the end wall.

ACKNOWLEDGMENTS

This research was conducted as part of the activity of the "Three-Dimensional Flow in Turbomachine Research Project" of the M.I.T. Gas Turbine Laboratory, under the sponsorship of

General Electric Company, Westinghouse Electric Corporation, Curtiss-Wright Corporation, Allison Division of General Motors Corporation. This research was under the supervision of Prof. E. S. Taylor, Director of the Gas Turbine Laboratory, and R. C. Dean, Jr., Assistant Professor of Mechanical Engineering. Special thanks are due Mr. Hans Kraft of the General Electric Company, for providing the turbine-nozzle sections used in the investigation.

Discussion

HANS KRAFT.^{*} It is certainly highly welcome to observe that at last fundamental work is being done about the secondary flow in turns. It is an old phenomenon and has been discussed in literature already somewhere around the beginning of the century. Unfortunately, like the weather, it is a complicated and unattractive fluid-flow problem and hence there was more talking about it than doing. For a long time engineers, as contrasted to interested physicists, have tried to do something about it along technical lines. The writer can hardly remember a young engineer entering this field who has not tried to find ways to eliminate or mitigate the secondary flow. The end result was always the same—negative. Only on a recent trip to England the writer found one attempt which claims to have succeeded. However, a check has not yet been made whether the difference in observation has been due to a difference in the adaptability of air to experiment which sometimes seems to exist between the two countries.

The sharply defined streak on the suction side of the nozzle which the author described has been observed in all steam turbines since their very beginning. The author is probably correct when he ascribes this streak to the one-dimensional separation of the fluid from the wall, this separation occurring in a spanwise direction only. It is difficult to change this pattern. Only once has the writer succeeded in doing so. The change resulted from very large fillets (about $3/4$ in. radius) around the entrance nose of the blade. The fillets ended before the final large acceleration was started in the nozzle. This had the effect that apparently the spanwise separation was eliminated and that the boundary-layer flow was inclined away from the end walls right up to the center of the span. However, it may be noted here that no beneficial effect could be found as far as performance was concerned.

The writer agrees with the author when he states that the loss created by the secondary flow in a nozzle of large span is probably not too serious in so far as the nozzle itself is concerned. However, in nozzles of normal turbine dimensions and approximately from 2 to 3 in. high, the additional end-wall loss about equals the friction loss around the profile, and in this case is an unwelcome addition.

Furthermore, as the author states, the variation both in angle and velocity magnitude of the issuing velocity vector can well be expected to affect the flow through the rotating part of the turbine rather materially if it can trigger some separation within the moving-bucket passage. Such a trigger action is not entirely impossible, although in view of the comparatively low energy deficiency, it may be somewhat difficult to explain it. It certainly can be said that some action seems to occur in the rotating member of the turbine which as yet cannot be explained fully. If this secondary flow should be the prime culprit, it must be expected that its nonsteady character is primarily to blame. This, of course, does not make the problem any simpler.

It is certainly to be hoped that more work of this nature will be undertaken and published. In view of the difficulty of the

^{*} Aerodynamic Engineer, Large Steam Turbine-Generator Department, General Electric Company, Schenectady, N. Y.

undertaking, it cannot be expected that a technically useful explanation of this phenomenon will be furnished quickly. However, if a number of capable experimenters expend some effort along this line the time should come when the effect of the various parameters, especially that of the profile contours, will be understood fully.

While it does not contribute really to the subject matter, the writer would like to discuss the separation, as it is called by the author, which occurs at the exit of the suction surface. The phenomenon is exaggerated here on account of the rather low Reynolds number at which the experiment was run. It seems that this kind of separation comes very close to that discussed by Schmieden around 1940.

The author correctly observes that the air does flow from the pressure to the suction side around the exit edge and joins the suction flow on the suction side. It does that in mid-span as well as near the wall. It does not appear as if this behavior detracts from the efficiency of the nozzle. Rather it seems to be connected with the fact that the wake behind such a nozzle, especially at lower Reynolds numbers, is a Karman street. This can be seen in some of the pictures which have been shown by Faulders in the publications already mentioned.

YASUTOSHI SENOO.² The investigation of the end-wall boundary layer of a turbine-nozzle cascade was continued after the author left the Institute. In the continued investigation, the end-wall boundary layer was measured directly in the nozzle. Since the author's investigation was mainly based on the flow behavior downstream of the cascade, the writer's experiment may serve to supplement the data for the author's investigation. As a whole, the boundary-layer measurement supports the author's statement, but there are a few results to be added.

² Gas Turbine Laboratory, Massachusetts Institute of Technology, Cambridge, Mass.; on leave of absence from Kyushu University, Japan.

1 The end-wall boundary layer was observed to be laminar independently of the inlet boundary layer.

2 The displacement thickness of the end-wall boundary layer was not very different from the prediction based on a two-dimensional laminar boundary-layer theory. The main flow component of the shear stress was also predicted by the two-dimensional boundary-layer theory with a reasonable accuracy. The end-wall boundary layer becomes thin owing to the sweeping effect of the crossflow, but the boundary layer becomes thick because of the converging effect of the side walls (or blades). The writer suspects that in the present case these two effects almost cancel each other; that is, the agreement of the two-dimensional theory prediction is fortuitous.

3 The maximum crossflow velocity and the secondary-flow behavior near the end wall (order of 0.05 in.) are essentially unchanged by the inlet boundary layer, but the behavior outside the thin layer depends upon the inlet boundary layer; i.e., the layer with crossflow is thick if the inlet boundary layer is thick. Since the velocity defect is limited to a thin layer near the end wall, the accumulation of the low stagnation-pressure fluid carried by the crossflow is essentially unchanged by the inlet boundary layer.

4 A two-dimensional laminar boundary-layer calculation shows that the separation of the boundary layer on the suction surface of the blade is completely suppressed by a slight variation of the pressure distribution on the blade surface. As a matter of fact, an experiment showed that an inaccuracy of blade mounting was sufficient to cause the boundary-layer separation. It is expected, however, that the boundary-layer behavior on the blade-suction surface does not affect the end-wall boundary layer.

AUTHOR'S CLOSURE

In closure, the author wishes to thank Mr. Kraft and Dr. Senoo for adding their greater experience and further work on this problem to the discussion.

Jet-Pump Theory and Performance With Fluids of High Viscosity¹

By R. G. CUNNINGHAM,² WOOD RIVER, ILL.

Performance characteristics of the jet pump when handling viscous oil have been established. Theoretical relations describing the jet pump are developed in this paper in terms of dimensionless ratios and friction coefficients. In addition, an energy analysis is made which separates friction losses and unavoidable mixing losses. In an experimental program eight jet pumps, with nozzle-to-throat area ratios of 0.1 to 0.6, were operated over a range of jet Reynolds numbers from 700 to 30,000. Mineral and synthetic lubricating oils used covered a 5 to 100-centistoke viscosity range of the jet fluid. The results of these theoretical and experimental studies permit application of the jet pump to lubrication systems. For design use the experimental data are reduced to friction coefficients and correlated versus jet and throat Reynolds numbers. To facilitate rapid estimates of viscosity effects, simplified empirical relations are also included. It is concluded from this study that the jet pump is indeed suitable for use with viscous fluids.

NOMENCLATURE

The following nomenclature is used in the paper:

- W = mass flow rate, lb_m/sec
 P = static pressure, psf or psi
 \bar{P} = total pressure, psf
 V = velocity, fps
 E = energy, ft-lb_f/sec
 ρ = density, lb_m/ft³
 A = area, sq ft
 d = diameter, ft or in.
 L = throat length, ft or in.
 S = nozzle-to-throat spacing, ft or in.
 g_c = dimensional constant, $\frac{\text{lb}_m \text{ft}}{\text{lb}_f \text{sec}^2}$
 (lb_m, lb_f are pound mass and force, respectively)
 b = area ratio, A_n/A_m
 ϕ = flow ratio, W_s/W_n
 K_1 = nozzle coefficient
 K_t = throat-friction coefficient
 K_d = diffuser-friction coefficient
 N = dimensionless pressure ratio
 R = Reynolds number
 ν = kinematic viscosity, centistokes or ft²/sec

μ = viscosity, centipoises or $\frac{\text{lb}_m}{\text{sec ft}}$

η = efficiency, $= \phi N$
 e = slope, N versus ϕ
 sg = specific gravity

Subscripts

- n = primary nozzle fluid
 s = secondary or pumped fluid
 t = total flow
 o = side flow entry to jet pump
 i = nozzle entry
 a = throat entry
 m = throat exit, diffuser entry
 d = diffuser exit
 jl = jet loss
 ml = mixing loss
 fl = friction loss
 l = total losses
 mep = maximum efficiency point on η versus ϕ plot
 opt = optimum
 h = high Reynolds number
 op = operating flow ratio: $\phi_{op} \approx \frac{2}{3} \phi_{mep}$

INTRODUCTION

The simplicity and light weight of the jet pump render it attractive for use in lubrication systems—particularly for aircraft engines. A major advantage of the fluid-powered jet pump is the elimination of the mechanical-drive train necessary for conventional pumps.

A broad study of the jet pump as a lubrication-oil scavenge pump was carried out at The Pennsylvania State University. Included in the work were (a) the effect of viscosity, which comprises the following paper; (b) cavitation (altitude ceiling) characteristics; and (c) jet-pump behavior with air-oil mixtures inducted at the suction port (7).³

The jet pump functions by turbulent mixing. At low Reynolds numbers, where viscous forces predominate over inertial forces, impaired performance may be expected. The results of this theoretical and experimental study permit design and application of the jet pump over a wide range of Reynolds numbers.

1 JET-PUMP THEORY AND EXPERIMENT

JET-PUMP THEORY

A jet pump is a device by means of which a fluid may be pumped by the action of a high-velocity jet of the same, or other fluid. The pumping action is a result of a transfer of momentum from the jet fluid to the fluid being pumped.

Because of the complex nature of the problem, development of the theory of jet pumps has been slow, particularly for compressible flow. Of the references on the subject the contributions of Flügel (1) and Keenan and Neumann (2, 3) are probably the most significant.

In the case of incompressible flow, the analyses by Gibson (4),

¹ Numbers in parentheses refer to the Bibliography at the end of the paper.

¹ Material in this paper is based on work conducted by the author at The Pennsylvania State University, 1953-1954, which was sponsored by the Wright Air Development Center (WADC Technical Report 55-143).

² Research Group Leader, Shell Oil Company, Wood River Research Laboratory. Formerly, Associate Professor of Engineering Research, The Pennsylvania State University, Department of Engineering Research, University Park, Pa. Assoc. Mem. ASME.

Contributed by the Hydraulic Division and presented at the Annual Meeting, New York, N. Y., November 25-30, 1956, of THE AMERICAN SOCIETY OF MECHANICAL ENGINEERS.

NOTE: Statements and opinions advanced in papers are to be understood as individual expressions of their authors and not those of the Society. Manuscript received at ASME Headquarters, July 26, 1956. Paper No. 56-A-58.

Gosline and O'Brien (5), Flügel (1), and Hussmann (6) are of interest in the present problem, that of pumping lubricating oil.

Mechanism of Pumping Action. As a jet of fluid penetrates a stagnant or slowly moving fluid, a dragging action occurs on the boundary of the jet between the high and low-velocity particles. Mixing occurs between the jet fluid and the low-velocity fluid; and transfer of momenta accelerates the latter in the direction of the flow. As the two flows progress, the mixture stream spreads. The undisturbed high-velocity core progressively decreases in diameter until it disappears, Fig. 1. Confined by parallel throat walls, the secondary fluid enters a region of decreasing area, that area being the annulus between the mixture stream and the throat wall. At the throat entrance the annular area is the difference between jet and throat area. At the throat exit the mixture stream has spread until it touches the wall of the throat. Then all of the side fluid has been mixed with the primary jet.

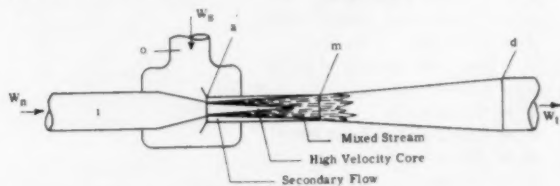


FIG. 1 JET PUMP, SHOWING MIXING PROCESS

Assumptions. In common with other solutions, the approach used in this paper leads to what may be termed an "approximate" theory, since the details of the mixing process are avoided by use of impulse-momentum relations:

- 1 The flow streams are one-dimensional at throat entrance and exit.
- 2 Mixing is completed in the constant-area throat, against an adverse pressure gradient.
- 3 Primary and pumped fluids are incompressible and of equal density.

Continuity Relations. The annular area available to the side-flow stream at throat entry is

$$A_{as} = A_m - A_{ns} = A_m - A_n$$

and, with $W = \rho AV$

$$V_{as} = \frac{W_s}{\rho A_{as}} = \frac{\phi b}{1-b} V_{ns} = \frac{\phi b}{1-b} V_n \dots [1]$$

The throat flow is the sum of the nozzle and side flows, $W_t = W_n + W_s$,

$$V_m = \frac{W_t}{\rho A_m} = b(1 + \phi) V_n \dots [2]$$

Nozzle-Energy Equation

$$\frac{P_t}{\rho} + \frac{V_t^2}{2g_c} = \frac{P_s}{\rho} + \frac{V_s^2}{2g_c} + \frac{P_{f1}}{\rho}$$

where P_{f1}/ρ is energy lost by friction in the nozzle.

$$\text{Let } \bar{P}_t = P_t + \frac{\rho V_t^2}{2g_c} \quad (\text{total pressure})$$

$$P_{f1} = K_1' \frac{\rho V_n^2}{2g_c}$$

The nozzle-energy equation becomes

* Hereafter the location subscript *a* will be dropped, i.e., *n* in place of *na*.

$$\bar{P}_t - P_s = (1 + K_1') \frac{\rho}{2g_c} V_n^2 \dots [3]$$

Side-Flow-Energy Equation. By analogy with Equation [3], the energy relationship between suction port (*a*) and throat entry (*a*) may be written*

$$\bar{P}_s - P_s = \frac{\rho V_{as}^2}{2g_c} = \frac{\rho V_n^2}{2g_c} \frac{\phi^2 b^2}{(1-b)^2} \dots [4]$$

Momentum Equation in Throat

$$\frac{W_n V_n}{g_c} + \frac{W_s V_{as}}{g_c} - \frac{W_t V_m}{g_c} - F_{f1} = A_m (P_m - P_s) \dots [5]$$

The term F_{f1} refers to wall-friction drag accompanying the flow of a real fluid in a tube

$$F_{f1} = f A_{wall} \frac{\rho}{2g_c} V_m^2$$

where f is the friction factor and $A_{wall} = \pi d_m L$ is the wall surface area of the tube, L and d_m are length and diameter of the throat. Upon introducing the throat cross-sectional area A_m

$$F_{f1} = f \frac{L A_m V_m^2}{d_m 2g_c}$$

Let $K_2 = f L/d_m$, then

$$F_{f1} = K_2 A_m \frac{\rho}{2g_c} V_m^2 \dots [6]$$

By inserting Equations [1], [2], and [6] in Equation [5]

$$P_m - P_s = \frac{\rho}{2g_c} V_n^2 \left[2b + \frac{2\phi^2 b^2}{1-b} - (2 + K_2) b^2 (1 + \phi)^2 \right] \dots [7]$$

Diffuser-Energy Equation

$$\frac{P_m}{\rho} + \frac{V_m^2}{2g_c} = \frac{P_d}{\rho} + \frac{V_d^2}{2g_c} + \frac{P_{f2}}{\rho}$$

$$\text{let } \bar{P}_d = P_d + \frac{\rho V_d^2}{2g_c}, \text{ and } P_{f2} = K_4 \frac{\rho V_m^2}{2g_c}$$

$$\text{then } \bar{P}_d - P_m = (1 - K_4) b^2 (1 + \phi)^2 \frac{\rho}{2g_c} V_n^2 \dots [8]$$

By combining Equations [3], [4], [7], and [8], the three significant pressure-difference expressions may be obtained

$$\bar{P}_t - \bar{P}_s = \frac{\rho}{2g_c} V_n^2 \left[1 + K_1' - \frac{\phi^2 b^2}{(1-b)^2} \right] \dots [9]$$

$$\bar{P}_d - \bar{P}_s = \frac{\rho}{2g_c} V_n^2 \left[2b + (1-2b) \frac{\phi^2 b^2}{(1-b)^2} - (1 + K_2 + K_4) b^2 (1 + \phi)^2 \right] \dots [10]$$

$$\bar{P}_t - \bar{P}_d = \frac{\rho}{2g_c} V_n^2 \left[1 + K_1' - 2b - \frac{2\phi^2 b^2}{1-b} + (1 + K_2 + K_4) b^2 (1 + \phi)^2 \right] \dots [11]$$

Hereafter the sum K_2 plus K_4 will be expressed as K_{24} .

* A throat-entry coefficient, K_1 , could be included, corresponding to K_1' above. Of negligible effect on pump-characteristic curves, it has been omitted.

Jet-Pump Efficiency. Pump efficiency η is obtained as the ratio of energy output to energy input

$$E_{out} = \frac{W_s}{\rho} (P_s - P_d) \text{ ft-lb/sec}$$

$$E_{in} = \frac{W_n}{\rho} (P_i - P_d)$$

$$\eta = \frac{E_{out}}{E_{in}} = \phi \frac{P_s - P_d}{P_i - P_d} = \phi N \dots \dots \dots [12]$$

where N is the dimensionless pressure ratio

$$N = \frac{2b + (1 - 2b) \frac{\phi^2 b^2}{(1 - b)^2} - (1 + K_{11})b^2(1 + \phi)^2}{1 + K_1' - 2b - \frac{2\phi^2 b^2}{1 - b} + (1 + K_{11})b^2(1 + \phi)^2} \dots [13]$$

Note also that
$$\frac{N}{N + 1} = \frac{P_s - P_d}{P_i - P_d} \dots \dots \dots [14]$$

The pressure characteristic is thus a function of area ratio b , flow ratio ϕ , and the friction-loss coefficients K_1' and K_{11} . Although the method employed and the form of the final N -equation are somewhat different, the relations between N and the variables noted are essentially the same as established by Gosline and O'Brien (5).

PERFORMANCE OF OIL-JET PUMPS

In order to investigate design variables, primarily area ratio b and spacing S , the pump shown in Fig. 2 was constructed. It consists of one body with three interchangeable nozzles and three throat-diffuser sections of similar design. Thus up to nine jet pumps could be assembled in the one body. Additional throat-diffuser sections were made to check effect of throat length and throat-entry shape. All diffuser angles were 8 deg (total included angle).

A commercial pump of conventional conic nozzle and throat design also was tested with two nozzle sections and provisions for varying the spacing S , Fig. 3. All pumps are identified by three numbers; e.g., No. 141/318/308. The numbers refer to nozzle diameter, throat diameter, and nozzle-to-throat spacing in thousandths of an inch.

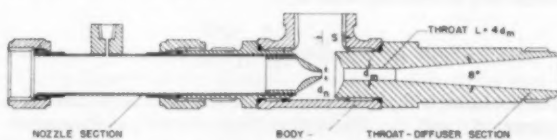


FIG. 2 EXPERIMENTAL JET PUMP WITH VARIABLE NOZZLE-TO-THROAT SPACING, S . EQUIPPED WITH THREE NOZZLE SECTIONS AND THREE THROAT-DIFFUSER SECTIONS
(Performance measured at $b = 0.1, 0.13, 0.2, 0.3, 0.4$, and 0.6 .)

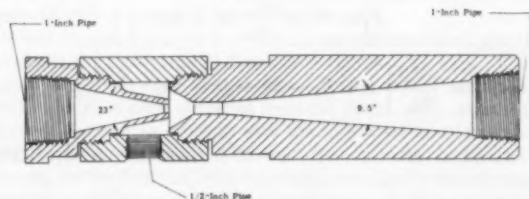


FIG. 3 CONVENTIONAL JET PUMP No. 177/240/455 AREA RATIO, $b = 0.544$, ALSO MODIFIED TO 177/240/255. SAME BODY USED FOR No. 100/240/277, 445, $b = 0.174$.
(Numbers refer to $d_n/d_m/S$, in thousandths. Throat length $L = 0.846$ in.)

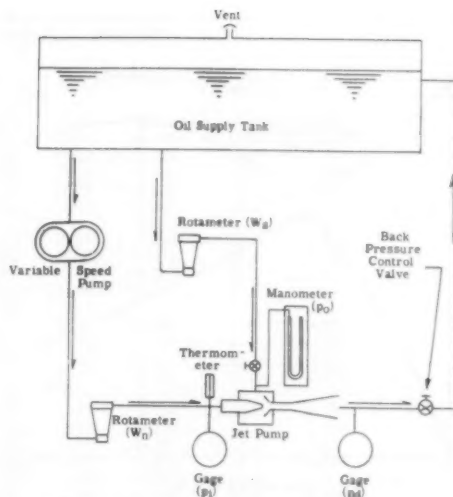


FIG. 4 FLOW DIAGRAM, JET-PUMP TEST STAND

Test Procedure. Testing a jet pump consists of measuring three pressures P_i , P_s , P_d , and the two flow rates, W_n and W_s . Generally tests were made at a selected nozzle flow rate W_n and side-port pressure P_s . A unique relationship exists for each pump between back pressure P_d and side flow rate W_s —much the same as for a centrifugal-pump discharge, similarly dependent on back pressure. The test is made by varying P_d from the "cutoff" pressure where $W_s = 0$ to the minimum obtainable (back-pressure valve wide open). At a number of operating points, usually about 10 to 15 for each performance curve, pressures and flow rates are recorded.

Fig. 4 shows the test-stand flow circuit. Primary flow was supplied with a positive-displacement pump driven by a variable-speed d-c motor. The rotameters shown were calibrated and used with oils of low viscosity. For viscous oils mass-flow rates were determined by timing the pump discharge into a tank placed on beam scales; the rotameters then served only to indicate steady-flow conditions during a run.

For each run the five measured quantities were converted to dimensionless flow and pressure ratios: The flow ratio, $\phi = W_s/W_n$ and the pressure ratio N

$$N = \frac{P_s - P_d}{P_i - P_d} \dots \dots \dots [15]$$

where P_i , P_s , and P_d are nozzle, side-port, and discharge pressures, psig. Velocity heads were negligible, thus permitting this substitution of static pressures.

Results. In Fig. 5 measured N -values are plotted versus flow ratio ϕ for a high head-ratio pump ($b = 0.6$). (The theoretical N and $\eta = \phi N$ -curves are discussed later.) The N - ϕ characteristic curve completely describes the jet pump. Similar performance curves for a high flow-ratio type ($b = 0.2$) are presented in Fig. 6. (Both of these tests were at high Reynolds numbers.) Agreements between theory and test results for six other area ratios were virtually identical with these. Numerical results are given in Table 1 where the high-Reynolds number test for each pump is identified with an asterisk.

By means of Equations [9] and [10] experimental data can be expressed in terms of dimensionless friction coefficients K_1' and K_{11} . Friction coefficients are dependent on Reynolds number and relative boundary roughness and should be unaffected by other parameters. This was true of the throat-diffuser coefficient

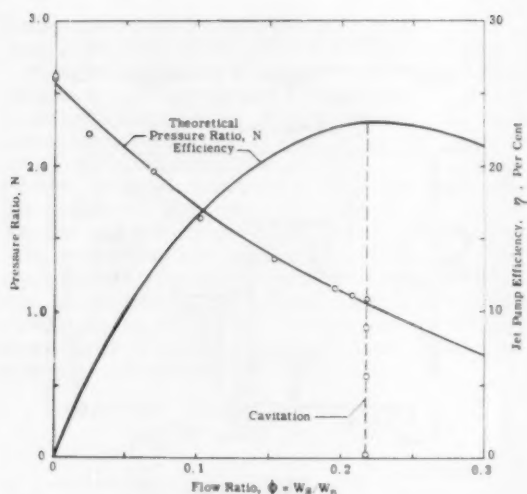


FIG. 5 EXPERIMENTAL VALUES OF PRESSURE RATIO N VERSUS FLOW RATIO ϕ . THEORY SHOWN AS SOLID LINE CURVES. AREA RATIO $b = 0.60$; JET REYNOLDS NUMBER $R_n = 21,370$

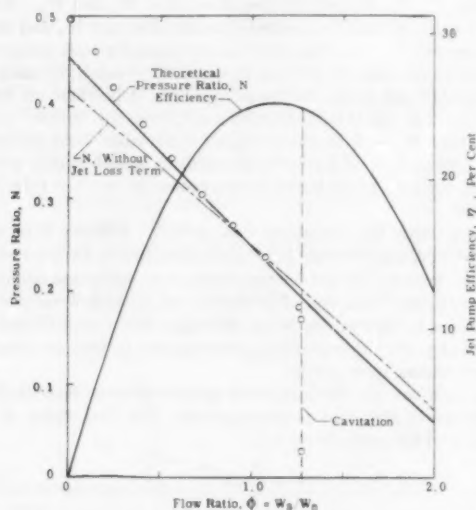


FIG. 6 EXPERIMENTAL VALUES OF PRESSURE RATIO N VERSUS FLOW RATIO ϕ . THEORY SHOWN AS SOLID AND BROKEN-LINE CURVES. JET-PUMP AREA RATIO $b = 0.2$; JET REYNOLDS NUMBER $R_n = 19,230$

K_{11} . However, early calculations revealed a disturbing influence of flow ratio on the value of the nozzle coefficient, K_1' . Rearranging Equation [9], K_1' is expressed in terms of pressures and flow rates

$$K_1' = \frac{P_4 - P_s}{\frac{\rho}{2g_s} V_n^2} - 1 + \frac{\phi^2 b^2}{(1-b)^2} \quad [16]$$

The nozzle velocity V_n is found from nozzle flow rate by

$$V_n = \frac{W_n}{\rho A_n} \quad [17]$$

The analytical solution was originally based on the assumption

that the pressure at the nozzle tip was equal to that in the plane of the entrance of the throat. An annular area $A_{n1} - A_n$ is available for the side flow. As the side flow W_s (hence ϕ) increases, the throat-entry pressure—therefore also the nozzle-discharge pressure—must of necessity decrease relative to the side-port pressure P_s . The growth of the last term in Equation [16] compensates the supposed decrease in $P_4 - P_s$; so that K_1' is theoretically unaffected by flow ratio.

In practice, the tip of the nozzle is withdrawn from the throat entry by as much as several nozzle diameters. Furthermore, these jet pumps were provided with large-area unrestricted side-entry ports, minimizing pressure loss (Figs. 2, 3). The nozzle evidently experienced a discharge pressure higher than the throat-entry pressure, for all practical purposes, equal to P_s . The result is that the first term in Equation [16] does not decrease at the same rate as the last term increases. It remains constant for a given nozzle flow rate. Thus, K_1' may be defined as

$$K_1' = K_1 + \frac{\phi^2 b^2}{(1-b)^2} \quad [18]$$

where

$$K_1 = \frac{P_4 - P_s}{\frac{\rho}{2g_s} V_n^2} - 1 \quad [19]$$

K_1 is simply K_1' at zero side flow, where $\phi = 0$. The nozzle coefficient K_1 reflects the effect of Reynolds number and nozzle design. The second term in Equation [18] is a consequence of the departure in practice from the theoretical configuration of the pump parts.

Jet-Loss Hypothesis. In over 200 tests with eight jet pumps, $b = 0.1$ to 0.6 , the nozzle-to-side port pressure drop did not vary with change in ϕ , but remained constant for a given primary-flow rate. Evidently the jet discharges from the nozzle tip to static pressure P_s and then penetrates the short distance S , before entering the throat where the static pressure is P_s . This traverse of the jet from P_s down to P_s may be thought of as a fluid frictional energy loss E_{fl} . This energy loss is

$$E_{fl} = \frac{W_n}{\rho} (P_s - P_s), \frac{\text{ft lb}_F}{\text{sec}}$$

By substituting for the pressure difference with Equation [4] (neglecting the velocity head at s)

$$E_{fl} = W_n \frac{V_n^2}{2g_s} \frac{\phi^2 b^2}{(1-b)^2} \quad [20]$$

The last factor in Equation [20] will be recognized as the difference between K_1' and K_1 . The flow of the jet from P_s to P_s is a loss distinct from the nozzle loss proper.

Revised Basic Equations. The basic equations of jet-pump behavior (Equations [9], [10], [11], [13]) incorporating the jet-loss concept appear as

$$P_4 - P_s = \frac{\rho V_n^2}{2g_s} [1 + K_1] \quad [9b]$$

$$P_4 - P_s = \frac{\rho V_n^2}{2g_s} \left[1 + K_1 - 2b - (1-2b) \frac{\phi^2 b^2}{(1-b)^2} + (1 + K_{11})b^2(1 + \phi)^2 \right] \quad [11b]$$

$$N = \frac{2b + (1-2b) \frac{\phi^2 b^2}{(1-b)^2} - (1 + K_{11})b^2(1 + \phi)^2}{1 + K_1 - \text{numerator}} \quad [13b]$$

TABLE 1 SUMMARY OF EXPERIMENTAL RESULTS

Pump Number and Area Ratio, b	R_n	K_1	At ϕ_{op}		At Max Eff Point			
			R_n	K_{24}	ϕ	η	η_{max}	σ
100/316/307 $b = 0.10$	754	1.024	382	5.58	0.60	0.0175	1.05	0.209
	2,480	0.560	2,270	0.382	1.90	0.0895	15.9	0.826
	3,410	0.414	3,020	0.291	2.12	0.089	18.9	0.898
	3,620	0.483	3,550	0.274	2.10	0.089	18.7	0.908
	8,720	0.273	9,380	0.276	2.35	0.096	22.6	1.0
	*13,020	0.208	10,760	0.294	2.40	0.095	22.8	1.0
141/387/311,411 $b = 0.133$	2,180	0.422	1,710	0.450	1.15	0.136	15.6	0.842
	5,290	0.264	5,030	0.356	1.65	0.131	21.6	0.961
	16,350	0.085	15,450	0.446	1.65	0.138	22.8	1.0
	*19,300	0.104	16,900	0.400	1.65	0.144	23.8	1.0
100/240/445 $b = 0.174^*$	760	0.773	427	3.80	0.35	0.052	1.83	0.276
	1,720	0.444	1,290	1.69	0.85	0.077	6.55	0.510
	2,120	0.462	1,810	0.505	1.05	0.117	12.3	0.726
	2,790	0.378	2,560	0.258	1.35	0.164	22.1	0.959
	2,840	0.411	2,840	0.352	1.35	0.143	19.3	0.908
	3,420	0.391	3,350	0.286	1.35	0.154	20.8	0.946
	3,490	0.365	3,273	0.232	1.25	0.176	22.0	0.976
	3,680	0.322	4,580	0.207	1.40	0.169	23.6	1.01
	5,610	0.300	5,490	0.182	1.60	0.165	26.1	1.02
	10,340	0.218	10,340	0.347	1.40	0.164	23.0	1.0
	*13,410	0.189	13,410	0.386	1.35	0.166	22.4	0.982
141/316/308 $b = 0.20$	656	0.878	410	2.71	0.35	0.077	2.70	0.326
	2,510	0.372	2,350	0.372	1.08	0.177	19.1	0.809
	5,160	0.246	5,060	0.315	1.15	0.198	22.8	0.935
	7,160	0.202	6,710	0.282	1.10	0.220	24.2	0.965
	9,530	0.158	9,140	0.315	1.15	0.218	25.0	0.986
	19,300	0.106	16,380	0.322	1.15	0.228	26.2	1.0
	*19,300	0.100	17,240	0.358	1.15	0.220	25.3	1.0
	20,130	0.096	17,100	0.357	1.15	0.226	26.0	1.0
173/316/237,337 $b = 0.30$	3,920	0.275	3,650	0.229	0.70	0.350	23.1	0.883
	5,720	0.208	4,580	0.185	0.70	0.355	25.0	0.909
	7,550	0.196	7,040	0.254	0.70	0.355	25.0	0.909
	21,200	0.096	19,700	0.220	0.80	0.360	28.8	0.986
	*31,500	0.090	29,350	0.206	0.80	0.370	29.6	1.0
141/224/291 $b = 0.40$	3,180	0.352	2,700	0.196	0.45	0.445	20.0	0.876
	4,510	0.255	3,830	0.235	0.45	0.455	20.4	0.898
	*25,840	0.068	24,400	0.272	0.52	0.502	26.1	1.0
177/240/455 $b = 0.544^*$	3,580	0.252	3,170	0.395	0.28	0.515	14.4	0.721
	*21,970	0.114	19,400	0.154	0.29	0.840	24.4	1.0
173/224/020 $b = 0.60$	*21,370	0.076	19,800	0.176	0.23	1.00	23.0	1.0

* Basic high Reynolds-number test, maximum efficiency.

* Conical nozzle and throat entry, Fig. 3. Other pumps, Fig. 2.

NOTE: Pump number refers to nozzle diameter/throat diameter/nozzle-to-throat spacing, in thousandths of an inch.

(The output pressure rise remains unchanged as Equation [10].)

Theory-Experiment Comparison. Theoretical $N-\phi$ curves were calculated for each test, from measured K_1 and K_{24} values to insure agreement with the experiment at the one flow ratio ϕ_{op} . The validity of the theory is judged by the agreement of data with the theoretical curve at values of ϕ greater and less than ϕ_{op} . Figs. 5 and 6 show that the theory agrees quite well with actual test results over a wide range of flow ratios. The sudden break in the data points and departure from theory at high flow ratios is the result of cavitation (7) (see the following).

It will be noted that for $b = 0.2$ the experimental data points fall above the theoretical at flow ratios approaching zero. This was characteristic of all pumps with b less than 0.3, and is attributed to separation of the jet from the throat wall, or rather, failure of the flow to conform with the throat wall until well beyond the throat entrance. Thus wall friction would be less, accounting for the fact that actual performance slightly exceeds the theoretical prediction at ϕ -values near zero. Such a tendency should be greatest for small area ratios.

The broken-line curve in Fig. 6 represents the theoretical solution without the "jet loss." This curve is based on the same K_{24} -value and on a K_1' nozzle coefficient evaluated at the flow ratio,

ϕ_{op} . In every case best agreement with experiment required inclusion of the jet-loss factor.

The virtue of the jet-loss hypothesis is this: It permits retention of the one-dimensional, impulse-momentum analysis of the otherwise complex mixing process while producing theoretical characteristic curves which accurately predict test performance of jet pumps.

Effect of Absolute Pressure. Since the head-flow ratio characteristics are expressed in terms of pressure differences ($P_t - P_o$, $P_s - P_o$, etc.) the absolute pressure level (psia) should have no effect on pump performance. This was confirmed experimentally: $N-\phi$ curves measured with P_o at 1 atm ("sea level"), and at simulated altitudes, were identical (7).

Performance is affected in one respect, however; cavitation-limited flow. The vertical lines in Figs. 5 and 6 show the effect of cavitation. Side-flow quantity fails to increase in response to a reduction in back pressure, and remains constant in W_{sL} the "limiting flow."

The original object of this study was aircraft use of jet pumps; a considerable portion of reference (7) is devoted to cavitation. Cavitation-limited, oil-flow data for the pumps described herein were well represented by a "limiting-flow function" correlated

with the absolute side-port pressure, psia. From these relations, altitude-ceilings of aircraft jet pumps may be predicted. Ceiling may be extended to altitudes of the order of 60,000 to 70,000 ft by use of low area-ratio pumps, designing for operation at reduced flow ratios, and by use of lower jet velocities (7). Although no water tests were made, this same method of correlating cavitation-limited performance of water-jet pumps should be satisfactory.

REYNOLDS-NUMBER CORRELATION OF MEASURED FRICTION COEFFICIENTS

One of the primary questions to be answered in judging the feasibility of using an oil-jet pump as in a lubrication system is the effect of viscosity. The jet-pumping process, a momentum interchange, depends upon turbulent mixing of the primary and secondary streams. Turbulence can persist only when the viscous stresses in the flow are insufficient to damp out local fluctuations in velocity.

By means of dimensional analysis it can be shown that in the nozzle, and in the throat and diffuser, the dynamic pattern of flow will depend upon the value of the Reynolds number. The Reynolds number expresses the relative importance of viscous action, being a ratio of inertial to viscous forces. In any two flows in which viscosity plays an important role, dynamic similitude exists when the boundaries are geometrically similar and the Reynolds numbers are the same.

A free jet-mixing process depends upon a "stability parameter" (8) which resembles a Reynolds number. Whether or not turbulent mixing occurs between the free jet and the surrounding fluid depends on the value of the stability parameter. As in the case of the transition from turbulent to laminar pipe flow at a Reynolds number of about 2100, a critical value exists for the free jet.

The case of the jet pump is complicated by the fact that the mixing occurs in an adverse pressure gradient, and is confined by the parallel walls of the throat. The latter will be a stabilizing influence tending to delay the onset of turbulent flow (9). As developed later, tests show that pump efficiency is affected relatively little by viscosity down to a jet Reynolds number of about 3800. Below this, performance decreases rapidly—operation in the laminar region should be avoided.

Mineral oil MIL-L-6081A, Grade 1005, and synthetic oil MIL-L-7808 were used for testing at high Reynolds numbers. To simulate low-temperature operation, three blends of Grades 1005 and 1100 were used at controlled temperatures from 80 to 200 F, producing a range of viscosity from 5 to 100 centistokes at the pump. Nozzle pressure drops ranged from 40 to 100 psi; primary flow rates from 0.17 to 1.1 lb/sec (7).

In Fig. 7 experimental characteristic curves are given for a jet pump at several viscosities. The uppermost $N-\phi$ line is the "normal" pressure-ratio characteristic. Reynolds numbers are noted on the curves. Reynolds numbers were calculated with

$$R_n = \frac{V_n d_n}{\nu} = \frac{4W_n}{\pi d_n \mu} \quad [21]$$

for the nozzle jet. By continuity the throat Reynolds number is

$$R_m = \sqrt{b(1 + \phi)} R_n \quad [22]$$

It is interesting to note that $R_m = R_n$ for $\phi = \frac{1}{\sqrt{b}} - 1$, which is the condition for equality between throat and jet momentum. As discussed later this forms a good approximation to ϕ_{max} . At jet Reynolds numbers over 3800 the throat Reynolds number R_m at the experimental ϕ_{max} was always found to be essentially equal to the jet Reynolds number R_n .

Nozzle Coefficient. Nozzle coefficients calculated from test results (with Equation [9b]) are plotted versus nozzle Reynolds

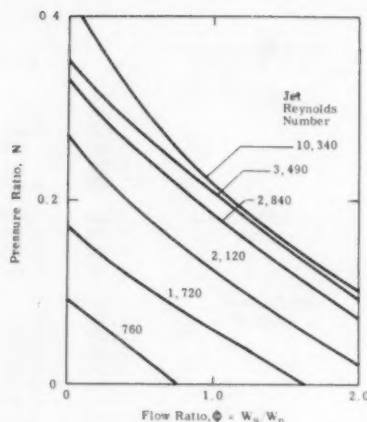


FIG. 7 PERFORMANCE CURVES SHOWING EFFECT OF REYNOLDS NUMBER. JET-PUMP AREA RATIO $b = 0.174$. NOZZLE PRESSURE DIFFERENCES $P_t - P_s = 40$ TO 100 PSI, VISCOSITIES 6.5 TO 100 CENTISTOKES

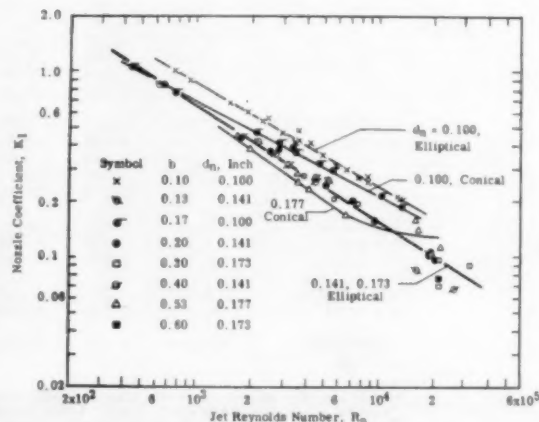


FIG. 8 EXPERIMENTAL NOZZLE COEFFICIENTS K_1 VERSUS JET REYNOLDS NUMBER. DATA FROM TABLE 1 AND NOZZLE TESTS

number R_n in Fig. 8. These data consist of K_1 -values from 40 performance tests on eight jet pumps plus a few nozzle tests. Included are coefficients for (a) three nozzles with elliptical profile (Fig. 2), $d_n = 0.100, 0.141, 0.173$ in.; and (b) for two nozzles with conical approach profile, $d_n = 0.100, 0.177$ in. (Fig. 3).

In general K_1 varies inversely as R_n to about the one-half power, from 500 to 20,000. At very high Reynolds number K_1 probably approaches a constant value (independent of R_n); $K_1 = 0.1$ is a good general assumption for these small nozzles. As would be expected, the smallest nozzle exhibits the highest loss coefficient at any one value of R_n . For design use K_1 -values may be taken from Fig. 8. These curves will be conservative for application to larger nozzles ($d_n > 0.177$ in.).

Throat-Diffuser Coefficient. K_{1d} -values are plotted versus throat Reynolds number R_m in Fig. 9. For each of 40 tests on eight jet pumps, coefficients were evaluated (Equation [10]) from data at $\phi_{\text{op}} \approx (2/3)\phi_{\text{max}}$. These measured K_{1d} -values, as well as performance characteristics at the maximum efficiency point for each test, are included in Table 1. A horizontal line, $K_{1d} = 0.3$, best represents results for $R_m > 3800$.

Maximum Efficiency. Values of η_{max} versus jet Reynolds num-

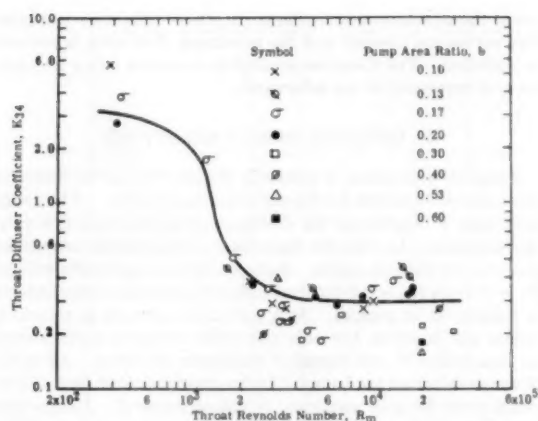


FIG. 9 THROAT-DIFFUSER FRICTION COEFFICIENT VERSUS THROAT REYNOLDS NUMBER. OIL-VISCOSITY RANGE 5 TO 100 CENTISTOKES

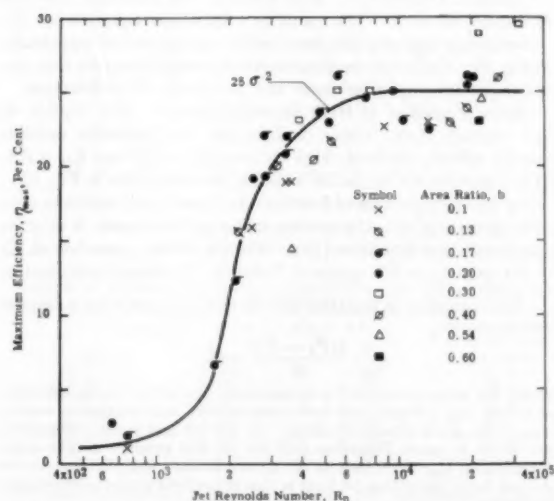


FIG. 10 EXPERIMENTAL VALUES OF MAXIMUM EFFICIENCY VERSUS JET REYNOLDS NUMBER. CURVE REPRESENTS $25\sigma^2$; σ FROM FIG. 17

ber appear in Fig. 10. Performance improves rapidly up to about $R_n = 3800$, beyond which Reynolds number has comparatively little effect. (The curve $\eta_{max} = 25\sigma^2$ stems from an empirical correlation explained later.)

JET-PUMP ENERGY ANALYSIS

In addition to fluid frictional losses—which also occur in mechanical pumps—an unavoidable “mixing loss” takes place in the jet pump. The following energy analysis demonstrates the ultimate efficiencies which may be expected of the jet pump.

The Mixing Loss. The momentum Equation [5] contains the throat-pressure rise. A second expression for $P_m - P_a$ is obtained from the energy equation between throat entry and exit

$$P_m - P_a = \frac{W_n}{W_t} \frac{\rho V_n^2}{2g_c} + \frac{W_s}{W_t} \frac{\rho V_{ss}^2}{2g_c} - \frac{\rho V_m^2}{2g_c} - \frac{\rho E_{ml}}{W_t} - \frac{\rho E_{fl}}{W_t} \dots [23]$$

Noting that $\frac{F_{fl}}{A_m} = \frac{\rho E_{fl}}{W_t}$

the mixing loss is obtained by eliminating the pressure difference between Equations [5] and [23]

$$E_{ml} = W_n \frac{(V_n - V_m)^2}{2g_c} + W_s \frac{(V_m - V_{ss})^2}{2g_c} \dots [24]$$

Upon combining with the continuity relations Equations [1] and [2]

$$E_{ml} = W_n \frac{V_n^2}{2g_c} \left[1 - 2b(1 + \phi) + b^2(1 + \phi)^2 + \frac{\phi^2 b^2}{(1 - b)^2} - 2\phi^2 b^2 \frac{1 + \phi}{1 - b} \right] \dots [25]$$

At zero side flow, ($\phi = 0$), Equation [25] reduces to

$$E_{ml} = \frac{W_n V_n^2}{2g_c} (1 - b)^2 \dots [25b]$$

which is simply the expression for a “sudden enlargement” loss in a pipeline.

The Friction Losses. The friction-loss terms are all expressed as constants multiplied times the kinetic-energy expression of the stream in question. These plus the continuity relations yield the following

$$\text{Nozzle loss: } E_1 = K_1 W_n \frac{V_n^2}{2g_c}$$

$$\text{Throat loss: } E_2 = K_2 W_t \frac{V_m^2}{2g_c} = K_2 b^2 (1 + \phi)^2 W_n \frac{V_n^2}{2g_c}$$

$$\text{Diffuser loss: } E_4 = K_4 W_t \frac{V_m^2}{2g_c} = K_4 b^2 (1 + \phi)^2 W_n \frac{V_n^2}{2g_c}$$

Total friction loss is the sum of the three foregoing equations

$$E_{fl} = W_n \frac{V_n^2}{2g_c} [K_1 + K_{12} b^2 (1 + \phi)^2] \dots [26]$$

The jet loss has been derived previously

$$E_{jl} = W_n \frac{V_n^2}{2g_c} \frac{\phi^2 b^2}{(1 - b)^2} \dots [20]$$

The total energy loss is the sum of Equations [25], [26], and [20], $E_{ml} + E_{fl} + E_{jl}$

$$E_t = W_n \frac{V_n^2}{2g_c} \left[1 + K_1 - 2b(1 + \phi) - (1 - 2b)(1 + \phi) \frac{\phi^2 b^2}{(1 - b)^2} + (1 + K_{12})b^2(1 + \phi)^2 \right] \dots [27]$$

Comparison of Characteristic Curves. Theoretical curves of pressure ratio N and efficiency $\eta = \phi N$ are shown in Fig. 11. The three sets of curves in Fig. 11 are discussed as follows:

(a) **Ideal Jet Pump.** Examination of Equation [24] shows that the mixing loss decreases as the side-flow throat-entry velocity V_{ss} approaches the jet velocity V_n and is zero when these are equal. This occurs at $\phi = (1 - b)/b$ or unity for $b = 0.5$, the design area ratio assumed for these curves. Fig. 11 shows that at $\phi = 1.0$ the efficiency is 100 per cent—but output and input are zero for this case. Two high-velocity jets simply pass through the throat together and in the diffuser the kinetic energy is recovered as a pressure equal to the inlet pressure; i.e., $P_t = P_d =$

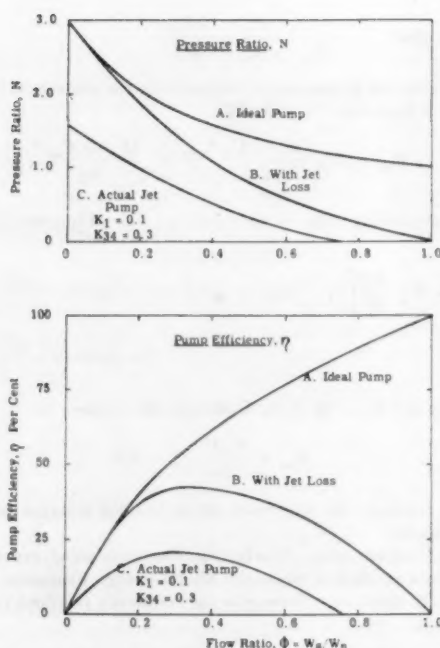


FIG. 11 PRESSURE RATIO AND EFFICIENCY CURVES SHOWING EFFECTS OF A—MIXING, B—JET, AND C—FRICTION LOSSES; $b = 0.5$

P_s . It can be shown that the maximum energy output occurs at $\phi = 0.534$; from curve A, $\eta_{\max} = 72.4$ per cent. Higher efficiencies can be obtained only at the expense of energy output, and lowered N pressure ratio.

For flow ratios greater than that for zero mixing loss ($\phi > 1.0$ in Fig. 11) the side-flow throat velocity exceeds the jet velocity, and the role of the two streams is interchanged.

(b) Frictionless Flow With Jet Loss. Curves B show the considerable effect of jet loss on efficiency and pressure ratio. It should be added here that A and B are two extremes; either no jet loss occurs, or all of the energy represented by jet flow from P_s to P_n (in the throat entry) is assumed lost. An intermediate case could well be postulated, wherein a part of this energy is considered utilized in the pumping process. Efficiency curve B reaches a maximum of 42 per cent at $\phi = 0.35$ as shown; and this represents a sort of ultimate in improvement through reduction of friction losses.

(c) Actual Jet Pump. By introducing friction losses,* the lowest curves C are constructed assuming that $K_1 = 0.1$ and $K_{34} = 0.3$. From test experience these values represent

* The increased energy losses at low Reynolds numbers have been accounted for in the friction coefficients (Figs. 8 and 9). In addition to frictional losses the increase of K_{34} may be considered to include a viscous-damping effect on the turbulent mixing process. Separation of these two components would require additional information (i.e., throat-diffuser, friction-loss characteristics without mixing, $W_n = 0$). A "mixing-process Reynolds coefficient" might thus be established.

about the minimum obtainable in practice. Efficiency and pressure curves are lowered and the maximum flow ratio is reduced as indicated. The C-curves accurately represent pump performance as measured in the laboratory.

2 OPTIMUM DESIGN RELATIONS

Design of a jet pump is primarily the selection of the best nozzle-to-throat area ratio for the particular application. The design area ratio b determines the discharge pressure-versus-flow ratio characteristic. In Fig. 12 theoretical characteristic curves are given for several area ratios. Assumed friction-loss coefficients are $K_1 = 0.1$ and $K_{34} = 0.3$ (approximately the minimum encountered in testing oil-jet pumps). At a particular value of ϕ , several b -values will function, but only one yields optimum performance, i.e., maximum N , and therefore maximum efficiency. All of the N versus ϕ -curves are bounded by an envelope curve (not shown) which is the locus of maximum N values versus ϕ . An envelope curve across the top of the efficiency curves (locus of maximum efficiencies with the assumed friction factors 0.1 and 0.3) is included in Fig. 12.

Optimum Area Ratio b . This is found from Equation [13b] for N and $\partial N / \partial b = 0$. The result⁷ is a fifth-order equation in b (7).

For design use, optimum area ratios b are presented graphically in Fig. 13. These curves demonstrate that optimum area ratio decreases as flow ratio increases and as friction (K_{34}) increases.

Design Procedure at High Reynolds Number. For liquids of low viscosity (e.g., water or light oil) jet Reynolds number usually will be sufficiently high for use of $K_1 = 0.1$ and $K_{34} = 0.3$. (The b - ϕ curve for the latter is shown as a heavy line in Fig. 13.)

For any combination of flow ratio and associated optimum area ratio (from Fig. 13), the corresponding pressure ratio N may be calculated from Equation [13b]. Results of this procedure at $K_1 = 0.1$ and $K_{34} = 0.3$ appear in Table 2. On linear co-ordinates,

⁷ Differentiation of Equation [10] to find optimum b for maximum energy output

$$\frac{\partial(P_d - P_n)}{\partial b} = 0$$

yields the same equation for optimum b . In other words, selection of b from Fig. 13 will yield both maximum N and maximum energy output for given ϕ and K -values. If the jet loss is not recognized, $\partial N / \partial b = 0$, using Equation [13] for N , will produce a fifth-order equation for b_{opt} dependent on K_1 as well as K_{34} . Justification for the simpler form (including jet loss) is that it predicts actual performance far better.

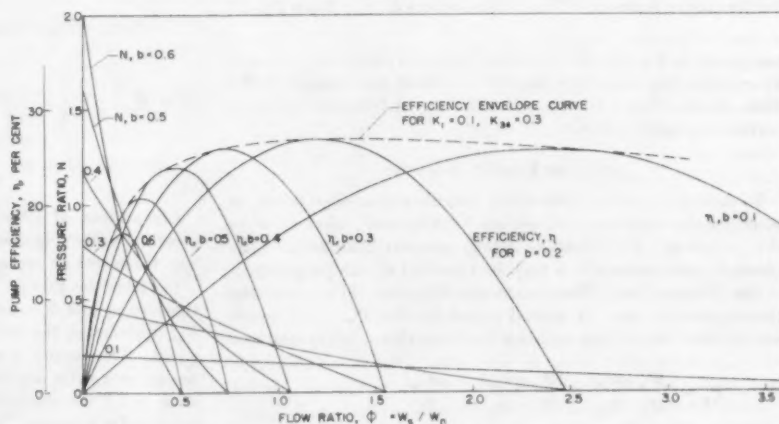


FIG. 12 PRESSURE-DIFFERENCE RATIOS AND EFFICIENCIES VERSUS FLOW RATIO, FOR PUMPS WITH DESIGN-AREA RATIOS $b = 0.1$ TO 0.6 . FRICTION COEFFICIENTS $K_1 = 0.1$, $K_{34} = 0.3$

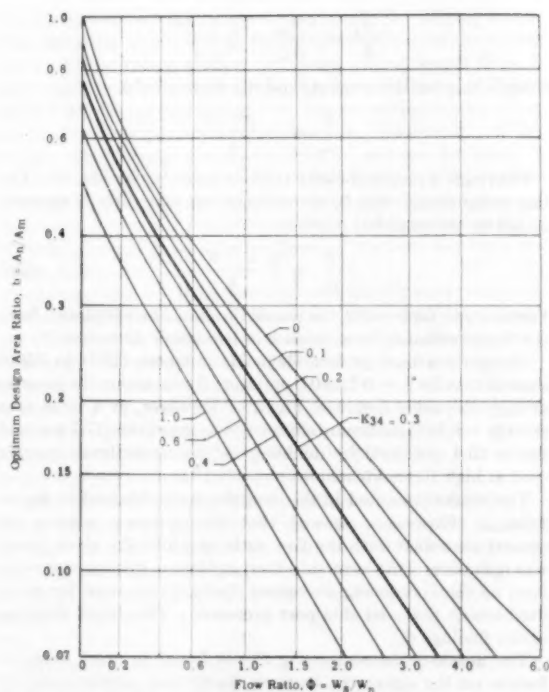


FIG. 13 OPTIMUM DESIGN-AREA RATIO AS FUNCTION OF FLOW RATIO AND FRICTION COEFFICIENT

TABLE 2 THEORETICAL OPTIMUM DESIGN RELATIONS FOR LOW FRICTION

$K_1 = 0.1, K_{34} = 0.3$			
ϕ	b_{opt}	N	$\eta = \phi N (100)$, per cent
5.0	0.046	0.043	21.7
2.54	0.10	0.101	25.6
2.0	0.127	0.132	26.4
1.2	0.20	0.225	27.0
0.67	0.30	0.387	25.9
0.37	0.40	0.620	22.9
0.20	0.50	0.937	18.7

this relation between ϕ and N comprises the "envelope" curve for the family of N - ϕ characteristic curves in Fig. 12. The efficiencies of these optimum designs vary with area ratio. As shown by the last column in Table 2, the maximum is $\eta = 27$ per cent for $b = 0.2$ operating at a flow ratio of $\phi = 1.2$.

The optimum relations between b , ϕ , and N for $K_1 = 0.1$ and $K_{34} = 0.3$ are shown graphically in Fig. 14. (The ϕ versus b curve is a duplicate of the heavy-line curve in Fig. 13.) Entering with any one of the three dimensionless ratios, b , ϕ , or N , the other two may be read directly from Fig. 14.

Experimental values of ϕ_{map} and N_{map} from Table 1 are included in Fig. 14 for comparison. Data points do not coincide with the theoretical curves over the entire range of b for two reasons: (a) Actual friction coefficients (at high Reynolds numbers) varied from 0.07 to 0.2 for K_1 , and K_{34} ranged from a low of 0.15 to a high of 0.4 (see Table 1); (b) design via the optimum area ratio (Fig. 13) does not necessarily result in "operation" of the pump at ϕ_{map} . Note that the envelope curve in Fig. 12 touches the efficiency curve at ϕ_{map} only for $b = 0.2$. This point is discussed later under Dual Optimum.

Optimum Flow Ratio, ϕ_{map} . For any given area ratio b and friction factors K_1 and K_{34} , pump efficiency versus flow ratio ϕ passes through a maximum. This particular value of flow ratio ϕ_{map} is found from $\partial(\phi N)/\partial\phi = 0$. The solution is a fourth-order

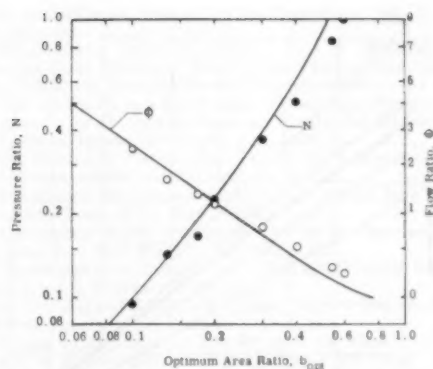


FIG. 14 RELATION OF THEORETICAL OPTIMUM AREA RATIO TO FLOW AND PRESSURE RATIOS. CALCULATED FOR LOW FRICTION CONDITIONS $K_1 = 0.1, K_{34} = 0.3$. EXPERIMENTAL VALUES OF ϕ_{map} AND N_{map} FROM TABLE 1 ARE INCLUDED FOR COMPARISON

equation for ϕ_{map} as a function of b , K_1 , and K_{34} (7). Theoretical ϕ_{map} -values are later compared with test values in Table 7.

Dual Optimum. There are two optimizing equations between b and ϕ ; for b_{opt} at a particular ϕ (Fig. 13); for optimum ϕ_{map} at a particular b -value. Optimization at one friction condition is a function of two variables, thus forming a three-dimensional surface. For $K_1 = 0.1$ and $K_{34} = 0.3$ the optimum combination is $b = 0.2$ operating at $\phi = 1.2$ and $N = 0.225$. The corresponding efficiency is $\eta = 27$ per cent. For this case $b_{opt} = \phi$ and $\phi_{map} = b$ are identical. Note in Fig. 12 that the η -curve for $b = 0.2$ is tangent to the envelope curve at its maximum point, whereas larger b -value curves are tangent at $\phi < \phi_{map}$, and smaller values at $\phi > \phi_{map}$.

Table 3 contains results of similar analyses at other friction conditions. The pump with area ratio $b = 0.2$ operating at $\phi = 1.2$ remained approximately the best "dual optimum" condition.

TABLE 3 ENVELOPE-CURVE STUDY

Friction coefficients	Max η
$K_1 = 0.05$ $K_{34} = 0.10$	37.5
$K_1 = 0.10$ $K_{34} = 0.20$	30.5
$K_1 = 0.10$ $K_{34} = 0.30$	27.0
$K_1 = 0.20$ $K_{34} = 0.40$	22.0

Maximum Flow Ratio. The maximum flow capacity ϕ_s of a pump occurs at $N = 0$ (see Fig. 12). Graphical solutions, ϕ_s versus b , are presented in Fig. 15 for K_{34} -values from 0 to 1.0. For frictionless flow, $\phi_s = (1 - b)/b$, which will be recognized as the condition for zero mixing loss.

Optimum Nozzle-Throat Spacing. Jet-pump theory based on impulse-momentum relations does not predict the axial location of the nozzle relative to the throat. As a rule it is assumed that the nozzle tip and the throat entry coincide, Fig. 1. In practice the nozzle tip is generally withdrawn by as much as several nozzle diameters to secure optimum performance.

The experimental jet pump in Fig. 2 was specially designed to permit study of the nozzle-throat spacing, S . The nozzles were mounted in sections of No. 16 thin-wall tubing, which were inserted into the pump body through an O-ring seal. By loosening the nut, the nozzle could be moved axially without interrupting pump operation. Scribe marks on the nozzle tube indicated the internal spacing, S . For each area ratio, optimum S was found by

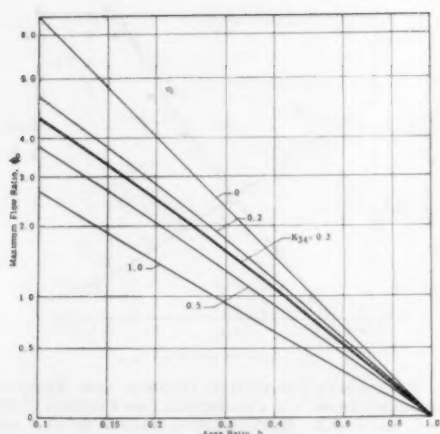


FIG. 15 MAXIMUM FLOW RATIO AS FUNCTION OF AREA RATIO AND FRICTION COEFFICIENT

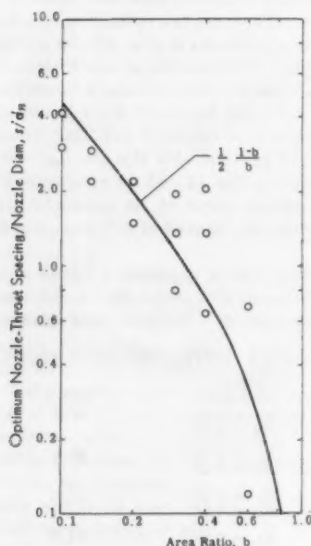


FIG. 16 OPTIMUM NOZZLE-THROAT SPACINGS FROM TESTS ON SIX JET PUMPS

(Multiple points at each area ratio indicate range over which maximum efficiency is obtained. Four-diameter throat lengths.)

varying the nozzle position in steps to obtain maximum secondary flow W_s with W_n and all three pressures held constant. This was carried out at flow ratios of $\phi_{opt} \approx (2/3)\phi_{max}$, at high jet Reynolds numbers.

Experimental results are shown in Fig. 16 as ratios of S to nozzle diameters; S/d_n . Multiple points indicate for each pump the range within which efficiency was relatively insensitive to variation in spacing, S . The ratio S/d_n reveals a consistent decrease with increase in b . It will be recalled that a large b means a small flow ratio (see Fig. 12). Thus, S decreased with flow ratio.

This suggests that the exposed cylindrical surface area of the "free" jet, $A_f = \pi d_n S$, decreases with ϕ as does the annular area A_{as} . The latter is defined as $A_n - A_a$ or $A_n(1-b)/b$ (assuming the jet enters the throat with stream area equal to A_n).

Let $A_f = CA_{as}$, where C is a constant. Then

$$\frac{A_f}{A_n} = \frac{CA_{as}}{A_n} = C \frac{1-b}{b}$$

Substituting for the areas A_f and A_a , there results

$$\frac{S}{d_n} = C' \frac{1-b}{b}$$

That such a proportionality exists is indicated by Fig. 16. For this pump design, Fig. 2, the optimum spacing ratio is approximated by the empirical relation

$$\frac{S}{d_n} = \frac{1}{2} \frac{1-b}{b} \quad [28]$$

For example, for $b = 0.2$, the nozzle tip should be withdrawn from the throat entrance by a distance of two nozzle diameters.

Comparison tests at low Reynolds numbers (1800 to 3500) showed that for $b = 0.1$ to 0.4 , optimum S was about the same as at high Reynolds numbers, Fig. 16. However, at a large area ratio ($b = 0.544$) maximum efficiency was improved (17.7 per cent versus 15.4 per cent) by doubling the nozzle-to-throat spacing used at high Reynolds numbers.

The results presented in the foregoing were obtained at $\phi_{sp} \approx 2/3\phi_{max}$. Experience showed that the optimum spacing increased somewhat with the flow ratio at which the given pump was operating. (At zero side flow, optimum spacing was redefined as that producing maximum discharge pressure for given fixed nozzle flow and side port pressure.) This trend confirms earlier findings (6).

The nozzle-to-throat spacing S was found to exert some influence on the agreement between theory and experimental results. For each of the eight jet pumps, theoretical $N-\phi$ curves were compared with measured characteristic curves—Figs. 5 and 6 are typical examples. The theoretical $N-\phi$ curve was found to agree with experimental results best when the spacing S had been adjusted to optimum (best efficiency). The effect of changing S is to alter the slope of the experimental $N-\phi$ curve: An increase in S decreases the slope, moving the maximum efficiency point to the right (increases ϕ_{max}). This sensitivity of slope and hence of agreement between theory and test results was noticeable only at the two highest area ratios. At $b = 0.1$ to 0.4 , theory-test data agreement was affected slightly, if at all, by S .

Throat Length. In the literature on jet pumps, recommended values for the length of the parallel-wall throat section range from 4 diameters up to 10 diameters. With compressible flow little departure from optimum performance has been noted for lengths from 4 to 14 diameters. The value of 7 to 7.5 has been recommended by three investigators, cited by Kroll (11).

Tests on oil-jet pumps reported by Husemann (6) showed that 4 diameters were slightly better than 2 diameters. For this work it was decided to adopt 4 diameters as the "standard" length, Fig. 2.

To check the effect of a short throat, particularly as regards cavitation-limited flow (7), the throat-diffuser section for pump No. 141/316/307 was duplicated except with $L = 2d_n$ instead of $4d_n$. Test results are summarized in Table 4, including the optimum spacings. Evidently the short throat causes only a small loss in efficiency.

The spacing S required for optimum performance was nearly

TABLE 4 COMPARISON OF TWO AND FOUR-DIAMETER THROAT LENGTHS

Pump Nos. 141/316/308, 141/316-S/548; $b = 0.2$. MIL-L-7808 synthetic oil at 150 F Nominal $P_s - P_e = 100$ psi, $R_n = 20,000$					
L/d_n	η_{max} , per cent	K_1	K_{21}^*	S , in.	
4	25.5	0.0956	0.337	0.208-0.308	
2	23.3	0.0954	0.448	0.548	

* Evaluated at $\phi = 0.9$. Theory agreement with test results equally good with both throat lengths.

doubled in this halving of the throat length L . Mixing length along the pump axis is $S + L$, assuming completion of the mixing process in the throat section. Perhaps mixing length $S + L$ should vary with design area ratio b through adjustment of L , and not of S (as was the case in Fig. 16). Longer mixing lengths along the jet are required as b is reduced (hence ϕ_{opt} increased). If the throat lengths were progressively increased as b was decreased, it is quite possible that optimum S/d_n would be essentially the same for every b -value. Further theoretical and experimental study of the relation between b , L , and S is in order. Only limited work on jet mixing length in an adverse pressure gradient has been reported (1, 14).

The pump with $b = 0.3$ gave best maximum efficiency, nearly 30 per cent. Efficiencies at $b = 0.1$ and 0.6 were lowest, about 23 per cent (Table 1). It is possible that this variation in efficiency with b was in part a result of the fixed throat length. At or near $b = 0.3$, an L of 4 diameters was perhaps "optimum," while at lower b -values $L = 4d_m$ was inadequate. At $b > 0.3$, the 4-diameter throats were probably too long for best results. Through proper adjustment of throat lengths it should be possible to reduce the variation of efficiency with design-area ratio.

Throat-Entrance Shape. The throat-entry profile for the experimental jet pump was a short cone with an included angle of 120 deg. A small radius at the entrance eliminated the sharp edge, Fig. 2. A longer conical entry with an angle of 60 deg was present in the "conventional" pumps, Fig. 3. Comparison of performance curves reveals no advantage from using the longer cone.

Converging nozzles of high efficiency are obtained from a profile consisting of a quarter of an ellipse (used for the nozzles in the experimental jet pump). A throat diffuser, part 0.317-E, was machined with such a profile at the throat entry and compared with the simpler conical entry. As shown in Table 5, the rounded throat entry somewhat improves performance.

TABLE 5 EFFECT OF THROAT ENTRY SHAPE
Pump Nos. 141/316/308 and 141/317-E/438, $b = 0.2$
Throat length: $L = 4d_m$

Throat-entry shape	R_n	η_{max} , per cent	K_1	K_M
Conical	20,000	25.5	0.096	0.337
Ellipse	20,000	26.4	0.096	0.314
Conical	5,000	22.8	0.246	0.318
Ellipse	5,000	23.4	0.302	0.243

ACKNOWLEDGMENTS

This material is based on a research project sponsored by the U. S. Air Force, Wright Air Development Center, at The Pennsylvania State University. The program was conducted by the Department of Engineering Research, Prof. E. R. Queer, Director. Application of the jet pump as an oil scavenge pump was originally suggested by Dr. P. H. Schweitzer, who supervised the initial phases. Dr. A. W. Hussmann's helpful suggestions and counsel also are gratefully acknowledged. A majority of the laboratory tests and calculations of results was carried out by Mr. R. M. Law. The author wishes to thank the sponsor and The Pennsylvania State University for permission to present this paper.

BIBLIOGRAPHY

- 1 "The Design of Jet Pumps," by G. Flügel, NACA TM 982, 1939.
- 2 "A Simple Air Ejector," by J. H. Keenan and E. P. Neumann, Trans. ASME, vol. 64, 1942, pp. A-75-81.
- 3 "An Investigation of Ejector Design by Analysis and Experiment," by J. H. Keenan, E. P. Neumann, and F. Lustwerk, *Journal of Applied Mechanics*, Trans. ASME, vol. 72, 1950, pp. 299-309.
- 4 "Hydraulics and Its Applications," by A. H. Gibson, Constable London, England, fourth edition, 1930, p. 264.
- 5 "The Water Jet Pump," by J. E. Gosline and M. P. O'Brien,

University of California Publications in Engineering, vol. 3, no. 3, 1934, pp. 167-190.

6 "Educators for Hydraulic Systems," by A. W. Hussmann, The Pennsylvania State University, Department of Engineering Research, University Park, Pa., Bulletin No. 64, February, 1955.

7 "The Jet Pump as a Lubrication Oil Scavenge Pump for Aircraft Engines," by R. G. Cunningham, Wright Air Development Center Technical Report No. 55-143, July, 1954.

8 "Jet Mixing of Two Liquids," by R. G. Folsom and C. K. Ferguson, Trans. ASME, vol. 71, 1949, pp. 73-77.

9 "Elementary Mechanics of Fluids," by H. Rouse, John Wiley & Sons, Inc., New York, N. Y., 1946, p. 171.

10 "Elementary Fluid Mechanics," by J. K. Vennard, John Wiley & Sons, Inc., New York, N. Y., 1940, p. 257.

11 "The Design of Jet Pumps," by A. E. Kroll, *Chemical Engineering Progress*, vol. 1, February, 1947, pp. 21-24.

12 "Centrifugal and Axial Flow Pumps," by A. J. Stepanoff, John Wiley & Sons, Inc., New York, N. Y., 1948, p. 413.

13 "Design of Injectors for Low-Pressure Air Flow," by G. E. McElroy, U. S. Bureau of Mines Technical Paper 678, 1945.

14 "Investigation of the Mixing of Parallel Flowing Plane Air Streams in the Pressure Gradient of a Jet Eductor," by C. K. Ferguson, MS thesis, University of California, Berkeley, Calif., 1948.

Appendix

STRAIGHT-LINE APPROXIMATE RELATIONS

The N versus ϕ characteristic curve can be approximated with a straight line (5, 12). Inspection of Fig. 12 shows that the theoretical N - ϕ line is slightly concave down, at $b = 0.1$, essentially linear at $b = 0.2$, but concave up for large b -values. Thus, particularly for $b < 0.3$, this linearity approach is quite useful. A straight line on N versus ϕ co-ordinates is drawn between ϕ_s (Fig. 15) on the abscissa and N_s (Equation [13b], with $\phi = 0$) on the ordinate. The efficiency curve will be a parabola and the following relations apply: $N = N_s - e\phi$ where $e = N_s/\phi_s$, the slope; also, $\phi_{max} = \phi_s/2$, $\eta = \phi N_s - e\phi^2$, and $\eta_{max} = N_s\phi_s/4$.

Empirical Correlation of Reynolds-Number Effect. Inspection of Fig. 7 suggests that at low Reynolds numbers the N - ϕ curves be considered as depressed below and parallel to the "base" or high Reynolds-number characteristic curve. By combining this observation with the assumption that the N - ϕ curve is a straight line, performance of a jet pump at all Reynolds numbers may be expressed by one equation

$$N = \sigma N_{ab} - e\phi \quad [29]$$

where σ is the "Reynolds influence coefficient," N_{ab} is the ordinate intercept of the high Reynolds number "base" line; and e is the slope assumed to be common to all operating conditions for the pump in question. Measured values of N_{ab} , ϕ_{ab} , and e appear in Table 6. The right-hand column of Table 1 contains measured values of σ

$$\sigma_{a,b} = \frac{N_{s,a,b}}{N_{ab}} \quad [30]$$

where $N_{s,a,b}$ are the ordinate intercepts of experimental N - ϕ lines at $R_{n,a,b}$. These straight lines were constructed parallel to the base line with elevation to intercept experimental N points for each test at $\phi \approx 2/3\phi_{max}$. (At high Reynolds numbers, $\sigma = 1.0$, by definition.) The critical effect of jet Reynolds number on jet-pump performance is shown by Fig. 17, a plot of σ versus R_n .

TABLE 6 INTERCEPTS AND SLOPES FOR EMPIRICAL N - ϕ CURVES AT HIGH-JET REYNOLDS NUMBERS: 13,000 < R_n < 31,000

Area ratio b	Pressure ratio N_{ab}	Flow ratio ϕ_{ab}	Slope $e = N_{ab}/\phi_{ab}$ (negative)
0.10	0.196	4.64	0.042
0.133	0.285	3.24	0.088
0.174	0.336	2.74	0.123
0.20	0.460	2.20	0.209
0.30	0.770	1.54	0.500
0.40	0.980	1.06	0.925
0.544	1.80	0.540	3.34
0.60	2.10	0.433	4.85

Utility. This approximate linear approach coupled with the σ versus R_n curve forms a complete description of pressure-head characteristics. In terms of σ_a , and the high Reynolds-number line for the same pump (N_{oh} , ϕ_{oh} , ϵ) the following relations apply:

$$\text{Pressure ratio: } N_a = \sigma_a N_{oh} - \epsilon \phi \dots \dots \dots [31]$$

$$\text{Efficiency at any flow ratio: } \eta_a = \sigma_a \phi N_{oh} - \epsilon \phi^2 \dots \dots \dots [32]$$

At the same flow ratio as the high Reynolds-number case, efficiency varies directly as σ_a

$$\eta_a = \sigma_a \eta_h \text{ } \phi = \text{const.} \dots \dots \dots [33]$$

Maximum efficiency

$$\eta_{\max, a} = \sigma_a^2 \frac{N_{oh}^2}{4\epsilon} = \sigma_a^2 \eta_{\max, h} \dots \dots \dots [34]$$

This maximum efficiency occurs at a flow ratio which is

$$\phi_{\text{mep}, a} = \frac{\sigma_a \phi_{oh}}{2} = \sigma_a \phi_{\text{mep}, h} \dots \dots \dots [35]$$

Maximum flow ratio (abscissa intercept)

$$\phi_{o, a} = \sigma_a \phi_{oh} \dots \dots \dots [36]$$

Maximum pump efficiency (η_{\max}), was in general about 25 per cent for this group of oil-jet pumps at high Reynolds numbers. The curve $\eta_{\max} = 25\sigma^2$ has been included in Fig. 10 for comparison with η_{\max} data. Agreement with the individual test values is

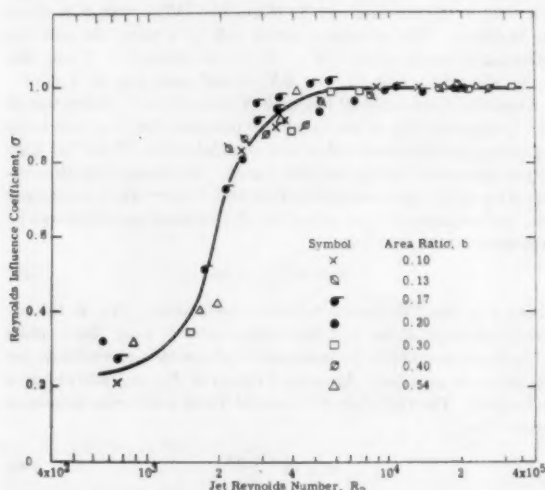


FIG. 17 REYNOLDS INFLUENCE COEFFICIENT VERSUS JET REYNOLDS NUMBER

TABLE 7 COMPARISON OF MAXIMUM-EFFICIENCY FLOW RATIOS

Pump No. and area ratio	R_n	K_1	K_{21}	Maximum-efficiency flow ratios, $\left(\frac{\phi_{\text{mep}}}{d_n} - 1\right)^2$			
				Experimental	Theoretical ^a	$\phi_o/2b$	$\left(\frac{\phi_{\text{mep}}}{d_n} - 1\right)^2$
100/316/307 $b = 0.10$	8720	0.273	0.276	2.35	2.46	2.40	2.16
100/240/445 $b = 0.174$	3420	0.391	0.286	1.35	1.35	1.44	1.40
141/316/308 $b = 0.20$	9530	0.188	0.315	1.15	1.18	1.22	1.24
141/224/291 $b = 0.40$	25840	0.068	0.272	0.52	0.52	0.56	0.59
177/240/255 $b = 0.544$	21970	0.114	0.154	0.29	0.29	0.36	0.36

^a From the solution of $\frac{\partial(\phi N)}{\partial \phi} = 0$.

^b ϕ_o from theoretical equation. $\phi_{\text{mep}} = \phi_o/2$, by assuming linear N - ϕ characteristic curve

^c Momentum-equality rule of thumb, Equation [37].

good. (Values of σ were obtained from the smoothed curve of σ versus R_n (Fig. 17) at corresponding jet Reynolds numbers.)

Momentum-Equality Rule of Thumb. In previous work (13) it has been noted that maximum efficiency occurs when the mixture

momentum equals the jet momentum, $\frac{W_m V_m}{g_c} = \frac{W_a V_a}{g_c}$. Combined with the continuity relations this yields

$$\phi_{\text{mep}} = \frac{d_m}{d_n} - 1 \dots \dots \dots [37]$$

That this simple relation does predict maximum efficiency-flow ratio quite well was confirmed in this work (see Table 7).

Comparison of Theoretical and Empirical Methods. In Table 7 experimental maximum-efficiency flow ratios ϕ_{mep} , for five jet pumps are compared with the theoretical prediction and the two empirical equations, $\phi_{\text{mep}} = \phi_o/2$, and Equation [37]. All three agree well with actual performance at small area ratios. At $b = 0.544$ the theoretical optimum equation is best: For $b > 0.4$, a linear N - ϕ curve is a rather poor approximation (see Fig. 12).

Design Example I. Design a jet pump to deliver a secondary flow of $W_a = 0.527$ lb/sec from atmospheric pressure against a back pressure of 23.5 psig. (Oil of 0.836 specific gravity and 7 centistokes kinematic viscosity (75.5×10^{-6} ft²/sec) at the pump.)

In view of the moderate back-pressure requirement, an area ratio of $b = 0.2$ is selected for high flow ratio and good efficiency. At the given viscosity and flow conditions assume that the jet Reynolds number is high: $R_n > 10^4$.

For a pump with $b = 0.2$ the empirical linear N - ϕ curve is valid. From Table 6, $N_o = 0.46$, $\phi_o = 2.2$, $\epsilon = 0.209$, so that, $N = 0.46 - 0.209 \phi$ represents the relation between head and flow ratios.

For conservative design (with regard to cavitation), operate the pump at

$$\phi = 2/3 \phi_{\text{mep}} = \frac{\phi_o}{3} = 0.734$$

Thus, $W_a = 0.527/0.734 = 0.718$ lb/sec. The operating head ratio is

$$N_{\text{op}} = 0.46 - 0.209 \times 0.734 = 0.307$$

From the relation

$$\frac{N}{N+1} = \frac{P_d - P_o}{P_i - P_o}, P_i - P_o = \frac{1 + 0.307}{0.307} \times 23.5 = 100 \text{ psi}$$

is the nozzle pressure drop. Since P_o is here atmospheric pressure, $P_i = 100$ psig. The nozzle diameter can now be calculated from Equation [9b] and the continuity equation $W_a = \rho A_n V_n$

$$d_n^4 = \frac{16 W_a^2 (1 + K_1)}{\pi^2 2 g_c \rho (P_i - P_o)} (\text{ft}^4) \dots \dots \dots [38]$$

With $K_1 = 0.1$ for the assumed high Reynolds number, $d_n = 0.141$ in. Throat diameter is $0.141/\sqrt{b} = 0.316$ in. Throat length (4 diameters) is 1.25 in.; and from Equation [28] the nozzle-to-throat spacing is $2d_n$ or 0.28 in. Checking the jet Reynolds number, Equation [21]

$$R_n = \frac{4 \times 0.718 \times 12 \times 10^4}{\pi \times 0.836 \times 62.4 \times 0.141 \times 75.5} = 19,700$$

Thus, the original assumptions ($\sigma = 1.0$ and $K_1 = 0.1$) are satisfactory. Pressures at other flow ratios (and vice versa) may be calculated from the N - ϕ equation.

Design Example II. Alter this pump to operate at a reduced temperature where $\nu = 70$ cs, $sg = 0.875$. Pump duty remains $W_s = 0.527$ lb/sec and $P_d = 23.5$ psig.

Both W_n and d_n will be increased, so that major change in jet Reynolds number will be from the tenfold rise in viscosity; hence assume $R_n = 2000$. From Fig. 17 the Reynolds influence coefficient is $\sigma = 0.67$ and the (parallel) characteristic curve is $N' = 0.308 - 0.209 \phi$. The prime identifies quantities in the case II design. As with case I, let $\phi_{op} = 2/3\phi_{nop}$, and thus

$$\phi_{op}' = \sigma\phi_{op} = 0.491, \text{ and } N_{op}' = \sigma N_{op} = 0.206$$

With identical secondary flow rates ($W_s' = W_s$)

$$W_n' = W_n/\sigma = 1.07 \text{ lb/sec}$$

From the $N/(N+1)$ equation and the equality $(P_d - P_s)' = (P_d - P_s)$, the case II nozzle pressure drop is increased by the ratio

$$\frac{(P_i - P_s)'}{P_i - P_s} = \frac{1 + \sigma N_{op}}{\sigma(1 + N_{op})}$$

where $N_{op} = 0.307$ from case I. Applying this ratio, $P_i = 138$ psig (versus 100 psig for case I). Substituting the foregoing relations in Equation [38] and forming the ratio of nozzle diameters

$$\left(\frac{d_n'}{d_n}\right)^4 = \frac{(1 + K_1') sg (1 + N_{op})}{(1 + K_1) sg' \sigma (1 + \sigma N_{op})} \dots \dots \dots [39]$$

With $K_1' = 0.42$ from Fig. 8 at $R_n = 2000$, Equation [39] yields $(d_n'/d_n)^4 = 2.0$; thus $d_n' = 0.174$ in. Other pump dimensions, d_m' , L' , and S' are calculated as in case I. The jet Reynolds number may now be calculated

$$R_n' = \frac{4 \times 1.07 \times 12 \times 10^4}{\pi \times 0.875 \times 62.4 \times 0.174 \times 755} = 2280$$

For greater accuracy the calculations of pump dimensions should be repeated with adjusted K_1 and σ -values. For most precise results, the full theoretical solution for the N - ϕ characteristic curve should be used, including both K_1 and K_{31} friction coefficients

Discussion

R. G. FOLSOM.⁸ Over a period of years, the writer has been amazed to see the number of important engineering applications of jet-mixing phenomena and, in particular, the large number of uses of the jet pump. The author is to be congratulated on his presentation of extensive and careful work on jet-pump performance with viscous fluids. It was gratifying to find that his work on fluids with low viscosity produced experimental results again confirming the analytical predictions developed by Gosline and

O'Brien, including cavitation limitations. The applicability of these analytical predictions have been confirmed elsewhere using water as a fluid.^{9,10} In addition, through extension of the same fundamental methods of approach, it has been possible to plot a type of head difference and capacity curve for a given jet pump (with low-viscosity fluids) providing essential information conveniently for determination of jet-pump performance in a specific installation.^{9,10}

With viscous fluids, the experimental results shown in Figs. 7 and 9 are very important. It is helpful to know that a single almost straight line on the dimensionless head ratio versus flow ratio co-ordinate system represents all operating conditions when a highly viscous fluid is concerned. Also, analysis has been clarified in that a Reynolds-number limit has been found below which the viscosity of the fluid begins to have an appreciable influence on performance.

The writer has given some consideration as to why that critical throat Reynolds number should be about 3800. A study of Fig. 8, taking into account available information on nozzle coefficients at low Reynolds numbers, leads to the conclusion that the critical value cannot be determined from nozzle flow phenomena alone. As Reynolds numbers increase, the curves of Fig. 8 will become flat; i.e., tend toward a constant coefficient or region of no influence of Reynolds number, similar to the tendency shown for the curve marked "0.117 conical." Thus the value of 3800 is in a region where the nozzle coefficient has shown a marked change with Reynolds number. Considering the complexities of flow in the complete jet pump, it is doubtful if the critical Reynolds number for normal pipe flow has any real significance in this problem.

The conclusion reached by the writer is that, owing to the different flow situations existing in the various portions of the jet pump, the critical Reynolds number to determine limits of jet-pump performance for the neglect of viscosity may be different for pumps of different size and design. If this conclusion is correct, additional work on larger pump units would appear to be desirable before acceptance of a critical Reynolds number of 3800 for all normal jet pumps.

AUTHOR'S CLOSURE

Dr. Folsom's comments and observations are appreciated. The question of why pump performance changes so radically in a narrow range of Reynolds number is an intriguing one. Compared with the Reynolds number correlation of fully developed pipe flow, or with nozzle flow, the jet pump is complex.

The following considerations suggest that viscous damping of the mixing process, rather than a simple change in nozzle or throat flow, is responsible for the precipitous decline of pump efficiency at Reynolds numbers between 1000 and 4000. As pointed out in footnote 6, the increase of the combined throat-diffuser coefficient (K_{31} versus R_n , Fig. 9) includes two effects when viscous forces become important. These are (a) the frictional energy losses (corresponding to K_1 , see Fig. 8) and (b) the viscous damping of the turbulent mixing process. The latter is, of course, in addition to the inherent mixing loss (Equation [25]).

The nozzle coefficient K_1 does not undergo rapid change with R_n in the 1000-4000 range. Component (a) of K_{31} would be expected to behave in a similar manner. As additional evidence, note the relatively slow decrease in venturi-meter coefficients with Reynolds number even in the pipe-flow "critical" range. One is led to conclude that the radical change in K_{31} versus R_n (Fig. 9)

⁸ "Jet Pumps With Liquid Drive," by R. G. Folsom, *Chemical Engineering Progress*, vol. 44, no. 10, 1948, pp. 765-770.

¹⁰ "Predicting Liquid Jet Pump Performance," by R. G. Folsom, *Proceedings of the National Conference on Industrial Hydraulics*, vol. 2, 1949, pp. 105-115.

⁸ Director of Engineering Research Institute and Professor of Mechanical Engineering, University of Michigan, Engineering Research Institute, Ann Arbor, Mich. Mem. ASME.

—and reflected in pump efficiency versus R_n , Fig. 10—is caused by a sudden decline in the efficiency of the turbulent mixing process.

Regarding correspondence to pipe-flow phenomena, consider the familiar "pipe factor" versus Reynolds number correlation. This plot of the ratio of the average velocity divided by the maximum or center-line velocity, V/u_{max} , shows the rather sudden flattening of the laminar-flow parabolic distribution ($V/u_{max} = 0.5$) as turbulence sets in when $R > 2100$. In the literature, such curves are usually based on the data of Stanton and Pannell;¹¹ and recently Senecal and Rothfus¹² obtained precise measurements of velocity profile under critical flow conditions. The appearance of V/u_{max} versus R is almost identical with the η versus R_n plot, Fig. 10. From a laminar-flow value of 0.5 the pipe factor V/u_{max} increases rapidly (33 per cent) between $R = 2000$ and 4000. From $R = 4000$ the increase is quite gradual and V/u_{max} asymptotically approaches 0.81 at high R values.¹²

¹¹ "Similarity of Motion in Relation to Surface Friction of Fluids," by T. E. Stanton and J. R. Pannell, *Trans. Royal Society of London, Series A*, vol. 214, 1914, p. 199.

¹² "Transition Flow of Fluids in Smooth Tubes," by V. E. Senecal and R. R. Rothfus, *Chemical Engineering Progress*, vol. 49, 1953, p. 533.

This suggests that an abrupt shift of velocity profile of this sort occurs in the jet pump primary and/or secondary flow streams. Velocity traverses of jet pump flow of viscous fluids would be quite interesting.

In at least two respects correspondence of critical jet Reynolds number (i.e., comparison with pipe flow) is subject to question. In the first place, at corresponding Reynolds numbers fully developed flow in a long pipe is usually not the same as flow in a nozzle or in a short-tube annulus, which are the most important parts comprising a jet pump. Pump design factors promoting turbulence may be expected to influence Reynolds number correlations. Relative wall roughness, of course, affects frictional losses. As shown by Fig. 8 nozzle losses decrease as size increases because of decreasing relative wall roughness. In this investigation of jet pumps, data on size effect were limited; however, one direct comparison was made in which three geometrically similar pumps ($b = 0.2$) were tested at $R_n = 20,000$. Nozzle diameters were 0.100, 0.141, and 0.173 inch. Over-all performances of these pumps were essentially the same; nominal peak efficiencies were 26 per cent (7). Additional experimental data on larger jet pumps operating at low Reynolds numbers would be desirable.

An Experimental Study of Centrifugal-Pump Impellers¹

By A. J. ACOSTA² AND R. D. BOWERMAN³

Experimental investigations were made on four two-dimensional impellers and on a well-designed commercial three-dimensional Francis impeller. The over-all performance of each of these impellers was measured and internal-energy loss and pressure-distribution data were also obtained for several impellers. The exit angle of the two-dimensional impellers was fixed and the inlet angle was systematically varied. However, the hydraulic characteristics of these impellers were all found to differ, the source of the variation being in the various loss distributions and hence internal flow patterns in the impellers. The two-dimensional and three-dimensional impeller-loss distributions were also different. The Francis-impeller performance agreed better with potential theory than that of the two-dimensional impellers, and it is concluded that the different loss distributions of the two types are responsible.

NOMENCLATURE

The following nomenclature is used in the paper:

- A = area
- C = absolute velocity
- C_p = pressure coefficient = $p_s - p_t / \rho U_2^2 / 2$
- H = head, ft
- H_d = head developed by impeller
- Q = flow rate, ft³/sec
- T = torque
- U = tangential velocity of impeller ($r\omega$)
- W = relative velocity
- g = gravitational constant
- p = pressure
- r = radius
- z = axial co-ordinate
- α = angle of attack
- β = vane angle
- ζ_r = loss coefficient = $p_T - p_t / \rho U_2^2 / 2$ (measured in relative flow)
- η = efficiency = $\phi \psi / \tau$
- θ = angular co-ordinate
- ρ = density

$$\sigma = \text{Thoma cavitation parameter} = \frac{\text{inlet total head minus vapor pressure}}{\text{developed head}}$$

$$\phi = \text{flow-rate coefficient} = Q / A_2 U_2 = C_{m1} / U_2$$

- τ = torque coefficient = $T / \rho r_2 U_2^2 A_2$
- ψ = head coefficient = $H / U_2^2 / g$
- ψ' = input head or work coefficient = τ / ϕ
- ω = angular speed

Subscripts

- d = developed head
- e = design point for impeller
- l = loss
- m = meridional (or radial) component
- s = static pressure
- T = total pressure (or head) in impeller inlet
- t = total pressure (or head) at any other location
- u = tangential component
- 1 = impeller inlet
- 2 = impeller exit

INTRODUCTION

This paper summarizes experimental work on centrifugal-pump impellers carried out by the hydraulic machinery group of the Hydrodynamics Laboratory over a period of about three years. Some of the work discussed herein has been reported already as individual investigations by this project (1, 2, 3, 4).⁴ This paper embodies these earlier results together with more complete and recent investigations.

In the past, industry has developed a line of highly efficient pumps by considering only gross effects by a one-dimensional theory and then resorting to empirical development based on many years of experience in order to obtain acceptable designs. This procedure is partly justified by the fact that there is little actually known about the internal flow in pump passages even though the body of fluid-dynamic theory is available and applicable. The problem of turbomachine design (and in particular centrifugal-pump design) is complicated by the fact that only a relatively few of the factors involved can be included in a practical mathematical or analytical solution. However, the basic difficulty facing any rational analysis has been the lack of knowledge of the important internal-flow details. Thus in most instances the general applicability of analytical results must be left open until sufficient experimental evidence is available.

One of the objectives of an experimental program on pump-impeller research must be to obtain a sufficient amount of information on the internal and over-all flow characteristics so that their main features become clear and are understood. Although such knowledge may only substantiate design practices developed by experience, this result would in itself be of considerable interest. Moreover, this type of information, which is not generally available, makes possible, through the knowledge of the experimental coefficients found, extension of designs into new fields of application.

The preceding discussions outline the motivation for the work reported herein. A series of experiments was conducted on four "two-dimensional" impellers in which the inlet angle was the only variable. These data include head, torque, and efficiency measurements in addition to internal loss, velocity profiles, and pressure distributions. As an aid in the qualitative description of the flow, photographic techniques also were used.

⁴ Numbers in parentheses refer to Bibliography at end of paper.

¹ This work was supported by the Office of Naval Research, under Contract N6onr-244, Task Order II. Reproduction in whole or in part is permitted for any purpose of the U. S. Government.

² Assistant Professor of Mechanical Engineering, California Institute of Technology, Pasadena, Calif. Assoc. Mem. ASME.

³ Research Engineer, U. S. Industries Research and Development Corporation, Los Angeles, Calif. Assoc. Mem. ASME.

Contributed by the Hydraulic Division and presented at the Annual Meeting, New York, N. Y., November 25-30, 1956, of THE AMERICAN SOCIETY OF MECHANICAL ENGINEERS.

NOTE: Statements and opinions advanced in papers are to be understood as individual expressions of their authors and not those of the Society. Manuscript received at ASME Headquarters, July 26, 1956. Paper No. 56-A-41.

Meridian cross-section profiles of impellers range from those of the very narrow width, radial flow, through the Francis or mixed-flow type of impeller sections built on cones, and ultimately to the straight axial profile. Attention in the present work has been confined to that of the "three-dimensional" or Francis impeller in which the meridian flow is generally curved but leaves radially. The flow pattern for such geometries is quite complex, so, in order to reduce the variables involved, "two-dimensional" impellers were made. These test impellers have plane, annular shroud shapes with a fairly quick transition from the axial to radial direction at the inlet. Such shapes are of limited practical application; however, they are of value in experimental work because of the relative ease of observation and measurement offered. Thus, in order to complete the investigation, additional work was carried out on a "three-dimensional," high-efficiency, commercial impeller with similar operating characteristics, and the results compared with those of the two-dimensional experiments.

DESCRIPTION OF LABORATORY FACILITIES, INSTRUMENTATION, AND IMPELLERS

Facilities. A detailed description of the laboratory facilities may be found in references (1) and (2) so that only the salient features will be mentioned here. The test facility consists of a closed hydraulic circuit using water as the fluid medium with a circulating pump, venturi flowmeters, and a system of piping to distribute the flow to any one of three test basins in which the experimental models can be installed. Although the flow may be made to circulate in either direction through the test basin, for pump work the circuit is arranged so that flow approaches the impeller axially and leaves radially, discharging into the test basin at atmospheric pressure. The impellers are driven by a vertically mounted d-c dynamometer which is equipped with an accurate speed control. Fig. 1 shows the impeller and test-basin arrangement and Fig. 2 is a view of the experimental setup.

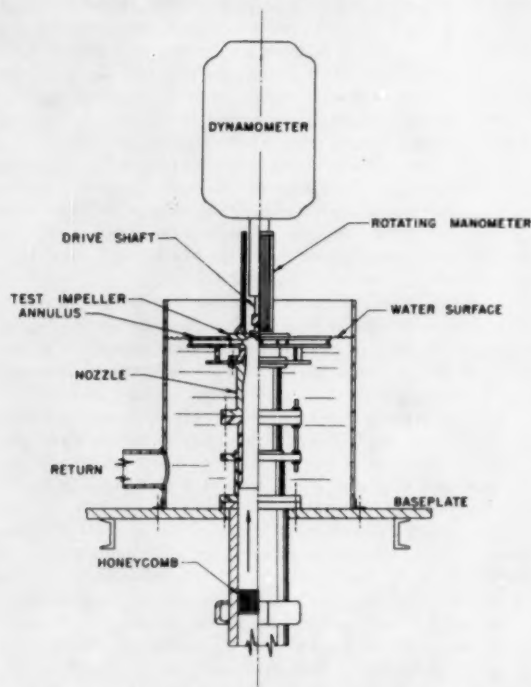


FIG. 1 CROSS SECTION OF IMPELLER AND TEST-BASIN ASSEMBLY

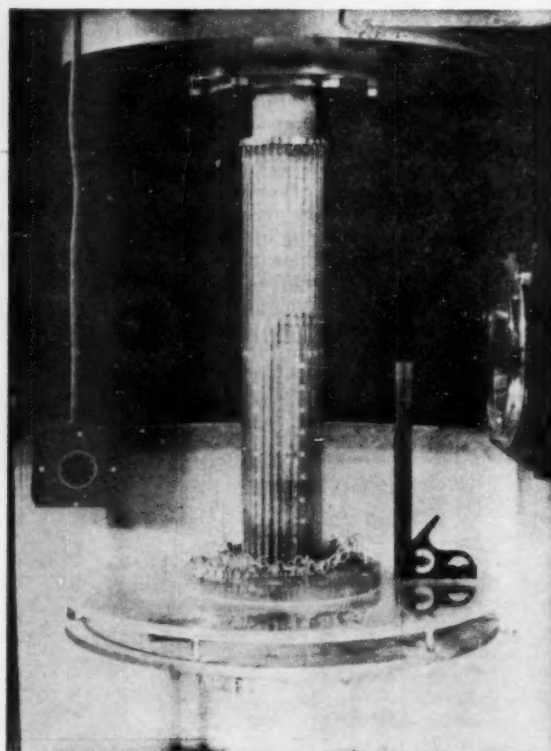


FIG. 2 VIEW OF EXPERIMENTAL SETUP

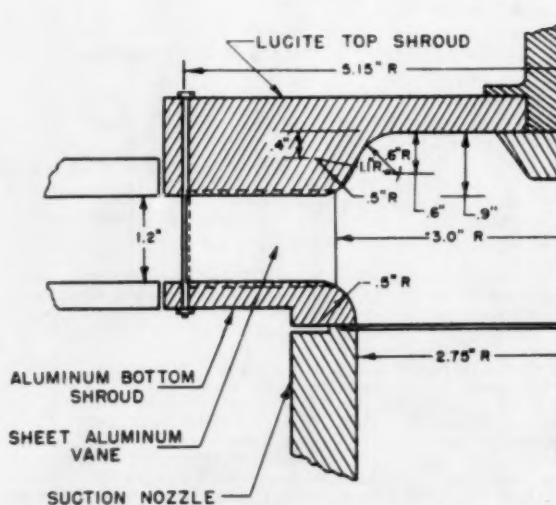


FIG. 3 CROSS SECTION OF TWO-DIMENSIONAL IMPELLER

of similar designs all with the same radius ratio, breadth, and exit-vane angle but with systematically varied inlet-angles.

In order to obtain a smooth and systematic variation of blade angle from inlet to exit, it was first assumed that the relative flow followed the blade shape exactly (i.e., an infinite number of vanes) and then the growth of the whirl or tangential component in the absolute flow was specified. In this particular case a linear variation was chosen. Even though it was realized that the foregoing assumption is incorrect, at least the resulting vane shapes are not completely arbitrary, and furthermore this procedure obviates shapes with excessive curvature. The various impeller geometrical constants are given in Table 1. Inasmuch as only the impeller-inlet angles are different for the four runners, they will be designated by these values throughout the text.

TABLE 1 IMPELLER GEOMETRICAL AND DESIGN CONSTANTS

Inlet angle β_1 (impeller designation), deg.	Two-dimensional				Three-dimensional
	20	17	14.5	12.5	23*
Outlet angle β_2 , deg.	23.5	23.5	23.5	23.5	17
Radius ratio (r_1/r_2)	0.583	0.583	0.583	0.583	0.525*
Outlet breadth/outside diameter (b_2/D_2)	0.086	0.086	0.086	0.086	0.116
Design flow rate ϕ (shockless inlet)	0.117	0.100	0.083	0.067	0.050
Number of vanes	6	6	6	6	5
Outside diameter, in.	10.30	10.30	10.30	10.30	12.875

* Suction shroud values.

Impeller Manufacture. The shape of the two-dimensional impeller series made fabrication particularly simple. The top shrouds were turned from lucite to permit photographic and visual observations to be made, and the bottom shroud was black anodized aluminum. The vanes were rolled to shape from $1/8$ -in. 2-S aluminum sheet, or from brass sheet in some cases, and were recessed in slots milled in the shrouds, six equally spaced vanes being employed in each case. The resulting impeller assembly was held together with $1/8$ -in. through-bolts at the exit edge of the individual blades. For reasons of economy, two sets of slots were installed in each of two sets of shrouds, the unused slots being waxed-in during operation. An assembled impeller is shown in Fig. 4.

Test Setup. The impeller was installed in the basin as shown in Fig. 2. Since only low rotative speeds were used, sealing was not a problem and in all cases running clearances of about 0.010 in. were found to be satisfactory. The flow from the impeller discharges into a set of parallel diffuser shrouds which serve to guide the flow and eliminate exterior disturbances.

In operation, the water surface was maintained slightly above the level of the impeller. The impeller was operated at a constant speed of 225 rpm. The flow rate was regulated by a manual throttle valve in the suction line and the speed-controlled circulating pump.

Instrumentation. Two types of information were sought in this work; namely, the over-all operating characteristics, i.e., head, torque, and flow rate; also internal flow data, viz., pressure distributions, velocity, and total head-loss profiles.

(a) **Flow Rate.** The volume flow rate was established and measured by any one of the three venturi meters available and a differential mercury manometer.

(b) **Torque.** The reaction torque of the motor case was balanced by graduated weights connected to the dynamometer torque arm by means of a wire and pulley system. A Statham electric strain gage attached to the arm was used as an indicator for the null position. Mechanical stops limit the motion to a few thousandths of an inch and protect the gage. The strain gage output was read by an optical galvanometer. Thus the procedure consisted of balancing the torque with small weights until the null position was achieved. This arrangement allows torque to be

measured with zero displacement, thus minimizing bearing friction. The resultant sensitivity of the system was about $1/400$ of the full-scale reading. With the relatively small torques measured in these tests (1.5 ft-lb max), vibration was found to be a problem so that to improve accuracy several readings at each operation point were taken and averaged.

With the setup employed, the tare reading was fairly large. In particular, the bearing friction and water drag on the shroud surfaces were large and as they took no part in the pumping operation their corresponding torques were treated as a tare.

(c) **Head.** The head developed by the impeller was measured with a water-air manometer and total-head probes, one being installed in the impeller inlet, or eye, and the other mounted at the impeller discharge. Both simple impact probes and Kiel venturi-type total-head probes were used at the impeller exit and were usually installed only $1/16$ in. away from the vane tips.

(d) **Internal-Flow Measurements.** All of the internal-flow measurements consist of pressures [except the photographic observations (1)] and hence a device to measure these pressures quickly and easily is necessary. For the work in this laboratory it was found to be expedient to use a manometer attached to and rotating concentric with the impeller (3, 4). The manometer employed consisted of thirty 6-mm tubes about 18 in. long with a common manifold to all tubes. One tube was reserved for a reference pressure (which was taken to be the inlet total head) and others were connected to various static or total-head piezometer connections. Thus, with a maximum economy of effort, static-pressure distributions, relative velocities, and relative "energy losses" could be found.

Static piezometer taps in the vane surfaces were installed by drilling down the breadth of the vane to an 0.030-in. perpendicular

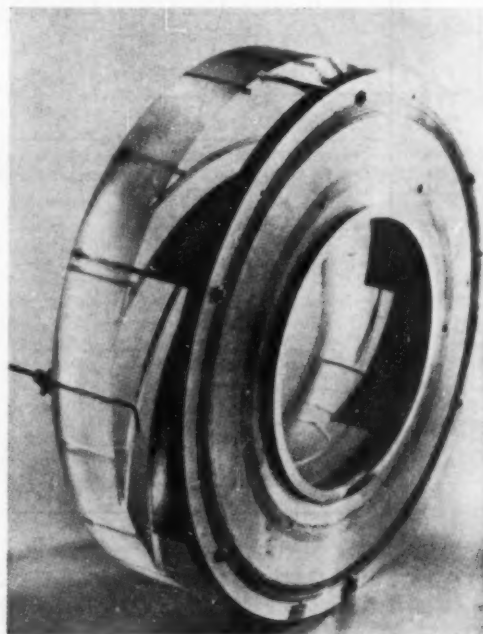


FIG. 4 VIEW OF ASSEMBLED TWO-DIMENSIONAL IMPELLER

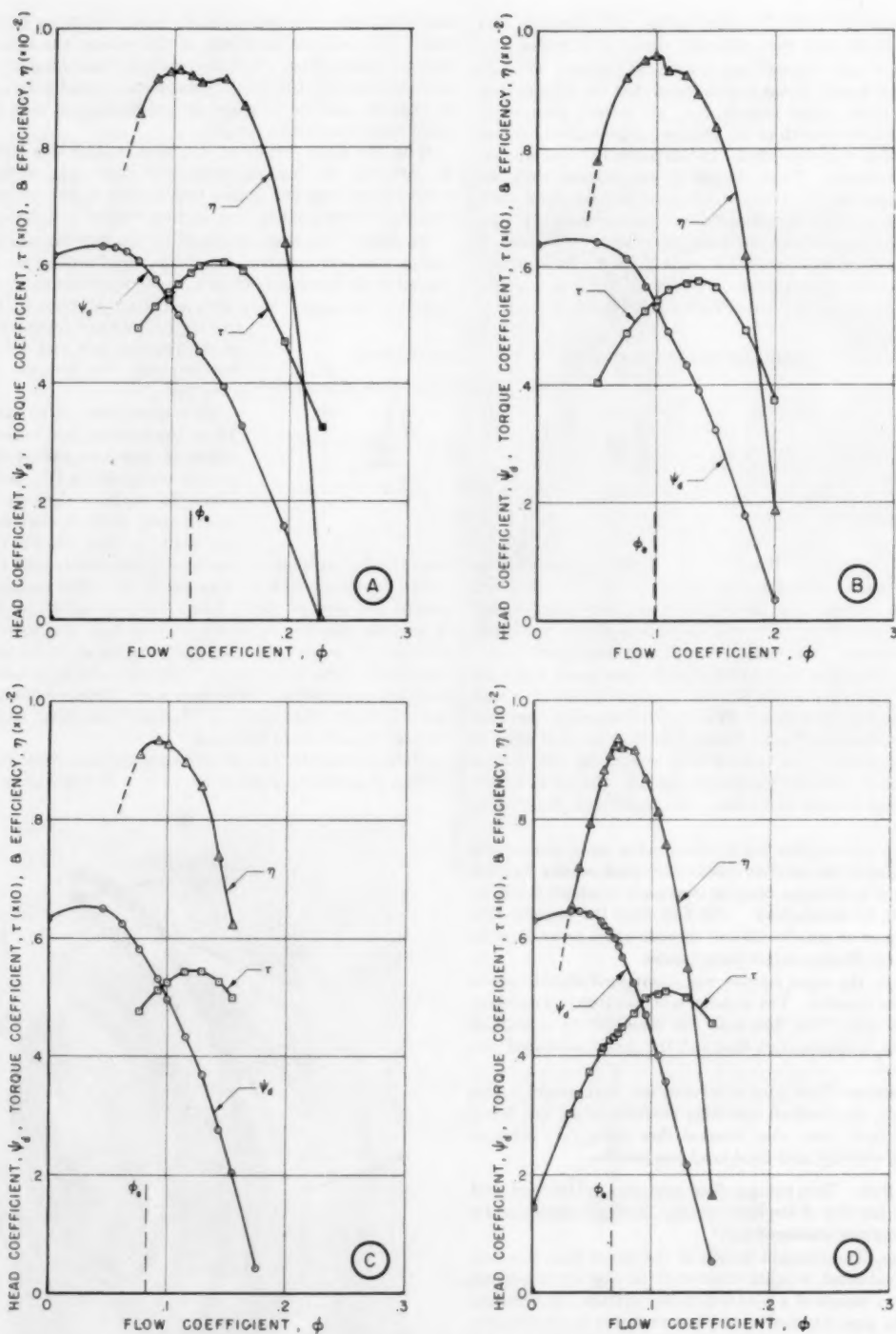


FIG. 5 HEAD COEFFICIENT, TORQUE COEFFICIENT, AND EFFICIENCY VERSUS FLOW-RATE COEFFICIENT FOR TWO-DIMENSIONAL IMPELLERS. IMPELLERS, (A) 20° , (B) 17.5° , (C) 15° , (D) 12.5°

lar hole and by soldering $1/16$ -in. brass tubing into vertically milled slots on the vane surface before it was bent to the proper contour. Both methods were found to be practicable.

Relative velocity heads were obtained with $1/16$ -in. simple impact probes mounted in the impeller passages and directed into the relative flow. In order to prevent flow asymmetry, such tubes usually were distributed throughout all of the passages.

It should be noted that the rotating manometer does not give the static-pressure distribution directly and that, in order to obtain it, the centrifugal effects in the connecting tubing must be accounted for (Appendix 2).

(e) *Flow Visualization.* The lucite shrouds of the test impellers permit both visual and photographic observation, as described in reference (1). Briefly, these techniques consist of injecting immiscible liquid globules into the flow and observing their subsequent history either in the relative or absolute reference frames. Both motion pictures and multiple-flash exposures on a single plate were taken. Some use also was made of stereographic photography.

Flow visualization by these methods has been found extremely valuable for qualitative exploratory investigations and provides a necessary complement to the internal flow measurements.

(f) *Accuracy.* Both the flow rate and speed were capable of being measured with an error of less than $1/2$ per cent. However, owing to the large tare, torque values were only known to within 1.5 per cent or so. The greatest difficulty was experienced in the determination of the pump head. Since the head reading varied somewhat over the passage height and depended also on the distance away from the impeller exit, there is some question as to what value of "head" should be used. The over-all accuracy of the performance measurements is thus about 3 to 4 per cent, depending somewhat on the value of the head.

Most of the relative measurements cannot be determined accurately. Instrumentation errors, manometer errors, and so on, probably are within 2 per cent for the most part and such varia-

tion would be typical of the pressure-distribution results also. Flow asymmetries, incorrect angles on the relative total head tubes, and the like, could cause additional errors that are quite difficult to detect.

EXPERIMENTAL WORK

Complete characteristic diagrams for the four two-dimensional impellers are presented in Fig. 5 in terms of the dimensionless developed head coefficient ψ_d , torque coefficient τ , flow-rate coefficient ϕ , and efficiency η . As mentioned in the preceding paragraphs, there is some arbitrariness in the definition of the impeller head. In particular, it was found that the distance between the discharge total-head probe and the impeller periphery was important. Fig. 6 shows this variation with the probe $1/16$ and $3/8$ in. from the impeller exit. The major difference is seen to occur at flow rates less than the design point. At such low flow rates, considerable mixing, and other real fluid effects can come into play since the path lines between the impeller and probe are long, flat spirals. Thus, in the rest of this work the $1/16$ -in. position was used as a standard. Any additional losses due to

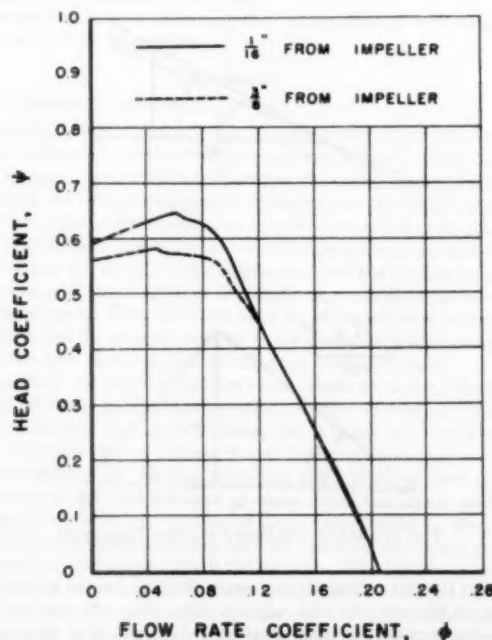


FIG. 6 DEVELOPED HEAD COEFFICIENT MEASURED AT $1/16$ IN. AND AT $3/8$ IN. RADIAL DISTANCE FROM IMPELLER

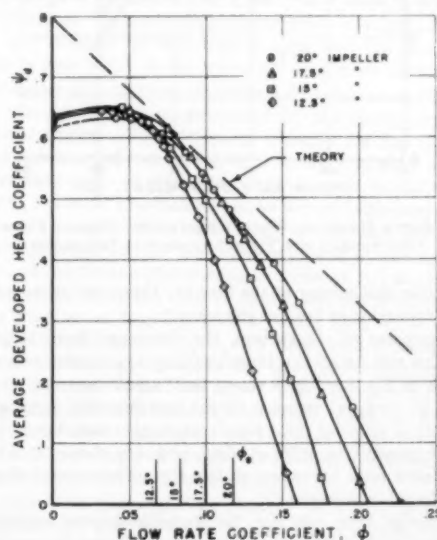


FIG. 7 DEVELOPED HEAD COEFFICIENT AND THEORETICAL HEAD COEFFICIENT VERSUS FLOW RATE COEFFICIENT FOR THE TWO-DIMENSIONAL IMPELLERS

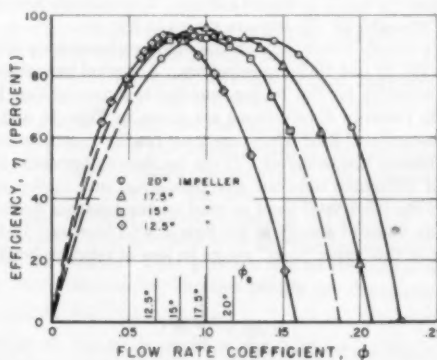


FIG. 8 EFFICIENCY VERSUS FLOW-RATE COEFFICIENT FOR THE TWO-DIMENSIONAL IMPELLERS

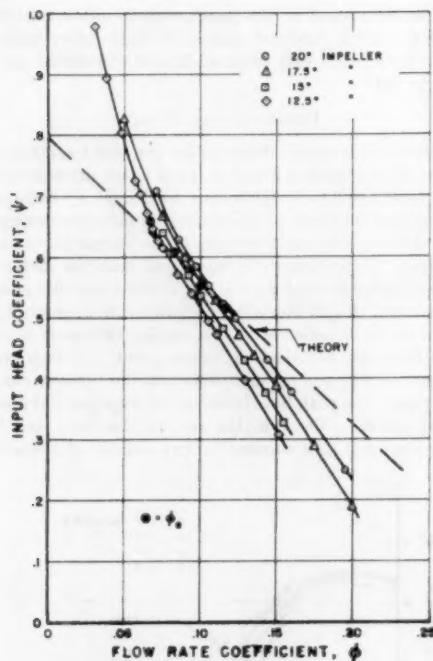


FIG. 9 INPUT HEAD OR WORK COEFFICIENT VERSUS FLOW-RATE COEFFICIENT FOR TWO-DIMENSIONAL IMPELLERS

equalization and mixing of the flow are therefore not counted in the determination of head or efficiency.

For purposes of comparison, the developed head is plotted versus flow rate for all four impellers (Fig. 7) and efficiency versus flow rate in Fig. 8. Fig. 9 shows the "input" head or work coefficient ψ' ($=\psi_d/\eta$) versus ϕ for the four impellers together with a theoretical estimate (6). Similar data also were taken on the three-dimensional impeller studied and are shown in Fig. 10. Performance data for other similar three-dimensional impellers may be found in reference (2).

The design flow rate for the two-dimensional impellers is designated by ϕ_d in Figs. 7 to 9 and was obtained by making the inlet relative-flow angle equal to the inlet-vane angle with the assumption that there is no prewhirl. It is realized that this procedure is inaccurate for potential flow (5, 6) but as the basis of a comparative study it should suffice. Typical inlet and outlet-velocity triangles for a pump are shown in Fig. 11.

Pressure-distribution data on the blade surfaces were obtained only for the 20 and 12.5-deg impellers. A typical piezometer-tap drilling schedule for the 20-deg impeller is shown in Fig. 13 and the static pressure distributions are given in Figs. 14 and 15.

Viscous and real fluid effects are most readily shown by contour plots of energy loss or defect. It can be shown (Appendix 2) that the head difference between any total-head tube in the relative flow and the inlet total head as read on the rotating manometer represents a loss of energy in the flow due to friction. In the remainder of this paper "loss" refers to loss of relative total head; i.e.,

$$p/\rho g + \frac{1}{2g} W^2$$

Energy-loss contours are given in terms of the per cent of input head or work coefficient for the 20-deg impeller for various flow

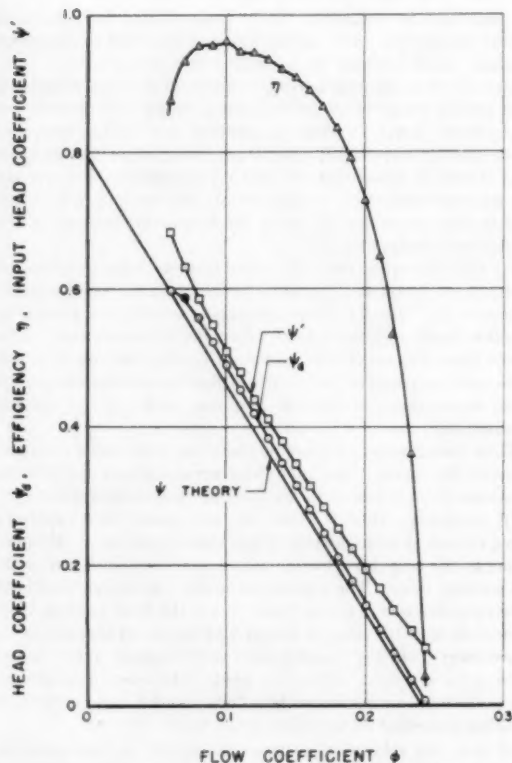


FIG. 10 HEAD COEFFICIENT AND EFFICIENCY VERSUS FLOW-RATE COEFFICIENT FOR THREE-DIMENSIONAL IMPELLER

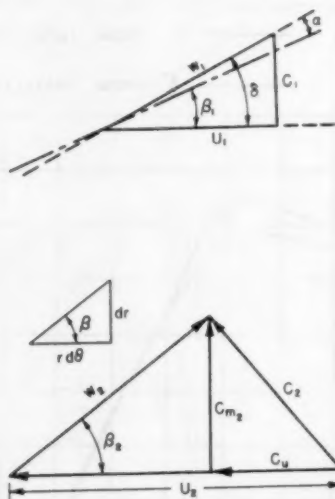


FIG. 11 INLET AND EXIT-VELOCITY TRIANGLES

rates at the exit section of the passage (Fig. 16), for the 15-deg impeller at the exit and mid-radius position (Fig. 17), and for the 12.5-deg impeller at three locations; i.e., exit (Fig. 18), mid-radius (Fig. 19), and inlet (Fig. 20). Static-pressure distributions between the vanes along top and bottom shrouds also were taken

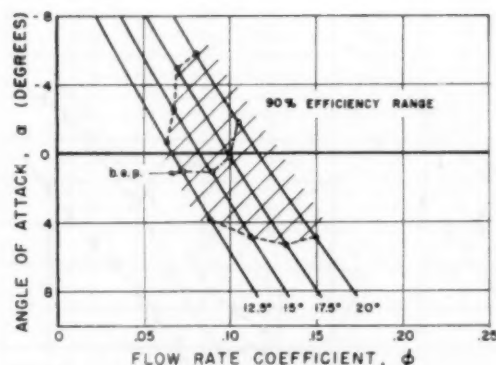


FIG. 12 INLET ANGLE OF ATTACK VERSUS FLOW-RATE COEFFICIENT FOR TWO-DIMENSIONAL IMPELLERS

for the 12.5-deg impeller, so that with the aid of the loss coefficients relative velocities in the passage section could be computed. Velocity profiles across the height of the passage and for several positions between the vanes are given for the 12.5-deg impeller at three radial stations in Fig. 21.

Similar data also were taken for the three-dimensional impeller. Loss contours at the exit are shown in Fig. 24 and at the inlet in Fig. 25. Relative velocity computations also were made at the exit section, but owing to the high curvature of the meridian flow at the inlet, static pressures could not be measured there, hence velocities could not be determined.

The three-dimensional impeller performance was obtained with a setup quite similar to that of the other impeller (Fig. 2), i.e., with plane annular diffuser shrouds. However, the exit-loss measurements had to be made without the top shrouds. Additional work also was done on the effect of these shrouds by removing the bottom shroud as well.

The results of these tests and their interpretation will be discussed in the following section.

DISCUSSION

Two-Dimensional Impellers

Over-All Characteristics. It is immediately clear from the plots of head versus flow rate for the four impellers in Figs. 7 and 9 that the inlet angle has a profound effect upon the entire characteristic. In general, the best efficiency point is seen to move to the left (Fig. 8) for the reduced inlet angles, as would be expected. At relatively high rates of flow ($\phi = 0.1 - 0.12$) larger heads are seen to be developed for the high inlet angles than for the smaller ones, and the slope of the $H-Q$ curve progressively steepens as the inlet angle is reduced. The developed head for all impellers is seen to be more or less the same at about $\phi = 0.06$, indicating that in this region the flow does not depend much on the inlet angle.

One should not assume that the losses which occur away from the best efficiency point are solely responsible for the variations in performance even though this assumption is commonly found in pump literature (7). An inspection of the brake horsepower or torque coefficient for the four impellers (Fig. 5) shows that the input work is different for each of them. The maximum peak value goes from about $\tau = 0.061$ for the 20-deg impeller to about 0.051 for the 12½-deg impeller, and the flow-rate coefficient for the maximum decreases from 0.135 to 0.11. The difference between each of these quantities is thus on the order of 20 per cent and from the torque characteristics one can see that attributing the variations in head performance to internal fluid losses cannot alone explain the discrepancies. It should be pointed out also that inlet-blade-angle variations of the magnitude in these tests

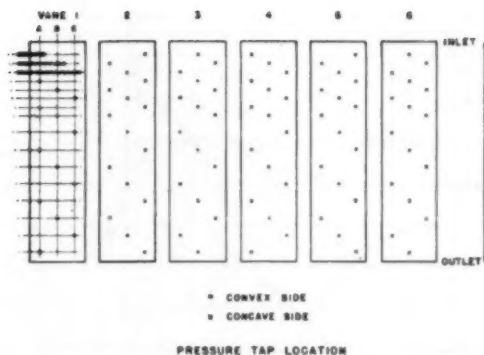


FIG. 13 PIEZOMETER-TAP DRILLING SCHEDULE FOR THE 20-DEG IMPELLER VANES

can only account for about 1 or 2 per cent change in the $H-Q$ characteristic on the basis of potential-flow calculations (10). Also it is of interest to note that in each case the maximum efficiency is seen to fall to the left of the maximum torque.

The design points of these impellers were taken to be the flow rate for shockless entry as calculated by the elementary one-dimensional theory. Vector-velocity triangles for the impeller inlet and outlet are shown in Fig. 11. In order to show the influence of local angle of attack or incidence angle to the blade-inlet edges, the angle of attack for the 90 per cent efficiency range versus flow rate is plotted for each of the four impellers in Fig. 12. The angle of attack for the best efficiency point is seen to vary from the -2 deg for the 20-deg impeller to about 1½ deg for the 12-deg impeller. From the slope of the 90 per cent envelope it is doubtful whether an impeller with a 10-deg inlet angle would ever achieve this efficiency. Again, this observation is taken to be a result of operation at extremely low flow-rate coefficients and not primarily a result of the inlet angle. This effect also shows up in the fact that the ratio of the high-efficiency operating range to the design flow rate is smaller for the low angles than the larger ones. If the inlet angle of attack were the sole criterion, this ratio should increase as the inlet angle is reduced.

Correlation With Potential-Flow Theory. In Figs. 7 and 9 are shown theoretical $\psi-\phi$ curves computed on the basis of potential-flow theory (6). Although these ideal characteristics were determined for logarithmic spiral vane shapes, small perturbations in inlet angle do not affect the $\psi-\phi$ characteristic materially. The outstanding feature on both of these figures is the rather large discrepancy in slope between the ideal performance and both developed and input heads. The same phenomenon also was noticed in reference (5) in which a series of experiments was conducted on 30-deg log-spiral, two-dimensional impellers. In this work the discrepancy was attributed to the influence of the inlet boundary layer arising from the sharp turn.

In Fig. 9 it is seen that the design points of the four impellers all fall nearly on the computed characteristic. The experimental $\psi-\phi$ curves must intersect the ideal $\psi-\phi$ characteristic at some flow rate. However, the coincidence of the design ψ' values with the computed characteristic must be regarded as fortuitous, at least for the present. This question will be considered again when the three-dimensional impeller results are discussed.

Pressure-Distribution Measurements

Knowledge of the static-pressure distributions on the vanes gives a direct measurement of the vane loading and hence evaluation of the design of the blade shape. Pressure-distribution measurements on the 20-deg impeller were first reported in reference

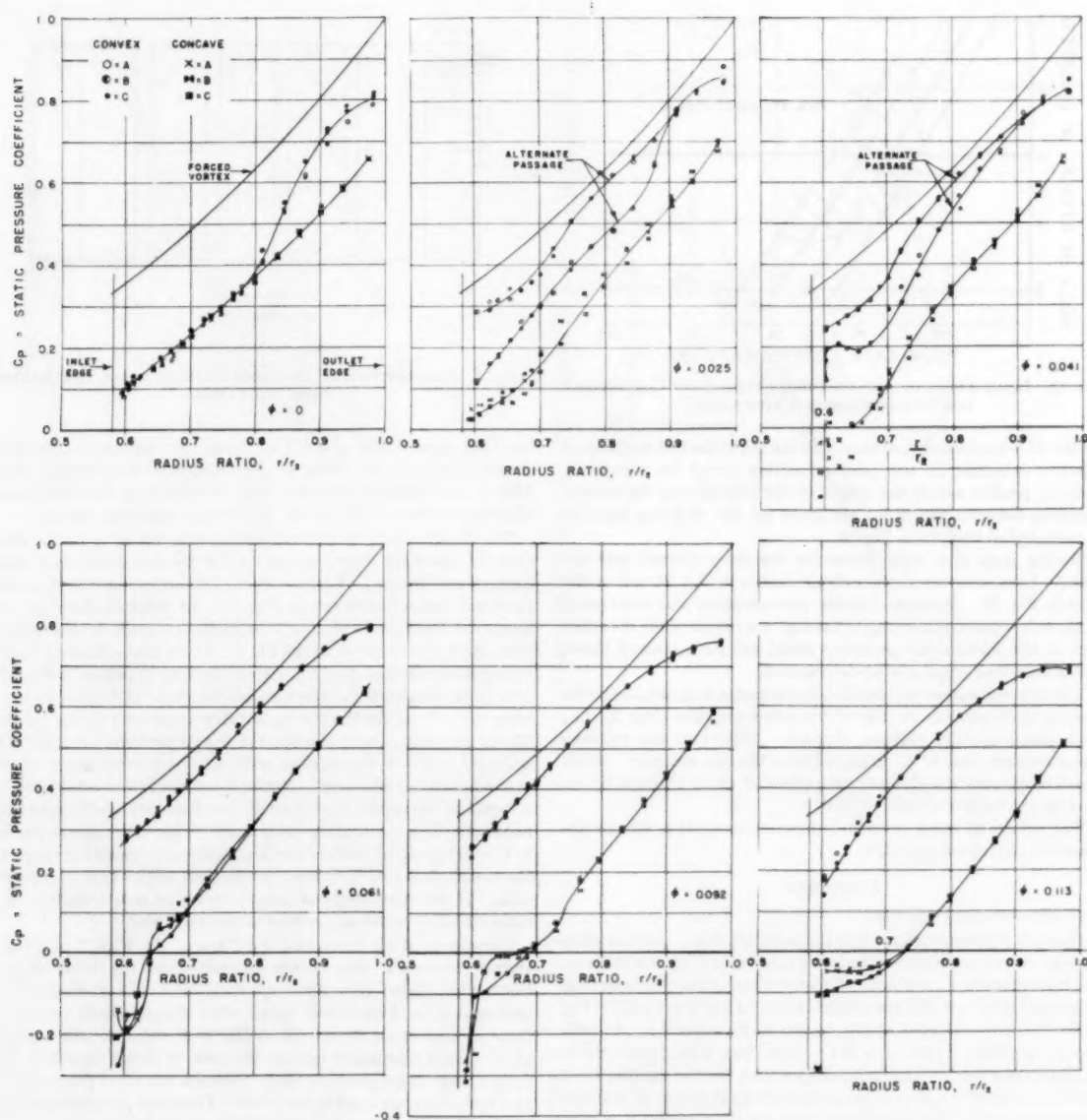


FIG. 14 STATIC-PRESSURE DISTRIBUTIONS ON VANES OF 20-DEG IMPELLER FOR SEVERAL FLOW RATES

(4) and additional measurements on the 12.5-deg impeller are reported herein.

In both Figs. 14 and 15 it is seen that the pressure distributions or loading curves near the design point are relatively smooth and show no unusual reversals. This fact is, no doubt, a consequence of the smooth curvature of the vanes, and supports the contention that for radial-flow machinery, the exact blade design is not of paramount importance provided abrupt changes in curvature are avoided, and that the blade angle smoothly increases or decreases.

"Shockless" Flow Rate. As mentioned before, the design points of these impellers were chosen so that the relative flow would stream smoothly onto the leading edge with no velocity discontinuities. The flow rate for this operating condition is termed

"shockless entry" in the pump literature. For the 20-deg impeller the nearest approach to shockless entry occurs about $\phi = 0.140$, whereas according to the simple theory, shockless entry should occur at $\phi = 0.117$. Thus, shockless entry occurs at a flow rate greater by 20 per cent than that computed on the basis of the infinite-vane theory. According to potential-flow calculations (6, 10) the shockless flow rate for this impeller geometry should be 32 per cent greater than that based on the infinite-vane theory. It seems reasonable that boundary-layer blockage and other real fluid effects could account for the discrepancy between this and the observed value. Similar results also were observed in reference (5) in experiments conducted on impellers with 30-deg log-spiral vanes.

The pressure-distribution measurements of Fig. 15 on the 12 $\frac{1}{2}$ -

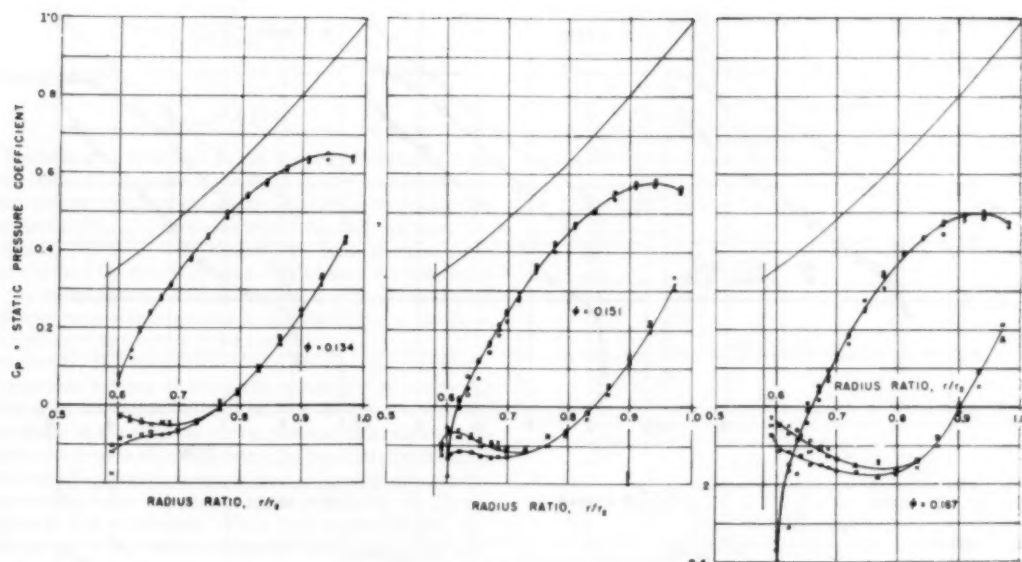


FIG. 14 (continued)

deg impeller show that shockless entry is about at $\phi = 0.06$, whereas the design calculations were for $\phi = 0.067$. This result does not fall on the trend established by the 20-deg impeller (5) or the theoretical predictions. As previously pointed out, real fluid effects become of increasing importance for such low flow coefficients, and the different behavior is attributed to this effect.

Loading Distribution. At or near the shockless-entry operating point it is clear from the head-flow rate characteristic that the vanes of the 12.5-deg impeller are considerably less loaded than those of the 20-deg impeller. The fact is reflected in the pressure-distribution diagrams which are slimmer and more elongated for the smaller angle. As previously noted, the load distributions for both of these impellers is "reasonable" near shockless, indicating that as long as the change in angle from inlet to outlet is not rapid and continuously increases (or decreases), any blade design should be satisfactory. This observation is mainly qualitative and is principally intended to point out the difference in importance that the vane shape has for axial and radial pumps. It will be shown later that the 12.5-deg impeller, although having a smooth increase in vane angle, does have certain undesirable internal-flow features as compared with the 20-deg impeller.

At flow rates less than shockless entry, large velocity discontinuities are seen to appear at the inlet on both impellers. In a similar fashion at high flow rates, the distributions on the two faces intersect and cross over.

Operation at Low Flow Rates. At shockless entry there is a stagnation point at the leading or inlet edge of the blade. As the flow rate is reduced, it is evident from the pressure distributions and also from physical considerations that the stagnation point moves onto the leading or pressure face of the blade. This point continues to move away from the inlet edge toward the outlet as the flow rate is reduced until shut-off has been reached. The final position of the stagnation point depends upon the blade angle, radius ratio, and so on. Thus, whatever the particular design, back flow can occur over a considerable extent of the pressure side of the blade at low flow rates. Such back flows are not conducive to high efficiency or stable operation. The excessive path length and highly unfavorable pressure gradient that must exist may

cause large-scale separation and other real fluid effects. At shut-off these effects become even more predominant. Motion pictures show that, in general, the fluid in the inner portions of the impeller rotates like a solid body and that an irregular pulsating rotation opposite to the direction of impeller rotation occurs at the exit.

The foregoing sequence of events which occurs as the flow rate is lowered, as determined by motion pictures, is that a separation zone appears first on the suction side of the blade. With a further decrease in flow rate, alternate passages are seen to "stall out" completely, the flow then being much like a solid body rotation. The stalled pattern seems to be stable with respect to the impeller and does not propagate around the periphery as is observed in axial-flow compressors (11). This situation occurs at about a flow rate of $\phi = 0.05$ or so and can be verified by the pressure distributions taken in alternate passages on the 20-deg impeller shown in Fig. 14. This configuration remains until the flow rate becomes very low, and finally near shut-off all the passages stall out with the inner portions rotating like a solid body. Near the exit there is a large-scale irregular eddy rotating in the opposite sense to the impeller direction. The pressure distributions for $\phi = 0$ are shown in Figs. 14 and 15. It can be seen that at the inlet the static pressure is near zero and is considerably below the forced vortex line, indicating that there is little or no rotation of the fluid in the impeller eye. From the inlet edge to about $r/r_2 = 0.8$ the pressure is distributed like that of rigid-body rotation and the small loop in the discharge portions represents the work going into the eddy maintained at the exit.

Cavitation Susceptibility. The knowledge of the pressure distributions permits one to make some estimation of the cavitation susceptibility of an impeller. In terms of the pressure coefficient C_p , it can be shown that the value of Thoma's σ for the inception of cavitation is

$$\sigma_{\text{inception}} = \left| \frac{C_{p(\min)}}{2\psi} \right|$$

where ψ is the head coefficient. For the 20-deg impeller near the design flow rate ($\phi = 0.117$) this becomes

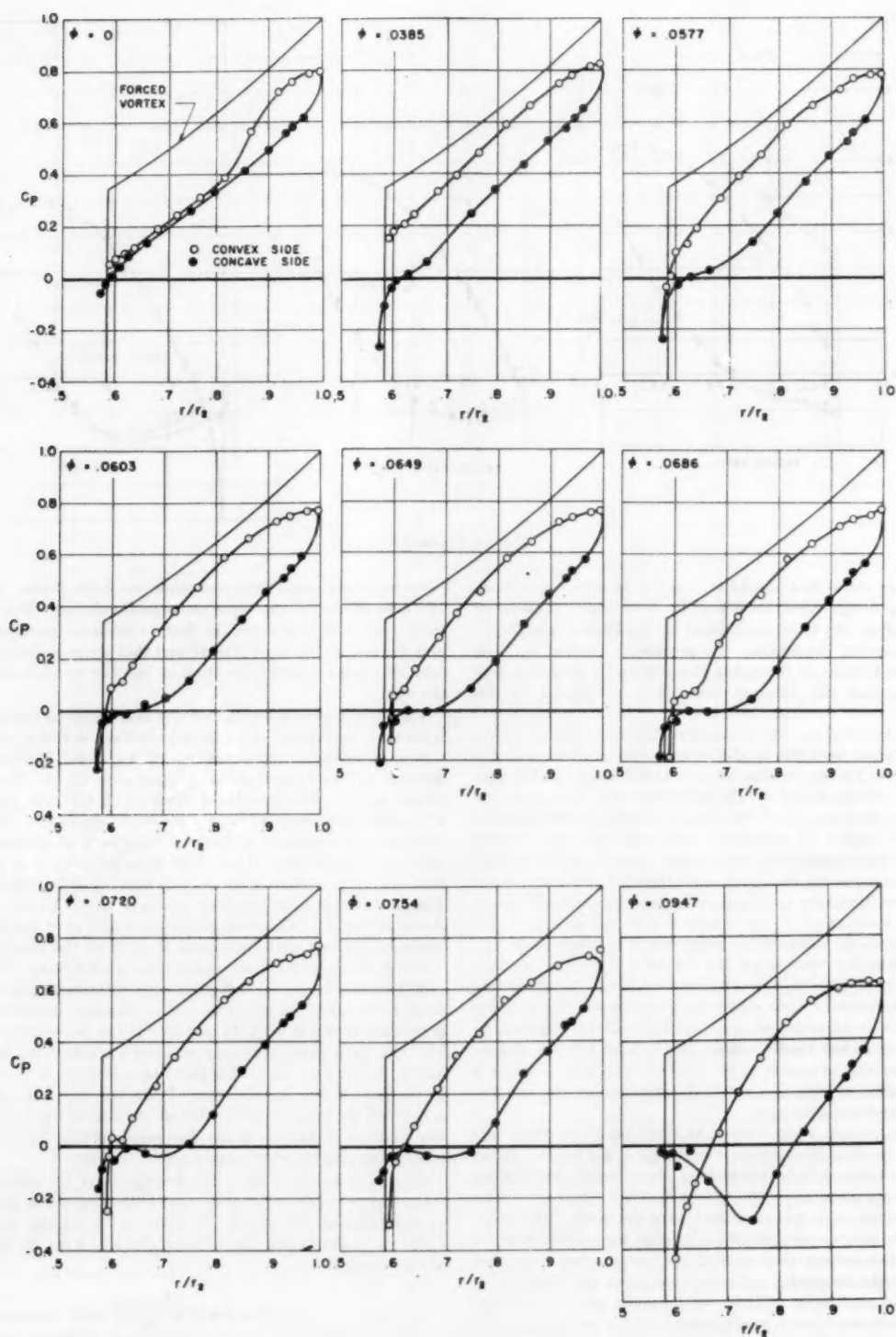


FIG. 15 STATIC-PRESSURE DISTRIBUTIONS ON VANES OF 12.5-DEG IMPELLER FOR SEVERAL FLOW RATES

$$\sigma_{\text{incept}} = \frac{0.3}{(2)(0.5)} = 0.3$$

and at shockless entry

$$\sigma_{\text{incept}} = 0.10$$

It is interesting to note that as the flow rate is reduced from shockless, the absolute value of the minimum pressure continues to increase and the values of σ_{incept} increase. However, when stall is encountered, $|C_{p \text{ min}}|$ decreases and near shut-off even becomes slightly positive. This means that lower absolute pressures are required for cavitation inception at very low flow rates than at the design points. This situation is in contrast to that of the axial-flow pump which requires increasing suction pressure to prevent cavitation as the flow is reduced (7).

Unfortunately, the knowledge of the noncavitating pressure distribution tells nothing of the performance during cavitating conditions or of cavitation "breakdown" or choking. However, from the shape of the pressure curves one can make some rough deductions: At or near shockless entry the pressure distributions are smooth and the pressure is nearly constant on the suction side. If this pressure is below the known vapor pressure of the liquid, the fluid must boil or cavitate. For a first approximation, the work represented by the area between the vapor-pressure line and pressure loop is not put into the flow as head. An inspection of these distributions at low flow rates shows that there are quite sharp pressure peaks of small area. Hence, one would infer that less head may be lost when cavitating under such circumstances than at shockless, although cavitation inception occurs sooner. According to these ideas, serious cavitation from the standpoint of head loss would not occur before $\sigma = 0.08$ or so at a flow rate coefficient of $\phi = 0.117$ for the 20-deg impeller. For the given characteristics of this impeller, this value agrees with the expected cavitation performance.⁶

Loss Contours. The internal velocity and relative total-head profiles probably give the best indication of the location and magnitude of real fluid effects possible with the experimental setup. The energy-loss contours at the exit section for the 20-deg impeller (Fig. 16) give a qualitative idea of the distribution of these effects for various flow rates. In these and the following contour plots, the loss in relative head is expressed as a fraction of the total developed head. It can be seen that up to and somewhat beyond the design point the regions of high loss are concentrated on the trailing (suction) side of the vane. At higher flow rates, the low-loss fluid moves over to the leading (pressure) side of the passage in accordance with the adverse negative angle of attack existing then at the vane-inlet edge.

Loss contours are also shown for the 15-deg impeller at a high flow rate (about 70 per cent greater than design) midway through the passage ($r/r_2 = 0.75$) and at the exit (Fig. 17). The high rate of flow is responsible for gross separation and flow detachment seen in the loss contours at mid-radius.

It is well known that such nonuniformities in relative total head give rise to circulating or secondary flows perpendicular to the main stream direction. Such evidence is offered by the outlet survey of Fig. 17 which shows how the areas of high-loss fluids have been distorted and displaced toward the trailing or suction side of the passage.

More extensive loss data are shown in Figs. 18 to 20 for the 12.5-deg impeller. Fig. 18 shows loss contours at the exit ($r/r_2 = 1.00$) at various flow rates. A difference between these distributions and those of the 20-deg impeller is immediately clear; namely, that a zone of large energy loss is always located next to the trailing side of the vane, even for flow rates about 60 per cent

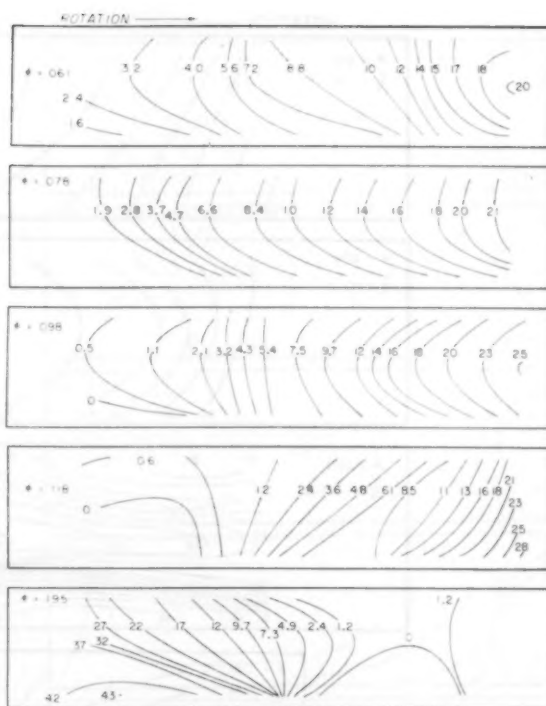


FIG. 16 RELATIVE TOTAL HEAD-LOSS CONTOURS FOR 20-DEG IMPELLER AT IMPELLER EXIT ($r/r_2 = 1.0$)

greater than the design. In fact, the percentage loss continuously increases with flow rate starting at the lowest value of $\phi = 0.048$. The inner survey ($r/r_2 = 0.73$) of Fig. 20 shows, in general, a thick region of relative energy defect on the trailing side of the passage and on the bottom shroud. These loss distributions remain more or less unchanged until the flow rate exceeds about $\phi = 0.072$. At flow-rate coefficients greater than this value, high loss areas are seen to occur on the pressure face of the vane. The pressure-distribution data, Fig. 15, for these flow rates show the static-pressure curves on leading and trailing-blade surfaces of the inlet crossing over at about this flow rate, so that unfavorable incidence angles occur at the inlet. Any further increase in flow rates results in regions of extreme loss probably associated with local flow detachment.

This sequence of events is roughly followed by the internal surveys at $r/r_2 = 0.89$ (Fig. 19) except that, in general, the profiles indicate greater losses near the trailing surfaces and less near the pressure (leading) surface. This behavior may be expected to follow from the general shape of the leading pressure-distribution curves.

Thus, it can be seen that the exit surveys on the 12.5-deg impeller do not follow the trend established by the inner surveys or the 20-deg impeller. The possibility that the flow separates along the trailing side of the vane near the exit immediately suggests itself. The velocity surveys discussed in the next paragraph further support this idea.

Velocity Profiles. From the loss measurements and static-pressure determinations on the impeller top shroud it is possible to calculate the relative velocity in the passage. Fig. 21 presents this information as relative velocity plotted against the channel height for several stations across the passage. An outstanding feature of each of these diagrams is that the velocity profile near

⁶ As given in reference (7), p. 267.

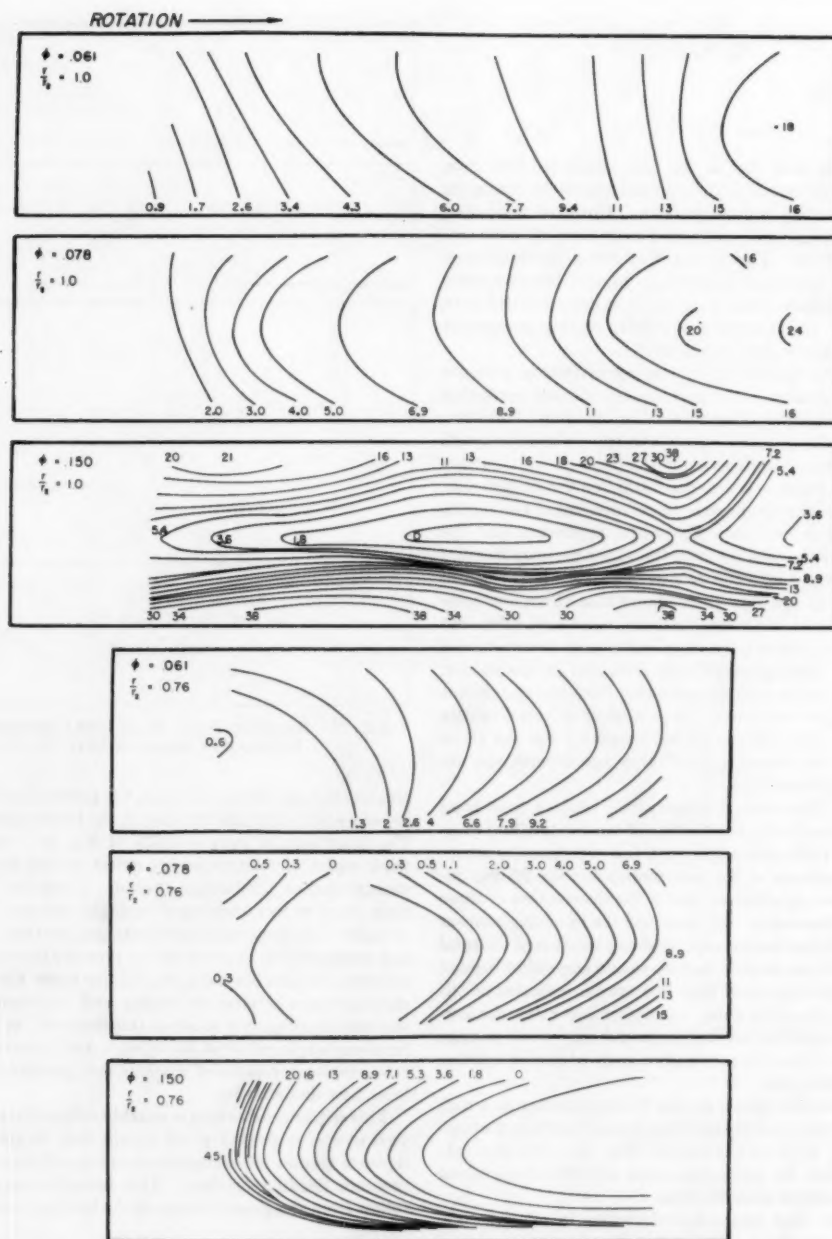


FIG. 17 RELATIVE TOTAL HEAD-LOSS CONTOURS AT EXIT ($r/r_2 = 1.0$) AND MID-RADIUS ($r/r_2 = 0.76$) FOR 15-DEG IMPELLER

the suction side of the vane progressively deteriorates from the inner to the outer radial stations. In fact, for all flow rates except the very highest the velocity distributions near the exit strongly suggest that flow separation occurs near there. The other salient feature of Fig. 21 is the pronounced boundary layer that appears on the lower shroud at the inner radius at a flow rate coefficient of about $\phi = 0.06$. Also interesting is the "inverted" shape of the exit-velocity profiles somewhat above the design point. It would appear that the low-energy regions are being

centrifuged out of the impeller. This behavior has been noted before on rotating shrouds with no blades (12), wherein it was observed that a substantially separated main stream could be stabilized and reattached by sufficient shroud rotation.

Loss Coefficients. With the velocity profiles having been determined, it became possible to calculate weighted loss coefficients through the impeller. A true loss coefficient would be weighted with the radial velocity to account for variations in work of each fluid stream. Because flow angle was difficult to

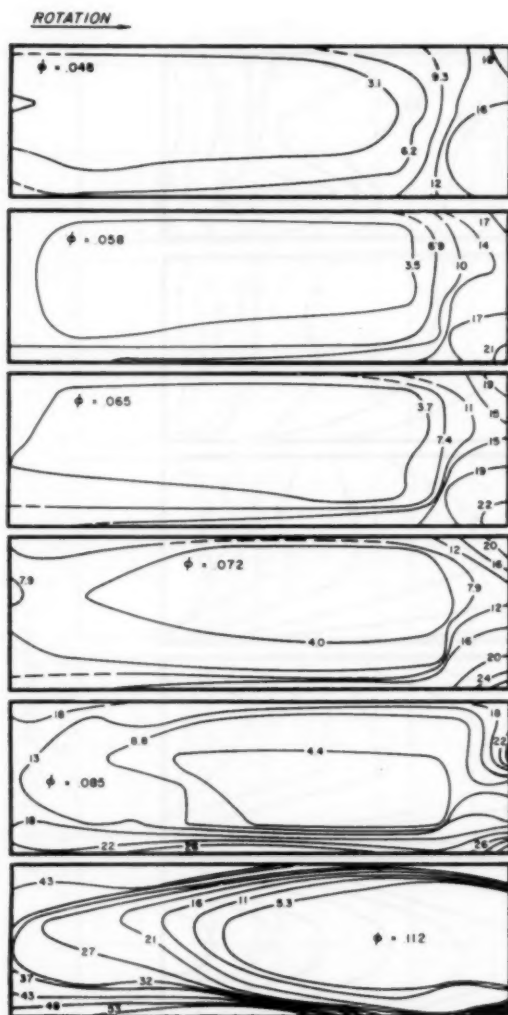


FIG. 18 RELATIVE TOTAL HEAD-LOSS CONTOURS FOR 12.5-DEG IMPELLER NEAR INLET ($r/r_1 = 0.73$)

measure, the loss coefficients were computed with relative velocity. Consequently, for flow rates much different from the design condition, errors must occur, and the resulting value must be too low. Fig. 22 shows this coefficient for the inlet and exit stations as a function of flow rate. At the design point it is seen that about 60 per cent of the total loss through the impeller has occurred at the inlet station $r/r_1 = 0.73$. It is interesting to note that the inlet loss rises sharply on either side of the design point. The exit-loss coefficient fails to show a rise for flow rates less than ϕ , probably because of the afore-mentioned errors incurred in the weighting procedure. At the design point, however, computation of efficiency by means of the weighted loss coefficients agrees to within a per cent or so with the measured value.

Comparison of Two-Dimensional Impellers. The over-all characteristics of the four two-dimensional impellers are similar and show the trends to be expected from the progressive decrease in inlet-vane angle. The internal flow patterns are unquestionably different, however, because of their different torque or brake-horsepower curves (Fig. 5). Qualitative information to this

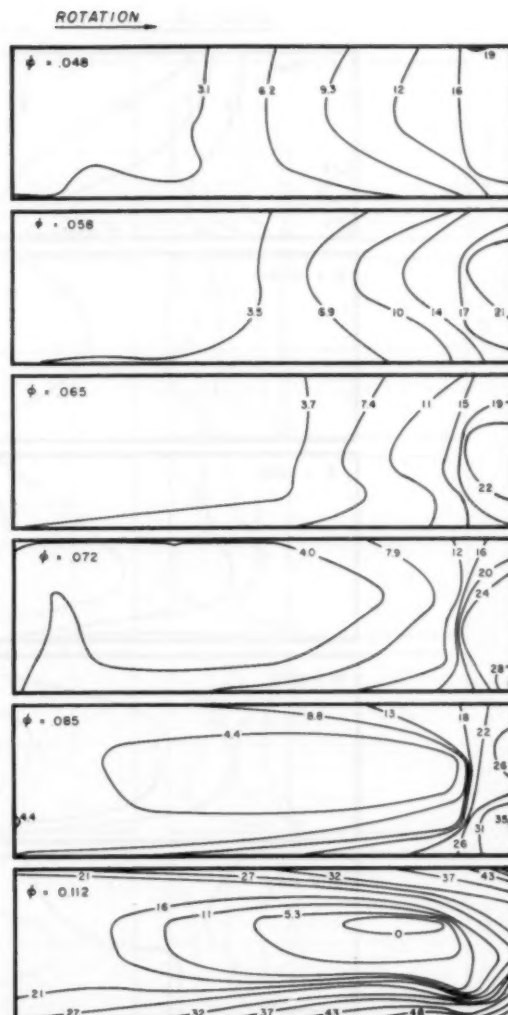


FIG. 19 RELATIVE TOTAL HEAD-LOSS CONTOURS FOR 12.5-DEG IMPELLER AT MID-RADIUS POSITION ($r/r_1 = 0.89$)

effect is offered by the loss contour plots of the 20 and 12.5-deg impellers. It is seen that, in general, fluid of low energy tends to be concentrated more behind the trailing side of the vane for the 12.5-deg impeller than the 20-deg one for all flow rates. Because of this fact the 12.5-deg impeller actually shows separated profiles near the exit at the design point, whereas the 20-deg impeller showed a much more uniform profile there. The difference is probably due to the excessive vane length of the 12.5-deg runner coupled with a continuous adverse pressure gradient.

It should be noted that separated flow in a pump will have a forced vortex-pressure rise through it rather than constant pressure as would be found on a stationary airfoil or blade of a cascade. The result is to centrifuge the separated region radially outward. Thus, separation in radial-flow machinery will not in general have as deleterious effects as it does in axial-flow machinery.

Three-Dimensional Impeller

Over-All Characteristics. In reference (2) Osborne and Morelli

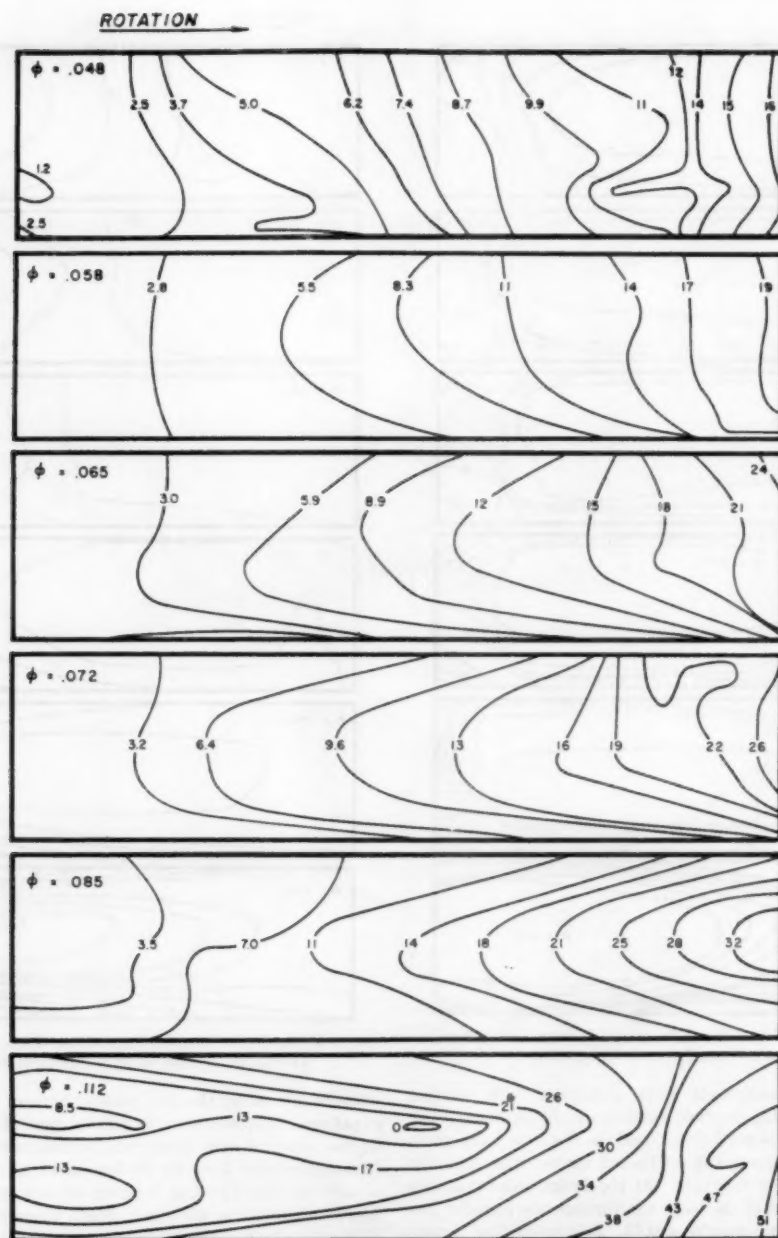


FIG. 20 RELATIVE TOTAL HEAD-LOSS CONTOURS FOR 12.5-DEG IMPELLER AT IMPELLER EXIT ($r/r_1 = 1.0$)

present complete characteristic data on several "three-dimensional" impellers, and the data on a 17-deg-exit-angle impeller is reproduced in Fig. 10. Fig. 23 shows a profile sketch of the impeller. It is clear from Fig. 10 and those of reference (2) that the three-dimensional characteristics agree much better with the theoretical calculations than do the two-dimensional ones. The fact that the measured head on the 17-deg impeller is slightly higher than the theoretical prediction is not understood at the present time, and in (2) this difference is attributed to real fluid effects.

A surprising fact is that the head curves of the 17-deg three-dimensional impeller do not fall off with increasing flow rate as rapidly as do the 23.5-deg two-dimensional impellers. This result appears (as is discussed later) to be due to the differences in inlet loss and velocity distribution of the two impeller types.

Internal-Loss Distributions. Loss contours for different flow rates are shown in Fig. 24 at the exit and in Fig. 25 at the inlet. Near and above best efficiency conditions the exit contours indicate a moderate boundary layer on the bottom shroud and some

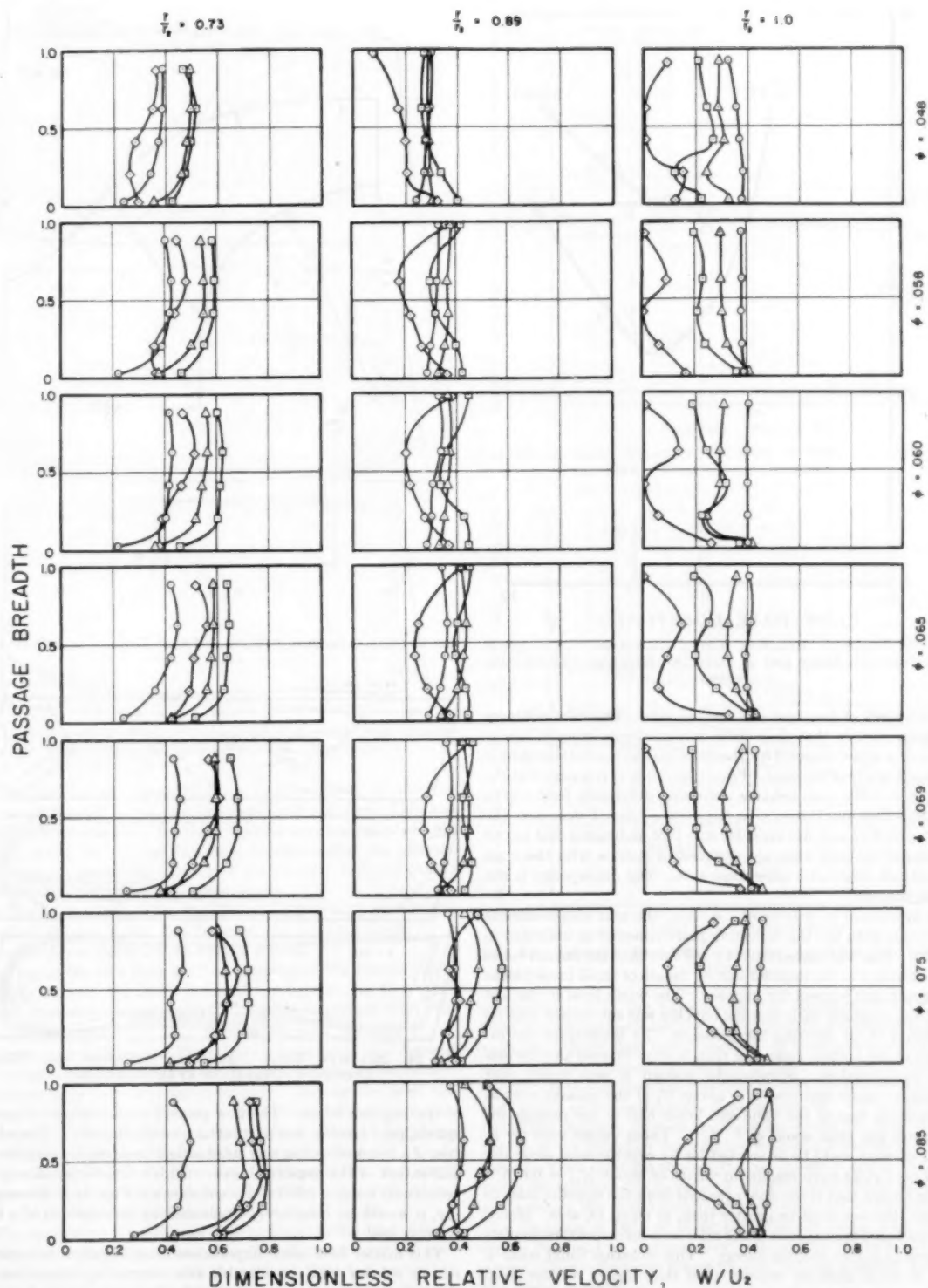


FIG. 21 RELATIVE VELOCITY PROFILES FOR 12.5-DEG IMPELLER AT THREE RADII FOR SEVERAL FLOW RATES
(Fraction of passage width, measured from pressure-face of vane: $\circ = 0.2$, $\triangle = 0.5$, $\square = 0.8$, $\diamond = 0.95$.)

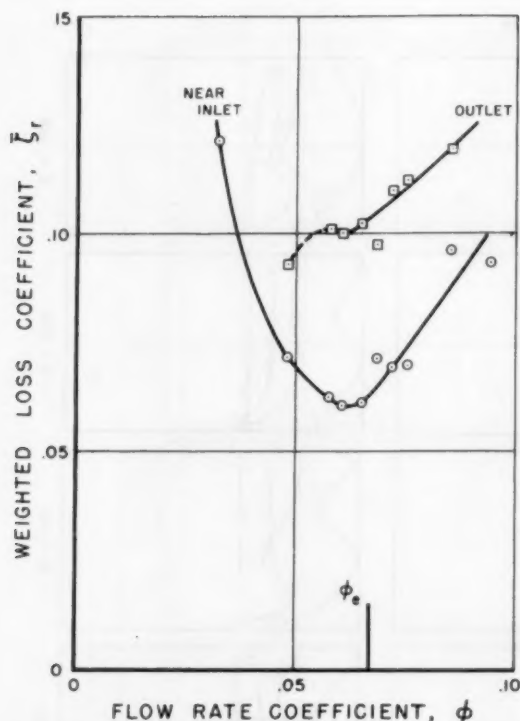


FIG. 22 WEIGHTED RELATIVE TOTAL HEAD-LOSS COEFFICIENTS NEAR IMPELLER INLET AND AT IMPELLER EXIT FOR 12.5-DEG IMPELLER

concentration of loss near the trailing side. The inlet contours are instructive in that they show only moderate areas of loss at higher flow rates, confined for the most part to the bottom shroud and trailing side of the vane. From Figs. 25(b, c) it is seen that the inlet edge of the vane behaves somewhat differently from top to bottom. Less loss is seen near the bottom shroud than near the top at $\phi = 0.12$ and vice versa for $\phi = 0.16$, indicating that not all sections of the inlet vane are designed to operate with the same inlet attack angle at a given flow rate. The discrepancy is not severe, however.

As mentioned in a foregoing section, the exit measurements were made with the top collecting plate removed as indicated in Fig. 23. This was necessitated by the fact that the impact tubes were attached to the impeller exit by means of small brass blocks that protruded beyond the impeller. The water level in the test basin was normally such that the impeller was submerged with no possibility of air entering the passages. To investigate the influence of the bottom collecting ring, it was removed and the loss data were retaken. Surprisingly enough it was found that "negative" losses occurred over about $1/3$ of the passage next to the pressure face of the vane and lower half of the passage for flow rates less than about $\phi = 0.10$. These values were far in excess of what could be accounted for by experimental error and based on $U_s^2/2g$ have maximum values of about $|\xi_r| = 0.075$.

It is known that if the flow proceeds from the impeller inlet to the exit, the loss must be greater than, or equal to, zero. Hence it is concluded the negative losses arise from an external recirculating flow of higher relative energy. This situation could occur if fluid of small absolute velocity (and thus higher relative total head) would circulate from the region exterior to the impeller discharge along the shrouds to the outer portions of the pressure side

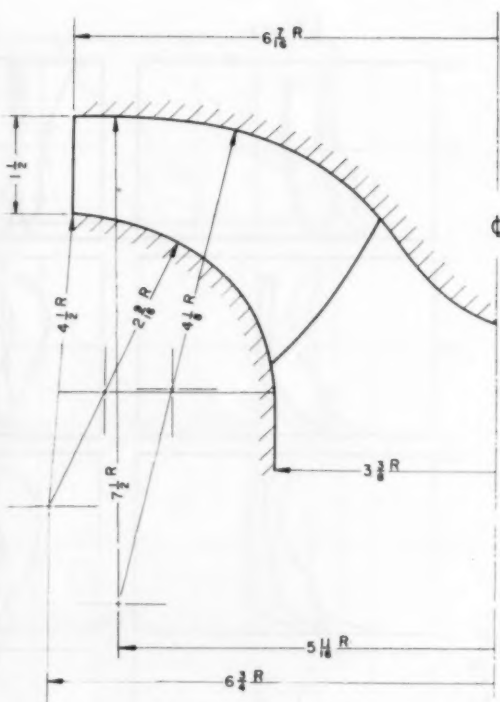


FIG. 23 CROSS-SECTION SKETCH OF THREE-DIMENSIONAL IMPELLER

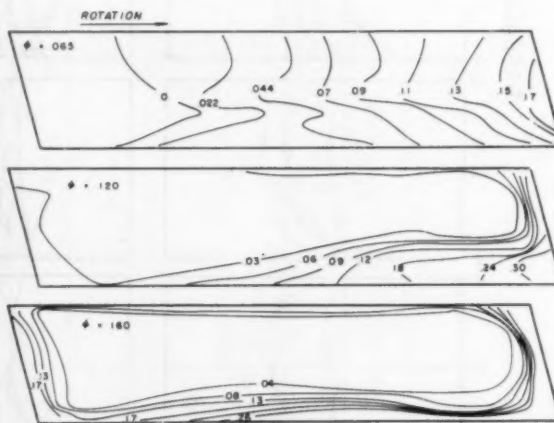


FIG. 24 RELATIVE TOTAL HEAD-LOSS CONTOURS FOR THREE-DIMENSIONAL IMPELLER AT IMPELLER EXIT

of the impeller blade. The flow picture would consist of loose spirals, part exterior and part interior to the impeller. The addition of a lower collecting ring substantially reduces the magnitude and extent of the negative losses. (This relatively small region occurs only for $\phi < 0.065$ and is not shown in Figs. 24.) Presumably, it would be completely eliminated by the addition of a top plate as well.

This matter is of some importance since impellers frequently run in volutes with considerable side clearance. According to these observations the velocity distributions and presumably also the head would be slightly different for such operation.

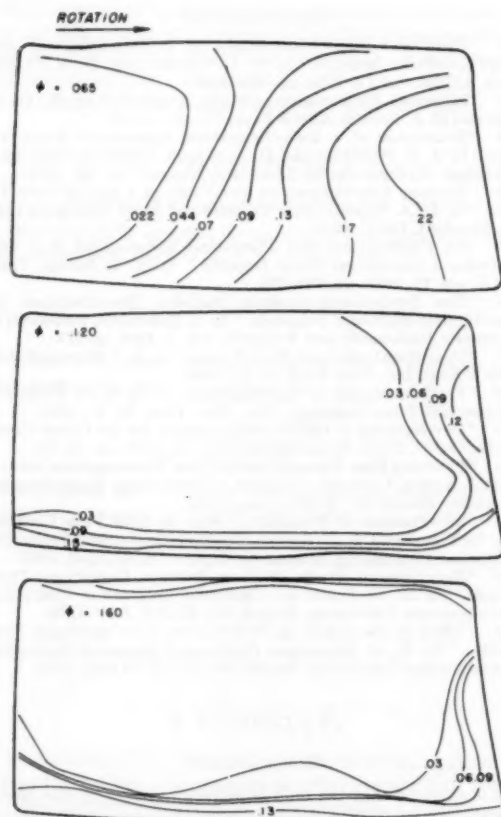


FIG. 25 RELATIVE TOTAL HEAD-LOSS CONTOURS FOR THREE-DIMENSIONAL IMPELLER NEAR IMPELLER INLET

Velocity Profiles. Static-pressure measurements on the top shroud at the exit of the impeller were made and from these and the loss determinations, relative velocities were computed and are shown in Fig. 26. It was necessary to assume that the pressure was constant across the breadth of the impeller, but this should not introduce serious error into the results.

It can be seen from these figures that for $\phi \geq 0.10$ the velocity distributions are fairly flat between the blades except for a boundary-layer region on the bottom shroud.

Owing to the fact that the inlet portions of the impeller were strongly curved, the static pressure throughout the flow could not be measured. Thus it was not possible to present inlet relative-velocity plots.

Comparison of Two and Three-Dimensional Impellers. Several of the salient differences between the two and three-dimensional impellers have been mentioned already. Among the most important of these is the difference in the head and flow-rate characteristics. In fact, the flow rate for zero head of the 17-deg three-dimensional impeller is higher than any of the 23.5-deg two-dimensional impellers. Furthermore, the slope of the ψ - ϕ curve agrees much better with potential theory (as mentioned before) and also is less steep than the two-dimensional results.

The reasons for this behavior may be found in the inlet surveys for the two cases (Figs. 20 and 25). The abrupt turn of the two-dimensional impeller gives rise to the large inlet loss previously mentioned and a large boundary layer on the bottom shroud. This behavior occurs more or less throughout the entire region of

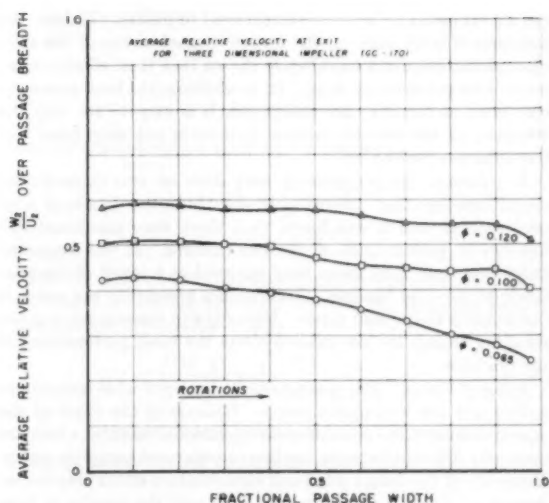


FIG. 26 AVERAGE RELATIVE VELOCITY AT IMPELLER EXIT FOR THREE-DIMENSIONAL IMPELLER

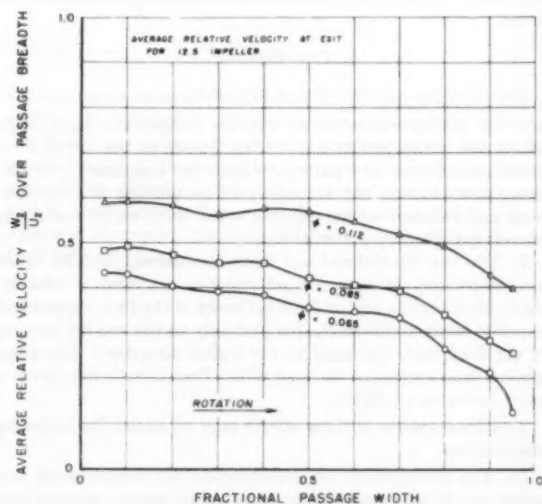


FIG. 27 AVERAGE RELATIVE VELOCITY AT EXIT OF 12.5-DEG IMPELLER

good efficiency in the two-dimensional impellers, but for the three-dimensional impeller the inlet performance is seen to be good until the highest flow rate observed. A comparison of the two and three-dimensional exit-velocity profiles is shown in Figs. 26 and 27. It is seen that the two-dimensional runners do not have exit profiles as flat as the three-dimensional one. In view of these facts, the simplest over-all explanation would be that the influence of the boundary layer at the inlet and subsequent formation of a thick retarded zone on the low-pressure side of the vane lower the effective blade angle of the two-dimensional impellers and increase the radial velocity by the blockage of the passage. The direction of both of these effects is the same; i.e., to decrease the head at a given flow rate and to steepen the ψ - ϕ curve. These effects are larger for the 12.5-deg impeller than for the 20-deg impeller.

Thus, it is not surprising that steeper head-flow-rate curves

can be exhibited by the two-dimensional impellers. In fact, the influence of inlet angle on the torque characteristics of the two-dimensional impellers has already shown that their effects on internal-flow patterns are large. If, in addition, the head losses encountered at the inlet are considered, it is easy to see why the efficiency of the two-dimensional runners is not only lower but has a sharper peak as well.

In reference (2) experiments were done on two three-dimensional impellers that differed only slightly in the details of inlet construction, and it was found that there were significant differences in performance of the two runners. It was suggested there that large inlet losses were incurred as a result of the relatively minor inlet changes. That such a possibility can occur is borne out in the present paper. Not only can losses occur, but the resulting change in flow pattern alters the basic performance of the machine.

Effect of Volute. The present results are applicable only to impellers and not a complete pump. Because of the effect of the case or volute, there are numerous operational features which are decidedly different between the free impeller and complete pump. However, at the design point and somewhat on either side the influence of the case is not marked (13) and the results of free-impeller tests may be applied there. At flow rates much lower, and particularly much higher than the volute-design point, significant deviations from the free-impeller performance are found.

CONCLUSIONS

The principal experimental results are:

1 In the two-dimensional impeller series, the inlet angle affects the entire performance characteristic of the impeller by initiating different flow patterns within the impellers. The differing flow patterns are demonstrated by varying loss distributions and different torque requirements. Such major variations are not indicated by potential theory.

2 The two-dimensional and three-dimensional impeller types have important differences in performance as a result of inlet design. Roughly one half of the total losses of the two-dimensional impeller occur at the inlet, due probably to the sudden turning of the fluid from the axial to the radial direction. The more gradual fluid turning at the inlet of the Francis-type impeller is a more favorable condition.

As a consequence of these effects may be added the following observations:

(a) The performance of well-designed three-dimensional impellers can be predicted closely by potential theory, whereas this cannot be done for the two-dimensional impeller; (b) a higher and broader range of efficiency is found for the three-dimensional impellers; (c) the head flow-rate characteristic of the two-dimensional impellers is steeper than that for the three-dimensional impellers (even for vane angles exceeding the three-dimensional value); (d) with the two-dimensional impeller, as inlet angle is reduced, the flow rate for maximum efficiency decreases with the efficiency value remaining about the same, but the range of flow rates (in percentage) for high efficiency is reduced.

The present experiments, although fairly extensive, do not begin to explain many of the important problems that remain. However, it is hoped that the data and results given will prove to be of some use to designers and experimenters in this field.

ACKNOWLEDGMENT

The authors would like to express their appreciation to Dr. D. A. Morelli and Prof. A. Hollander for many helpful suggestions and discussions.

BIBLIOGRAPHY

- 1 "Head and Flow Observations on a High-Efficiency Free Centrifugal-Pump Impeller," by W. C. Osborne and D. A. Morelli, *Trans. ASME*, vol. 72, 1950, pp. 999-1007.
- 2 "Measured Performance of Pump Impellers," by W. C. Osborne and D. A. Morelli, ASME Paper No. 50-A-90.
- 3 "Evaluation of a Two-Dimensional Centrifugal Pump Impeller," by J. H. Beveridge and D. A. Morelli, California Institute of Technology Hydrodynamics Laboratory Report No. 90, 1950.
- 4 "Pressure Distributions on the Vanes of a Radial Flow Impeller," by D. A. Morelli, *Heat Transfer and Fluid Mechanics Institute*, Stanford, Calif., 1951.
- 5 "An Experimental and Theoretical Investigation of a Two-Dimensional Centrifugal Pump Impeller," by A. J. Acosta, *Trans. ASME*, vol. 76, 1954, pp. 749-763.
- 6 "Das Förderhohenverhältnis Radialer Kreispumpen mit Logarithmisch-Spiraligen Schaufeln," by A. Busemann, *Zeitschrift für angewandte Mathematik und Mechanik*, vol. 8, 1928, p. 372.
- 7 "Centrifugal and Axial Flow Pumps," by A. J. Stepanoff, John Wiley & Sons, Inc., New York, N. Y., 1948.
- 8 "Fluid Mechanics of Turbomachinery," by G. F. Wislicenus, McGraw-Hill Book Company, Inc., New York, N. Y., 1948.
- 9 "Development of the Hydraulic Design for the Grand Coulee Pumps," by C. Blom, *Trans. ASME*, vol. 72, 1950, pp. 53-70.
- 10 "Potential Flow Through Radial Flow Turbomachine Rotors," by A. J. Acosta, California Institute of Technology Hydrodynamics Laboratory Report No. E-19.5, June, 1954.
- 11 "Observations of Propagating Stall in Axial Flow Compressors," by T. Iura and W. D. Rannie, California Institute of Technology Mechanical Engineering Laboratory Report No. 4, April, 1953.
- 12 "Experimental Study of Flow Between Centrifugal Pump Shrouds," by H. N. Tyson, Jr., California Institute of Technology Hydrodynamics Laboratory Report No. E-19.6, July, 1954.
- 13 "Effect of the Volute on Performance of a Centrifugal Pump Impeller," by R. D. Bowerman, California Institute of Technology Hydrodynamics Laboratory Report No. E-19.7, March, 1955.

Appendix 1

BLADE DESIGN

It is assumed that the fluid is perfectly guided by the blades. The blade shape is then chosen to make the tangential or circumferential component of the absolute velocity increase linearly with radius. Thus, from the velocity triangle (Fig. 11) it can be seen that the equation of the streamlines or blade surface is

$$\tan \beta = \frac{dr}{r d\theta} = \frac{C_u}{U - C_u} \dots \dots \dots [1]$$

For constant impeller breadth $C_m = C_{m2} r_2/r$. The growth of C_u is now specified as

$$C_u = K_1(r - r_0)\omega$$

where K_1 and r_0 are constants. Equation [1] can be integrated to obtain

$$\theta = \frac{U_2}{C_{m2}} \left[\frac{1 - K_1}{2} \left(\frac{r}{r_2} \right)^2 + K_1 \frac{r_0 r}{r_2^2} \right] \dots \dots \dots [2]$$

The constant K_1 is evaluated at the impeller exit by stipulating the blade angle β_2 there; i.e.

$$C_{u2} = U_2 - \cot \beta_2 C_{m2} = K_1 \omega (r_2 - r_0)$$

or

$$K_1 = \frac{1 - (C_{m2}/U_2) \cot \beta_2}{1 - r_0/r_2} \dots \dots \dots [3]$$

The blade-exit angle β_2 of all impellers was chosen arbitrarily as $\beta_2 = 23.5$ deg. The four impeller designs were then obtained by selecting $C_{m2}/U_2 = 0.110$ with r_0/r_2 taking the values 0.55, 0.60, 0.65, 0.70, respectively. The inlet-blade angle β_1 is given by

$$\beta_1 = \cot^{-1} \left\{ \frac{1}{0.110} \left(\frac{r_1}{r_2} \right)^2 \left[1 - K_1 \left(1 - \frac{r_0}{r_1} \right) \right] \right\} \dots \dots [4]$$

The flow rate for "shockless" or smooth entry is designated as the design flow rate ϕ_d and is computed as that value for which the relative flow angle is equal to the blade angle (blade thickness is accounted for in this computation).

A summary of the design constants is given in Table 1.

Appendix 2

MEASUREMENT OF LOSS AND RELATIVE VELOCITY

The Bernoulli equation in rotating co-ordinates for a frictionless, incompressible flow is

$$p_s + \frac{\rho}{2} (W^2 - U^2) = \text{const} = p_T \dots \dots \dots [5]$$

If the total pressure p_t and static pressure p_s are measured at the same point, then

$$W = \left(\frac{p_t - p_s}{\rho/2} \right)^{1/2} \dots \dots \dots [6]$$

The quantity $p_t - p_s$ can be read directly on the rotating manometer, or p_t and p_s may be read individually as was done in the present experiments.

If the flow is not frictionless, then Equation [5] is modified by the loss in relative total head p_h , i.e.

$$p_t = p_T - p_h$$

where the subscripts are defined in notation, thus

$$p_s + \frac{\rho}{2} (W^2 - U^2) = p_T - p_h \dots \dots \dots [7]$$

The quantity p_h is measured directly on the rotating manometer by comparing the total pressure p_t with the inlet total pressure p_T (both pressures being read at the same radius, i.e., the manometer radius).

The loss coefficient is defined as

$$\zeta_r = \frac{p_h}{\frac{1}{2} \rho U_s^2}$$

and the static-pressure coefficient is defined as

$$C_p = \frac{p_s - p_T}{\frac{1}{2} \rho U_s^2}$$

Then the relative velocity, as a dimensionless quantity, can be calculated by solving Equation [7] with the foregoing substitution of dimensionless coefficients

$$\left(\frac{W}{U_s} \right)^2 = \left(\frac{r}{r_2} \right)^2 - C_p - \zeta_r \dots \dots \dots [8]$$

EFFICIENCY AND WEIGHTED-LOSS COEFFICIENT

It can be shown that the impeller efficiency is

$$\eta = \frac{\psi_d}{\psi_d + \zeta_{r/2}} = \frac{\psi_d}{\psi'}$$

where ζ_r is a weighted loss coefficient defined as

$$\zeta_r = \frac{\int \zeta_r W \sin \beta dA}{\int W \sin \beta dA} \dots \dots \dots [9]$$

both integrals being evaluated over the discharge area of the impeller. The angle β is the relative flow angle. Since this angle is difficult to measure, it is assumed constant over the passage cross section. This assumption can only be correct near the design or best efficiency point of the impeller. At other flow rates, and in particular low flow rates, the result must be low. In the figures of the report, the loss coefficients are usually expressed as fractions of the head.

Computer Representations of Engineering Systems Involving Fluid Transients

By F. D. EZEKIEL¹ AND H. M. PAYNTER,² CAMBRIDGE, MASS.

This paper deals with the applications of modern analog and digital computing machines to engineering solutions of fluid-transient problems. It is not concerned with the structural or operating details of the computers themselves. Rather, described here are methods for computer representations of various physical elements commonly used in hydraulic and pneumatic systems such as conduits, valves, pumps, and so forth. These are presented in such forms that they can be incorporated readily as component parts into a simulated engineering installation. Such methods permit rapid determination of critical dimensions as well as ready exploration of alternatives for balances between cost and performance.

NOMENCLATURE

The following nomenclature is used in the paper:

A	= area, sq ft
B	= controller adjustment parameter
C	= fluid capacitance, sq ft
$F(\)$	= function of
F	= stroking force, lb
g	= acceleration of gravity, ft/sec ²
g	= a constant
G	= a constant
H	= fluid head, ft
IP	= horsepower, ft-lb/sec
I	= fluid inertia, sec ² /ft ²
J	= pump rotary inertia, ft-lb-sec ² /rev
k	= a constant
K	= a constant
L	= conduit length, ft
M	= torque, lb-ft
N	= speed of rotation, rev/sec
P	= absolute stagnation pressure, psfa
P_s	= absolute static pressure, psfa
Q	= volumetric rate of flow, ft ³ /sec
s	= distance along a conduit, ft
$\text{sgn}(\)$	= signum function = $(-)/ - $
S	= weight storage, lb
t	= time, sec
T	= time parameter, sec
T_α	= downstream wave travel time, sec
T_β	= upstream wave travel time, sec
U	= transformed pressure variable, lb/ft sec ^{1/2}
V	= fluid velocity, fps
\mathcal{V}	= volume, cu ft

\mathcal{V}	= transformed flow variable, lb/ft sec ^{1/2}
W	= weight rate of flow, lb/sec
X	= stroking lever position parameter
X	= general input variable
\mathbf{X}	= vector input
Y	= general output variable
\mathbf{Y}	= vector output
z	= height above a datum level, ft
Z	= conduit surge impedance, sec/ft ²
β	= fluid bulk modulus, psf
γ	= fluid weight density, pcf
ρ	= fluid mass density, lb-sec ² /ft ⁴

Subscripts a and b generally denote the upstream and downstream ends of a conduit, respectively.

INTRODUCTION

Within a brief ten years, the coming into existence of electronic computing machines has made accurate calculations describing complex physical situations entirely practical in cases formerly beyond reach. Contemporary literature is now replete with examples in all branches of technology employing every type of commercially available equipment (1-10).³ The present effort will be restricted to outlining particular forms of analysis and representation of hydraulic components with citation of but a few recurrent engineering problems involving hydraulic transients (11-15).

1-PROBLEM FORMULATION

PHYSICAL PROCESSES AND THE SYSTEM CONCEPT

It is possible to make a fairly clear-cut distinction between basic physical and chemical processes and complex engineering systems. In the former, isolation is both assumed and established; and the problems are concerned chiefly with the ascertainment of predictive relationships between significant variables. In the engineering situation on the other hand, interconnection of primitive components is essential, the problems being concerned with determination of over-all system behavior given a set of specific components (16).

In either case, from an abstract viewpoint, one is confronted with a *system* in which generally a multiplicity of observed variables Y_i is at least assumed to be related to another multiplicity of known or unknown variables X_k . The first multiplicity we can think of as the *output vector* \mathbf{Y} and the second group as the *input vector* \mathbf{X} . Thus, the functional dependency may be expressed as

$$\mathbf{Y} = \Psi(\mathbf{X})$$

Historically, the \mathbf{X} quantities have also been called *independent* or *exogenous* variables and by contrast, the \mathbf{Y} quantities, the *dependent* or *endogenous* variables. Fig. 1 shows how these concepts can be applied to a general system. The arrows indicate the *directional causal sense* of information or signal flow, while the balloons or blocks house the functional operators.

³ Numbers in parentheses refer to the Bibliography at the end of the paper.

¹ Assistant Professor of Mechanical Engineering, Massachusetts Institute of Technology. Mem. ASME.

² Assistant Professor of Mechanical Engineering, Massachusetts Institute of Technology; President, Pi-Square Engineering Company, Inc., Boston, Mass. Mem. ASME.

Contributed by the Hydraulic Division and presented at the Annual Meeting, New York, N. Y., November 25-30, 1956, of THE AMERICAN SOCIETY OF MECHANICAL ENGINEERS.

NOTE: Statements and opinions advanced in papers are to be understood as individual expressions of their authors and not those of the Society. Manuscript received at ASME Headquarters, August 6, 1956. Paper No. 56-A-120.

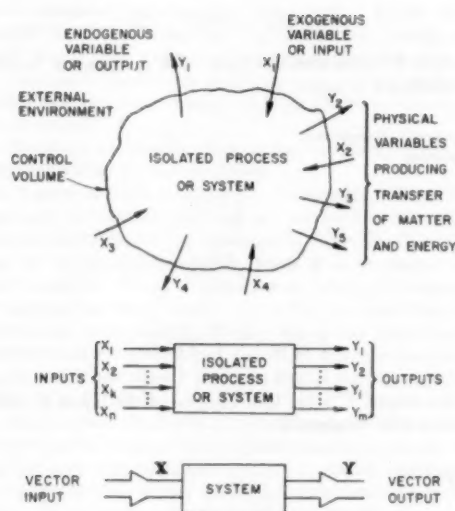
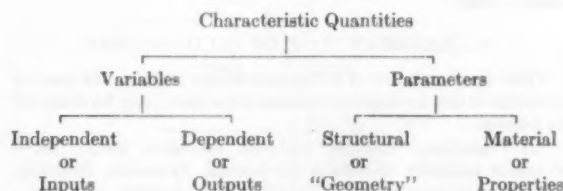


FIG. 1 THE SYSTEM CONCEPT

Besides these X and Y -quantities, a physical system also is generally described by means of its *geometry or structural parameters* and by its *properties or material parameters*.

The foregoing characteristic quantities may be arranged usefully in a table as follows:



It is the task of basic science to determine the characteristic parameters for the processes of interest; it is the task of engineering and the applied science to so interconnect the variables in system complexes as to put this knowledge to productive use.

MODELS

Whenever an engineering problem must be studied other than by direct manipulation of the actual system involved, it is necessary to have recourse to *models* of some type (17, 18, 19). Often these are *conceptual models* existing only as abstractions and idealizations of a real situation. In other circumstances, *actual models* in the form of physical counterparts are involved. In either case, one is concerned with the quantitative and qualitative extent to which the model is a copy of the system. All modeling in this paper is that of the conceptual type since the simulation is primarily directed toward the use of computers. However, it should be noted that such computer assemblies do themselves constitute physical models.

SCHEMATA AND BLOCK DIAGRAMS

Since early days, pictorial representations of real and abstract systems have been of great practical use in all branches of science and engineering. These run the gamut from portrayals giving complete, explicit photographic detail to simplified symbolic formulas with only abstract, implicit significance. Among such

representations, we encounter schematic and circuit diagrams. These attempt to reduce a system to its skeletal features only, with emphasis on representing functional and behavioral aspects, alone, without distracting details. The task of constructing and interpreting such diagrams necessarily involves the application of human subjective judgment. For example, electrical engineering has been advanced no small degree due to the ease with which physical systems can be conceived and constructed through the use of circuit diagrams. Moreover, particularly in the fields of electronics and communication, even without skilled training, it is possible to obtain a strong intuitive feeling for behavior from such diagrams.

This trend toward schematization has been carried further in the modern fields of communication and control; the use of *causally directed schemata* or *block diagrams* which originated in these fields is now diffusing throughout every branch of science. In such representations, only the interconnected flow and transformations of the various system signals are represented. In the particular case of the "signal flow graphs" (American) or "schemes of dependency" (British), often even the specific functional relationships are made secondary (that is, the "blocks" are suppressed), with primary emphasis on *causal dependencies* alone.

FIRST PRINCIPLES OF FLUID DYNAMICS

The basic principles governing unsteady-flow situations are just as for steady flow, the conservation of both matter and energy as influenced by appropriate standard geometries. The available mechanical-energy content in a fluid stream at a given point can still be measured in terms of the total pressure P , where

$$P \equiv P_s + \gamma z + \frac{\rho V^2}{2} \dots \dots \dots [1]$$

where P_s is the static pressure at a given point in the flow. Because changes in elevation z and stream velocity V represent negligible fractions of the energy content of the stream in most high-pressure systems, it is often only necessary to measure the static pressure in a stream to approximate its total pressure. However, in certain applications the energy effects of changes in elevation and stream velocity are important.

The rate of mechanical-energy flow, or *fluid-power transfer* across any normal section of a fluid stream is given by

$$IP = \frac{P \cdot W}{\gamma} = \gamma H \cdot Q = H \cdot W = P \cdot Q \dots \dots \dots [2]$$

The particular choice of any of the foregoing formulations depends both on the nature of the fluid and the system under consideration. For example, when dealing with liquids, the volumetric flow rate Q is generally preferred, and if the system contains free surfaces, then the total head H is convenient. However, in certain other applications, the total pressure P is found to be more appropriate. Moreover, when dealing with compressible fluids where changes in densities are substantial, the use of the weight-rate of flow W and the total pressure P is preferred both for convenience in measurements and for proper accounting of the conserved mass.

2-COMPUTING OPERATIONS

Although various modern computing machines differ in many respects, they can generally be classified into two major types:

(a) *Digital computers* which compute by counting. Their operations consist of simple arithmetical operations plus storage of information and other logical functions (1-4).

(b) *Analog computers* which compute by measuring. Their operations consist of making such physical quantities as voltages obey the same mathematical relations as the physical quantities in

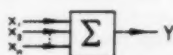
the system to be studied with accompanying display and recording of these computer variables (5-10).

UNIVERSAL OPERATIONS

Given in the following paragraphs are certain universal operations, which can be realized easily in both digital and analog computers and which will be employed throughout this paper. It should again be emphasized that this paper is concerned only with the logical programming and not with the detailed operations of particular computing devices.

(a) Static Operations

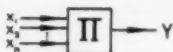
Summation



$$Y = X_1 + X_2 + \dots + X_n = \sum_{k=1}^n X_k \quad [3]$$

where the output Y is the summation of the input variable X_1, X_2, \dots, X_n .

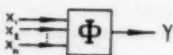
Product



$$Y = X_1 \cdot X_2 \cdot \dots \cdot X_n = \prod_{k=1}^n X_k \quad [4]$$

where the output Y is the product of all the inputs X_1, X_2, \dots, X_n .

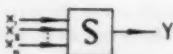
Functional Dependency



$$Y = \Phi(X_1, X_2, \dots, X_n) \quad [5]$$

where the output Y is a function of all the inputs X_1, X_2, \dots, X_n .

Selection (Reference 6)

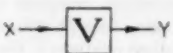


$$\text{Upper selection: } Y = l.u.b.(X_k) = S^+(X_k) \quad [6a]$$

$$\text{Lower selection: } Y = g.l.b.(X_k) = S^-(X_k) \quad [6b]$$

The output Y is either the *least upper bound* (upper selection) or *greatest lower bound* of the inputs X_1, X_2, \dots, X_n .

Rectification (special case of selection)

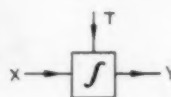


$$Y = |X| = S^+(X, -X) \quad [7]$$

The output Y is the absolute value of X or, what is the same thing, whichever is larger, X or $-X$.

(b) Temporal Operations

Integration



$$Y(t) = \frac{1}{T} \int X(t) dt \quad [8]$$

where the output Y is the time integral of the input X , with an integrating time constant T .

Delay



$$Y(t) = X(t - T) = \Delta(X) \quad [9]$$

where the output Y is identical to the input X but delayed by T units of time.

3-TRANSIENT FLOW OF FLUID ENERGY

From the standpoint of power and energy transfer, the various elements in any hydraulic or pneumatic system may be classified as follows:

(a) *Transducers* (pumps, turbines, actuators, etc.). These elements normally transform mechanical, hydraulic, electrical, etc., types of energies into one another. For example, a pump receives a torque M at a speed N and delivers a fluid flow Q at pressure P as is shown by the block diagram in Fig. 2. Here, Q and N are taken as inputs and P and M as outputs. The indicated Φ 's are functional operators whose specific nature depends on the so-called "complete characteristics" of the pump (13, 14). In certain cases, a limited amount of modulation (see below) can be imposed on a transducer as is the case in a variable-displacement pump. In this latter situation, another signal (X) such as a stroke lever position must be introduced in the block diagram in Fig. 2.

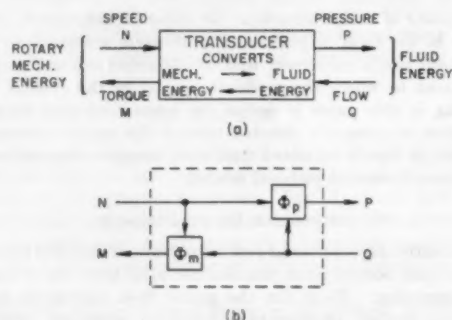


FIG. 2 TRANSDUCER BLOCK DIAGRAM

(b) *Modulators* (valves, throttles, etc.). These elements normally control or modulate the amount of energy passing through them. Generally they can be classified into two types:

1 *Dissipative modulators* (such as relief valves, gate valves, and throttles) which necessarily dissipate available fluid energy in order to control.

2 *Structural modulators* (such as needle valves) which modulate by controlling the flow geometry.

Fig. 3 shows a block diagram for a modulator. Here, the upstream and downstream pressures are assumed to determine the flow as modulated by the stroke variable. Thus, P_a , P_b , and X are inputs or independent variables, while Q is an output or dependent variable. In many applications, where it is necessary to know the reaction force of the stem so that the power to position the valve can be calculated, another functional block should be introduced that will give the magnitude of this force as a function of the hydraulic variables P and Q as well as the valve position X as is shown in Fig. 3(c).

(c) *Transmitters* (fluid conduits, tanks, etc.). These elements serve to transmit or store fluid momentum and/or mass. Fig. 4 shows the only four realizable configurations for representing a fluid transmitter, involving simple permutations of inputs and outputs. In these diagrams the subscript a signifies the upstream and b , the downstream end of the transmitter, respectively.

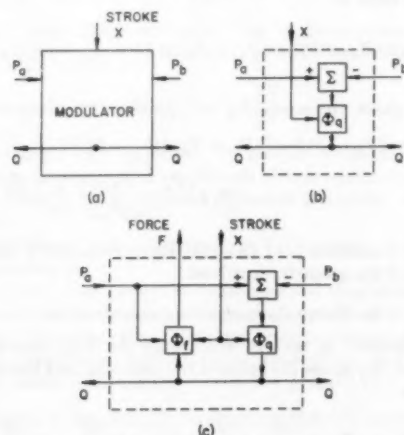


FIG. 3 MODULATOR BLOCK DIAGRAM

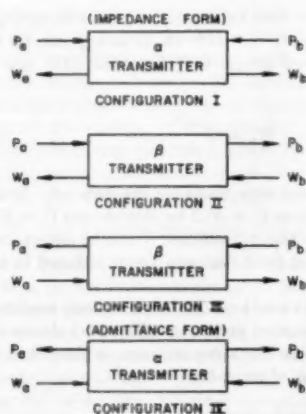


FIG. 4 BLOCK DIAGRAM FOR FLUID TRANSMITTERS

Power-transfer considerations, as described later, limit the possibilities to just those four configurations shown in Fig. 4.

Configuration I

Inputs or independent variables: P_a and P_b
Outputs or dependent variables: W_a and W_b

Configuration II

Inputs: P_a and W_b
Outputs: P_b and W_a

Configuration III

Inputs: P_b and W_a
Outputs: P_a and W_b

Configuration IV

Inputs: W_a and W_b
Outputs: P_a and P_b

The α and β labels merely signify that the inputs are of like or unlike kind, respectively. By analogy to the corresponding electrical situations, the two possible α -type transmitter representations may be considered as *impedances* or *admittances*, depending on whether they are pressure or flow driven, respectively.

It should be noted that in all the foregoing cases the fluid-power transfer at each end of the device must be determined by one input variable and one output variable.

The remainder of the paper will be devoted to a detailed discussion of the contents of the block diagrams in Figs. 2, 3, and 4 in terms of specific computer operations. Fig. 5 shows how a simple fluid system can be conceived in terms of the various elements cited. The particular choice of inputs and outputs, of course, primarily depends on the specific nature of elements involved.

4—PHYSICAL OPERATIONS AND TRANSFORMATIONS

The following three classical elementary concepts form the basic physical components for analyzing any fluid-conduit control or storage medium.

A—FLUID RESISTANCE AND CONDUCTANCE

While available energy is dissipated as heat throughout the extent of any fluid device, the effects of friction can be "lumped" by hypothetically establishing "friction joints" at which all the losses are assumed to occur. These so-called "friction losses" of available energy manifest themselves in the form of a pressure drop in the direction of flow, which may be expressed as

$$P_a - P_b = F(W) \dots \dots \dots [10]$$

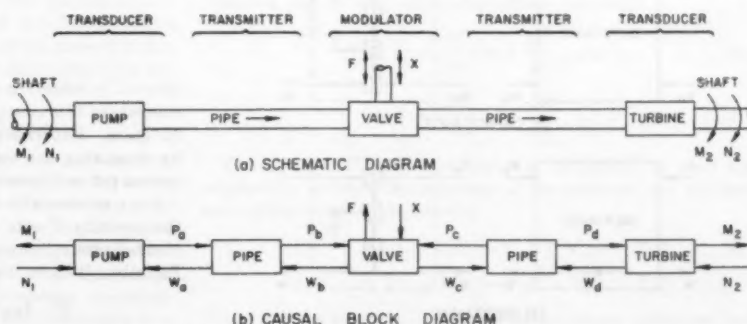


FIG. 5 CAUSAL REPRESENTATION OF A FLUID SYSTEM

The function $F(W)$ is readily determined for steady-state operation; however under transient conditions a rather different dissipative mechanism is involved. Fig. 6(a) shows a block diagram of a generalized resistance in the form of a modulator. Thus the upstream and downstream flows W are identical and, together with the downstream pressure P_b , determine the upstream pressure P_a . For most engineering purposes the loss term for liquid flows can be taken either as directly proportional to the flow (for laminar-flow conditions) or as proportional to the square of the flow rate (assuming turbulent-flow conditions with constant boundary-layer thickness)

$$P_a - P_b = K|W| \quad W = K \cdot \text{sgn } W \cdot W^2 = K\Phi_k(W) \dots [11]$$

where

$$\Phi_k(W) = |W|W$$

For gases, density variations alter this relationship to the form which may be approximated by the expression

$$P_a^2 - P_b^2 = k|W|W = k \cdot \text{sgn } W \cdot W^2 = k\Phi_k(W) \dots [12]$$

It is evident that k and K in Equations [11] and [12] are necessarily functions of the particular geometry involved. Fig. 7 depicts the diagram representing Equations [9] and [10].

In a manner similar to treating a resistance, the dual concept of fluid conductance, such as a nozzle, can now be represented since the flow through such an element is a function of the pressure drop across it

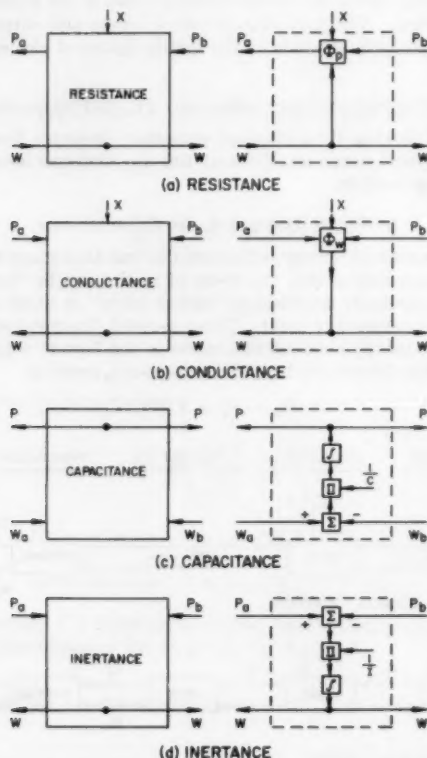


FIG. 6 BLOCK DIAGRAMS FOR FLUID ELEMENTS

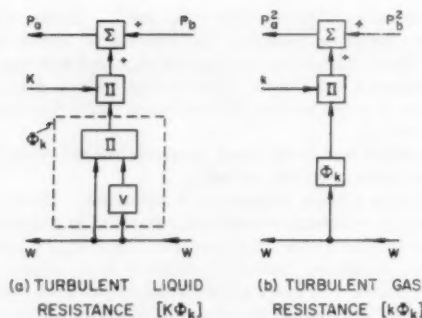


FIG. 7 TURBULENT-FLUID RESISTANCES

$$W = F(P_a - P_b) \dots [13]$$

A block diagram for representing a general conductance is shown in Fig. 6(b) as an α -transmitter. The pressure difference $P_a - P_b$ determines the flow W . The representation of a variable resistance and conductance falls under the general scheme of representing modulators as has been discussed earlier.

For liquids, an expression corresponding to Equation [13] takes the form of

$$W = G \cdot \text{sgn } (P_a - P_b) \cdot \sqrt{|P_a - P_b|} = G \frac{(P_a - P_b)}{\sqrt{|P_a - P_b|}} \dots [14]$$

while for gases, corresponding to Equation [12], there results

$$W = g \cdot \text{sgn } (P_a - P_b) \cdot \sqrt{[(P_a + P_b)(P_a - P_b)]} = g \frac{(P_a - P_b) \sqrt{(P_a + P_b)}}{\sqrt{|P_a - P_b|}} \dots [15]$$

Again, in Equations [14] and [15] the parameters G and g are functions of the geometry involved.

B—FLUID CAPACITANCE (MASS STORAGE)

For a conduit or tank in which only the fluid capacitance is considered, Equation [16] relates the incoming and the outgoing flow rates

$$W_a - W_b = \frac{dS}{dt} = \frac{d}{dt} (\gamma U) = \gamma \frac{dU}{dt} + U \frac{d\gamma}{dt} \dots [16]$$

where S is the weight of the fluid in the tank or conduit having a volume U and weight density γ . If both U and γ can be assumed functions of the total pressure P , Equation [16] can be written

$$W_a - W_b = C \frac{dP}{dt} \dots [17]$$

where C is defined as the fluid capacitance of the element. In the case where U is constant, then $C = S/\beta$ for liquids and $C = S/P$ for gases. Experimentally the capacitance C can be determined by measuring the weight of fluid that can be introduced in the system per unit pressure rise.

For a process with small variations about some mean condition the quantity C can be assumed constant. Fig. 6(c) shows the block-diagram representation for a capacitance as described by Equation [17], in the form of an α -transmitter.

C—INERTANCE (MOMENTUM STORAGE)

For a frictionless conduit in which only the effects of fluid

inertia are considered, Euler's equation for fluid flow may be written in the following form

$$-\frac{\partial P}{\partial s} = \rho \frac{\partial}{\partial t} \left(\frac{W}{\gamma A} \right) = \frac{1}{gA} \frac{\partial W}{\partial t} + \frac{\rho W}{A} \frac{\partial}{\partial t} \left(\frac{1}{\gamma} \right) + \frac{W}{g} \frac{\partial}{\partial t} \left(\frac{1}{A} \right) \dots [18]$$

or

$$-\frac{\partial P}{\partial s} \approx \frac{1}{gA} \frac{\partial W}{\partial t} \dots [18a]$$

where P is defined as the stagnation pressure. The last two terms on the right-hand side of Equation [18] can be neglected in considering inertia only, since all volume and density changes are necessarily included in the capacitance effect above.

Equation [18a] may then be spatially integrated to the form

$$P_a - P_b = I \frac{dW}{dt} \dots [19a]$$

where

$$I \equiv \frac{1}{g} \int_0^L \frac{ds}{A}$$

is defined as the fluid inductance. For an incompressible fluid, Equation [19a] is usually expressed in terms of head H and flow Q

$$H_a - H_b = I \frac{dQ}{dt} \dots [19b]$$

The inductance I in Equations [19] can be determined experimentally by measuring the weight rate of fluid acceleration in the element when a given pressure difference is applied across its terminals.

Fig. 6(d) shows a block diagram for an inductance, in the form of an α -transmitter.

It should be noted from the definitions and diagrams that resistance and conductance, as well as inductance and capacitance, are respective dual concepts. Moreover, resistance and inductance are both impedance aspects while conductance and capacitance are admittance aspects of any flow geometry.

SPATIALLY DISTRIBUTED ASPECTS OF FLUID CONDUITS

All fluid-transmission systems extend through space and time and may be concentrated at one or more points in space only when the spatial variations in flow variables are negligible with respect to temporal changes. Thus a system may be characterized roughly by means of such concentrated, discrete, or lumped models whenever the significant wave lengths of all variables are reasonably large as compared to the physical dimensions of the system. Otherwise, the actual distributed nature of the system may produce appreciable effects not present in any lumped model. Nevertheless, the lumping approximations frequently prove to be useful and convenient.

LUMPED-PARAMETER CONDUIT MODELS

In a conduit where the fluid capacitance, inductance, and resistance (or conductance) are all to be considered, a model can be visualized that incorporates the effect of each of these elements in a concentrated manner occurring one after another in space rather than all of them interacting in the same region. Fig. 8 shows how a conduit can be represented crudely in such a lumped elemental form by using the physical operations previously described. The most important effect of lumping the various elements in a conduit in this particular fashion is to replace a system having an

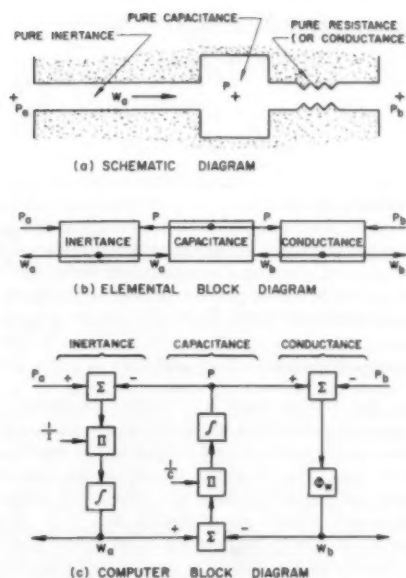


FIG. 8 LUMPED MODEL OF A FLUID CONDUIT

infinite number of degrees of freedom with a system having only one such degree. Although in many applications the error involved is quite tolerable, the behavior of the model bears no resemblance to that of the actual conduit for certain other cases. While the space sequence of the three elements was arbitrarily chosen in Fig. 8, the resulting system is only suitable for pressure inputs from both ends. For other systems having different terminal conditions, the fact that differentiating elements are usually avoided makes this lumped approximation impractical. Thus, the choice of the sequence of the elements also should be governed by the type of terminations to which the conduit is subjected.

REPRESENTATION OF CONDUIT WITH DISTRIBUTED PARAMETERS

A general variable-section conduit can always be approximated by a finite or infinite set of differing uniform, dissipationless transmitters separated by lumped resistances or friction joints. In practical cases, only a few such sections are required for each pipe, with friction lumped at either or both ends as indicated in Fig. 9.

For the foregoing reasons considerable attention centers upon the representation of a single, uniform frictionless pipe. The following pair of differential equations is then valid

$$-L \frac{\partial P}{\partial s} = I \frac{\partial W}{\partial t} \dots [20]$$

$$-L \frac{\partial W}{\partial s} = C \frac{\partial P}{\partial t} \dots [21]$$

The solution of these equations may be written to yield the relationship between the measures of the pressures and the flow rates at both ends of the conduit

$$U_b(t) + V_b(t) = U_a(t - T_a) + V_a(t - T_a) \dots [22]$$

$$U_a(t) - V_a(t) = U_b(t - T_b) - V_b(t - T_b) \dots [23]$$

These may be contracted in terms of time-delay operators (see Equation [9]) to the forms

$$U_s + V_s = \Delta_s(U_s + V_s) \dots \dots \dots [22a]$$

$$U_s - V_s = \Delta_s(U_s - V_s) \dots \dots \dots [23a]$$

where

$$U \equiv \frac{P}{\sqrt{Z}}; V \equiv W \sqrt{Z}$$

With parameters defined by

$$\text{Downstream wave travel time: } T_a \equiv \left[\frac{1}{\sqrt{IC}} + \frac{W}{LA\gamma} \right]^{-1}$$

$$\text{Upstream wave travel time: } T_b \equiv \left[\frac{1}{\sqrt{IC}} - \frac{W}{LA\gamma} \right]^{-1}$$

$$\text{Conduit surge impedance: } Z \equiv \sqrt{I/C}$$

The reason for writing these relationships in terms of time-difference equations and in the specific forms given is to enable one to construct a simple and universal block diagram, readily suitable for computer use. Fig. 10 shows the set of the four different representations of Equations [22a] and [23a], each configuration having inputs and outputs corresponding to Fig. 4. Fig. 11(a) shows a particular case (Configuration I) for P and W -variables. Fig. 11(b) illustrates the reduction in operations made possible when P_a is constant and the value of W_a is not required. This simplification is that used in Case 1 and Fig. 12 which follow.

5—SOME SPECIFIC APPLICATIONS

It is possible here to outline only a few of the many recurrent engineering problems involving fluid transients for which, in the experience of the authors, analysis and design have benefited from the use of modern electronic computers.

Specifically these selected problems are concerned with design decisions involving:

- 1 Water hammer in a pipeline system.
- 2 Air chamber and check valve in a pumping plant.
- 3 Control of flows and levels in a sewage tunnel system.

Here, only essential information has been given on the steps leading up to the formulation of the problems in mathematical terms starting from the basic physical situations. For further details, it will be necessary for most readers to refer to the many excellent existing books and papers, some of which have been indicated in the short Bibliography at the end of this paper. Moreover, we shall assume here that the mathematical formulation is correct, and will be concerned only with the steps necessary to obtain useful computer results.

The problems were chosen primarily to demonstrate the benefits of machine computing but otherwise represent excessive oversimplification resorted to only for the sake of brevity. However, from the versatility and generality of the methods used, the extensions to actual cases should be apparent.

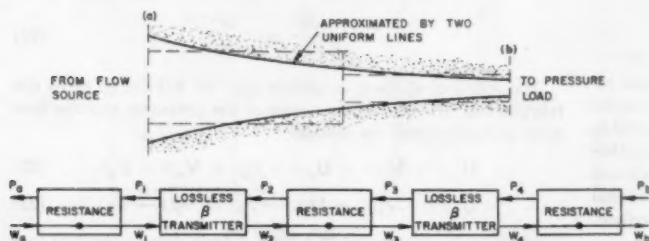


FIG. 9 PIPELINE OF VARIABLE CROSS SECTION

CASE 1—WATER HAMMER IN A PIPELINE SYSTEM

Let us consider the representative physical situation depicted in Fig. 12(a). A motor-operated valve located just below the junction is to be used for emergency shutoff of the water supply. In drawing up specifications for this valve it is necessary to consider in particular the effect of the closing-stroke characteristics on water-hammer pressures upstream and downstream of the valve.

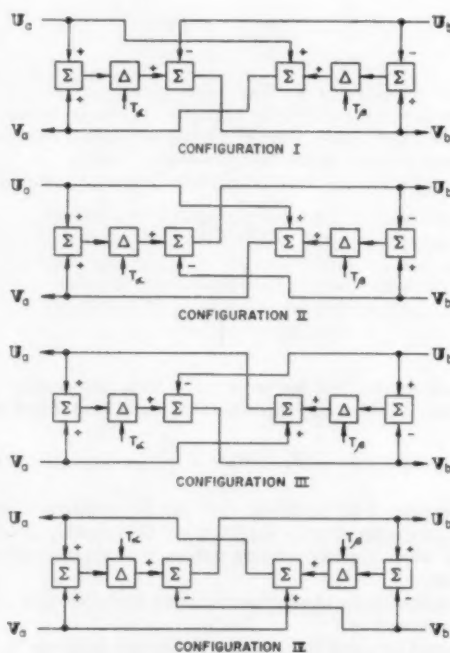
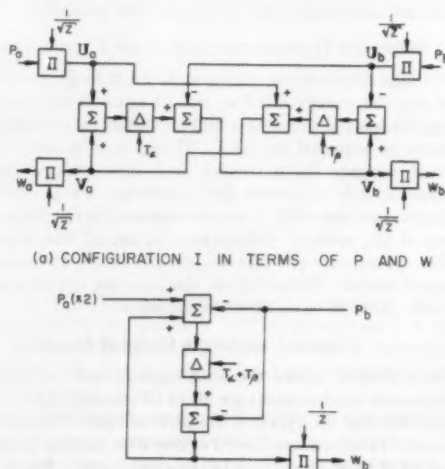


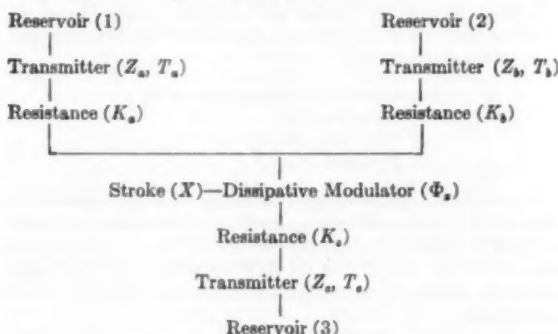
FIG. 10 DISTRIBUTED LOSSLESS CONDUIT MODELS



(a) CONFIGURATION I IN TERMS OF P AND W
(b) SPECIAL CASE WITH P_a = CONSTANT AND W_a NOT REQUIRED

FIG. 11 SPECIAL CASES OF LOSSLESS CONDUITS

This system is readily interpreted in terms of the concepts previously described, in the following form:



The assumed equations governing the performance of this system are the following

$$\text{Pipe a} \begin{cases} Z_a Q_a(t) = 2H_1 - H_a(t) + Z_a Q_a(t - T_a) \\ \quad - H_a(t - T_a) \dots [24] \\ H_a = H_s + K_s |Q_s| Q_s \dots [25] \end{cases}$$

$$\text{Pipe b} \begin{cases} Z_b Q_b(t) = 2H_2 - H_b(t) + Z_b Q_b(t - T_b) \\ \quad - H_b(t - T_b) \dots [26] \\ H_b = H_s + K_b |Q_b| Q_b \dots [27] \end{cases}$$

$$\text{Junction} \quad Q_s = Q_a + Q_b \dots [28]$$

$$\text{Valve} \quad H_v = H_d + K(X) |Q_v| Q_v \dots [29]$$

$$\text{Pipe c} \begin{cases} H_d = H_s + K_d |Q_d| Q_d \dots [30] \\ H_c(t) = 2H_3 + Z_c Q_c(t) - Z_c Q_c(t - T_c) \\ \quad - H_c(t - T_c) \dots [31] \end{cases}$$

These performance relationships are programmed for solution by electronic computer following the block diagram of Fig. 12(b). The symbols in the blocks correspond to those given in Section 2. All the variables in such a computer correspond to instantaneous signals and when the computer is properly interconnected it becomes, in effect, a flexible working model of the system.

It is flexible in the sense that every physical characteristic in the actual system corresponds to an adjustable constant in the computer setup so that changes in design or in operating conditions can be explored fully. It is a working model because it reproduces both transient and steady-state phenomena present in the actual setup but usually to different scales and in a different medium. For engineering studies of this sort, a high-speed, repetitive analog computer has many advantages.

For the foregoing case, in particular, curves showing pressure transients upstream and downstream of the control valve for different valve strokes may be obtained readily. Optimum stroking can be determined by simple experimentation in this way for any specific pipeline circumstance.

CASE 2—AIR CHAMBER AND CHECK VALVE IN A PUMPING PLANT

Fig. 13 depicts a fairly typical centrifugal-pump installation, which has been equipped with a throttled air chamber to protect the discharge main from excessive water-hammer pressures upon power failure and subsequent closure of the check valve.

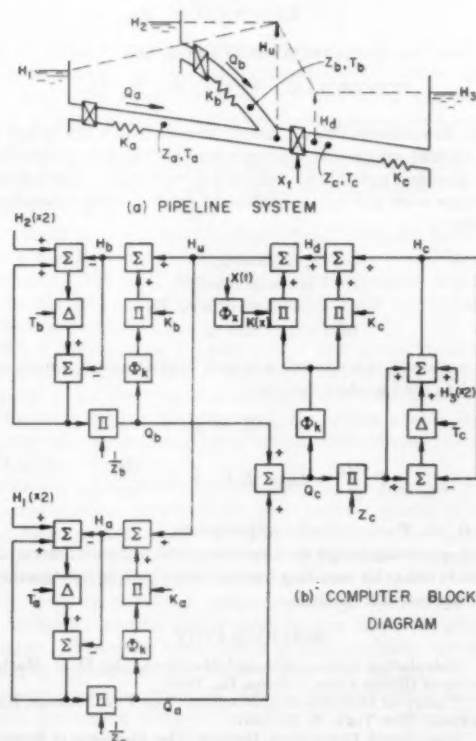


FIG. 12 WATER HAMMER IN A PIPELINE SYSTEM

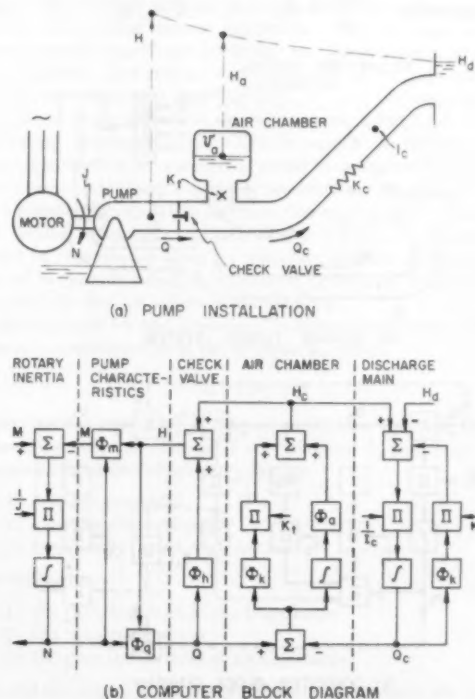
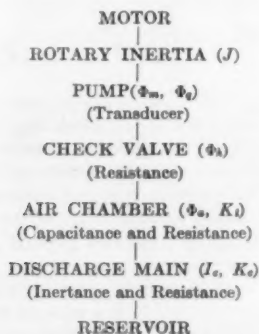


FIG. 13 AIR CHAMBER AND CHECK VALVE IN A PUMPING PLANT

The physical situation here also can be conceived in terms of the previous basic operations as:



The performance equations for this case can be taken as the following

$$\text{Pump acceleration} \quad J \frac{dN}{dt} = M_d - M \dots \dots \dots [32]$$

$$\text{Pump characteristics} \quad M = \Phi_m(N, H) \dots \dots \dots [33]$$

$$Q = \Phi_p(N, H) \dots \dots \dots [34]$$

$$\text{Check valve} \quad H = H_s + \Phi_h(Q) \dots \dots \dots [35]$$

$$\text{Air chamber} \quad \begin{cases} \frac{dV_a}{dt} = Q_s - Q = Q_i \dots \dots \dots [36] \\ H_s = \Phi_a(V_a) + K_i|Q_i|Q_i \dots \dots \dots [37] \end{cases}$$

$$\text{Discharge main} \quad I_s \frac{dQ_s}{dt} = H_s - H_d - K_s|Q_s|Q_s \dots \dots \dots [38]$$

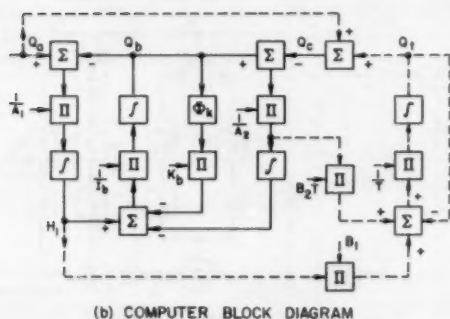
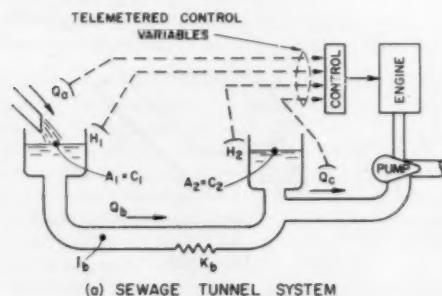


FIG. 14 CONTROL OF FLOWS AND LEVELS IN A SEWAGE TUNNEL SYSTEM

The computer block diagram for this case is shown in Fig. 13 (b).

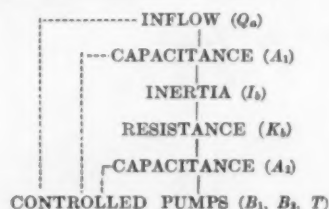
Typical engineering studies are concerned with effects on transient pressures in the discharge main of the following physical constants, among others:

- (a) Check-valve characteristics Φ_h
- (b) Air storage V_a
- (c) Throttling loss K_i
- (d) Flywheel effect J

In particular, such investigations (which, of course, correspond to those made conventionally by graphical or numerical methods) are used to determine the economic size of the control features, such as the air storage and the flywheel effect, and the design values of such items as the throttling constant and check-valve parameters.

CASE 3—CONTROL OF FLOWS AND LEVELS IN A SEWAGE TUNNEL SYSTEM

One of the authors was called upon to investigate the hydraulic transients occurring in a sewage-disposal system involving several deep-rock tunnels and to recommend schemes of control for the associated pumping installation. A simplified schematic of a comparable situation is portrayed in Fig. 14, where the dashed components denote the flow and level-control action. The physical elements are interconnected as follows:



If the downstream flow Q_s merely tries to follow the inflow Q_0 , rather violent surges will develop whenever the flow is disturbed. In the practical case, these could not be tolerated. Accordingly, the pumps were put under control of the following telemetered variables:

- (a) Input flow Q_0
- (b) Upstream level H_1
- (c) Downstream level H_2
- (d) Output flow Q_c

The nature of this control was such that the pumps were constrained to hold to the relations

$$\left. \begin{aligned} Q_c &= Q_0 + Q_i \\ T \frac{dQ_i}{dt} + Q_i &= B_1 H_1 + B_2 T \frac{dH_2}{dt} \end{aligned} \right\} \dots \dots \dots [39]$$

where B_1, B_2, T are controller-adjustments.

The engineering design studies were concerned with determining changes in behavior resulting from changes both in flow geometry as well as controller settings.

BIBLIOGRAPHY

- 1 "Calculating Instruments and Machines," by D. R. Hartree, University of Illinois Press, Urbana, Ill., 1949.
- 2 "Theory of Mathematical Machines," by F. J. Murray, Kings Crown Press, New York, N. Y., 1947.
- 3 "High-Speed Computing Devices," by Engineering Research Associates, McGraw-Hill Book Company, Inc., New York, N. Y., 1950.

- 4 "Giant Brains," by E. C. Berkeley, John Wiley & Sons, Inc., New York, N. Y., 1949.
- 5 "Electrical Analogies and Electronic Computers: Surge and Water Hammer Problems," by H. M. Paynter, Trans. ASCE, vol. 118, 1953, p. 962.
- 6 "A Palimpsest on the Electronic Analog Art," H. M. Paynter, Editor, G. A. Philbrick Researches, Inc., Boston, Mass., 1955.
- 7 "Analog Methods in Computation and Simulation," by W. W. Soroka, McGraw-Hill Book Company, Inc., New York, N. Y., 1954.
- 8 "Linear Transient Analysis," by E. Weber, John Wiley & Sons, Inc., New York, N. Y., 1954.
- 9 "Electronic Analog Computers," by G. A. Korn and T. M. Korn, McGraw-Hill Book Company, Inc., New York, N. Y., 1952.
- 10 "Introduction to Electronic Analog Computers," by C. A. A. Wass, McGraw-Hill Book Company, Inc., New York, N. Y., 1955.
- 11 "Methods and Results from M.I.T. Studies in Unsteady Flow," by H. M. Paynter, *Boston Society of Civil Engineers Journal*, vol. 39, April, 1952, pp. 120-165.
- 12 "Effect of a Hydraulic Conduit with Distributed Parameters on Control Valve Stability," by F. D. Ezekiel, ScD thesis, Department of Mechanical Engineering, Massachusetts Institute of Technology, Cambridge, Mass., 1955.
- 13 "Hydraulic Transients," by G. R. Rich, McGraw-Hill Book Company, Inc., New York, N. Y., 1951.
- 14 "Waterhammer Analysis," by J. Parmakian, Prentice-Hall, Inc., New York, N. Y., 1955.
- 15 "Engineering Fluid Mechanics," by C. Jaeger, Blackie & Son, London, England, 1956.
- 16 "Response of Physical Systems," by J. D. Trimmer, John Wiley & Sons, Inc., New York, N. Y., 1950.
- 17 "Similitude in Engineering," by G. Murphy, Ronald Press, New York, N. Y., 1950.
- 18 "Dynamical Analogies," by H. F. Olson, D. Van Nostrand, Inc., New York, N. Y., 1943.
- 19 "Analogy of Hydraulic, Mechanical, Acoustic, and Electric Systems," by J. C. Schoenfeld, *Applied Scientific Research*, section B, vol. 3, 1951-1953, pp. 417-450.

Discussion

S. L. KERR.⁴ The use of the analog computer and other automatic computing devices has increased rapidly within the past few years. The extent to which it is now being applied on so many different problems has made the apparatus itself generally available.

The authors have given us an excellent presentation of the procedures required for adapting the analog computer to problems in hydraulic transients.

It should be noted that the elastic-wave theory for water hammer and surge computation has been well confirmed in actual field tests. The agreement between the theoretical and actual results has been remarkably close, providing the theory has been applied properly.

Where discrepancies between theory and actual results have occurred, it is usually due to the theory having been applied improperly or incorrect assumptions or approximations used.

The same caution must be used in applying analog or other types of computers to surge problems since the results are only as good as the assumptions.

With arithmetic-integration procedures or the graphical method for surge analysis, errors usually show up very quickly since the basic diagrams are being referred to constantly. These methods also permit the analysis of discontinuous functions that otherwise might not be susceptible of determination.

The question of cost of apparatus and the cost of setting up the equations, circuits and procedures is a matter of great importance. Where the apparatus is already available, the cost of setting up an individual problem should not be great. On many problems where a variety of possible solutions needs to be explored, the analog computer or other types of automatic computers undoubtedly result in a great saving of time.

Where only a relatively few potential variations need to be studied, the writer questions whether the use of such computers can be justified. The economics of such procedures, of course, must be established in each individual case.

AUTHORS' CLOSURE

The authors would like to acknowledge both the kind remarks of Mr. Kerr and a long standing debt of gratitude for his interest and support. We wish to emphasize again that without people like him to pioneer in analysis and to pave the way for computing methods, our paper would have fallen on barren ground.

From his comments, we gather Mr. Kerr may have slightly misunderstood some of our points and purposes. These differences we shall attempt to set to rights.

It was our purpose to present all formulations so as to be applicable either to digital or to analog computing machines. Mr. Kerr has perhaps correctly read through to our occupational preferences and biases, but both authors have had vital experiences employing digital programs for engineering problems such as these.

Moreover, we wish to correct the impression that human computation is less prone to error than that of machines. Indeed, errors in electronic computer solutions and formulations usually show up at least as rapidly and obviously as in hand methods. Particularly in the case of analog machines, this fast "proving out" process permits continuing reformulation at a minimum of waste, cost, and expense. It should be clear that all of the checks useful and appropriate to hand methods are also applicable to machine solutions, but, by and large, the machines, unless sadly abused, are more reliable than human calculations.

We had intended to make clear and apparent the fact that functional articulation in modern computers is almost unlimited. That is, if the component characteristics are either known or can be assumed within reasonable limits, there is absolutely no difficulty representing them on computers. This, of course, includes the physically significant nonlinear and discontinuous functions to which Mr. Kerr refers. Referring back to the paper itself, it should be understood that Equation [5] and the corresponding functional block pertain to the most general static functional relationship between variables that is conceivable. With digital machines this can be represented either by constructible algebraic operations or through storage of an arbitrary number of values and suitable interpolation schemes (see references 1 through 4). On analog computers, such arbitrary functional dependencies could be represented again by algebraic schemes or through the use of n -variable function generators (references 6 through 10, particularly the last article in reference 6).

In the paper we had attempted to demonstrate these possibilities in our introduction of the function Φ_A , where

$$\Phi_A(x) \equiv |x|x$$

This function represents a class of easily instrumented algebraic operations. On the other hand, the functions Φ_p and Φ_m of Fig. 2 represent functions which can either be

- (1) linearly generated
- (2) algebraically generated
- (3) nonlinearly function-generated

depending on

- (1) the specific nature of the transducer
- (2) the conditions of use
- (3) the permissible level of approximation.

We did not intend in the paper to become involved in the detailed mechanics of such representations since these matters also depend to a great extent on the specific computer to be employed. But

⁴ Consulting Engineer, Flourtown, Pa. Fellow ASME.

neither did we intend to leave the impression that the engineer is necessarily limited in the degree of permissible articulation.

It is particularly worth while at this point to make more general and precise our definition of fluid energy storage elements and the associated definitions of *inertance* and *capacitance*. Fig. 15 represents an important generalization of Fig. 6(c) and (d), with X_1 as inputs (Pressures or Flows) and Y as output (Flows or Pressures). Thus Fig. 15(a) demonstrates the generally nonlinear storage relationship while Fig. 15(b) is suitable for cases of *variable* inertance and capacitance, which are the *slopes* of the corresponding storage function.

This correction is made necessary since the diagrams of Fig. 6(c) and (d) are useful only when the inertances and capacitances are *constant* for any particular solution. This explanation will justify the use of Φ_s in the diagram of Fig. 13.

Lastly, Mr. Kerr has raised the always important point of cost and justification for computer studies. We should like to temper his remarks with the balance between cost and *benefits*, and not restrict attention to cost alone. If minimizing cost of analysis were the sole criterion of value, very few analyses and computations would ever be made, by hand or any other method. But it is well understood that engineering costs are well justified so long as they result in proportionate decreases in ultimate plant or equipment costs and/or improvements in safety, reliability, and over-all economy. In addition, we should clearly distinguish between the cost to *purchase* computing machines and the cost to *use* them.

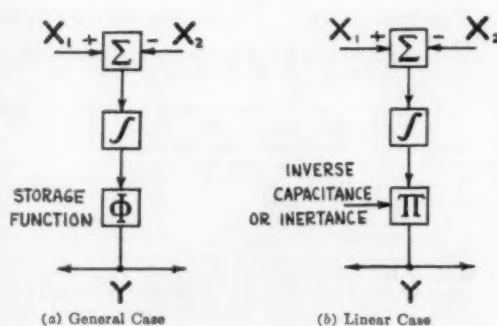


FIG. 15 GENERALIZED STORAGE ELEMENT

In this last connection it is only fair to point out that there are now a sizeable number of modern privately operated and also academically supported *computing centers*, most of which are well equipped with talented staffs and ample machinery for all the problems we are here considering. In at least one of these centers known to the authors, routine problems involving hydraulic transients are solved for a modest fixed fee. Such information is readily available merely for the asking. This would go far to settle the question of cost in any particular case.

Method for Presenting the Response of Temperature-Measuring Systems

By ROBERT LOONEY,¹ ROCHESTER, N. Y.

A single time-constant approximation of the lag of temperature-measuring systems is often adequate for evaluating the effect of the system lag on the control loop and for indicating the fidelity with which transients are recorded. The value of this approximate time constant is dependent upon the system and on the properties of the fluid whose temperature is being controlled. This paper suggests a method of presenting information on systems from which the user can determine the single time-constant approximation for his operating conditions. Experimental procedures for obtaining the necessary information are discussed.

INTRODUCTION

IF THE design of process-control systems is to be carried out on a rational basis the designer needs an adequate representation of the lags in the various components of the loop. One of the frequently used components is a temperature-measuring system.

Lags in a temperature-measuring system contribute to the total lag in the loop and tend to make control sluggish. Consequently it is desirable to use temperature-measuring systems that contribute only a small phase lag at the frequency where the open-loop lag is 180 deg. Lags in nonresonant measuring systems also tend to make the recorded amplitude of transients smaller than the actual amplitude. If the phase lag is small at the dominant frequency of the transient, the attenuation of the transient tends to be small.

Many temperature-measuring systems have distributed capacities. Several papers have been written which show how the response of such systems may be approximated by several lumped capacities. The response of a mercury-filled thermometer in a well was investigated by Fishwick (1)² with the temperature system being approximated as a two-time-constant interacting system. Aikman (2) considered various thermal elements in wells using a similar approximation while a single-time-constant approximation was considered valid for certain cases. Both authors used the response to a constant-rate temperature change (ramp input) as a common basis to represent and compare the performance of temperature systems. A recent paper by Linahan (3) considers the response of industrial thermometers in wells.

In a companion paper (4) it is shown that, at frequencies where the phase lag is small, the response of many systems may be represented adequately by a single time constant. It is interesting to note for these systems this time constant is equal to the maximum time lag for a ramp input and that even for complicated systems it often is roughly equal to the 63 per cent response time for a step input.

¹ Research Engineer, Taylor Instrument Companies. Assoc. Mem. ASME.

² Numbers in parentheses refer to the Bibliography at the end of the paper.

Contributed by the Instruments and Regulators Division and presented at the Annual Meeting, New York, N. Y., November 25-30, 1956, of THE AMERICAN SOCIETY OF MECHANICAL ENGINEERS.

Note: Statements and opinions advanced in papers are to be understood as individual expressions of their authors and not those of the Society. Manuscript received at ASME Headquarters, August 1, 1956. Paper No. 56-A-102.

This single time constant is dependent on the properties of the fluid whose temperature is being measured as well as the parameters of the system. Fortunately, the time constant turns out to be no more complicated than the sum of two numbers, one of which is dependent on the fluid properties and velocity and one which is dependent only on the parameters of the measuring system. This leads to a variety of simple methods of presenting data on systems. One of these will be discussed later. Before doing so it may be helpful to discuss the response of a particular system.

VERIFICATION FOR APPROXIMATION

In the paper presented by G. A. Coon (4), an approximation has been developed relating the maximum time lag for a ramp input with the frequency response. Here it has been shown that by neglecting s -terms higher than the first power in the polynomial representing the complex thermal system, the resulting expression will approximate the frequency response to a frequency of approximately $1/(4\pi L)$ where L is the maximum value of lag for a ramp input. The significance of the approximation is that for frequencies below $1/(4\pi L)$ a temperature-measuring system behaves essentially as a single-time-constant system with the effective time constant being equal to the lag.

Consider an example case of a gas-filled tube system with the thermal bulb, the temperature-sensitive element, centered in a well. The temperature system may be considered a two-time-constant interacting system with Fig. 1 representing the electrical

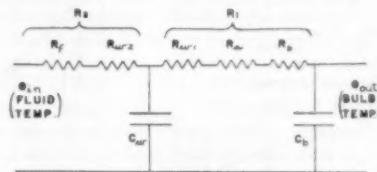


FIG. 1 ELECTRICAL ANALOG FOR EXAMPLE THERMAL SYSTEM

circuit analogous to the system. It can be shown mathematically that the lag to a constant-temperature rate-of-change input after the initial transient has dissipated is

$$\text{Lag } (L) = R_1 C_1 + R_2 C_2 + R_3 C_3 \dots [1]$$

and the transfer function representing the system is

$$\frac{\theta_{out}}{\theta_{in}}(s) = \frac{1}{1 + (R_1 C_1 + R_2 C_2 + R_3 C_3)s + R_1 C_1 R_2 C_2 s^2} \dots [2]$$

or

$$\frac{\theta_{out}}{\theta_{in}}(s) = \frac{1}{(1 + T_2 s)(1 + T_1 s)} \dots [2a]$$

The values of T_2 and T_1 are the equivalent noninteracting time constants and are

$$T_1, T_2 = \frac{(R_1 C_1 + R_2 C_2 + R_3 C_3)}{2} \pm \sqrt{\left\{ \left[\frac{(R_1 C_1 + R_2 C_2 + R_3 C_3)^2}{4} - R_1 C_1 R_2 C_2 \right] \right\}} \dots [3]$$

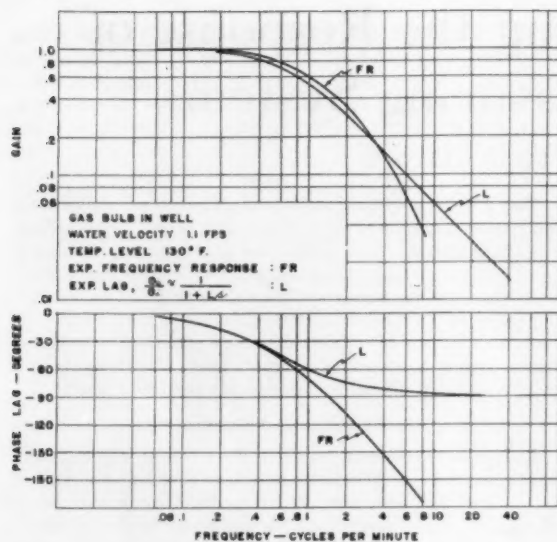


FIG. 2 FREQUENCY RESPONSE OF GAS-FILLED SYSTEM IN WELL ($V = 1.1$ FPS; TEMP AMP = 10 F)

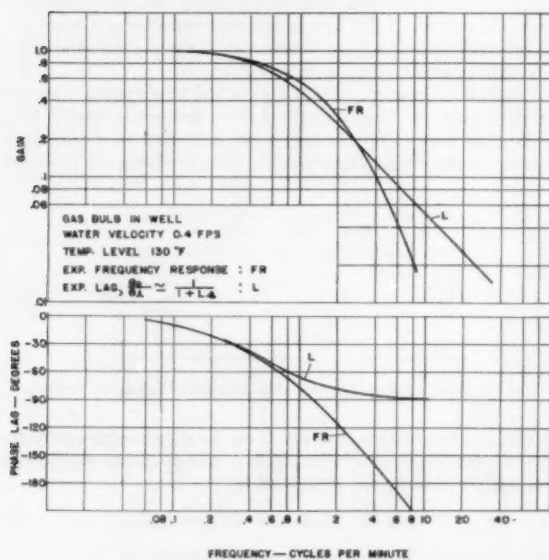


FIG. 3 FREQUENCY RESPONSE OF GAS-FILLED SYSTEM IN WELL ($V = 0.4$ FPS; TEMP AMP = 10 F)

The approximation applied to Equation [2] results in

$$\frac{\theta_{out}}{\theta_{in}}(s) \approx \frac{1}{1 + (R_2 C_w + R_3 C_b + R_1 C_b)s} \text{ for } f \leq \frac{1}{4\pi L} \quad [4]$$

$$\text{or} \quad \frac{\theta_{out}}{\theta_{in}}(s) \approx \frac{1}{1 + Ls} \text{ for } f \leq \frac{1}{4\pi L} \quad [5]$$

where L is the lag in seconds and f is the frequency in cycles per second.

Both the experimental frequency response and the experimental lag to a ramp input for a gas-filled tube system in a well were ob-

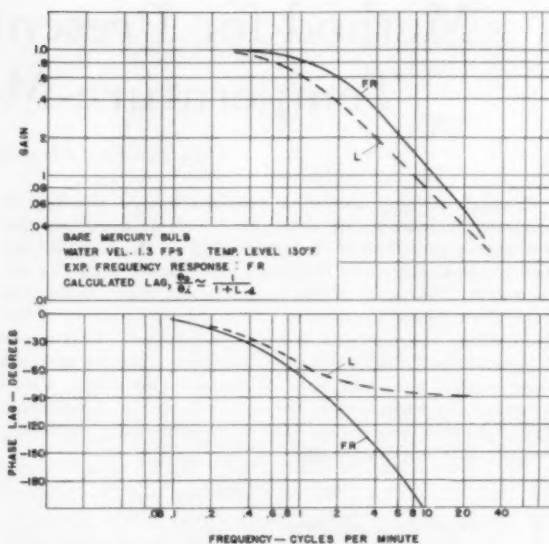


FIG. 4 FREQUENCY RESPONSE OF MERCURY-FILLED SYSTEM

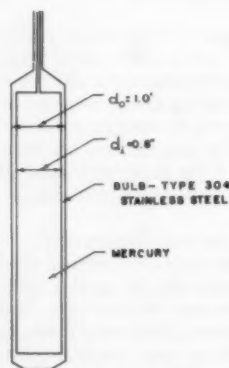


FIG. 5 MERCURY-FILLED TUBE SYSTEM

tained at two water velocities and at identical temperature levels. Figs. 2 and 3 show the degree of correlation between the approximation of the frequency response using the lag L for the value of the single time constant and the observed frequency response. The experimental values of lag for these figures are 16 and 18 sec, respectively.

The experimental frequency-response data shown in Fig. 4 are for the mercury-in-steel thermometer represented by Fig. 5. Muller-Girard (5) has developed an approximation for the response of liquid-filled tube systems. The frequency-response approximation based on a computed value is compared with the frequency response in Fig. 4. The correlation of the phase is good up to $1/(4\pi L) = 0.4$ cpm. In this frequency range, the approximation shows greater attenuation than the actual system.

BASIS FOR PRESENTATION

Thermal resistances and capacitances of the example temperature system represented by Fig. 1 may be treated in detail. The following assumptions are made:

- (a) Radiant heat transfer does not occur.
- (b) Heat transfer is radial only.

(c) Physical properties of the metals constituting the well and bulb are temperature independent.

A unit length is used in defining the resistances and capacitances represented in Fig. 1.

R_2 is the sum of two resistances one of which is the film resistance defined as

$$R_f = \frac{1}{\pi h_f D_o} \quad [6]$$

where h_f is the film coefficient of heat transfer and D_o is the external well diameter.

The well resistance may be separated into two parts, R_{w2} and R_{w1} , where R_{w2} is

$$R_{w2} = \frac{\ln(D_o/D_m)}{2\pi k} \quad [7]$$

Here k is the thermal conductivity of the well material

$$D_m = [(D_o^2 + D_i^2)/2]^{1/2}$$

and D_i is the internal well diameter. The purpose of using the diameter D_m is to lump the heat capacity of the well at the midpoint of the distributed well capacity.

An air annulus is formed by the shell and bulb causing a resistance to heat flow defined as

$$R_a = \frac{\ln(D_o/d_o)}{2\pi k_a} \quad [8]$$

where d_o is the external bulb diameter and k_a is the thermal conductivity of air. The resistance of the air annulus R_a will be much larger than either the second part of the shell resistance R_{w1} or the bulb resistance R_b

$$R_1 = R_a \quad [9]$$

The well capacitance is

$$C_w = \frac{\pi}{4} \rho c_p (D_o^2 - D_i^2) \quad [10]$$

and the bulb capacitance is

$$C_b = \frac{\pi}{4} \rho c_p (d_o^2 - d_i^2) \quad [11]$$

where ρ and c_p are the density and specific heat with d_i being the internal bulb diameter. The capacitance of the gas fill in the bulb is negligible compared to the bulb capacitance.

An effective time constant for the system shown in Fig. 1 is then the sum of two numbers

$$T_s = \frac{1}{h_f} \left[\frac{C_w + C_b}{\pi D_o} \right] + [R_{w2}(C_w + C_b) + R_a C_b] \quad [12]$$

Thermal resistances and capacitances in Equation [12] are arranged in two groups, one of which is dependent on fluid properties and velocity. The second is dependent only on the parameters of the measuring system and will be a constant for a given temperature system if temperature variations are small.

GRAPHICAL PRESENTATION OF DATA

The single-time-constant approximation with the effective time constant being the sum of two numbers lends itself to a wide variety of nomograph and graphical methods of presentation. A combined graphical and tabular method will be developed to demonstrate how the information contained in Equation [12] may be presented to the user. Let that portion of Equation [12] dependent on the film coefficient be

$$T_f = \frac{1}{h_f} \left[\frac{C_w + C_b}{\pi D_o} \right] \quad [13]$$

A dimensionless heat-transfer equation of the Nusselt type for the fluid-film coefficient is

$$\frac{h_f D_o}{k} = K_1 \left(\frac{\rho V D_o}{\mu} \right)^m \left(\frac{c_p \mu}{k} \right)^n \quad [14]$$

where h_f is the coefficient of heat transfer of the fluid, k is the thermal conductivity, ρ is the density, μ is the viscosity, c_p is the specific heat, and V is the average fluid velocity. Thus

$$\frac{1}{h_f} = \left[\frac{D_o}{D_o^m K_1} \right] \left[\frac{1}{k \left(\frac{\rho}{\mu} \right)^m \left(\frac{c_p \mu}{k} \right)^n} \right] \left[\frac{1}{V^m} \right] \quad [15]$$

and

$$T_f = \left[\frac{C_w + C_b}{\pi D_o} \right] \left[\frac{D_o}{D_o^m K_1} \right] \left[\frac{1}{k \left(\frac{\rho}{\mu} \right)^m \left(\frac{c_p \mu}{k} \right)^n} \right] \left[\frac{1}{V^m} \right] \quad [16]$$

We note that T_f is a function of the following variables:

- (a) A particular temperature system.
- (b) The fluid velocity.
- (c) Temperature of the fluid.
- (d) The physical properties of the fluid.

For some reference fluid, such as water at a standard temperature, T_f can be calculated for various flow velocities using one particular temperature-measuring system. A plot of T_f versus water velocity on log-log paper would result in a straight-line graph at a negative slope of m . Such a procedure would be applicable to any temperature system providing the constants of the system were calculable. A family of straight-line graphs would result, one for each system. There is the possibility that one line may represent several systems if the combinations of capacitances and diameters in Equation [13] are numerically equal.

It is apparent Equation [14] could be used to evaluate the effects of temperature changes of the reference fluid (water), the effects of fluids other than water, and the effects of temperature changes of other fluids. A table of correction factors could be computed and tabulated and that portion of the effective time constant dependent on fluid conditions would be

$$T_1 = M T_f \quad [17]$$

where

$$M = \frac{\left[k \left(\frac{\rho}{\mu} \right)^m \left(\frac{c_p \mu}{k} \right)^n \right]_{\text{water at } \theta = \text{standard}}}{\left[k \left(\frac{\rho}{\mu} \right)^m \left(\frac{c_p \mu}{k} \right)^n \right]_{\text{process fluids}}} \quad [18]$$

Such a series of computations also could be conducted using air at standard temperature as a reference gas thus resulting in two separate M -tables, one for liquids and one for gases.

If a particular fluid were not included in the two M -tables, an M -value could be computed from Equation [18] where the quantities in the denominator are the physical properties of the liquid or gas in question at the temperature of use. The value in the numerator would be the physical properties of either water or air at standard temperature.

The coefficient of heat transfer must be established. Empirical equations for the film coefficient generally agree with experimental data to ± 20 per cent. It would be advantageous if the exponents of the Reynolds number and Prandtl number in Equation

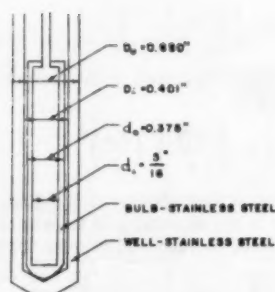


FIG. 6 GAS-FILLED TUBE SYSTEM IN WELL

[14] were the same for both liquids and gases. For both liquids and gases, heated or cooled outside single tubes, direction of flow normal to tube, $Re > 100$, Stoevers (6) uses

$$\frac{h_f D_o}{k} = 0.385 \left(\frac{\rho V D_o}{\mu} \right)^{0.64} \left(\frac{c_p \mu}{k} \right)^{0.3} \dots [19]$$

A log-log plot of T_f versus fluid velocity would be a straight-line graph at a slope of -0.56 for both liquids and gases. Temperature-correction factors using 100-F reference temperature are included in Stoevers while a fluid-correction factor may be computed from graphs. Calculations for the tables of M -values are thus simplified.

It was assumed earlier in defining the resistances and capacitances that the physical properties were temperature independent. While the thermal conductivity and density of metals are essentially constant, the specific heat does vary (Fe about 10 per cent for a 180 F temperature rise). Of greater importance is the conductivity of the air annulus formed by the well and bulb. Data from McAdams (7) indicate the conductivity will increase linearly by 23 per cent from 100 to 250 F. An evaluation to include temperature effects is beyond the scope of this paper. However, it is of importance to note that the resistance of an air gap to heat flow is inversely proportional to the thermal conductivity of air. Hence computations concerning air-gap resistance at 100 F reference temperature would be high compared to the thermal resistance at higher temperatures. That portion of the effective time constant dependent only on the parameters of the system is

$$T_e = R_{wg}(C_w + C_b) + R_b C_b \dots [20]$$

The total effective time constant is

$$T_s = MT_f + T_e \dots [21]$$

Computations have been made to determine the system parameters of a gas-filled tube system, see Fig. 6, for which the experimental frequency-response data were obtained. A plot of T_f versus water and air velocity at 100 F reference temperature together with a brief table of M -values for some common liquids only is shown in Fig. 7.

If we wish to know the effective time constant for the preceding thermal system in water at a velocity of 1.1 fps, flow direction normal to the longitudinal axis, and temperature level 130 F, enter the plot of Fig. 7 at 1.1-fps water velocity. From this point on the abscissa project a line vertically until the graph is intersected. At the point of intersection, project a line horizontally to the ordinate T_f . Multiply the value of T_f by the correction factor M for water at 130 F (about 1.1). Add the 14-sec value of T_e to the product of MT_f . The resulting value, T_s , equals about

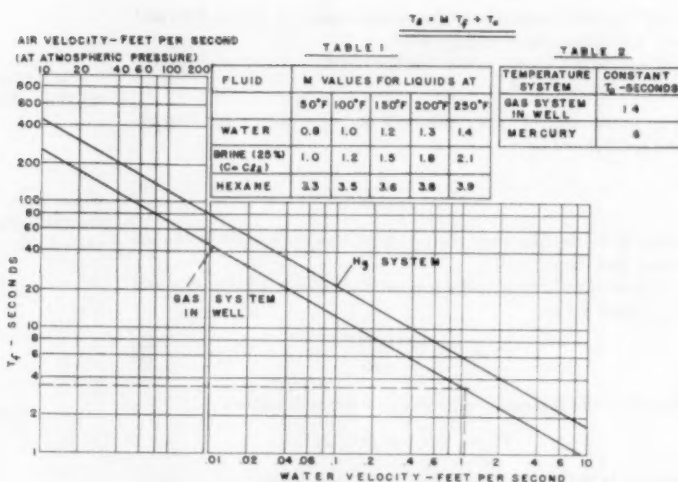


FIG. 7 GRAPHICAL PRESENTATION OF RESPONSE

18 sec, will approximate the frequency response to a frequency of about $1/(4\pi L)$ or approximately 30-deg phase lag.

The mercury-filled tube system, see Fig. 4 for the actual frequency-response data, has been included in the presentation of Fig. 7. A glance at the T_e -values in Table 2 and at the graph of Fig. 7 reveals that the mercury system has less lag (T_e) at high water velocities while the gas system in the well has less lag at lower water velocities and in air. The presentation of approximate frequency-response data in this form would be helpful to the user in selecting a temperature-measuring system with the least lag for his process.

EXPERIMENTAL DETERMINATION OF CONSTANTS

The development of the graphical presentation of data in Fig. 7 has depended on knowledge of the physical construction of the temperature system and assuming an equation for the film coefficient. Another important assumption was that of the bulb being centered in the well, or geometrical symmetry. A few of the number of conditions tending to make the analysis of a system both difficult and inaccurate will be mentioned. Manufacturing tolerances for a given type of system would result in slightly different system constants. Some degree of eccentricity between the bulb and well is possible while some bulbs are deliberately off-center in the well. The value of the effective capacitance for the liquid fill of a vapor system will vary with temperature. Resistance thermometers are sometimes encased in a flat sheath.

An experimental determination for the constants of a system would be more reliable. By combining Equations [12] and [15] the effective time constant may be written as

$$T_s = \frac{A}{V^\infty} + B \dots [22]$$

or

$$T_s - B = \frac{A}{V^\infty} \dots [23]$$

where $B = T_e$ and $A = T_f V^\infty$. A plot of $T_s - B$ versus the fluid velocity on log-log paper would be the straight line at a negative slope of m .

Experimentally, several values of L could be obtained by using several known fluid velocities. Then by subtracting from the

total lag an arbitrary constant that yields a straight line on log-log paper for the difference versus velocity, the conditions of Equation [23] are realized. The arbitrary constant would be B and the slope m would be the power of the velocity term under experimental conditions.

Frequency-response data may be used to determine the constants of a system. By means of curve-fitting a single-time-constant template to the frequency-response diagrams for several known velocities, values for the single-time-constant approximation may be obtained. The procedure described in the preceding paragraph may then be followed to obtain the system constant B . With B known, the approximate frequency response of the system at many fluid conditions may be arrived at.

By testing several identical systems at similar test conditions, the accuracy of the system constant could be established. This information should be supplied to the user.

CONCLUSIONS

A method for representing the speed of response of temperature-measuring systems has been developed through the use of an approximation relating the time lag for a constant-rate temperature change with the frequency response. The frequency response may be approximated as a single time constant to a frequency of $1/(4\pi L)$ or about 30-deg phase lag. The representation is not applicable in processes where the temperature-measuring system constitutes the principal lag of the process. A more complete analysis would be necessary for this case.

The illustrative graphical and tabular representation may be enlarged to include the numerous process fluids found in the industrial field. Although fluid-filled tube systems have been used as examples, the method of presentation should be valid for other types of temperature systems. Although approximations have been worked out for various types of systems, it is recommended that the information used in a presentation be based on experimental data.

This method for representing the frequency response of temperature-measuring systems is proposed by the author for consideration as a means for specifying the response of temperature systems. The several advantages are as follows: (a) The single-time-constant approximation may be used to represent the frequency response of complex temperature systems; (b) this single time constant may be obtained experimentally with relative ease if a constant-rate, temperature-change input is used; (c) this single time constant may be presented in a graphical form quite simple to use; (d) the effects of numerous process fluids may be included in the presentation; and (e) data could be compiled into a handbook which should be of immediate practical value to the user.

BIBLIOGRAPHY

- 1 "Time-Lags in Thermometer Pockets," by W. Fishwick, Transactions of the Society of Instrument Technology, vol. 4, March, 1952, p. 29.
- 2 "Static and Dynamic Performance of Sheathed Industrial Thermometers," by A. R. Aikman, J. McMillan, and A. W. Morrison, Transactions of the Society of Instrument Technology, vol. 5, December, 1953, p. 138.
- 3 "The Dynamic Response of Industrial Thermometers in Wells," by T. C. Linahan, Trans. ASME, vol. 78, 1956, p. 759.
- 4 "Response of Temperature-Sensing Element Analogs," by G. A. Coon, ASME Paper No. 56-A-101.
- 5 "The Dynamics of Filled Temperature-Measuring Systems," by O. Muller-Girard, Trans. ASME, vol. 77, 1955, p. 591.
- 6 "Applied Heat Transmission," by H. J. Stoever, McGraw-Hill Book Company, Inc., New York, N. Y., 1941.
- 7 "Heat Transmission," by W. H. McAdams, McGraw-Hill Book Company, Inc., New York, N. Y., 1942.
- 8 "A Method for Measuring Surface Heat Transfer Using Cyclic Temperature Variations," by J. C. Bell and E. F. Katz, Heat Transfer and Fluid Mechanics Institute, 1949, p. 243.

9 "Response and Phase-Lag of Thermometers," by E. G. J. Eykman and C. J. D. M. Verhagen, included in contents of "Frequency Response," edited by R. Oldenburger, MacMillan Book Company, New York, N. Y., p. 158.

10 "A Thermal Sine-Wave Apparatus for Testing Industrial Thermometers," by S. P. Higgins, Jr., and J. R. Keim, ASME Paper No. 54-SA-20.

11 "A Thermal Sine-Wave Generator for Speed-of-Response Studies," by R. Looney, ASME Paper No. 54-SA-28.

Discussion

R. D. COOK¹ This paper is based on the idea that only the low-frequency end of the response is of interest (where lags are less than 30 deg). This is usually an acceptable qualification since lags due to the thermal measuring element are secondary ones. If they are not, the system should be redesigned so that they are.

If then it is only the low-frequency portion which is desired, a single negative real root seems the simplest and most logical approximation. The derivation of the heat-transfer equation seems straightforward. The approximations to make it first order seem agreeable.

The validity of the effective single time constant for many different physical arrangements should be more completely verified by experimental measurement. Once this has been done and the condensed data compiled, it would be of great value to the designer of thermal-control systems.

The writer strongly suspects that the accuracy of these calculations would be rather poor: (a) The derivations utilize general heat-transfer equations which cannot exactly match all the varying conditions encountered in temperature measurement; (b) then there is the practical matter of determining accurately the physical constants of the system, particularly where two-phase flow is encountered or a chemical reaction is taking place. In spite of this possible limitation, such a compilation of data would be useful.

H. M. PAYNTER⁴ In the writer's discussion of the companion paper by G. A. Coon, he has pointed out the connection of the theory of monotone processes to the problems presented in this paper.¹⁻³

The time constant L used by the author is identical to the writer's mean time delay T_m . Since this constant is always the low-frequency value of the slope of the curve of phase lag versus frequency for all monotone processes, it would be much more significant in these cases to plot either (1) phase lag versus frequency or (2) log phase lag versus log frequency.

This latter plot has been used by the writer and Takahashi⁵ and obviates the need of any templates to determine the value of L from experimental data.

J. McMILLAN⁶ The author is to be congratulated on his excellent method of presenting dynamic data for temperature-measuring systems. Such information is extremely useful to

¹ Shell Chemical Corporation, Martinez, Calif.

⁴ Assistant Professor of Mechanical Engineering, Massachusetts Institute of Technology, Cambridge, Mass. Mem. ASME.

⁵ "A New Method of Evaluating Dynamic Response of Counter-Flow and Parallel-Flow Heat Exchangers," by H. M. Paynter and Y. Takahashi, Trans. ASME, vol. 78, 1956, pp. 749-758.

⁶ Discussion by H. M. Paynter of reference (3) of the Bibliography of the paper.

⁷ "On an Analogy Between Stochastic Processes and Monotone Dynamic Systems," by H. M. Paynter, Tagung Regelungstechnik, Heidelberg, Germany, September, 1956, Paper No. 37.

⁸ "Specifying Stable Control Systems," by R. J. Medkoff, Askania Report TSD 48, Askania Regulator Company, 1955.

⁹ Central Instrument Laboratory, Imperial Chemical Industries, Ltd., Reading, Berks, England.

the user in selecting equipment for a process and it will become even more useful as more data become available on the dynamic characteristics of the processes themselves.

The approximation devised in the paper by G. A. Coon¹⁰ and used in this paper, obviously has wider applications, but has the author shown it to be exceptionally useful in this particular case? The graphical presentation is exact so long as all we want is the "total" or "thermal" lag (as measured with ramp input) and often this is good enough for comparing alternative systems, without calculating the frequency response. If the frequency response is required no more information is required than that used to calculate the total lag and individual calculations probably are worth while.

The discussor would like to ask the author if he has any data which confirm (or otherwise) the heat-transfer relationship given in the paper by Aikman, McMillan, and Morrison (2). In that paper experiment indicated that for a temperature installation pointing upstream (parallel flow) the heat-transfer coefficient is given by the accepted relationship for cross-flow (normal to tube) with an increased constant coefficient. This was thought to be due to the increased turbulence of the fluid stream caused by impingement on the end of the thermometer well. This discussor feels that this is important because thermometer installations are usually mounted this way—to give sufficient immersion for negligible static error.

AUTHOR'S CLOSURE

The author appreciates the interesting discussions contributed

¹⁰ Printed in this issue of Transactions pp. 1857-1868.

to this paper. Mr. Cook pointed out the need for experimental verification concerning the effective single time constant using many different physical arrangements. There is also the need for verification using fluids other than water. A general heat-transfer equation such as the one used would not be sufficient to cover the numerous process fluid conditions. Perhaps it would be more advantageous if system constants were related to the film coefficient leaving the user to choose the heat-transfer equation applicable to his particular process conditions. To do this, system constants for a given physical arrangement would be determined experimentally to minimize calculation errors. Then the constants would be related to the film coefficient by the heat-transfer equation matching the physical arrangement. The effective time constant would be

$$T_s = \frac{A'}{h_f} + B$$

In the discussion by Professor Paynter, the reader is cautioned to note that the low-frequency value of the slope of the log phase lag versus log frequency curve is equal to one regardless of the value of the time constant. The time constant L or the mean time delay T_m may be computed, however, from known relationship of phase lag, time constant, and frequency at low frequencies

$$\phi \approx 2\pi fL$$

The author regrets that he does not have any data concerning the heat-transfer relationship given in the paper by Aikman, McMillan, and Morrison (2).

Responses of Temperature-Sensing-Element Analogs

By G. A. COON,¹ ROCHESTER, N. Y.

From the standpoint of stability, temperature-sensing elements used in control systems should not contribute much phase lag at the frequency where the open-loop phase lag is 180 deg. For those cases where the temperature-sensing element does not contribute appreciable (less than 30 deg) phase lag around 180 deg, it would be advantageous to have a low-frequency approximation which works for complicated thermal systems. This paper presents such an approximation and establishes its validity for the electrical analogs of many sensing elements. In addition, it shows how the approximation is related to the thermal lag measured during a ramp input and the 63 per cent response time. These results, which are obtained in terms of transfer functions, can be applied to other systems having the same analogs.

INTRODUCTION

THE behavior of a temperature-sensing element may be described by its response to a disturbance in input. Disturbances commonly used for this purpose are the step change, the ramp, and the sine wave. The step response is often characterized by the time when the response is 63.2 per cent complete. If a ramp input is used, it is customary to measure the thermal lag. While these quantities give an indication of the speed of response, no one value by itself can define the complete response of any but the simplest systems.

Sinusoidal inputs form the basis of frequency-response techniques commonly employed in analyzing control loops. In judging system performance, one usually wants the controlled variable to recover from a load disturbance in a reasonably short time. Since this recovery time is associated with the frequency where the open loop has 180 deg phase lag, for good performance the latter should be fairly high. The phase lag of the sensing element, as a component of the open loop, has the effect of lowering the frequency at which the open-loop phase lag is 180 deg. Thus the sensing element ordinarily should not be allowed to contribute more than 20 or 30 deg in phase lag at this frequency.

Usually, for fidelity of recording, it is desirable that the gain of the sensing element be relatively constant in the working range of frequency. Obviously, the phase lag of a process using sensing element (a) of Fig. 1 will be reduced by changing to sensing element (b). If the same control actions are employed, this change will increase the frequency where the open loop has 180 deg phase lag, which will give a shorter recovery time following a load disturbance in the loop. Since the process gain is generally lower at

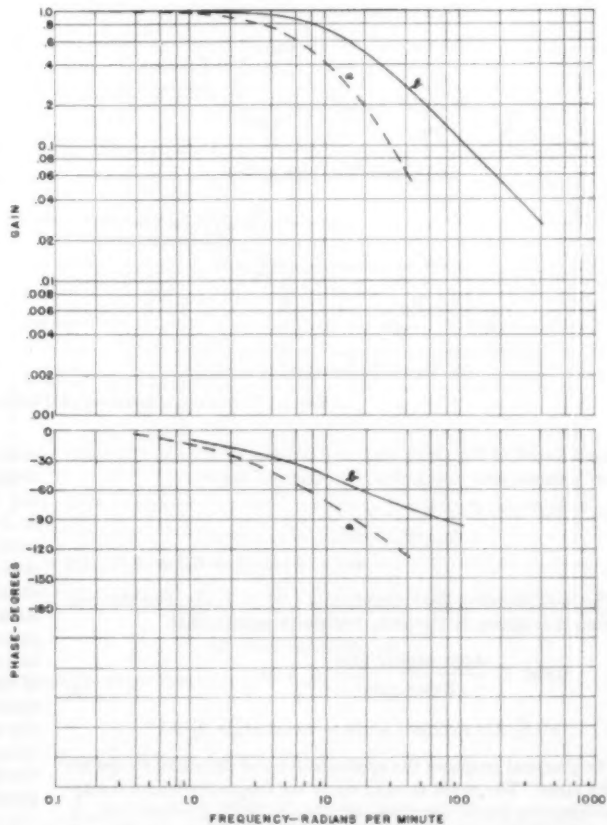


FIG. 1 FREQUENCY RESPONSES OF TWO TEMPERATURE SENSING ELEMENTS

the higher frequency, the controller gain can be increased with a corresponding reduction in the size of deviations.

This paper will show that the frequency responses of many thermal systems can be represented adequately by a single time constant in the frequency range corresponding to 0 to 30 deg phase lag. For the systems studied, this time constant is equal to the thermal lag L (maximum time lag for a ramp input). Thus in the region of 0 to 30 deg phase lag the transfer function of the sensing element can be approximated by $1/(1 + Ls)$. The lag L may be determined by experimental tests or by direct calculation. It is an easy matter to sketch the approximate frequency response.

This low-frequency approximation is valid between 0 and 30 deg phase lag, which is precisely the region of interest when the thermal element is used in a control loop. By using the approximation, complicated thermal elements may be included in the loop with very little difficulty.

This paper will show the validity of the low-frequency approximation mentioned for the network analogs of Fig. 2. For

¹ Mathematician, Taylor Instrument Companies.

Contributed by the Instruments and Regulators Division and presented at the Annual Meeting, New York, N. Y., November 25-30, 1956, of THE AMERICAN SOCIETY OF MECHANICAL ENGINEERS.

NOTE: Statements and opinions advanced in papers are to be understood as individual expressions of their authors and not those of the Society. Manuscript received at ASME Headquarters, August 1, 1956. Paper No. 56-A-101.

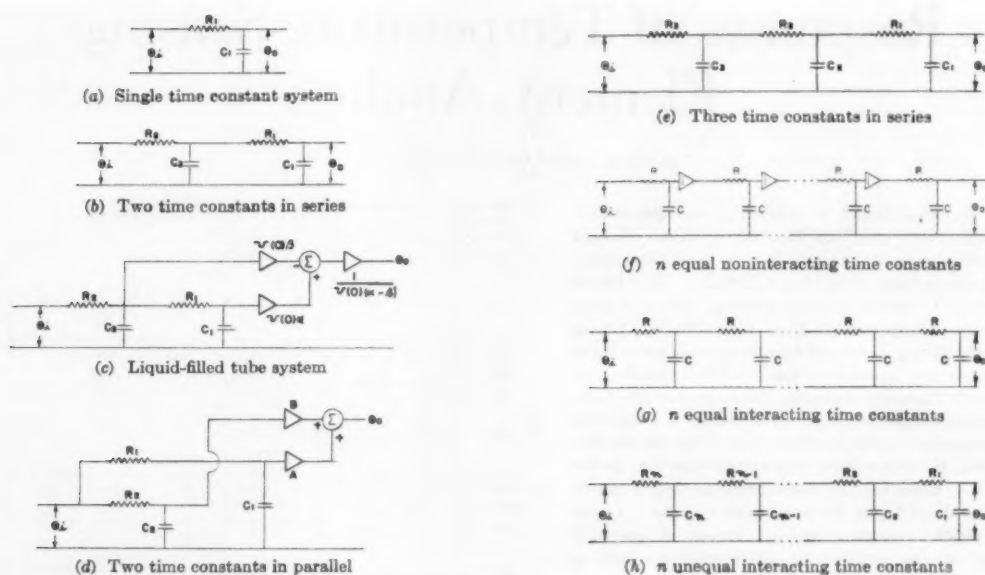


FIG. 2 ELECTRICAL ANALOGS OF TEMPERATURE SENSING ELEMENTS

the network of Fig. 2(h), with any number of R 's and C 's which are unequal and interacting, the thermal lag is

$$L_n = R_n(C_n + C_{n-1} + \dots + C_1) + R_{n-1}(C_{n-1} + C_{n-2} + \dots + C_1) + \dots + R_2(C_2 + C_1) + R_1 C_1 \quad [1]$$

The low-frequency approximation is $1/(1 + L_n s)$. For this network it is shown in Theorem 1 of the Appendix that

$$\left. \begin{aligned} 0.866 &\leq \frac{\text{Approximate gain}}{\text{Exact gain}} \leq 1.00 \\ 0^\circ &\leq \text{Approximate angle} - \text{exact angle} \leq 3.1^\circ \end{aligned} \right\} \dots [2]$$

For practical purposes the approximate and the exact values are the same. The result is valid up to the frequency where the approximation has 30 deg phase lag; that is, for $0^\circ \geq -\tan^{-1} \omega L_n \geq -30^\circ$. This is the same as the frequency range $0 \leq \omega \leq 0.577/L_n$.

If a distance-velocity lag T_d is added to the system simulated in Fig. 2(h), the thermal lag L_d equals $L_n + T_d$, where L_n is given by Equation [1]. Thus the low-frequency approximation is $1/(1 + L_d s)$. The same inequalities [2] hold for the new system in the frequency range $0 \leq \omega \leq 0.577/L_d$.

As a matter of fact inequalities [2] are valid for all of the networks of Fig. 2 with the exception of Fig. 2(d). It will be shown that the thermal lag, which is used as the time constant in the low-frequency approximation, is about equal to the 63 per cent response time for many types of thermal systems.

These results, which were derived for sensing elements, obviously have a much wider range of application. They hold for any systems which can be simulated by the electrical networks of Fig. 2.

SINGLE TIME-CONSTANT SYSTEM

In simple cases a thermometric system may be adequately represented by a single time constant. Harper³ has cited a

³ "Thermometric Lag," by D. R. Harper, 3rd, *Bulletin of the Bureau of Standards*, vol. 8, 1912, pp. 659-715.

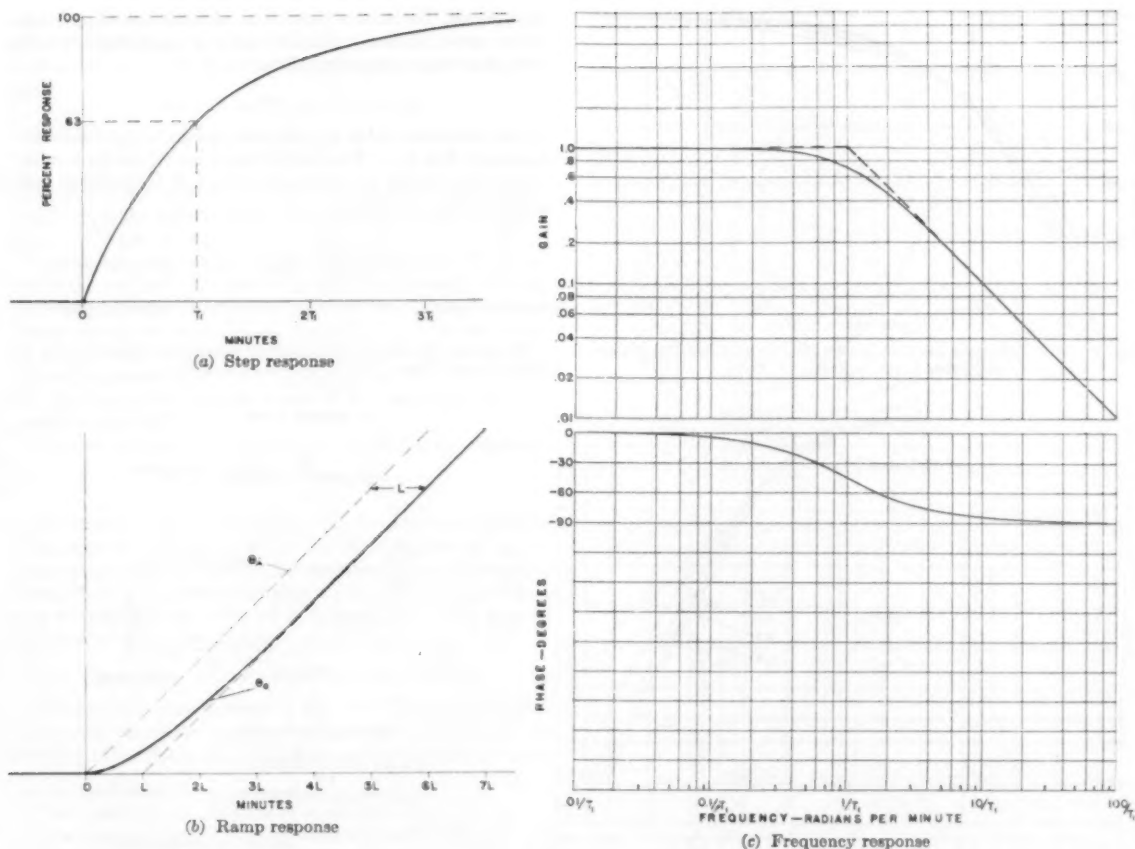
mercury-in-glass thermometer as an example. A step change in temperature may be made by plunging the bulb into well-agitated hot water. Resistance to heat flow is provided by (1) the film between the water and bulb glass, (2) the glass wall, and (3) a portion of the mercury fill. The relative size of these resistances depends upon the dimensions of the glass bulb, the thermal conductivity of the glass, the coefficients of heat transfer, and so on. Assume that the resistance due to the water film is large as compared with the other two and that the thermal capacity of the mercury is larger than that of the bulb glass. Then the response of the thermometer can be approximated by assuming all the resistance to heat flow to be in the water-to-glass film and all the thermal capacity to be in the mercury. In doing this, the thermal capacity and resistance to heat flow have been "lumped." Thus, the thermal system can be represented schematically by the diagram of Fig. 2(a) where

- θ_i = temperature input, deg F
- θ_o = temperature of bulb fill, deg F
- R_1 = resistance to heat flow, deg F/(Btu/min)
- C_1 = thermal capacity, Btu/deg F
- $T_1 = R_1 C_1$ = time constant, min

The transfer function is
$$\frac{\theta_o}{\theta_i}(s) = \frac{1}{1 + T_1 s} \dots \dots \dots [3]$$

The behavior of a system consisting of a single time constant T_1 is well known. The response to a step change in external temperature, Fig. 3(a), is 63 per cent complete when the elapsed time is T_1 minutes. If the system is subjected to a ramp input, then the output will lag the input as indicated in Fig. 3(b). For this simple system, the thermal lag L is equal to the time constant ($L = T_1$). Its frequency response, Fig. 3(c), is characterized by a gain of 0.707 and a phase lag of 45° at the frequency $1/T_1$ radians per minute.

A single time-constant system is described completely by its 63 per cent response time or by its lag. But in more complex systems neither value by itself gives a complete picture.

FIG. 3 RESPONSES OF A SINGLE TIME-CONSTANT SYSTEM $1/(1 + T_1s)$

TWO TIME CONSTANTS IN SERIES

Usually in order to get a sufficiently accurate picture of the response, it is necessary to include the effects of several resistances and capacities. Fig. 2(b), for example, may represent a bulb-in-well where the resistances and capacities are interpreted in the following manner

R_2 = resistance to heat flow due to film between water and well

R_1 = resistance to heat flow due to air space between well and bulb

C_2 = capacity of well

C_1 = capacity of bulb wall and fill

This is an interacting system with transfer function

$$\frac{\theta_o}{\theta_i}(s) = \frac{1}{1 + (R_2C_2 + R_2C_1 + R_1C_1)s + R_2C_2R_1C_1s^2} \dots [4]$$

The response of this system is the same as that of a system with two noninteracting time constants suitably chosen. In this case the equivalent noninteracting system is

$$\frac{\theta_o}{\theta_i}(s) = \frac{1}{(1 + T_1s)(1 + T_2s)} \quad T_1 \geq T_2 \dots [5]$$

where

$$T_1 = \frac{1}{2} (R_2C_2 + R_2C_1 + R_1C_1) + \left[\frac{1}{4} (R_2C_2 + R_2C_1 + R_1C_1)^2 - R_2C_2R_1C_1 \right]^{1/2}$$

$$T_2 = \frac{1}{2} (R_2C_2 + R_2C_1 + R_1C_1) - \left[\frac{1}{4} (R_2C_2 + R_2C_1 + R_1C_1)^2 - R_2C_2R_1C_1 \right]^{1/2}$$

If R_2C_1 is small in comparison with $R_2C_2 + R_1C_1$, then interaction effects are negligible and the noninteracting time constants T_1 and T_2 are about equal to R_2C_2 and R_1C_1 .

Both the noninteracting system [5] and the interacting system [4] respond to a given input in exactly the same way. For either system, the thermal lag is

$$L = T_1 + T_2 = R_2C_2 + R_2C_1 + R_1C_1 \dots [6]$$

Either system responds to a step change in input as shown on Fig. 4, the time scale being in terms of the thermal lag L . For all possible ratios of T_1/T_2 the response is 63 per cent complete when the time elapsed after the step change is between $1.0L$ and $1.1L$. For this system, then, the thermal lag is a good approximation to the 63 per cent response time. From the other point of view

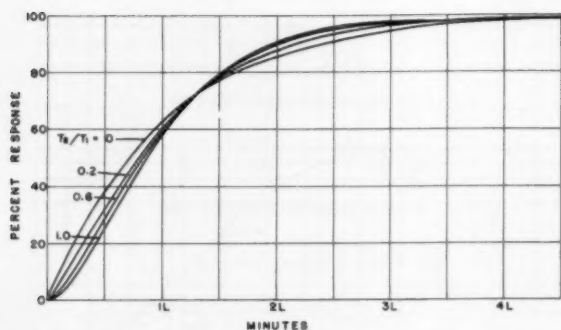


FIG. 4 STEP RESPONSE OF TWO NONINTERACTING TIME CONSTANTS IN SERIES $1/[(1 + T_1s)(1 + T_2s)]$

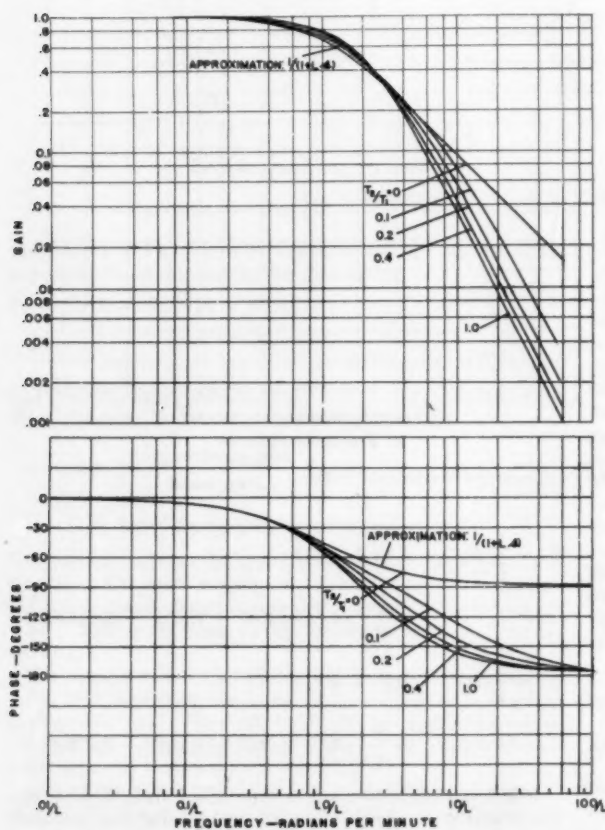


FIG. 5 FREQUENCY RESPONSE OF TWO NONINTERACTING TIME CONSTANTS IN SERIES $1/[(1 + T_1s)(1 + T_2s)]$

when the elapsed time equals the thermal lag, the response is between 58 and 63 per cent complete.

Fig. 5 shows the variation in frequency responses for various ratios of T_2/T_1 . There is very little difference in them between zero frequency and the frequency of 30 deg phase lag. The frequency-response approximation recommended for this region, $1/(1 + Ls)$ where L is the thermal lag, is represented on this plot by the same curves as $T_2/T_1 = 0$. If $1/(1 + Ls)$ is taken as an approximation for any system of this type in the region of 0 to 30

deg phase lag, the maximum error in phase is less than 3 deg. Over the same frequency range, the ratio of approximate gain to actual gain always lies between 0.9 and 1.0.

LIQUID-FILLED TUBE SYSTEM

The filled system of Fig. 6(a) may be represented by the electrical analog of Fig. 2(c). Under appropriate conditions the transfer function relating the indicated temperature θ_o to the input temperature θ_i may be written³

$$\frac{\theta_o}{\theta_i}(s) = \frac{1 - T_2s}{(1 + T_1s)(1 + T_2s)} \quad \begin{matrix} (T_1 \geq T_2) \\ (T_1 \geq T_2 > 0) \end{matrix} \quad [7]$$

Actually T_1 and T_2 are the equivalent noninteracting time con-

³ "Dynamics of Filled Temperature-Measuring Systems," by O. Muller-Girard, Trans. ASME, vol. 77, 1955, p. 591.

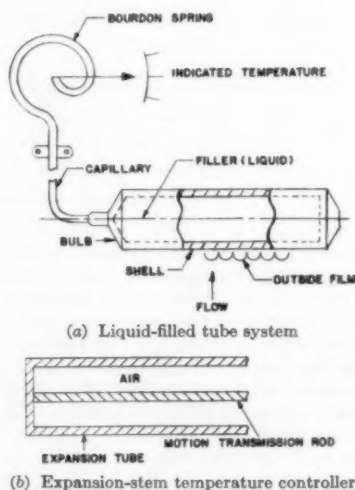


FIG. 6 TYPES OF THERMAL SYSTEMS

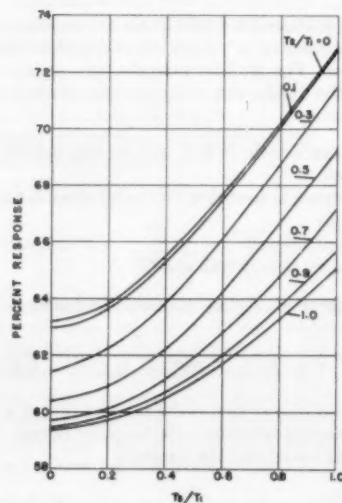


FIG. 7 PER CENT RESPONSE OF $(1 - T_2s)/[(1 + T_1s)(1 + T_2s)]$ WHEN ELAPSED TIME AFTER A STEP CHANGE EQUALS THERMAL LAG

stants associated with the network of Fig. 2(b). The time constant T_3 depends on R_1C_1 and also on α and β , the volumetric coefficients of expansion of the filling liquid and of the shell material

$$T_3 = \frac{\beta}{\alpha - \beta} R_1 C_1$$

Since $\alpha > \beta$, the time constant T_3 is positive. The amplification factor $v(0)$ is the volume of the bulb prior to a change in temperature.

In this case, the thermal lag is $L = T_1 + T_2 + T_3$. Fig. 7 shows the per cent response when the time elapsed following a step change in input is equal to L . This value lies between 59 and 73 per cent for any system of this type $T_1 \geq T_3$. Obviously there are many combinations of time constants for which the response is close to 63 per cent when $t = L$. In particular, if T_3/T_1 is less than 0.5, the response is between 59 and 67 per cent complete for all possible ratios of T_3/T_1 .

It is now of interest to see how well the frequency response of

$$1/(1 + Ls) = 1/[1 + (T_1 + T_2 + T_3)s]$$

approximates a liquid-filled system. Up to frequencies where the approximation has 30 deg phase lag, the approximate angle is always larger than the exact angle, as the maximum difference between them is less than 3.1 deg. The ratio of approximate gain to exact gain lies between 0.866 and 1.00. This is shown analytically in Theorem 1 of the Appendix.

EXPANSION-STEM TEMPERATURE CONTROLLER

The physical system is shown in Fig. 6(b). The expansion-stem temperature controller has the same electrical analog as the liquid-filled tube system [Fig. 2(c)] if proper interpretation is made

- α' = coefficient of expansion of rod
- β' = coefficient of expansion of expansion tube
- R_2 = resistance to heat flow provided by outside film
- C_2 = capacity of expansion tube
- R_1 = resistance to heat flow provided by air layer separating tube and rod
- C_1 = capacity of rod

It is assumed that the major source of heat transfer is by radial conduction. If $\alpha' > \beta'$, the two systems have the same electrical analog and so they must respond in the same manner to changes in input temperature.

TWO TIME CONSTANTS IN PARALLEL

If a change is made in the external temperature θ_i of the system shown in Fig. 2(d), the heat may flow in either of two directions. The output of each mesh is amplified, and the indicated temperature is the sum of the amplified outputs. The transfer function is

$$\frac{\theta_o(s)}{\theta_i(s)} = \frac{1 + T_2 s}{(1 + T_1 s)(1 + T_3 s)} \quad \begin{matrix} (T_1 \geq T_3) \\ (T_1 \geq T_3 > 0) \end{matrix} \quad [8]$$

where $A + B = 1$, $T_1 = AR_2C_2 + BR_1C_1$, and T_1 and T_2 are, respectively, the larger and smaller of the time constants R_2C_2 and R_1C_1 . In this case the thermal lag is $L = T_1 + T_2 - T_3$.

Fig. 8 shows the per cent response when the elapsed time after the step change is equal to L . If $T_2 \geq 0.3T_1$ and $T_1 \geq T_3$, the response is between 58 and 70 per cent complete when $t = L$.

How well the low-frequency approximation $1/(1 + Ls)$ works in this case is shown in Figs. 9 and 10. For some values of the time constants the ratio of approximate gain to exact gain increases steadily as the frequency increases from 0 to $0.577/L$, the frequency range corresponding to 0-30 deg phase lag. Thus the

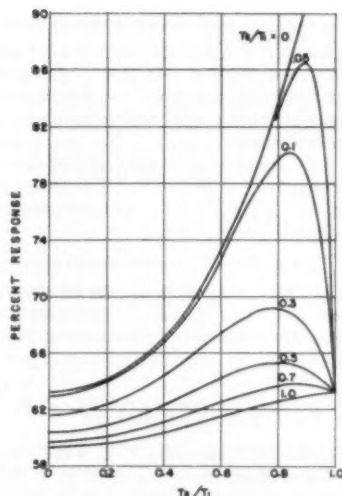


FIG. 8 PER CENT RESPONSE OF $(1 + T_{2s})/[(1 + T_{1s})(1 + T_{3s})]$ WHEN ELAPSED TIME AFTER A STEP CHANGE EQUALS THERMAL LAG

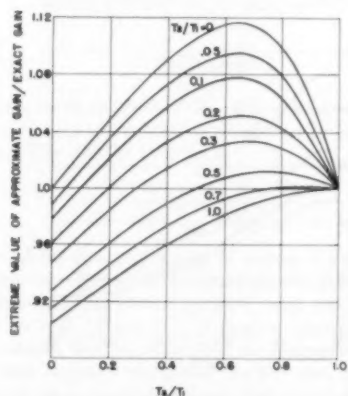


FIG. 9 EXTREME VALUE OF GAIN RATIO FOR $(1 + T_{2s})/[(1 + T_{1s})(1 + T_{3s})]$

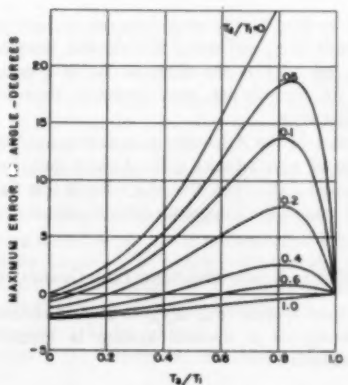


FIG. 10 EXTREME VALUE OF PHASE ERROR FOR $(1 + T_{2s})/[(1 + T_{1s})(1 + T_{3s})]$

largest value of the gain ratio occurs at the upper end of the frequency range and it is this extreme value which is plotted in Fig. 9. For other values of the time constants the gain ratio decreases steadily as the frequency increases over the range so that the gain ratio is smallest at the upper end of the range. Fig. 9 also shows this smallest value.

The phase error (approximate angle minus exact angle) also exhibits this same type of behavior. The extreme values are plotted in Fig. 10. If $T_1 \geq 0.3T_1$, the maximum error in using the approximation is less than 5 deg.

THREE TIME CONSTANTS IN SERIES

The circuit of Fig. 2(e) consists of three interacting time constants in series. This may be replaced by an equivalent circuit with three noninteracting time constants whose transfer function has the form

$$\frac{\theta_2}{\theta_1}(s) = \frac{1}{(1 + T_1s)(1 + T_2s)(1 + T_3s)} \quad (T_1 \geq T_2 \geq T_3) \dots [9]$$

where T_1 is the largest time constant, T_2 is the next largest, and T_3 is the smallest. Here $L = T_1 + T_2 + T_3$.

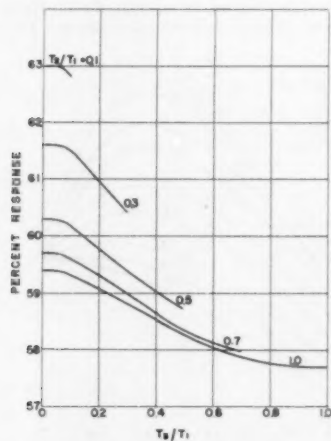


FIG. 11 PER CENT RESPONSE OF $1/[(1 + T_1s)(1 + T_2s)(1 + T_3s)]$ WHEN ELAPSED TIME AFTER A STEP CHANGE EQUALS THERMAL LAG

According to Fig. 11 the step response is between 57 and 63 per cent complete when the elapsed time equals the thermal lag. Thus the thermal lag is a good approximation to the 63 per cent response time for all systems of this type.

In Theorem 1 of the Appendix it is shown analytically that the ratio of approximate gain to exact gain lies between 0.866 and 1.00 when the phase lag is less than 30 deg. In this region the maximum error in phase angle is less than 3.1 deg.

n EQUAL NONINTERACTING TIME CONSTANTS

This is an easy system [Fig. 2(f)] to discuss although its practical importance as a thermal system is questionable. Its transfer function is

$$\frac{\theta_2}{\theta_1}(s) = \frac{1}{(1 + T_1s)^n}$$

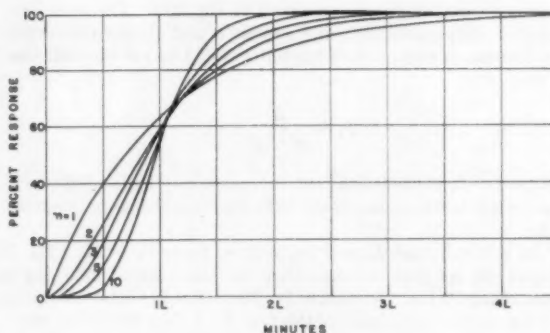


FIG. 12 STEP RESPONSE OF n EQUAL NONINTERACTING TIME CONSTANTS IN SERIES $1/(1 + T_1s)^n$

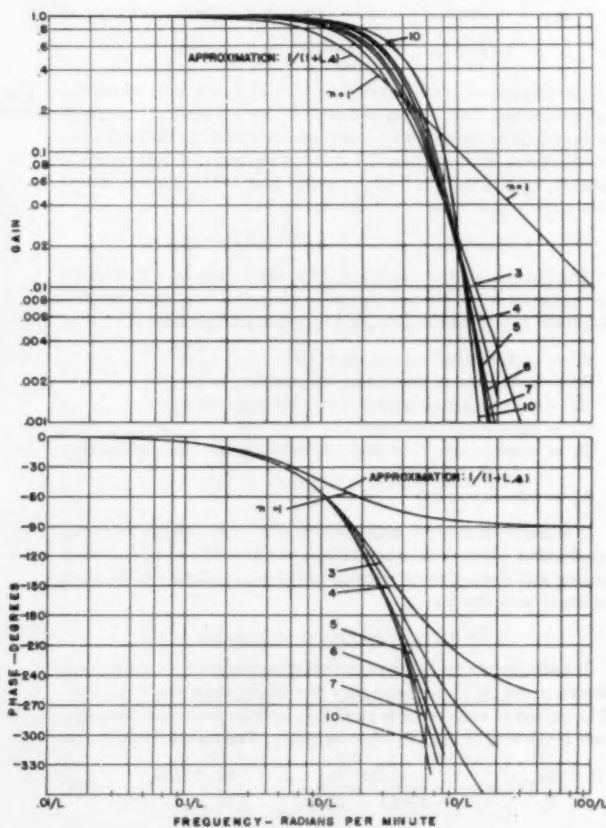


FIG. 13 FREQUENCY RESPONSE OF n EQUAL NONINTERACTING TIME CONSTANTS IN SERIES $1/(1 + T_1s)^n$

$$= \frac{1}{1 + n(T_1s) + \frac{n(n-1)}{2}(T_1s)^2 + \dots + (T_1s)^n} \dots [10]$$

where $T_1 = RC$ is the time constant and n is the number of stages. The thermal lag $L = nT_1$. According to Fig. 12 the response is 63 per cent complete when the elapsed time after the step change is between $1.0L$ and $1.1L$, up to ten equal stages.

When the elapsed time equals the thermal lag, the response is between 54 and 63 per cent complete for $n \leq 10$. Again, then, the lag is a good approximation to the 63 per cent response time.

In this case the approximate transfer function is $1/(1 + Ls) = 1/(1 + nT_1s)$, the corresponding frequency response being plotted in Fig. 13. Up to 30 deg phase lag the ratio of approximate gain to actual gain lies between 0.866 and 1.00 and the maximum error in phase is less than 3 deg.

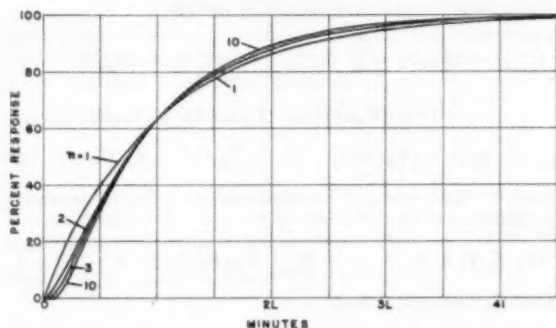


FIG. 14 STEP RESPONSE OF n EQUAL INTERACTING TIME CONSTANTS IN SERIES

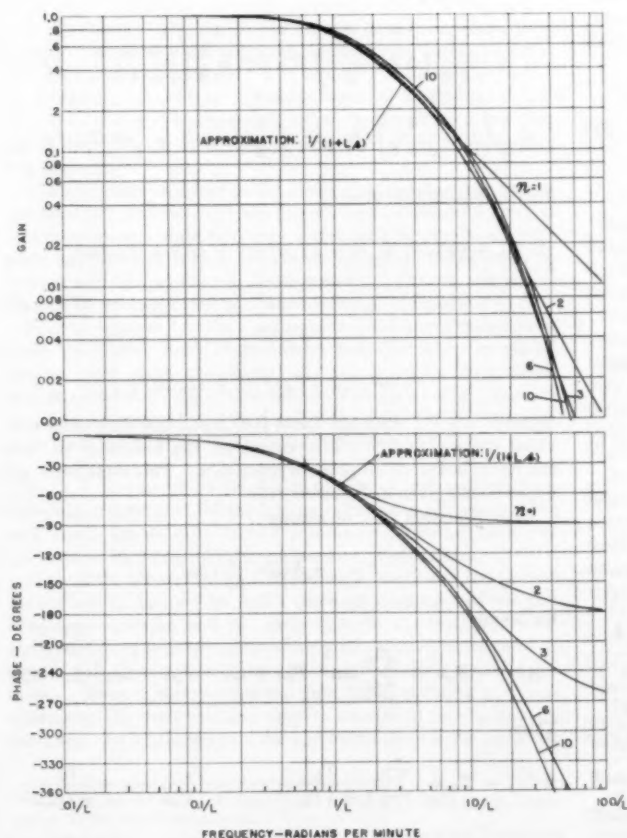


FIG. 15 FREQUENCY RESPONSE OF n EQUAL INTERACTING TIME CONSTANTS IN SERIES

n EQUAL INTERACTING TIME CONSTANTS

Another possibility is to have a series of equal time constants which are interacting [Fig. 2(g)]. The step responses of Fig. 14 show that the thermal lag L , which in this case equals $n(n+1)RC/2$, is a good approximation for the 63 per cent response time if the number of stages does not exceed 10.

On setting $T_1 = RC$, the transfer function is

$$\frac{\theta_0(s)}{\theta_i(s)} = \frac{1}{1 + (n+1)n(T_1s)/2 + \dots + (T_1s)^n}$$

where the coefficient of $(T_1s)^k$ is $(n+k)/(2k)(n-k)!$. The approximation to the frequency response is $1/(1 + Ls) = 1/[1 + n(n+1)T_1s/2]$. According to Fig. 15 the maximum error in phase is less than 2 deg between 0 and 30 deg phase lag, the corresponding ratio of approximate gain to actual gain being greater than 0.866.

ACKNOWLEDGMENT

The author wishes to express appreciation to Mr. W. I. Caldwell, Director of Research, Taylor Instrument Companies, for recommending this study and making valuable suggestions.

REFERENCES

"Method for Presenting the Response of Temperature-Measuring Systems," by R. Looney, published in this issue, pp. 1851-1856.

Appendix

The n -mesh network of Fig. 2(h) consists of interacting resistances and capacities which may be equal or unequal. The transfer function is

$$\frac{\theta_0(s)}{\theta_i(s)} = \frac{1}{\Delta_n(s)} \quad [11]$$

where $\Delta_n(s)$ is a polynomial of degree n with positive coefficients. The characteristic equation $\Delta_n(s) = 0$ has n roots and it was proved by Bode⁴ that all of the roots must be real. Since it is a passive network, it is always stable, that is, all roots of the characteristic equation have negative real parts. In this case, then, the n roots are all real and negative. This means that the interacting network can be replaced by an equivalent network with noninteracting time constants. The equivalent transfer function is

$$\frac{\theta_0(s)}{\theta_i(s)} = \frac{1}{(1 + T_1s)(1 + T_2s) \dots (1 + T_ns)} \quad [12]$$

where $T_1 \geq T_2 \geq \dots \geq T_n > 0$. Both Equations [11] and [12] give the same response to a disturbance in input. In proving the following theorem, it is more convenient to use Equation [12].

The theorem is made more general by considering the transfer function of Equation [13] rather than Equation [12]. It allows for the possibility of a distance-velocity lag being added to any of the systems since Equation [13] includes a factor $e^{-T_d s}$, which is the transfer function of an element characterized by a distance-velocity lag T_d . A liquid-filled tube system is included as a special case of Equation [13] by setting $T_d = 0$ and $n = 2$ (see Equation [7]). Therefore, the results of the following

⁴ "Network Analysis and Feedback Amplifier Design," by H. W. Bode, D. Van Nostrand Company, Inc., New York, N. Y., 1945, p. 134.

theorem apply to all of the networks of Fig. 2, except Fig. 2(d):
Theorem 1. Let

$$\frac{\theta_0}{\theta_i}(s) = \frac{e^{-T_d s} (1 - T_d s)}{\prod_{k=1}^n (1 + T_k s)} \quad (T_1 \geq T_2 \geq \dots \geq T_n > 0) \quad [13]$$

and let

$$\frac{\theta_0}{\theta_i}(s) = \frac{1}{1 + L_n s} \left(L_n = T_d + T_a + \sum_{k=1}^n T_k \right) \quad [14]$$

If $0 \leq \omega \leq 0.577/L_n$, then

$$0.866 \leq \left| \frac{\theta_a}{\theta_0}(j\omega) \right| \leq 1.00 \dots \dots \dots [15]$$

$$0^\circ \leq \text{Angle } \frac{\theta_a}{\theta_0}(j\omega) \leq 3.1^\circ \dots \dots \dots [16]$$

Proof. From the definitions

$$\frac{\theta_a}{\theta_0}(j\omega) = \frac{e^{T_d \omega j} \prod_{k=1}^n (1 + T_k \omega j)}{(1 - T_d \omega j)(1 + L_n \omega j)} \dots \dots \dots [17]$$

so that

$$\left| \frac{\theta_a}{\theta_0}(j\omega) \right|^2 = \frac{\prod_{k=1}^n [1 + (T_k \omega)^2]}{[1 + (T_d \omega)^2][1 + (L_n \omega)^2]} \\ = \frac{[1 + (T_d \omega)^2] \prod_{k=2}^n [1 + (T_k \omega)^2]}{[1 + (T_d \omega)^2][1 + (L_n \omega)^2]} \dots [18]$$

Since $T_1 \geq T_a$

$$\left| \frac{\theta_a}{\theta_0}(j\omega) \right|^2 \geq \frac{\prod_{k=2}^n [1 + (T_k \omega)^2]}{1 + (L_n \omega)^2} \geq \frac{1}{1 + (L_n \omega)^2}$$

Now $L_n \omega \leq 0.577$ and so

$$\left| \frac{\theta_a}{\theta_0}(j\omega) \right| \geq \frac{1}{[1 + (L_n \omega)^2]^{1/2}} \geq \frac{1}{[1 + (0.577)^2]^{1/2}} = 0.866$$

which provides the lower bound of Equation [15]

Next the upper bound of Equation [15] will be established by using the principle of finite induction. If $n = 1$, then

$$\left| \frac{\theta_a}{\theta_0}(j\omega) \right|^2 = \frac{1 + (T_1 \omega)^2}{[1 + (T_d \omega)^2][1 + (L_1 \omega)^2]}$$

which is obviously less than or equal to unity. For the case $n = 2$, using the fact that

$$T_1 T_2 \omega^2 \leq (T_1 + T_2)^2 \omega^2 / 2 \leq (L_2 \omega)^2 / 2 \leq (0.577)^2 / 2 < 2$$

Then

$$[1 + (T_1 \omega)^2][1 + (T_2 \omega)^2] = 1 + (T_1^2 + T_2^2) \omega^2 + 2 T_1 T_2 \omega^4 \\ < 1 + (T_1^2 + T_2^2) \omega^2 + 2 T_1 T_2 \omega^2 \\ = 1 + (T_1 + T_2)^2 \omega^2 \leq 1 + (L_2 \omega)^2 \\ \leq [1 + (T_d \omega)^2][1 + (L_2 \omega)^2]$$

Thus the numerator of Equation [18] is less than the denominator so that the ratio is less than unity for $n = 2$.

Assume that the ratio has an upper bound of unity for $n = i$, that is, for $L_i \omega \leq 0.577$

$$\frac{\prod_{k=1}^i [1 + (T_k \omega)^2]}{[1 + (T_d \omega)^2][1 + (L_i \omega)^2]} \leq 1$$

It is necessary to show that for $n = i + 1$ the Ratio [18] is less than unity when $L_{i+1} \omega \leq 0.577$. Since $0 \leq L_i \omega \leq L_{i+1} \omega \leq 0.577$, the previous inequality may be applied

$$\prod_{k=1}^{i+1} [1 + (T_k \omega)^2] = [1 + (T_{i+1} \omega)^2] \prod_{k=1}^i [1 + (T_k \omega)^2] \\ \leq [1 + (T_d \omega)^2][1 + (T_{i+1} \omega)^2][1 + (L_i \omega)^2] \\ = [1 + (T_d \omega)^2][1 + (L_i^2 + T_{i+1}^2) \omega^2 + T_{i+1}^2 L_i^2 \omega^4] \dots [19]$$

Since the time constants are numbered according to decreasing magnitude

$$k T_k \leq T_1 + T_2 + \dots + T_k \leq L_{i+1} \text{ for } k = 1, 2, \dots, i + 1$$

Thus $T_k \leq L_{i+1}/k$ so that

$$T_{i+1} L_i \omega^2 = T_{i+1} (T_d + T_a + T_1 + \dots + T_i) \omega^2 \\ \leq \frac{1}{i+1} \left(1 + 1 + 1 + \frac{1}{2} + \dots + \frac{1}{i} \right) (L_{i+1} \omega)^2 \\ \leq \frac{1}{i+1} \left(3 + \frac{i-1}{2} \right) (L_{i+1} \omega)^2 = \frac{1}{2} \left(\frac{i+5}{i+1} \right) (L_{i+1} \omega)^2 \\ \leq \frac{1}{2} \left(1 + \frac{4}{i+1} \right) (L_{i+1} \omega)^2 \leq \frac{3}{2} (L_{i+1} \omega)^2 \leq \frac{3}{2} (0.577)^2 < 2$$

Substitution in [19] gives

$$\prod_{k=1}^{i+1} [1 + (T_k \omega)^2] \leq [1 + (T_d \omega)^2][1 + (L_i^2 + T_{i+1}^2) \omega^2] \\ + 2 T_{i+1} L_i \omega^2 \\ = [1 + (T_d \omega)^2][1 + (L_i + T_{i+1})^2 \omega^2] \\ = [1 + (T_d \omega)^2][1 + (L_{i+1} \omega)^2]$$

When $n = i + 1$, then the Ratio [18] is still less than unity provided $L_{i+1} \omega \leq 0.577$. This completes the induction so that the result holds for all positive integers n . This establishes the upper bound given in Equation [15].

From Equation [17], on setting

$$A(\omega) = \text{Angle } \frac{\theta_a}{\theta_0}(j\omega)$$

for brevity

$$A(\omega) = T_d \omega + \sum_{k=1}^n \tan^{-1} T_k \omega + \tan^{-1} T_a \omega - \tan^{-1} L_n \omega \quad [20]$$

Then

$$A'(\omega) = T_d + \sum_{k=1}^n \frac{T_k}{1 + (T_k \omega)^2} + \frac{T_a}{1 + (T_a \omega)^2} - \frac{L_n}{1 + (L_n \omega)^2} \\ = T_d + \frac{T_a}{1 + (T_a \omega)^2} + \sum_{k=1}^n \left[\frac{T_k}{1 + (T_k \omega)^2} - \frac{T_k}{1 + (L_n \omega)^2} \right]$$

$$\begin{aligned}
& - \frac{T_d}{1 + (L_n \omega)^2} - \frac{T_a}{1 + (L_n \omega)^2} \\
& = \frac{T_d(L_n \omega)^2}{1 + (L_n \omega)^2} + \frac{T_a(L_n^2 - T_a^2 \omega^2)}{[1 + (T_d \omega)^2][1 + (L_n \omega)^2]} \\
& \quad + \sum_{k=1}^n T_k \left[\frac{(L_n^2 - T_k^2) \omega^2}{[1 + (T_k \omega)^2][1 + (L_n \omega)^2]} \right]
\end{aligned}$$

Since each $T_k \leq L_n$ and $T_a < L_n$, this quantity is nonnegative and hence A is a monotone nondecreasing function of ω . Therefore, for $\omega \geq 0$, $A(\omega) \geq A(0) = 0$.

The function $A(\omega)$ also may be written

$$\begin{aligned}
A(\omega) &= L_n \omega - \tan^{-1} L_n \omega - [T_a \omega - \tan^{-1} T_a \omega] \\
&\quad - \sum_{k=1}^n [T_k \omega - \tan^{-1} T_k \omega]
\end{aligned}$$

Since the function $X - \tan^{-1} X$ is 0 when $X = 0$ and is an increasing function of X for $X > 0$, each term in brackets ≥ 0 and so

$$\begin{aligned}
A(\omega) &\leq L_n \omega - \tan^{-1} L_n \omega = 0.577 - 0.524 \\
&= 0.053 \text{ rad} < 3.1 \text{ deg}
\end{aligned}$$

which is the second part of Equation [16].

Discussion

R. D. COOK.⁵ The lag due to thermal-measuring elements is usually a secondary one compared to the larger lags inherent in the process equipment itself. If it is not, then the system should be redesigned so that it is. Thus the region of interest is the low-frequency end of the response, or where the phase lag is less than 30–40 deg. This is in agreement with the fundamental basis of this paper.

The responses analyzed in the paper are not uniquely those of temperature elements, but are general combinations of positive and negative real roots and poles, which may be used to approximate any complex system. With the exception of the work by Harper and Muller-Girard, these transfer functions are rather arbitrarily selected as being representative of thermal systems.

It is of interest to note that these several transfer functions have nearly the same low-frequency response when correlated against their constant-velocity lag. Particularly, they all resemble a first-order lag in this region. This fact can be especially useful in selecting the form of a transfer function to use to approximate the response of a particular physical component.

E. G. J. EYKMAN.⁶ In the design of control systems simplifications in the description of the frequency response are certain to be welcomed. On the other hand it is most desirable that such simplifications are attended with the necessary restrictions.

Now in the theoretical and experimental studies of the present author and R. Looney⁷ we find a thorough treatment of one possible approximation and the restrictions of it. With the enormous variation in temperature-sensing elements it remains to be seen if all these elements can be described with a linear behavior. Even in simple cases the fluid film is in fact a nonlinear resistance. In most practical cases this seems to be of minor importance. As is pointed out, the approximation for the phase lag

is valid in the range 0–30 deg. For higher frequencies the exact phase lags will be greater than the approximated values. Therefore it may have preference to present the phase lags as $\varphi = \omega L$, which will be valid in the same range. The approximated phase lags being now mostly greater than the exact values, the user himself will feel safer.

H. M. PAYNTER.⁸ The author has explored the use of what the writer calls "single-lag models" of monotone processes, occurring, in this case, in temperature-sensing elements. The basic calculus underlying the problems of parameter determination for these as well as more accurate models, has been presented in considerable detail by the writer and colleagues in several publications.^{9–12}

The author's equivalent time lag L , is identical to the writer's mean time delay T_m . However, the writer has established the existence of a complete set of derived time constants, which permit simple and direct modeling of any monotone process such as those treated by the author.

By direct analogy to the central limit theorem of mathematical statistics, any cascade and/or paralleling of a sufficiently large number of elemental monotone processes must necessarily converge in the limit to the normal or Gaussian process having the transform

$$F(s) = \frac{\theta_0}{\theta_1}(s) = e^{-T_m s} + \frac{1}{2} T_d s^2 \dots \dots \dots [21]$$

with mean delay T_m and dispersion time T_d .

For an operation of the form of the author's Equation [13], these time constants are given by the expressions

$$T_m (= L_n) = T_d + T_a + \sum_{k=1}^n T_k$$

$$T_d^2 = -T_a^2 + \sum_{k=1}^n T_k^2$$

Statisticians call the ratio T_d/T_m the "coefficient of variation." For a pure delay, this has the value zero; and for a first-order lag, the value unity. For most commonly encountered monotones, the coefficient will vary between these extremes.

Thus, as pointed out by the author, a single-lag model will necessarily almost always have more low-frequency attenuation than the prototype process. Ignoring this fact in control studies may lead to errors on the unsafe side. For this reason the writer prefers always to use at least two-parameter models (matching both T_d and T_m), following methods similar to those outlined in the references cited.

As to determining the value of $L = T_m$ from step-response data, it is helpful to realize that this time constant measures the time interval from the instant of application of the step to the centroid of the impulse response. In other words, the mean delay measures the equivalent pure delay and therefore bisects the step-response curve as indicated in Fig. 16.

Instead of estimating $L = T_m$ as the time for 63 per cent recovery, a considerably more accurate value can be obtained as the

⁵ Assistant Professor of Mechanical Engineering, Massachusetts Institute of Technology, Cambridge, Mass. Mem. ASME.

⁶ "A New Method of Evaluating Dynamic Response of Counter-Flow and Parallel-Flow Heat Exchangers," by H. M. Paynter and Y. Takahashi, Trans. ASME, vol. 78, 1956, pp. 749–758.

⁷ "The Dynamic Response of Industrial Thermometers in Wells," by T. C. Linahan, Trans. ASME, vol. 78, 1956, pp. 759–763.

⁸ "On an Analogy Between Stochastic Processes and Monotone Dynamic Systems," by H. M. Paynter, Tagung Regelungstechnik, Heidelberg, Germany, September, 1956, Paper No. 37.

⁹ "Specifying Stable Control Systems," by R. J. Medkoff, Askania Report TSD 48, Askania Regulator Company, 1955.

⁵ Shell Chemical Corporation, Martinez, Calif.

⁶ Laboratorium voor Technische Physica der Technische Hogeschool, Delft, The Netherlands.

⁷ This discussion also includes discussion of "Method for Presenting the Response of Temperature-Measuring Systems," by Robert Looney, appearing on pp. 1851–1856 of this issue of Transactions.

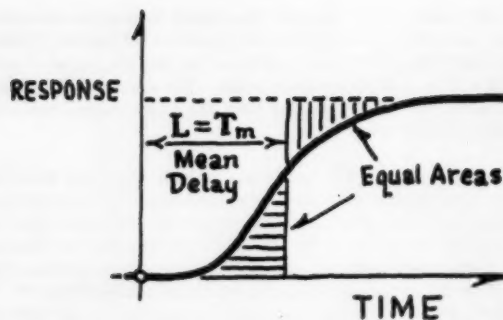
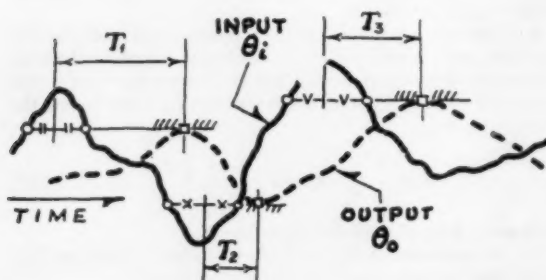
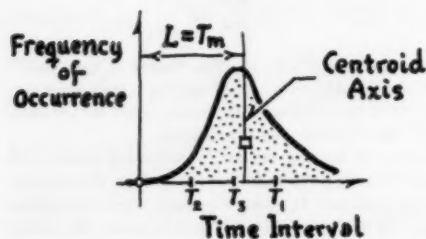


FIG. 16 DETERMINATION OF MEAN DELAY FROM STEP RESPONSE



(a) Sampled Values of Equivalent Delay



(b) Determination of Mean Delay

FIG. 17 EQUIVALENT DELAY FROM ARBITRARY SIGNALS

arithmetical mean of the times for 16 per cent and 84 per cent recoveries. Methods for using "probability paper" and other useful devices to determine both T_m and T_r are indicated elsewhere.¹²

Based on the use of a binomial model,¹³ the equivalent lag (T_m) may be determined rapidly for arbitrary curves of θ_i and θ_o as indicated in Fig. 17. However, it is necessary that the gains and scales of the two variables be identical in the steady state, in order to use this technique.

J. McMILLAN.¹³ The author is to be congratulated on discovering such a simple working approximation. Mathematicians do not always direct their energies toward these lines.

The main question in the discussor's mind concerned the appli-

¹³ Central Instrument Laboratory, Imperial Chemical Industries, Ltd., Reading, Berks, England.

cation of the approximation. The answer was found in the paper by Robert Looney.¹⁴

As the author says, her results have a range of application wider than that of temperature-sensing elements. These and similar approximations may well be invaluable when the dynamic characteristics of the more complex plant elements have been defined in suitable terms.

AUTHOR'S CLOSURE

It should be emphasized that the frequency responses are plotted on a frequency scale which involves the thermal lag L . In Fig. 5, for example, $L = T_1 + T_2$ so that the value of L changes from curve to curve. Each curve on the graph is plotted against the appropriate " L " for that particular system.

The thermal lag L is simply related to the system transfer function. If

$$\frac{\theta_o}{\theta_i} = \frac{1}{1 + a_1s + a_2s^2 + a_3s^3 + \dots + a_ns^n}$$

then L is the coefficient of s in the denominator, that is, $L = a_1$.

The author concurs with the philosophy of Mr. Cook. Published data on thermal systems, although not extensive, support the use of the approximation in the low-frequency range. On the other hand, the results of the paper can be used by anyone who finds that his system can be represented by one of the transfer functions under consideration.

Mr. Eykman's remarks are relevant and practical. If one is interested in approximating the phase lag at higher frequencies, the approximation $\phi = \omega L$ is indeed safer. However, in the specified region of interest, 0 to 30 deg phase lag, there is at most 3 deg difference between the two approximations.

The author feels that the present paper is original and distinctly different from Professor Paynter's work in the following respects:

1 The main objective of this paper is to state and prove the limits of error in using a simple one-parameter approximation. This is done in Theorem 1 of the Appendix where the errors in gain and phase are precisely stated in the range of 0 to 30-deg phase lag. The proof applies to a large class of dynamic systems including some systems which are not monotone.

Professor Paynter has not given any estimate of the error involved in using any of his models. Indeed, he has not indicated that some of the infinite series expansions in his paper¹¹ converge only in restricted regions. To quote, "The transmission operator, $\log \hat{P}$, corresponding to any monotone \hat{P} , can also be expanded in a power series of the form

$$\log \hat{P} = \sum_{k=0}^{\infty} \frac{c_k}{k!} (-s)^k \dots \dots \dots [26]$$

where the coefficients c_k are called (by statisticians) the *cumulants* or semi-invariants of the distribution $F(t)$." Now consider a transfer function such as

$$\hat{P}(s) = 1/(1 + T_L s)$$

Then

$$\log \hat{P} = -\log(1 + T_L s) = \sum_{k=1}^{\infty} \frac{1}{k} (-T_L s)^k$$

This series converges only for $|T_L s| < 1$. The corresponding series for gain and phase

$$\text{Gain} = \exp[-1/2(T_L \omega)^2 + 1/4(T_L \omega)^4 - 1/6(T_L \omega)^6 + \dots]$$

¹⁴ Printed in this issue of Transactions, pp. 1851-1856.

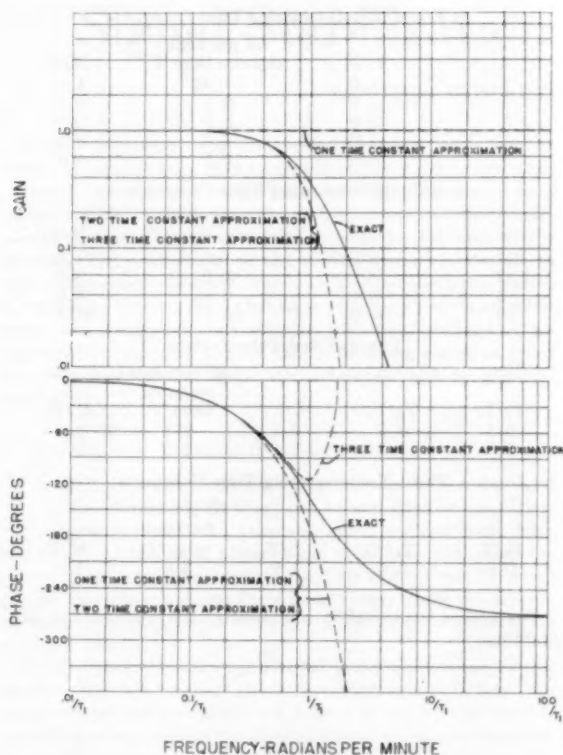


FIG. 18

$$\text{Phase} = -(T_L\omega) + 1/2(T_L\omega)^2 - 1/6(T_L\omega)^3 + \dots$$

do not converge for $T_L\omega > 1$. Therefore in this frequency range the approximation cannot be made to approach the exact frequency response by using an increasing number of derived time constants.

The solid curve of Fig. 18 represents the exact frequency response of a process with three equal time constants. The dashed curves are successive approximations using one, two, and three derived time constants according to Professor Paynter's scheme. When the dimensionless frequency is greater than unity, the addition of the third derived time constant actually decreases the accuracy of the approximation. This is not surprising since a divergent series is being used to approximate the exact frequency response.

2 In a recently presented paper¹¹ Professor Paynter defines monotone processes as follows: "A large number of fluid, thermal, chemical, and other industrial and organic processes are characterized by a step response which is monotonic nondecreasing in time as in Fig. 1(b). The corresponding frequency response would have a nonincreasing amplitude and nondecreasing phase lag with increasing frequency as indicated in Fig. 1(c). All linear systems giving rise to such response might be called *monotone processes*."

The author is puzzled by the second statement of the preceding quotation which appears to imply that a process whose step response is monotonic nondecreasing must be characterized by a gain curve which is nonincreasing. Obviously this is not the case. The step response of the averaging process shown in the inset of Fig. 19 is monotonically nondecreasing. Its transform is $(1 - e^{-T/s})/T$. The curve of gain versus frequency, plotted on

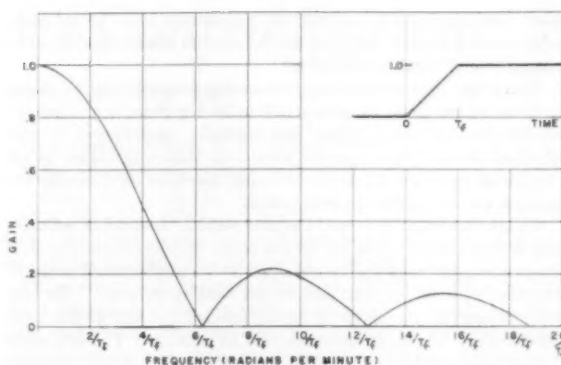


FIG. 19

linear paper on Fig. 19, has an oscillatory character in contradiction to Professor Paynter's statement.

The above definition is ambiguous since it is not clear whether the words "to such response" in the third sentence refer to the step or the frequency response. However, since he wishes to draw analogy between monotone processes and the distribution functions of probability theory which are monotone between 0 and 1, he means undoubtedly that the step response is monotone. But if this is the proper interpretation of "monotone process," then this paper considers several types of processes which are not monotone: Liquid-filled tube systems which show a dip in the initial portion of the step response and some systems in parallel which overshoot the final value. Also the classification "monotone" does not include processes without self-regulation.

3 The present paper is concerned with establishing the validity of an approximation which uses a *single* time constant. As Professor Paynter indicates above, he prefers to use at least two time constants in modeling a process. There is no practical need for using more than one time constant in the region of 0 to 30 deg phase lag as shown in this paper.

The author questions Professor Paynter's statement that his set of derived time constants permits simple and direct modeling of any monotone process. Certainly his formulas for determining the stochastic parameters of a parallel-flow heat exchanger are not simple. Neither will most engineers enjoy the determination of T_m and T_s by plotting step responses on probability paper.

The reader is cautioned that the transform [21] given by Professor Paynter is not the familiar Laplace transform, but the bilateral Laplace transform where the range of integration is from $-\infty$ to $+\infty$. Its inverse is

$$F(t) = \frac{1}{\sqrt{(2\pi)T_s}} \int_{-\infty}^{\infty} \exp[-(\tau - T_m)^2/2T_s^2] d\tau \dots [22]$$

For finite values of T_m/T_s , this transient is not zero at zero time. Further the response is 50 per cent complete when $t = T_m = L$. If one refers to Figs. 4, 7, 8, 11, 12, 14 of this paper, one sees that these systems show about 60 per cent response when $t = T_m = L$. Thus the approximation [22] cannot be expected to represent all monotone systems at all frequencies so that one needs to know when the approximation is valid.

In his discussion Professor Paynter remarks that "... any cascade and/or paralleling of a sufficiently large number of elemental monotone processes must necessarily converge in the limit to the normal or Gaussian process. . . ." Since it is a question of convergence, which implies the existence of an infinite set of processes, the words "a sufficiently large number" seem superfluous.

ous. One needs to know how many processes must be taken in order to insure approximation by the normal process and also the magnitude of the errors involved.

The single time constant approximation suggested in this paper is intended for use in the region of 0 to 30 deg phase lag, which includes the amount of phase lag normally contributed by the thermal element in a control loop. In this range there is no danger of errors on the unsafe side and therefore no necessity for using a more complex approximation.

In his discussion Professor Paynter states, "Instead of estimating $L = T_m$ as the time for 63 per cent recovery, a considerably more accurate value can be obtained as the arithmetical mean of the times for 16 per cent and 84 per cent recoveries." To test this statement, a number of representative systems of the type discussed in this paper were selected at random. The following tables compare the actual value of L with the 63 per cent response time and with M , the arithmetic mean of the 16 per cent and 84 per cent response times. These results indicate that M is not "considerably more accurate" for the systems studied.

Two-Time-Constant System

T_2/T_1	L/T_1	63 per cent response time/ T_1	M/T_1
0	1.0	1.0	1.0
0.2	1.2	1.2	1.2
0.4	1.4	1.5	1.4
0.6	1.6	1.7	1.6
0.8	1.8	1.9	1.8
1.0	2.0	2.1	2.0

n Equal Non-Interacting Time Constants

n	L/T_1	63 per cent response time/ T_1	M/T_1
1	1.0	.95	1.0
2	2.0	2.1	2.0
3	3.0	3.2	3.0
4	4.0	4.3	3.8
5	5.0	5.3	4.9

n Equal Interacting Time Constants

n	L/T_1	63 per cent response time/ T_1	M/T_1
1	1.0	1.0	1.0
2	3.0	3.0	3.0
3	6.0	6.0	6.0
10	55.0	55.0	55.3

Liquid-Filled Tube System

T_2/T_1	T_3/T_1	L/T_1	63 per cent response time/ T_1	M/T_1
0.5	0.6	2.1	2.1	2.0
0.3	1.0	2.3	2.0	2.0

Three Noninteracting Time Constants

T_2/T_1	T_3/T_1	L/T_1	63 per cent response time/ T_1	M/T_1
0.5	0.4	1.9	2.0	1.9

The author is pleased to acknowledge the comments of Mr McMillan.

Signal Stabilization of a Control System

By RUFUS OLDENBURGER,¹ LAFAYETTE, IND.

Linear automatically controlled systems with two or more dominant lags may be stabilized by the introduction of noise, or a signal of sufficiently high frequency, or a signal with sufficiently high-frequency components, provided that the hunt of the system is not excessively severe. The amplitude of the signal must be enough to run a bounded element, such as a governor pilot valve, through its full stroke. One or multiple-lag systems with optimum nonlinear controls also may be stabilized by an appropriate signal. Unless the stabilizing signal is great the response to the larger disturbances will be affected negligibly.

SIGNAL STABILIZATION

IN THE past, automatic control systems have been stabilized by the use of a stable linear band about equilibrium. Thus control systems that otherwise are nonlinear have been stabilized with the use of a linear band in the sense that, when the errors in the controlled variable and its derivatives are small enough, the system behaves like a linear system whose characteristic roots are satisfactory. Stability in this paper is achieved by nonlinear means.

MacColl and Minorsky contributed to the general area of this paper. MacColl treated² on-off servomechanisms, where the output of the nonlinear element is A , zero, or $-A$ for a number A , according as the input of the element is positive, zero, or negative. By the introduction of a sinusoidal signal, the system behaves like a linear system for small inputs superimposed on this signal. The output of the nonlinear element in the present paper is assumed to be proportional to the input for a range of values of the input.

Minorsky treated³ the use of a signal to excite or quench the hunt of a physical system described by a second-order differential equation in the variable $x(t)$, for time t , where the coefficient of the "damping" term in dx/dt is an even polynomial in x . The stabilization of Minorsky depends on properties of asymptotic solutions of the differential equation.

In every problem involving a hydraulic servo, the servo-piston speed is bounded, Fig. 1. In this figure the system to be controlled is shown in one block. The variable m is the controlling variable, such as the throttle on a gasoline engine. If the controller is a governor, m can be taken to be servo-piston position. The output of the controlled system is denoted by c . For a governor-engine system, c is engine rpm (revolutions per minute). The input to the controller is $r - c + r_s$, where r is the reference value of the controlled variable (speed setting in the case of a governor engine system), and r_s is the value of the extra input signal used to stabilize the system. The variables r , c , and r_s are measured

as deviations from an equilibrium state for which $r = r_s = c = 0$. Owing to physical limitations we have

$$|m'| \leq K \dots \dots \dots [1]$$

for a constant K , where $|m'|$ is the absolute value of m' , and m' denotes the derivative dm/dt of m with respect to time t .

Physical systems always involve lags. The systems to which the stabilization technique to be described here applies are systems with two or more lags where one of the lags does not dominate the others, and at the same time the controller is based on the use of a linear control function as is customary; that is, on the use of integral, proportional, and derivative control (all three types need not be involved simultaneously). The technique also applies to physical systems with one or more lags where the control function involves the absolute value of the derivative error m' as described in a recent paper⁴ by the author, and/or higher derivatives. Instead of the absolute value other nonlinearities may be involved.

Suppose now that the system of Fig. 1 hunts with a frequency f when $r_s = r = 0$; i.e., when there is no input signal r_s , and the

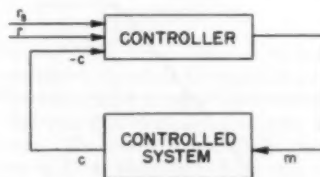


FIG. 1 SYSTEM WITH CONTROLLER

normal input r is zero. It is assumed that the hunt is not completely wild. The technique to be described generally applies to systems with a hunt that does not exceed 10 per cent of the full range of the controlled variable, such as 10 per cent of base speed in the case of a prime-mover system.

By the introduction of a sinusoidal signal r_s with frequency greater than or equal to $10f$, and amplitude more than enough to make m' reach its limits when the system is not disturbed, but not excessive, the hunt amplitude is diminished substantially or reduced to zero. The amplitude of r_s , for example, can be 1.2 to 4 times the value needed to make m' reach its limits, but should not be 20 times this value.

For a system with a linear-control function the stabilizing signal r_s may be introduced anywhere in the controller ahead of the bounded output element. In place of a sinusoidal signal, random noise may be employed. Also r_s can be taken to be a triangular wave, pulse, or other appropriate repetitive signal, with a frequency greater than or equal to $10f$, or containing components of this size and sufficient amplitude to run m' to its limits. A reasonable proportion of the time must be spent away from saturation of the bounded element. Thus a square wave will not work (there should be a one to one correspondence between values of r and c).

Stabilization with r_s will be called "signal stabilization." The frequency of the stabilizing signal does not have to be a multiple of the hunt frequency f .

⁴"Optimum Nonlinear Control," by Rufus Oldenburger, Trans. ASME, vol. 79, 1957, pp. 527-542.

¹Professor of Mechanical Engineering and Engineering Sciences, Purdue University; formerly, Director of Research, Woodward Governor Company, Rockford, Ill. Mem. ASME.

²"Fundamental Theory of Servomechanisms," by L. A. MacColl, D. Van Nostrand Company, Inc., New York, N. Y., 1945, pp. 78-87.

³"On Asynchronous Action," by N. Minorsky, *Journal of the Franklin Institute*, vol. 259, no. 3, 1955, pp. 209-219.

Contributed by the Instruments and Regulators Division and presented at the Annual Meeting, New York, N. Y., November 25-30, 1956, of THE AMERICAN SOCIETY OF MECHANICAL ENGINEERS.

NOTE: Statements and opinions advanced in papers are to be understood as individual expressions of their authors and not those of the Society. Manuscript received at ASME Headquarters July 31, 1956. Paper No. 56-A-92.

Instead of bounding servo speed some other quantity may be limited, such as the driving torque on the rotor of an electric motor or the current that gives rise to this torque.

REASONS WHY SIGNAL STABILIZATION WORKS

Signal stabilization changes the gains in the channels for which it is effective. The presence of available supply frequencies of 60 cps, 400 cps, or some other "high" frequency in the case of electrical devices makes the introduction of signal stabilization a simple matter in such applications.

Consider an ordinary hydraulic servo composed of the usual valve-piston arrangement. That the servo speed is bounded is equivalent to the stroke of the valve being bounded. The input-output characteristic of a bounded element, such as this valve, is shown in Fig. 2. Its gain is plotted in Fig. 3, where the describing function⁴ is employed for the gain. As the amplitude of the input to the bounded element is increased the gain of this element is diminished. The equation of a servo is normally taken to be

$$m' = kx \dots \dots \dots [2]$$

for a constant k , pilot-valve position x , and velocity m' of the servo. Consider a controller with the control function

$$\Sigma = c_1 + \alpha c_1' \dots \dots \dots [3]$$

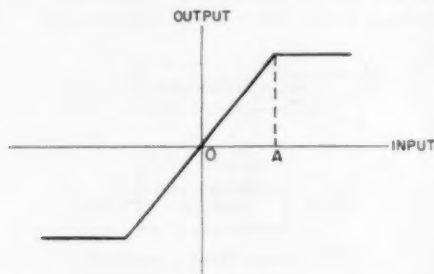


FIG. 2 CHARACTERISTIC CURVE OF BOUNDED ELEMENT

for a constant α and derivative c_1 of c_1' , where

$$x = -K_1 \Sigma \dots \dots \dots [4]$$

for a constant K_1 , and $c_1 = r - c + r_s$. The introduction of signal stabilization reduces the gains of the proportional and derivative channels, which both feed to the bounding element, improving the system stability accordingly.

Let $\psi = c_1$ or $c_1 + Tc_1'$ for a constant T . If the control function is

$$\Sigma = \psi + \beta |\psi'| \psi' \dots \dots \dots [5]$$

for a constant β , or

$$\Sigma = c_1 + \gamma c_1' + \lambda |c_1'| c_1' \dots \dots \dots [6]$$

for constants γ and λ , the introduction of signal stabilization reduces the gains in the linear channels (corresponding to the ψ , c_1 , and $\gamma c_1'$ -terms), but increases the gain in the absquare channel. In the case of Equation [5] the gain of the channel corresponding to the absquare term $|\psi'| \psi'$ is zero at $\psi' = 0$. This gain should be raised to make the loop stable. The introduction of signal stabilization achieves this, provided that the signal is inserted before the absquare element, and not after it. Injecting this signal

⁴See ASME book "Frequency Response," The Macmillan Company, New York, N. Y., 1958, p. 242. Here the describing function is called the "equivalent admittance."

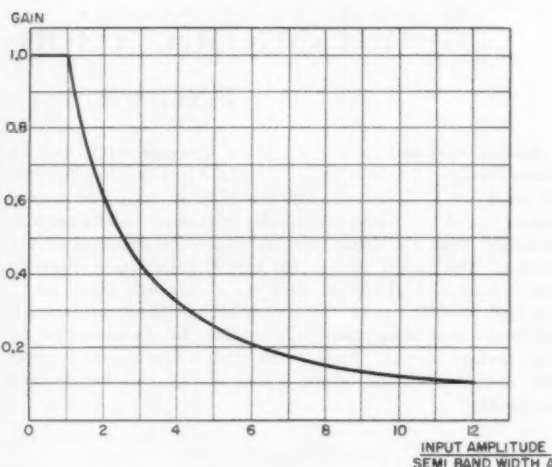


FIG. 3 GAIN CURVE FOR BOUNDED ELEMENT

after the absquare element is not effective. Similar remarks hold for the nonlinear control based on Equation [6].

EXPERIMENTAL RESULTS

In Fig. 4 is shown signal stabilization obtained experimentally on a Philbrick computer. This is for a simulated governor-engine system. The engine is given by the torque equation

$$c' = \frac{m}{(0.1D + 1)^2} + L \dots \dots \dots [7]$$

where D represents the derivative with respect to time t , and L is a load term. Also

$$|m'| \leq 10 \dots \dots \dots [8]$$

which implies that the servo-piston speed is bounded. The denominator in the torque equation corresponds to two first-order lags with 0.1-sec time constants. The governor equations are

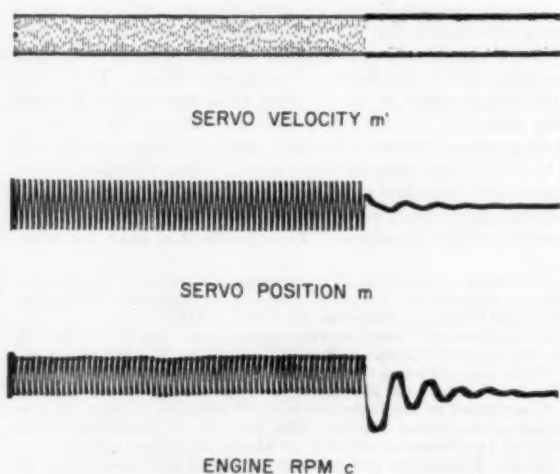


FIG. 4 STABILIZATION OF A SIMULATED GOVERNOR-ENGINE SYSTEM WITH TWO LAGS

$$\left. \begin{aligned} m' &= 100 \Sigma \\ c_1 &= r - c + r_s \\ \Sigma &= 0.8 c_1 + \frac{|c_1'|c_1'}{5} \end{aligned} \right\} \dots\dots\dots [9]$$

where Σ is the control function.

The top trace in Fig. 4 shows servo velocity m' , the second servo position m , and the third engine rpm c all versus time. The oscillation on the left is the natural 1-cps hunt of the system. Stabilization with a sinusoidal 30-cps signal is introduced suppressing the hunt as shown on the right half of the record.

Fig. 5 shows experimental results obtained for a system linear except for the fact that the servo speed is bounded. The system

is one with two lags with identical 0.1-sec time constants. The natural hunt of 1 cps appears on the left followed by a portion stabilized by a 30-cps sinusoidal signal. The relations for the system are

$$\left. \begin{aligned} c' &= \frac{m}{(0.1D + 1)^2} + L \\ |m'| &\leq 10 \end{aligned} \right\} \dots\dots\dots [10]$$

and for the control

$$\left. \begin{aligned} m' &= 50 \Sigma \\ \Sigma &= c_1 + 0.8 c_1' \\ c_1 &= r - c + r_s \end{aligned} \right\} \dots\dots\dots [11]$$

This figure indicates that the response to disturbances is little modified when signal stabilization is introduced. The system was subjected to the same sequence of four disturbances during the stabilized and unstabilized portions of the runs, resulting in the transients of the figure. The traces in Fig. 6 were taken during a steady-state run on the same system. The natural hunt appears on the left. The performance of the system with signal stabilization is shown on the right. Sinusoidal signals at 30 cps and 300 cps were used as indicated. Irregularities in the rpm trace are due to random drift of the computer.

Discussion

KEISUKE IZAWA.* The author restricts his treatment of systems with linear control functions to those with second and higher order lags. The writer is led to ask whether or not this restriction is essential. Systems with dominant first-order lags occur quite often in practice. The author might clarify the distinction between the work of L. A. MacColl and his own, since the on-off case can be obtained by taking the limit for a servo with velocity saturation by assuming infinite acceleration or deceleration at the origin.

It appears to the writer that a stabilization signal can be employed to make round ports for hydraulic valves behave more or less like rectangular ones. Also, how does one apply the technique of the paper in a practical example?

AUTHOR'S CLOSURE

Consider a controlled system with a first order lag given by the equation

$$c' = \frac{K_1 m}{(TD + 1)} \dots\dots\dots [12]$$

where T and K_1 are constants. Let the controller be given by the equation

$$m' = -K_2(c + ac') \dots\dots\dots [13]$$

for constants K_2 and a . The controlled variable c satisfies the differential equation

$$c''' + \frac{1}{T} c'' + \frac{K_1 K_2 a}{T} c' + \frac{K_1 K_2}{T} c = 0 \dots\dots [14]$$

where c'' and c''' denote the second and third derivatives of c with respect to time t . The system is stable if and only if the characteristic roots for Equation [14] have negative real parts. A change in the value of the loop gain constant $K_1 K_2$ will not

* Assistant Professor of Tokyo Institute of Technology; Visiting Fellow, Massachusetts Institute of Technology, Cambridge, Mass.

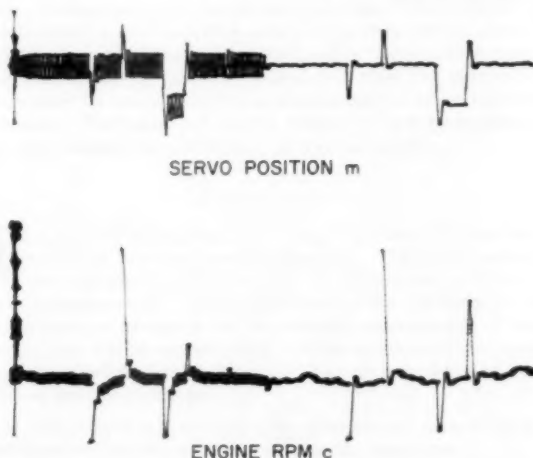


FIG. 5 SIGNAL STABILIZATION OF A LINEAR SYSTEM SUBJECT TO STEP DISTURBANCES

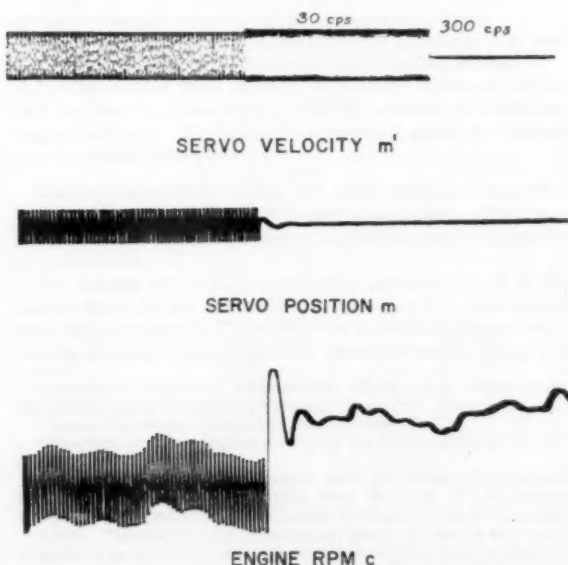


FIG. 6 SIGNAL STABILIZATION OF LINEAR SYSTEM

affect the stability of the system. Introduction of signal stabilization to vary the "gain" K_1 of the controller will thus not affect the stability of the system, a fact first established experimentally.

MacColl was interested in linearizing the response of an on-off element, rather than in stabilizing a system with such an element. The writer's concern is with stability, and nonlinearities are acceptable if they do not deteriorate the stability.

In hydraulic applications a low gain is associated with small openings of round ports of spool valves. The gain (rate of flow versus opening) must sometimes be raised to prevent hunting. The introduction of a stabilizing signal raises the gain for small openings and makes the round ports appear more like rectangular ones. The cost of machining rectangular ports is high compared to the cost of making round ports. It is often cheaper to introduce the stabilizing signal, and retain the round ports, than go to rectangular ones. Also the gain for small openings can often be

readily varied by changing the signal, whereas the cutting of new ports is expensive.

Suppose that the input to a nonlinear element is x and the output a differentiable function $f(x)$ of x . If for $x > 0$, the second derivative $f''(x)$ is negative, and for $x < 0$, we have $f''(x) > 0$, introduction of an extra sinusoidal signal will decrease the slope $f'(x)$ at $x = 0$ to a low gain. Similarly, if

$$f''(x) > 0 \text{ for } x > 0$$

$$f''(x) < 0 \text{ for } x < 0$$

introduction of an extra sinusoidal input signal will raise the gain at $x = 0$. A rigorous treatment of gain for the phenomenon of this paper has been developed and will be published elsewhere along with theoretical considerations involved in applying stabilization techniques.

Design Basis for Cascade-Type Positional Servomechanisms

BY SIDNEY LEES¹ AND T. C. BLASCHKE²

A design basis, previously developed for multiloop positional servomechanisms, has been extended to cascade-type systems. The design basis attempts to co-ordinate specifications, dynamic characteristics, interferences, and uncertainties from a consideration of the generation of torques by the system. The limitations of the system performance are distinguished from component characteristics. The concept of frequency-dependent coefficients is applied to the lead modifier damping model, the lag modifier, viscous damping model, and to the lag modifier, lead modifier damping model. It is shown that the performance may be understood from knowledge of second-order systems. Estimates of useful values of the parameters for each model are confirmed by analog studies.

INTRODUCTION

IN A PREVIOUS paper (1),³ a design basis was developed for multiloop, positional servomechanisms. The design basis is now extended to the treatment of cascade-type positional servomechanisms (2). In the interest of brevity, the background of the concepts necessary for the complete understanding of the design basis will be omitted when it exists in the previous paper hereinafter referred to as Paper I. The characteristics of the method are repeated here.

1 The method is developed taking interference, uncertainties, and dynamic factors into account, all at the same time.

2 Only the closed-chain performance equation is required.

3 A distinction is made between system and component performance. Component characteristics may be bettered by improving the individual components. Limitations exist for system performance even when all components are perfect.

4 The design basis is developed from the limitation on system performance caused by equivalent output member inertia.

5 The method leans strongly on a study of torque sources and the torque summation equation for systems with rotating output members. For linear displacement systems, the method uses forces and force summation.

The examples and discussion deal with torques and rotational positional servomechanisms for convenience only. The functional diagrams are based on electrical systems, again as a matter of convenience.

The torques acting on the controlled member in each of the models shown in the functional diagrams may be attributed to four distinct sources. These are inertia reaction torque $M_{(ir)}$, viscous damping torque M_d , torque generator output $M_{(tg)}$, and

interference torque $M_{(infr)}$. The sum must be zero, or in symbols

$$M_{(ir)} + M_d + M_{(tg)} + M_{(infr)} = 0 \dots \dots \dots [1]$$

Expressions for the torques in terms of the controlled member motion and the input are given in Table 1 for each of the models. Performance equations may be obtained by introducing the torque expressions into the torque summation equation. The performance equations for the cascade-type models are given in Table 2, first with dimensional coefficients and then with parametric coefficients. Nondimensional forms of the associated performance functions are provided in Table 3.

It was shown in Paper I that a comprehension of the performance of positional servomechanisms can be developed from a knowledge of second-order systems. A physical analysis of the basic model performance is given in Paper I. The functional diagram shown in Fig. 1 and associated mathematics is included here for comparison with the other cascade-type models. In order to assist the mathematical aspects of the design, the technique has been adopted of expressing the performance equations and performance functions as second-order forms with frequency-dependent coefficients. The entire frequency range is divided into suitable frequency subranges in each of which the frequency dependent coefficients may be assumed to be practically constant. The actual frequency response is approximated in terms of the appropriate second-order frequency response for each subrange. It is demonstrated that reasonable estimates for the system parameters can be made from the second-order approximations and a knowledge of the system requirements and limitations. Some skill is necessary, as in most approximation techniques, in order to obtain the desired simplification without sacrificing essential information. However, this skill is not too hard to acquire with practice.

As in the discussion in Paper I of multiple-loop positional servomechanisms design, it is necessary to understand the performance characteristics and limitations associated with the basic model in order to see the physical reasons for introducing additional cascaded elements into the loop.⁴ The performance equations of the basic model in Table 2 as well as the following characteristics are abstracted from Paper I.

A maximum practical value exists for the stiffness coefficient. In many instances the stiffness coefficient necessary to reduce interference torques to tolerable levels completely defines the dynamic character of the system. The range of adjustment in the dynamic properties is determined by the range in the stiffness coefficient between the minimum set by the interference torques and the practically available maximum. The stability depends on the residual damping of the system, the torque generator damping being included in the residual damping. The damping ratio is fortuitous. It may very well happen that the theoretical damping ratio becomes so small that the system actually becomes unstable when the system is made stiff enough to meet the requirements. The stability may be improved by increasing the

⁴ Cascade-type positional servomechanisms are defined as positional servomechanisms with a single unity-feedback loop. All the signal components are in series with the power-controlling components. These systems are also called series servos and tandem servos by some authors.

¹ Assistant Professor, Aeronautical Engineering Department, Massachusetts Institute of Technology, Cambridge, Mass.

² Sperry Gyroscope Company, Lake Success, N. Y.

³ Numbers in the parentheses refer to the Bibliography at the end of the paper.

Contributed by the Instruments and Regulators Division and presented at the Annual Meeting, New York, N. Y., November 25-30, 1956, of THE AMERICAN SOCIETY OF MECHANICAL ENGINEERS.

NOTE: Statements and opinions advanced in papers are to be understood as individual expressions of their authors and not those of the Society. Manuscript received at ASME Headquarters, August 1, 1956. Paper No. 56-A-105.

TABLE 1 EXPRESSIONS FOR TORQUES ACTING ON SERVOMECHANISM CONTROLLED MEMBER

	Inertia Reaction Torque $M_{(ir)}$	Damping Torque M_d	Torque Generator Output Torque $M_{(tg)}$	Interference Torques $M_{(intr)}$
Basic (b)	$-I_{(cm)}\ddot{\theta}_{(cm)}$	$-S_{(qt)}^2 c_{d(res)} \dot{\theta}_{(cm)}$	$S_{(ps)}[A;M](C) \dot{\theta}_{(cm)} - S_{(qt)}^2 S_{(tg)}[\dot{\lambda};M] \dot{\theta}_{(cm)}$	$M_{(intr)}$
Lead modifier damping (ld)	"	"	$S_{(ps)}[A;M] S_{(ld)} \frac{1 + \nu_{ld} \tau_{ld} p}{1 + \tau_{ld} p} (C) \dot{\theta}_{(cm)} - S_{(qt)}^2 S_{(tg)}[\dot{\lambda};M] \dot{\theta}_{(cm)}$	"
Lag modifier viscous damping (lg)(vd)	"	$-S_{(qt)}^2 (c_{d(res)} + c_{d(vls)}) \dot{\theta}_{(cm)}$	$S_{(ps)}[A;M] \frac{1 + \nu_{lg} \tau_{lg} p}{1 + \tau_{lg} p} (C) \dot{\theta}_{(cm)} - S_{(qt)}^2 S_{(tg)}[\dot{\lambda};M] \dot{\theta}_{(cm)}$	"
Lag modifier lead modifier damping (lg)(ld)	"	$-S_{(qt)}^2 c_{d(res)} \dot{\theta}_{(cm)}$	$S_{(ps)}[A;M] S_{(ld)} \frac{1 + \nu_{lg} \tau_{lg} p}{1 + \tau_{lg} p} \frac{1 + \nu_{ld} \tau_{ld} p}{1 + \tau_{ld} p} (C) \dot{\theta}_{(cm)} - S_{(qt)}^2 S_{(tg)}[\dot{\lambda};M] \dot{\theta}_{(cm)}$	"

Definitions:

$$I_{(cm)} = I_{(cm)} + S_{(qt)}^2 (I_{(tmm)} + I_{(qt)}(eff))$$

= equivalent controlled member inertia

$I_{(cm)}$ = controlled member inertia

$I_{(tmm)}$ = torque summing member inertia

$I_{(qt)}(eff)$ = effective gear train inertia at torque summing member

$$S_{(qt)} = S_{(qt)}[A_{(cm)}; \dot{\theta}_{(tmm)}]$$

= gear train sensitivity for controlled member angle input, torque summing member angle output

$c_{d(res)}$ = residual damping measured at torque summing member

$S_{(ps)}[A;M]$ = positional servomechanism sensitivity for angle input, torque output

$S_{(tg)}[\dot{\lambda};M]$ = torque generator sensitivity for torque summing member angular velocity input, torque output

$c_{d(vls)}$ = viscous damping coefficient

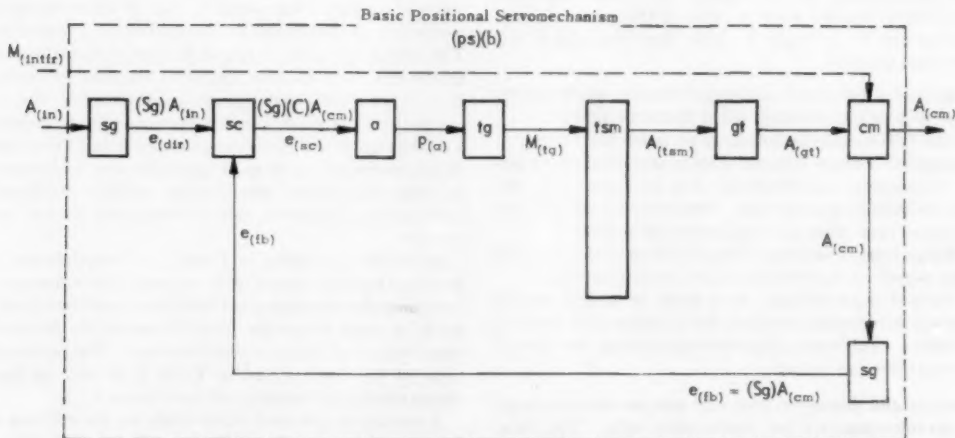
τ_{ld} = lead modifier characteristic time

ν_{ld} = lead modifier characteristic time ratio

$S_{(ld)}$ = lead modifier sensitivity = $1/\nu_{ld}$

τ_{lg} = lag modifier characteristic time

ν_{lg} = lag modifier characteristic time ratio



$A_{(in)}$ = input angle

(sg) = signal generator

(a) = amplifier

(tmm) = torque summing member

(cm) = controlled member

$A_{(cm)}$ = controlled member angle

(sc) = signal comparator

(tg) = torque generator

(gt) = gear train

$(C)A_{(cm)} = A_{(in)} - A_{(cm)}$ = controlled member correction

$e_{(dir)} = (Sg)A_{(in)}$ = input angle signal = direct voltage

$e_{(fb)} = (Sg)A_{(cm)}$ = controlled member signal = feedback voltage

$e_{(nc)} = (Sg)(C)A_{(cm)}$ = correction signal

$P(a)$ = amplifier power output

$M_{(tg)}$ = torque generator output torque

$M_{(intr)}$ = interference torque

$A_{(tmm)}$ = torque summing member angle

$A_{(gt)}$ = gear train output angle

FIG. 1 FUNCTIONAL DIAGRAM FOR A BASIC POSITIONAL SERVOMECHANISM

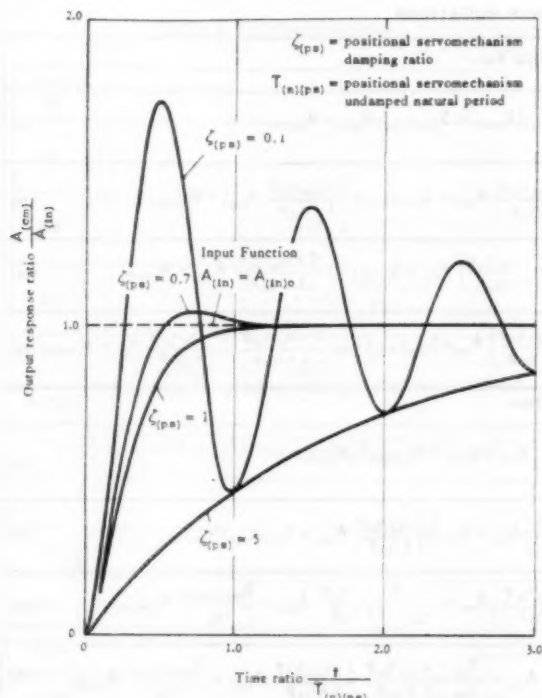


FIG. 2 STEP FUNCTION RESPONSES OF BASIC POSITIONAL SERVOMECHANISM MODELS AS A FUNCTION OF DAMPING RATIO

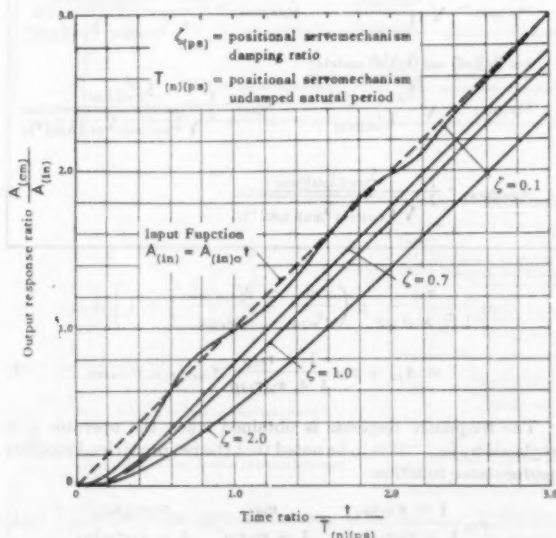


FIG. 3 RAMP FUNCTION RESPONSES OF BASIC POSITIONAL SERVOMECHANISM MODELS AS A FUNCTION OF DAMPING RATIO

damping coefficient at the expense of introducing forced dynamic error for ramp inputs. When the forced dynamic error is excessive it is necessary to modify the model. The price for eliminating the forced dynamic error for ramp inputs is increased complexity in the system and its performance. A cascaded lead

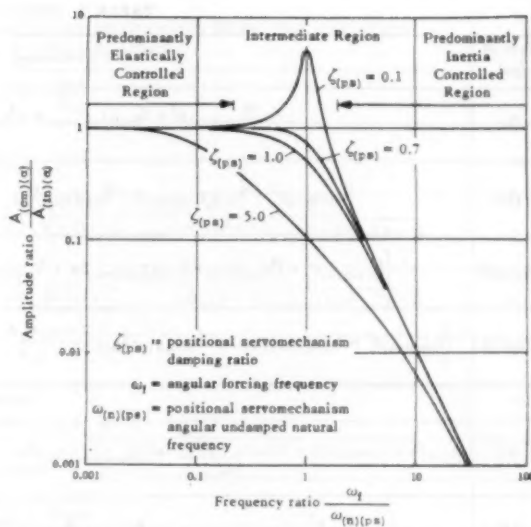


FIG. 4 FREQUENCY RESPONSE CHARACTERISTICS OF BASIC POSITIONAL SERVOMECHANISM MODELS AS A FUNCTION OF DAMPING RATIO

modifier is sometimes introduced with the idea of adding simple damping, but as it will be shown, it corresponds to the modified velocity signal damping model discussed in Paper I. This is a model designed to minimize the forced dynamic error for ramp inputs.

LEAD MODIFIER DAMPING POSITIONAL SERVOMECHANISM MODEL

It is shown in Paper I that damping is only necessary in the frequency subrange that includes the resonance calculated from the coefficients of the basic model. The lead modifier circuit shown in Fig. 5 has an output that depends on both the input and its derivative in proportions that vary with frequency. For low and intermediate frequencies, the dependence is approximately as the sum of the input and its derivative but at higher frequencies the proportion of the derivative contribution decreases. A functional diagram of a positional servomechanism model with cascaded lead modifier is given in Fig. 6. The problem at hand is how to select the parameters of the lead modifier in terms of the parameters of the basic model.

The performance equation associated with the lead modifier damping model is given in two forms by Equations [2a] and [2b] in Table 2. The equations are not as readily interpreted in terms of second-order approximations as the equations associated with multiloop systems taken up in Paper I. The reason lies in the physical situation. In multiloop systems, each loop performs a specialized function readily identified and controlled independently of the other loops. In the cascade-type system, the cascaded component operates on the correction signal for the purpose of producing the various modifications as the need arises. The multiloop systems in effect produce an independent torque contribution from each loop with the aid of suitable signal generators. The cascade-type systems attempt to achieve the same effect from the time variation of the correction signal. For example, a velocity signal generator loop is added to introduce damping torques in multiloop systems, while lead circuits are used in cascaded systems. The damping ratio is easily controlled by adjusting the velocity signal generator sensitivity in the one instance, but a change in the lead-modifier parameters alters the

TABLE 2 PERFORMANCE EQUATIONS

Type of (ps)	Dimensional Coefficient Form
(h)	$[I_{(cm)(eq)} p^2 + S_{(ps)}[\dot{A}; M](res) p + S_{(ps)}[A; M] A_{(cm)} - S_{(ps)}[A; M] A_{(in)} + M_{(intfr)}] A_{(cm)} = S_{(ps)}[A; M] A_{(in)} + M_{(intfr)} \quad (1a)$
(ld)	$\left[I_{(cm)(eq)} p^2 + S_{(ps)}[\dot{A}; M](res) p + S_{(ps)}[A; M] S_{(ld)} \frac{1 + \nu_{ld} \tau_{ld} p}{1 + \tau_{ld} p} \right] A_{cm} = S_{(ps)}[A; M] \frac{1 + \nu_{ld} \tau_{ld} p}{1 + \tau_{ld} p} A_{(in)} + M_{(intfr)} \quad (2a)$
(lg)(vd)	$\left[I_{(cm)(eq)} p^2 + (S_{(ps)}[\dot{A}; M] + S_{(ps)}[\dot{A}; M](res)) p + S_{(ps)}[A; M] \frac{1 + \nu_{lg} \tau_{lg} p}{1 + \tau_{lg} p} \right] A_{cm} = S_{(ps)}[A; M] \frac{1 + \nu_{lg} \tau_{lg} p}{1 + \tau_{lg} p} A_{(in)} + M_{(intfr)} \quad (3a)$
(lg)(ld)	$\left[I_{(cm)(eq)} p^2 + S_{(ps)}[\dot{A}; M](res) p + S_{(ps)}[A; M] S_{(ld)} \frac{1 + \nu_{lg} \tau_{lg} p}{1 + \tau_{lg} p} \frac{1 + \nu_{ld} \tau_{ld} p}{1 + \tau_{ld} p} \right] A_{cm} = S_{(ps)}[A; M] S_{(ld)} \frac{1 + \nu_{lg} \tau_{lg} p}{1 + \tau_{lg} p} \frac{1 + \nu_{ld} \tau_{ld} p}{1 + \tau_{ld} p} A_{(in)} + M_{(intfr)} \quad (4a)$
Parameter Form	
(h)	$\left[\frac{p^2}{\omega_{(n)(ps)}^2} + 2 \zeta_{(ps)(res)} \frac{p}{\omega_{(n)(ps)}} + 1 \right] A_{cm} = A_{(in)} + S_{(ps)}[M; A] M_{(intfr)} \quad (1b)$
(ld)	$\left[\frac{p^2}{\omega_{(n)(ps)}^2} + 2 \zeta_{(ps)(res)} \frac{p}{\omega_{(n)(ps)}} + S_{(ld)} \frac{1 + \nu_{ld} \tau_{ld} p}{1 + \tau_{ld} p} \right] A_{cm} = S_{(ld)} \frac{1 + \nu_{ld} \tau_{ld} p}{1 + \tau_{ld} p} A_{(in)} + S_{(ps)}[M; A] M_{(intfr)} \quad (2b)$
(lg)(vd)	$\left[\frac{p^2}{\omega_{(n)(ps)}^2} + (2 \zeta_{(ps)} + 2 \zeta_{(ps)(res)}) \frac{p}{\omega_{(n)(ps)}} + \frac{1}{\nu_{lg}} \frac{1 + \nu_{lg} \tau_{lg} p}{1 + \tau_{lg} p} \right] A_{cm} = \frac{1}{\nu_{lg}} \frac{1 + \nu_{lg} \tau_{lg} p}{1 + \tau_{lg} p} A_{(in)} + \frac{S_{(ps)}[M; A]}{\nu_{lg}} M_{(intfr)} \quad (3b)$
(lg)(ld)	$\left[\frac{p^2}{\omega_{(n)(ps)}^2} + 2 \zeta_{(ps)(res)} \frac{p}{\omega_{(n)(ps)}} + \frac{S_{(ld)}}{\nu_{lg}} \frac{1 + \nu_{lg} \tau_{lg} p}{1 + \tau_{lg} p} \frac{1 + \nu_{ld} \tau_{ld} p}{1 + \tau_{ld} p} \right] A_{cm} = \frac{S_{(ld)}}{\nu_{lg}} \frac{1 + \nu_{lg} \tau_{lg} p}{1 + \tau_{lg} p} \frac{1 + \nu_{ld} \tau_{ld} p}{1 + \tau_{ld} p} A_{(in)} + \frac{S_{(ps)}[M; A]}{\nu_{lg}} M_{(intfr)} \quad (4b)$
Definitions:	
$\omega_{(n)(ps)}$	= high-frequency-response positional servomechanism undamped natural frequency or positional servomechanism undamped angular natural frequency
$\zeta_{(ps)}$	= high-frequency-response positional servomechanism damping ratio due to specific components or positional servomechanism damping ratio
$\zeta_{(ps)(res)}$	= high-frequency-response positional servomechanism damping ratio due to residual sources or positional servomechanism residual damping ratio
$S_{(ps)}[M; A]$	= $\frac{1}{S_{(ps)}[A; M]}$
For (b) and (ld) models:	
$\omega_{(n)(ps)} = \sqrt{\frac{S_{(ps)}[A; M]}{I_{(cm)(eq)}}}$	$\zeta_{(ps)(res)} = \frac{1}{2} \frac{S_{(ps)}[\dot{A}; M](res)}{\sqrt{I_{(cm)(eq)} S_{(ps)}[A; M]}}$
For (lg)(vd) and (lg)(ld) models:	
$\omega_{(n)(ps)} = \sqrt{\frac{S_{(ps)}[A; M] \nu_{lg}}{I_{(cm)(eq)}}}$	$\zeta_{(ps)} = \frac{1}{2} \frac{S_{(ps)}[\dot{A}; M]}{\sqrt{I_{(cm)(eq)} S_{(ps)}[A; M] \nu_{lg}}}$
$\zeta_{(ps)(res)} = \frac{1}{2} \frac{S_{(ps)}[\dot{A}; M](res)}{\sqrt{I_{(cm)(eq)} S_{(ps)}[A; M] \nu_{lg}}}$	

stiffness and the undamped natural frequency of the cascaded-type system. It would appear that the design of cascade-type positional servomechanisms is more difficult and less flexible than multiloop systems. This conclusion may surprise anyone who is not familiar with the torque summation concept.

The use of a judicious amount of mathematical legerdemain can alter the form of the lead modifier damping model performance equation to make it more amenable to interpretation. The parametric form of the performance equation, Equation [2b] of Table 2, may be rewritten as

$$\left[\nu_{ld} \frac{1 + \tau_{ld} p}{1 + \nu_{ld} \tau_{ld} p} \left(\frac{p^2}{\omega_{(n)(ps)}^2} + 2 \zeta_{(ps)(res)}^* \frac{p}{\omega_{(n)(ps)}} \right) + 1 \right] A_{(cm)} = A_{(in)} + \nu_{ld} \frac{1 + \tau_{ld} p}{1 + \nu_{ld} \tau_{ld} p} S_{(ps)}[M; A] M_{(intfr)} \dots \dots [2]$$

or again as

$$\left[\frac{\nu_{ld} \tau_{ld} p}{1 + \nu_{ld} \tau_{ld} p} \left(\frac{p^2}{\omega_{(n)(ps)}^2} + 2 \zeta_{(ps)(res)}^* \frac{p}{\omega_{(n)(ps)}} \right) \right]$$

$$+ \frac{\nu_{ld}}{1 + \nu_{ld} \tau_{ld} p} p \left(\frac{p^2}{\omega_{(n)(ps)}^2} + 2 \zeta_{(ps)(res)}^* \frac{p}{\omega_{(n)(ps)}} \right) + 1 \Big] A_{(cm)} = A_{(in)} + \nu_{ld} \frac{1 + \tau_{ld} p}{1 + \nu_{ld} \tau_{ld} p} S_{(ps)}[M; A] M_{(intfr)} \dots \dots [3]$$

The frequency response is obtained when the operator p is replaced by $j\omega_f$. It is to be noted that the reciprocal lead modifier performance function

$$\nu_{ld} \frac{1 + \tau_{ld} j\omega_f}{1 + \nu_{ld} \tau_{ld} j\omega_f} = \frac{\nu_{ld}}{1 + \nu_{ld} \tau_{ld}} + \frac{\nu_{ld} \tau_{ld} j\omega_f}{1 + \nu_{ld} \tau_{ld} j\omega_f} \dots \dots [4]$$

is equal to the characteristic time ratio ν_{ld} for small values of the forcing frequency ω_f and approaches unity as the frequency gets large. In particular, the partial fraction

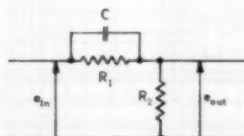
$$\frac{\nu_{ld}}{1 + \nu_{ld} \tau_{ld} j\omega_f} \dots \dots [5]$$

is equal to the characteristic time ratio ν_{ld} for small values of

TABLE 3 NONDIMENSIONAL PERFORMANCE FUNCTIONS ASSOCIATED WITH THE EQUATION

$$A(s) = [PF](ps)[A;A]A(s) + [PF](ps)[M;A]M(s)$$

Type of (ps)	$[PF](ps)[A;A] = \frac{A(s)}{A(s)}$
(h)	$\frac{1}{p^2 + 2\zeta_{(ps)}(res)p + 1}$ (1a)
(ld)	$\frac{1}{v_{ld} \left(\frac{1 + 2\pi R_{ld} p}{1 + 2\pi v_{ld} R_{ld} p} \right) (p^2 + 2\zeta_{(ps)}(res)p + 1)} = \frac{1 + 2\pi v_{ld} R_{ld} p}{v_{ld} [2\pi R_{ld} p^3 + (1 + 2\zeta_{(ps)}(res) 2\pi R_{ld}) p^2 + (2\zeta_{(ps)}(res) + 2\pi R_{ld}) p + 1]}$ (2a)
(lg)	$\frac{1}{v_{lg} \left(\frac{1 + 2\pi R_{lg} p}{1 + 2\pi v_{lg} R_{lg} p} \right) (p^2 + 2\zeta_{(ps)}(res)p + 1)} = \frac{1 + 2\pi v_{lg} R_{lg} p}{v_{lg} [2\pi R_{lg} p^3 + (1 + 2\zeta_{(ps)}(res) 2\pi R_{lg}) p^2 + (2\zeta_{(ps)}(res) + 2\pi R_{lg}) p + 1]}$ (3a)
(lg)(ld)	$\frac{1}{v_{ld} v_{lg} \left(\frac{1 + 2\pi R_{ld} p}{1 + 2\pi v_{ld} R_{ld} p} \right) \left(\frac{1 + 2\pi R_{lg} p}{1 + 2\pi v_{lg} R_{lg} p} \right) (p^2 + 2\zeta_{(ps)}(res)p + 1)} = \frac{(1 + 2\pi v_{ld} R_{ld} p)(1 + 2\pi v_{lg} R_{lg} p)}{v_{ld} v_{lg} (2\pi)^2 R_{ld} R_{lg} p^4 + [2\zeta_{(ps)}(res) (2\pi)^2 R_{ld} R_{lg} + 2\pi R_{ld} + 2\pi R_{lg}] p^3 + [1 + 2\zeta_{(ps)}(res) (2\pi R_{ld} + 2\pi R_{lg}) + (2\pi)^2 R_{ld} R_{lg}] p^2 + [2\zeta_{(ps)}(res) + (2\pi R_{ld} + 2\pi R_{lg})] p + 1}$ (4a)
	$[PF](ps)[M;A] = \frac{A(s)}{M(s)}$
(h)	$S_{(ps)}[M;A] [PF](ps)[A;A]$ (1b)
(ld)	$S_{(ps)}[M;A] v_{ld} \frac{1 + 2\pi R_{ld} p}{1 + 2\pi v_{ld} R_{ld} p} [PF](ps)[A;A]$ (2b)
(lg)(vis)	$S_{(ps)}[M;A] v_{lg} \frac{1 + 2\pi R_{lg} p}{1 + 2\pi v_{lg} R_{lg} p} [PF](ps)[A;A]$ (3b)
(lg)(ld)	$S_{(ps)}[M;A] v_{ld} \frac{1 + 2\pi R_{ld} p}{1 + 2\pi v_{ld} R_{ld} p} \frac{1 + 2\pi R_{lg} p}{1 + 2\pi v_{lg} R_{lg} p} [PF](ps)[A;A]$ (4b)
Definitions: $p = \frac{p}{\omega_n(ps)}$ = nondimensional derivative operator $R_{ld} = \frac{\tau_{ld}}{\tau_n(ps)}$ = lead modifier characteristic time - positional servomechanism undamped natural period ratio $R_{lg} = \frac{\tau_{lg}}{\tau_n(ps)}$ = lag modifier characteristic time - positional servomechanism undamped natural period ratio	



$$e_{out} = S_{ld} \frac{1 + v_{ld} \tau_{ld} p}{1 + \tau_{ld} p} e_{in} \quad v_{ld} > 1$$

$$S_{ld} = \frac{R_2}{R_1 + R_2} = \frac{1}{v_{ld}} = \text{lead modifier sensitivity}$$

$$\tau_{ld} = \frac{R_2}{R_1 + R_2} R_1 C = \text{lead modifier characteristic time}$$

$$v_{ld} = \frac{R_1 + R_2}{R_2} = \text{lead modifier characteristic time ratio}$$

FIG. 5 TYPICAL LEAD MODIFIER CIRCUIT

 TABLE 4 FORCED DYNAMIC ERROR FOR RAMP FUNCTION INPUT ($\dot{A}(cm) = \text{CONST}$)

Type of (ps)	Forced Dynamic Error		
	Dimensional Coefficient Form	Parametric Form	Nondimensional Parametric Form
(h)	$-\frac{S_{(ps)}[\dot{A};M](res)}{S_{(ps)}[A;M]} \dot{A}(cm)$	$-2\zeta_{(ps)}(res) \frac{\dot{A}(cm)}{\omega_n(ps)}$	$-2\zeta_{(ps)}(res) p \dot{A}(cm)$
(ld)	$-\frac{S_{(ps)}[\dot{A};M](res)}{S_{(ps)}[A;M]} \dot{A}(cm)$	$-2\zeta_{(ps)}(res) \frac{\dot{A}(cm)}{\omega_n(ps)}$	$-2\zeta_{(ps)}(res) p \dot{A}(cm)$
(lg)	$-\frac{S_{(ps)}[\dot{A};M] + S_{(ps)}[\dot{A};M](res)}{S_{(ps)}[A;M]} \dot{A}(cm)$	$\dot{A}(cm) - (2\zeta_{(ps)} + 2\zeta_{(ps)}(res)) \frac{\dot{A}(cm)}{\omega_n(ps)}$	$-(2\zeta_{(ps)} + 2\zeta_{(ps)}(res)) p \dot{A}(cm)$
(ld)	$-\frac{S_{(ps)}[\dot{A};M](res)}{S_{(ps)}[A;M]} \dot{A}(cm)$	$-2\zeta_{(ps)}(res) \frac{\dot{A}(cm)}{\omega_n(ps)}$	$-2\zeta_{(ps)}(res) p \dot{A}(cm)$

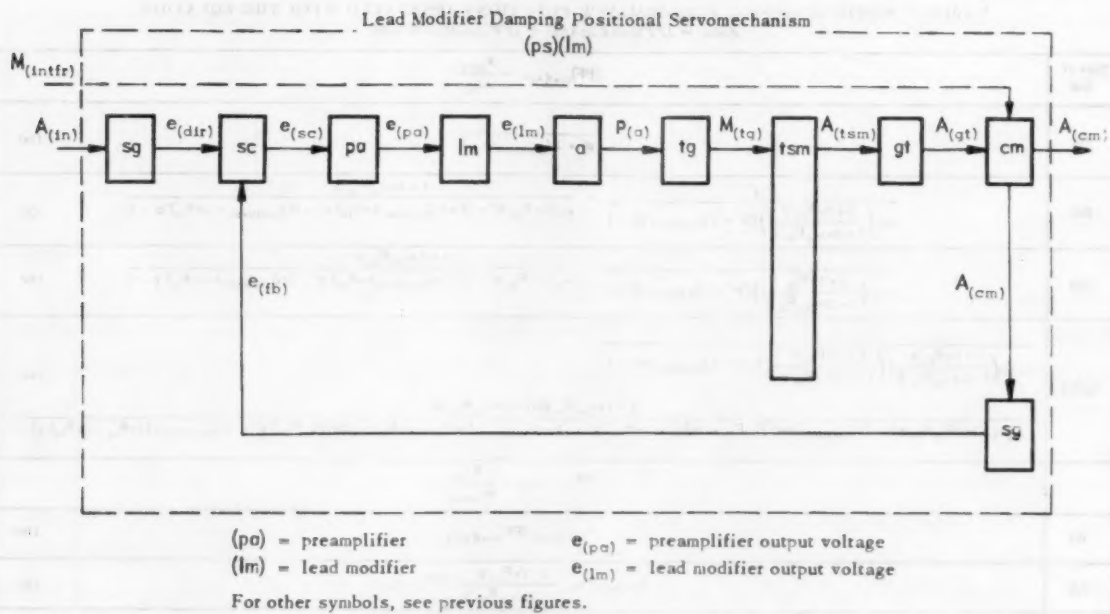


FIG. 6 FUNCTIONAL DIAGRAM FOR A LEAD MODIFIER DAMPED POSITIONAL SERVOMECHANISM

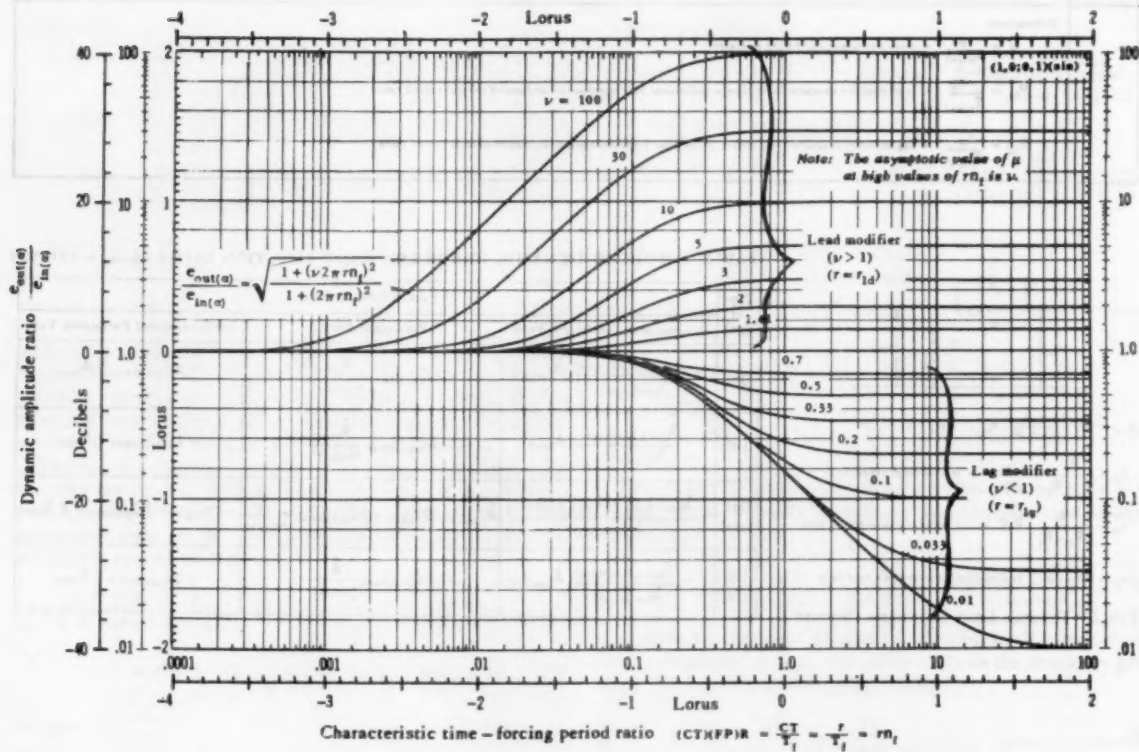


FIG. 7(a) FREQUENCY RESPONSE CURVES OF LEAD MODIFIERS AND LAG MODIFIERS (LOG DYNAMIC AMPLITUDE RATIO VERSUS LOG CHARACTERISTIC TIME-FORCING PERIOD RATIO)

(Adapted from Chapter 18, *Instrument Engineering*, vol. II, by C. S. Draper, W. McKay, and S. Lees.)

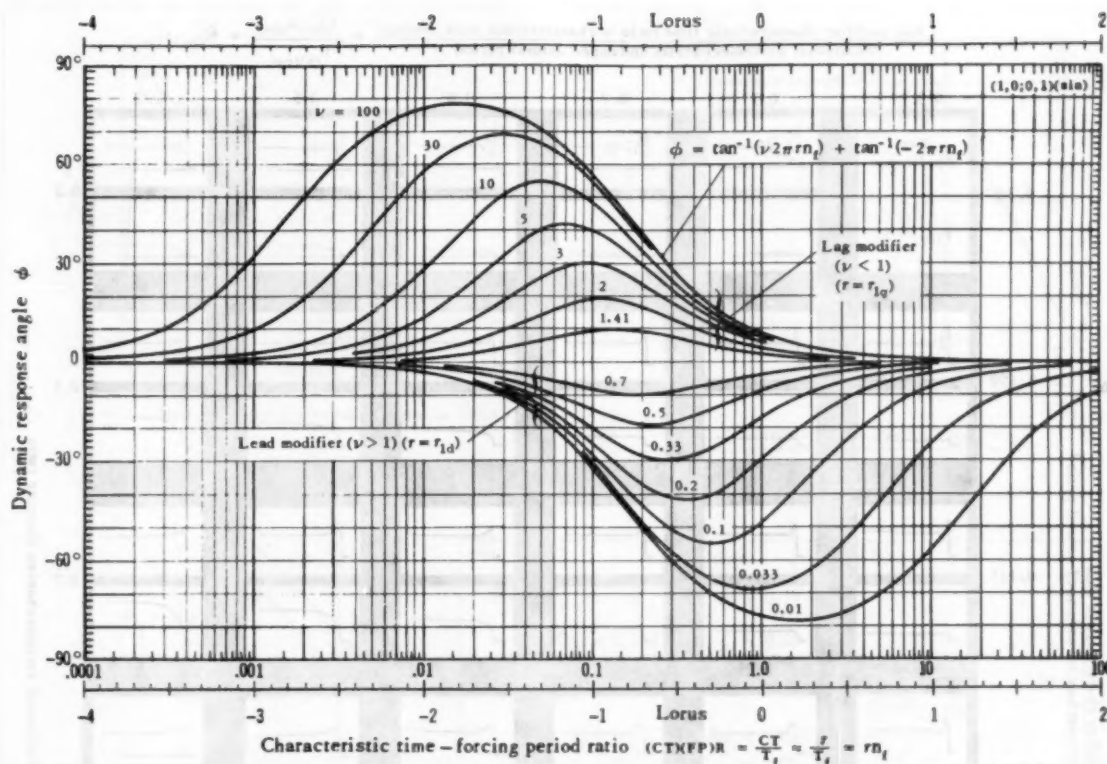


FIG. 7(b) FREQUENCY RESPONSE CURVES OF LEAD MODIFIERS AND LAG MODIFIERS (DYNAMIC RESPONSE ANGLE VERSUS LOG CHARACTERISTIC TIME-FORCING PERIOD RATIO)

(Adapted from Chapter 18, *Instrument Engineering*, vol. II, by C. S. Draper, W. McKay, and S. Loos.)

the frequency, and goes to zero as the frequency becomes very large. On the other hand, the partial fraction

$$\frac{\nu_{ld} \tau_{ld} j \omega_f}{1 + \nu_{ld} \tau_{ld} j \omega_f} \dots \dots \dots [6]$$

is zero for zero frequency and tends to unity as the frequency increases. Functions of the form of Equation [6] were used in Paper I to supply the requisite frequency dependence for coefficients. In particular, it was shown in Paper I that

$$\left| \frac{\nu_{ld} \tau_{ld} j \omega_f}{1 + \nu_{ld} \tau_{ld} j \omega_f} \right| = 0.99 \text{ for } \omega_f = \frac{1}{\nu_{ld} \tau_{ld}} \dots \dots \dots [7]$$

The performance equation has been cast into the form of Equation [3] to take advantage of the known properties of the function in Equation [6]. For low frequencies the performance equation may be approximated by the expression

$$\left[\nu_{ld} \left(\frac{p^2}{\omega_{n(pa)}^2} + \frac{2\zeta_{(pa)}(rea)p}{\omega_{n(pa)}} \right) + 1 \right] A_{(em)} = A_{(in)} + \nu_{ld} S_{(pa)} [M; A] \bar{M}_{(instr)} \dots \dots \dots [8]$$

For intermediate frequencies the approximation is

$$\left[\frac{p^2}{\omega_{n(pa)}^2} + 2\zeta_{(pa)}(rea) \frac{p}{\omega_{n(pa)}} + \frac{p}{\tau_{ld} \omega_{n(pa)}} + \frac{2\zeta_{(pa)}(rea)}{\tau_{ld} \omega_{n(pa)}} + 1 \right] A_{(em)} = A_{(in)} + \left(1 + \frac{1}{\tau_{ld} p} \right) S_{(pa)} [M; A] \bar{M}_{(instr)} \dots \dots \dots [9]$$

For sufficiently high frequencies, the performance equation becomes

$$\left[\frac{p^2}{\omega_{n(pa)}^2} + 2\zeta_{(pa)}(rea) \frac{p}{\omega_{n(pa)}} + 1 \right] A_{(em)} = A_{(in)} + S_{(pa)} [M; A] \bar{M}_{(instr)} \dots \dots \dots [10]$$

The reason for using the lead modifier is to introduce damping because the residual damping ratio is too small. It is assumed that

$$\frac{2\zeta_{(pa)}(rea)}{\tau_{ld} \omega_{n(pa)}} \ll 1 \dots \dots \dots [11]$$

When the quantity [11] is neglected in Equation [9], it may be identified as a second-order equation with an undamped natural frequency

$$\omega_{n(pa)} = \sqrt{\left\{ \frac{S_{(pa)} [A; M]}{I_{(em)}} \right\}} \dots \dots \dots [12]$$

and a damping ratio

$$\zeta_{(pa)}(rea) + \zeta_{(pa)} \dots \dots \dots [13]$$

where

$$\zeta_{(pa)} = \frac{1}{2} \frac{1}{\tau_{ld} \omega_{n(pa)}} \dots \dots \dots [14]$$

The development leads to a point of view of the lead modifier damping in the performance of the positional servomechanism that is much like that associated with the modified velocity sig-

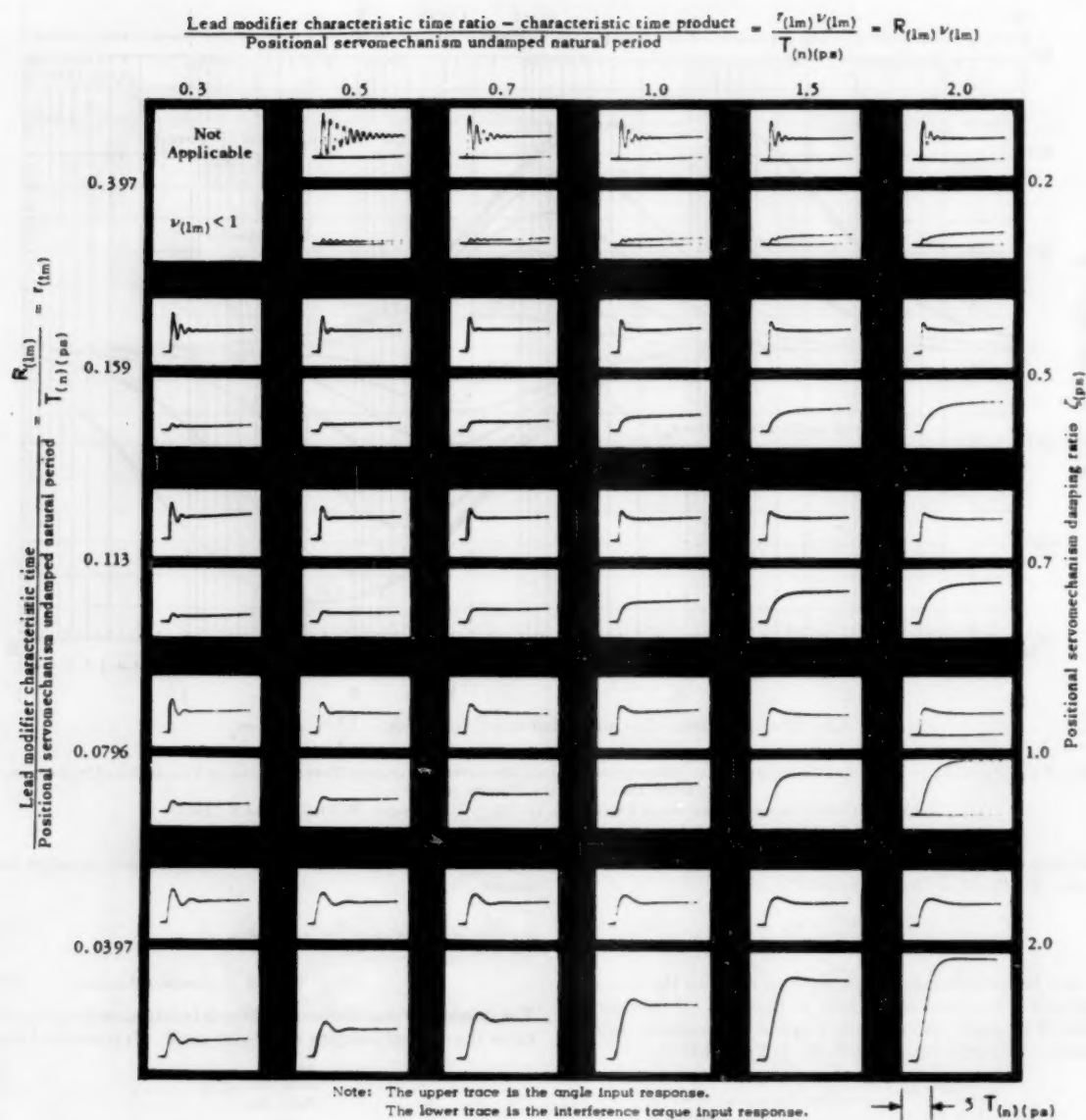


FIG. 8 STEP FUNCTION RESPONSES FOR LEAD MODIFIER DAMPED POSITIONAL SERVOMECHANISMS WITH HIGH-FREQUENCY STIFFNESS HELD CONSTANT

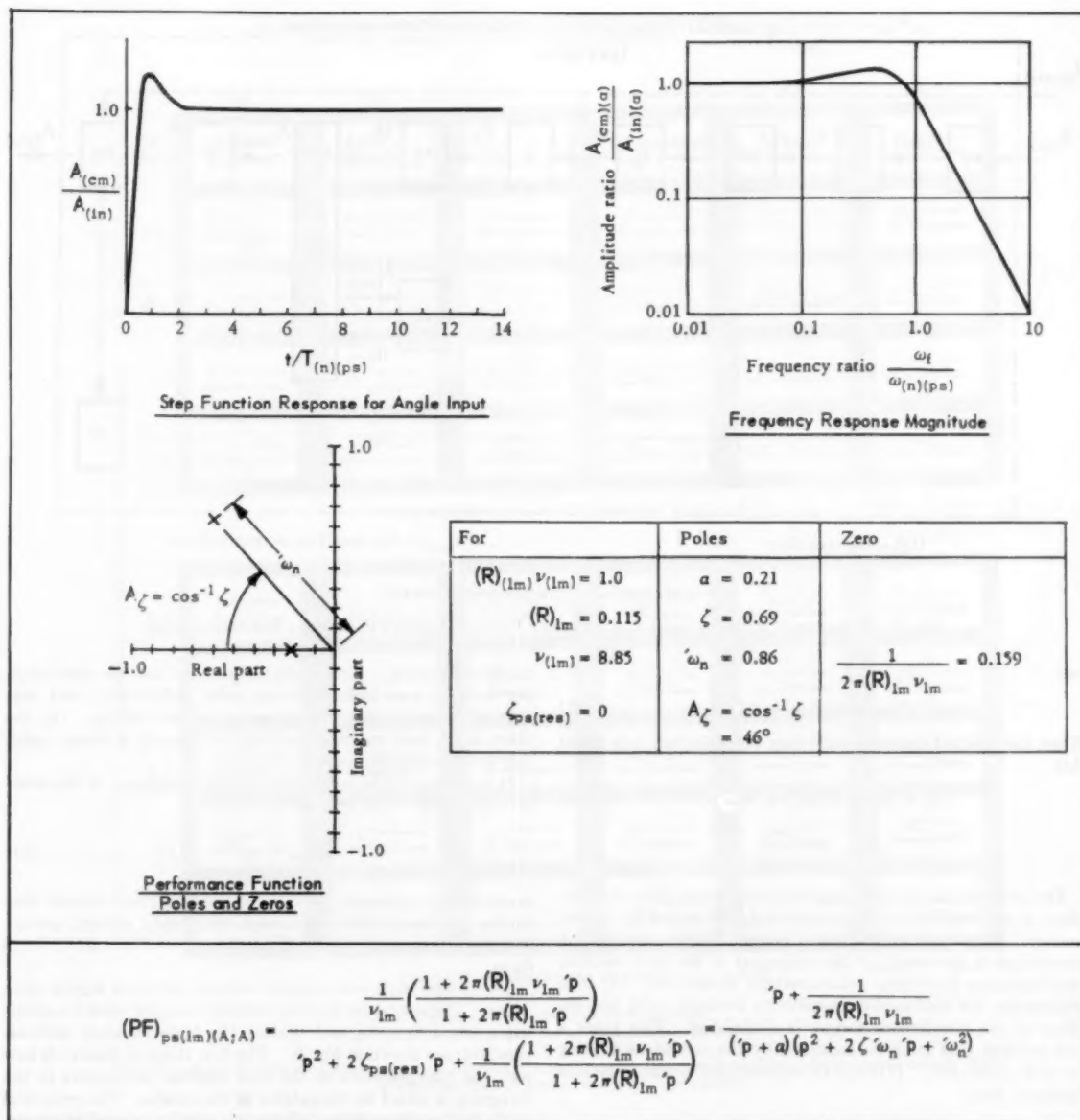


FIG. 9 TYPICAL DYNAMIC CHARACTERISTICS OF A LEAD MODIFIER DAMPED POSITIONAL SERVO MECHANISM FOR AN ANGLE INPUT

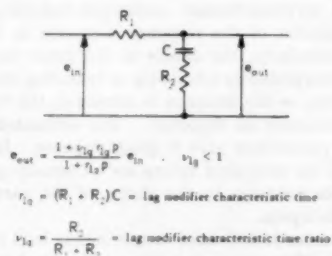


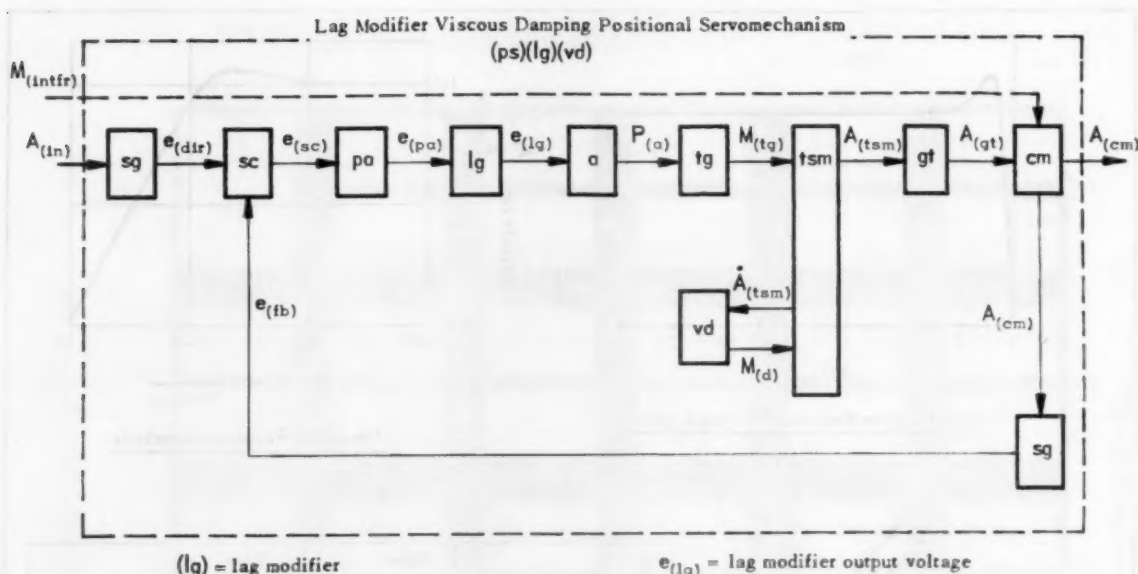
FIG. 10 TYPICAL LAG MODIFIER CIRCUIT

nal damping model discussed in Paper I. At low frequencies, the system performs like a lightly damped system with undamped natural frequency

$$\omega_{n(lf)} = \frac{\omega_{n(ps)}}{\sqrt{\nu_{ld}}} \quad [15]$$

At frequencies comparable to the positional servomechanism undamped natural frequency $\omega_{n(ps)}$, the system can be made to perform as a well-damped second-order system with an undamped natural frequency given by Equation [12]. From the arguments presented in Paper I, this condition may be achieved by selecting

$$\nu_{ld} T_{ld} = \frac{1}{\omega_{n(ps)}} \quad [16]$$



For other symbols, see previous figures.

FIG. 11 FUNCTIONAL DIAGRAM FOR A LAG MODIFIER VISCOUS DAMPING POSITIONAL SERVOMECHANISM

and

$$\zeta_{(ps)(res)} + \zeta_{(ps)} = 0.7 \dots \dots \dots [17]$$

When the residual damping ratio may be neglected, it is found that

$$\tau_{ld} = 0.113 T_{n(ps)}; \nu_{ld} = 8.85 \dots \dots \dots [18]$$

$$T_{n(ps)} = \frac{2\pi}{\omega_{n(ps)}}$$

The performance equation approximations also show that the effect of the interference torque is strongly influenced by the frequency. At low frequencies, from Equation [8], the basic system compliance is increased by the reciprocal of the lead modifier zero-frequency sensitivity (characteristic time ratio). At high frequencies, the lead modifier sensitivity becomes unity and the effect of the interference torque is diminished. This poses a real problem that must be answered by the conditions existing for each application. If the zero-frequency stiffness must be held constant, then

$$\frac{S_{(ps)}[A;M]}{\nu_{ld}} = \text{const}, \omega_{n(ps)} = \omega_{n(ps)(ref)} \sqrt{(\nu_{ld})} \dots \dots [19]$$

For this condition, the positional servomechanism undamped natural frequency increases as the square root of the characteristic time ratio. When the high-frequency stiffness is held constant

$$S_{(ps)}[A;M] = \text{const}, \omega_{n(ps)} = \text{const} \dots \dots \dots [20]$$

and the bandwidth is unaltered. However, this condition requires that the compliance be increased for low frequencies in proportion to the characteristic time ratio. The choice is between increasing the bandwidth and making the system softer.

When the maximum available gain from practical considerations is required before the lead modifier is introduced then it is necessary to make the system softer at zero frequency for lead

modifier damping. Also, it should be noted that the lead modifier tends to pass high-frequency noise very readily and contributes to saturating the power amplifier thereby. On the other hand, lead modifier damping is certainly a cheap, quick way to introduce damping.

It is convenient to nondimensionalize using $\omega_{n(ps)}$ as the reference quantity. The symbol

$$R_{ld} = \frac{\tau_{ld}}{T_{n(ps)}} \dots \dots \dots [21]$$

is adopted to represent the ratio of the lead characteristic time to the positional servomechanism undamped natural period. The performance functions in Table 3 are given in nondimensional form.

The design basis was verified with the aid of an analog computer. The results for the lead modifier damping model, neglecting residual damping and holding the high-frequency stiffness constant, are shown in Fig. 8. The first thing to observe is how well the interpretation of the lead modifier parameters in the foregoing is suited to the pattern of the results. The reciprocal of the lead modifier characteristic time was interpreted as proportional to the damping ratio in Equation [14]. The analog studies show that as the characteristic time decreases in proportion to the positional servomechanism undamped natural period, the oscillatory character of the response decreases as if damping were added. Similarly, the choice of the other lead modifier parameter is interpreted as advancing or retarding the damping. Fig. 8 shows that, as the damping is advanced, the response becomes less oscillatory as expected. The estimated values of lead modifier parameters give a good response. In fact, the regions around the estimated values are all equally good, showing considerable tolerance in the choice of the parameters for command angle inputs.

The responses for interference torque inputs hold no surprises as the lead modifier parameters vary. The final value of the output increases for unit input as the characteristic time ratio in-

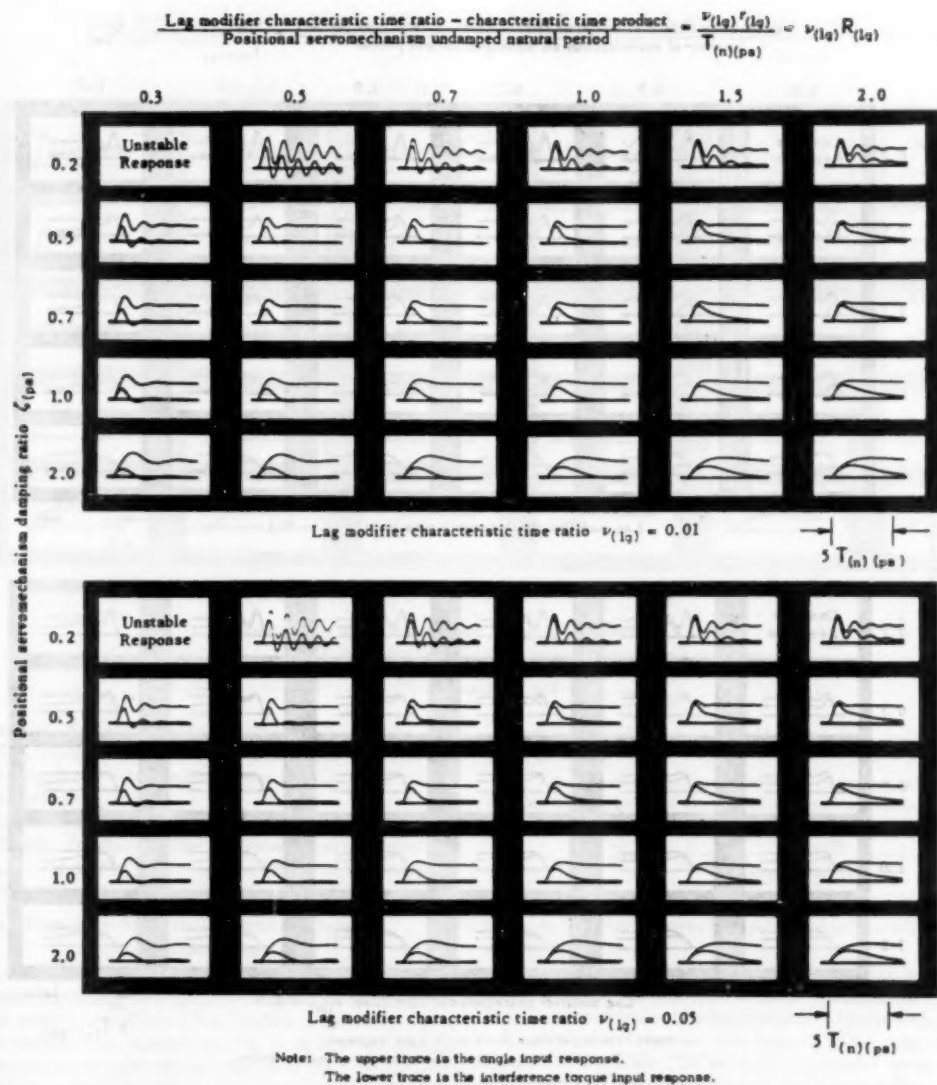


FIG. 12 STEP FUNCTION RESPONSES FOR LAG MODIFIER VISCOUS DAMPED POSITIONAL SERVOMECHANISMS WITH HIGH-FREQUENCY STIFFNESS HELD CONSTANT

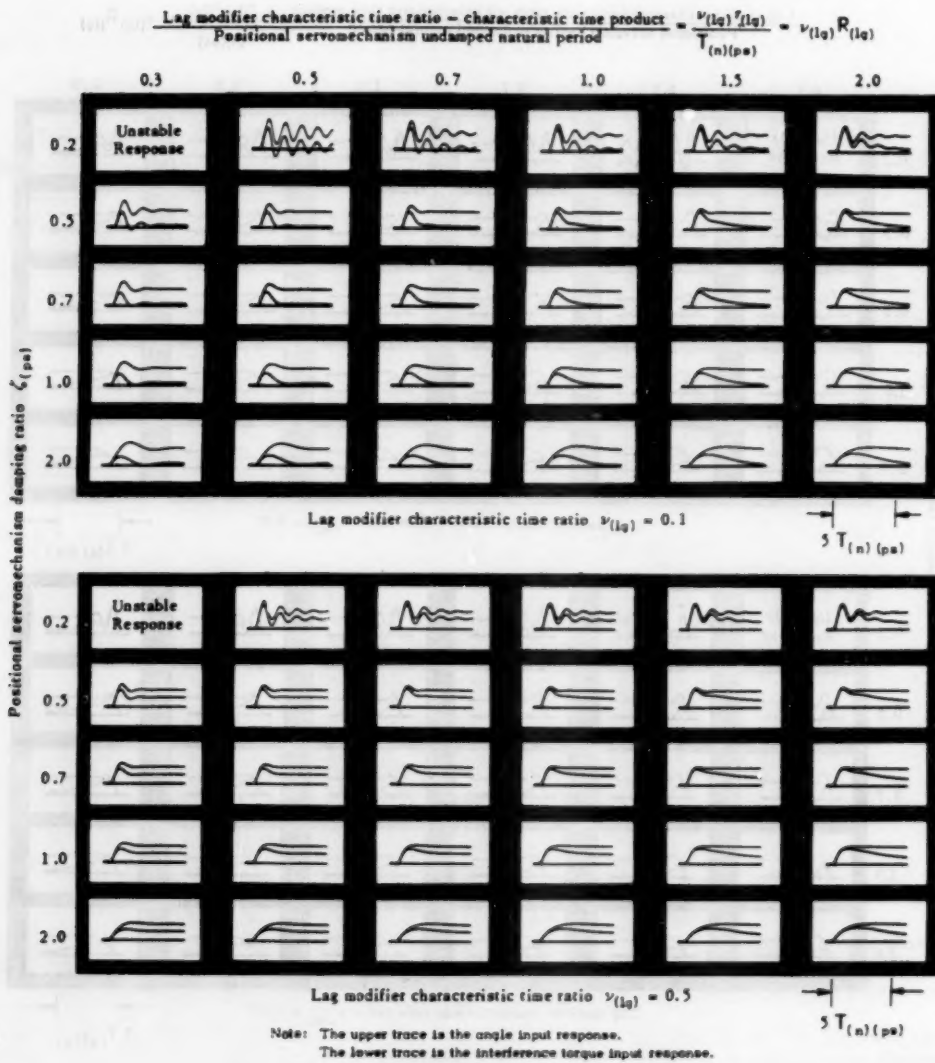


Fig. 12 (continued)

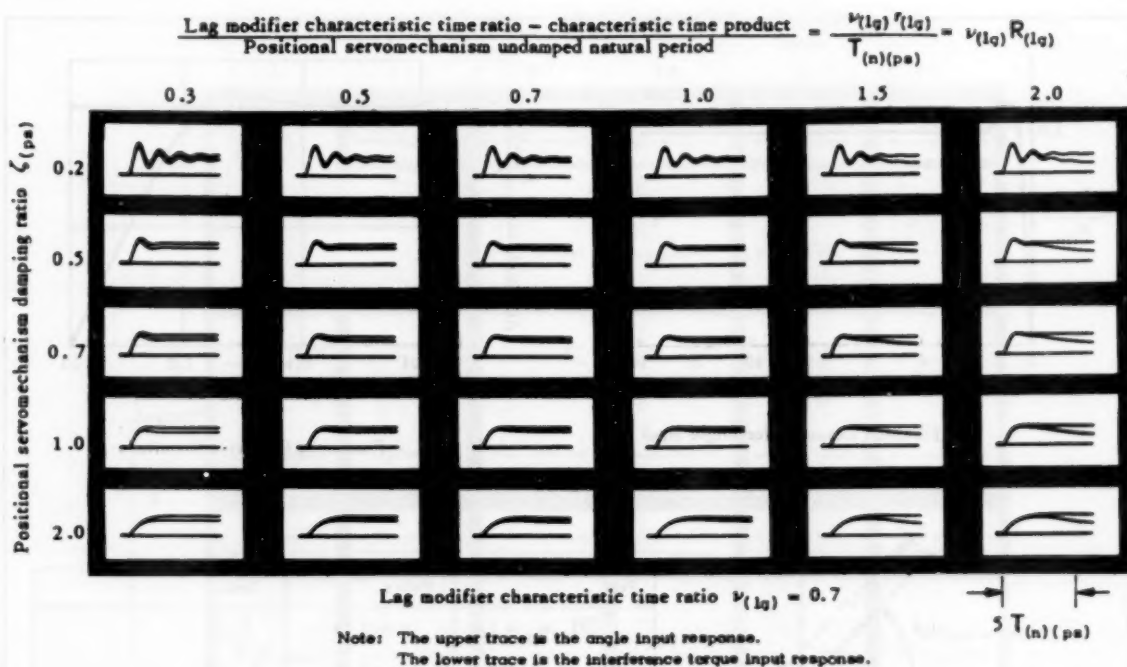


FIG. 12 (continued)

creases, because the zero-frequency stiffness decreases. The choice of lead modifier parameters is seen to be more critical from the standpoint of interference torque inputs than for command angle inputs.

A comparable study has been carried out holding the low-frequency stiffness constant. The command angle input responses are similar to Fig. 8 but the final values of the responses to interference torque inputs are constant and different from zero.

LAG MODIFIER, VISCOUS DAMPING POSITIONAL SERVOMECHANISMS

It may be seen from Fig. 7 that the sensitivity of lag modifiers decreases with increasing frequency in contrast to the performance of lead modifiers. When a lag modifier is introduced into the basic servomechanism model as in Fig. 11, it is to be expected that the zero-frequency stiffness will be greater than the high-frequency stiffness. Furthermore, an examination of the torque variations from Table 1 as well as the performance equations, [3a] and [3b] in Table 2, shows that a lag modifier does not contribute damping. When the residual damping is inadequate, it is necessary to supplement it by some other means. For the simplest case, simple viscous damping will do.

From a study of second-order approximations, quite similar to the lead modifier damping study, it becomes possible to deduce several design guides. These are summarized as follows:

- 1 The low-frequency stiffness coefficient is $S_{(ps)}[A;M]$.
- 2 The high-frequency stiffness coefficient is $\nu_{lg} S_{(ps)}[A;M]$, where the characteristic time ratio ν_{lg} is less than unity.
- 3 The positional servomechanism undamped natural frequency is based on the high-frequency stiffness

$$\omega_{n(ps)} = \sqrt{\left\{ \frac{\nu_{lg} S_{(ps)}[A;M]}{I_{(cm)(eq)}} \right\}} \dots \dots \dots [22]$$

The importance of identifying $\omega_{n(ps)}$ is that the associated

undamped natural period provides the time scale for selecting parameters.

- 4 The positional servomechanism damping ratio $\zeta_{(ps)}$ is calculated on the basis of the high-frequency stiffness

$$\zeta_{(ps)} = \frac{1}{2} \frac{\zeta_{(ps)}[A;M]}{\sqrt{\{I_{(cm)(eq)} \nu_{lg} S_{(ps)}[A;M]\}}} \dots \dots \dots [23]$$

- 5 The choice of the lag modifier characteristic times, τ_{lg} or $\nu_{lg} T_{lg}$, is of lesser importance and plays only a minor role in the system dynamics.

- 6 The choice of the characteristic time ratio is most marked by its effect on the interference torque response for a given positional servomechanism undamped natural frequency, $\omega_{n(ps)}$.

Since the characteristic time ratio ν_{lg} is less than unity, it follows from Equation [22] that the bandwidth is effectively decreased with this quantity when the low-frequency stiffness is held constant. On the other hand, if the high-frequency stiffness is fixed, the bandwidth is invariant but the low-frequency stiffness increases inversely as the characteristic time ratio. The loss of stiffness at higher frequencies makes this model subject to the influence of sudden changes in interference-torque levels. When the undamped natural frequency is decreased significantly, the actual performance in the presence of relatively slowly changing torques may be unsatisfactory, despite the low compliance at zero frequency.

The choice of the damping ratio, together with the two lag modifier parameters, requires several arrays of analog computer responses in order to show the effects of three parameters. The several arrays of Fig. 12 were prepared with the characteristic time ratio held constant for each array and the high-frequency stiffness coefficient the same for all arrays. The responses verify the statements just enumerated. The effect of the lag modifier characteristic time on the final value of the response to interference torque inputs is very striking. The damping ratio

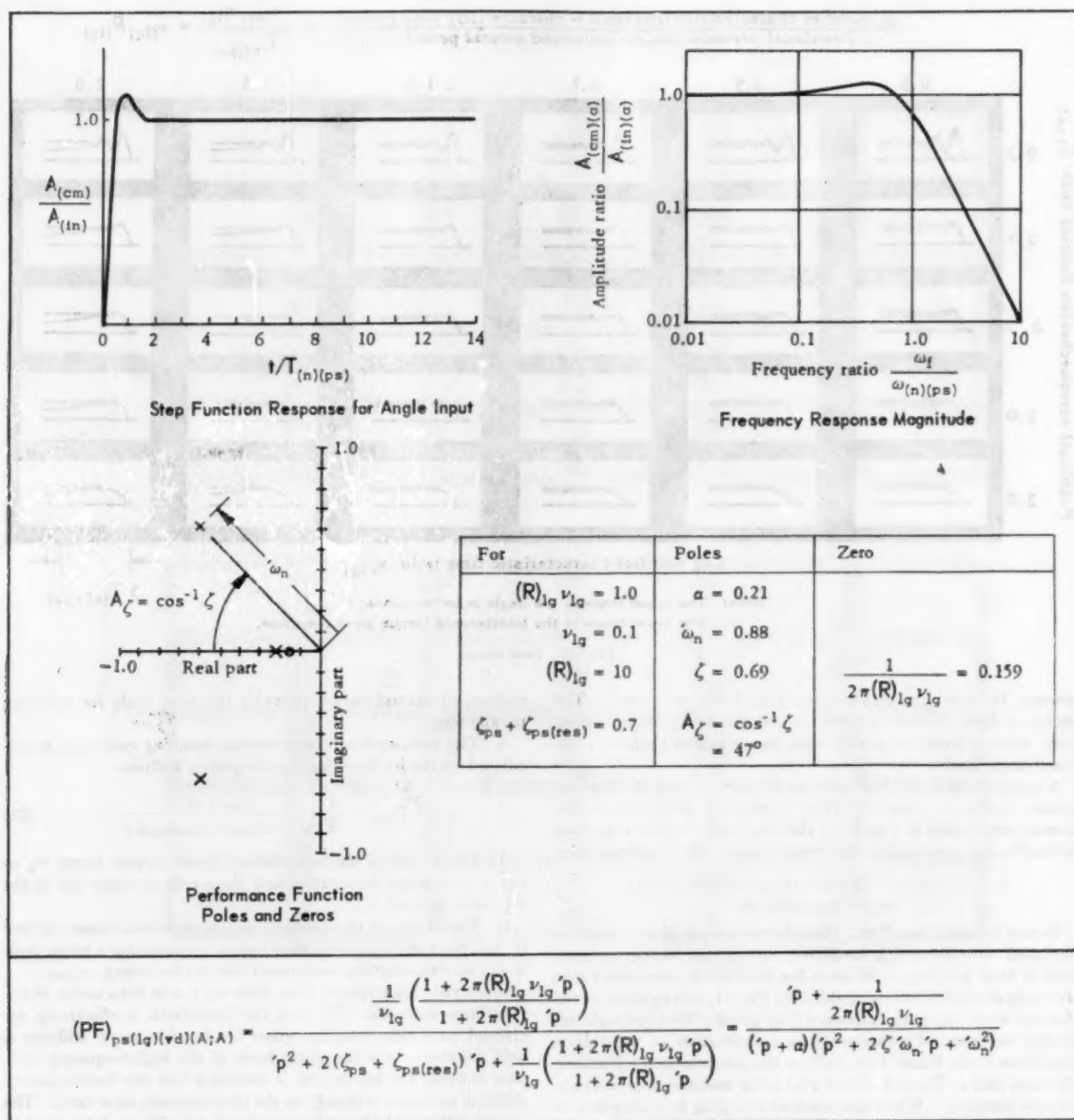
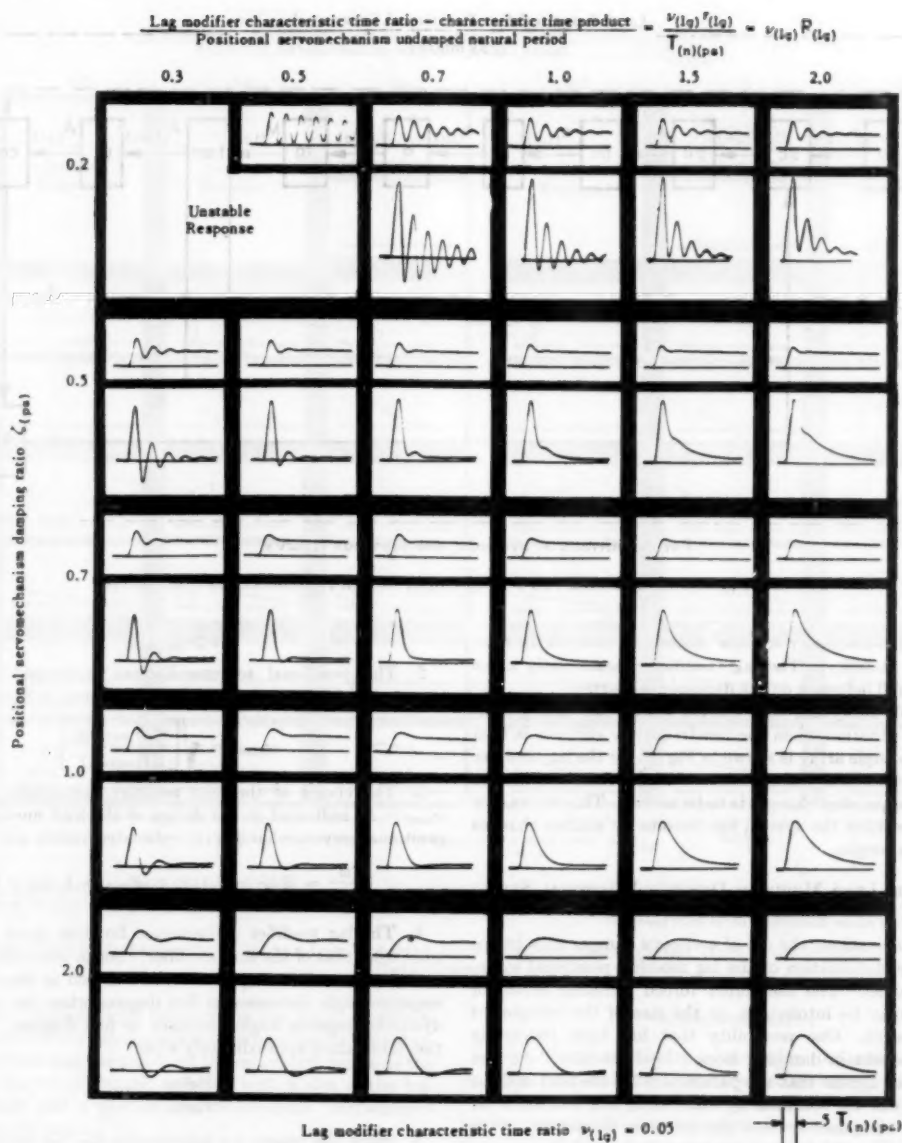


FIG. 13 TYPICAL DYNAMIC CHARACTERISTICS OF A LAG MODIFIER VISCOUS DAMPED POSITIONAL SERVO MECHANISM FOR AN ANGLE INPUT



Note: The upper trace is the angle input response.
The lower trace is the interference torque input response.

FIG. 14 STEP FUNCTION RESPONSES FOR LAG MODIFIER VISCOUS DAMPED POSITIONAL SERVOMECHANISMS WITH LOW-FREQUENCY STIFFNESS HELD CONSTANT

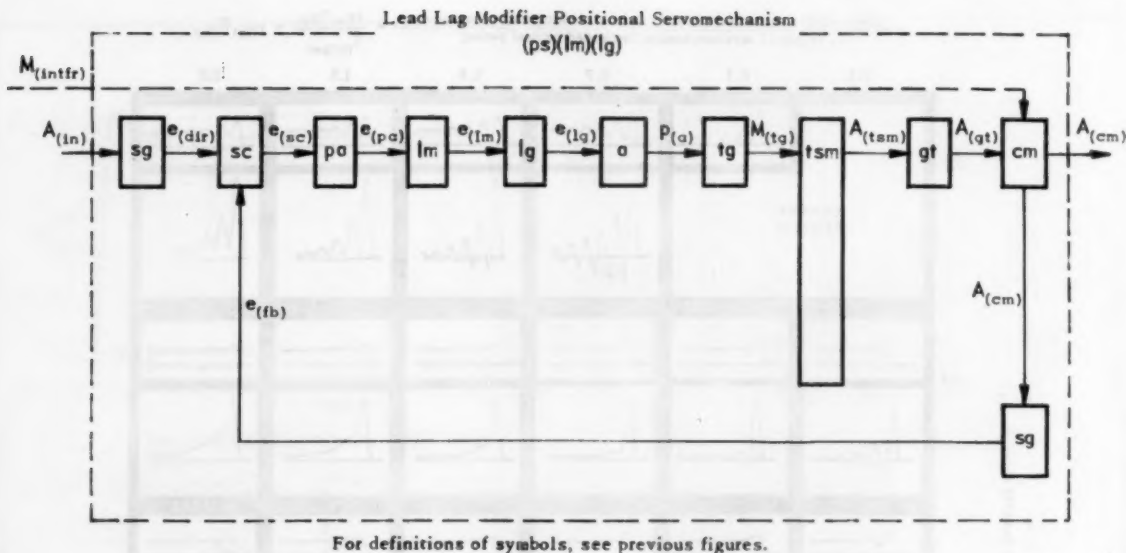


FIG. 15 FUNCTIONAL DIAGRAM FOR A LEAD-LAG MODIFIER POSITIONAL SERVO MECHANISM

based on the high-frequency stiffness essentially controls the relative transient stability. The lag modifier characteristic times have only a small influence on the dynamic properties.

A comparable study has been carried out on the analog computer for the situation when the low-frequency stiffness is held constant. A sample array is shown in Fig. 14 for the lag modifier characteristic time ratio equal to 0.05. The violent response to interference torque step changes is to be noted. This shows how much more sensitive the system has become to sudden changes in interference torque.

LAG MODIFIER, LEAD MODIFIER DAMPING POSITIONAL SERVO MECHANISM MODEL

For some applications, the use of a viscous damper may be unsuitable in the stabilization of the lag modifier positional servomechanism model. The associated forced dynamic error for ramp inputs may be intolerable, or the size of the component may be excessive. One possibility that has been frequently employed is to obtain damping from a lead modifier. At first thought, it may appear that the parameters for the lead and the lag modifiers can be obtained by combining the estimates for each of these components from the previous discussion. It is necessary to be careful because for some choices of the parameters the lead modifier may cancel out the effect of the lag modifier, a condition that may be deduced from Fig. 7.

The study of this model is summarized as follows:

- 1 The stiffness coefficient varies in three steps:

(a) At zero frequency, it is

$$S_{ld}S_{(ps)}[A;M] = \frac{S_{(ps)}[A;M]}{\nu_{ld}} \quad [24]$$

(b) At an intermediate frequency where the lag modifier reaches its minimum sensitivity, the stiffness coefficient is

$$S_{ld}\nu_{lg}S_{(ps)}[A;M] = \frac{\nu_{lg}}{\nu_{ld}} S_{(ps)}[A;M] \quad [25]$$

(c) At high frequencies, the stiffness coefficient becomes

$$\nu_{lg}S_{(ps)}[A;M] \quad [26]$$

- 2 The positional servomechanism undamped natural frequency is calculated from the high-frequency stiffness coefficient

$$\omega_n(pa) = \sqrt{\frac{\nu_{lg}S_{(ps)}[A;M]}{(I_{(cm)})(m_q)}} \quad [27]$$

- 3 The choice of the lead modifier parameters is based on $\omega_n(pa)$. As indicated in the design of the lead modifier damping positional servomechanism the estimated values are

$$\frac{\tau_{ld}}{T_n(pa)} = R_{ld} = 0.113; \nu_{ld}R_{ld} = 1, \nu_{ld} = 8.85 \dots [28]$$

- 4 The lag modifier performance function must be kept distinct from that of the lead modifier. As an estimate, the characteristic times of the lag modifier are chosen so that its dynamic response angle decreases to five degrees when the lead modifier dynamic response angle increases to five degrees. This condition is obtained approximately when

$$\frac{\nu_{lg}\tau_{lg}}{\nu_{ld}\tau_{ld}} = 10 \quad [29]$$

- 5 Since the reason for introducing the lag modifier is to increase the zero-frequency stiffness with respect to the higher frequency stiffness

$$\nu_{lg} > \nu_{ld} \quad [30]$$

- 6 The response characteristics are identified as essentially similar to the lag modifier viscous damping model. The final value of the output to interference-torque step changes depends on the value of ν_{lg} . The system is sensitive to derivatives of interference torque and should produce large overshoots for step changes.

The analog computer studies undertaken to verify the design basis are shown in Fig. 16. The responses correspond to the situation where the high-frequency stiffness is held constant. The situations where the low-frequency stiffness and the intermediate-frequency stiffness are held constant have not been investigated. Several arrays have been assembled corresponding to the varia-

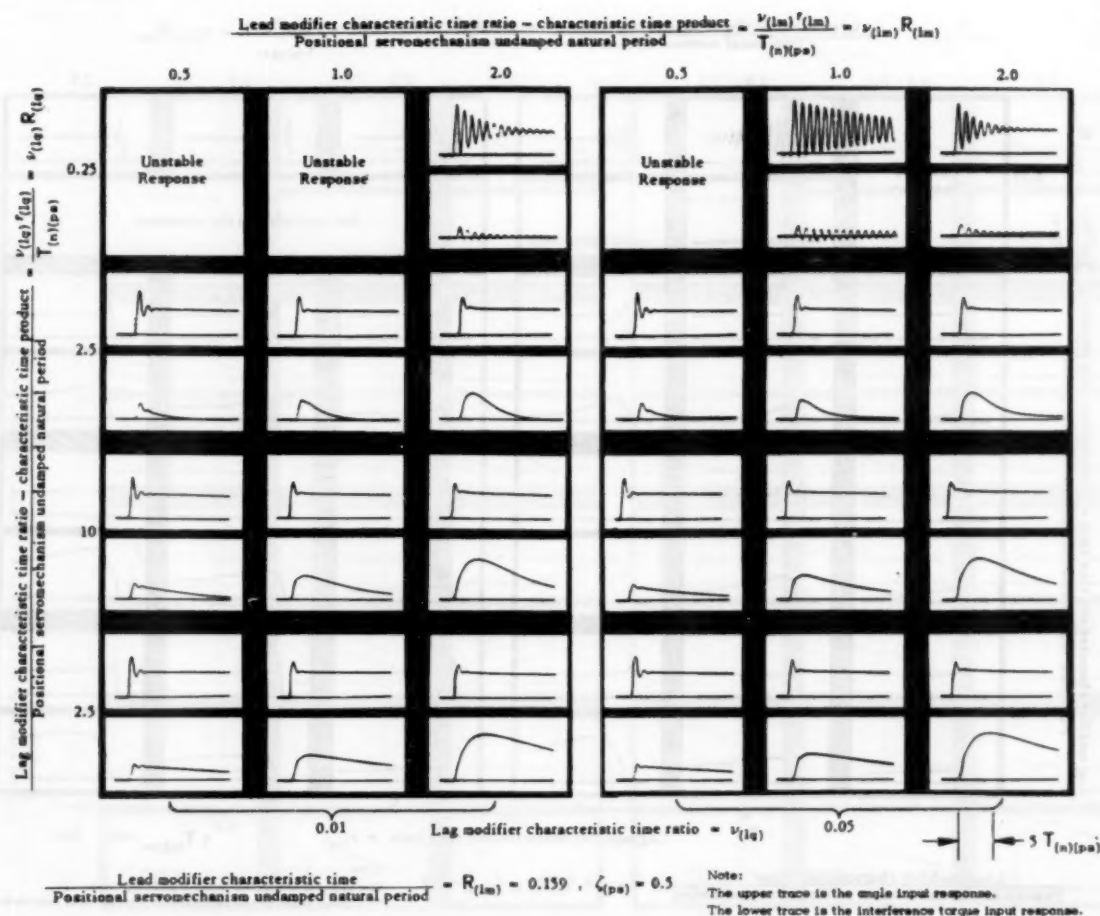


FIG. 16 STEP FUNCTION RESPONSES FOR LEAD-LAG MODIFIER POSITIONAL SERVOMECHANISMS WITH HIGH-FREQUENCY STIFFNESS HELD CONSTANT

tions of the four characteristic times of the two signal modifiers. The study bears out the conclusions enumerated in the foregoing. The response to an angular input for the estimated values of the parameters is shown in Fig. 17, together with a plot of the frequency response and a plot of the closed-chain performance function poles and zeros.

CONCLUSIONS

The design basis developed for multiloop positional servomechanisms has been successfully extended to cascade-type systems. It has been shown that the ultimate limit on the dynamic performance is still the equivalent controlled member inertia. Again, as for the multiloop systems, it is recognized that interference torques on the controlled member, uncertainties in the actuating quantities, and a practical limit to the available torque generator output and component sensitivities establish an upper bound on the static sensitivity. The upper bound is closely coupled to the upper limits of dynamic performance. The complete discussion of these bounds is given in Paper I.

In the present paper, the use of the concept of frequency-dependent coefficients has been extended to provide estimates of the system parameters. The technique provides a first approximation method to establish the bounds of performance.

ACKNOWLEDGMENT

The authors gratefully acknowledge the assistance of Mr. James L. Stockard and Miss Athena Korogis of the Instrumentation Laboratory, Massachusetts Institute of Technology. The analog computer studies were carried out on the General Purpose Simulator of the Instrumentation Laboratory. The authors are indebted to the staff of the Jackson & Moreland Technical Publications Division for their assistance in preparing the manuscript and figures.

The work involved in preparing this paper was supported in part with funds provided by U. S. Air Force Contract No. AF 33(616)-2039 to the Massachusetts Institute of Technology.

BIBLIOGRAPHY

- 1 "Design Basis for Multiloop Positional Servomechanisms," by Sidney Lees, Trans. ASME, vol. 78, 1956, pp. 1339-1366.
- 2 "Stabilization of Positional Servomechanisms With Cascaded Elements," by Theodore C. Blaschke, SM thesis submitted to Aeronautical Engineering Department, Massachusetts Institute of Technology, Cambridge, Mass.
- 3 "Instrument Engineering," by C. S. Draper, W. McKay, and S. Lees, vol. I, vol. II, and vol. III, McGraw-Hill Book Company, Inc., New York, N. Y.

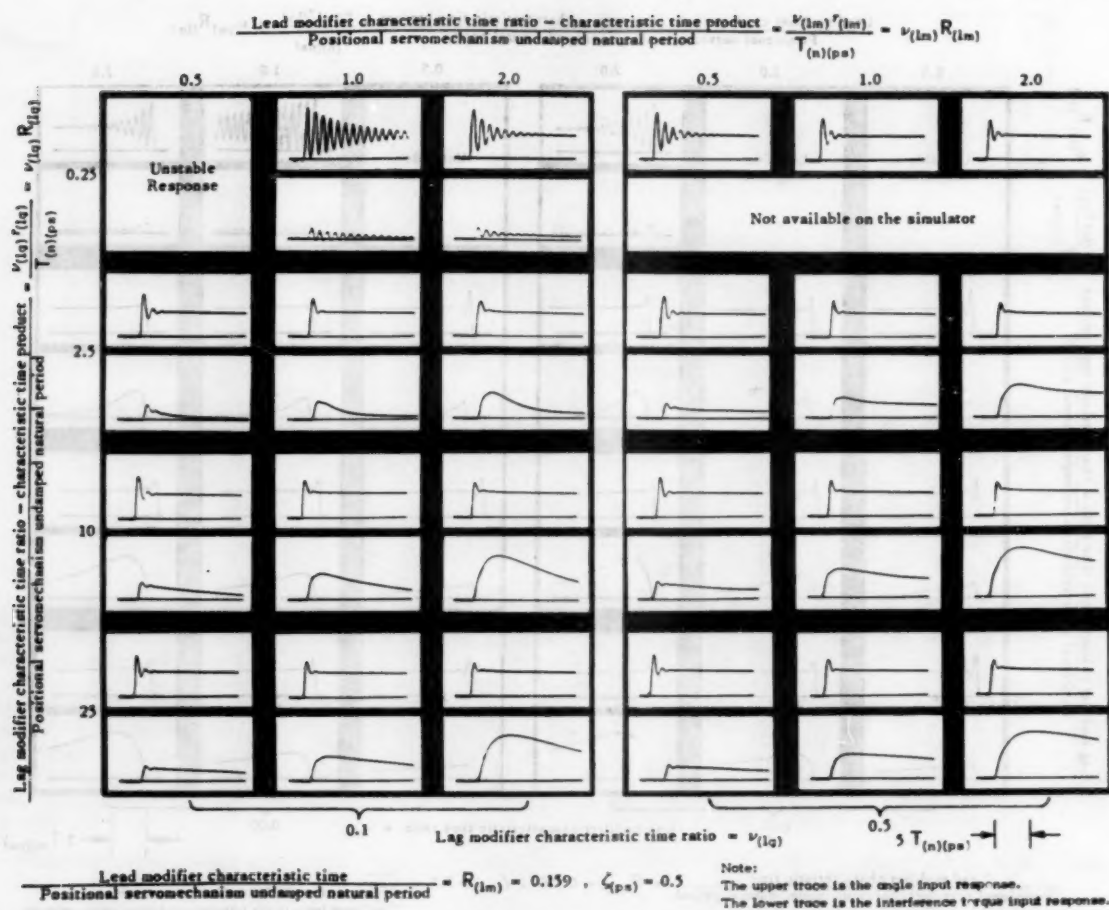


FIG. 16 (continued)

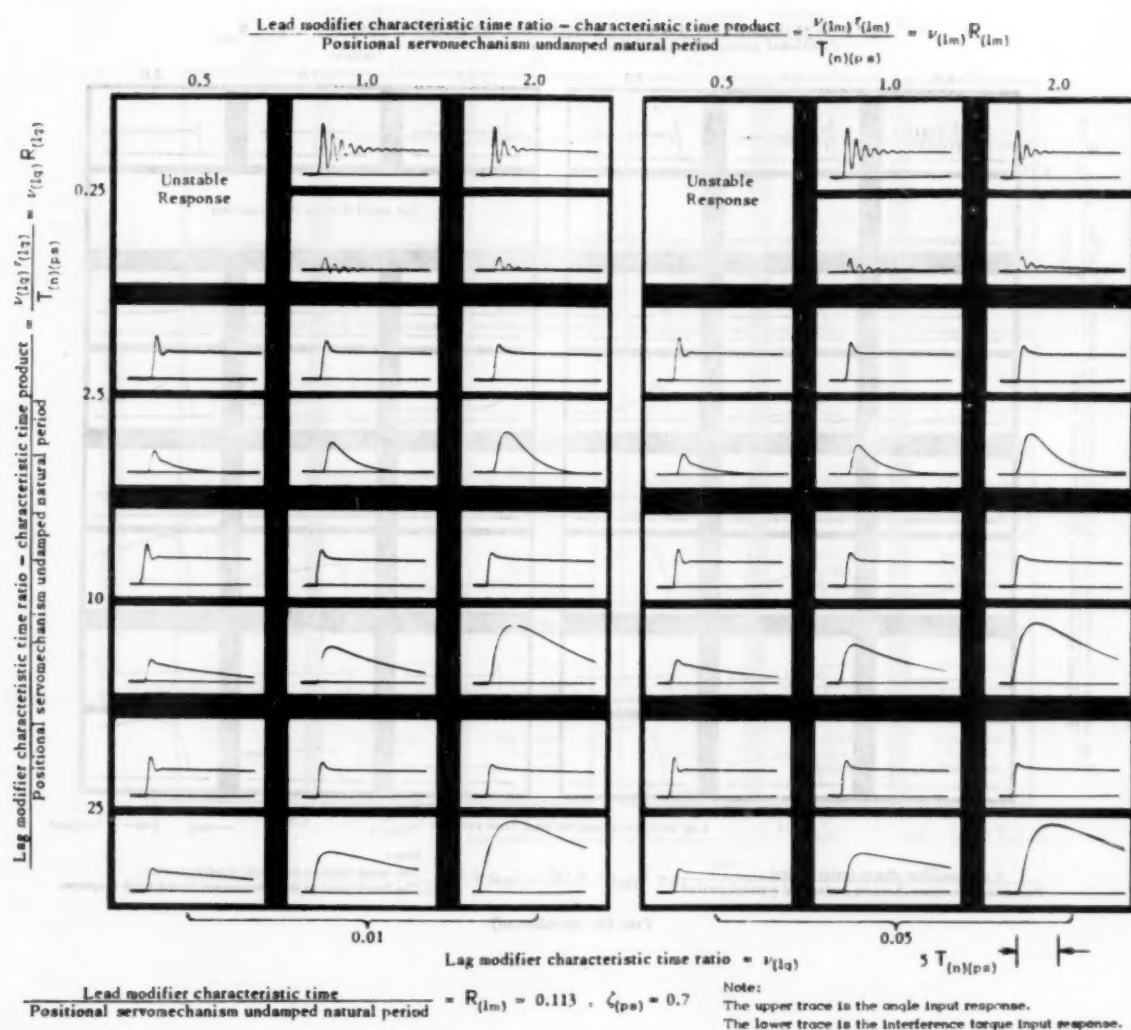


Fig. 10 (continued)

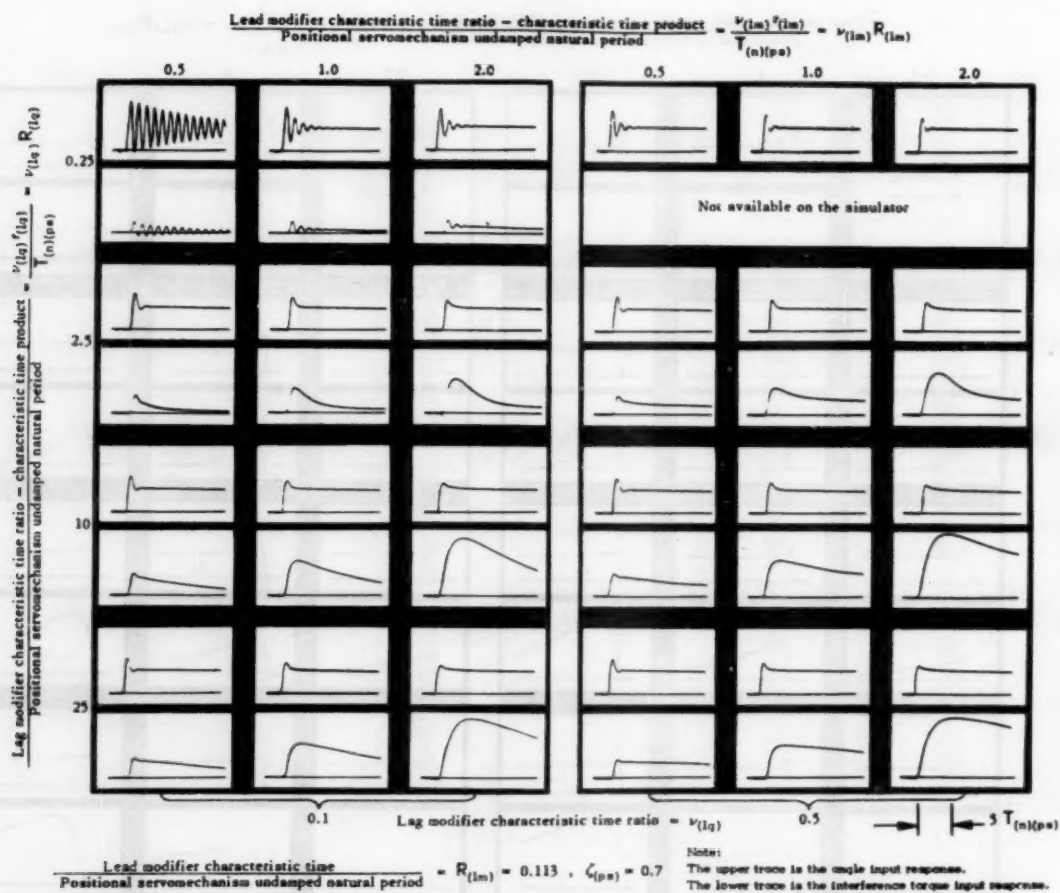


Fig. 16 (continued)

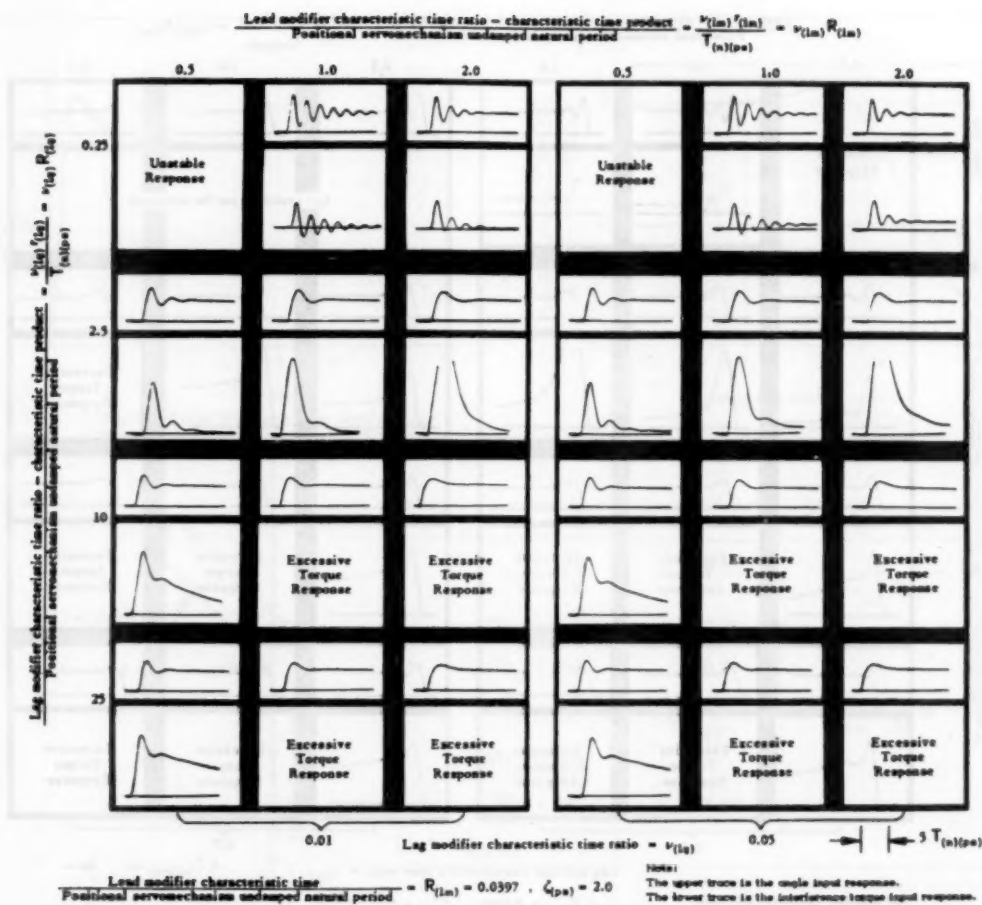


FIG. 16 (continued)

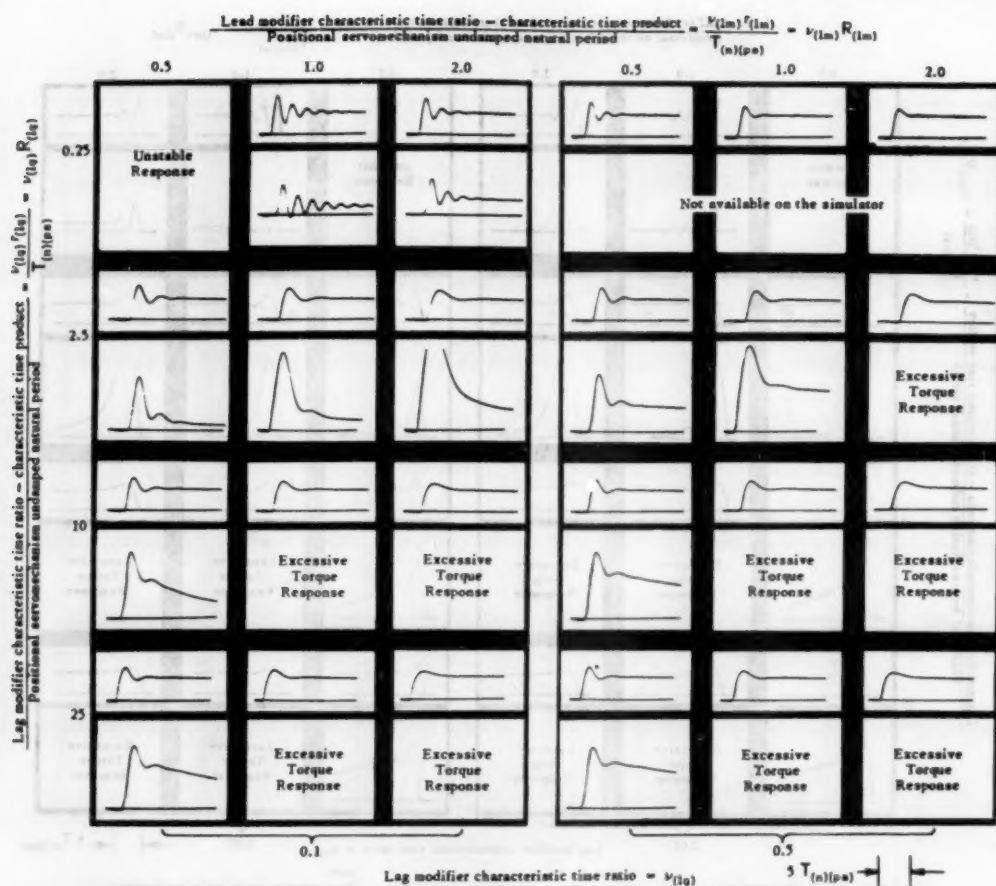


FIG. 16 (continued)

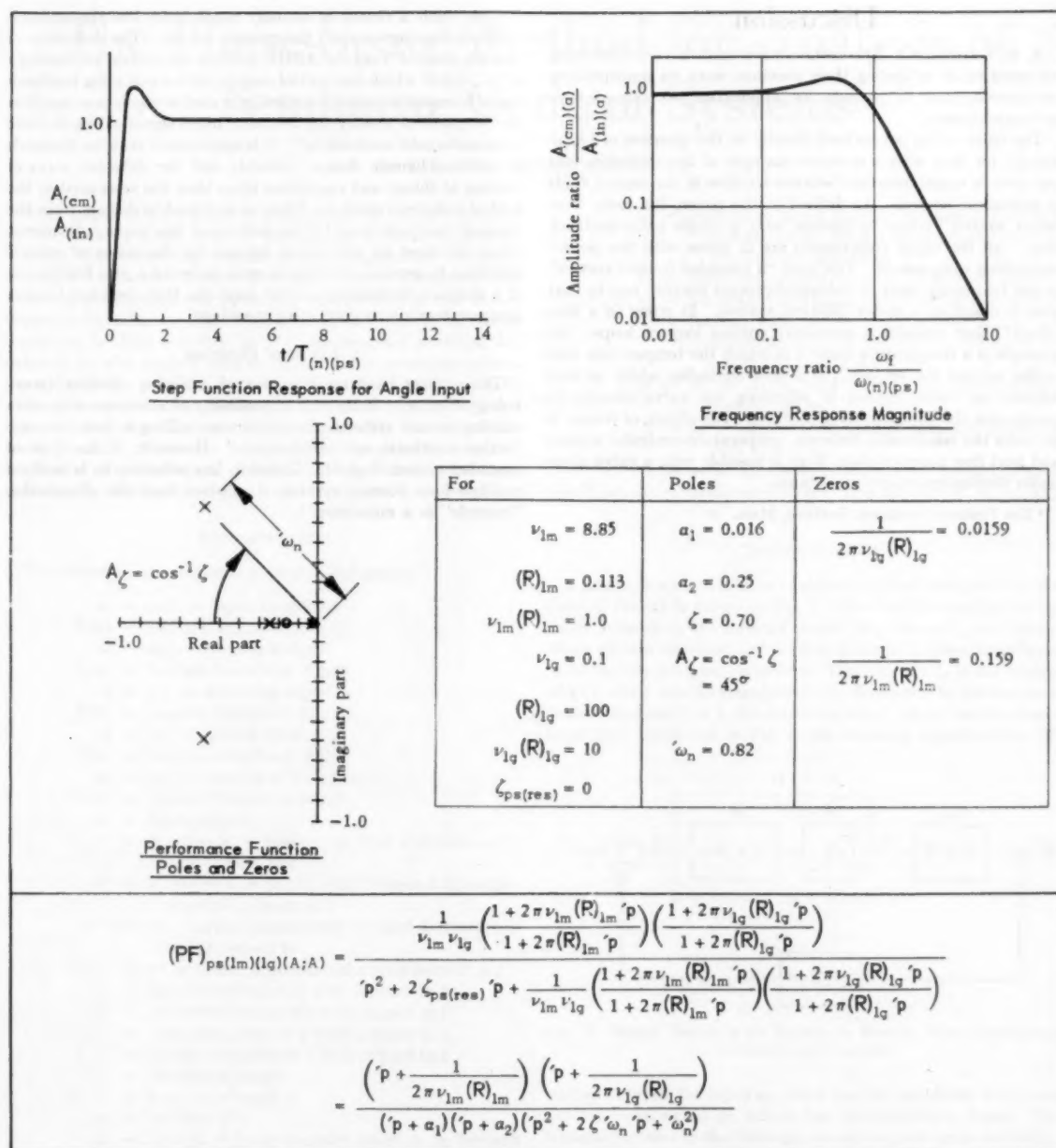


FIG. 17 TYPICAL DYNAMIC CHARACTERISTICS OF A LEAD-LAG MODIFIER POSITIONAL SERVOMECHANISM FOR AN ANGLE INPUT

Discussion

A. R. CATHERON.⁵ The authors have made a very interesting contribution in extending their previous work on multiple-loop servomechanisms to include its application to cascade-type servomechanisms.

The titles of the papers lead directly to the question of terminology, for they offer a concrete example of the confusion that can exist in communication between workers in the several fields of automatic control. As defined in the paper, the term "cascaded control" refers to devices with a single unity-feedback loop. All the signal components are in series with the power-controlling components. The term "a cascaded control system" is one frequently used in industrial-process control, but in that area it describes a rather different system. It refers to a loop (chain?) that contains a secondary control loop or loops. An example is a temperature control in which the temperature controller adjusts the set point of a flow controller which in turn adjusts the valve instead of adjusting the valve directly to manipulate the flow of heating medium. The object, of course, is to make the relationship between temperature-controller output and heat flow more constant than is possible with a valve alone under fluctuating supply conditions.

⁵ The Foxboro Company, Foxboro, Mass.

Now, such a circuit is actually much more like the authors' multiple-loop servos than the cascade servos. The definition of cascade control from the ASME bulletin on control terminology is "...one in which the control output, or the actuating feedback signal from one automatic controller is used to regulate or readjust the set-point or modify the reference input signal of one or more other automatic controllers." It is appreciated that the demands of servomechanism design probably call for different ways of looking at things and expressing ideas than the ones used in the field of industrial control. There is no intent to detract from the value of the work done by the authors of this paper. However, where we meet on a common ground for discussion of control problems in general, it seems in order to make a plea for the use of a common terminology, or at least one that does not involve common terms with conflicting meanings.

AUTHORS' CLOSURE

The authors have no intention of initiating another terminology dispute. If there is a possibility of confusion with other existing control systems, the authors are willing to use the name "series positional servomechanism." However, if the type of cascaded system that Mr. Catheron has reference to is really a multiple-loop control system, it appears that the designation "cascade" is a misnomer.

The Phase-Space Method for Analysis of Nonlinear Control Systems

By Y. H. KU,¹ PHILADELPHIA, PA.

This paper gives a general procedure for the analysis of a feedback system with a nonlinear control function. Taking the actuating signal as the dependent variable, a single nonlinear differential equation is obtained, the order of which depends upon the complexity of the linear transfer functions. This high-order nonlinear differential equation is then solvable by the phase-space method developed by the author and detailed in his previous papers (1, 2, 3).² The method is further extended to the analysis of a system with one nonlinear controller in the forward branch and another nonlinear controller in the feedback branch. The two phase-plane equations obtained from the simultaneous differential equations are then solvable by the method given in reference (4).

NOMENCLATURE

The following nomenclature is used in the paper:

- $x_1 = x_1(t)$ = input to system
- $X_1(s)$ = Laplace transform of $x_1(t)$
- $x_2 = x_2(t)$ = feedback signal
- $X_2(s)$ = Laplace transform of $x_2(t)$
- $\epsilon = \epsilon(t)$ = actuating signal
- $E(s)$ = Laplace transform of $\epsilon(t)$
- $f = f(t)$ = control effort
- $F(s)$ = Laplace transform of $f(t)$
- $x_0 = x_0(t)$ = output of the system
- $X_0(s)$ = Laplace transform of $x_0(t)$
- x = displacement
- $x' = dx/dt = v$ = velocity or first derivative of x with respect to t
- $x'' = d^2x/dt^2 = w$ = acceleration or second derivative of x with respect to t
- $x''' = w' =$ rate of acceleration or third derivative of x with respect to t
- $x'''' = w'' =$ fourth derivative of x with respect to t
- ϵ' = first derivative of ϵ with respect to t
- ϵ'' = second derivative of ϵ with respect to t
- ϵ''' = third derivative of ϵ with respect to t
- ϵ'''' = fourth derivative of ϵ with respect to t
- $F(t)$ = function of time t
- $f(v, x)$ = function of v and x
- $f_1(x)$ = function of x
- $L_1 = K_1 G_1(s)$ = linear transfer function in forward branch, where K_1 is a constant and $G_1(s)$ is the function transform involving the complex variable s

- $L_2 = K_2 G_2(s)$ = linear transfer function in feedback branch, where K_2 is a constant and $G_2(s)$ is the function transform
- N_1 = nonlinear control function in forward branch
- $n_1(\epsilon'', \epsilon', \epsilon)$ = nonlinear function as a function of ϵ , ϵ' , and ϵ''
- A_1 = limiter, with limits $\pm A_m$, where A_m is the maximum value of $f(t)$, the control effort, on account of limiter A_1
- $N = N_1 + A_1$ = total control function including both N_1 and A_1
- $n = n_1 + A_1$ = total control function including both n_1 and A_1
- N_2 = nonlinear control function in feedback branch
- $n_2(x_0'', x_0', x_0)$ = nonlinear function as a function of x_0 , x_0' , and x_0''

INTRODUCTION

A feedback system with a nonlinear control function N in the forward branch is shown in Fig. 1. The transfer function of the linear network in the forward branch is given as $L_1 = K_1 G_1(s)$, where K_1 is a constant and $G_1(s)$ is given in Laplace transforms involving the complex variable s . The input to L_1 is the control effort f , which has the transform $F(s)$. The input to the nonlinear control function N is ϵ , the actuating signal, which has the transform $E(s)$. As shown in Fig. 1, the actuating signal ϵ is the dif-

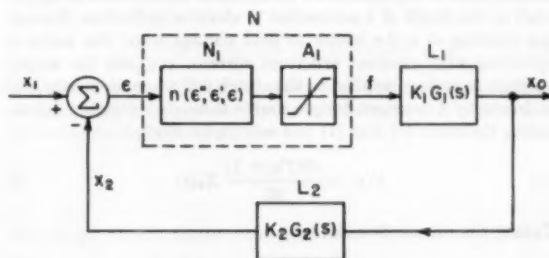


FIG. 1 BLOCK DIAGRAM OF FEEDBACK SYSTEM WITH NONLINEAR CONTROL AND LIMITER

ference between the input x_1 , which has the transform $X_1(s)$, and the feedback signal x_2 , which has the transform $X_2(s)$. The transfer function in the feedback branch is given as $L_2 = K_2 G_2(s)$, where K_2 is a constant and $G_2(s)$ is given in Laplace transforms and represents a linear network. The input to L_2 is the output x_0 , which has the transform $X_0(s)$.

As the system is nonlinear, it is not possible to analyze the whole problem by standard methods in Laplace transforms. It is the purpose of this paper to derive the nonlinear differential equation for the feedback system with a nonlinear control function in the forward branch and then establish the corresponding phase-plane equations which are solvable by the method detailed in the author's previous papers (1, 2, 3). Extension of the application of the phase-space method to the analysis of a system with nonlinear functions in both the forward branch and the feedback branch is made at the end of this paper. Two simultaneous non-

¹ Professor, Moore School of Electrical Engineering, University of Pennsylvania.

² Numbers in parentheses refer to the Bibliography at the end of the paper.

Contributed by the Instruments and Regulators Division and presented at the Annual Meeting, New York, N. Y., November 25-30, 1956, of THE AMERICAN SOCIETY OF MECHANICAL ENGINEERS.

NOTE: Statements and opinions advanced in papers are to be understood as individual expressions of their authors and not those of the Society. Manuscript received at ASME Headquarters, August 1, 1956. Paper No. 56-A-103.

linear differential equations are transformed into a corresponding set of simultaneous phase-plane equations which are solvable by the method given in reference (4).

FUNDAMENTAL EQUATIONS OF THE SYSTEM

There are two sets of fundamental equations: The first set involving linear elements can be expressed in terms of Laplace transforms assuming known initial conditions; while the second set involving nonlinear elements can be given best in the form of differential equations.

Referring to Fig. 1, the Laplace-transform equations (assuming the system initially quiescent) that can be written down are

$$X_0(s) = K_1 G_1(s) F(s) \dots \dots \dots [1]$$

$$X_2(s) = K_2 G_2(s) X_0(s) \dots \dots \dots [2]$$

$$X_1(s) - X_2(s) = E(s) \dots \dots \dots [3]$$

As the relation between $\epsilon(t)$ and $f(t)$ is nonlinear, the following differential equation is given as a typical example

$$n(\epsilon'', \epsilon', \epsilon) = f(t) \dots \dots \dots [4]$$

where n stands for the combination of $n_1(\epsilon'', \epsilon', \epsilon)$ and the limiter A_1 , which limits the value of $f(t)$ to $\pm A_m$, where A_m is the maximum value.

PRINCIPAL TRANSFER FUNCTION

In order to illustrate the general procedure for analyzing the nonlinear control system represented by the foregoing equations, let the principal transfer function $L_1 = K_1 G_1(s)$ be chosen as

$$K_1 G_1(s) = \frac{K_1}{s^2(Ts + 1)} \dots \dots \dots [5]$$

where T is a time constant. This transfer function is a good approximation to the function which relates the altitude of an aircraft or the depth of a submarine to elevator deflection, the output position of a d-c motor to field voltage when the motor is operating with constant armature current, and also the output position to voltage applied to the clutch coil when an inertia load is driven by a constant-torque source through a clutch. Substituting Equation [5] into [1] and solving for $F(s)$

$$F(s) = \frac{s^2(Ts + 1)}{K_1} X_0(s) \dots \dots \dots [6]$$

Taking the inverse transform

$$f(t) = (T/K_1)x_0''' + (1/K_1)x_0'' \dots \dots \dots [7]$$

where x_0'' and x_0''' are the second and third derivatives of $x_0(t)$ with respect to t , respectively.

FEEDBACK-TRANSFER FUNCTION

The feedback-branch transfer function is designated as $L_2 = K_2 G_2(s)$. While $K_2 G_2(s)$ can be chosen as $K_2/(Ts + 1)$ for example, three simpler cases can serve as well to illustrate the procedure

Case I: $L_2 = 1$ (Fig. 2)

$$\text{Case II: } L_2 = K_2 G_2(s) = \frac{K_2}{s} \dots \dots \dots [8]$$

$$\text{Case III: } L_2 = K_2 G_2(s) = K_2 s \dots \dots \dots [9]$$

Cases II and III are shown in Figs. 3 and 4, respectively.

Substituting the various values of $K_2 G_2(s)$ into Equation [2], solving for $X_2(s)$ and taking the inverse form, the relation between $x_2(t)$ and $x_0(t)$ is obtained.

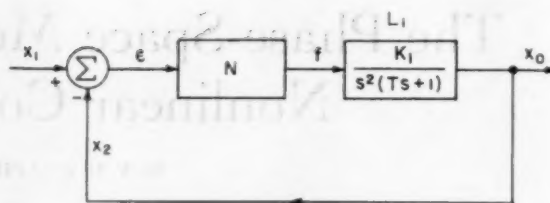


FIG. 2 NONLINEAR CONTROL SYSTEM WITH DIRECT FEEDBACK

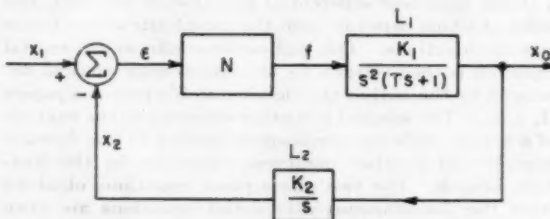


FIG. 3 NONLINEAR CONTROL SYSTEM WITH INTEGRAL FEEDBACK

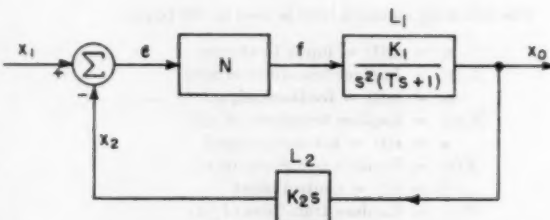


FIG. 4 NONLINEAR CONTROL SYSTEM WITH DERIVATIVE FEEDBACK

Corresponding to Equation [3], the following general relation

$$x_1(t) - x_2(t) = \epsilon(t) \dots \dots \dots [10]$$

holds for any form of feedback-transfer function.

CASE I—SIMPLE FEEDBACK SYSTEM WITH NONLINEAR CONTROL

Consider the simple feedback system with nonlinear control function N as shown in Fig. 2. As $L_2 = 1$, $X_2(s) = X_0(s)$, and $x_2(t) = x_0(t)$. Substituting x_2 for x_0 in Equation [7]

$$f(t) = (T/K_1)x_2''' + (1/K_1)x_2'' \dots \dots \dots [11]$$

From Equation [10], $x_2 = x_1 - \epsilon$. Substituting this relation into Equation [11]

$$f(t) = (T/K_1)x_1''' + (1/K_1)x_1'' - (T/K_1)\epsilon''' - (1/K_1)\epsilon'' \dots \dots \dots [12]$$

Substituting Equation [4] into Equation [12] and rearranging terms

$$(T/K_1)\epsilon''' + (1/K_1)\epsilon'' + n(\epsilon'', \epsilon', \epsilon) = (T/K_1)x_1''' + (1/K_1)x_1'' \dots \dots \dots [13]$$

Dividing through by (T/K_1)

$$\epsilon''' + (1/T)\epsilon'' + (K_1/T)n(\epsilon'', \epsilon', \epsilon) = x_1''' + (1/T)x_1'' \dots \dots \dots [14]$$

This equation preserves the total form of the nonlinear control function which in the chosen illustrative example includes $n_1(\epsilon'', \epsilon', \epsilon)$ and the effect of a limiter A_1 . In choosing the actuating signal ϵ as the dependent variable, a third-order nonlinear differential equation is obtained. The solution of Equation [14] will be deferred until later. Once ϵ is found, the feedback signal $x_2 = x_1 - \epsilon$ is known. In Case I, the feedback signal is equal to the output x_2 .

CASE II—NONLINEAR SYSTEM WITH INTEGRAL FEEDBACK

Consider the feedback system with nonlinear control function N and the transfer function L_1 in the forward branch and the transfer function $L_2 = K_2/s$ as shown in Fig. 3. Substituting Equation [8] into Equation [2]

$$X_2(s) = (1/K_2)sX_1(s) \dots \dots \dots [15]$$

Taking the inverse transform

$$x_2(t) = (1/K_2)x_1' \dots \dots \dots [16]$$

Differentiating, Equation [10] becomes

$$x_1' - x_2' = \epsilon' \dots \dots \dots [17]$$

Substituting Equation [17] into Equation [16]

$$x_2 = (1/K_2)(x_1' - \epsilon') \dots \dots \dots [18]$$

As in Equation [7], high derivatives of x_2 are needed, these can now be obtained from Equation [18]

$$x_2'' = (1/K_2)(x_1'' - \epsilon'') \dots \dots \dots [19]$$

$$x_2''' = (1/K_2)(x_1''' - \epsilon''') \dots \dots \dots [20]$$

Substituting Equations [19] and [20] into Equation [7]

$$f(t) = (T/K)(x_1''' - \epsilon''') + (1/K)(x_1'' - \epsilon'') \dots [21]$$

where $K = K_1K_2$.

Substituting the explicit nonlinear function given in Equation [4] for $f(t)$ into Equation [21], dividing by (T/K) and transposing terms, a high-order nonlinear differential equation like the following is obtained

$$\epsilon'''' + (1/T)\epsilon''' + (K/T)n(\epsilon'', \epsilon', \epsilon) = x_1'''' + (1/T)x_1''' \dots [22]$$

Notice that the right-hand member of Equation [22] depends on the third and fourth derivatives of the input x_1 , while in Equation [14] the right-hand member depends on the second and third derivatives of the input x_1 . The solution of Equation [22] will be deferred until later.

CASE III—NONLINEAR SYSTEM WITH DERIVATIVE FEEDBACK

Consider the nonlinear system with derivative feedback as shown in Fig. 4. In this case, $K_2G_2(s) = K_2s$. The preliminary steps will be carried out in terms of Laplace transforms. Combining Equations [1] and [2]

$$X_2(s) = K_2G_2(s)K_1G_1(s)F(s) \dots \dots \dots [23]$$

Substituting Equations [5] and [9] into Equation [23]

$$X_2(s) = \frac{K}{s(Ts + 1)}F(s) \dots \dots \dots [24]$$

Solving for $F(s)$

$$F(s) = (1/K)s(Ts + 1)X_2(s) \dots \dots \dots [25]$$

From Equation [3], $X_2(s) = X_1(s) - E(s)$. Substituting this relation into Equation [25]

$$F(s) = (1/K)s(Ts + 1)[X_1(s) - E(s)] \dots \dots [26]$$

Taking the inverse transform

$$f(t) = (T/K)x_1'' + (1/K)x_1' - (T/K)\epsilon'' - (1/K)\epsilon' \dots [27]$$

Substituting Equation [4] for $f(t)$ in Equation [27], dividing by (T/K) and transposing terms, there is obtained

$$\epsilon'' + (1/T)\epsilon' + (K/T)n(\epsilon'', \epsilon', \epsilon) = x_1'' + (1/T)x_1' \dots [28]$$

Notice that this is a second-order nonlinear differential equation and the right-hand member depends on the first and second derivatives of the input. In the following section, the method for solving Equation [28] will be outlined first. The method is then extended to the solution of the third-order nonlinear differential Equation [14] and the solution of the fourth-order nonlinear differential Equation [22]. It may be mentioned that according to the method given in reference (1), still higher order differential equations involving nonlinear functions can be solved in a similar way. Thus the procedure is general and is by no means limited by the particular forms of $K_1G_1(s)$ and $K_2G_2(s)$ discussed in the foregoing.

DERIVATION OF THE PHASE-PLANE EQUATION

Consider a general second-order nonlinear differential equation

$$x'' + f(x', x)x' + f_1(x) = F(t) \dots \dots \dots [29]$$

where x is the dependent variable, t is the independent variable, $F(t)$ is a forcing function, x' and x'' are, respectively, first and second derivatives of x with respect to t , $f(x', x)$ is a function of x' and x , and $f_1(x)$ is a function of x . In mechanical systems, x may represent linear or angular displacement, $x' = v$ may represent linear or angular velocity, and $x'' = w$ may represent linear or angular acceleration. Introducing the symbols $v = dx/dt$ and $w = dv/dt = d^2x/dt^2$, Equation [29] can be rewritten as

$$w + f(v, x)v + f_1(x) = F(t) \dots \dots \dots [29a]$$

Thus the acceleration function (or the second derivative) is given as

$$w = F(t) - f(v, x)v - f_1(x) = w(t, v, x) \dots \dots [30]$$

Now, since $w = dv/dt$ by definition and $dv/dt = (dv/dx)(dx/dt)$, where dx/dt can be replaced by the symbol v , there is obtained the following fundamental relation

$$v \frac{dv}{dx} = w \dots \dots \dots [31]$$

Dividing by v , the phase-plane equation is derived

$$\frac{dv}{dx} = \frac{w}{v} \dots \dots \dots [32]$$

This is the fundamental equation for the v - x curve or v - x trajectory in the v - x plane which is known as the phase plane. The equation says that the slope of the v - x curve anywhere in the phase plane is given by the ratio of the acceleration to the velocity at the corresponding instant. This relation is true whether the system is linear or nonlinear. This equation can be used to solve any second-order nonlinear differential equation whether the equation represents a mechanical system or an electrical system or any other physical system. Notice that Equation [28] is a specific form of Equation [29] and its phase-plane equation, according to Equation [32], can be derived similarly as follows

$$\frac{d\epsilon'}{d\epsilon} = \frac{\epsilon''}{\epsilon'} = \frac{x_1'' + (1/T)x_1' - (1/T)\epsilon'' - (K/T)n(\epsilon'', \epsilon', \epsilon)}{\epsilon'} \dots [33]$$

where $x_1'' + (1/T)x_1'$ corresponds to $F(t)$ in Equations [29] and [30], and ϵ , ϵ' , and ϵ'' correspond, respectively, to x , v , and w in Equation [32].

SOLUTION OF THE PHASE-PLANE EQUATION

There are a number of analytical and graphical methods for solving the phase-plane equation given in standard treatises (5, 6, 7). The author has developed the acceleration-plane method in which the acceleration function w is plotted against x for different values of v and the slope dw/dx is determined from the ratio of w and v for a given set of values of v and x . The interested reader is referred to references (8, 9, 10) in the Bibliography.

For a given point on the v - x trajectory (with a set of values of v and x), there corresponds a definite value of t . Starting from the initial conditions at $t = t_0 = 0$, $x = x_0$ and $v = v_0$, let there be a small change in time, say, Δt . The ratio $\Delta x/\Delta t$ can be designated as v_1 , the average velocity during this interval. So from a given v - x curve, if one picks any interval Δx and takes the average value of v during this interval, the corresponding value of Δt can be found as equal to $\Delta x/v_{avg}$, where v_{avg} stands for the average value of velocity during Δt . Denoting t_1 and x_1 as the values of t and x in the middle of the first interval (starting from initial conditions), it can be seen that the phase-plane equation corresponding to the set of values v_1 , x_1 , and t_1 becomes

$$\left(\frac{\Delta v}{\Delta x}\right)_{v=v_1, x=x_1} = \frac{w(t_1, v_1, x_1)}{v_1} = \frac{w_1}{v_1} \dots \dots \dots [34]$$

It may be mentioned here that, since the initial value of acceleration w_0 is also known, the following relation determines the initial slope of the v - x curve

$$\left(\frac{\Delta v}{\Delta x}\right)_0 = \frac{w(t_0, v_0, x_0)}{v_0} = \frac{w_0}{v_0} \dots \dots \dots [35]$$

So for an assumed value of Δx initially, the corresponding value of Δv can be obtained from Equation [35]. A more accurate way of determining Δv is to go back to Equation [34] and solve for Δv for a known value of Δx

$$\left(\frac{\Delta v}{\Delta x}\right)_{v_1=v_0+\Delta v/2, x_1=x_0+\Delta x/2} = \frac{w[(t_0 + \Delta x/(2v_0 + \Delta v)), (v_0 + \Delta v/2), (x_0 + \Delta x/2)]}{v_0 + \Delta v/2} \dots \dots \dots [36]$$

If small increments of Δx are used, the slopes thus determined can be rather accurate. If graphical methods are used, a few trials are usually sufficient to find the correct slope that satisfies Equation [32]. The interested reader may try this method on the solution of a known linear differential equation and then extend its application to nonlinear problems.

THE PHASE-SPACE METHOD

The phase-space method is a logical extension of the phase-plane method. Since w represents the acceleration function or the second derivative, w' represents the rate of acceleration or the third derivative. Thus

$$w' = \frac{dw}{dt} = \left(\frac{dw}{dv}\right) \left(\frac{dv}{dt}\right) = \left(\frac{dw}{dv}\right) w \dots \dots \dots [37]$$

Dividing by w , the following phase space equation is obtained

$$\frac{dw}{dv} = \frac{w'}{w} \dots \dots \dots [38]$$

Now in general w' is a function of w , v , x , and t . Equation [38] represents the physical relationship that the slope of the ac-

celeration-velocity trajectory anywhere in the w - v plane is equal to the ratio of the rate of acceleration w' to the acceleration w . A three-dimensional phase space with co-ordinates w , v , and x is needed for the space trajectory (11). The other phase-space equation needed is already given in Equation [32]. Taking its reciprocal form

$$\frac{dx}{dv} = \frac{v}{w} \dots \dots \dots [39]$$

Applying the phase-space method outlined in the foregoing to the solution of Equation [14], let the actuating signal ϵ be replaced by the symbol x and the right-hand member be designated by $F(t)$. Equation [14] then becomes

$$w'' + (1/T)w' + (K_1/T)n(w, v, x) = F(t) \dots \dots \dots [40]$$

The phase-space Equation [38] gives

$$\frac{dw}{dv} = \frac{w'}{w} = \frac{F(t) - (1/T)w' - (K_1/T)n(w, v, x)}{w} \dots \dots [41]$$

Equation [39] and Equation [41] constitute the desired phase-space equations where $x = \epsilon$, $v = \epsilon'$, and $w = \epsilon''$. In Equations [40] and [41], $w' = \epsilon'''$ is a function of ϵ'' , ϵ' , ϵ , and t , and $F(t) = x_1''' + (1/T)x_1''$.

The reader is referred to references (2, 3, 4) for actual examples in the simultaneous solution of these phase-space equations. It may be pointed out here that if one chooses a small interval Δv , there are corresponding increments of Δw and Δx determined by the slopes of the projections of the space trajectory in the w - v plane and in the x - v plane. From Equations [39] and [41], another equation

$$\frac{dw}{dx} = \frac{w'}{v} \dots \dots \dots [42]$$

representing the projection in the w - x plane is derived.

Extending the phase-space method to fourth-order nonlinear differential equations like Equation [22], let the actuating signal be replaced by the symbol x and the right-hand member of Equation [22] be designated by $F_1(t)$. Equation [22] then becomes

$$w'' + (1/T)w' + (K/T)n(w, v, x) = F_1(t) \dots \dots \dots [43]$$

Since $w'' = dw'/dt = (dw'/dw)(dw/dt) = (dw'/dw)w'$, the following general phase-space equation is obtained

$$\frac{dw'}{dw} = \frac{w''}{w'} \dots \dots \dots [44]$$

Equations [32], [38], and [44] are general phase-space equations for solving any fourth-order differential equation. It is shown in reference (1) that the general slope equation is

$$\frac{dx^{(n-1)}}{dx^{(n-2)}} = \frac{x^{(n)}}{x^{(n-1)}} \dots \dots \dots [45]$$

Starting from the highest order of the derivatives (n), one writes down such phase-space equations according to Equation [45] until Equation [32] is obtained.

In bringing Equation [22] to the proper form for its solution by the phase-space method, one substitutes for w'' in Equation [44] by the various terms involving w' , w , v , x , and t given in Equation [43]. Thus

$$\frac{dw'}{dw} = \frac{w''}{w'} = \frac{F_1(t) - (1/T)w' - (K/T)n(w, v, x)}{w'} \dots \dots [46]$$

where

$$x = \epsilon, v = \epsilon', w = \epsilon'', w' = \epsilon''', w'' = \epsilon'''' \text{, and } F_1(t) = x_1'''' + (1/T)x_1'''$$

Equations [46], [38], and [32] are sufficient for solving the problem of Case II representing a nonlinear system with integral feedback. The three phase-space equations represent three projections of the four-dimensional space trajectory in the w - v plane, the w - x plane, and the v - x plane. If the nonlinear control function $n(w, v, x)$ in Equation [46] is known, the problem can be solved to any desired degree of accuracy.

GENERAL SYSTEM WITH ADDITIONAL NONLINEAR FEEDBACK

Consider the system as shown in Fig. 5. The nonlinear function in the forward branch is given as

$$\epsilon' + n_1(\epsilon) = f(t) \dots \dots \dots [47]$$

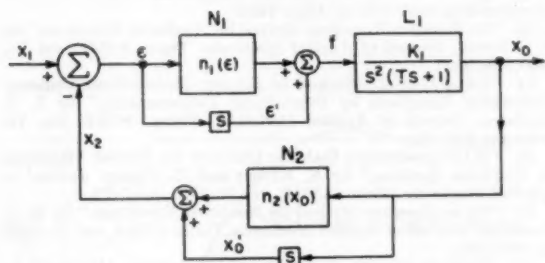


FIG. 5 FEEDBACK SYSTEM WITH TWO NONLINEAR CONTROLLERS

The nonlinear function in the feedback branch is given as

$$x_0' + n_2(x_0, x_0') = x_2(t) \dots \dots \dots [48]$$

The transfer function in the forward branch is the same as that given in Equation [5].

Substituting Equation [47] into Equation [7]

$$\epsilon' + n_1(\epsilon) = (T/K_1)x_0''' + (1/K_1)x_0'' \dots \dots \dots [49]$$

Substituting Equation [10] into Equation [48]

$$x_0' + n_2(x_0) = x_1 - \epsilon \dots \dots \dots [50]$$

Differentiating

$$x_0'' + n_2'(x_0) = x_1' - \epsilon' \dots \dots \dots [51]$$

Differentiating again

$$x_0''' + n_2''(x_0) = x_1'' - \epsilon'' \dots \dots \dots [52]$$

Substituting Equations [51] and [52] into Equation [49], dividing by (T/K_1) and rearranging terms

$$\begin{aligned} \epsilon'' + [(K_1 + 1)/T]\epsilon' + (K_1/T)n_1(\epsilon) \\ = x_1'' + (1/T)x_1' - n_2''(x_0) - (1/T)n_2'(x_0) \dots [53] \end{aligned}$$

Notice that Equations [51] and [53] are two simultaneous second-order nonlinear differential equations. According to the phase-plane method discussed before, any second-order nonlinear differential equation can be transformed to a first-order phase-plane equation like Equation [32]. Let x_0 and ϵ be the two dependent variables. Since $dx_0/dt = x_0'$ and $d\epsilon/dt = \epsilon'$, Equation [32] gives

$$\frac{dx_0'}{dx_0} = \frac{x_0''}{x_0'} \dots \dots \dots [54]$$

Similarly, since $d\epsilon/dt = \epsilon'$ and $d\epsilon'/dt = \epsilon''$

$$\frac{d\epsilon'}{d\epsilon} = \frac{\epsilon''}{\epsilon'} \dots \dots \dots [55]$$

Substituting Equation [51] into the general phase-plane Equation [54]

$$\frac{dx_0'}{dx_0} = \frac{x_1' - \epsilon' - n_2'(x_0)}{x_0'} \dots \dots \dots [56]$$

Substituting Equation [53] into the phase-plane Equation [55]

$$\begin{aligned} \frac{d\epsilon'}{d\epsilon} = \left(\frac{1}{\epsilon'}\right) \{x_1'' + (1/T)x_1' - n_2''(x_0) - (1/T)n_2'(x_0) \\ - [(K_1 + 1)/T]\epsilon' - (K_1/T)n_1(\epsilon)\} \dots [57] \end{aligned}$$

The reader is referred to reference (4) for detailed methods of solving two simultaneous phase-plane equations like Equations [54] and [55]. Equations [56] and [57] can be similarly solved simultaneously if the nonlinear functions n_1 and n_2 are known. It may be mentioned that the nonlinear function given in Equation [47] is similar to the form of nonlinear control by Mr. John L. Preston in fig. 1-8 of reference (12). The function $n_1(\epsilon)$ may represent a diode. A limiter for keeping the maximum value of the control effort f (see Fig. 5) within $\pm A_m$ may be added in the actual network similar to that shown in Fig. 1.

Consider next the system as shown in Fig. 6. The nonlinear functions are

$$\epsilon' + n_1(\epsilon', \epsilon) = f(t) = (T/K_1)x_0''' + (1/K_1)x_0'' \dots [58]$$

$$x_0'' + n_2(x_0', x_0) = x_2(t) = x_1 - \epsilon \dots \dots \dots [59]$$

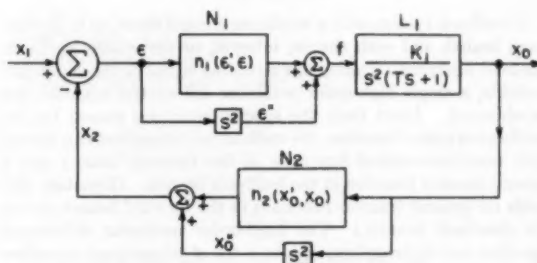


FIG. 6 FEEDBACK SYSTEM WITH TWO NONLINEAR CONTROLLERS

Differentiating, Equation [59] gives

$$x_0''' + n_2'(x_0', x_0) = x_2' = x_1' - \epsilon' \dots \dots \dots [60]$$

Substituting Equations [59] and [60] in Equation [58] and rearranging terms

$$\begin{aligned} \epsilon'' = (T/K_1)x_1' + (1/K_1)x_1 - (T/K_1)\epsilon' \\ - (1/K_1)\epsilon - (T/K_1)n_2'(x_0', x_0) \\ - (1/K_1)n_2(x_0', x_0) - n_1(\epsilon', \epsilon) \dots \dots \dots [61] \end{aligned}$$

The phase-plane equations for Equations [59] and [61] are

$$\frac{dx_0'}{dx_0} = \frac{x_0''}{x_0'} = \frac{x_1 - \epsilon - n_2}{x_0'} \dots \dots \dots [62]$$

$$\begin{aligned} \frac{d\epsilon'}{d\epsilon} = \frac{\epsilon''}{\epsilon'} = \left(\frac{1}{\epsilon'}\right) [(T/K_1)(x_1' - \epsilon' - n_2') \\ + (1/K_1)(x_1 - \epsilon - n_2) - n_1] \dots [63] \end{aligned}$$

It is interesting to note that with more complicated nonlinearities specified in Equations [58] and [59] than those given in Equations [47] and [48], the final phase-plane Equations [62] and [63] are simpler than Equations [56] and [57].

It is also possible to derive one single high-order nonlinear differential equation for the foregoing example by the following steps: From Equation [59]

$$\epsilon = x_1 - x_0'' - n_2 \dots \dots \dots [64]$$

Taking derivatives

$$\epsilon' = x_1' - x_0''' - n_2' \dots \dots \dots [65]$$

$$\epsilon'' = x_1'' - x_0'''' - n_2'' \dots \dots \dots [66]$$

Substituting Equation [66] into Equation [58]

$$x_0'''' + (T/K_1)x_0''' + (1/K_1)x_0'' + n_2'' = x_1'' + n_1 \dots \dots [67]$$

where n_1 is a function of x_1 , x_1' , x_0'' , x_0''' , n_2 , and n_2' .

The phase-space equations are

$$\frac{dx_0'''}{dx_0''} = \frac{x_0''''}{x_0'''} \dots \dots \dots [68]$$

$$\frac{dx_0'}{dx_0''} = \frac{x_0''}{x_0'} \dots \dots \dots [69]$$

$$\frac{dx_0}{dx_0'} = \frac{x_0'}{x_0} \dots \dots \dots [70]$$

where the highest derivative x_0'''' can be expressed in terms of other quantities according to Equation [67].

CONCLUSIONS

A feedback system with a nonlinear control function in the forward branch and with simple, integral, or derivative feedback, has been analyzed. Taking the actuating signal as the dependent variable, a single high-order nonlinear differential equation can be obtained. Apart from the specific examples chosen for the feedback-transfer function, the method can be applied to a system with nonlinear-control functions in the forward branch and a general transfer function in the feedback branch. (Equation [23] holds for general transfer functions in the forward branch and in the feedback branch.) The high-order nonlinear differential equation can be transformed into a set of phase-space equations that can be solved simultaneously by known techniques in the field of nonlinear mechanics. The method of analysis is further extended to the study of feedback systems with one nonlinear function in the forward branch and one nonlinear function in the feedback branch. Two simultaneous phase-plane equations are obtained and these can be solved by the method developed by the author. A linear transfer function and a nonlinear element may be present in the feedback branch. In this case, instead of choosing the output x_0 as the second dependent variable, the quantity between the linear network L_2 and the feedback-branch nonlinear function N_2 should be chosen as the second dependent variable. Hence the phase-space method can be applied to the analysis of nonlinear control systems either with linear or nonlinear feedback.

BIBLIOGRAPHY

- 1 "A Method for Solving Third and Higher Order Nonlinear Differential Equations," by Y. H. Ku, *Journal of the Franklin Institute*, vol. 256, September, 1953, pp. 229-244.
- 2 "Analysis of Multi-Loop Nonlinear Systems," by Y. H. Ku, *Proceedings of IRE*, vol. CT-1, December, 1954, pp. 6-12.
- 3 "Analysis of Nonlinear Coupled Circuits," by Y. H. Ku, *Trans. AIEE*, vol. 73, part I, 1954, pp. 626-631.
- 4 "Analysis of Nonlinear Coupled Circuits—II," by Y. H. Ku, *Trans. AIEE*, vol. 74, part I, 1955, pp. 439-443.
- 5 "Nonlinear Vibrations," by J. J. Stoker, Interscience Publishers, Inc., New York, N. Y., 1950.
- 6 "Ordinary Nonlinear Differential Equations," by N. W. McLachlan, Clarendon Press, Oxford, England, 1950.

7 "Mechanical Vibrations," by J. P. den Hartog, McGraw-Hill Book Company, Inc., New York, N. Y., 1947.

8 "Nonlinear Analysis of Electro-Mechanical Problems," by Y. H. Ku, *Journal of the Franklin Institute*, vol. 255, January, 1953, pp. 9-31.

9 "Acceleration Plane Method for Nonlinear Oscillations," by Y. H. Ku, *Proceedings of the Symposium on Nonlinear Circuit Analysis*, Polytechnic Institute of Brooklyn, Brooklyn, N. Y., April, 1953, pp. 129-153.

10 "Acceleration Plane Method for Analysis of a Circuit with Nonlinear Inductance and Nonlinear Capacitance," by Y. H. Ku, *Trans. AIEE*, vol. 73, part I, 1954, pp. 619-626.

11 "Analysis of Nonlinear Systems With More Than One Degree of Freedom by Means of Space Trajectories," by Y. H. Ku, *Journal of the Franklin Institute*, vol. 259, February, 1955, pp. 115-131.

12 "Nonlinear Control of a Saturating Third-Order Servomechanism," by J. L. Preston, MIT Servomechanisms Laboratory Technical Memorandum 6897-TM-14, May, 1954.

13 "An Iterative Numerical Method for Nonlinear Vibrations," by J. E. Brock, *Journal of Applied Mechanics*, Trans. ASME, vol. 73, 1951, pp. 1-11.

14 "On a General Method of Solving Second-Order Ordinary Differential Equations by Phase-Plane Displacements," by L. S. Jacobsen, *Journal of Applied Mechanics*, Trans. ASME, vol. 74, 1952, pp. 543-553.

15 "A Comprehensive Stability Criterion for Forced Vibrations in Nonlinear Systems," by K. Klotter and E. Pinney, *Journal of Applied Mechanics*, Trans. ASME, vol. 75, 1953, pp. 9-12.

16 "On an Iterative Method for Nonlinear Vibrations," by R. E. Roberson, *Journal of Applied Mechanics*, Trans. ASME, vol. 75, 1953, pp. 237-240.

17 "Analysis of a Nonlinear Dynamic Vibration Absorber," by L. A. Pipes, *Journal of Applied Mechanics*, Trans. ASME, vol. 75, 1953, pp. 515-518.

18 "The Existence and Stability of Ultraharmonics and Subharmonics in Forced Nonlinear Oscillations," by T. K. Caughey, *Journal of Applied Mechanics*, Trans. ASME, vol. 76, 1954, pp. 327-335.

19 "Free Oscillations of Systems Having Quadratic Damping and Arbitrary Restoring Forces," by K. Klotter, ASME Paper No. 55-APM-34.

Appendix

The following example is taken from the field of torpedo-control systems. Referring to Fig. 1, the transfer function L_1 relates depth (the output x_0) to elevator deflection (the control effort f). The mechanical limits of elevator deflection correspond to the limiting of the control effort and are represented by A_1 , which has the maximum values $\pm A_m$.

In reference (12), a conventional linear control system and two nonlinear control systems are given. Fig. 7 shows the conventional linear control system. Fig. 8 shows the optimum nonlinear control system. The optimum nonlinear system has a function $n_1(\epsilon)$, ϵ which is obtained, not in analytical form, but in graphical form by using an analog computer. The actuating signal must be differentiated twice, and a device to generate a nonlinear function

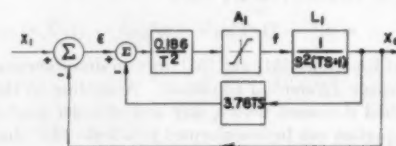


FIG. 7 LINEAR CONTROL SYSTEM

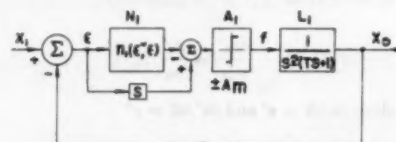


FIG. 8 OPTIMUM NONLINEAR CONTROL SYSTEM

of ϵ'' and ϵ is needed. The optimum nonlinear system might not be practical but it serves not only as a basis for comparison between linear and nonlinear-system responses but also as a starting point from which simplified nonlinear systems can be evolved.

From the point of view of analysis, this direct feedback in Fig. 8 gives $L_2 = 1$ (Case I, Fig. 2). Referring to Equation [6], $K_1 = 1$

$$F(s) = s^2(Ts + 1)X_0(s) \dots [71]$$

From Fig. 8 the nonlinear function in Equation [5] is specifically

$$f(t) = n(\epsilon'', \epsilon', \epsilon) = \epsilon' - n_1(\epsilon'', \epsilon) \dots [72]$$

Then Equation [14] becomes

$$\epsilon''' + (1/T)\epsilon'' + (1/T)[\epsilon' - n_1(\epsilon'', \epsilon)] = x_1''' + (1/T)x_1'' \dots [73]$$

Note that the quantity inside the square brackets represents the control effort f and the magnitude of f is limited by $\pm A_m$.

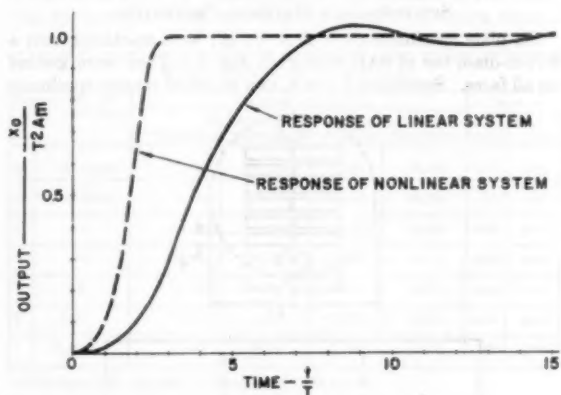


FIG. 9 COMPARISON OF RESPONSES OF LINEAR AND NONLINEAR SYSTEMS

Fig. 9 shows the comparison of step responses of the linear and optimum nonlinear systems. Using the integral of time-multiplied absolute value of actuating function

$$I = \int t |e| dt \dots [74]$$

as a criterion, the response of the linear system gives $I = 1.56$ and the response of the optimum nonlinear system gives $I = 6.25$, which is four times that of the linear control system.

A simplified nonlinear control system is shown in Fig. 10. The nonlinear function $n_1(\epsilon'', \epsilon)$ is replaced by a diode network, which gives a nonlinear gain. The new nonlinear function is simply a function of the actuating signal as shown by $n_1(\epsilon)$ in Fig. 11.

Fig. 10 also may be considered as a simplified block diagram of Fig. 5, with direct feedback.

From Fig. 10, $K_1 = 1$, and the nonlinear function in Equation [4] is specifically

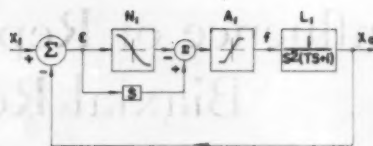


FIG. 10 SIMPLIFIED NONLINEAR CONTROL SYSTEM

$$f(t) = \epsilon' - n_1(\epsilon) \dots [75]$$

Then Equation [14] becomes

$$\epsilon''' + (1/T)\epsilon'' + (1/T)[\epsilon' - n_1(\epsilon)] = x_1''' + (1/T)x_1'' \dots [76]$$

From Equations [41] and [32], the phase-space equations are

$$\frac{d\epsilon''}{d\epsilon'} = \frac{x_1''' + (1/T)x_1'' - (1/T)\epsilon'' - (1/T)[\epsilon' - n_1(\epsilon)]}{\epsilon''} \dots [77]$$

$$\frac{d\epsilon'}{d\epsilon} = \frac{\epsilon''}{\epsilon'} \dots [78]$$

The $\epsilon' - \epsilon$ trajectories (or the $\epsilon' - \epsilon$ projections of the space trajectories) are shown in Fig. 11 for different initial values of ϵ . This is taken from fig. 3.1 of reference (12). In this case, both x_1''' and x_1'' are zero. The constants for the numerical example are

$$T = 1$$

$$A_m = 1$$

$$\text{Limited gain} = 1/T$$

$$\text{Differentiator gain} = 1$$

$$\text{Nonlinear gain as shown in Fig. 11}$$

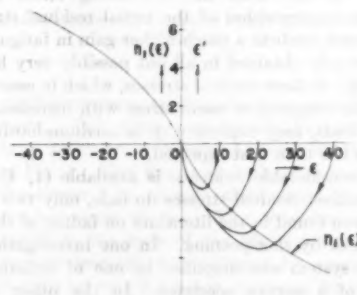


FIG. 11 PHASE-PLANE TRAJECTORIES

As mentioned in reference (12), the system of Fig. 10 was simulated on a Reeves electronic analog computer. The simplified nonlinear system was tested not only with step inputs of position and velocity, but also with continuous time-varying functions. It behaves like a linear system for small inputs and it approximates very closely the step response of an optimum nonlinear system for large inputs.

Influence of Repeated Bending Loads on Biaxial Residual Stresses in Shot-Peened Plates

By T. M. ELSESSER,¹ URBANA, ILL.

The utility of shot-peening certain members to increase their fatigue strength may be explained by the reduction of the initial residual stresses with increased numbers of repeated loads. The purpose of this investigation was to determine the changes in the biaxial residual stresses, induced by shot-peening, in steel plates subjected to cyclic bending loads. The plates were sectioned by etching, and curvature measurements were made to evaluate the residual-stress distributions in the region of the peened surface. The residual stresses were found to "fade" or decrease to at least 50 per cent of their initial value in 10,200 load cycles in the medium-hard (SAE 4340) steel investigated.

INTRODUCTION

SHOT-PEENING and cold-rolling are frequently used to increase the fatigue strength of members subjected to repeated loads (1, 2).² Qualitatively this increase may be explained by considering that the compressive residual stresses induced by these operations produce a beneficial compressive mean stress about which the alternating stress fluctuates. However, the superposition of the initial residual stresses and the load stresses predicts a much higher gain in fatigue strength than that actually obtained in all but possibly very hard steels (3). "Fading" of these residual stresses, which in essence is a reduction of the compressive mean stress with increased numbers of repeated loads, may explain why in medium-hardness steels the benefit is less than that expected.

Although considerable evidence is available (1, 4) that mechanically induced residual stresses do fade, only two investigations have been found in the literature on fading of the residual stresses induced by shot-peening. In one investigation (3) the biaxial-stress system was simplified to one of uniaxial stresses by the use of a narrow specimen. In the other study (5) only qualitative data were obtained by observing curvative changes in the specimen. Since the maximum shearing stress is sometimes used as a criterion for fatigue performance, this gives increased importance to the magnitudes of both of the biaxial residual stresses, not immediately after peening but after a prescribed number of load cycles when the residual stresses have been reduced.

PURPOSE

It was the purpose of this study to:

- (a) Evaluate the biaxial residual-stress distributions at the

¹ Assistant Professor, Theoretical and Applied Mechanics, University of Illinois.

² Numbers in parentheses refer to the Bibliography at the end of the paper.

Contributed by the Metals Engineering Division and presented at the Annual Meeting, New York, N. Y., November 25-30, 1956, of THE AMERICAN SOCIETY OF MECHANICAL ENGINEERS.

NOTE: Statements and opinions advanced in papers are to be understood as individual expressions of their authors and not those of the Society. Manuscript received at ASME Headquarters, August 1, 1956. Paper No. 56-A-109.

surface and to small depths below the shot-peened surface of small steel plates.

(b) Observe the variation of these biaxial residual stresses with the number of repeated bending loads. The bending loads stressed the peened face of the specimens between zero and a compressive stress 94 per cent of the yield point.

SPECIMENS AND MATERIAL PROPERTIES

Six plate specimens ($8 \times 2 \times \frac{1}{4}$ in.) were machined from a $3\frac{1}{2}$ -in.-diam bar of SAE 4340 steel, Fig. 1. They were ground on all faces. Specimens 1 and 8, two standard tension specimens

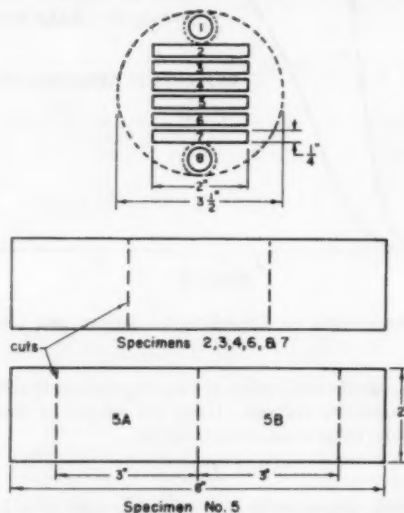


FIG. 1 LOCATION OF PLATE SPECIMENS IN THE SAE 4340 BAR AND THE CUTS MADE TO OBTAIN THE 3-IN. SPECIMENS

(0.505-in. diam), were also cut from the same bar. They were heat-treated by quenching in oil from 1500 F and drawn at 1050 F for 24 hr in a vacuum. This procedure was used to minimize both the scale formation and the residual stresses resulting from machining and quenching. The sectioning technique described later was used on two of the original specimens before they were shot-peened to insure that they were stress-free. This heat-treatment gave a Rockwell C hardness of approximately 20 and the test of the tension specimens gave the following average properties:

Yield point, 95,500 psi
Ultimate strength, 100,400 psi
Elongation in 2 in., 19.5 per cent
Reduction of area, 61.7 per cent

SHOT-PEENING TREATMENT

The flat specimens were polished using 3/0 emery paper and the initial dimensions were recorded. The plates were then

shot-peened on one 2 X 8-in. face. The other faces were protected by masking. The peening treatment employed S170 size steel shot through a nozzle 6 in. from the specimens using air pressure of 50 psi. Each was given 12 passes at 4 fpm equivalent to 2 min peening time per specimen. The peening intensity was measured by an Almen C strip which gave an arc height of 0.003 in. This treatment was used to give a "saturated" condition of residual stresses which would be almost unaffected by small variations in exposure time. The measurement of curvature changes caused by the peening was nearly equal in all the specimens indicating the residual stresses were uniform. Small shot, having an average diameter of 0.017 in., was employed due to its wide use in industry and to minimize the roughness of the peened face.

LOADING OF SPECIMENS

Five of the six plate specimens were subjected to repeated loads. Each specimen was loaded to a different number of cycles, as shown in Table 1. The specimens were loaded in pure bending, as shown in Fig. 2, such that a nominal compressive stress of

TABLE 1 VARIATION OF THE SURFACE AND PEAK STRESSES WITH NUMBERS OF CYCLES

Spec. No.	No. of Load Cycles	Residual Stresses psi						Depth to Maximum - in.
		At Surface		Maximum				
		Transverse	Longitudinal	Transverse	Longitudinal	Trans.	Long.	
5A	0 "As Formed"	67,000	67,000	89,600	88,000	.001	.001	
5B	0 "As Formed"	72,000	75,000	94,300	90,700	.001	.001	
2	1	72,000	36,000	75,700	37,000	.0006	.0007	
3	10	50,000	25,000	74,300	43,500	.0008	.0007	
4	100	43,000	14,000	75,500	52,000	.001	.0005	
6*	1200	37,000	39,000	79,100	44,300	.0004	.0004	
7	10,200	31,200	25,000	71,500	41,000	.0004	.0006	

* This specimen slightly overloaded at 1200 cycles.

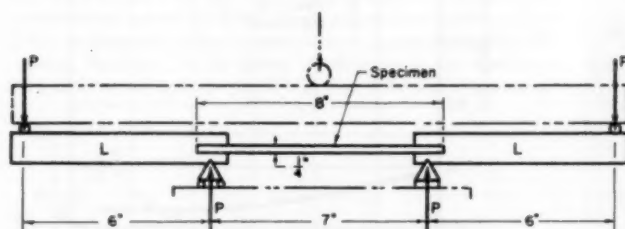


FIG. 2 LOADING ARRANGEMENT FOR PLATE SPECIMENS

90,000 psi (94 per cent of the original yield-point stress) was produced on the peened face of the specimen. It was believed that this loading would produce significant changes in the residual stress. The plates loaded through 1, 10, and 100 cycles were loaded in a 10,000-lb-capacity universal testing machine using the fixtures shown in phantom in Fig. 2. The specimens were slightly "bowed" due to the shot-peening so they were not clamped at the ends but were free to slide in the loading levers (L). The flexure formula was used to determine the load stresses which were assumed constant across the top and bottom faces since the bow was quite small. The plates loaded through 1200 and 10,200 cycles were loaded in the Instron machine shown in Fig. 3 using the loading levers (L) shown in Fig. 2. The loads P shown in Fig. 2 were applied by means of the vertical steel straps shown in Fig. 3.

Specimen no. 5, which was not loaded, was used to measure the

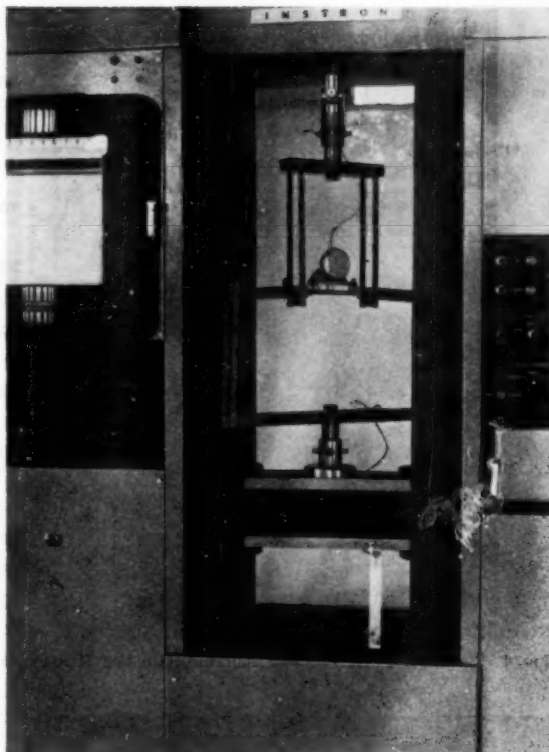


FIG. 3 ARRANGEMENT FOR LOADING PLATE SPECIMENS IN INSTRON MACHINE

residual stresses resulting from the shot-peening treatment. This plate was cut into two specimens 3 in. long which are numbered 5A and 5B at the bottom of Fig. 1. The five loaded plates were cut such that the center 3 in. of each plate would be used for the residual-stress studies. This procedure was used to eliminate the ends of the plates where the residual stresses possibly were affected by contact with the loading levers. Each 3-in. specimen for residual-stress measurements was therefore obtained by cuts on both ends using a 1/16-in. milling cutter as shown in Fig. 1. Care was used to keep the machining stresses small by using a slow feed and speed and sufficient coolant was used to prevent localized heating. The effect of the machining stresses at the cut surface was kept to a minimum by making measurements at least 1/2 in. from the cut.

MEASUREMENT OF RESIDUAL STRESSES

A sectioning technique similar to that used by Letner (6) was employed to measure the residual stresses on and slightly below the shot-peened surface. Thin layers (of approximately 0.0001 in.) were removed from the shot-peened face by etching in 5 to 10 per cent nitric acid and water solutions. Scotch electrical tape was used to mask the remaining faces to prevent acid attack. While in the acid bath the bubbles produced on the peened face were continually swept away by a soft bristle brush. The uniformity of the thickness of the removed layer was verified by measurements on a precision micrometer. Preferential etching, which roughens the etched face, became a problem as the thick-

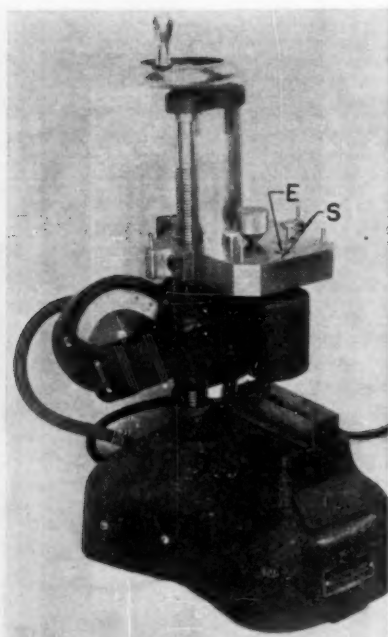


FIG. 4 SPECIALLY OUTFITTED ELECTRO-ARC GAGE FOR MEASURING ARC HEIGHTS

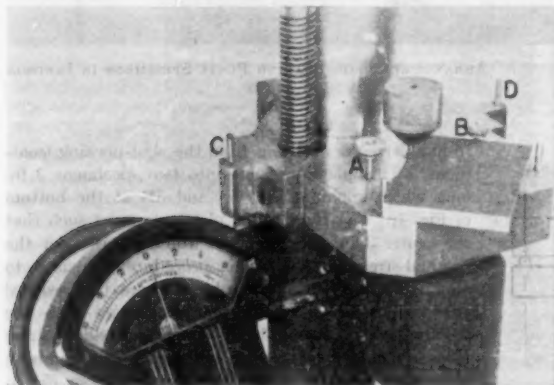


FIG. 5 CLOSEUP OF FIXTURE ON ELECTRO-ARC GAGE SHOWING LOCATING PINS AND SPECIMEN IN POSITION

ness removed increased. However, for a total thickness removal of less than 0.010 in. this roughening was found to be quite small.

The amount of material removed by each etch was determined by measuring the weight loss of the specimen on a Christian Becker chain balance. These weights were measured to the nearest milligram. The ratio of the thickness of the removed layer and the weight loss was considered equal to the ratio of the original thickness to weight of the specimen.

Curvature measurements were made following each etch on a specially outfitted Pratt and Whitney electro-arc gage shown in Figs. 4 and 5. The specimen was assumed to bend into the arc of a circle and the curvature was determined from the arc height (measured by the sensing element E) relative to the two spherical supports (S) shown in Fig. 4. The span between supports was 1.800 in. The locating pins shown in Fig. 4 permitted

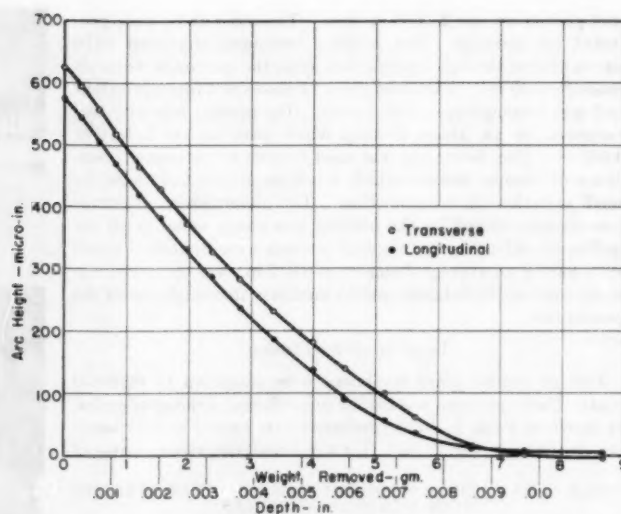


FIG. 6 ARC HEIGHT-DEPTH CURVES FOR AS-PEENED SPECIMEN NO. 5A

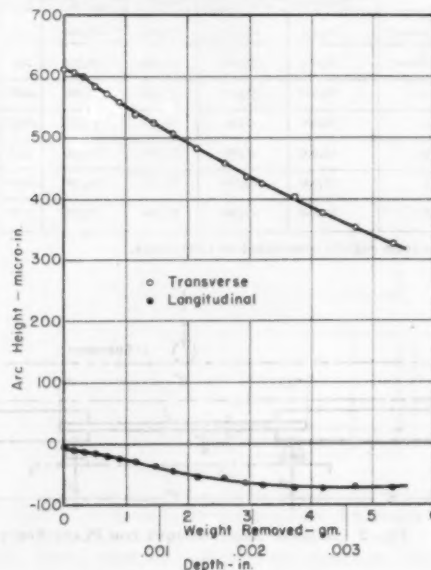


FIG. 7 ARC HEIGHT-DEPTH CURVES FOR SPECIMEN NO. 7 SUBJECTED TO 10,200 LOAD CYCLES

curvature measurements to be made on the center lines of the polished 2×3 -in. face, parallel to the 3-in. dimension (longitudinal) as shown in Fig. 5, or by rotating the specimen 90 deg to the right, parallel to the 2-in. dimension (transverse). These pins permitted the specimen to be placed in precisely the same position for each measurement. The large knurled knob was used to weight the corner of the specimen which held it in a horizontal plane. The smallest division on the electro-arc dial (see Fig. 5) is 25 microin., but readings were interpolated to the nearest 5 microin. Preceding each measurement of arc height the dial was zeroed using a standard bar known to be flat. At least three readings were taken in this way and averaged to obtain the arc height.

By progressively etching, weighing, and measuring arc height of the specimens, data were obtained to plot the curves shown in Figs. 6 and 7. These curves show the decrease in the arc height for both the longitudinal and transverse directions for specimens 5A (Fig. 6) and 7 (Fig. 7) as the weight or thickness is reduced. Curves similar to those shown in Fig. 6 were obtained for specimen 5B and curves similar to those shown in Fig. 7 were obtained for the specimens subjected to repeated loads.

The residual stresses at the thickness w were then obtained by using the following equation

$$\sigma_1(w) = \frac{E}{6(1-\mu^2)} \left\{ w^2 \left[\frac{dC_1(w)}{dw} + \mu \frac{dC_2(w)}{dw} \right] + 4w [C_1(w) + \mu C_2(w)] + 2(w_0 - 3w) [C_1(w_0) + \mu C_2(w_0)] - 2 \int_w^{w_0} [C_1(z) + \mu C_2(z)] dz \right\} \dots [1]$$

which was derived in reference (7).

Equation [1] for the longitudinal residual stress $\sigma_1(w)$ was modified to obtain the equation for the transverse residual stresses $\sigma_2(w)$ by interchanging the subscripts 1 and 2. The modulus of elasticity E was taken as 30,000,000 psi and Poisson's ratio (μ) of 0.30 was used; w_0 is the initial thickness of the specimen and w is the thickness as the layers are removed; z is the co-ordinate parallel to the thickness of the specimens; C_1 and C_2 are the curvatures of the specimen in the longitudinal and transverse directions. To convert from arc height h to curvature it was assumed that the curvature was the arc of a circle over the span of 1.800 in. If the arc height is small, the radius of curvature R determined by simple geometry becomes

$$R = \frac{1.800^2}{8h} \quad \text{or} \quad \frac{1}{R} = C = h/0.405$$

The terms $dC_1(w)/(dw)$ and $dC_2(w)/(dw)$ are the slope of the curvature thickness curves which were evaluated as the slope $dh(w)/(dw)$ of the arc-height-thickness curves divided by the constant 0.405.

Using Equation [1] the stress distributions in the specimens were determined and are plotted in Fig. 8 for the "as-peened"

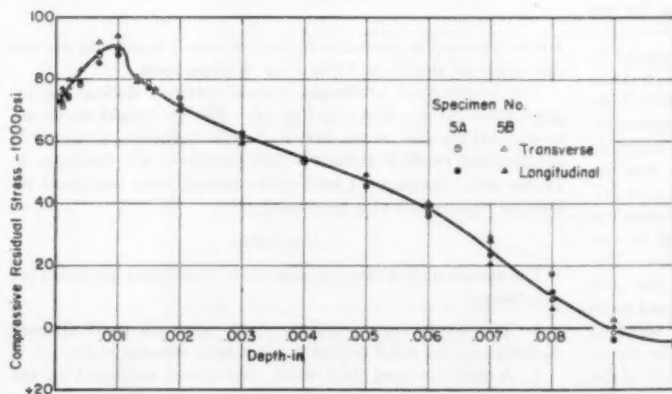
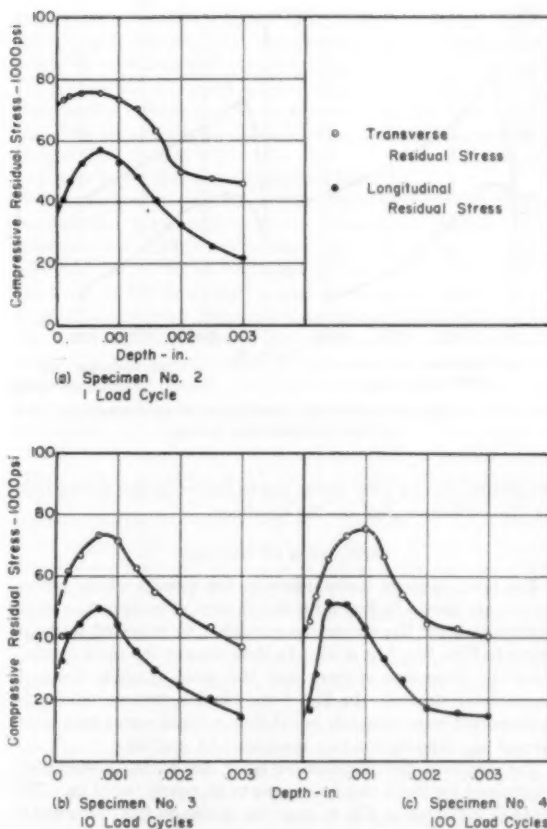


FIG. 8 RESIDUAL-STRESS DISTRIBUTION IN AS-PEENED SPECIMENS

specimens and in Figs. 9(a, b, c, d, e) for the specimens after being subjected to repeated loads. The plotted points indicate the arbitrary depths which were chosen to calculate the residual stresses and are unrelated to the depths removed by etching. Fig. 9 shows the changes in the residual stresses due to the



FIGS. 9(a, b, c) RESIDUAL-STRESS DISTRIBUTION IN SPECIMENS SUBJECTED TO REPEATED LOADS

repeated loads if it is presumed that all the specimens had the same original residual stresses as those shown in Fig. 8.

A qualitative measure of the change in the longitudinal residual stresses with increased numbers of load cycles is indicated by the changes in the longitudinal arc height of the specimens at zero load. A plot of the decrease in arc height with number of cycles is shown in Fig. 10 for five of the specimens. The transverse arc height also was measured in specimens 2, 3, and 4, but no observable change occurred. In specimens 2, 3, and 4 the arc heights were obtained by removing the specimens from the load jig and making measurements in the electro-lim gage shown in Figs. 4 and 5. During the loading the specimens were 8 in. long, making it necessary to remove the pins A and B and use the pins C and D to locate the specimen centrally. The specimens, which sustained 1200 and 10,200 cycles, were measured while in the Instron machine employing a 0.0001-in. dial on a 4-in. span, Fig. 3. Assuming the plates bent into the arc of a circle, the arc heights for these two specimens were converted to the corresponding values for a span of 1.800 in. and plotted in Fig. 10. The arc heights are

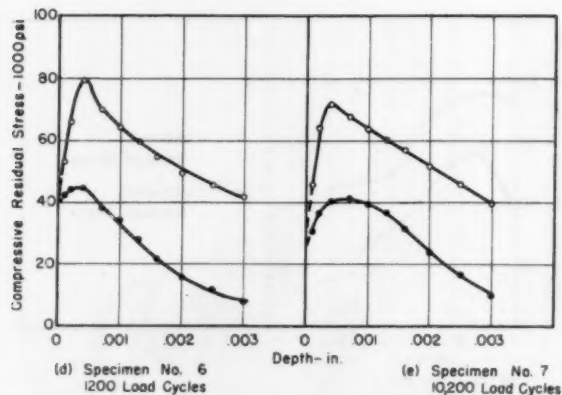


Fig. 9(d, e) RESIDUAL-STRESS DISTRIBUTION IN SPECIMENS SUBJECTED TO REPEATED LOADS

not plotted beyond 1000 cycles due to failure of the device holding the curvature gage on the specimen.

DISCUSSION OF RESULTS

The residual-stress distributions in the vicinity of the peened surface are shown in Fig. 8 for the as-peened specimens, and the distributions for the specimens subjected to repeated loads are shown in Figs. 9(a, b, c, d, e). In these figures the open symbols designate transverse stresses and the solid symbols designate longitudinal stresses. In Fig. 8 the biaxial stresses induced by shot-peening were so nearly equal that a single curve was drawn through the data for the two specimens 5A and 5B.

The depth of the cold-worked layer due to the peening was determined for these two specimens to be nearly 0.010 in. This depth is indicated in Fig. 6 since the specimen (5A) returned to the configuration (zero arc height) it had before peening, indicating the "stressed layer" was removed. In addition, the zero slope of these curves indicates the material removed is stress-free. Since the maximum residual stresses occur at a depth of approximately 0.001 in., it was considered unnecessary to evaluate the stress distributions beyond a depth of 0.003 in. for the remaining specimens.

In Fig. 9 the residual stresses in the specimens subjected to repeated loads are unequal in the transverse and longitudinal directions and are considerably reduced in magnitude from those shown in Fig. 8 for the as-peened specimens. The surface stresses were mainly determined by extrapolation of the data shown in Fig. 9. In a few instances the extrapolated curve was influenced by a calculation of the surface stress using Equation [1].

The maximum residual stresses and the surface stresses are summarized in Table 1. The surface stresses reduced to less than 45 per cent of their initial values in 10,200 cycles. The longitudinal surface stresses reduced abruptly after the first load cycle, whereas the transverse surface stresses reduced more gradually. The maximum or peak stresses which occurred slightly below the surface are plotted in Fig. 11. The transverse peak stresses reduced to approximately 85 per cent of the initial value after the first load cycle and remained essentially unchanged. The longitudinal peak stresses reduced to 64 per cent of the value induced by the shot-peening in the first cycle and continued to decrease to 46 per cent of the induced value at 10,200 cycles. Although data are scant, the reduction is linear on a stress-log N plot after the first load cycle. In addition the peak stresses have a tendency to move closer to the surface as the number of cycles of load increases. A slight overload,

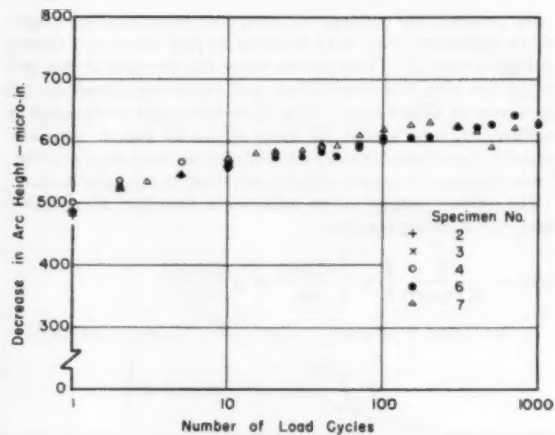


Fig. 10 DECREASE IN ARC HEIGHT WITH INCREASED NUMBERS OF REPEATED LOADS

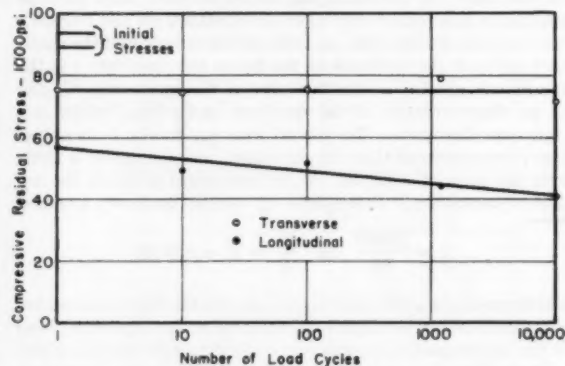


Fig. 11 DECREASE IN PEAK RESIDUAL STRESSES WITH INCREASED NUMBERS OF REPEATED LOADS

which occurred in specimen 6, may or may not account for the discrepancies shown in Table 1 for this specimen.

The longitudinal arc-height values obtained during the repeated loading are shown in Fig. 10. The arc height decreased nearly 500 microin. in the first load cycle indicating a release of longitudinal residual stresses which permitted the specimen to flatten out. Subsequent load cycles caused some continued release of stresses but at a decreasing rate.

CONCLUSIONS

The results of this investigation seem to warrant the following conclusions:

- 1 The sectioning technique yields accurate residual-stress distributions for small depths in a biaxially stressed plate.
- 2 A medium-hard SAE 4340 steel plate, subjected to the shot-peening treatment described, had equal biaxial compressive residual stresses that were a maximum at a depth of 0.001 in. and were approximately equal to 91,000 psi.
- 3 Cyclic loads between zero and a maximum, which produced a compressive stress 94 per cent of the yield point on the peened face, caused the biaxial stresses to become unequal, with the longitudinal residual stresses decreasing at a greater rate than the transverse residual stresses.

4 The repeated loading caused a decrease in the biaxial residual stresses with the most rapid decrease occurring during the first load cycle. The longitudinal residual stresses were reduced to about 64 per cent of their initial value by the first load cycle, and as the number of cycles increased to 10,200 the residual stresses continued to decrease to 46 per cent of their initial value.

ACKNOWLEDGMENT

The research studies described in this paper were conducted in the Department of Theoretical and Applied Mechanics as part of the work of the Engineering Experiment Station.

The author wishes to acknowledge Prof. T. J. Dolan, Head of the Department, Prof. H. T. Corten, and the many other members of the Department for their helpful suggestions. Special acknowledgment is made to Mr. J. C. Straub of the American Wheelabrator Company who kindly consented to shot-peen the specimens.

BIBLIOGRAPHY

- 1 "Residual Stresses," by O. J. Horgner, Handbook of Experimental Stress Analysis, John Wiley and Sons, Inc., New York, N. Y., 1950, p. 459.
- 2 "Shot Peening," by H. F. Moore, American Foundry Equipment Company, Mishawaka, Ind., 1944.
- 3 "Effect of Shot Peening Variables and Residual Stresses on Fatigue Life," by R. L. Mattson and W. S. Coleman, Jr., summary of original paper in *Metal Progress*, vol. 65, May, 1954, pp. 108-112.
- 4 "Relief and Redistribution of Residual Stresses in Metals," by D. G. Richards, Residual Stress Measurements, ASM, Cleveland, Ohio, 1951, pp. 129-191.
- 5 "A Study of Residual Stresses and Size Effect and a Study of the Effect of Repeated Stresses on the Residual Stresses due to Shot Peening of Two Steels," by H. F. Moore, *Experimental Stress Analysis*, vol. 2, no. 1, 1944, p. 170.
- 6 "Residual Grinding Stresses in Hardened Steel," by H. R. Letner, ASME Paper No. 54-A-56.
- 7 "A Mechanical Determination of Biaxial Stress in Sheet Metals," by R. G. Trenting and W. T. Read, Jr., *Journal of Applied Physics*, vol. 22, 1951, pp. 130-134.

Discussion

J. FRISCH.³ The author is to be commended for a fine study of

³ Assistant Professor of Engineering Design, University of California, Berkeley, Calif. Assoc. Mem. ASME.

fading out of residual stresses under repeated loading. Since it is fairly well accepted that shot-peening increases fatigue life, it would be very helpful if the author could include *S-N* curves for the peened and unpeened specimens of his experiment. Despite considerable reduction of the compressive surface stresses during initial cycling, the shot-peened material may still exhibit a higher fatigue life. If that is the case, then the fading of some of the compressive residual stresses may not be critical.

Since fatigue cracks tend to start at the surface it is quite important that the change of the surface residual stresses be considered. The author has evaluated the peak-stress behavior at approximately 0.001 in. below the surface, and Fig. 11 shows the reduction of the longitudinal peak stresses after the first cycle with transverse peak stresses remaining essentially constant past the first cycle. However, if one considers the stress level after removal of the first layer only, at approximately 0.0001 in. below the surface, the residual compressive stresses in both directions for peened specimens as well as for those subjected to cyclic loading can be plotted in a manner similar to Fig. 11. Such a semilog plot of the decrease of transverse and longitudinal residual surface stresses with increased numbers of repeated loads is shown in Fig. 12. As in Fig. 11 the largest single stress reductions take place during the first cycle. While in the author's plot the transverse peak stresses remain constant after the first cycle, regardless of the subsequent number of repeated loads, the plot in Fig. 12 shows that during the first 100 cycles the surface stresses in both the transverse and longitudinal directions decrease at the same rate. However, after 100 cycles the residual surface stresses do not follow a set pattern. This may be an indication that variables other than cycling must be contributing to the change of the surface compressive stresses.

The reduction of the longitudinal surface stresses from an initial value of 73,000 psi in the peened condition to 17,000 psi after 100 cycles constitutes a loss of 76.4 per cent. While it may be only coincidence it nevertheless is interesting to note that Moore in Table II-A of the author's reference (5) lists a reduction of 76 per cent in the residual stresses due to peening of structural steel after only 1 to 25 cycles at $\pm 50,000$ psi.

In conclusion it may be said that the results only point up the need for further research on the changes which residual stresses undergo during cyclic loading.

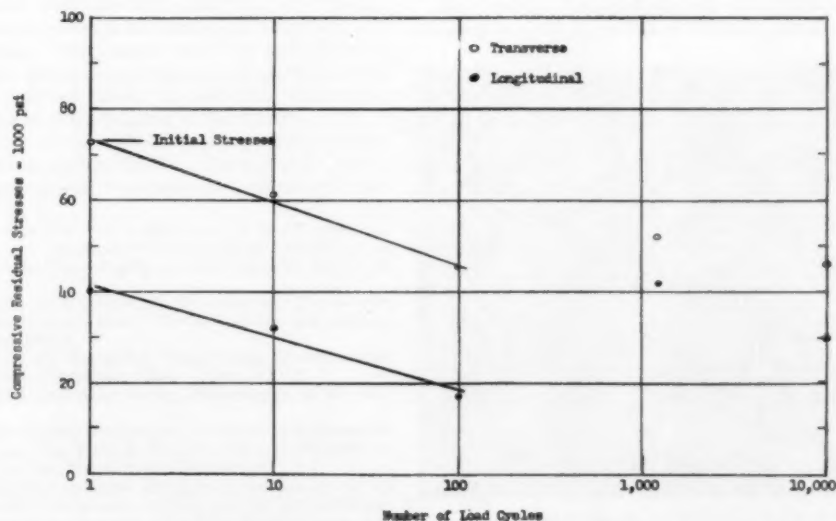


FIG. 12 DECREASE IN SURFACE RESIDUAL STRESSES WITH INCREASED NUMBERS OF REPEATED LOADS

AUTHOR'S CLOSURE

In general, I am in full agreement with the discussion submitted by Professor Frisch. $S-N$ curves for the specimens would have been interesting and I agree that such data would probably indicate a higher fatigue strength for peened specimens than for unpeened specimens. However, the great reduction in the beneficial compressive residual stresses induced by peening may make a peening operation uneconomical for the small benefit derived. I did not include $S-N$ data for the peened specimens which were used in this study because we considered it would give little or no correlation to the residual stresses

measured. Since the specimens were shot peened on one face only, the fatigue crack would initiate on the unpeened face and this $S-N$ data would be unrelated to the residual stresses measured on the peened face of the specimen.

We had considered a plot of the surface stresses shown in Table 1 similar to that shown in Fig. 11 for the peak stresses. However, it had not occurred to us to plot the values of the residual stress measured at a depth of 0.0001 in. as was done by Professor Frisch in Fig. 12.

I would like to express my gratitude for the discussion presented by Professor Frisch and agree with him that further research is needed on the subject of fading of residual stresses.

The Flow and Fracture of Nodular Cast Iron¹

By W. R. CLOUGH² AND M. E. SHANK³

Combined stress tests on pearlitic nodular iron show this material possesses a constant valued modulus of elasticity and Poisson's ratio. The maximum shear criterion for yielding is conservative, but is sufficiently accurate for design purposes. In addition, it appears to yield in accordance with the distortion-energy theory, providing stress concentrations at the graphite nodules are taken into account. There is a density change with plastic deformation due to separation of the matrix from the graphite. Stress and strain variables may be reasonably correlated by plotting plastic work against octahedral shear stress. A smooth fracture envelope has been obtained, and fracture occurs in a direction normal to the greatest applied tensile stress. A considerable internal crack network may be opened up before fracture. Brittle cleavage facets in pearlitic nodular iron are revealed by the fractographic technique. Cleavage fracture is not obtained in ferritic nodular iron in tension, but may be obtained in the presence of notches or by low temperature of test.

INTRODUCTION

THE desirable properties of gray cast iron entail the presence (and adverse shape) of graphite flakes. These desirable properties are thus obtained at a sacrifice of strength and ductility. It had long been felt that a smaller loss in strength properties would result if the graphite could be dispersed in well-rounded spherical nodules which would not so disrupt the continuity of the matrix. In the past this had been partially accomplished in malleable iron, but only by long and expensive heat-treatment. In May, 1948, it was announced that a workable process for producing nodular-type gray iron from the melt had been developed. Interest in this material was great; between April, 1948 and January, 1951, at least 206 technical articles appeared primarily concerned with this new product (1).⁴ Its properties, compared with previous materials, are unique. Knowledge of these properties is still somewhat incomplete and will be for some time. The present work was undertaken to study the mechanical properties of this material, particularly in the presence of combined stress. In addition, microscopic observations were made of the behavior of the material.

Some of the findings of others which are of interest to the work contained herein will be outlined briefly. The material appears, in the generally accepted sense, to exhibit elastic behavior (2) and

the yield point is sharp enough so that tensile testing machine operators may observe it by a sharp change in loading rate (3). The comparatively high modulus of approximately 25,000,000 psi is apparently independent of section size and heat-treatment (2, 4). The high damping capacity usually associated with gray cast iron is not exhibited, and nodular iron has been found to be pressure-tight for hydraulic applications (2, 5).

The fracture has a "metallic" appearance and does not have the characteristic gray appearance of flake cast iron. Nodular irons can show transition from ductile to brittle behavior when tested in impact, and at room temperature it has been found that annealed ferritic nodular cast iron could fail in impact with a relatively high impact value, or in a brittle manner with a relatively low impact value, depending on the composition and treatment. Ductile fracture is found to be predominantly dark in appearance while brittle failure gives a predominantly bright fractured surface.

Combined stress tests have been made with gray cast iron by several workers, the more recent investigations being those of Grassi and Cornet (6), Coffin (7), and Clough and Shank (8). This method of testing was considered to be particularly applicable for deformation and fracture studies of pearlitic nodular cast iron.

MATERIAL USED FOR TESTS

The iron from which the combined stress specimens were machined was supplied by the International Nickel Company in the form of 60 castings 2 in. × 2 in. × 6 in. It is denoted as iron A and the chemical composition is given in Table 1. The matrix was almost entirely pearlitic. Small patches of ferrite were present, surrounding the nodules of graphite. This iron was manganese treated and was supplied in the as-cast conditions. A lineal analysis, by means of a microscope with a motorized stage, of several metallographically polished specimens revealed that the graphite nodules comprised 8.7 per cent of the total volume of the material. A photomicrograph is shown in Fig. 1.

Other nodular irons, both ferritic and ferritic-pearlitic as cast (referred to as B, C, and D in Tables 1 and 2), were prepared

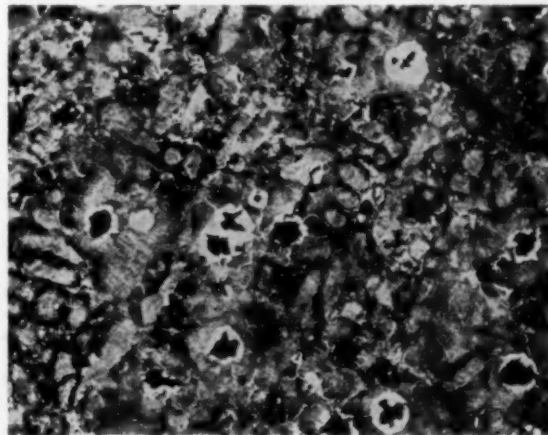


FIG. 1 PHOTOMICROGRAPH OF NODULAR IRON A USED FOR COMBINED-STRESS TESTS. ×100, NITAL ETCH

¹ This paper is abstracted from a portion of a thesis presented by W. R. Clough to the Massachusetts Institute of Technology, in partial fulfillment of the requirements for the degree of Doctor of Science.

² Research Engineer, Metals Research Laboratories, The Electro Metallurgical Company, a division of Union Carbide and Carbon Corporation, Niagara Falls, N. Y.

³ Associate Professor of Mechanical Engineering, Massachusetts Institute of Technology, Cambridge, Mass. Mem. ASME.

⁴ Numbers in parentheses refer to the Bibliography at the end of the paper.

Contributed by the Metals Engineering Division and presented at the Annual Meeting, New York, N. Y., November 25-30, 1956, of THE AMERICAN SOCIETY OF MECHANICAL ENGINEERS.

NOTE: Statements and opinions advanced in papers are to be understood as individual expressions of their authors and not those of the Society. Manuscript received at ASME Headquarters, August 1, 1956. Paper No. 56-A-110.

TABLE 1 CHEMICAL ANALYSIS OF NODULAR CAST IRONS

Iron	Total % C	% Si	% Mn	% P	% S	% Ni	Condition
A.....	3.42	2.33	0.42	0.07	0.008	1.63	Pearlitic, as-cast
B.....	3.38	3.19	0.24	0.04	0.016	...	Ferritic, as-cast
C.....	3.30	2.91	0.38	0.04	0.009	1.20	Ferritic, as-cast
D.....	3.47	1.90	0.27	0.085	0.033	0.63	Mixed ferrite and pearlite, as-cast

TABLE 2 MECHANICAL PROPERTIES OF NODULAR CAST IRONS

Iron	Bhn	Proportional limit, psi	Tensile strength, psi	Elongation in 2 in., per cent	Modulus of elasticity $\times 10^6$, psi	Poisson's ratio
A.....	270	41,000	92,600	0.9	25.0	0.295
B.....	164	30,000	68,750	22.3	25.0	0.275
C.....	168	31,000	65,500	22.0	25.2	0.280
D.....	192	42,000	79,000	14.0	23.5	0.285

by the Metals Processing Laboratory at Massachusetts Institute of Technology. None of these irons was used for combined-stress testing, but were used for preliminary work and to study by microscopic means the effects of stress.

Some typical mechanical properties of these irons as determined by hardness tests, and from 0.505-in.-diam tensile specimens equipped with Type A-8 wire resistance strain gages, are given in Table 2.

COMBINED-STRESS TEST PROGRAM

Some preliminary tests were carried out on iron D. Threaded-end 0.505-in.-diam cylindrical samples were tested in tension and compression, and a hollow tube of 1.000 in. ID and 1.100 in. OD was tested in torsion between centers in a lathe. In tension and compression initial yielding commenced in iron D at axial stresses of 42,000 psi. In torsion, yielding took place at a shear stress of 24,500 psi. The ratio of torsion yield stress to tension yield stress is in almost exact accord with the distortion-energy (Hencky-von Mises) theory as opposed to the maximum-shear (Tresca) condition of yielding. In these tests, as in all others, loading was in increments of stress. The strain was noted after each additional load was applied, and yielding was considered to have taken place at the stress at which the strain increment increased from the comparatively constant value obtained in the elastic range.

In order to check directional properties in pearlitic iron A (used in the biaxial tests) standard and substandard tensile specimens were cut in the longitudinal and transverse directions from eight of the castings. These gave comparable stress-strain curves and fracture stresses. Such behavior was interpreted as indicating negligible directional properties as well as mechanical uniformity of material from casting to casting.

Since the largest part of the test program was concerned with combined stress, a great deal of attention was paid to the design of suitable grips. The grips used in this work transmitted axial loads, as well as containing the fluid which supplied internal pressure for biaxial stressing. They are shown in Fig. 2. A Baldwin 60,000-lb-capacity hydraulic testing machine was used to supply axial loading.

An Amsler pendulum dynamometer (17,000 psi maximum pressure) supplied pressure to the interior of the hollow specimen. The specimens employed had an internal diameter of $1\frac{1}{4}$ in., a wall thickness of 0.05 in., and an over-all length of 6 in. The same machining operations were followed as were used by Coffin (7). Each specimen was measured carefully in order to determine the actual internal diameter and wall thickness after machining.

Strain in the combined-stress tests was measured by means of SR-4 wire resistance strain gages. Two diametrically opposite Type A-8 gages placed at mid-specimen length, on the outer surface, and connected in series, were used in the tube axial direction, and two more in the tangential or hoop direction. For

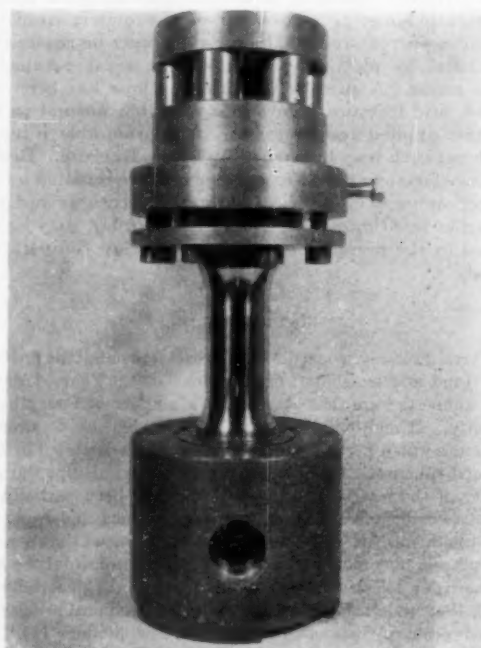


FIG. 2 GRIPS USED IN COMBINED-STRESS TESTING

tension-tension tests, this arrangement allowed strain measurement directly to fracture. In tension-compression tests, however, the strain-gage capacity was often exceeded. Testing procedure consisted of measuring the strains as the load on the tube was increased in increments. The ratio of axial to tangential stress was preselected before each test and was maintained constant during testing. Stresses were calculated by simple thin-walled-tube equations.

Altogether, combined-stress tests were carried out on 32 hollow specimens of pearlitic iron A. A résumé of combined-stress data is given in Table 3. The column entitled "fracture mode" indicates that a number of those specimens which supported large compressive axial stresses failed by buckling which took the form of radial bulges at either or both ends of the gage length. When such buckling occurs it probably introduces tensile stresses at the bulge. Such stresses would play a large part in the fracture process. Consequently, these specimens which failed by buckling cannot be interpreted as defining a true fracture strength and envelope, but indicate only a failure mode for the particular design of specimen. Radial bulges are evident also in the combined-stress specimens of gray cast iron used by Coffin (7) and

TABLE 3 BIAxIAL TEST DATA FOR PEARLITIC NODULAR IRON

Spec. No.	Stress ratio, σ_2/σ_1	Proportional limit —		Fracture stress, psi	Strain data	Fracture mode
		σ_2	σ_1			
N 1	∞	41900	0	92650	Complete	Circumferential
N 27	∞	41250	0	91650	Complete	Circumferential
N E	∞	42000	0	90000	Axial	Circumferential
N 21	8/3	40850	15300	95700	Axial	Circumferential
N 19	2/1	41700	20850	90520	Complete	Circumferential
N 20	6/5	40400	33600	91100	Complete	Oblique
N A	1	42750	42750	90200	Complete	Oblique
N 11	1	92250	None	Oblique
N 18	7/8	36750	42000	92800	Complete	Oblique
N 2	4/5	35800	44400	92200	Complete	Oblique
N 22	5/8	27000	43250	94200	Complete	Longitudinal
N 3	1/2	20600	41250	92800	Complete	Longitudinal
N 12	1/2	91900	None	Longitudinal
N 25	1/3	14950	44900	93050	Complete	Longitudinal
N 8	1/4	10850	43450	85000	Complete	Longitudinal
N 26	1/7	6150	43000	90300	Complete	Longitudinal
N 4	0	91900	Complete	Longitudinal
N 14	-1/8	-5050	40400	95800	Complete	Longitudinal
N 13	-1/4	-8700	34800	88800	Complete	Longitudinal
N 15	-1/3	-12600	37700	91800	Complete	Longitudinal
N 7	-1/2	-14700	29000	89400	Complete	Longitudinal
N 16	-2/3	-20050	30100	86500	Complete	Longitudinal
N 17	-3/2	-30201	20134	76600	Complete	Buckling
N 9	-2/1	-32000	16000	-92200	Complete	Buckling
N 10	-5/2	-103100	Complete	Buckling
N 24	-4/1	-36600	9200	-109600	None	Buckling
N D	∞	-42035	0	-120750	Complete	Buckling
N 6	∞	-48300	0	-145000	Complete	Buckling
N 28	∞	-136000	Complete	Buckling
N 29	∞	-143000	None	Buckling
N 30	∞	-270000	None	45° Shear
				-265000	None	45° Shear

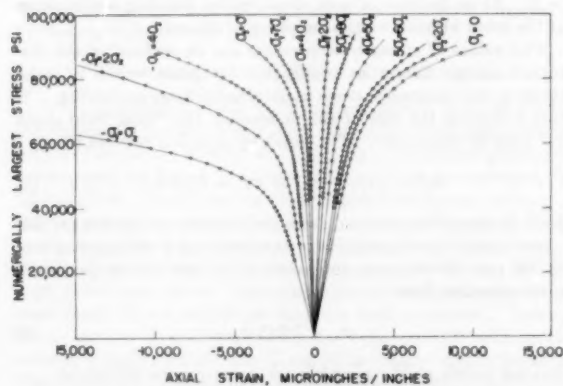


FIG. 3 STRESS-AXIAL STRAIN CURVES UNDER COMBINED STRESS FOR PEARLITIC NODULAR IRON

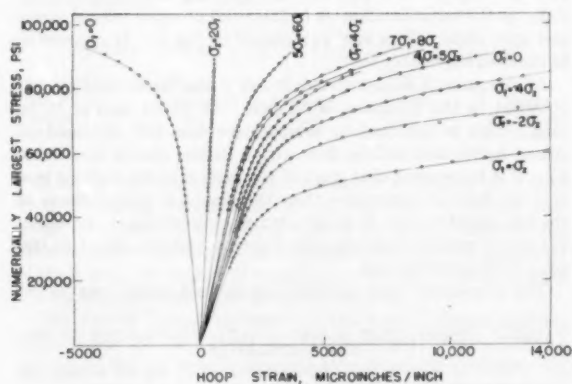


FIG. 4 STRESS-TANGENTIAL STRAIN CURVES UNDER COMBINED STRESS FOR PEARLITIC NODULAR IRON

Grassi and Cornet (6). Buckling was avoided in some compression tests by use of solid, threaded-end specimens. A number of representative stress-strain curves are included in

Figs. 3 and 4. The individual data points are shown for the plastic range only. Owing to the proximity of the lines, data points could not be included on these figures for the elastic range.

YIELDING UNDER COMBINED STRESS

Each biaxial test, regardless of the ratio of axial to tangential stress involved gave an initial linear stress-strain relation which prevailed to quite high stress values. In this elastic region the modulus of elasticity and Poisson's ratio determined from the tensile test (given in Table 2) were maintained practically constant at the stated values for all biaxial-stress ratios involved. The actual state of stress on the outer surface of the cylindrical tubes may be calculated by the elastic Lamé solutions for a thick-walled cylinder. By substituting these values into Hooke's laws and using the mentioned values of modulus and Poisson's ratio, values of strains may be calculated for each combination of stresses. The elastic stress-strain curves thus obtained were found to coincide almost exactly, in most cases, with the measured elastic portions of the stress-strain curves. The elasticity on initial stressing has been noted by several workers and would appear to be a distinguishing characteristic of this type of cast iron. Initial elasticity exists not only for the pearlitic-matrix iron but also for the ferritic-matrix and mixed-matrix irons.

The lowest stresses of departure from elastic behavior have been listed as the proportional limit in Table 3. In subsequent discussion the proportional limit so determined is assumed to be synonymous with yielding. Actually, this limit cannot be determined with all of the precision that may be desired since no sharp yield point exists. Also, the method of strain-increment loading limits accurate placing of the yield point to the range of the resulting stress increment. In this program the resulting increments were about 1000-2000 psi.

The yield data have been reproduced in Fig. 5 in the form of a yield envelope. The great majority of the many yield theories that have been suggested for metals are now only of historic importance. They conflict with experiments by predicting that a hydrostatic stress always influences yielding. The two simplest theories that do not have this fault are the criterion of Tresca (9) and that of von Mises (10) which have become known as the maximum-shear stress theory and the distortion-energy theory, respectively. The pertinent part of the maximum-shear-stress hexagon has been plotted (solid line) in Fig. 5, as has one half

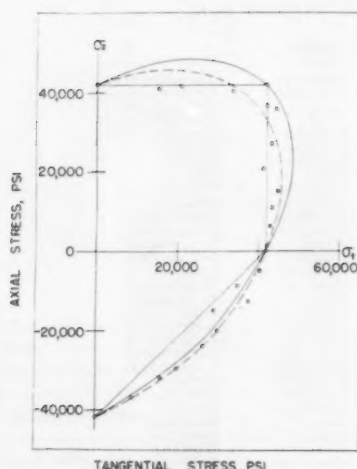


FIG. 5 EXPERIMENTAL YIELD ENVELOPE FOR PEARLITIC NODULAR IRON

(Solid curves represent distortion-energy and shear theories. Dashed line takes account of stress concentrations at nodules.)

of the distortion-energy ellipse, and the experimental data appear to agree better with the former theory in the tension-tension quadrant and the latter in the tension-compression region. Explanation for this behavior may be arrived at by considering the influence of the graphite nodules.

The graphite nodules may be considered as spherical voids in the matrix, due to the large difference between the moduli of graphite and the steel matrix. The elastic solution for the case of a single spherical cavity in an infinite matrix subjected to uniform biaxial stress at infinite distance from the cavity has been set forth by Southwell and Gough (11) and Goodier (12). At a distance of four diameters away from the cavity, the stress distribution (which would be uniform without the cavity) is not modified by more than one per cent, and at two diameters by about five per cent. As a consequence the results may be considered reasonably valid for cavities which are, say, four diameters or more away from a boundary or from other cavities. Certainly all the basic assumptions are not entirely fulfilled in the case of nodular iron, where the spherulites may be separated by much smaller distances and where a number of nodules intersect the specimen surface. In addition, the size of the spherulites is of the same order as the size of the matrix grains. Even so, as will be seen, the proposed theory seems to fit the yield envelope with good agreement.

In accordance with Goodier's solution, maximum stress concentrations (expressed as local principal stresses σ_1 , σ_2 , and σ_3) in the neighborhood of spherical cavities may be calculated for various combinations of biaxial stress. In all cases, it is assumed that Poisson's ratio for the matrix is 0.3. Stress combinations of particular interest are as follows:

(a) Simple tension or simple compression: The equator of the cavity lies in a plane perpendicular to the direction of the applied stress σ_x . The worst combination of stress is then at the tangent of the equator where

$$\begin{aligned}\sigma_1 &= 2.045 \sigma_x \text{ (parallel to } \sigma_x) \\ \sigma_2 &= 0.136 \sigma_x \text{ (tangent to equator)} \\ \sigma_3 &= 0 \text{ (radial to cavity)}\end{aligned}$$

(b) Two equal principal stresses of opposite sign (pure shear):

Consider the average applied stresses to be σ_x and $\sigma_y = -\sigma_x$. The cavity equator is taken in a plane perpendicular to the X-Z plane. Two severe stress concentrations will exist under these conditions. The first is at the intersection of the X-Z plane and the equator, where

$$\begin{aligned}\sigma_1 &= 2.727 \sigma_x \text{ (parallel to } \sigma_x) \\ \sigma_2 &= 0.818 \sigma_x \text{ (tangent to equator)} \\ \sigma_3 &= 0 \text{ (radial to cavity)}\end{aligned}$$

The second is on the equator, 90 deg removed from the first case, where

$$\begin{aligned}\sigma_1 &= 1.91 \sigma_x \text{ (parallel to } \sigma_x) \\ \sigma_2 &= -1.91 \sigma_x \text{ (tangent to equator)} \\ \sigma_3 &= 0 \text{ (radial to cavity)}\end{aligned}$$

If either the distortion-energy or maximum-shear theory is used for yielding, it is easily shown that yielding would occur initially at the latter location.

(c) Two equal principal stresses of same sign: If applied stress orientations are as described in (b) again two concentrations will exist in the same locations. They are $\sigma_1 = 1.364 \sigma_x$, $\sigma_2 = -0.545 \sigma_x$, $\sigma_3 = 0$ and $\sigma_1 = 2.182 \sigma_x$, $\sigma_2 = 2.182 \sigma_x$, and $\sigma_3 = 0$. As in the case of pure shear, initial yielding would occur at the latter location on the periphery of the void.

The values of stress concentration can be utilized in the distortion-energy theory as multipliers for gross values of axial stress σ_x and tangential stress σ_t obtained in tests at yielding. If this is done in the case of simple tension, the "local yield stress σ_0 " may be calculated. The resulting equation reduces to

$$\sigma_1^2 - \sigma_1 \sigma_2 + \sigma_2^2 = \sigma_0^2 = 3.92 \sigma_x^2 \dots \dots \dots [1]$$

Since in simple tension the gross yield stress was 41,900 psi this would imply that the matrix of this iron had a yield strength of 83,000 psi. If the same procedure is applied to the maximum-shear criterion, then

$$\sigma_0 = 2.045 \sigma_x \dots \dots \dots [2]$$

and the matrix yield strength would appear to be 85,900 psi.

The "local yield stress" obtained from the distortion-energy theory in the case of simple tension may be used to calculate a yield envelope, if it is assumed that yielding always occurs initially at the same location as in the cases of equal biaxial stress and pure shear. This is shown dotted in Fig. 5. It appears to fit the data reasonably well.

At this point it is appropriate to ask if the "local yield stress" obtained in the foregoing is realistic. It would appear to be high. This is indicated by comparative data (13) obtained on silicon ferrite and nodular iron with a ferritic matrix (see Table 4). If it is assumed that most of the carbon in the nodular iron is in the form of spherulites then the chemical compositions of the two matrices may be considered as quite similar. Equation [1] would require that the silicon ferrite yield at about 83,000 psi. This is not the case.

The excessively high apparent "local yield stress" can be ex-

TABLE 4 COMPARISON OF MECHANICAL PROPERTIES OF TWO FERRITIC ALLOYS

	Silicon ferrite	Ferritic nodular iron
Tensile strength, psi.....	76000	65000
Yield strength, psi.....	53000	45000
Per cent elongation in 2 in.	24.5	20
Per cent reduction in area.	53.5	20
Modulus of elasticity, psi		
× 10 ⁶	30	24
Brinell hardness.....	181	150
Chemical analysis.....	0.06 C	3.40 C
	2.35 Si	2.20 Si
	0.16 Mn	0.15 Mn
	0.10 P	0.02 F

plained in several ways. One possibility is that, since yielding occurs initially in a very localized region adjacent to a nodule, it may be taking place entirely in one grain. If the orientation of the grain is favorable relative to the direction of applied local stress, stress levels above the normal polycrystalline yield stress may be reached. This mechanism seems unlikely. A second mechanism may be termed "elastic superstrengthening." X-ray measurements (23) have indicated that the upper yield point of low-carbon steels may rise abnormally high, up to 2 or 3 times the value of the lower yield point, if the high stress is concentrated in a very small volume, such as the root of a notch. Certainly the matrix of the nodular iron may be considered as a steel. Since the nodules are surrounded by ferrite in the case here considered (i.e., low carbon) perhaps some superstrengthening may occur. However, the most logical and straightforward reason for the apparent high yield stress of the matrix appears to be due to the fact that average strains were measured by SR-4 gages during the tests. When actual initial yielding occurred adjacent to a cavity, the strain was so highly localized that the SR-4 gages could not detect it. When the gross proportional limit had been reached, considerable local work-hardening must have occurred already in previously yielded regions adjacent to the cavities. The value of local yield stress calculated by distortion-energy theory, then, is a figure which is increased by work-hardening of the initially yielded material.

DENSITY CHANGES IN PLASTIC DEFORMATION

In the application of the mathematical theory of plasticity to the solution of particular problems, one of the usual assumptions is that of constancy of volume. One of the advantages of such an assumption, so far as combined stress testing is concerned, is that it allows the calculation of three principal strains, although only two may be measured. In a previous publication (14), it has been shown that nodular iron undergoes a striking density change when subjected to tensile or compressive stresses. Strain-gage measurements and immersion-type density determinations were used. Some additional data are here presented. Again, the immersion-type determination has been used for solid specimens of ferritic nodular iron C tested in tension and in torsion. The procedure consisted of determining the density of the whole specimen, straining it, cutting out the strained-gage section, and determining the final density of this section. Results are given in Table 5.

TABLE 5 DENSITY CHANGE FOR NODULAR IRON C

Stress	Unstressed density	Final density	Density decrease, per cent	Strain
Tension.....	7.1408	6.9426	2.78	0.20 tensile
Torsion.....	7.1408	7.0644	1.15	0.785 shear

Some of the fractured combined-stress specimens also were used for density determinations. In this case the method consisted of cutting sections from each of the large, relatively unstressed ends of the specimens and comparing the average density of these with the density of a specimen cut from the gage section. Values thus determined are listed in Table 6.

The data of Table 6 indicate that the density change depends considerably upon the stress state. The largest density decrease was found for the equally stressed biaxial-tension specimen, the

smallest decrease for the stress state in which the axial stress was compressive.

In several publications attention has been given to the quantity known as the "plastic Poisson's ratio," which for a tensile test would represent the negative ratio of the plastic tangential strain to the plastic axial strain. The idea of incompressibility associated with the ideally plastic body necessitates this ratio having a value of one half. Gleyzal (15) has shown that, for steel, the quantity increased from 0.33 at initial yielding to 0.48 after very little plastic strain, and thereafter asymptotically approaches a value of one half. For nodular cast iron it is clear that a value of one half cannot prevail since a density change has been found. Strain-gage measurements from tensile tests on the pearlitic nodular iron indicate a value of 0.25 shortly after the proportional limit, and a value of 0.38 at fracture.

CORRELATION OF STRESS AND STRAIN VARIABLES

Figs. 3 and 4 present a series of smooth curves for each ratio of combined stresses. When the results obtained with different stress ratios are to be correlated, or when the state and history of deformation for complex loading paths are to be described, it is again desirable to obtain a single curve. What is usually sought for this purpose is some function of the stress, such as effective stress, plotted against a function of the strain, such as the effective strain. Curves showing maximum shear stress $\frac{1}{2}(\sigma_1 - \sigma_2)$ versus maximum shear strain $(\epsilon_1 - \epsilon_2)$ also are used. Test results of Davis (16) for mild steel and of Osgood (17) for aluminum have been so plotted and quite a good correlation obtained. For nodular cast iron, which has been shown to undergo a volume change after stressing, the calculation of shear strain is necessarily limited since the assumption of incompressibility cannot be made in order to calculate values of radial strain. However, for the tensile test, values of shear strain may be calculated. Also, for those combined-stress tests in which σ_2 is compressive it may be assumed that the tangential strain is the largest and the axial strain the smallest, so that the shear strain may be calculated for these test conditions. A plot of maximum shear stress against maximum shear strain, for four cases, is shown in Fig. 6, and poor correlation is indicated. The curves deviate from each other in a systematic manner.

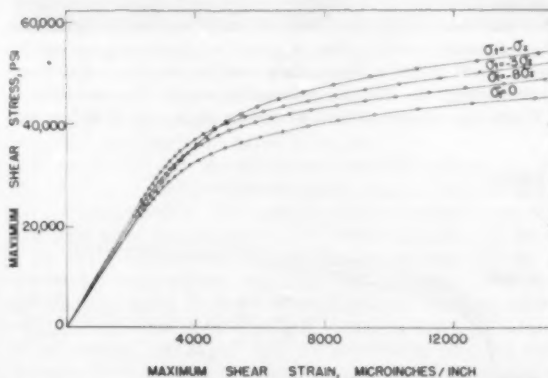


FIG. 6 MAXIMUM SHEAR STRESS VERSUS MAXIMUM SHEAR STRAIN FOR PEARLITIC NODULAR IRON

TABLE 6 DENSITY OF COMBINED-STRESS SPECIMENS

Stress system	Density of end No. 1	Density of end No. 2	Average unstressed density	Gage section density	Density decrease, per cent
$\sigma_x = \sigma_y$	7.2401	7.2419	7.2410	7.1810	0.83
$\sigma_x = 2\sigma_y$	7.2414	7.2420	7.2417	7.1940	0.66
$\sigma_1 = -2\sigma_2$	7.2388	7.2402	7.2395	7.2144	0.35

The tensile test curve is the lowest on the plot. Values of ordinates increase for a given shear strain as the ratio σ_2/σ_1 decreases from 0 to -1, thus placing the pure shear curve at the top.

Even though, because of volume changes, radial strains could not be calculated, an attempt was made to correlate data by plotting effective stress versus plastic work. Plastic work has been held (18) to be a fundamental measure of the amount of plastic deformation. Effective stress is given by

$$\sigma^* = \frac{1}{\sqrt{2}} \sqrt{(\sigma_1 - \sigma_2)^2 + (\sigma_2 - \sigma_3)^2 + (\sigma_3 - \sigma_1)^2} \quad [3]$$

and the increment of plastic work has been defined as

$$dW^P = \sigma^* d\epsilon^* \quad [4]$$

It has been shown (19) that, if the material work-hardens isotropically and obeys a simple stress-strain relationship, then the effective plastic strain increment $d\epsilon^*P$ of Equation [4] is given by

$$d\epsilon^*P = \frac{\sqrt{2}}{3} \sqrt{[(d\epsilon_1^P - d\epsilon_2^P)^2 + (d\epsilon_2^P - d\epsilon_3^P)^2 + (d\epsilon_3^P - d\epsilon_1^P)^2]} \quad [5]$$

The use of plastic work as a fundamental unit has also been discussed by Hill (20) in the form that

$$\sigma^* = F(W^P) \quad [6]$$

where σ^* is as defined in Equation [3]. It is not clear when the relation [6] was first introduced into the literature, but Taylor and Quinney (21) and Schmidt (22) proposed a hypothesis to which Equation [6] reduces when the elastic strain increment can be neglected. Schmidt (22) has shown that as good a correlation of combined-stress data can be obtained by plotting σ^* against W^P as by plotting σ^* against ϵ^* . Hill (20) has discussed the conditions for which Equation [6] reduces to an effective stress-effective strain relationship.

In the present case an approximate value of plastic work has been taken as the area under the stress-plastic strain curves, or

$$W^P = \int \sigma_x d\epsilon_x + \int \sigma_y d\epsilon_y + \int \sigma_z d\epsilon_z \quad [7]$$

The last term involving radial stress and strain has been neglected. This has some justification, because for the size of specimen used the tangential stress is always about 14 times as great as the radial stress at the inside surface. Of course, the radial stress varies through the wall thickness and is zero at the outer surface.

Curves of effective stress σ^* versus plastic work W^P as cal-

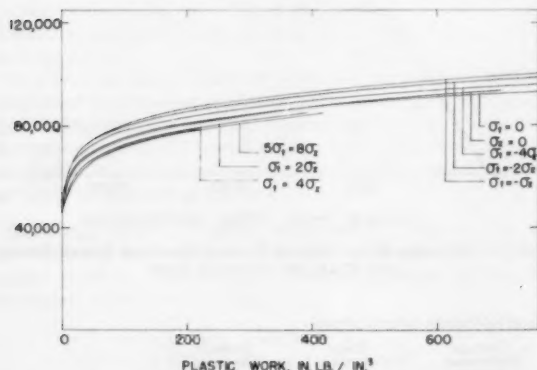


FIG. 7 EFFECTIVE STRESS VERSUS PLASTIC WORK FOR PEARLITIC NODULAR IRON

culated by Equation [7] have been presented in Fig. 7. Only a fair degree of correlation is obtained. As in the shear-stress plots, the curves for combined-stress tests in which σ_2 is compressive are found to be above the tensile-test plot, while curves for combined-tensile-stress tests lie below the pure tensile curve. This behavior is believed to be a direct result of the compressibility of the material; the volume change per unit stress is certainly less in the former cases than in the latter, as shown by the immersion-type density measurements. Correlation of data obtained by plotting effective stress versus effective strain showed no better results.

FRACTURE

Pearlitic nodular iron fractures in a direction perpendicular to the greatest tensile stress whether the other stress is tensile or compressive. This is the case at least for all specimens which did not buckle. The fracture mode is more complicated for the cases of nearly equal biaxial tension. In such cases fracture consists of a short longitudinal crack and two other cracks at approximately 45 deg to the former. The same type of fracture was noted by Coffin (7) and by Clough and Shank (8) for biaxial tensile tests of gray iron.

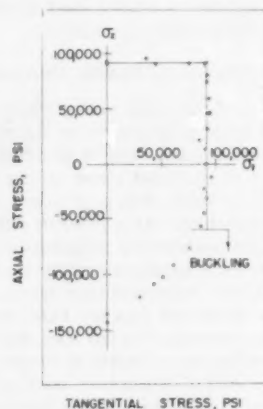


FIG. 8 FRACTURE ENVELOPE FOR PEARLITE NODULAR IRON

The fracture data plotted in Fig. 8 for those test specimens in which buckling did not play a part may be interpreted as conforming to the maximum tensile stress-fracture theory. If a complete biaxial-fracture envelope could be obtained, it probably would be of about the same shape as that found for gray iron by Grassi and Cornet (6), Coffin (7), and Clough and Shank (8). For both materials the compressive-fracture stress is approximately three times the tensile-fracture stress. Compressive fracture takes place on a plane at approximately 45 deg to the applied stress for both materials.

MICROSCOPIC OBSERVATIONS

The effect of nodules on initial yielding is no doubt strongly influenced by the number and locations of the surrounding grains of the matrix, and by the crystallographic orientations of these grains. The distance of approach of the nearest neighbor of graphite is probably also of importance, as indicated in Fig. 9. This photomicrograph was taken from the polished and etched surface of nodular iron B after it had been stressed in tension to a value of 24,000 psi. Numerous slip lines are shown although strain measurements indicated that the material remains "elastic" to 30,000 psi tensile stress. The area contained by the

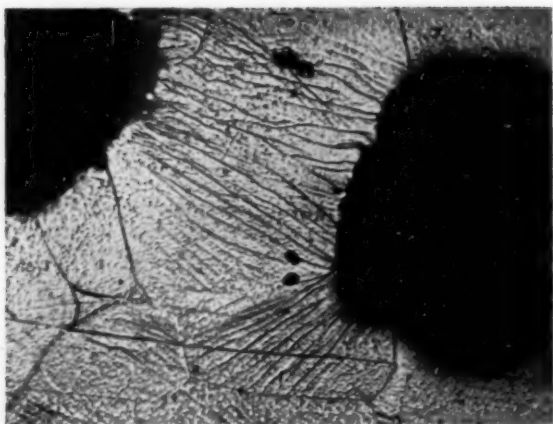


FIG. 9 SLIP LINES PRESENT WHEN FERRITIC NODULAR IRON B WAS STRESSED TO 24,000 PSI TENSION. $\times 1500$; NITAL ETCH



FIG. 10 IRON B. POLISHED AND ETCHED BEFORE STRAINING TO 0.5 PER CENT. TENSION DIRECTION VERTICAL. $\times 750$; NITAL ETCH

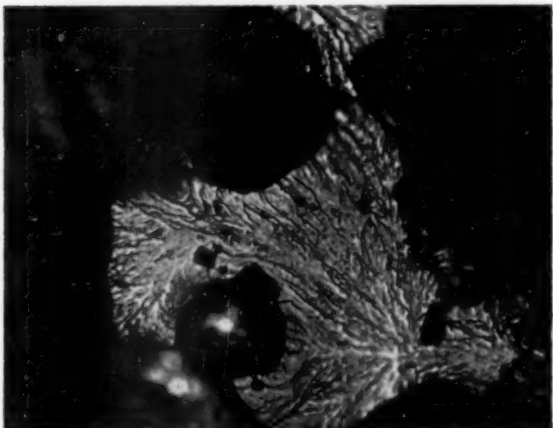


FIG. 11 FRACTOGRAPH OF PEARLITIC NODULAR IRON FRACTURED IN TENSION, $\times 750$

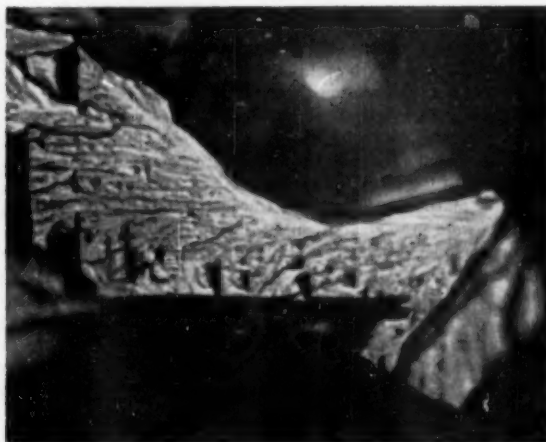


FIG. 12 FRACTOGRAPH OF PEARLITIC NODULAR IRON UNDER TWO EQUAL TENSILE STRESSES, $\times 1500$

photomicrograph was one of very few containing such slip lines. All such areas were located between two nodules separated by comparatively short distances, in this case only one ferrite grain in width.

A previous publication (14) showed that the density decrease of nodular iron is due to the creation of voids between the matrix and the graphite material; this behavior is also indicated by Fig. 10. When it is considered that the material was only strained $\frac{1}{2}$ per cent in tension, the amount of void area is quite surprising. It has been noted often by the authors that separation of materials does not occur at the graphite-matrix boundary, but occurs in the nodule itself by the separation of a thin ring of graphite. This is probably a result of the crystal structure and grain orientations of the nodule. Fig. 10 and two photomicrographs shown in reference (14) indicate two reasons why the tensile-plastic Poisson's ratio has values of less than one half. Since voids are created, a density decrease should be expected and a ratio of less than one half is necessary. Across the nodule, in a direction perpendicular to the tensile axis, there is very little, if any, lateral contraction. If there were any such contraction, the remaining graphite would be crushed, or at least strongly deformed out of round. Instead, it appears that

the graphite separates from the matrix not only in the direction of tension, but also in the lateral direction.

There can be little doubt that all fractured surfaces for the pearlitic nodular iron, combined-stress specimens may be classified as largely brittle. Mechanical evidence consists of the fact that very rapid fracture occurred at very small strains (order of 1 per cent) without the specimen passing through a point of maximum load-carrying capacity (the ultimate or tensile strength). Further evidence of brittleness is shown by microscopic examination of the fractured surface, a technique termed "fractography" by Zappfe and his co-workers. Typical fractographs for specimens of various stress ratios are indicated in Figs. 11 and 12. Each cleavage facet is bounded on at least one of its sides by a graphite nodule. In Fig. 11, a hole left by a nodule is shown at the upper center and a hole still containing its nodule is shown at the lower center. A vacant hole is also indicated in Fig. 12. Either the graphite nodule can easily fall out of its hole, which is likely since previous photomicrographs have shown separation between nodule and matrix, or it clings to the other piece of the fracture. Cleavage facets are no doubt in the ferrite which surrounds the nodules.



FIG. 13 FERRITIC NODULAR IRON C SECTIONED AFTER 20 PER CENT ELONGATION, $\times 750$

While the fracture of pearlitic nodular irons does appear to be largely brittle, this is not necessarily the case for iron with a ferritic matrix. Pearlitic iron A heat-treated into a ferritic state and tested in tension showed an elongation of 14 per cent in a 2-in. gage length of a 0.505-in.-diam test specimen. The testing-machine load dial rose to a maximum and appeared to remain virtually constant until fracture occurred. Visual examination of the fractured surface showed it to be generally dull and of a matted appearance. However, a few bright reflective surfaces were present and could be identified as cleavage facets under the microscope. The tensile fractured surfaces of irons B and C, those which were ferritic as-cast and exhibited an elongation of more than 20 per cent, did not show any cleavage facets. These ferritic materials, however, could be made to exhibit considerable brittle cleavage fracture by testing at room temperature in the form of V-notched Charpy specimens. In this case, the energy absorption, as measured by the pendulum of the machine, was negligible—of the order of 1 ft.-lb. Evidently, the material is one which is particularly susceptible to the phenomenon of notch brittleness.

It is of interest to consider the ductile mode of fracture in ferritic irons. Examples of what may be called the beginnings of ductile fracture are shown in Fig. 13, which was made by sectioning and polishing the necked portion of a sample of nodular iron C. The opening up of a ductile crack is indicated. There are points at which the upper and lower matrix material across the crack exactly match, and there would appear to be some justification for thinking of the fracture of ductile nodular iron as the sum of a number of fractures of smaller tensile specimens composed of the matrix material between the nodules. Further proof of this theory is offered by the data of Table 4, which indicate that chemically equivalent tensile specimens of silicon ferrite and nodular iron may show approximately equal elongations over the gage length, but that the reduction in area is more than twice as great for the former material than for nodular iron. The silicon ferrite develops a comparatively short and sharp neck, say at the center of the gage length, and the remainder of the gage section is little reduced in diameter. The nodular iron does not develop such a localized neck, but instead the diameter decrease is more evenly spread over the entire gage length. The deformation between nodules has the effect of spreading the neck over a longer gage length. The fracture of the silicon ferrite may be ascribed to a single crack opening up at the center

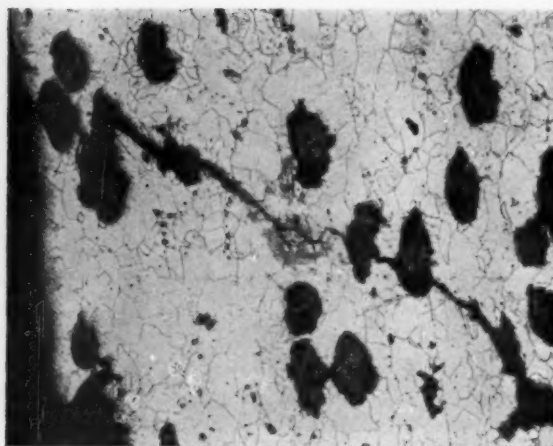


FIG. 14 IRON B. PHOTOMICROGRAPHY OF SECTIONED NECKED PORTION OF 0.505 IN. TENSILE SPECIMEN ELONGATED 21 PER CENT. TENSION DIRECTION VERTICAL. $\times 100$, NITAL ETCH

of the neck, and spreading to near the periphery, where final failure is by shear, resulting in a cup-and-cone fracture. The fracture of ductile iron is distinctly different, as shown in Fig. 13. The fracture can occur by the separation of graphite from the matrix which causes a high degree of local strain in the matrix. Ductile fracture may start at several points on the surface on a tensile specimen of nodular iron, and a cup-and-cone fracture never results. Such a crack is indicated in Fig. 14. The crack passes through a large number of spaces which contain graphite nodules, and in this plane of polish terminates at the large void shown at the lower right corner. It appears that quite an extensive crack network may be opened up through the matrix before final rupture takes place.

CONCLUSIONS

Nodular cast iron has several mechanical properties which offer considerable improvement over gray iron. This improvement is mainly due to the change of shape of the graphite particles. The continuity of the matrix is not nearly so disturbed by the smooth, well-rounded particles as by flakes. The internal notching effect is so small that elastic behavior can be exhibited by nodular iron. A constant modulus of elasticity and Poisson's ratio, approaching in value those of steel, are maintained up to yielding regardless of the stress system imposed.

Pearlitic nodular iron appears to yield in conformity with the distortion-energy theory, provided the effect of stress concentration of the nodules acting as voids is considered. Since actual initial yielding is quite localized and adjacent to the nodules, it is undetectable even by wire resistance strain gages. When gross yielding is detected, local yielding and work-hardening have progressed to such an extent that an extremely high figure of matrix yield stress is required to satisfy the distortion-energy equation. This fact should not be a bar to employing the distortion-energy criterion (considering stress concentrations at nodules) providing the "matrix yield strength" which results is treated as a fictitious quantity. As an alternative, the maximum-shear criterion, based on the gross yield stress in simple tension, may be employed. This latter is a somewhat conservative approach. Application of the distortion-energy theory based on the gross yield stress results in a yield envelope which lies outside experimental results, particularly in the tension-tension region.

At equivalent stress levels, the density change is greater for biaxial tension than for uniaxial tension, and less for tension-compression than for pure tension. The density decrease has been attributed to the opening up of holes or voids around the graphite nodules as a result of the action of tensile stresses. There appears to be little or no contraction in directions across the holes perpendicular to the direction of applied stress, which explains the small value of the plastic Poisson's ratio.

There is very little uniqueness of stress-strain results of combined-stress tests when maximum shear stress is plotted against maximum shear strain. The correlation is somewhat better when octahedral shear stress and plastic work are used. In either case a systematic deviation is obtained, and this is believed to be due to the systematic behavior of density changes.

All specimens uninfluenced by buckling fractured in a direction perpendicular to the greatest applied tensile stress, and for these specimens a fracture envelope is obtained which may be interpreted as conforming to the maximum normal stress-fracture theory. The complete biaxial fracture envelope is believed to have a form similar to that of gray iron. Compressive failure is at a strength level approximately three times that of tensile fracture, and occurs on a plane approximately 45 deg to the applied stress.

Fracture of pearlitic iron can be by brittle cleavage, as may be the case for ferritic irons which fracture before or at the ultimate strength, or for ferritic irons containing a notch. Cleavage patches are not present in ferritic irons fractured in tension after a considerable elongation, and after the passing of the point of maximum load-carrying capacity. In this case, the fracture is ductile and is the result of a fine network of cracks opening up before final rupture takes place. There is evidence to show that the matrix between the graphite flakes may act as if it were composed of a large number of small individual tensile specimens, each of which necks and fractures in a ductile manner.

BIBLIOGRAPHY

- 1 "Report on Nodular Cast Iron," anonymous, *SAE Journal*, vol. 59, December, 1951, pp. 23-24, 26.
- 2 "Engineering Applications of Ductile Cast Iron," by A. P. Gagnebin, K. D. Millis, and N. B. Pilling, *Machine Design*, vol. 22, January, 1950, pp. 108-114.
- 3 "Progress Report on Nodular Iron," by C. O. Burgess, *Foundry*, vol. 77, May, 1949, pp. 112-115, 218, 220-222, 224-225, 228, and 230.
- 4 "Symposium on Nodular Graphite Cast Iron," by D. J. Reese, *Transactions of the American Foundrymen's Society*, vol. 57, 1949, pp. 576-587.
- 5 "Properties and Application of Ductile Iron," by G. L. Cox, *Iron and Steel Engineer*, vol. 28, December, 1951, pp. 75-83.
- 6 "Fracture of Gray-Cast-Iron Tubes Under Biaxial Stresses," by R. C. Grassi and I. Cornet, *Journal of Applied Mechanics*, Trans. ASME, vol. 71, 1949, pp. 178-182.
- 7 "The Flow and Fracture of a Brittle Material," by L. F. Coffin, Jr., *Journal of Applied Mechanics*, Trans. ASME, vol. 72, 1950, pp. 233-248.
- 8 "The Deformation and Rupture of Gray Cast Iron," by W. R. Clough and M. E. Shank, to be published in *Trans. ASM*, vol. 49, 1957 (now in preprint form).
- 9 Mémoire sur l'écoulement des corps solides soumis à de fortes pressions," by H. Tresca, *Comptes Rendus de l'Académie des Sciences*, Paris, France, vol. 59, 1864, pp. 754-758; vol. 64, 1867, p. 809.
- 10 "Mechanik der festen Körper im plastisch-deformablen Zustand," by R. von Mises, *Göttinger Nachrichten (Math.-Phys. Klasse)*, 1913, pp. 582-592.
- 11 "On the Concentration of Stress in the Neighborhood of a Small Spherical Flow, and on the Propagation of Fatigue Fractures in 'Statistically Isotropic' Materials," by R. V. Southwell and H. J. Gough, *Philosophical Magazine*, series 7, vol. 1, January, 1926, pp. 71-97.
- 12 "Concentration of Stress Around Spherical and Cylindrical Inclusions and Flaws," by J. N. Goodier, *Trans. ASME*, vol. 55, 1933 APM-55-7, pp. 39-44.
- 13 By E. M. Mielnik, unpublished SM thesis, Metallurgy Department, Massachusetts Institute of Technology, Cambridge, Mass., August, 1952.
- 14 "Decrease of Density During Plastic Deformation of Nodular Cast Iron," by W. R. Clough and M. E. Shank, *Trans. ASME*, vol. 200, 1954, pp. 1093-1094.
- 15 "General Stress-Strain Laws of Elasticity and Plasticity," by A. Gleyzal, *Trans. ASME*, vol. 68, 1946, p. A-261.
- 16 "Yielding and Fracture of Medium-Carbon Steel Under Combined Stress," by E. A. Davis, *Trans. ASME*, vol. 67, 1945, p. A-13.
- 17 "Combined-Stress Tests on 24 S-T Aluminum-Alloy Tubes," by W. R. Osgood, *Trans. ASME*, vol. 69, 1947, p. A-147.
- 18 "Effective Stress and Effective Strain in Relation to Stress Theories of Plasticity," by G. N. White, Jr. and D. C. Drucker, *Journal of Applied Physics*, vol. 21, October, 1950, pp. 1013-1021.
- 19 "Die Bedeutung des Gleit- und Reisswiderstandes für die Werkstoffprüfung," by P. Ludwik, *Zeitschrift-VDI*, vol. 71, 1927, pp. 1532-1538.
- 20 "The Mathematical Theory of Plasticity," by R. Hill, Clarendon Press, Oxford, England, 1950.
- 21 "The Plastic Distortion of Metals," by G. I. Taylor and H. Quinney, *Philosophical Transactions of the Royal Society of London*, series A, vol. 230, 1931, pp. 323-362.
- 22 By R. Schmidt, *Ingenieur-Archiv*, vol. 3, 1942, p. 215.
- 23(a) "Über die röntgenographische Messung elastischer Spannungen," by H. Möller and J. Barbers, *Mitt. der Kaiser Wilhelm-Institut für Eisenforschung*, vol. 16, 1934, pp. 21-31.
- (b) "Röntgenographische Untersuchung über Spannungsverteilung und überspannungen in Flussetahl," by H. Möller and J. Barbers, *Mitt. der Kaiser Wilhelm-Institut für Eisenforschung*, vol. 17, 1935, pp. 157-166.

Discussion

L. F. COFFIN, JR.¹ The results reported in this paper give further support to the proposal first made by Fisher² and extended by the writer³ that properties of composite materials may be studied rationally by adjusting the state of stress in the ductile phase or matrix to account for the local effects of the randomly distributed aggregate. The information given should be of considerable value to metallurgists and designers seeking a clearer understanding of the mechanics of flow and fracture of this useful material.

There are two points of particular interest which the writer would like to raise. The first relates to the determination of the conditions for local yielding and the value of the matrix yield strength. The authors have determined the state of stress existing at yielding from an elastic analysis for a spherical cavity in an infinite matrix. While these elastic stresses would very likely give the state of stress for initial yielding, a small amount of local plastic flow would quickly modify the stress-concentrating effects produced by the cavity. It would be expected that this local flow would have little effect on the gross stress-strain curve, such that the onset of local flow would be quite difficult to detect until a reasonable proportion of the total matrix volume has become plastic. As soon as plastic flow occurs, the concentrating effects of the stresses near the cavity decrease, since in the plastic zone the stresses remain constant, or actually decrease, while elsewhere the elastic stresses increase. Thus in determining the matrix yield strength from the gross yield stress, the multiplying factor should be considerably less than the approximate value of 2.0 arrived at by the authors. This would then give better agreement between the actual properties of the matrix material and the calculated value. It does not seem necessary to explain the

¹ Research Associate, General Electric Research Laboratory, Schenectady, N. Y. Mem. ASME.

² "A Criterion for the Failure of Cast Iron," by J. C. Fisher, General Electric Research Laboratory Report, 1949, 7 pages, unpublished.

³ "The Flow and Fracture of a Brittle Material," by L. F. Coffin, Jr., *Journal of Applied Mechanics*, Trans. ASME, vol. 72, 1950, pp. 233-248.

differences in yield strength by strain-hardening, as is done by the authors.

A second point relates to the correlation of stress and strain as a function of combined stress. In the writer's work on gray cast iron, the correlation was attempted by calculating a "notch effective stress" found from the actual stresses in the matrix at the tip of the graphite flake. The writer wonders whether such might not be done for the present material, using as a stress concentration, not 3, as was used in the writer's work (this being approximately the theoretical upper limit for a stress-concentration factor of an infinitely sharp notch with complete plastic flow) but rather some lower value, such as the yield-strength ratios of the silicon ferrite to the ferritic nodular iron, given in Table 4 of the paper. This might result in an improved correlation of effective stress versus effective strain over what was obtained in Fig. 6.

AUTHORS' CLOSURE

The comments of Dr. Coffin are greatly appreciated. Many of the techniques employed in the present investigations are modifications of those developed by Dr. Coffin in a previous investigation of gray cast iron.

The authors believe that Dr. Coffin's first point has a great deal of validity. It is indeed probable that the local plastic flow

which occurs at initial yielding in the immediate vicinity of the nodules has little effect on the subsequent gross stress-strain curve of the material as determined by the SR-4 gages. This is pointed out by Fig. 9, which shows that local slip occurs at relatively low stress levels, while the gross stress-strain relationship is still linear and therefore assumed to be elastic.

Concerning correlation of stress and strain, the authors agree that a better type of correlation of stress and strain as a function of combined stress could be obtained. Actually, the authors were somewhat surprised to find that the degree of correlation obtained in Figs. 6 and 7 is as good as it is. As Dr. Coffin points out, one very good approach is the use of a "notch effective stress" value. However, a notch effective stress, with an equivalent strain parameter, may not result in simple relationships. It would probably be necessary to have different types of formulations for the case of tensile stresses, in which the graphite nodule may possibly be treated as a void, and for the case of compressive stresses, in which account may have to be taken of the fact that the cavities are actually filled with graphite. For example, other data obtained by the authors indicate that change of density, which is certainly a function of strain, is different, at equivalent stress levels, for tension as compared to compression.

Creep Characteristics of Type 347 Stainless Steel at 1050 and 1100 F in Tension and Compression

By M. J. MANJOINE,¹ PITTSBURGH, PA.

Cold-drawn and stress-relieved Type 347 heavy-wall tubing flows plastically at service temperatures (1050-1100 F) when subjected to a stress below the 10,000-hr rupture strength. Precipitation induced by the strain and temperature conditions causes an extended period of abnormally high creep resistance. The duration of this period increases with decreasing stress and is longer for compression than for tension. The creep and rupture strengths for service duration over 10,000 hr are poorer than those reported for Type 347 annealed bar stock.

INTRODUCTION

MOST published data for Type 347 stainless steel have been obtained for bar stock. The results described in this paper are for specimens machined from a cold-drawn and stress-relieved seamless tube. The interaction of stress, strain, and temperature, causes metallurgical changes which alter the physical properties during service. In this investigation an attempt was made to determine the nature of these metallurgical changes and their effect on the elevated-temperature strength characteristics for both tension and compression loading.

Other investigators have noted abnormal creep behavior in stainless steels at elevated temperatures. Smith, et al. (1)² reported that either annealed Type 304 or 316 stainless steel tested at elevated temperatures gave a false minimum creep-rate period shortly after loading. They attributed this abnormality to structural changes during tests. The structural changes were believed to be associated with the precipitation of carbides, ferrite, and sigma. Freeman, et al. (2) also noted the abnormally low creep rate at short-time periods and attributed it to the formation of sigma or the volume decrease accompanying the precipitation reaction. The Timken Roller Bearing Company reported anomalies in creep rate for specimens from a heavy-wall, Type 347, stainless-steel tube (3).

MATERIAL AND SPECIMENS

The test material was a section of cold-drawn seamless tube (9 in. OD \times 1.063 in. wall thickness) of Type 347 stainless steel. This alloy steel has been stabilized with niobium to render it insensitive to intergranular corrosion when exposed to temperatures in its service range. The chemical composition, Table 1, was supplied by the Metallurgical Department of the Westinghouse Steam Turbine Division. The material was stress-relieved at 1700 F.

¹ Westinghouse Research Laboratories. Mem. ASME.

² Numbers in parentheses refer to the Bibliography at the end of the paper.

Contributed by the Metals Engineering Division and presented at the Annual Meeting, New York, N. Y., November 25-30, 1956, of THE AMERICAN SOCIETY OF MECHANICAL ENGINEERS.

NOTE: Statements and opinions advanced in papers are to be understood as individual expressions of their authors and not those of the Society. Manuscript received at ASME Headquarters, July 25, 1956. Paper No. 56-A-40.

The specimens were cut axially from the tube. Those for tension loading had a 3-in. gage length of 0.505 in. diam; those for compression, a 2-in. gage length of 0.505 in. diam.

TABLE 1 CHEMICAL COMPOSITION

C—0.06;	Mn—1.57;	P—0.020;	S—0.010;	Si—0.70;	Ni—11.14;
Cr—18.07;	Nb—1.0;	Fe—balance			

The room-temperature properties in tension for this material are 81,700 psi ultimate strength; 50,700 psi yield strength (0.2 per cent offset); and 50 per cent elongation at fracture.

TEST RESULTS

Creep-Rupture Tests—Tension. The creep-rupture tests in tension were performed in conventional creep machines (4) at 1050 and 1100 F. All specimens were stabilized overnight at test temperature before loading. A stress-strain curve was obtained by incremental loading. It was observed that discontinuous yielding occurred on loading. A typical loading curve, Fig. 1, illustrates this type of yielding when the load is applied in increments of about 2500 psi. Two curves are shown; when the stress exceeds that of the upper curve the specimen yields to the lower curve at constant stress because of zero stiffness of lever-arm machine. This yielding appears to be macroscopically homogeneous over the gage section; that is, no local strain markings were visible on strained specimens.

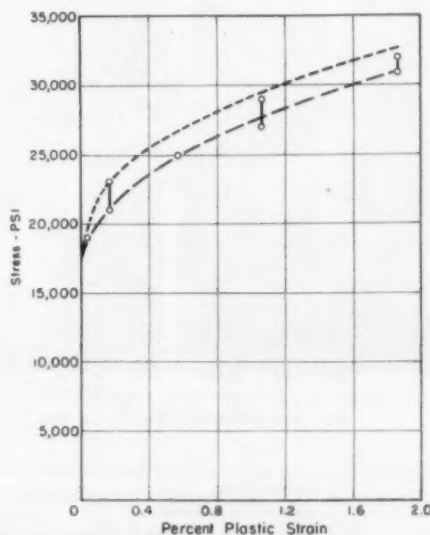


FIG. 1 LOADING CURVE FOR TYPE 347 STAINLESS-STEEL TUBE AT 1050 F TO A STRESS OF 32,000 PSI IN TENSION

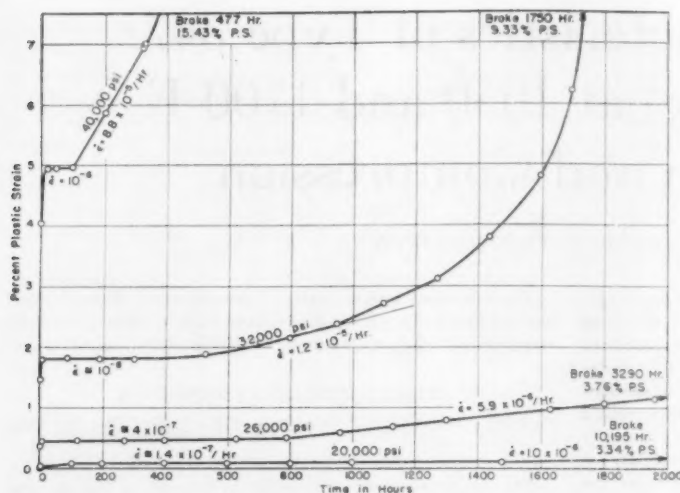


FIG. 2 TENSION-CREEP CURVES FOR TYPE 347 STAINLESS-STEEL TUBE AT 1100 F

Creep-rupture tests were made at several stress levels and the curves in Fig. 2 show the type of creep curves obtained for this material at 1100 F. They are typical of all the creep curves obtained. The creep characteristics of this material are abnormal. After a very short first stage in which the rate of creep is high, the creep rate drops to a very low value. This abnormally low rate continues for a time period which is an inverse function of the stress and/or the initial strain; that is, the period of abnormally low creep rate increases as the test stress is decreased. The material thus appears to go through an "aging period" during which it is very creep resistant. After this aging period a second period of higher constant creep rate is observed followed by a normal third stage of creep. This second constant creep rate corresponds to the normal "second stage of creep."

In addition to the usual creep-rupture data, Table 2 includes the plastic strain which occurs on loading, the time at which the aging period terminates, and the creep rate during this period.

The structural instability (in the temperature range of 1000 F and above) of 18-8 stainless steels containing niobium and titanium has been noted by other investigators. Smith, et al. (1), in the creep testing of stainless steels of AISI Types 304, 316, 321, and 347, noted structural changes during creep tests which resulted in "false minimum creep-rate periods." They detected a change in permeability after creep testing and showed that precipitation of ferrite and not Fe_3C caused the change. There was no indication that ferrite occurs as an intermediate phase in the precipitation of sigma from austenite or whether it is associated with formation of sigma. The false minimum creep-rate period

TABLE 2 TENSION-CREEP-RUPTURE DATA FOR TYPE 347 STAINLESS-STEEL TUBE

Spec. No.	Temp °F	Stress psi	Loading Strain %	Creep Rate 1/hr	Creep Data			Rupture Time hr	Rupture Strain %	Hardness DPH 50 KG No Stress		R.A. %
					Strain %	Time hr	Transition Time hr			Orig.	Final	
A13	1050	40,000	8.74	5.7×10^{-6} 9.8×10^{-5}	10.3 11.4	300 600	494 ⁽²⁾ 730	10.47 12.7	929	164	166	28.8
A25	1050	40,000	4.03	10^{-8} 2.0×10^{-5}	4.3 5.25	300 1700	1230 ⁽²⁾ 1980	4.5 5.90	2210 ⁽¹⁾	181	178	22.4
A14	1050	32,000	1.87	4×10^{-9} 4.1×10^{-6}	1.98 2.4	1000 3500	2390 ⁽²⁾ 4100	2.02 2.68	6808	165	173	10.9
B13	1100	40,000	4.03	$\sim 10^{-6}$ 8.8×10^{-5}	4.95 5.83	50 200	100 ⁽²⁾ 330	4.96 7.0	477	192	183	25.0
B14	1100	32,000	1.45	$\sim 10^{-8}$ 1.2×10^{-5}	1.8 2.15	300 800	530 ⁽²⁾ 950	1.87 2.38	1750	171	171	13.0
B15	1100	26,000	0.46	7×10^{-7} 8×10^{-7}	0.59 2.12	200 1000	400 ⁽⁴⁾ 1600	0.50 2.20	3455	181	193	9.0
C13	1100	26,000	0.36	4×10^{-7} 5.9×10^{-6}	0.46 1.05	400 1800	830 ⁽²⁾ 2300	0.50 1.38	3290	174	201	9.6
C14	1100	20,000	0.03	1.4×10^{-7} 1.0×10^{-6}	0.0075 0.243	600 3000	1355 ⁽²⁾ 4400 ⁽⁵⁾	0.1 0.39	10,195	170	187	6.0

(1) Plastic strain.

(2) Aging period terminus.

(3) Overheated to 1170F for 29 hours at 2040 hours.

(4) Overheated to 1300F for 8 hours at 400 hours, strained 1.47 per cent.

(5) Overheated to 1135F for 7 hours at 4400 hours.

was obtained for Type 304 stainless steel which did not develop sigma phase and it was not observed for the other steels (including Type 347) in which sigma phase was identified.

Freeman, et al. (2), who investigated the creep properties of titanium-stabilized stainless steels with several Ti/C ratios and heat-treatments, report that "steels which developed sigma phase had abnormal creep characteristics with first-stage creep virtually absent and increasing creep rates at short-time periods and low creep rates." They offered several reasons for the abnormal creep behavior which includes sigma-phase formation, precipitation-hardening followed by overaging, and volume decrease accompanying precipitation with solid-solution depletion.

Creep Tests—Compression. The period of low creep rate observed in the tension-creep test may be the result of a metallurgical change which involves a decrease in volume; e.g., precipitation of chromium carbide. As mentioned previously (2), the precipitation reaction may reach completion so that the volume decrease would cease. If this volume decrease is effective, then its presence in compression-creep tests would cause an increase in creep rate during the period of precipitation. To check this hypothesis, a series of compression-creep tests was performed at 1100 F to determine the effect of the direction of stress on the metallurgical change. The compression loading was accomplished by a special fixture, Fig. 3, which can be used in the conventional tensile machine, Fig. 4.

The abnormal aging period was found to depend on the stress level of the creep test, but since this material yields on loading the effect may be related to the resulting strain rather than to the stress *per se*. A compression-creep test at 44,000 psi and 1100 F was made on a specimen which had been prestrained 4 per cent in tension at room temperature. From the compression-creep tests in Fig. 5 it can be seen that this pretreatment eliminated the abnormal creep behavior. The yield strength of the prestrained specimen is slightly higher and this, therefore, reduced the strain on loading. The final creep rate, however, is about the same or slightly higher than that for other specimens at 44,000 psi which had not been prestrained at room temperature.

The creep curves for these compression tests, Fig. 5, illustrate the abrupt transition in creep rate from the low creep-rate period, "aging period," to the "second stage of creep" (see curve for 40,000 psi). The gradual increase in creep rate for the final parts of the curves for 44,000 psi is a result of buckling. The curves and the data from these curves recorded in Table 3 show that the creep rate in compression during the aging period is lower than that which follows, just as it is in tension, Fig. 2.

Constant-Strain-Rate Test in Compression. A constant-strain-rate compression test at 1100 F was run to determine the influence of strain-rate history on the yielding behavior. The results of this test traced from the original autographic load-elongation curve and corrected to obtain nominal stress and plastic strain is shown in Fig. 6. At the initial strain-rate of 0.9 per hr discontinuous yielding starts after about 0.1 per cent plastic strain. The amplitude of the drop in load on yielding increases with strain (or flow stress). Yielding is accompanied by an audible clicking. After yielding, the stress builds up elastically to about the same as that before the last yielding, plastic flow continues but the slope of the stress-strain curve is greater than that of the envelope of the yielding peaks; that is, the rate of strain-hardening is greater. After about 0.01 per cent plastic strain, yielding again occurs with a drop in stress of about 3 to 5 per cent. At 2.5 per cent plastic strain, the rate of strain was increased to 2.5 per hr. The stress-strain curve follows a continuation of the previous envelope;

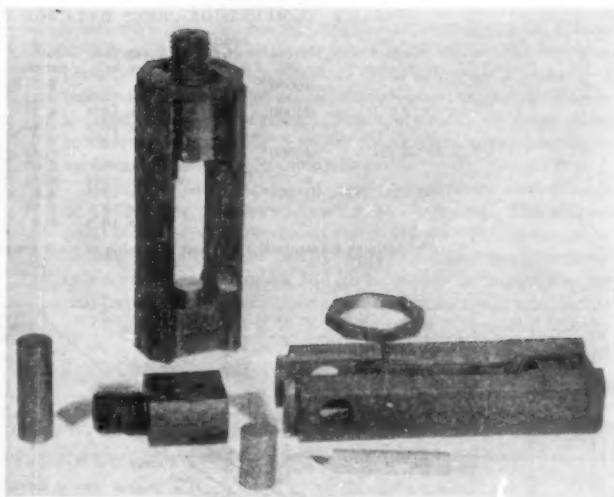


FIG. 3 SPECIAL COMPRESSION FIXTURE FOR TENSILE MACHINES

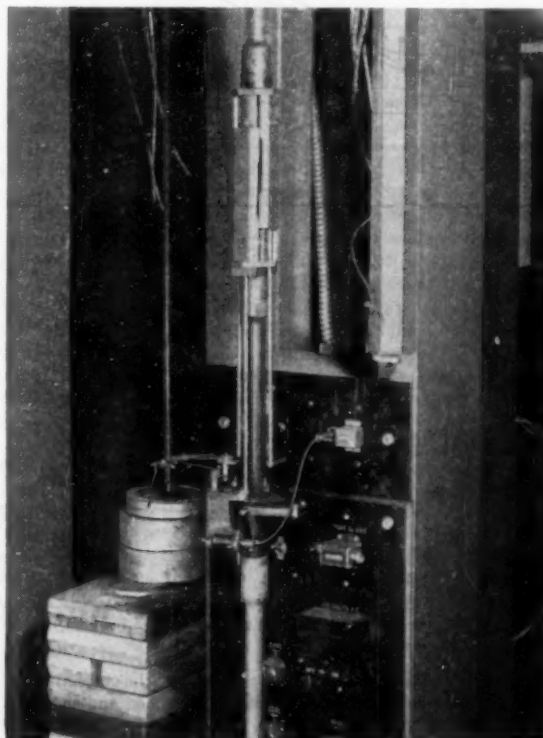


FIG. 4 SETUP OF COMPRESSION FIXTURE IN CONVENTIONAL TENSILE-CREEP MACHINE

the flow is still discontinuous but the region of higher work-hardening has disappeared (see enlarged portion of curve) except for an occasional cycle.

When the strain rate was lowered to 3.6×10^{-3} per hr, discontinuous yielding stopped and the flow stress increased to a value which is about 5 per cent higher than the extrapolation of the

TABLE 3 COMPRESSION-CREEP DATA FOR TYPE 347 S.S. TUBE AT 1100 F

Spec. no.	Stress, psi	Loading strain per cent	Creep rate per hr	Strain, per cent	Time, hr	Aging time, hr	Strain, per cent	Test time, hr	Strain, per cent
C 1.....	40000	3.05	10^{-4}	3.55	300	575	3.6	1608	5.0
C 2.....	44000	3.48	1.4×10^{-3}	4.15	1000				
			3.2×10^{-3}	4.23	300	390	4.26		
			1.7×10^{-3}	4.45	500				
C 3.....	44000	4.32	$\sim 10^{-4}$	4.55	300	410	4.56	1368	6.48
			2×10^{-3}	5.07	700				
			3.2×10^{-3}	6.44	1200			1319	6.89
C 12 ^a	44000	2.1	3.4×10^{-3}	4.0	300				
			3.2×10^{-3}	6.25	1000				
			4.2×10^{-3}	8.4	1600			3051	18.2

^a Specimen prestrained 4 per cent in tension at room temperature.

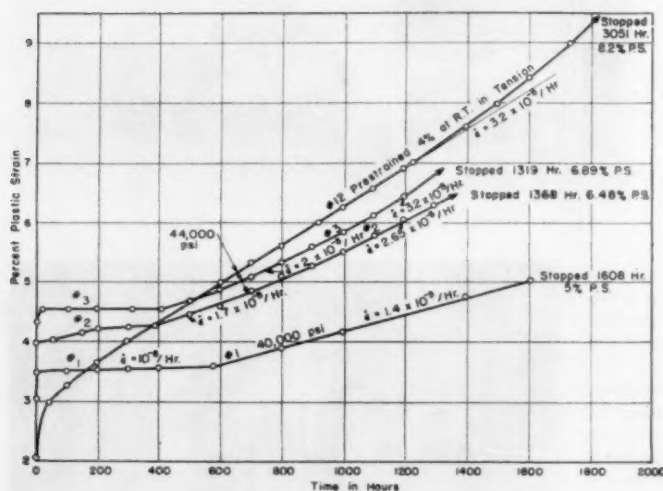
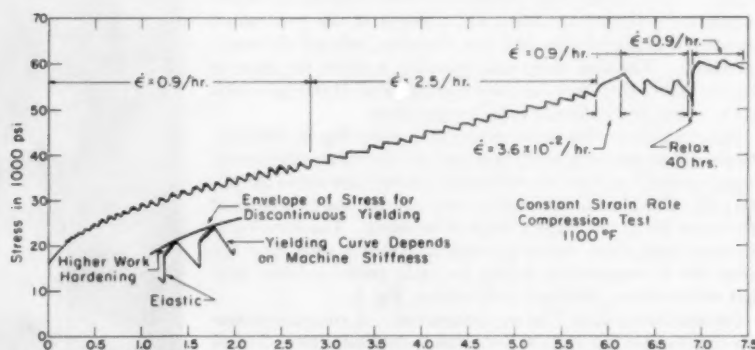


FIG. 5 COMPRESSION-CREEP CURVES FOR TYPE 347 STAINLESS-STEEL TUBE AT 1100 F

FIG. 6 CONSTANT-STRAIN RATE COMPRESSION TEST OF TYPE 347 STAINLESS-STEEL TUBE AT 1100 F



envelope of the previous curve. On returning to the original strain rate of 0.9 per hr, discontinuous yielding resumed and the yield stress dropped to that corresponding to the envelope. The drop in load on yielding appeared to be much greater than before. To check the effect of aging, the head motion was stopped and the specimen was aged for 40 hr at 1100 F. During this time the load relaxed slightly. When the head motion was restored at a rate of 0.9 per hr, the yield stress had increased about 7 per cent (aging), but the slope of the envelope had decreased. The latter strain-rate cycle was repeated with essentially the same result; that is, discontinuous yielding at a rate of 0.9/hr but none for the strain rate of 3.6×10^{-2} /hr.

Thermal-Expansion Tests. To discover if any phase change

occurs in this material due to temperature in the absence of stress, thermal-expansion curves were run to over 1300 F for specimens in both "as-received" and "prestrained" conditions. The curves shown in Fig. 7 are practically identical and indicate that no anomalies occurred in either specimen. In both conditions the strains were reversible on cooling.

Freeman, et al., (2) report that an unstrained specimen of Type 321 stainless steel exhibited a decrease in length of 0.0002 in. per in. when heated for 300 hr at 1200 F. Smith, et al., (1) conclude from density measurements before and after creep tests of specimens of Types 304, 316, 321, and 347 stainless steels that as a result of structural instabilities the changes of length, *per se*, are unimportant in determining the shape of the creep curve.

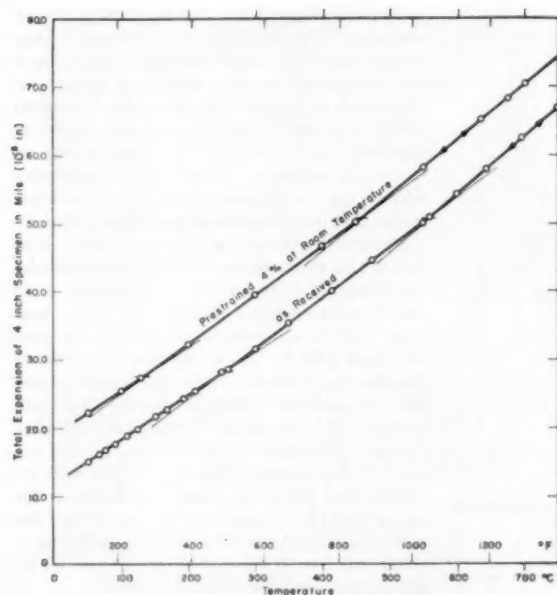


FIG. 7 THERMAL-EXPANSION CURVES FOR TYPE 347 STAINLESS-STEEL TUBE

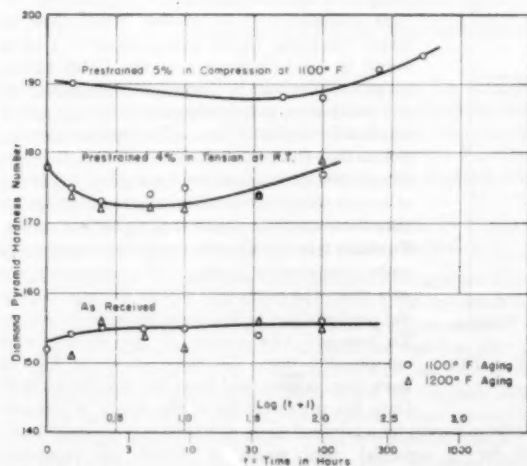


FIG. 8 AGING CURVES FOR TYPE 347 STAINLESS-STEEL TUBE

Aging Tests. If a metallurgical change occurs as a function of time at temperature, it may be detected by a change in hardness. Specimens of as-received and prestrained materials were aged at various times at 1100 and 1200 F (without external stress). The resulting hardness values (DPH-30 kg load) are given in Fig. 8 and are practically the same for either aging temperature for as-received and room-temperature prestrained specimens. The specimens from the material prestrained 5 per cent at 1100 F were, therefore, aged at 1100 F only. The hardness for as-received material did not change significantly up to 100 hr aging time. The room-temperature prestrained specimens have a higher initial hardness because of the cold work. The hardness decreases slightly up to 10 hr and then increases slightly. The specimens

which were prestrained 5 per cent in compression at 1100 F have an initial hardness of about 10 points DPH higher than for those prestrained at room temperature. This difference is probably a result of the same metallurgical change which causes the discontinuous yielding on loading. The aging curve of these latter specimens, top curve Fig. 8, shows only a slight initial decrease in hardness followed by a slight increase.

Magnetic Measurements. Magnetic measurements were made on all the aging samples discussed in the foregoing. The Magne-gage³ was used and the results are as follows: (a) No magnetic indication was obtained for the as-received and room-temperature prestrained specimens, and (b) indication in "equivalent per cent ferrite," for some of the specimens which were prestrained at 1100 F as given in Table 4. Thus it appears that a small amount of some magnetic phase is present shortly after deformation at 1100 F, but this phase disappears on aging (without stress).

TABLE 4 MAGNETIC MEASUREMENTS OF SPECIMENS PRE-STRAINED 5 PER CENT IN COMPRESSION AT 1100 F

Aging time, hr	Equivalent per cent ferrite
0	0
0.5	0.4
50	0.1
100	0.1
245	0.2
525	0

DISCUSSION OF RESULTS

The data from the tension-creep tests at 1050 F are summarized in the design curves of Fig. 9. The "points" of the creep curve which are identified in this plot are as follows: (A) The "terminus of the aging period" or the end of the low-creep-rate period which occurs shortly after loading. The time for this terminus is taken at the intersection of the tangents to the creep curve at the low-creep-rate portion and at the normal second stage of creep. In many cases this terminus was abrupt and easily picked from the creep curve. (See curve for 40,000 psi, Fig. 2). (B) The "transition point" is the time at the transition from the second to third stages of creep where the creep rate increases. (C) The time to "rupture" is plotted together with the final plastic strain. (D) Finally the creep rate "during aging" (dashed curve) and "after aging" are included to illustrate the large difference in rates which was observed. The abscissa scale for the creep rates is given at the top of the graph.

The duration of the aging period, Fig. 9, increases with decreasing stress but drops off more rapidly than the transition point or rupture curves. This may be a result of the lower plastic flow on loading at the lower stresses.

The difference in creep rates before and after the aging period increases with decreasing stress in the range investigated. At 40,000 psi and 1050 F the creep rate shortly after loading is three orders of magnitude lower (1/1000) than that which occurs after 1230 hr. These data show how short-duration creep tests of this and similar materials might be misinterpreted. If a creep test at 32,000 psi and 1050 F had been made for a duration of only 2000 hr then only the false minimum creep rate would have been measured.

At 1100 F the metallurgical and flow reactions are accelerated. The design curves for tension loading, Fig. 10, now exhibit a "knee" which has been shown to be a result of a metallurgical change or a change in the mechanism of flow (5). The creep rate during the aging period (dashed curve) shows a discontinuity at a stress of about 30,000 psi. The creep-rate curve increases abruptly about a hundredfold for lower stresses. It is suggested that this is a result of the lower plastic flow on loading at the lower stresses (see Table 2). The terminus of this low-creep-rate period also,

³ Registered trade name.

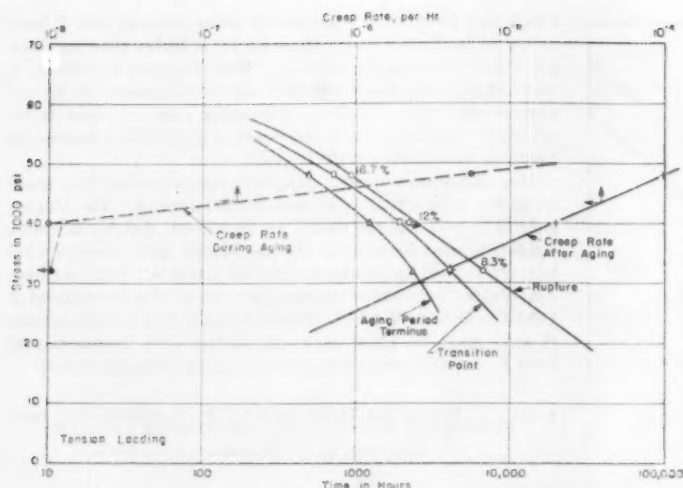


FIG. 9 DESIGN CURVES FOR TYPE 347 STAINLESS-STEEL TUBE AT 1050 F IN TENSION

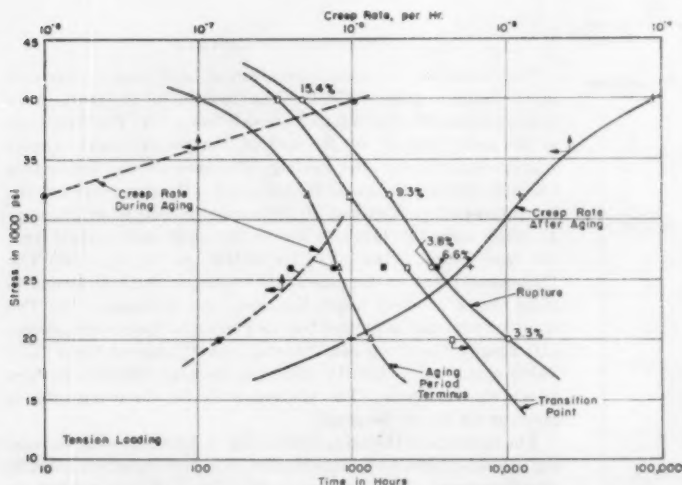


FIG. 10 DESIGN CURVES FOR TYPE 347 STAINLESS-STEEL TUBE AT 1100 F IN TENSION

drops more rapidly than the transition-point curve below a stress of 30,000 psi.

The elongation at rupture, Fig. 10 and Table 2, decreases sharply with decreasing stress at 1100 F and is only 3.3 per cent at a stress of 20,000 psi. This loss in ductility in stainless steels has often been associated with the formation of sigma phase. The presence of sigma in Type 347 stainless steel as a result of exposure at elevated temperature has been reported (1, 6, 7). The presence of delta ferrite in stainless steels has been observed by Smith, et al. (6). They believe that the delta ferrite can transform to sigma on further exposure at 1150 F. This is similar to the observation made in the magnetic tests described previously. The magnetic indication found shortly after aging the samples prestrained 5 per cent at 1100 F is probably due to ferrite. This indication disappears on further exposure and is accompanied by an increase in hardness. These measurements indicate that the abnormal creep behavior is associated with the formation of ferrite and sigma. The mechanism of strengthening during the aging

period following plastic flow on loading is very complex. The formation of the weaker phase, ferrite, should not cause a strengthening unless it is accompanied by other metallurgical changes. Bain, et al. (8) reason that the ferrite is rejected locally because of the carbon and chromium depletion consequent to the precipitation of chromium carbides. Thus the strengthening may be due to the precipitation of the carbides rather than the presence of the ferrite or sigma.

Photomicrographs, Fig. 11, were made of samples of this stainless-steel tube for the following conditions: (a) As received; (b) strained 5 per cent in compression at 1100 F; and (c) strained 5 per cent in compression at 1100 F and aged 525 hr at 1100 F. In the as-received condition (a) the fine-grain structure shows a finer carbide precipitation which is slightly more pronounced at the grain boundaries and twin planes. The other microstructures, (b) and (c), are not noticeably different. It was not expected that the small amount of ferrite or the sigma would be detected and it appears that the precipitate which causes the strengthening is either too fine to be resolved or is obscured by the coarser precipitate that is present.

As mentioned in the introduction, the lower creep rate during the aging period has been associated with the volume contraction which accompanies the precipitation of carbides (2). This speculation is as follows: Plastic flow on initial loading causes precipitation just as is found in carbon steels in the "blue brittle range," this results in discontinuous yielding (9) and could account for the period of strengthening which follows plastic flow. The further speculation is that the period terminates when the continued precipitation ceases because of depletion of excess constituents. The volume contraction also ceases and the result is a higher net strain. To check this speculation, creep tests were made under compressive loading. If a contraction occurs, then the creep rate should increase during the precipitation period for compression loading. To compare the results of the tension and compression tests, the creep curves of Fig. 12 have been constructed from the data at 1100 F. Only the magnitude of the strain is plotted.

The creep curves for a nominal stress of 40,000 psi (constant load) and for a constant true stress of 40,000 psi (constant stress) are compared. From these curves it can be noted that (a) the plastic strain on loading to a true stress of 40,000 psi is the same for either loading, (b) the creep rate is practically the same during the "aging period" for either loading, (c) the duration of the aging or low-creep-rate period is longer for compression than for tension loading, and (d) the time to a given strain or to rupture is much greater for compression than that for tension.

We can conclude, therefore, that:

1 If a precipitation occurs during the aging period it either involves no volume change or is combined with the formation of other phases which involve an expansion* thus resulting in no net volume change.

2 Compressive loading inhibits the disappearance of the

* The formation of ferrite would cause an expansion.

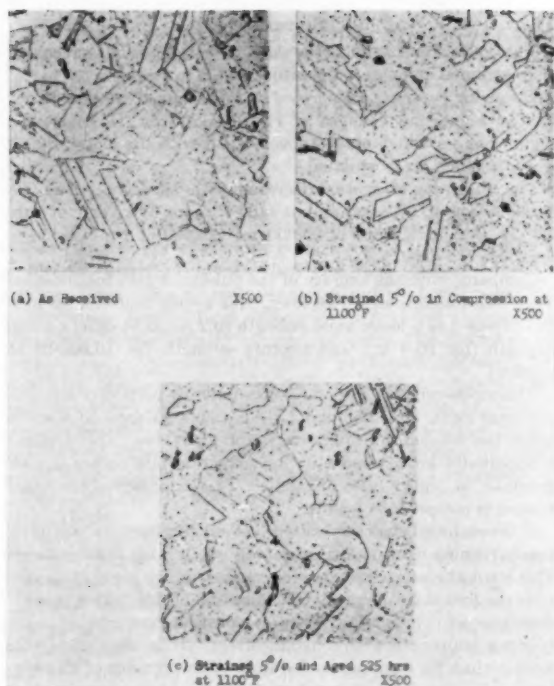


FIG. 11 MICROSTRUCTURE OF TYPE 347 STAINLESS-STEEL TUBE

metallurgical process or factors which cause the strengthening; or conversely, tensile loading accelerates the disappearance of the high creep resistance. This latter conclusion must be reconciled with the fact that for either type of loading the duration of the aging period is a function of the stress, the duration increasing with decreasing stress.

3 The creep strength and rupture strength are higher in compression than in tension (even on a true stress basis).

Although no anomalies were detected during most of the aging periods, one was noted just after loading the specimen tested at 32,000 psi and 1050 F in tension. This specimen strained 1.87 per cent on loading and an additional 0.15 per cent just after loading. During the next 200 hr it contracted 0.04 per cent after which there was no significant change in strain for the next 2000 hours. The contraction which can be expected from precipitation is about the same as measured.⁵ Thus it is possible that any change due to precipitation just after loading may be masked completely by the first-stage creep. The data and the curves of Fig. 12 do indicate, however, that no appreciable precipitation occurs during the latter portion of the aging period.

COMPARISON OF STRENGTH

From the published data for Type 347 stainless steel (10) a comparison can be made between the average strength of annealed Type 347 bar stock and this Type 347 tube for tension loading. In Fig. 13 the strength is plotted as a function of temperature. A band is given for the tensile strength and yield strength. The 0.2 per cent yield stress for this tube material at 1050 F is about 23,000 psi. This is much less than that shown for the band in Fig. 13. Single curves are shown for the 1000-hr

⁵ Reference (2). A contraction of 0.02 per cent was measured for a Type 321 stainless steel.

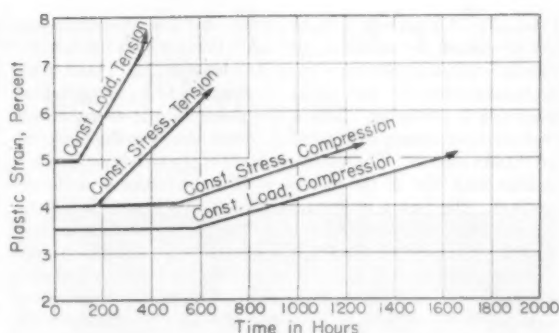


FIG. 12 CREEP CURVES FOR TENSION AND COMPRESSION AT 40,000 PSI AND 1100 F FOR TYPE 347 STAINLESS-STEEL TUBE

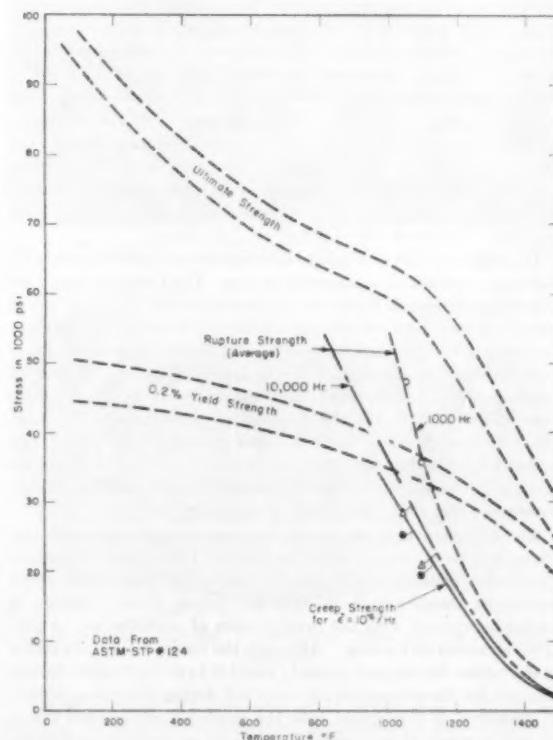


FIG. 13 STRENGTH OF ANNEALED TYPE 347 STAINLESS STEEL IN TENSION

rupture strength, 10,000-hr rupture strength, and creep strength for a rate of 10^{-3} per hr. The data for this tube material are plotted for comparison. The rupture strength for 1000 hr at 1050 F and at 1100 F (open circles) are the same as that for the bar stock but the rupture strength at 10,000 hr (open triangles) is considerably lower. The creep strength for a rate of 10^{-3} per hr (solid circles) is also lower at 1050 or 1100 F.

METALLURGICAL CHANGES

The microstructure of the as-received material, Fig. 11, shows a large amount of precipitate. The yield stress, however, is lower than that for annealed bar stock of Type 347 stainless steel (Figs.

1 and 13). We can conclude, therefore, that this precipitate does not strengthen the material; probably because it is incoherent.⁶ The discontinuous yielding observed on loading (Fig. 1) and in the constant-strain-rate test (Fig. 6) suggest that precipitation-hardening is occurring. This latter precipitate is strengthening because it is coherent and probably occurs on active slip planes by a diffusion process. The lattice constant of the usual precipitate is smaller than that of the matrix, so that the lattice is elastically strained. Hardening or strengthening results from this internal strain of the lattice and its influence extends beyond the slip plane on which it is formed. Plastic flow occurs under a constant stress for a creep test until all active planes of slip are strengthened after which there is no further plastic flow. This is the metallurgical state during the aging period or low-creep-rate period found in the creep tests.

As the material is aged it is suggested that the precipitate becomes incoherent at a rate which is a function of the stress on the precipitate. This also accounts for the influence of the direction of stress. The stress on the coherent precipitate is lower for an external compression load since a tensile stress is produced internally on the precipitate because of its smaller volume. When the precipitate becomes incoherent the rate of creep increases to the normal second-stage creep rate. The mechanism of flow during creep is apparently such that additional precipitates either do not form or form in an incoherent manner. This is similar to the yielding behavior observed in the constant-strain-rate compression tests where discontinuous yielding occurs at a strain rate of 0.9 per hour but not at the lower rate of 3.6×10^{-2} per hour.

In addition to the precipitate mentioned, strengthening may result from interstitial or impurity atoms. The Cottrell theory for this strengthening is based on an atmosphere of impurity atoms which diffuses into the strained lattice sites or into equilibrium positions of the dislocations thus locking them. It is also feasible that the dislocations migrate to the impurity atoms. Under an external stress a dislocation may move slowly by dragging its atmosphere with it. If the dislocation can escape the atmosphere, the result will be a much faster rate of strain. This may account for the low and high strain rates observed in the creep tests and the disappearance of discontinuous yielding in the constant-strain-rate tests at low strain rates.

The detection of a magnetic phase on aging of the specimen which had been prestrained 5 per cent at 1100 F and the subsequent disappearance with further aging indicates that other significant metallurgical changes are taking place. Ferrite is probably rejected with the precipitation of carbides at, or just after, straining on loading. Although the ferrite introduces strain in the lattice the amount present (about 0.4 per cent) could hardly account for the strengthening observed during the aging period. If, however, it segregated into the grain boundaries and transformed to sigma then it could be partially responsible for the decrease in ductility observed in the long time tests at 1100 F.

Prestraining at room temperature alters the structure so that no precipitation occurs when loaded at elevated temperature, and, therefore, no period of high creep resistance after the first stage of creep.

⁶ Not in atomic registry with matrix, thus not strengthening matrix.

SUMMARY

The thermal expansion is the same for this material as received or prestrained at room temperature and is reversible.

The aging curves of as-received and prestrained samples do not indicate significant changes at 1100 or 1200 F. However, the slight changes which occur are consistent with the metallurgical changes which are postulated.

The elongation at rupture decreases with decreasing stress (increasing time to rupture) and at 1100 F drops to a value of only 3.3 per cent at a stress of 20,000 psi (10,000-hr rupture life in tension).

Compared with the average of the published data for annealed Type 347 stainless-steel bar stock, this tubing material at 1050 and 1100 F has a lower yield strength (0.2 per cent offset), creep strength (for 10^{-6} hr), and rupture strength (at 10,000-hr in tension).

This stress-relieved Type 347 tube material has a very low proportional limit. At 1050 and 1100 F yielding occurs at a stress below the tension rupture strength for 10,000 hr. This yielding is apparently homogeneous on a macroscale but occurs discontinuously at higher rates of strain. This is observed for either tension or compression loading.

It is concluded that this material is strengthened by precipitation-hardening when deformed rapidly at elevated temperatures. This strengthening is reflected in a period of high creep resistance after the first stage of creep. The duration of this "aging period" decreases with increasing stress at constant temperature or increasing temperature at constant stress. It is also shorter for tension than for compression loading. The presence of this low-creep-rate period illustrates how the data from short-duration creep tests may be misleading.

No significant precipitation occurs during the aging period since no difference in creep rate was detected between tension and compression loading at the same stress and temperature. A volume change usually accompanies precipitation.

BIBLIOGRAPHY

- 1 "Creep and Rupture of Several Chromium-Nickel Austenitic Stainless Steels," by G. V. Smith, E. J. Dulis, and E. G. Houston, Trans. ASM, vol. 42, 1950, pp. 953-980.
- 2 "Rupture and Creep Characteristics of Titanium-Stabilized Stainless Steel at 1100 to 1300 F," by J. W. Freeman, G. F. Comstock, and A. E. White, Trans. ASME, vol. 74, 1952, pp. 793-801.
- 3 "Résumé of High Temperature Investigations Conducted During 1953-1954," by Timken Roller Bearing Company, p. 72.
- 4 "New Machines for Creep and Creep-Rupture Tests," Trans. ASME, vol. 67, 1945, pp. 111-116.
- 5 "Effect of Rate of Strain on the Flow Stress and Gas Turbine Alloys at 1200 and 1500 F," Proc. ASTM, vol. 50, 1950, pp. 931-950.
- 6 "Creep and Rupture of Chromium-Nickel Austenitic Stainless Steels," by E. J. Dulis, G. V. Smith, and E. G. Houston, Trans. ASM, vol. 45, 1953, pp. 42-76.
- 7 "The Structure and Properties of Stainless Steel After Exposure at Elevated Temperatures," by A. B. Wilder, and E. F. Ketterer, ASTM STP No. 128, 1952, pp. 237-249.
- 8 "The Nature and Prevention of Intergranular Corrosion in Austenitic Stainless Steels," by E. C. Bain, R. H. Aborn, and J. J. B. Rutherford, Trans. ASM, vol. 21, 1933, pp. 481-509.
- 9 "Influence of Rate of Strain and Temperature on the Yield Stress of Mild Steel," *Journal of Applied Mechanics*, Trans. ASME, vol. 66, 1944, pp. A-211-218.
- 10 "Report on the Elevated Temperature Properties of Stainless Steels," ASTM STP No. 124, 1952.

Design and Development of a Two-Cycle Turbocharged Diesel Engine

By P. J. LOUZECKY,¹ CLEVELAND, OHIO

The development of a successful design of two-cycle diesel engines for turbocharging involves many difficult problems, such as integrating the turbocharger to the engine, developing an exhaust manifold that will result in a minimum loss of heat energy, and making the engine components sufficiently rugged to carry the increase in engine loads. A solution to these problems, obtained by intensive study and testing, is presented in this paper. Also described are the favorable results achieved, which are improved fuel consumption, increased engine horsepower, and decreased engine size per horsepower as compared with nonturbocharged two-cycle diesel engines.

INTRODUCTION

THE successful turbocharging of two-cycle diesel engines has been a desirable goal for many years. Although various attempts were made by diesel-engine designers to solve the many problems involved, a satisfactory solution was not forthcoming until suitable turbochargers had been developed with pressure ratios from 2:1-3:1. Recently, however, rapid progress has been made and the excellent results obtained, reflected by nearly doubled engine output and much improved economy with only nominal increase in size and weight, more than justify the development efforts expended.

Although experimentation with turbocharging of two-cycle diesel engines has been carried out intermittently since 1942, the practical advantages demonstrated recently prompted the Cleveland Diesel Engine Division of General Motors Corporation to develop a new series of 6, 8, 12, and 16-cylinder two-cycle diesel engines, designated as the Model 498, specifically adapted for turbocharging. This new engine has the same bore and stroke, 8 $\frac{1}{4}$ in. by 10 $\frac{1}{2}$ in., as its successful nonturbocharged predecessor, the Model 278A engine.

FOUR-CYCLE DIESEL-ENGINE TURBOCHARGING EXPERIENCE

Turbocharging of engines is not new to the author's company as much work was done on four-cycle engines before and during World War II. In 1936, an 8 in. by 10 in., four-cycle, eight-cylinder engine was turbocharged, Fig. 1, to study the advantages that could be obtained with a small increase in over-all dimensions, weight, and cost of such a unit.

Another four-cycle, 9 $\frac{1}{4}$ in. by 12 in., sixteen-cylinder diesel, which was turbocharged for Navy applications during the late war, is shown in Fig. 2. This engine was used in many Navy "PC" boats.

TURBOCHARGING OF TWO-CYCLE DIESEL ENGINES

With the four-cycle turbocharging experience as a background,

¹ Mechanical Section Engineer, Cleveland Diesel Engine Division of General Motors Corporation. Mem. ASME.

Contributed by the Oil and Gas Power Division and presented at the Annual Meeting, New York, N. Y., November 25-30, 1956, of THE AMERICAN SOCIETY OF MECHANICAL ENGINEERS.

NOTE: Statements and opinions advanced in papers are to be understood as individual expressions of their authors and not those of the Society. Manuscript received at ASME Headquarters, August 10, 1956. Paper No. 56-A-100.

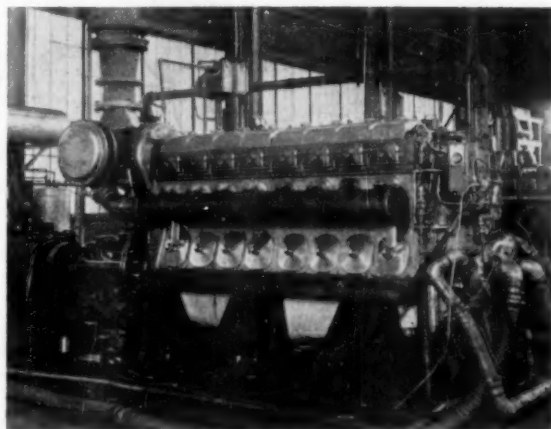


FIG. 1 MODEL 8-241 FOUR-CYCLE TURBOCHARGED DIESEL ENGINE

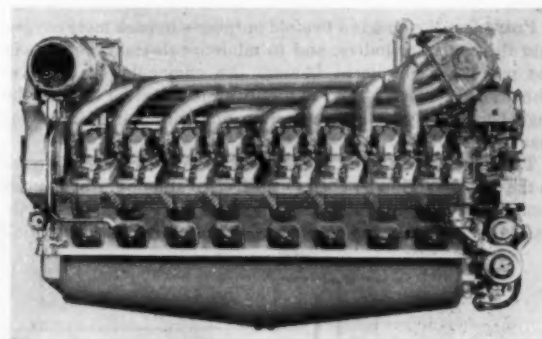


FIG. 2 MODEL 16-258S FOUR-CYCLE TURBOCHARGED DIESEL ENGINE

it was decided, in 1942, to investigate the feasibility of turbocharging two-cycle diesel engines. A preliminary survey showed that it would be practical to turbocharge two-cycle engines, except for a few serious problems such as starting and acceleration. In 1943, a two-cycle engine was equipped with a Buchi turbocharger, but this project was discontinued because of the war effort.

About two and a half years ago, the development of turbocharged two-cycle diesel engines was resumed. The very favorable results obtained at that time by the U. S. N. Engineering Experiment Station in its simulated turbocharger experiments, and the development work being sponsored by the Navy Department influenced this decision. Before actually designing a new two-cycle engine specifically for turbocharging, it was decided to do as much experimental work as possible on a standard Model 278A engine. This work was expected to supply engine-performance data such as heat rejections, firing pressures, exhaust temperatures, and so on under exact operating conditions.

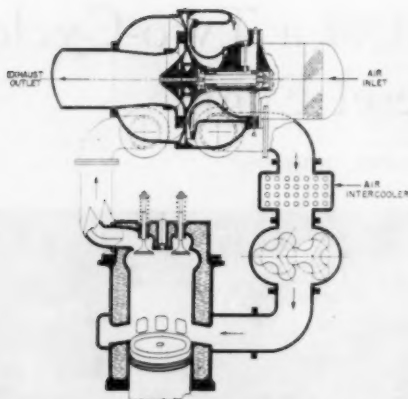


Fig. 3 DIAGRAM OF TWO-CYCLE TURBOCHARGING ARRANGEMENT

It had been thought, at one time, that it would be advantageous to simulate turbocharger operation by means of external air blowers, but while studying this problem it was learned that the De Laval Steam Turbine Company of New Jersey manufactures a turbocharger that could be matched quite closely to obtain the desired engine performance.

The turbocharging arrangement used is as shown in Fig. 3. The air compressed by exhaust-gas energy in the turbocharger is intercooled before entering the standard, positive-displacement, engine-driven blower where the second stage of compression takes place.

Precooling the air has a twofold purpose—to pack more oxygen into the engine cylinders, and to minimize thermal problems in the positive-displacement blower. An engine-driven positive-displacement blower is used to supply air required for starting the engine, and always to have a positive amount of air available for maneuvering.

The indicator diagram, Fig. 4, shows the percentage of power in the exhaust gas under both turbocharged and nonturbocharged conditions. If only a part of the heat energy which is ordinarily lost in the exhaust gas is recovered, the saving is substantial.

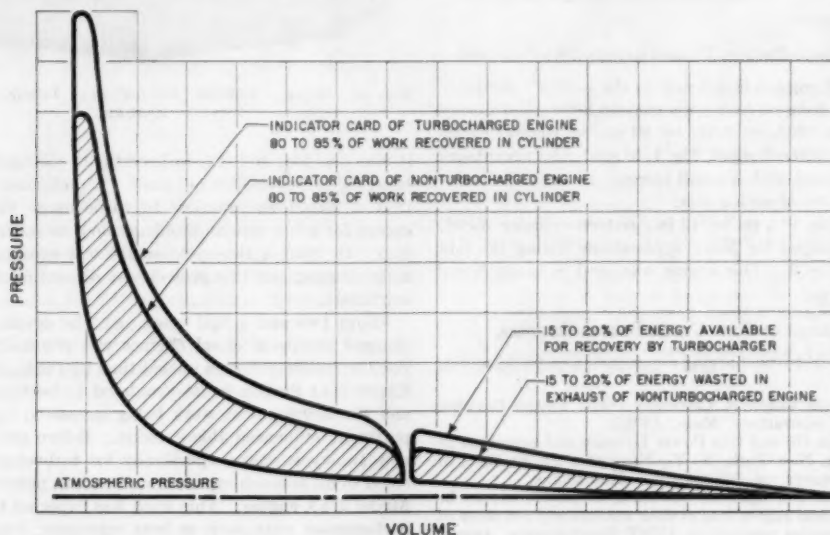


Fig. 4 TYPICAL DIESEL-ENGINE INDICATOR DIAGRAM

If the exhaust-heat energy is used to drive a turbocharger, an increase in engine horsepower and an improvement in fuel economy is obtained. An increase in engine horsepower results in higher brake mean effective pressure, which raises the expansion line of the indicator card. In a two-cycle diesel it means that the pressure in the cylinder at which the exhaust valves open increases for blowing down the cylinder. Experimental tests show that with an increase in engine power of 75 per cent, the pressure in the cylinder at the time the exhaust valves open increased from about 50 to 100 psi by turbocharging.

The actual test arrangement of this turbocharged engine is indicated in Fig. 5, which shows a branch-type of manifold used to recover the pulse energy in the exhaust from each cylinder. The firing sequence of the engine is such that there is very little overlap between the exhaust from the various cylinders. A study of the exhaust pulsations verified these conclusions. The two manifolds are joined together at a pulse converter, the purpose of which is to convert the kinetic energy in the exhaust pulsations into pressure energy by controlling the expansion through a diffuser. After the exhaust gases are slowed down through the pulse converter, they pass through the turbine and then out to the atmosphere. The centrifugal compressor driven by the turbine draws the air in through an air-inlet filter and silencer and discharges it through an intercooler to the positive-displacement blower on the engine. (Since this blower pumps denser air, its size is only about two thirds that of the standard blower used on a nonturbocharged engine.) The blower delivers the air to the engine air box and then to the engine cylinder. The compressor pressure ratio on this experimental turbocharger was 2:1.

Fig. 6 shows a cross section of the De Laval turbocharger as used on the engines. It is of the monorotor mixed-flow design with the compressor direct-connected to the turbine. The rotor is supported by bearings on the compressor side. The inlet air is used to cool the bearing housing and it protects the sleeve bearings from the high exhaust temperature. The turbochargers used for this line of engines are made by De Laval and are designed for operating at pressure ratios up to 3:1. For development work, turbochargers with a pressure ratio of approximately 2.5:1 were used.

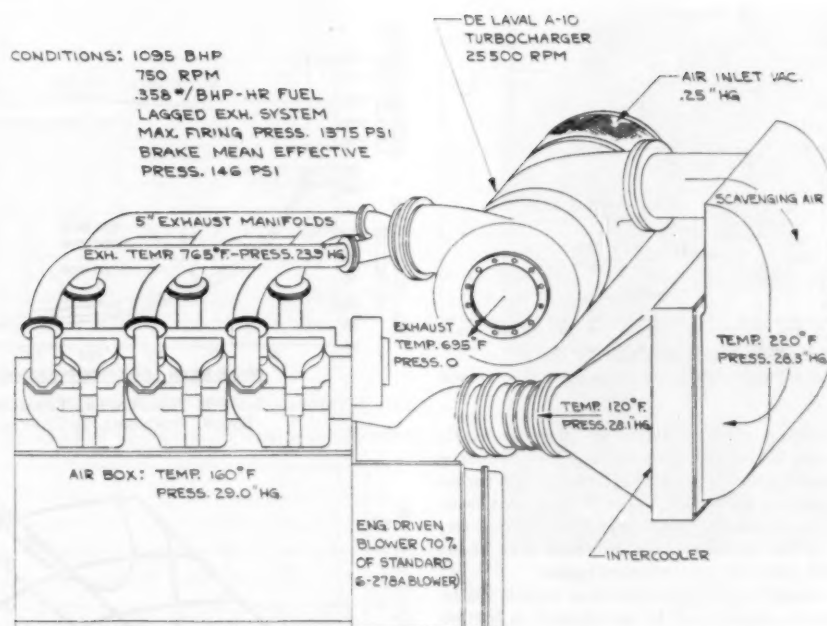


FIG. 5 MODEL 6-278BS TWO-CYCLE TURBOCHARGED DIESEL-ENGINE TEST ARRANGEMENT

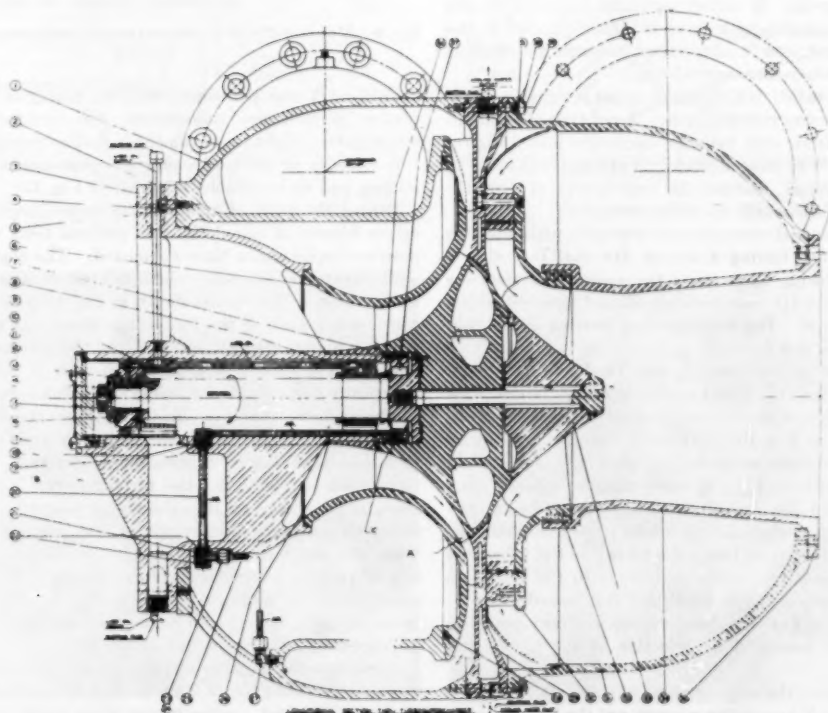


FIG. 6 CROSS SECTION OF DE LAVAL MONOROTOR MIXED-FLOW-TYPE TURBOCHARGER

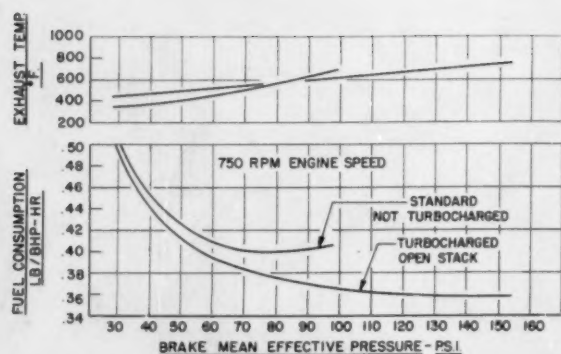


FIG. 7 MODEL 6-278BS TWO-CYCLE DIESEL-ENGINE PERFORMANCE CURVES

Some of the performance results obtained are shown in Fig. 7. Comparisons are made of the turbocharged engine performance with a nonturbocharged unit. The curve shows that the turbocharged engine output was increased almost 100 per cent, with very little increase in engine-exhaust temperature. However, the firing pressure in the cylinders only increased from about 1100 psi to about 1350 psi for the turbocharged engine.

Fig. 8 shows the change in fuel consumption at various engine speeds. This is almost proportional to the increase in friction horsepower. The exhaust temperature changes very little as the engine speed is increased.

Another problem that arises when adapting a turbocharger to an engine is matching its characteristics satisfactorily to the engine. Fig. 9 shows the engine horsepower at 750 rpm superimposed on the compressor-performance curve. It shows that at 750 rpm the compressor is almost perfectly matched to the engine. The engine-horsepower curve is almost parallel to the compressor surge line, and it also passes through the highest efficiency islands of the compressor curves.

During experimental studies, different types of exhaust manifolds were tried to evaluate their merits. A pot type of manifold where the exhaust from each cylinder discharges into a big receiver was tested. With this manifold, no attempt was made to recover any pulse energy, whereas the branch type of manifold attempts to recover the maximum pulse energy.

Fig. 10 shows the fuel consumption obtained with the two branch manifolds—one having a $3\frac{1}{2}$ -in. ID, and the other a 5-in. ID. Later, during these tests the pulse converter was removed from the 5-in-ID branch manifold, and replaced with a straight section of pipe. The corresponding increase in fuel consumption is shown in this figure.

The exhaust pulse for both the $3\frac{1}{2}$ and 5-in-ID branch manifolds is shown in Fig. 11. The magnitude of the initial pulse in the $3\frac{1}{2}$ -in. manifold was twice as great as in the 5-in. manifold, but, as shown by Fig. 10, there was no change in fuel consumption between the two manifolds. However, a closer study of the exhaust pulsations, Fig. 11, shows that the exhaust back pressure in the $3\frac{1}{2}$ -in-diam manifold exceeds the air-box or cylinder charging pressure when the air-intake ports are uncovered by the piston; and therefore, this pulse energy in the exhaust is not being utilized to scavenge the cylinder. In the 5-in-diam manifold the exhaust pulse is so small that it is not effective for cylinder scavenging. For the best engine performance, this condition should be corrected by selection of the proper size manifold.

Fig. 12 is a view of the experimental engine. It shows the branch manifold, the Y-type pulse converter at the turbocharger, the inlet silencer, and the exhaust piping. Much of the experi-

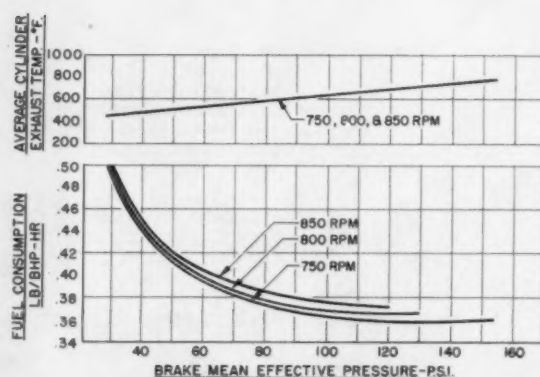


FIG. 8 MODEL 6-278BS TWO-CYCLE TURBOCHARGED DIESEL-ENGINE PERFORMANCE CURVES

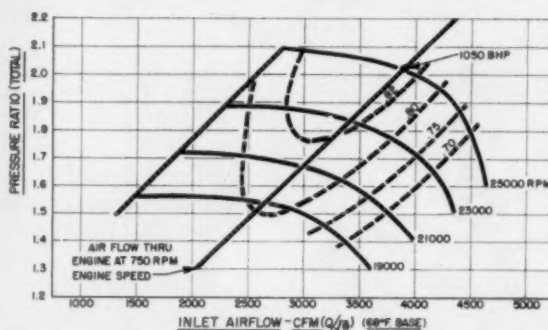


FIG. 9 MODEL 6-278BS TURBOCHARGER-COMPRESSOR PERFORMANCE CURVES

mental work was performed with an unlagged manifold. For further performance refinements, the manifold was lagged, which gave a slight improvement in fuel consumption.

A close-up of the turbocharger, compressor-discharger manifold, and air intercooler is shown by Fig. 13.

During the study of matching the turbocharger to the engine-driven blower, it was decided to perform tests with the engine positive-displacement blower removed. The engine was started with an external air source which was cut off after the engine was in operation. The results shown in Fig. 14 indicate that over a considerable part of the load range there was no difference in fuel consumption with or without the positive-displacement blower. The blower is designed so that at full load there is practically no pressure rise across it; and therefore, it is floating in the system. At lower loads, however, the blower develops some parasitic load. Also, the higher exhaust temperatures at part load, as shown by this curve, are due to the reduced quantity of air delivered by the turbocharger. The turbocharger being so dependent on the exhaust-gas temperature does not develop its full capacity, except at full engine-load conditions, while the positive-displacement blower delivers the same quantity of air at a particular speed regardless of the load. The reduction in firing pressures in the cylinder is due to this reduction in air to the cylinder, with corresponding reduction in compression pressure and oxygen deficiency.

A considerable number of other studies were made with various exhaust-port timings, and so on. It was surprising to learn that the standard engine timing gave about the best over-all performance. The results of these tests were so encouraging

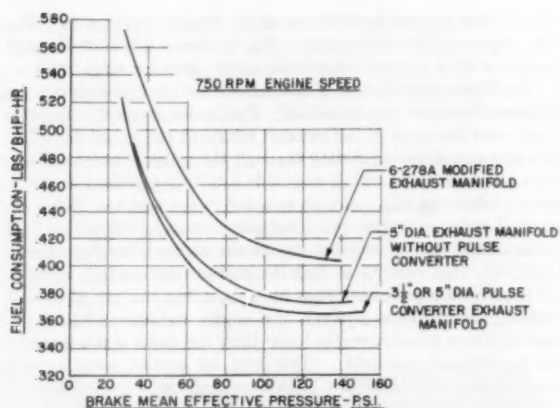


FIG. 10 MODEL 6-278BS FUEL-CONSUMPTION CURVES FOR VARIOUS TYPES OF MANIFOLDS

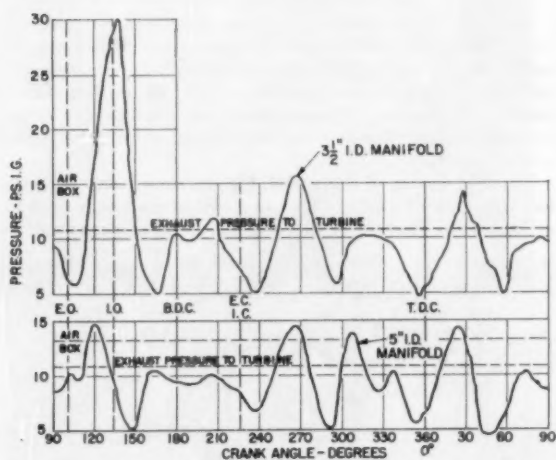


FIG. 11 PULSATIONS IN BRANCH-TYPE MANIFOLD FOR MODEL 6-278BS TURBOCHARGED ENGINE

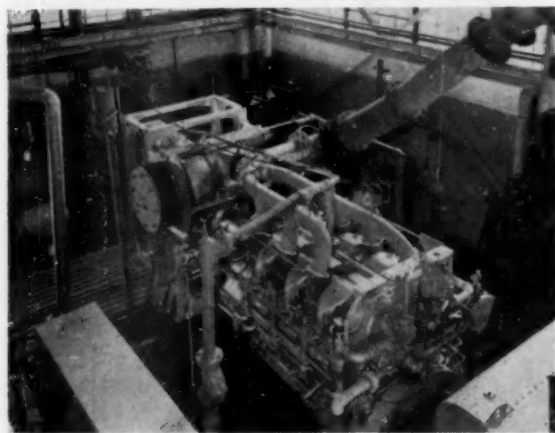


FIG. 12 MODEL 6-278BS TWO-CYCLE TURBOCHARGED DIESEL-ENGINE TEST-STAND SETUP

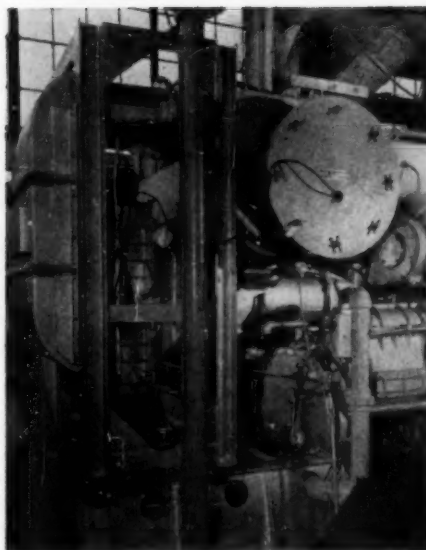


FIG. 13 MODEL 6-278BS TURBOCHARGED ENGINE—CLOSEUP OF TURBOCHARGER, COMPRESSOR-DISCHARGE MANIFOLDING, AND AIR INTERCOOLER

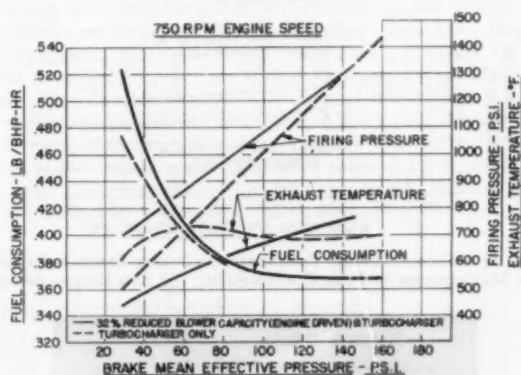


FIG. 14 MODEL 6-278BS PERFORMANCE CURVES WITH AND WITHOUT POSITIVE-DISPLACEMENT BLOWER ON ENGINE

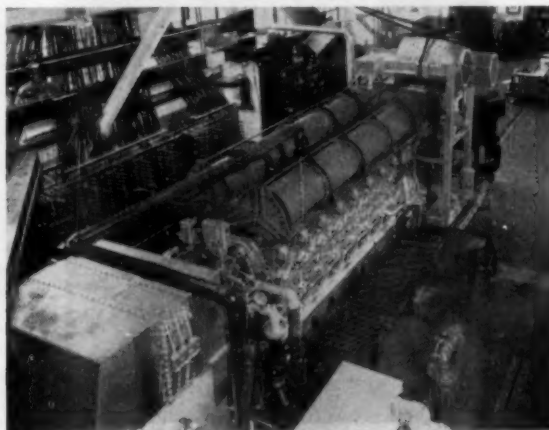


FIG. 15 MODEL 16-278A TWO-CYCLE TURBOCHARGED DIESEL-ENGINE TEST-STAND SETUP



FIG. 16 MODEL 16-278A TURBOCHARGED DIESEL ENGINE—CLOSEUP OF EXHAUST CONNECTION BETWEEN CYLINDER HEAD AND MANIFOLD

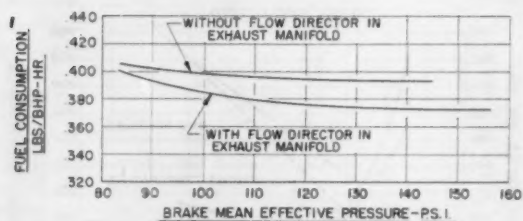


FIG. 17 MODEL 16-278BS TURBOCHARGED DIESEL ENGINE—EFFECT OF MANIFOLDING ON FUEL CONSUMPTION; 750 RPM ENGINE SPEED

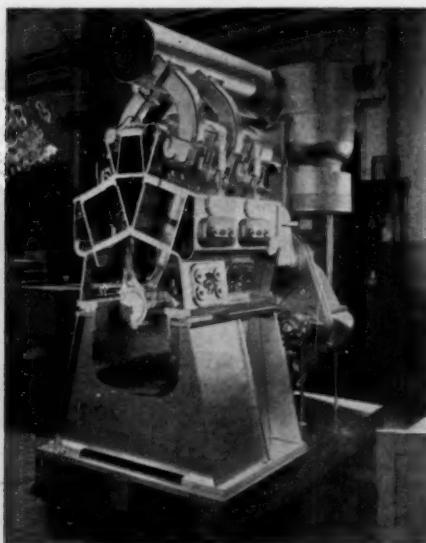


FIG. 18 MODEL 49S TURBOCHARGED DIESEL ENGINE—WOODEN MODEL

that it was decided to verify them by turbocharging a 16-cylinder engine of this same series. Fig. 15 shows this turbocharged engine with a double exhaust manifold—one for each bank.

Fig. 16 shows a closeup of the exhaust connection between the cylinder head to the manifold. The pulse converter for this setup was designed in the exhaust elbow at the manifold. The exhaust gas, after expanding through the pulse converter, flows into a flow director which was built into this manifold to maintain a relatively high exhaust velocity to the turbine. This design of pulse-converter manifold serves two functions: (1) It controls the flow of exhaust gas to the turbine, keeping it at a relatively high velocity so that the engine exhausts into a region of lower static pressure; that is, by keeping the gas at a high velocity in the flow director, the engine cylinder actually exhausts into a pressure region lower than the mean static pressure in the exhaust manifold. (This idea, of course, sounds quite theoretical; and therefore, tests were performed to evaluate it.) (2) It converts the velocity energy to pressure energy at the turbine by means of a diffuser. Fig. 17 shows the improvement in engine performance with the flow director.

DESIGN OF A TWO-CYCLE TURBOCHARGED DIESEL ENGINE

Based on this test information, it was decided to design a two-cycle diesel engine specifically for turbocharging. First a wooden model. Fig. 18, was built of this engine to study the integration of the various engine components, and to study the method of fabricating the crankcase, subbase, and oil pan. It also was used for studying the turbocharger-manifold problem, which proved to be a very important item.

The cross section of this model, Fig. 19, shows some of its interesting design features. The crankcase is made very rigid to withstand the increase in charging and firing pressures due to

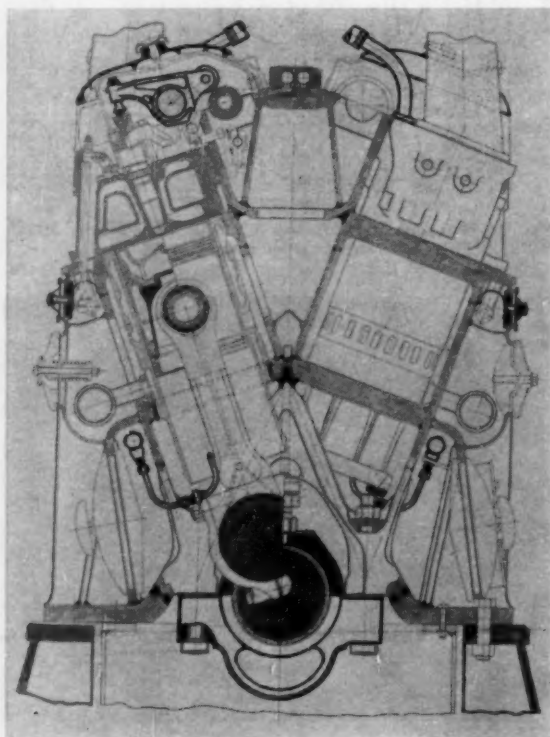


FIG. 19 MODEL 49S TURBOCHARGED DIESEL-ENGINE CROSS SECTION

turbocharging. The engine crankcase is supported at the four corners. The rear two corners are secured by bolting and doweling to the engine base, while the front corners are permitted to move in order to reduce the thermal stresses in the crankcase and to minimize thermal distortion. The resulting thermal stresses in the crankcase are very small.

The crankshaft is made larger than its nonturbocharged predecessor, to reduce bearing pressures and to control torsional vibrations. The bearing pressures are commensurate with the nonturbocharged Model 278A engine. This engine was designed to operate up to 900 rpm, and to be free from torsional vibrations through its entire operating speed range.

The pistons are of the floating type to reduce thermal distortion and give uniform wear. The piston is supported by a trunnion which carries the wristpin.

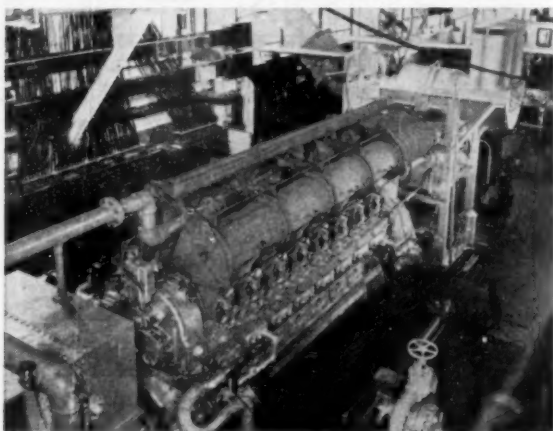


FIG. 20 MODEL 498 EXPERIMENTAL TWO-CYCLE TURBOCHARGED DIESEL-ENGINE TEST-STAND SETUP

The connecting rod is of strap construction (see Fig. 19), similar to that used successfully on other General Motors' engines. This makes it possible to use larger crankpin bearings and still remove the connecting rod with the piston through the cylinder liner.

The exhaust system was designed specifically for turbocharging. Besides the exhaust manifold which will be described later, all the exhaust passages through the cylinder head and elbows have been streamlined as much as practical. The exhaust passages were proportioned to regulate the gas flow from the cylinder to the manifold, so as to minimize the acceleration and deceleration of the exhausting gas. It was concluded that the improvement in engine performance warranted this consideration.

The experimental engine with its turbocharger is shown in Fig. 20. For testing convenience, the turbocharger was placed as shown, in front of the engine. In this way, it was possible to change the manifold without disturbing the other engine accessories. The turbocharger, for experimental reasons, was placed horizontally, but on production models it is possible to mount the turbocharger either vertically or horizontally to achieve the best engine-room arrangement.

Fig. 21 again shows the flow director in the manifold into which the exhaust discharges from each cylinder. This is a region of high velocity. The velocity energy in the exhaust gas is converted to pressure energy at the diffuser at the end of the manifold. The tapered cone at the end before the turbine is a screen which was built into the manifold for protecting the turbine from debris, weld splatter, and the like, that might be in the exhaust system. Provision also is made in the manifold for part of the exhaust to circulate around the outside of the high-velocity, flow-director section. This recirculating exhaust gas is at a relatively low velocity, and therefore it acts as an insulator for the main exhaust stream, making it possible to water-cool the outside of the exhaust manifold, thereby reducing the thermal-expansion problems existing in nonwater-cooled manifolds. Fig. 21 also shows the open end of the high-velocity section which

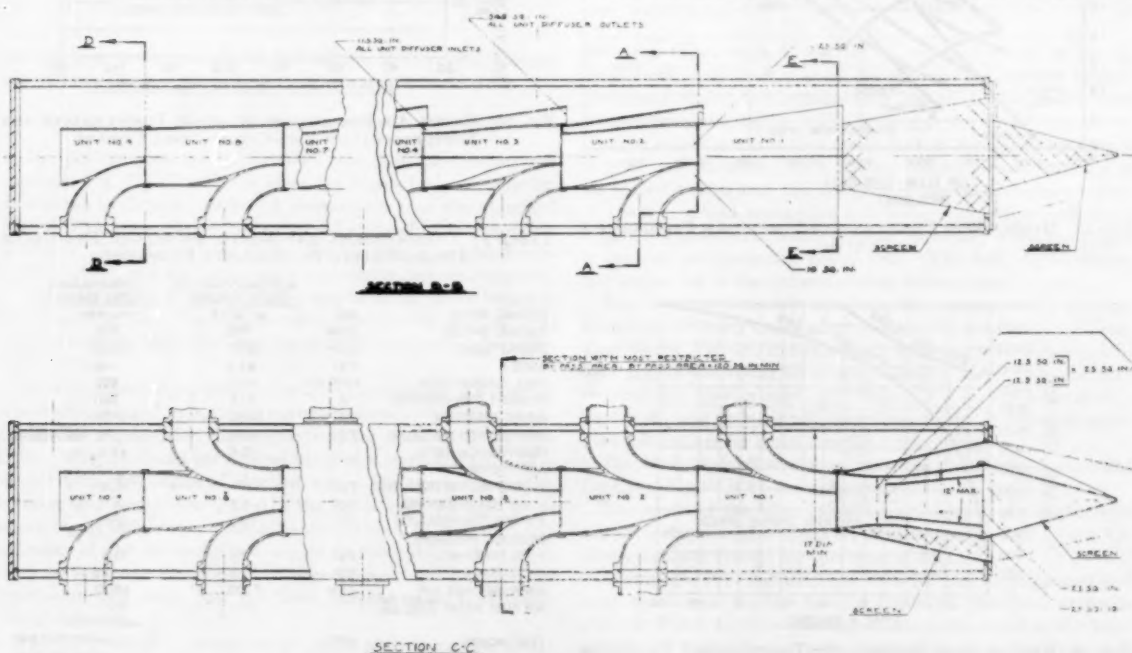


FIG. 21 DRAWING OF MODEL 498 TURBOCHARGED-ENGINE MANIFOLD

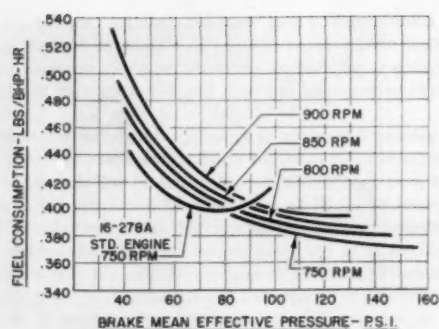


FIG. 22 MODEL 16-498 TWO-CYCLE TURBOCHARGED DIESEL-ENGINE FUEL-CONSUMPTION CURVES

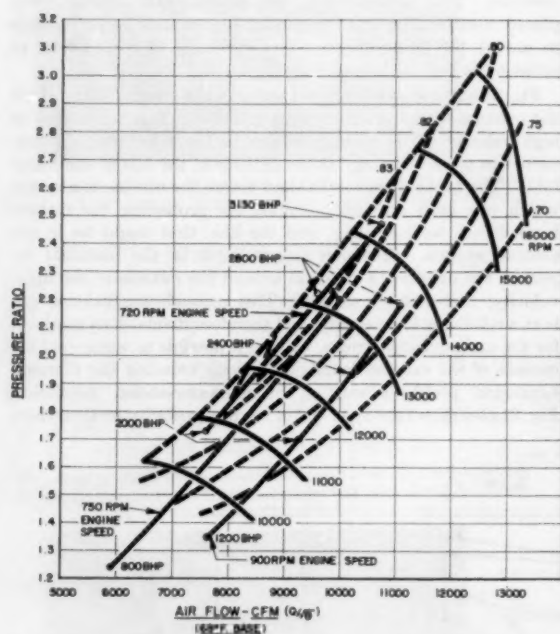


FIG. 23 MODEL 16-498 TURBOCHARGER-COMPRESSOR PERFORMANCE CURVES

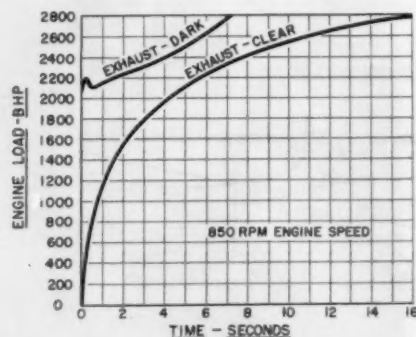


FIG. 26 RATE OF LOAD APPLICATION—TURBOCHARGED TWO-CYCLE DIESEL ENGINE

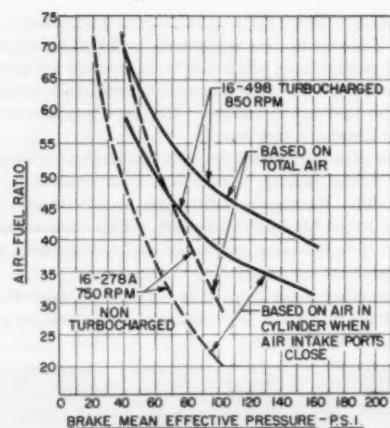


FIG. 24 AIR-FUEL RATIO OF TURBOCHARGED AND NONTURBOCHARGED TWO-CYCLE DIESEL ENGINES

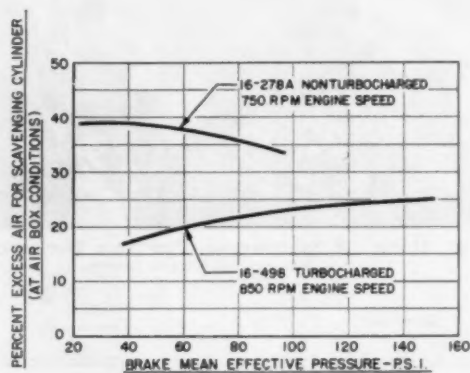


FIG. 25 EXCESS AIR REQUIRED TO SCAVENGE TURBOCHARGED AND NONTURBOCHARGED TWO-CYCLE DIESEL ENGINES

TABLE 1 TURBOCHARGED AND NONTURBOCHARGED TWO-CYCLE DIESEL-ENGINE PERFORMANCE COMPARISON

ENGINE MODEL	NO.	NONTURBOCHARGED DIESEL ENGINE		TURBOCHARGED DIESEL ENGINE	
		16-278A	750	16-498	750
ENGINE SPEED	RPM	750	750	2800	2800
ENGINE LOAD	BHP	1600	1600	146	146
B.M.E.P.	PSI	83.6	83.6	146	146
FUEL CONSUMPTION	LB/BHP-HR	400	400	374	374
EXHAUST TEMPERATURE	°F	615	615	740	740
FIRING PRESSURE	PSI	1050	1050	1335	1335
COMPRESSION PRESSURE	PSI	600	600	730	730
COMPRESSION RATIO		15.6	15.6	13.2	13.2
AIR PRESSURE					
COMPRESSOR DISCHARGE	PSI	—	—	15.0	15.0
AIR BOX PRESSURE	PSI	3.7	3.7	14.5	14.5
AIR BOX TEMPERATURE	°F	150	150	120	120
EXHAUST PRESSURE					
TO TURBINE	PSI	—	—	11.5	11.5
TO STACK	PSI	1.5	1.5	.25	.25
AIR FLOW—FREE AIR	CFM	5730	5730	9800	9800
AIR FUEL RATIO		38/1	38/1	40/1	40/1
TEST HOURS	HRS			1440 (TOTAL)	1440 (TOTAL)
				1150 (ABOVE 1600 BHP)	1150 (ABOVE 1600 BHP)
				880 (ABOVE 2800 BHP)	880 (ABOVE 2800 BHP)

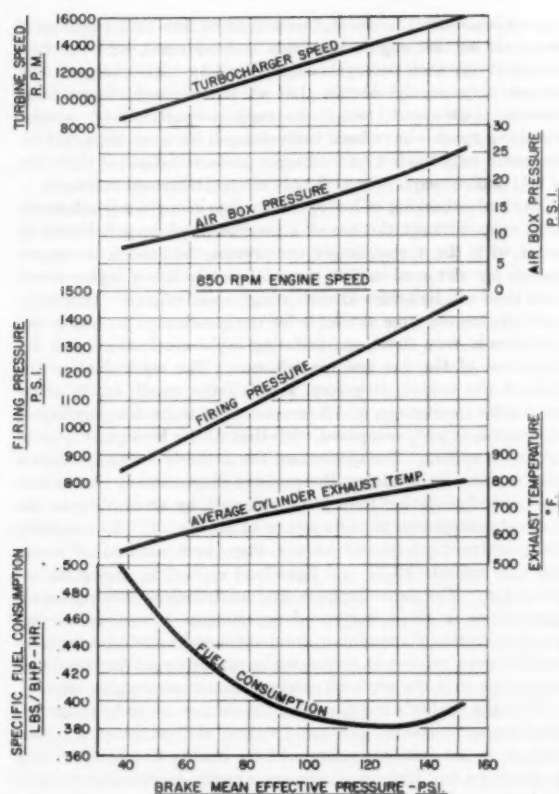


FIG. 27 MODEL 16-498 TURBOCHARGED TWO-CYCLE DIESEL-ENGINE PERFORMANCE CURVES

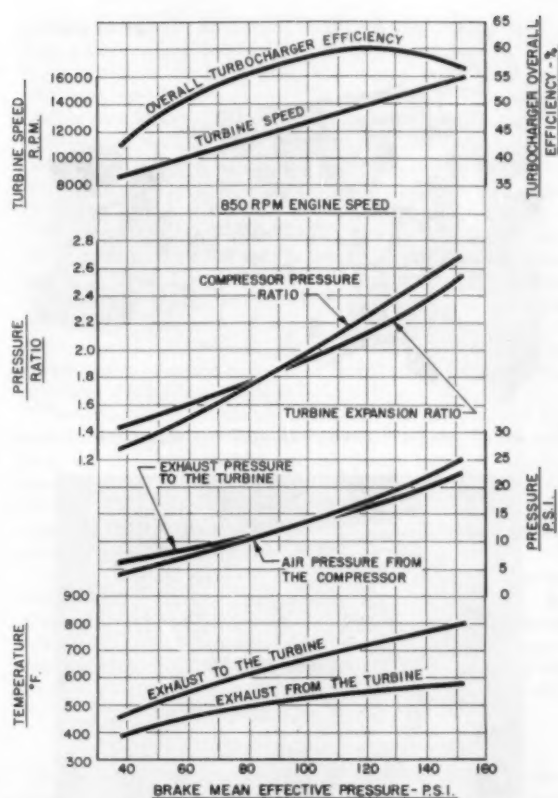


FIG. 28 MODEL 16-498 TURBOCHARGED TWO-CYCLE DIESEL-ENGINE PERFORMANCE CURVES

permits gas on the outside of this section to circulate, thereby maintaining the high velocity through the center section.

PERFORMANCE RESULTS

The performance results obtained with the new engine are shown in Fig. 22. This curve gives the engine fuel consumption at various loads and speeds. A comparison with the standard Model 278A two-cycle nonturbocharged engine fuel consumption is shown. This figure also shows the increase in engine-horsepower output, and the improvement in engine fuel consumption.

The satisfactory matching of this engine to its turbocharger is shown on Fig. 23. The horsepower curves for 720 and 750 rpm pass through the high-efficiency region of the compressor-performance curve.

Since a turbocharged two-cycle engine does not act the same as a nonturbocharged unit, it was necessary to determine the quantity of air required for combustion and for scavenging the cylinder. Fig. 24 shows the air-fuel ratio of a turbocharged and a nonturbocharged engine of identical size. The curve shows that considerably more air is required by the turbocharged engine when operating at higher output because the air used to scavenge the cylinder of the turbocharged engine is more dense than that used to scavenge the nonturbocharged diesel, and because the maximum load limit has not been reached with the turbocharged engine.

Fig. 25 shows the percentage of air at air-box conditions required to scavenge both the turbocharged and nonturbocharged,

two-cycle diesel engines. About 30 per cent excess air has always been considered a good design criterion for the nonturbocharged engine, yet considerably less air is used to scavenge the turbocharged engine. The density of the air at these turbocharged conditions is almost twice that of the nonturbocharged engine; and therefore, on a free-air basis a greater quantity of air is used to scavenge the cylinders of the turbocharged engine.

The rate of load application to a turbocharged two-cycle diesel engine is a problem of much concern, especially when the engine is used as an emergency power unit. The difficulty is due to the inertia lag of the exhaust-driven turbocharger.

Tests were performed to determine the minimum time required to obtain full load under clear and smoky exhaust conditions. The results, Fig. 26, indicate that, with a smoky exhaust, full-load application could be accomplished in about half the time required for clear exhaust. Therefore, if a smoky exhaust during the starting period is not objectionable, the time reduction is a desirable feature for certain engine applications.

The load-application curves were obtained with a standard De Laval Model B-17 turbocharger.

The results of the Model 16-498 turbocharged-engine performance at 850 rpm engine speed are summarized in Figs. 27 and 28. These data are typical for this type of engine.

A comparison of the principal data for the turbocharged and nonturbocharged engines having the same bore and stroke is given in Table 1. One particular item to be noted is the large increase in engine horsepower obtained by turbocharging, with very little increase in cylinder firing pressure.

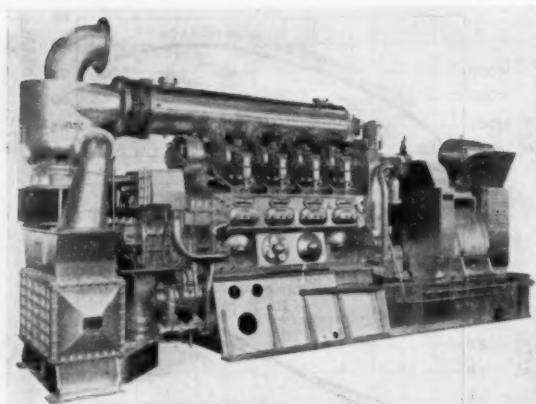


FIG. 29 MODEL 8-498 TURBOCHARGED TWO-CYCLE DIESEL ENGINE

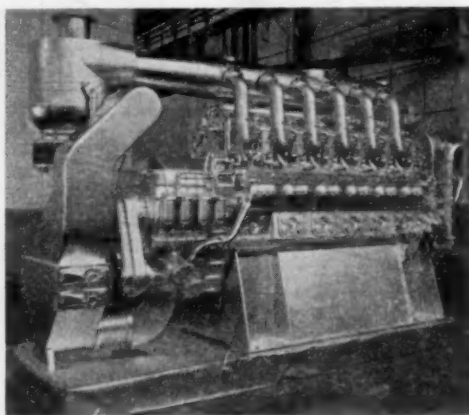


FIG. 30 MODEL 12-498 TURBOCHARGED TWO-CYCLE DIESEL ENGINE

MODEL 498 ENGINES

The Model 498 engine is currently being built in eight (Fig. 29), twelve (Fig. 30), and sixteen-cylinder sizes. As shown in these views, the compressor-discharge manifold is made sufficiently rigid to support the turbocharger, resulting in a very compact, lightweight, high-speed engine.

CONCLUSIONS

The result of this development work is a new series of two-cycle diesel engines, designed specifically for turbocharging, that have improved fuel consumption, increased engine output, and a larger reduction in size per horsepower as compared with non-turbocharged two-cycle diesel engines.

Discussion

RUDOLPH BIRMANN.² The author has presented an outstanding success story—success in many different respects, but chiefly with respect to the marriage of the reciprocating engine to the turbomachine (in the form of a highly turbocharged two-cycle diesel engine).

As pointed out in the paper, the turbocharging of two-cycle

engines is not new; however, this is the first time that a *high-speed* two-cycle service engine has been turbocharged, and the first time that any such two-cycle engine has been turbocharged to an output very nearly double that of its atmospheric-aspirated version. Low-speed two-cycle engines—particularly several European types—have been turbocharged for some time, but by the use of only modest turbocharger pressure ratios (of the order of 1.4) and consequently with only modest increases in output.

The turbocharging of low-speed two-cycle engines is relatively easy, even without the use of a positive-displacement blower in series with the turbocharger compressor, because a low-speed engine, by virtue of its low rpm, inherently has a higher merit ratio than can be achieved with a high-speed engine. In a high-speed engine the time available for the gas-change process in the cylinders is very short, necessitating rapid acceleration and deceleration of the gas and air columns. The equivalent orifice area of the engine, therefore, is relatively small, or, in other words, the merit ratio, which measures the turbochargeability of the engine, is poor compared with that of the low-speed type of two-cycle engine. For this reason the author's company made a wise decision in retaining the positive-displacement blower—at least initially—rather than going "all out" by attempting to use the turbocharger as the sole source of air supply. By retaining the positive-displacement blower they were assured of ready starting, reliable idling and light-load operation, and good acceleration. The paper explains that nevertheless, keeping future possibilities in mind, successful experiments have been carried out in operating the engine without the use of a positive-displacement blower, relying entirely on the turbocharger for supplying the engine with the required combustion and scavenging air.

Both the author's company and the author are to be congratulated for not following the usual course of "patching" a turbocharger on an existing engine, and for having had the foresight to develop a new high-speed two-cycle engine specifically designed for high-pressure turbocharging. This development work is described in the paper, and demonstrates clearly that if the proper design skill is applied, engine-firing pressures and turbocharger pressure levels need not be limited by considerations of engine structure (crankshaft, bearings, crankcase, cylinder heads, and so on).

High-pressure turbocharging, such as described in the paper, makes the role played by the turbocharger in the over-all picture an exceedingly important one. This can be recognized readily if it is considered that when the 16-498 engine develops 2800 hp the turbine of the turbocharger develops 1200 hp. Since it makes such a sizable contribution the turbocharger deserves a "break," particularly with regard to the ducting to and from the engine and the flow losses occurring therein. If we look at the photographs in the paper, we see that in this application things have been made rather difficult for the turbocharger, by the inadequate size of the turbine-exhaust ducting and the use of sharp elbows in the air and exhaust piping. This inadequate exhaust ducting makes it difficult for the turbine to show a good performance, which can be appreciated readily if it is realized that as much as 10 to 15 per cent of all the energy that is being made available to the turbine is in the form of kinetic energy at the turbine outlet. The high velocity corresponding to this large amount of kinetic energy should be converted into a pressure rise by the provision of a diffuser at the turbine exhaust. If the exhaust piping into which the diffuser discharges is of adequate size and does not contain too many restrictions in the form of sharp elbows, the pressure directly at the turbine outlet can easily become subatmospheric, which reflects in better utilization by the turbine of the energy in the engine exhaust.

While it would be desirable, from the point of view of engine performance, to have the advantage of the aerodynamic re-

² Consulting Engineer, De Laval Steam Turbine Company, Trenton, N. J. Mem. ASME.

finements just mentioned, thereby making the aerodynamic design of the engine-turbocharger combination match the superb mechanical design of the engine, such aerodynamic refinements become a "must" only when the positive-displacement blower is omitted. For the turbocharged engine to operate successfully without the positive-displacement blower, it is imperative that all flow and pressure losses in the engine-turbocharger system (which includes all air and exhaust piping, intercoolers, and intercooler headers) be reduced to the very minimum, and that as much of the energy contained in the exhaust gases as possible be made available to the turbine. Along these lines, it is also essential that the maximum amount of the energy in the exhaust pulsations be recovered. A step in this direction has been taken already, and is described by the author in conjunction with Figs. 17 and 21, the latter showing an eductor type of exhaust manifold designed for conversion of the energy in the exhaust pulsations into a pressure rise, giving the engine the benefit of a back pressure lower than the turbine nozzle-box pressure. This eductor manifold is a very promising development, but undoubtedly requires further study and experimentation to bring about the maximum possible improvements that can be accomplished by its use. Such experimentation undoubtedly will show that this type of manifold can be designed to produce the optimum eductor effect at either part load or full load.

The responsibility for improving the engine output and performance and eventually eliminating the positive-displacement blower does not rest entirely on the engine manufacturer, but also is shared by the turbocharger manufacturer, since the performance of a two-cycle engine is even more sensitive to turbocharger combined efficiency than is that of the four-cycle engine. For this reason systematic improvements have been made in the performance of the De Laval turbocharger, recently resulting in the development of improved turbine blading and substantially higher turbine efficiencies than were obtainable with the turbines used by the author's company in the past.

The fact that much remains to be done to further perfect the highly turbocharged two-cycle engine does not detract from the great accomplishment of Cleveland Diesel described by the author. Rather, this accomplishment holds out the hope that further equally substantial progress can be made, to the extent that the highly turbocharged two-cycle engine will occupy a wider and wider range in the spectrum of heat-power engines for a long time to come, in spite of the advent of other heat-power engines such as the gas turbine, even including that of the free-piston gas-generator type.

RALPH MILLER.³ This paper, while interesting, lacks many essential technical data. The writer is particularly concerned when he sees "Russian" curves such as a *P-V* diagram without a pressure scale. Also lacking is the thermal load in terms of total heat flow to cooling water and lubricating oil for the conventional and turbocharged versions. Scavenging efficiency data are missing. However, the abnormally high fuel consumption points to a very low scavenging efficiency, probably in the order of 75 per cent.

Poppet-exhaust-valve uniflow-scavenged engines were developed and built by the Burmeister & Wain Company some years before we made this discovery in the United States. That company also led all other engine builders by several years in turbocharging this type of engine; furthermore, their engines operate with scavenging efficiencies of 90 per cent, with resulting fuel consumptions of 0.33 lb per bhp-hr, all of which shows that, far from being the pioneers in this field as inferred in the

opening paragraph, we haven't even been able to copy successfully what has been accomplished already by others.

As mentioned by the author, the original exploratory work was done by extensive research in the U. S. N. Experiment Station on a Model 278A, at a time when turbocharging of two-cycle engines was held by others to be impractical. Many of the data presented here are based on the work carried out by the Experiment Station, which was very ably reported in a paper by W. G. Payne and W. S. Lang.⁴

In addition to studying what has now become the conventional method of turbocharging two-cycle engines, Payne and Lang studied and tested the variable-compression-ratio cycle, but only in a limited range and at low supercharging pressures. Nevertheless, their tests point toward the great advantage of this cycle as a means of obtaining very high output when using supercharging pressures of 3 atm or more. Will the author explain why this lead has not been followed?

The cycle was at one time known as the perfect cycle and was used in four-cycle gas engines. In their report, Payne and Lang call it the "controlled exhaust closure timing." Having been developed originally for naturally aspirated-engine application, it is today in its supercharged version known as the Miller supercharging system for two and four-cycle diesel and gas engines.

In this system the supercharging pressure can be varied or increased while holding the compression pressure constant. At constant air-fuel ratio and compression pressure, the indicated horsepower then increases directly with the absolute supercharging pressure to the power of 0.285. That is, doubling the supercharging pressure increases the bhp by about 25 per cent without increasing compression pressure.

AUTHOR'S CLOSURE

It was indeed fortunate to have Mr. Birmann and Mr. Miller discuss this paper on the turbocharging of two-cycle diesel engines.

The Model 498 line of engines was designed specifically for turbocharging and was made sufficiently rugged to carry the increase in engine loads. With the small increase in space required by the turbocharger and air intercooler, the engine is now developing nearly twice the horsepower of a conventional, non-turbocharged, two-cycle diesel engine and, as the development of both the engine and turbocharger progresses, the power output will increase. Currently, there are Model 498 engines in operation developing a brake mean effective pressure of 155 psi and it is expected that in the near future the bmep will be increased.

During the development stages of this engine, it was recognized that the prime requisites for successful operation would be satisfactory engine breathing and manifolding, and that a very thorough investigation of the scavenging and the gas flow through the engine would be necessary to obtain as high a merit ratio as possible with this type of high-speed, two-cycle diesel engine. Study of these items, therefore, has been in progress and, to date, three different cylinder heads have been made to study the flow of exhaust gas through the cylinder. Also being investigated are different types of exhaust manifolds. This project will continue because it is realized that energy is available in the exhaust gas which can be recovered by proper manifolding. Furthermore, to obtain an improvement in fuel consumption, more of the available energy in the exhaust gas must be recovered.

Elimination of the engine-driven positive displacement blower is desirable as it will result in an engine of approximately the same size as a nonturbocharged unit, and it eliminates the natural parasitic losses that are attributed to this blower. But, as

³ Consulting Engineer, Nordberg Manufacturing Company, Milwaukee, Wis. Mem. ASME.

⁴ "High Supercharging Development of a GM16-278A Two-Stroke Cycle Diesel Engine," by W. G. Payne and W. S. Lang.

pointed out, a positive displacement blower is used to supply a positive amount of air for starting and maneuvering the engine and, should trouble develop with the turbocharger, a sufficient amount of air is still available to develop about 40 per cent of the normal engine power which is adequate to maneuver the vessel into port.

As progress continues on both the engine and turbocharger, it should eventually be possible to build a turbocharged, two-cycle engine that will start satisfactorily without the positive displacement blower. However, due to the natural lag between the air supplied by the turbocharger and the power applied to the engine, for some applications it may not always be feasible to operate without a positive displacement blower, especially on units requiring very rapid acceleration with a minimum amount of smoke. Some work has already been done in connection with the study of improved engine performance by varying both the air inlet port timing and the exhaust valve timing. Results show that by varying the exhaust timing, it is possible to vary the amount of exhaust energy to the turbocharger. This is one problem that also must be given consideration when matching the turbocharger to the engine. By properly retarding the injection timing and controlling the opening of the exhaust valve, it is possible to supply a relatively large amount of pulse energy to the turbocharger for part load and very light load operation.

Some changes in both the injector and valve timing may prove to be beneficial to facilitate starting the engine with the turbocharger. Also, suggestions have been made concerning the burning of fuel in the exhaust manifold to supply quick energy to the turbocharger for starting or maneuvering.

Experimental work has been done on this engine with different compression ratio pistons. For this turbocharged engine, as indicated in the paper, it was found that 13.2:1 was the minimum compression ratio that would give satisfactory starting under all conditions.

This paper does not fully describe the experimental work done at the GMC Cleveland Diesel Engine Division on this engine. Information such as the heat rejection to the oil, water, and the air intercoolers with both wet and dry exhaust manifold, etc., was not included due to time limitations.

This engine is a compromise of power output, over-all power-plant size, fuel economy, maneuverability, and engine weight, which are required to produce the most economical over-all power plant. This results in a small, compact power plant having many applications such as small, powerful, and economical towboats for moving freight in inland waterway systems. In fact, two of the twelve-cylinder engines were recently installed in a new river towboat. This towboat has broken many of the speed records under tow on the Mississippi River.

Future Developments of the High-Speed Diesel Engine

By ERNEST CHATTERTON,¹ LONDON, ENGLAND

This paper has the main objective of exploring the lines of development which appear to offer greatest possibilities for the reduction of size and weight of the diesel engine. The author examines the increases in power output from a given size of cylinder which result from the combination of a diesel engine and exhaust-driven gas turbine operating with high degrees of supercharge. He discusses the limitations and draws conclusions as to the type of engine best suited to such developments.

NOMENCLATURE

The following nomenclature is used in the paper:

D	= cylinder diameter, in.
L_{tot}	= piston stroke, in.
L_{eff}	= effective stroke, in.
V_T	= volume of air trapped in cylinder per cycle, cu in.
V_a	= total air flow per cycle, cu in.
v	= clearance volume, cu in.
W_T	= weight of air trapped in cylinder per cycle, lb
W_a	= total weight of air per cycle, lb
w_f	= weight of fuel burned per cycle, lb
d	= weight of air per cubic inch, lb
R_t	= trapped air/fuel ratio
R_a	= over-all air/fuel ratio
r	= volumetric compression ratio in cylinder based on L_{eff}
r_s	= pressure ratio in supercharger
r_t	= pressure-expansion ratio across turbine
E_{ind}	= indicated thermal efficiency
E_{brake}	= brake thermal efficiency
n_c	= compression index
n_e	= expansion index
T_{ex}	= temperature of gas leaving cylinder, deg F abs
T_{tur}	= turbine inlet temperature, deg F abs
T_{sup}	= supercharging temperature, deg F abs
T_p	= peak temperature in cylinder, deg F abs
CV	= lower calorific value of fuel, Btu/lb
C_v	= specific heat of gas at constant volume, Btu/lb/deg F
C_p	= specific heat of gas at constant pressure, Btu/lb/deg F
γ	= ratio between specific heats

INTRODUCTION

Objectives of Paper. It is a well-established design fact that, for fundamental reasons which need not be explored here, an engine having multiple cylinders of small dimensions running at a high rate of revolutions can be made lighter and smaller for a given power output than one having a smaller number of larger cylinders running at lower speed.

A "high-speed diesel engine," for the purposes of this paper, is one which is designed specifically with the object of exploiting

this fact and achieving the minimum weight and space occupied per horsepower produced.

The paper has three main objectives: (1) To show that the development of the high-speed engine is justified on both technical and economic grounds. (2) To explore the lines of development which at present appear to offer the greatest possibilities for reduction of engine size and weight and consider the limitations which exist. (3) To assess the relative suitabilities of various basic types of engine for such developments.

THE CASE FOR THE HIGH-SPEED ENGINE

Applications for High-Speed Engines. There are many applications for diesel engines where minimum size and weight are important. Such cases occur in the propulsion of certain naval and similar craft, and in portable or mobile equipment of various kinds. In such applications high-speed engines are essential to permit technical requirements to be fulfilled.

There are, however, other applications for which heavier and larger types of engine are traditionally employed but which would show considerable technical and economic benefit from small and lighter engines. Two typical examples are considered in the following.

Marine Propulsion in Merchant Ships. Fig. 1 illustrates a machinery installation for a general cargo ship with engines placed aft. The shaded area shows a conventional slow-speed, direct-drive reversing engine of well-known type developing 6000 shp at 110 rpm.

The alternative installation is provided by four Napier Deltic engines, each delivering 1700 hp at 1500 rpm driving through fluid couplings into a reduction gear box containing reversing mechanism, the propeller speed remaining at 110 rpm. The costs of these two installations are comparable but the weight of the complete Deltic installation is about 68 tons, as compared with 460 tons for the slow-speed engines—a saving of 392 tons! Furthermore, the engine-room length is reduced from 68 ft to 28 ft, this permitting an addition to the total cargo space available in the ship of about 15 per cent.

These results are typical of a large number of similar installations examined and the technical and economic gains are obvious.

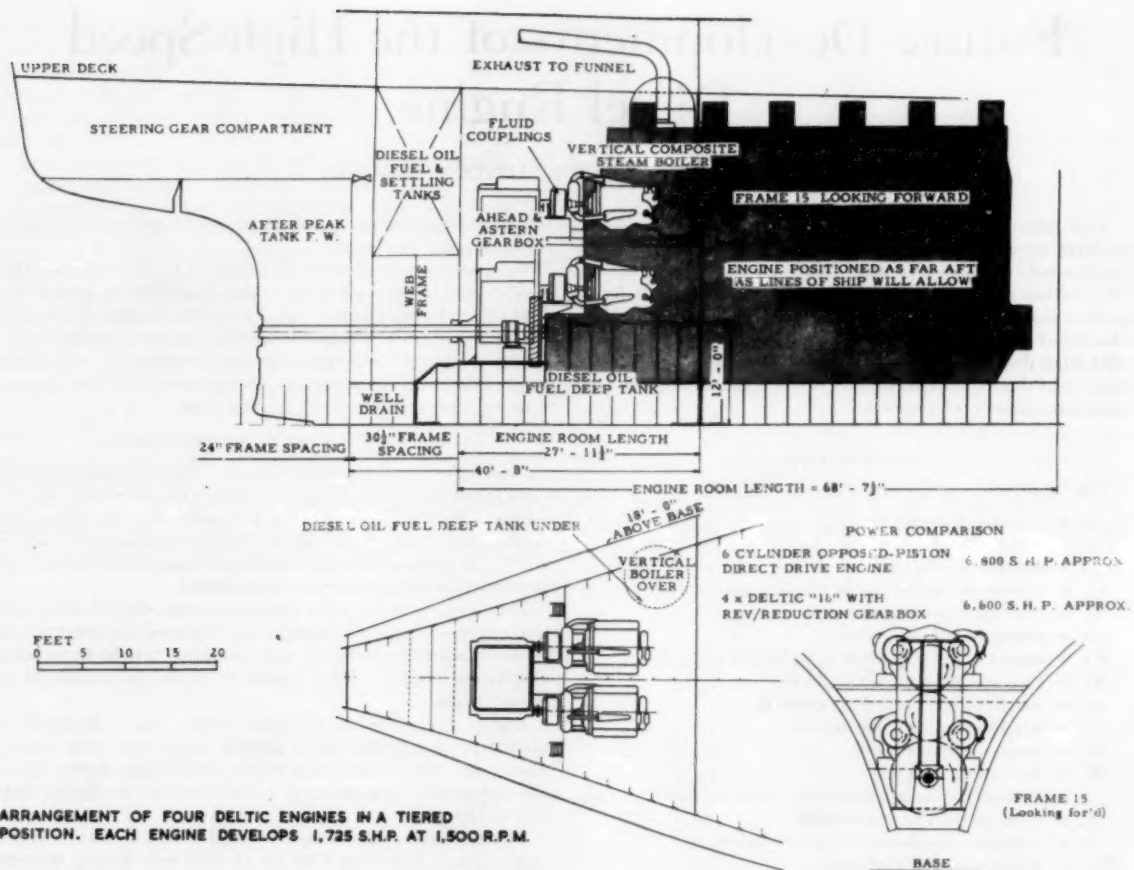
Rail Traction. There is an observable demand for locomotives of increased powers up to 4000 hp or more, this demand being accompanied by a requirement for reduced weight. The weight permissible, in any case, is limited by the maximum axle loads which can be used on certain railroads.

The ability to meet these requirements is governed almost entirely by the extent to which the specific weight and size of the engines can be reduced. Fig. 2 shows a 3400-hp locomotive constructed by The English Electric Company Limited which uses two Deltic engines with electric transmission and a Co-Co wheel arrangement. The axle load is below 19 tons when ready for service and the weight of the complete locomotive, including carriage heating equipment, is 240,000 lb, or 71 lb/hp, which is believed to be the lightest ever achieved.

Economic Advantages. Apart from the obvious advantages demonstrated in the two examples quoted, there is a further most important economic saving derived from the use of small light-weight engines; namely, the reduction in over-all maintenance

¹ Chief Engineer, Piston Engine Division, D. Napier & Son Limited. Contributed by the Oil and Gas Power Division and presented at the Annual Meeting, New York, N. Y., November 25-30, 1956, of THE AMERICAN SOCIETY OF MECHANICAL ENGINEERS.

NOTE: Statements and opinions advanced in papers are to be understood as individual expressions of their authors and not those of the Society. Manuscript received at ASME Headquarters, August 16, 1956. Paper No. 56-A-141.



ARRANGEMENT OF FOUR DELTIC ENGINES IN A TIERED POSITION. EACH ENGINE DEVELOPS 1,725 S.H.P. AT 1,500 R.P.M.

FIG. 1 ARRANGEMENT OF MARINE INSTALLATION

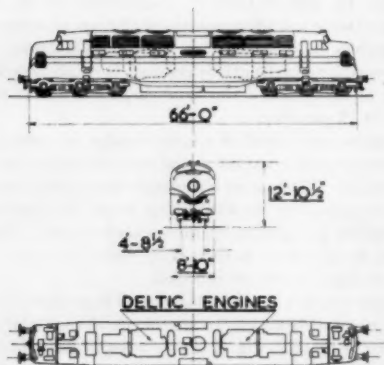


FIG. 2 ENGLISH ELECTRIC 3400-Hp "DELTIC" LOCOMOTIVE

costs. This arises mainly from the fact that small, lightweight engines allow the complete adoption of the "repair-by-replacement system."

The parts are small enough to permit complete interchangeability in manufacture and can be handled easily, so that running repairs may be carried out expeditiously without the need for skilled engineering services. Furthermore, it is possible to change en-

gines within a few hours, thus avoiding loss of service time and consequent economic penalties.

When all factors are taken into account, the repair-by-replacement system shows considerable savings in over-all maintenance costs.

Summary. For the reasons which have been stated, it is submitted that there are good technical and economic grounds to justify further development of the high-speed diesel engine. It is therefore of interest to explore those lines of development which would appear to offer the greatest promise in producing maximum power for minimum weight and space.

MAXIMUM POWER FOR MINIMUM SIZE AND WEIGHT

The Basic Problem. The problem to be explored is to produce maximum power from a cylinder of minimum dimensions; that is, to produce maximum BHP per cubic inch of cylinder volume. Power is derived from the combustion of fuel, so that the problem is to burn fuel at the greatest possible rate per cubic inch of cylinder volume.

Now fuel can be injected into a cylinder at any desired rate; it is the provision of air in appropriate quantities which presents difficulties, and this is the major problem in the development of high-speed engines for maximum power.

Limitations to Engine Speed. The most obvious way to increase the power output from a given size of cylinder is to increase the rpm at which it operates. There are, however, certain practical

limitations to this, the three main factors being as follows:

(a) *Mechanical difficulties in operation of valve gear.* As a matter of practical experience it may be said that in engines of the type considered, whether operating on the four-cycle or two-cycle systems, this problem begins to present design difficulties at about 2000 crankshaft rpm, these difficulties accentuating rapidly as the speed is increased above this.

(b) *Mechanical and hydraulic operation of fuel-injection gear.* This problem is similar in nature to the previous one and again becomes difficult on all engines at about 2000 crankshaft rpm, with rapidly increasing problems above this speed.

(c) *Piston speed.* The mean speed of the piston has become generally accepted as a practical indicator of engine life. This factor is an average empirical one established by experience and is less determinate than the two previous ones. It is probably true to say that mean piston speeds up to 2000 fpm would be generally regarded as acceptable, although speeds up to 2500 fpm are used on a number of well-known engines.

It will be apparent that the three limitations referred to are all somewhat indeterminate and must depend upon the individual engine and the skill of the designer.

In the present paper the objective is to explore maximum possibilities and for this reason the upper limit of rpm will be taken as 2200 and the upper limit of piston speed 2500 fpm.

It is not suggested that the use of these figures is necessarily permissible in an engine designed to give long life; they are intended as practical upper limits for use in determining what is possible. The conclusions derived in the paper would not be affected by the use of lower figures, it is only the maximum potentiality of achievement which would be affected.

An engine designed to operate at both the stated limits would have a piston stroke of about 6.8 in. which gives an indication of the size of cylinder concerned.

RANGE OF EXPLORATION

Types of Engines Considered. In assessing development possibilities, it is clearly necessary to take account of the differing characteristics of engines operating on four-cycle and two-cycle systems. Three basic types are therefore considered, as shown in the diagram of Fig. 3:

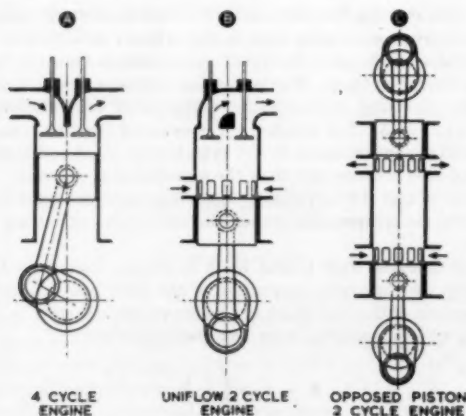


FIG. 3 TYPES OF ENGINE CONSIDERED

(a) 4-cycle engine with poppet valves.

(b) "Uniflow" 2-cycle engine with poppet valves and piston-controlled ports.

(c) Opposed-piston 2-cycle engine with piston-controlled ports.

As maximum power is the objective, supercharging is an essential requirement, which also implies the provision of an exhaust-driven turbine. All three engines are therefore considered to be equipped with both these items.

Clearly, it will not be possible to explore the potentialities of these three types of engine in more than the broadest possible terms, but there are certain fundamental factors involved which will safely permit the basic trends to be deduced.

BASIS FOR PERFORMANCE COMPARISONS

Primary Requirement. Before any assessment of development possibilities can be made as related to the three types of engine considered, it is necessary to establish a basis on which performance computations can be made. As pointed out previously, this resolves itself mainly into a problem of air supply, the various factors involved in this problem being summarized later.

Air Required for Combustion. Chemically each pound of fuel consumed requires 15 lb of air for its complete combustion, that is, the theoretical ideal air/fuel ratio by weight is 15/1. In practice the minimum air/fuel ratio which can be used is about 20/1. This refers to the air trapped in the cylinder and available for combustion which may be referred to as "trapped air/fuel ratio" R_t .

Relation Between Air Trapped in Cylinder and Total Air Flow:

(a) *4-cycle engines.* In the 4-cycle engine burned gases are expelled by piston movement. With moderate supercharge and careful selection of valve-opening periods it is possible to fill about 95 per cent of the total swept volume with air at the temperature and pressure at which air is delivered from the supercharger, the remaining 5 per cent being lost through the exhaust valves.

If the piston diameter is D and the stroke L_{tot} the volume of air trapped in the cylinder per cycle in terms of the cylinder dimensions V_T is

$$V_T = \frac{0.95\pi D^2 L_{tot}}{4} \text{ cu in.} \quad [1]$$

and the total air flow per cycle V_0

$$V_0 = \frac{1}{0.95} V_T = 1.05 V_T \text{ cu in.} \quad [2]$$

Where D is piston diameter (in.) and L_{tot} is piston stroke (in.).

If the trapped air/fuel ratio is R_t , the over-all air/fuel ratio R_0 based on the total air flow for the 4-cycle engine is

$$R_0 = 1.05 R_t \quad [3]$$

or

$$R_t = \frac{R_0}{1.05} \quad [4]$$

(b) *2-cycle uniflow engines.* In the 2-cycle engine the scavenging of burned gases has to be done by the incoming air from the supercharger, and both swept volume and clearance volume are scavenged to some extent. On the other hand, part of the total stroke is sacrificed by the valve or port-opening periods, the remainder being referred to as the effective stroke L_{eff} . The volume made up by the effective stroke plus the clearance volume can be filled with air at supercharge pressures and temperatures to the extent of about 90 per cent, the remainder being lost through exhaust valves. To achieve this it is necessary to pass through the cylinder about 50 per cent more air than can be trapped.

Based upon the foregoing assumptions the volume of air trapped in terms of cylinder dimensions can be derived as follows: If

v = clearance volume, cu in.

r = compression ratio based upon effective stroke

$$V_T = 0.90 \left(\frac{\pi D^3 L_{eff}}{4} + v \right) \text{ cu in.} \dots [5]$$

$$v = \frac{\pi D^3 L_{eff}}{4(r-1)} \text{ cu in.} \dots [6]$$

$$\therefore V_t = \frac{0.90 \pi D^3 L_{eff}}{4} \left(1 + \frac{1}{r-1} \right) \text{ cu in.} \dots [7]$$

The total air flow per cycle V_0 is 50 per cent more than this; i.e.

$$V_0 = \frac{1.35 \pi D^3 L_{eff}}{4} \left(1 + \frac{1}{r-1} \right) \text{ cu in.} \dots [8]$$

In the two-cycle engine therefore

$$R_0 = 1.5 R_t \dots [9]$$

$$R_t = 0.66 R_0 \dots [10]$$

In this paper the effective stroke for the two-cycle engine is assumed to be 78 per cent of the total stroke; i.e.

$$L_{eff} = 0.78 L_{tot} \dots [11]$$

(c) *2-cycle opposed-piston engine.* Based upon the same assumptions as used for the uniflow engine Equations [5] to [11] also apply to the opposed-piston engines, except that in this case L_{eff} is the sum of the effective strokes of the two pistons, which is also taken as $0.78 L_{tot}$.

Relation Between Fuel Consumed and Total Air Flow. If the weight of air W_T trapped in a cylinder is known, and a value is assumed for the trapped air/fuel ratio R_t , the weight of fuel burned per cycle w_f is established

$$w_f = \frac{W_T}{R_t} \dots [12]$$

If the volume of air trapped in the cylinder V_T is known in cubic inches the weight trapped is given by

$$W_T = V_T d \dots [13]$$

where d = weight of air per cubic inch at appropriate temperature and pressure conditions. Therefore

$$w_f = \frac{V_T d}{R_t}$$

$$w_f = \frac{1.05 V_T d}{R_0} \text{ for four-cycle engines.} \dots [14]$$

$$w_f = \frac{V_T d}{0.66 R_0} \text{ for two-cycle engines.} \dots [15]$$

Relation Between Supercharging Pressure and Maximum Cylinder Pressure. As the degree of supercharge applied to a cylinder is increased, it is necessary to take into account a further limitation imposed by practice; namely, the maximum cylinder pressure.

The maximum pressure attained in a cylinder may be taken as a direct function of the pressure at the end of compression. In normally aspirated or unsupercharged engines a compression ratio based on the effective stroke of 18/1 is in common use, this corresponding to a compression pressure of 690 psia. If, therefore, the effective compression ratio in the cylinder is reduced as the degree of supercharge is increased so that the compression pressure remains at a constant value of 690 psi, it may be assumed that the practical limitations on maximum cylinder pressure will not be exceeded.

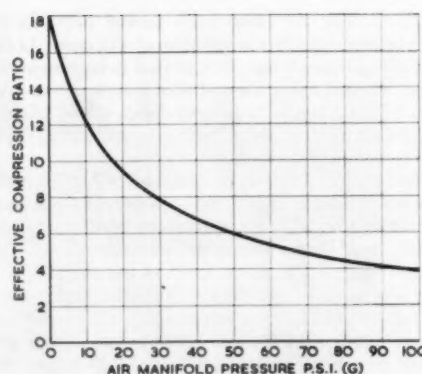


FIG. 4 VARIATION OF EFFECTIVE COMPRESSION RATIO WITH AIR MANIFOLD PRESSURE

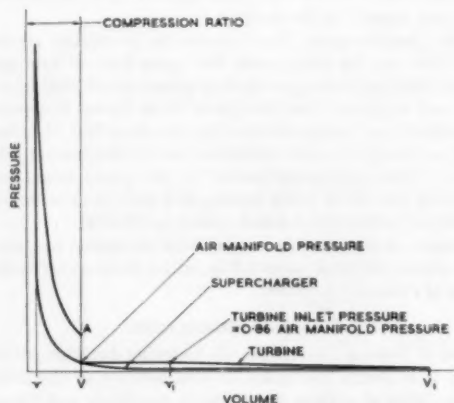


FIG. 5 ASSUMED INDICATOR DIAGRAM

A curve showing the relationship between supercharge pressure and effective compression ratio in the cylinder to achieve a constant value of 690 psi at the end of compression is shown in Fig. 4.

The Operating Cycle. The theoretical indicator diagram, showing the operating cycle used for performance computations, is shown in Fig. 5. For simplicity it is assumed that the compression and expansion ratios in the cylinder are equal and that the turbine-inlet pressure is 0.86 of the supercharging pressure. The position of line AV is variable depending upon the supercharge pressure, the compression pressure in the cylinder remaining constant.

Heat Converted Into Useful Work in Engine Cylinder. Theoretically the maximum proportion of the total heat released by combustion of the fuel which can be converted into work is given by the well-known formula for "air standard efficiency"

$$E = 1 - \left(\frac{1}{r} \right)^{\gamma-1} \dots [16]$$

where

E = air standard efficiency

r = expansion ratio

γ = ratio between specific heats

In practice it is found possible to achieve only about 72 per cent of the figures given by the formula, the resulting figures which

may be said to express the indicated thermal efficiency (E_{ind}) being plotted in Fig. 6 for varying expansion ratios.

From the figure for indicated thermal efficiency must be subtracted that proportion of the heat which is absorbed in friction and driving auxiliaries, the remaining figure being the brake thermal efficiency (E_{brake}), which expresses the proportion of the total heat which can be used as brake horsepower.

A graphical heat-balance diagram can be drawn as in Fig. 7.

For any particular proportion of the total fuel heat from the heat balance, horsepower may be derived as follows:

Let x = proportion of total fuel heat

$$\text{Heat units} = xw_f CV \text{ Btu/cycle}$$

where CV = calorific value of fuel Btu/lb

$$= xw_f CV \times 778 \text{ ft-lb/cycle}$$

$$\text{HP} = \frac{xw_f CV \times 778}{33,000} \times \text{cycles/min} \dots \dots \dots [17]$$

Alternatively the HP per cubic inch of cylinder is

$$\text{HP/cu in.} = \frac{xdCV \times 778}{R_0 \times 33,000} \times \text{cycles/min} \dots \dots \dots [18]$$

Proportion of Total Heat Absorbed by Supercharger. The work done per cycle in the supercharger expressed in heat units is

$$\text{Mass flow} \times \text{temperature rise} \times C_{p(\text{air})} \text{ Btu/cycle}$$

$$C_{p(\text{air})} = \text{specific heat at constant pressure} = 0.241 \text{ for air}$$

$$= W_0 \times \text{temperature rise} \times 0.241 \text{ Btu/cycle}$$

$$= w_f R_0 \times \text{temperature rise} \times 0.241 \text{ Btu/cycle}$$

The total heat in the fuel per cycle

$$= W_f \times CV \text{ Btu}$$

The proportion of the total heat absorbed in driving the supercharger is therefore

$$\frac{w_f R_0 \times \text{temp rise} \times 0.241}{w_f CV} = \frac{R_0 \times \text{temp rise} \times 0.241}{CV} \dots \dots \dots [19]$$

The temperature rise can be obtained from normal adiabatic formulas and is

$$\text{Temperature rise} = \frac{\text{intake temp} \times (r_s^{\frac{\gamma-1}{\gamma}} - 1)}{\text{adiabatic efficiency of supercharger}} \dots [20]$$

where

$$r_s = \text{pressure ratio} = \frac{\text{delivery pressure}}{\text{intake pressure}}$$

$$\gamma = 1.40 \text{ for air}$$

Curves showing the air-delivery temperatures T_{sup} and the weights of air per cubic inch d for varying supercharger pressures and three values of adiabatic efficiency are drawn in Fig. 8, and the proportion of the total fuel heat absorbed in driving the supercharger for four values of R_0 in Fig. 9.

The Turbine: (a) *Turbine-inlet temperature.* Here it is necessary to specify another practical limitation, for with the best modern materials the maximum turbine-inlet temperature which can be used is about 2000 F abs. This figure is assumed to apply for the purpose of this paper.

From the heat-balance diagram the proportion of the total fuel heat rejected in the exhaust is known and equals $1 - (E_{ind} + \text{heat to coolant})$. This quantity of heat is contained in the total

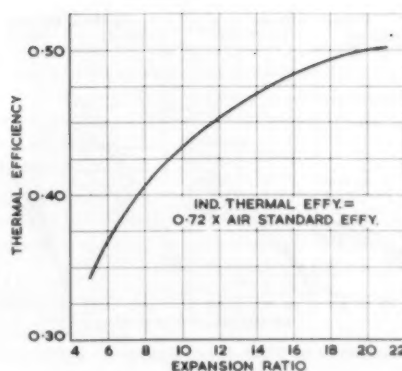


FIG. 6 VARIATION OF INDICATED THERMAL EFFICIENCY WITH EXPANSION RATIO

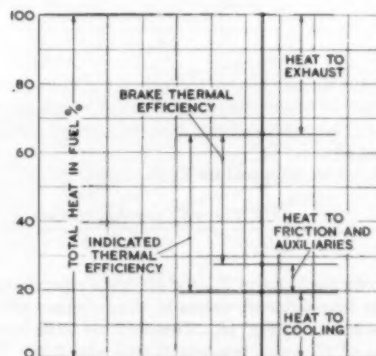


FIG. 7 TYPICAL HEAT-BALANCE DIAGRAM

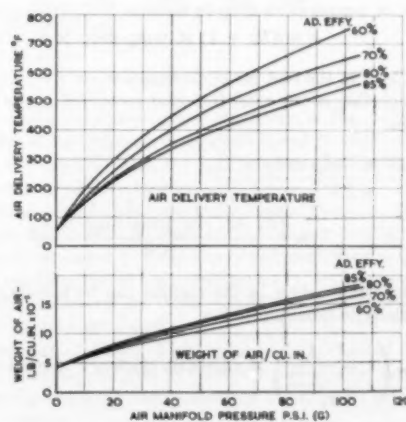


FIG. 8 SUPERCHARGER DATA

mass flow leaving the cylinder; that is, the total mass of air and fuel and equals $w_f(R_0 + 1)$.

The temperature rise from manifold temperature to exhaust temperature is therefore

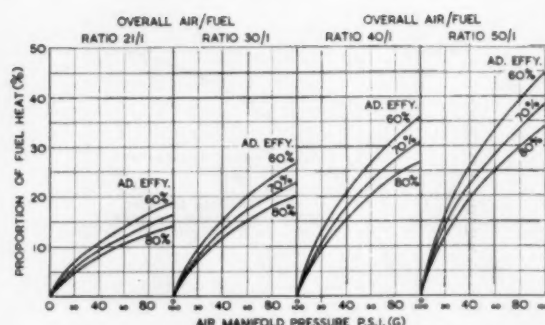


FIG. 9 PROPORTION OF FUEL HEAT ABSORBED IN DRIVING SUPERCHARGER

$$\frac{w_f CV}{C_p} \frac{1 - (E_{ind} + \text{heat to coolant})}{w_f (R_0 + 1)} = \frac{CV}{C_p} \frac{1 - (E_{ind} + \text{heat to coolant})}{(R_0 + 1)} \dots [21]$$

where C_p = the specific heat of the gas at constant pressure.

To this must be added the temperature at which air enters the cylinder; i.e., the supercharging temperature as obtained from the preceding section.

The turbine-inlet temperature T_{tur} is therefore

$$T_{tur} = T_{sup} + \left(\frac{CV}{C_p} \frac{1 - (E_{ind} + \text{heat to coolant})}{R_0 + 1} \right) \dots [22]$$

Curves showing the value of T_{tur} for different supercharging pressures and for four different values of R_0 and three adiabatic efficiencies are shown in Fig. 10. These curves have been plotted using values of C_p lying between 0.2465 and 0.288 depending upon the gas temperature and the value of R_0 .

(b) *Proportion of total heat recovered in turbine.* The work done per cycle in the turbine expressed in heat units is

$$\text{Mass flow} \times \text{temperature drop in turbine} \times C_p \text{ Btu/cycle} = w_f (R_0 + 1) \times \text{temp drop} \times C_p \text{ Btu/cycle}$$

The total heat in the fuel per cycle equals $w_f \times CV$ Btu.

The proportion of the total fuel heat recovered in the turbine is therefore

$$\frac{w_f (R_0 + 1) \times \text{temp drop} \times C_p}{w_f CV} = \frac{(R_0 + 1) \times \text{temp drop} \times C_p}{CV} \dots [23]$$

The temperature drop in the turbine can be calculated from normal adiabatic formulas and is

$$T_{tur} \left(1 - \frac{1}{r_t^{\gamma-1}} \right) \times \text{adiabatic efficiency of turbine} \dots [24]$$

When r_t = expansion ratio across turbine

$$= \frac{\text{turbine-inlet pressure}}{14.7}$$

For the purpose of this paper the turbine-inlet pressure is taken to be 86 per cent of the supercharging pressure, the adiabatic efficiency of the turbine is taken as 85 per cent and γ varies over

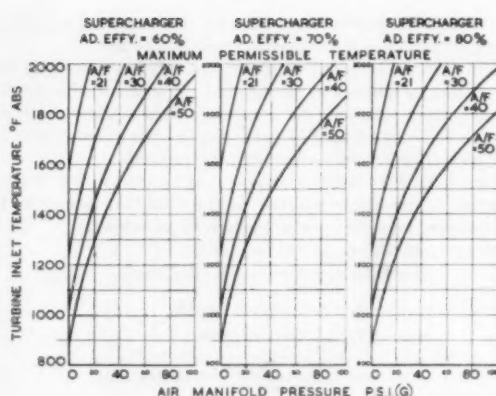


FIG. 10 TURBINE-INLET TEMPERATURE FOR VARIOUS AIR-MANIFOLD PRESSURES

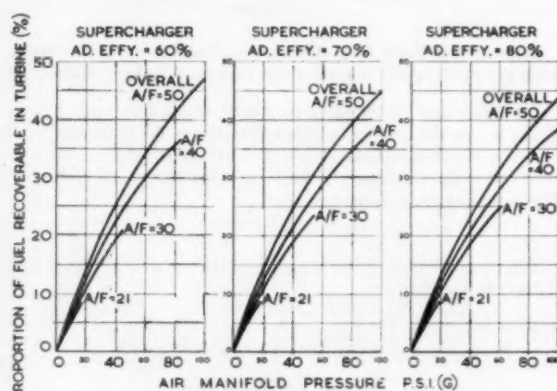


FIG. 11 PROPORTION OF FUEL HEAT RECOVERABLE IN TURBINE

the range 1.292 to 1.355. Curves showing the proportion of the total fuel heat recoverable in the turbine for various supercharging pressures and four over-all air/fuel ratios and three adiabatic efficiencies are given in Fig. 11.

PERFORMANCE COMPARISONS

Utilization of Fuel Heat. Having indicated the methods used, it is now possible to embark upon some performance assessments for actual cylinder designs.

As a first step a series of composite heat-balance diagrams may be constructed for various degrees of supercharge. It has been shown that the compressor and turbine are affected by the over-all air/fuel ratio and it is therefore necessary to evaluate separate diagrams for each air/fuel ratio. Four such examples are drawn, for ratios of 21/1, 30/1, 40/1, and 50/1, and these are shown in Fig. 12.

Basically these diagrams are applicable to all three types of engine mentioned earlier in the paper, but in fact the 21/1 ratio is applicable only to the 4-cycle engine as its use in the 2-cycle engine would reduce the trapped ratio to below the defined minimum of 20/1. The various steps used in construction of these diagrams are as follows:

- 1 Assess value of expansion ratio in cylinder for the super-

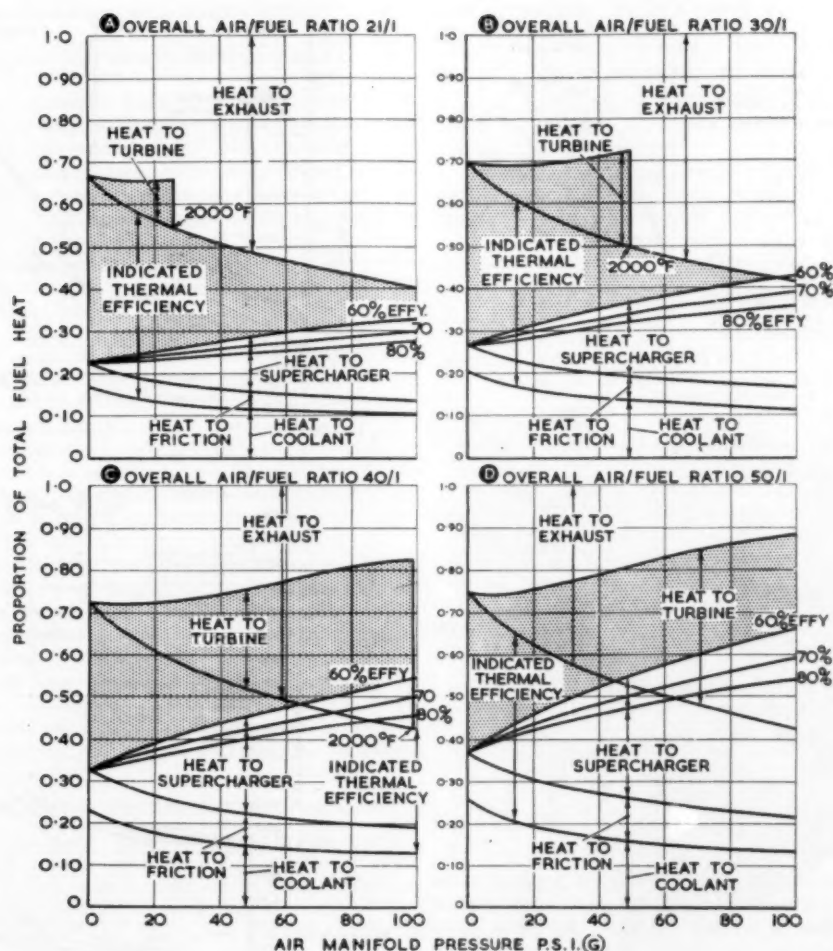


FIG. 12 HEAT-BALANCE DIAGRAMS

charging pressure used from Fig. 4 assuming that compression ratio = expansion ratio.

2 Plot assumed losses to coolant. These figures are based on practical experience and lie between 27.5 per cent of fuel heat for no supercharge, to 10.4 per cent for 100 psi supercharge.

3 Plot values for indicated thermal efficiency for these compression ratios from Fig. 6.

4 Add to coolant losses the assumed friction losses. These also are based on practical evidence and lie between 17.7 and 3.1 per cent over the range of pressures considered.

5 Add losses involved in driving supercharger from Fig. 9.

6 Add heat recoverable from turbine from Fig. 11.

It will be clear that the total proportion of fuel heat available as brake horsepower is

Ind. thermal efficiency - (friction + supercharger) + turbine
The value for this can be read directly off the diagrams.

Potential BHP per Cubic Inch of Cylinder. From the values for fuel heat available as BHP obtained from the heat-balance diagrams, and using the method described under Heat Converted Into Useful Work in Engine Cylinder, it is possible to evaluate the potential BHP per cubic inch of cylinder for both 4-cycle and

2-cycle engines. These figures are drawn in Fig. 13, all engines operating at the limiting crankshaft speed of 2200 rpm. These curves are terminated at the points where the limiting turbine-inlet temperatures are reached.

Practical Limit to BHP per Cubic Inch of Cylinder. The extent to which the potential power outputs shown in Fig. 13 can be practically achieved in cylinders of different sizes is determined by the resulting piston temperatures and it is therefore necessary to devise a method by which piston temperatures in various cylinders can be compared.

Assessment of Piston Temperature: (a) *Thermal loading on piston.* The thermal load to which the piston is subjected may be assessed by the mean temperature in the cylinder during the expansion stroke

$$= \frac{\text{peak temperature} + \text{exhaust temperature}}{2}$$

The peak temperature T_p in the cylinder is compounded of the temperature at end of compression and the temperature rise due to combustion

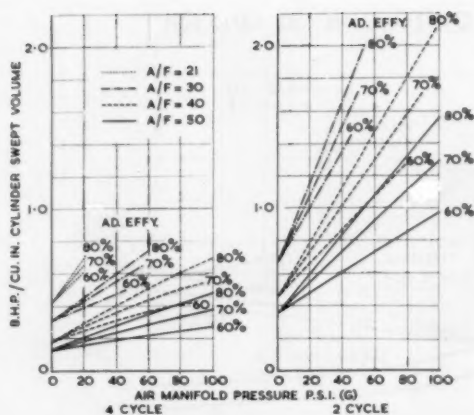


FIG. 13 BHP OBTAINABLE PER CUBIC INCH OF SWEEP VOLUME

$$\therefore T_p = T_{sup} r^{n_c-1} + \frac{CV}{C_s(R_t + 1)} \quad [25]$$

The temperature at which gases leave the cylinder (T_{ex}) is

$$T_{ex} = T_p \left(\frac{1}{r} \right)^{n_c-1} \quad [26]$$

and the thermal load comparator is therefore

$$\frac{T_p + T_{ex}}{2} = \frac{\left(T_{sup} r^{n_c-1} + \frac{CV}{C_s(R_t + 1)} \right) \left(1 + \left(\frac{1}{r} \right)^{n_c-1} \right)}{2} - 460 \text{ F.} \quad [27]$$

(b) *Piston temperatures.* The temperatures attained under the influence of the thermal loadings imposed depends on the ability of the piston to conduct heat away, the piston crown reaching an equilibrium temperature at which the heat lost balances the heat received. Other things being equal, the cooling effectiveness of various sizes of piston may be assessed by the factor (heat-input area)/(heat-loss area).

For the purpose of this paper all the pistons compared are assumed to be of the same design and dimensionally similar, all dimensions bearing a fixed relationship to the diameter. The cooling effectiveness of all pistons will therefore be equal and the mean temperature of the crown will depend only on the thermal-loading comparator given in Equation [27].

$$\therefore \text{Mean } T_{pist} = K \text{ (comparator given in Equation [27])} \quad [28]$$

where K is a constant which for oil-cooled aluminum pistons has a value based on practical evidence of 0.215, which has been used for this paper.

There is, however, a difference in the temperature distribution across the crown for pistons of different diameters, owing to the temperature gradient imposed by the conductivity of the material, this producing a different relationship between mean and maximum temperatures. If the temperature gradient is assumed linear from the center of the crown to the circumference and equal to k deg F per in., it can be shown that the maximum temperatures in the center of the crown will be

$$\text{Max } T_{pist} = \text{mean } T_{pist} + 0.3kD \quad [29]$$

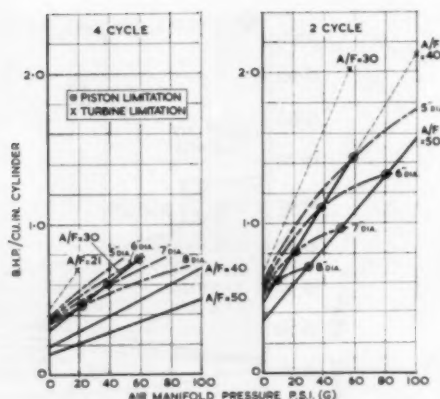


FIG. 14 BHP PER CUBIC INCH FOR LIMITING PISTON TEMPERATURE

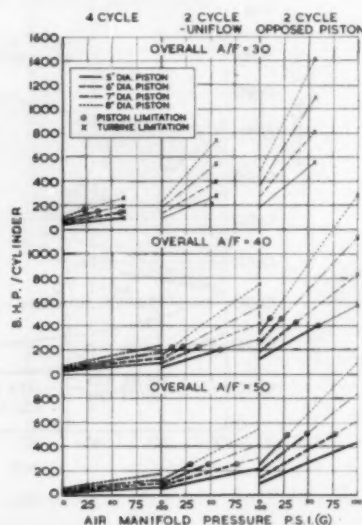


FIG. 15 BHP PER CYLINDER FOR VARIOUS PISTON DIAMETERS

The value of k for aluminum pistons appears to be about 60 deg F per in. The maximum temperature in the center of the crown, assuming a constant value for CV of 18,500 Btu/lb is therefore

$$\begin{aligned} \text{Max } T_{pist} \\ = K \left\{ \left[\frac{\left(T_{sup} r^{n_c-1} \right) + \frac{18,500}{C_s(R_t + 1)}}{2} \right] \left[1 + \left(\frac{1}{r} \right)^{n_c-1} \right] - 460 \right\} \\ + 20D \quad [30] \end{aligned}$$

The values taken in the foregoing formula in the paper are

$$n_c = 1.33 \quad n_s = 1.17$$

c_s varying between 0.219 and 0.261 depending upon gas temperature and air/fuel ratio.

This "Chatterton factor" for piston temperature may not be universally applicable, as different values for k and K will apply to pistons of different designs and materials. In the author's ex-

perience the values calculated are valid for aluminum, oil-cooled pistons.

In the comparisons which follow the limiting value for maximum T_{pist} is taken as 800 F.

Actual Powers Obtainable. From the data now available it is possible to evaluate the actual power obtainable from cylinders of different volumes with varying ratios of stroke to bore.

To bring comparisons onto a practical basis a range of cylinder diameters has been explored for the three basic designs. All cylinders operate at 2200 crankshaft rpm and have a total piston stroke of 7.0 in. giving a piston speed of 2560 fpm. For these fixed factors, cylinders of 5, 6, 7, and 8-in. bore have been evaluated by the foregoing methods for each cylinder design, the results being shown in Figs. 14 and 15.

Fig. 14 is a replotted of the figures from Fig. 13 and shows the BHP/cubic inch obtainable from each of the four cylinder diameters for the same limiting piston temperature. For simplification only the 80 per cent supercharger-efficiency case has been shown on this diagram.

This diagram shows clearly that the BHP/cubic inch of cylinder which can be used increases as the manifold pressure and the over-all air/fuel ratio are raised and that the smaller piston at any manifold pressure is capable of higher outputs than the larger piston.

Fig. 15 shows the BHP usable per cylinder for the various piston diameters and it will be observed that at any air/fuel ratio it is possible, by increasing manifold pressure, to extract as much power from the 5-in.-diam cylinder as from the 8-in. without increasing the piston temperature.

With the smaller piston with high manifold pressure and air-fuel ratios it also will be seen that the limitation imposed by the piston temperature more nearly coincides with that imposed by the turbine, this giving a more balanced cycle with consequent minimum specific weight.

DEDUCTIONS FROM PERFORMANCE COMPUTATIONS

Four Cycle or Two Cycle? The results plotted in Figs. 14 and 15 show conclusively that, in spite of its economy in the use of air, the four-cycle engine cannot compete on the basis of BHP per cubic inch of cylinder with the two-cycle engine.

Uniflow or Opposed Piston? The figures illustrated in Fig. 15 show that, because of its small piston diameter in relation to cylinder volume, the opposed-piston cylinder is able to produce higher powers for a given cylinder diameter than the uniflow engine for the same piston temperatures.

Supercharger Efficiency. The results plotted in Fig. 13 and the heat-balance diagrams of Fig. 12 demonstrate the very considerable influence exerted on the final power output by the efficiency of the supercharger, particularly when high degrees of supercharge are used. For high manifold pressures therefore an axial-flow supercharger may be regarded as essential.

Turbine Power. The heat-balance diagrams of Fig. 12 show that the turbine is capable of producing more power than is absorbed by the supercharger. To take full advantage of this excess power the turbine must therefore be geared back into the engine output, thus forming a "compound" engine.

In the free-running turbocharger the turbine power is limited to that demanded by the supercharger, this involving sacrifices in total power output.

Power Increase Possible. Fig. 14 shows that using a piston of 5-in. diam the BHP/cubic inch can be increased by supercharging to three times the value at zero manifold pressure with no increase in piston temperature.

Fuel Economy. The heat-balance diagrams of Fig. 12 show that the increased power resulting from increased supercharge

and air/fuel ratio can be achieved with very little sacrifice in specific fuel consumption.

CONCLUSIONS RELATIVE TO OBJECTIVES

From the deductions of the preceding section it is possible to derive the following conclusions relative to the objectives of this paper:

(a) The greatest possibility for reduction of engine size and weight is offered by a highly supercharged two-cycle engine compounded with a turbine driving an axial-flow compressor.

(b) The cylinder layout which offers the greatest potentiality for such development is the opposed-piston design.

DESIGN LAYOUT OF COMPLETE ENGINE

The Napier "Deltic" Engine. The conclusions just derived still leave the engine designer with the problem of producing a me-

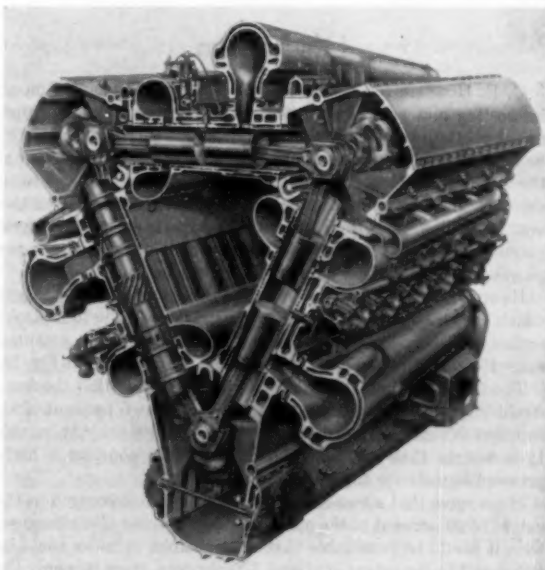


FIG. 16 PICTORIAL CROSS SECTION OF "DELTAIC" ENGINE

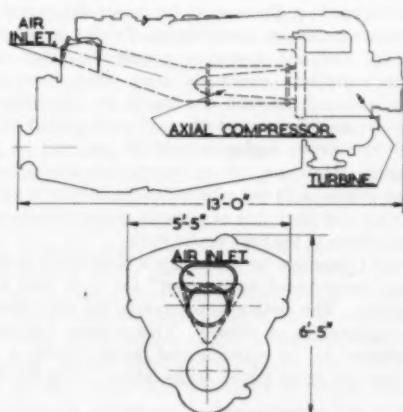


FIG. 17 COMPOUND "DELTAIC" ENGINE

chanical layout which will permit the merits of the compound arrangement to be exploited successfully.

An interesting solution is the one with which the author is associated, the Napier "Deltic" engine, which employs opposed-piston cylinders arranged in the form of a triangle, as shown in Fig. 16. This arrangement overcomes most of the technical objections to the opposed-piston layout. Furthermore, the space between the cylinders provides room for an axial-flow compressor, the complete compound engine being very compact, as shown in Fig. 17, and weighing only about $2\frac{1}{4}$ lb/BHP for an output of 5500 BHP.

ACKNOWLEDGMENT

The author expresses his thanks to the Board of Directors of D. Napier & Son Limited for permission to present this paper and also to his colleagues who helped in its preparation, particularly to Mr. C. A. Wood-Collins, without whose help the paper could not have been written.

Discussion

C. E. HOLVENSTOT.² The author is to be commended on an interesting and careful analysis of the turbocompound engine, based on the use of both the four-stroke piston engine and the two-stroke uniflow piston engine for the high-pressure portion of the cycle. The Napier Deltic engine is certainly eloquent testimony of the general soundness of the conclusion drawn from this analysis. The conclusion is that the two-stroke uniflow compound engine lends itself to the development of high output per pound of weight and per cubic foot of space occupied.

However, the writer disagrees with two points of the analysis which account for the apparent poor showing of the four-stroke engine. History has not shown the great difference in potential output between two and four-stroke engines indicated in Fig. 13.

The first objection is to the author's assumption that the four-stroke engine is not scavenged (or at best a mere 5 per cent of air supplied is permitted to be "lost" through the exhaust valve). It is certain that no modern designer would consider a high-pressure four-stroke engine without scavenging.

If we agree that a two-stroke cylinder can be scavenged to the extent of 90 per cent of the effective swept volume plus clearance, then it would be reasonable that a four-stroke cylinder could be scavenged to the extent of almost 100 per cent, since it is only the clearance space that needs cleaning. The swept volume is scavenged by positive displacement. Also, there is no reason why the scavenged four-stroke engine should not handle 150 per cent of the trapped air, the same as the two-stroke engine.

To illustrate the effect of scavenging, Table 1 is based on definite cylinder size and operating conditions, since numerical values are sometimes easier to grasp than formulas. The arithmetic is straightforward and based on the author's data. Note the last line shows that the potential output of the unscavenged four-stroke engine is only 38 per cent of the two-stroke engine. However, the scavenged four-stroke engine has a potential output of 71 per cent of the two-stroke engine. It is the writer's belief that this is a much more realistic appraisal of the capabilities of the four-stroke cycle.

The second objection to the author's methods is in his use of the same "thermal-load comparator" for both two and four-stroke pistons. The method is to average the peak temperature and the temperature at release. This average temperature is then multiplied by an experimental factor having a value of 0.215 to give the mean piston temperature. This factor appar-

TABLE 1 PERFORMANCE CALCULATIONS FOR THREE SPECIFIC ENGINE TYPES

Type of engine cycle	Two-stroke scavenged	Four-stroke unscavenged	Four-stroke scavenged
Cylinder diam, in....	5	5	5
Stroke, in.....	7	7	7
Swept volume, cu in...	137.6	137.6	137.6
Effective stroke, per cent.....	78	100	100
Effective swept volume, cu in.....	107.4	137.6	137.6
Assumed blower efficiency, per cent....	80	80	80
Supercharger pressure, psig.....	60	60	60
Effective compression ratio.....	5.3	5.3	5.3
Clearance volume, cu in.....	25.0	32.0	32.0
Effective swept volume plus clearance, cu in.	132.4	169.6	169.6
Manifold density, pci.	0.00013	0.00013	0.00013
Trapped volume, cu in.	119.0	130.6	169.6
Over-all air/fuel ratio.	40	40	40
Fuel per cycle, lb.....	0.00058	0.000447	0.000827
Thermal efficiency (Fig. 6), per cent...	35	35	35
Less friction (Fig. 12), per cent.....	-7	-7	-7
Less blower work @ 80% eff. (Fig. 9), per cent.....	-20	-20	-20
Plus turbine work @ 80% blower eff. and 85% turbine eff. (Fig. 11), per cent..	27.5	27.5	27.5
Net conversion of fuel to work, per cent...	35.5	35.5	35.5
Power cycles per minute.....	2200	1100	1100
Power per cu in. swept volume, calculated hp.....	1.435	0.553	1.02
Check on foregoing value from Fig. 13..	1.45	0.52	...
Power per cu in. swept volume, comparison, per cent.....	100	38	71

ently accounts for the fact that during scavenge and compression the piston top is exposed to considerably lower temperatures than the thermal-load-comparator temperature. There can be no objection to this procedure, since it seems to correlate experimental data on pistons of a given design and within certain ranges of size and operating conditions. However, the writer is sure the valid operating conditions do not include both two-stroke and four-stroke cycles, and particularly not a scavenged four-stroke cycle.

At the completion of the power stroke, during blowdown, the gas remaining in the cylinder undergoes an adiabatic expansion with a very marked drop in temperature. This occurs whether the cycle is two-stroke or four-stroke, but in the latter case, the piston is exposed to this reduced temperature during the entire exhaust stroke. Then the intake stroke exposes the piston to an even lower temperature for an appreciable period of time. It seems certain that the four-stroke piston would run cooler than the two-stroke piston under the same gas temperatures at peak and release. Table 2 shows some temperatures calculated according to the author's methods, and for the same operating conditions assumed previously for illustration.

The thermal-load comparator according to the method of the paper is 3340 F for the two-stroke engine. No attempt has been made to define a thermal-load comparator for the scavenged four-stroke engine. However, note that the exhaust-stroke gas tem-

² Engineer, Gas and Diesel Engineering Department, Ingersoll-Rand Company, Painted Post, N. Y.

TABLE 2 SOME TEMPERATURE CALCULATIONS FOR TWO SPECIFIC ENGINE TYPES

Type of engine cycle	Two-stroke scavenged	Four-stroke scavenged
Blower disch temp, deg F abs.....	900	900
Temp at end of compression, deg F abs.....	1560	1560
Temp rise during combustion, deg F.....	$\frac{18,500}{0.24[(40/1.5) + 1]}$ = 2780	2780
Peak temperature, deg F abs.....	4340	4340
Temp at end of expansion, deg F abs.....	$4340(1/5.3)^{1.17-1}$ = 3260	3260
Thermal-load comparator, deg F.....	3340	..
Mean piston temperature, deg F.....	718	..
Max piston temperature, deg F.....	818	..
Cyl pressure at release, psia.....	..	$(60 + 14.7)3260/900$ = 280
Back pressure after release, psia.....	..	$0.86(60 + 14.7)$ = 64.2
Expansion ratio during blowdown.....	..	$280/64.2 = 4.36$
Cylinder gas temp after blowdown, deg F abs.....	..	$3260(1/4.36)^{(1.3-1/1.5)}$ 2320
Average of temperatures at peak, release, exhaust, and intake, deg F.....	..	2015

perature is 2320 - 460 or 1860 F and the intake-stroke gas temperature is 900 - 460 or 440 F. The time-average of the four-stroke-cycle temperatures must be lower than for the two-stroke cycle.

A further beneficial effect, not evident in the calculated temperatures themselves, is the piston-cooling obtained from the powerful scrubbing action of the scavenge air in certain four-stroke engines. Especially in designs where inlet-port shape gives a "fire-nozzle" jet directed spirally down onto the piston to scour it and force gases up and out the exhaust valve, the four-stroke scavenging has an effectiveness in cooling the piston which cannot be matched in any method of two-stroke scavenging. The four-stroke clearance space is filled and emptied several times by the scavenge air, whereas the two-stroke cylinder (swept volume plus clearance) is filled only slightly more than once. Thus the four-stroke cylinder is not only scavenged much cleaner, but the conditions for heat transfer from the piston top are much better (high velocity and mass flow rate).

The net result of lowering the piston-temperature limitation is to bring still closer together the potential output of the four-stroke and two-stroke engines. One of the interesting facets of modern engineering technology is the strong competition between two-stroke and four-stroke engines, on nearly equal footing, in so many fields. Despite the sometimes fierce partisanship of their adherents, and the fundamental differences between the engines, we must admit that with equal development the two-stroke and four-stroke engines are pretty close in performance.

It is not meant to imply that Napier has made any but the correct choice in the selection of the operating cycle for the "Deltic" engine. It is meant to imply that it was not an easy choice.

A. W. HUSSMANN.³ In these days, when there seems to be no glamor left in anything but atomic or gas-turbine power plants or, at least, free-piston engines, it is gratifying, indeed, to have one of the authority of the author discuss the future of such a seemingly obsolete thing as the diesel engine. The case for the high-speed engine as shown in the application of the Napier-Deltic engine to locomotive and marine propulsion is certainly convincing, and the comparison with the low-speed ship engine is surely overwhelming.

The writer wishes to add a few remarks considering another field of widened application for the future high-speed diesel—that of the truck and tank engine. Particularly for military application the possibility of designing multifuel diesel engines

to digest a wide range of fuels becomes more and more important. Such developments as the M-combustion system for multifuel operation and turbocharging or turbocompounding four and two-stroke-cycle engines open up new fields for the diesel engine. Following the same analysis which the author has shown, we came to the same result; namely, that the engine with the highest power output for the smallest bulk and lowest weight will be a turbocharged, and possibly turbocompounded, two-stroke cycle engine. Multifuel engines of the 200-hp class with a weight ratio of less than 4 lb per hp are possible and are under development.

The author mentions as one of the limitations to increased power output the engine speed. In a discussion to one of the papers presented at the last diesel meeting of the SAE in Chicago, Mr. Klinge of Continental showed a slide with a most interesting statistic. He had plotted for a large number of naturally aspirated and turbocharged engines of various sizes the maximum smoke-free bmep against engine speed and could show that the obtainable mean effective pressure decreased about linearly with the absolute engine speed (not piston speed or $D \times N$ factor). Engines above the author's limit of 2500 rpm are, of course, possible and even commercially available, but it is obvious that we have to pay an increasingly higher price in the form of decreasing mep.

The author's mathematical analysis leads to some truly startling results. There may be a question or even a doubt here and there in the assumptions made. Such doubts are quickly dispelled by such authoritative statements as: Practical evidence has shown that the constants have such and such value. We feel, therefore, that we are on safer ground than if the analysis had been made by a college professor. However, the writer would still like to ask the author whether there is practical evidence for the startling result that it should be possible to extract as much power from a 5×7 -in. cylinder as from an 8×7 -in. cylinder; that is, from a cylinder of $2\frac{1}{4}$ times the displacement.

Qualitatively, the analysis makes a strong case for a fairly long stroke engine which is in agreement with experimental results reported by Caterpillar at the last SAE Diesel meeting.

In Fig. 15 of the paper the power output per cylinder is shown with the limitations for various piston diameters for the four-stroke cycle and the uniflow and opposed-piston two-stroke-cycle engine. The horsepower per cylinder of the OP engine was shown as double that of the uniflow engine, a fact which was explained as being due to the small piston diameter in relation to the cylinder volume. Actually, the reason is simply that the OP-engine cylinder is, in fact, a double cylinder. The power output per unit swept volume and, therefore, roughly per unit bulk of the

³ Professor of Engineering Research, Pennsylvania State University, University Park, Pa.

engine is the same for the uniflow and the OP engine as, of course, was assumed for the analysis. This is mentioned only because a superficial glance at Fig. 15 may mislead one in the belief that the OP-engine per se had the higher power capacity.

ISRAEL KATZ.⁴ The author makes a strong case for the high-speed diesel engine and focuses our attention on several influential factors that set early limits to the attainment of high power output at high speed; namely, the reduction of volumetric efficiency, difficulties with fuel-injection equipment, piston overheating, and excessive piston speeds. However, before the piston can be overheated the necessary heat must be released in the cylinder. Thus the supply of sufficient air to the cylinder is the decisive factor at present and will so remain well into the foreseeable future.

In arriving at the noteworthy conclusion that the opposed-piston configuration shows the greatest promise for the development of turbocompounded high-speed high-performance diesel engines, he compares the merits and anticipated performance capabilities of high-speed opposed-piston two-cycle engines having piston-controlled ports against comparable four-cycle poppet-valve engines and uniflow two-cycle engines having exhaust poppet valves and piston-controlled inlet ports. However, it is surprising that in making this comparison he neglects the turbocompounded loop-scavenged engine. Only two years ago the author and his colleague, Herbert Sammons, enthusiastically described the loop-scavenged Napier Nomad at the SAE summer meeting. The Napier Nomad seems to be a remarkable turbocompounded, two-cycle, 12-cylinder, high-speed diesel aircraft engine that can match the performance capabilities of the opposed-piston types. Because we are speaking here about high-speed diesel engines in general, it would be interesting to learn the author's views concerning the loop-scavenged engine as a competitive type.

Some of us who follow engine developments have been intrigued by the power and economy potentialities of turbocompounded two-stroke-cycle machines. Those who conjure up various schemes for realizing these potentialities, time and again, have postulated configurations similar to that of the Deltic engine. Considering that a certain aircraft engine with 28 cylinders has been quite popular in recent years and that very-highly developed engines with 36 and 42 cylinders also have been built, a cylinder arrangement involving 6 pistons per row and three crankshafts to accomplish tertiary opposed-piston action should not frighten us. But a question arises whether the obvious and obscure complexities of this configuration are justified by performance advantages over the simpler loop-scavenged engines. It should be borne in mind that the loop-scavenged diesel engine is far from being a dead issue.

About 8 years ago Col. A. A. Ambrose, USAF, while doing graduate work at Cornell under the writer's direction, developed a 7-cylinder radial aircraft engine that was mid-cylinder-port loop-scavenged and operated on a two-stroke Otto-cycle. He was able to demonstrate that, with appropriate supercharge, careful design of the inlet and exhaust ports, and proper choice of piston speed, it is possible to reduce substantially the weight-power ratio and mechanical complexity of an engine without sacrificing economy. It also was clear that the same engine could have been run successfully as a diesel, with minor modifications and addition of a high-pressure fuel-injection system. A portion of this work is described in the discussion of a paper by Schweitzer and Tsu.⁵

⁴ Consulting Engineer, Advanced Electronics Center, General Electric Company, Ithaca, N. Y. Mem. ASME.

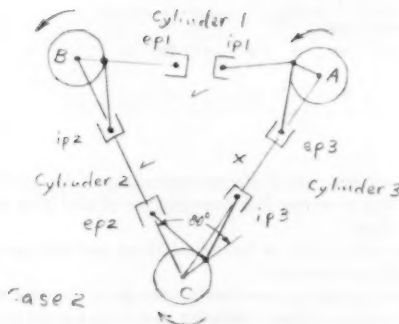
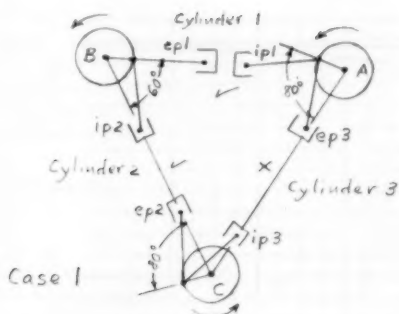
⁵ Israel Katz discussion of "Energy in the Engine Exhaust," by P. H. Schweitzer and T. C. Tsu, Trans. ASME, vol. 71, 1949, pp. 668-669.

In addition to indicating that the turbocompounded high-pressure loop-scavenged engine also merits most serious considerations as a promising high-speed diesel, the writer would like to comment on two other pertinent items: The first of these items concerns the relative timing between cylinder scavenging and charging events. In a loop-scavenged engine the timing of scavenging and charging events, normally a function of port geometry and crankshaft speed, remains inflexible unless auxiliary valves of some sort are operated in the exhaust system. With opposed-piston engines, however, the designer has considerable latitude by virtue of varying the linear extension of the ports and arranging a phase shift between the exhaust-port control and inlet-port control pistons. A common practice is to have the exhaust-port control piston lead the inlet-port control piston by as much as 12 deg of crankshaft travel. This much lead not only permits the cylinder gases to blow down to a pressure level below the supercharge pressure without gas blowback, but also allows the pressure of the fresh cylinder charge to approach the inlet-manifold pressure when the exhaust ports are closed before the intake ports are covered. The over-all gain is that, by careful phasing of the pistons, it is possible to trap a greater mass of air in an opposed-piston cylinder than in any other comparable two-cycle cylinder. But, while it appears from the sectional view of the Deltic engine that piston phasing may be present, it is curious that the author has not mentioned the matter and that his mathematics relating to effective cylinder displacement neglect this very important aspect of opposed-piston-engine action.

The writer makes special mention of this point because designs of opposed-piston engines with more than one cylinder per crankplane usually involve rigid, often unfavorable, piston phasing and crankshaft-vibration limitations. For example, unless there is a gimmick, which is not evident from the artist's representations and which the author has not seen fit to discuss either in his written or oral descriptions, in the Deltic configuration, all crankshafts must turn in the same direction and all exhaust-port control pistons must lead their respective inlet-port control pistons by 60 deg. This inflexible lead angle seems excessive, although lead-angle requirements usually increase as the crankshaft speed is raised, but in this case any departure from the directional and piston-phase requirements would make engine operation impossible. Also, only two firing orders are available; an unrealistic one where the three cylinders in each crankplane would fire simultaneously, and a realistic one where one cylinder would fire every 120 deg of crankshaft rotation. The arrangement of alternate inlet and exhaust-port control pistons around the engine seems like a wonderful idea until the transverse loading of the crankshaft is examined. With the sequence of inlet and exhaust ports around the engine shown (which, incidentally, is the only practical sequence), the crankshaft vibration may well be prohibitive. To understand this conclusion it is necessary to realize that even with a 12-deg phase angle between exhaust and intake control pistons, the intake-port control piston converts only about 25 per cent of the cylinder's indicated work. With a 60-deg phase lag the same piston could convert little or no energy, yet it would impose severe load fluctuations on the crankpin shared with the exhaust-port control piston of the adjacent cylinder.

(During the author's oral closure, he indicated that the Deltic engine's lead angle was 20 degrees and not 60 degrees as suggested by the writer. By use of the illustration below, the writer demonstrates that, on the basis of information given in the paper, the lead angle cannot be 20 degrees.

Case 1, where crankshafts A, B, and C all turn in the same direction: If the exhaust piston (epl) in cylinder number 1 leads the intake piston (ipl) in cylinder 1, then ip2 must be 60 degrees past its top center position because the fixed angle between all



cylinder banks is 60 degrees. Thus ep2 must be $60 + 20 = 80$ degrees after its top center position and ip3 will be $80 + 60 = 140$ degrees past its top center position. But, since ep3 is $60 + 20 = 80$ degrees before its top center position, ip3 should be only 60 degrees before its top center position. However, because ip3 actually is $360 - 140 = 220$ degrees before its top center position, there is a discrepancy in cylinder 3 of 120 degrees.

Case 2, where any one of the three cranks (such as C) turns in an odd direction: All pistons, except ip3, could be in the same positions relative to each other as above. However, ip3 would be only 20 degrees after its top center position. Thus, ip3 would lead ep3 by an angle of 100 degrees, whereas it should lag ep3 with an angle of 20 degrees.)

Another point is concerned with the writer's inability to arrive intuitively at the same conclusions regarding the striking effects of piston diameter, air/fuel ratio, and choice of engine action upon the power/displacement ratio at which the author does by methods of analysis. The writer makes no claim for extraordinary intuitive insight, but must state emphatically that the author's conclusions clash with the writer's experiences.

For example, the writer cannot persuade himself to believe that Equation [16], which is the underlying premise of the author's analysis, is applicable to the diesel engine. It is the writer's belief that the equation applies only to a nonsupercharged engine, utilizing constant-volume combustion and an expansion ratio equal to its compression ratio, whose peak cycle pressure occurs only at the top center position of the piston and whose pump-loop work, however achieved, is zero. The writer will readily admit that in practice the combustion processes in a high-speed diesel engine may occur during little volume change, but the other numerous practical deviations from the ideal render even a meticulous analysis of a complex cycle a crude approximation of real events.

A properly designed and operated turbosupercharged diesel engine usually achieves its peak economy at the design point. Departures from design-point operation introduce increasingly severe penalties in performance. This characteristic property arises from the diesel engine's requirement for a relatively fixed weight of trapped air per cylinder cycle to obtain compression ignition; the high heat losses through the combustion-space surfaces at low speeds, because of the extended residence time and the engine's relatively high compression ratio, and the consequent large surface/volume ratio of the combustion space; and the need for a high convertible energy content in the exhaust at all operating conditions to implement the supply of sufficient scavenge and supercharge air.

Thus, to raise the power level of an engine above its design-point value, it is necessary to increase the supercharge pressure, but is also necessary to increase the rate of fuel injection. Since the higher supercharge does not come cheaply, the power requirements of the turbine place an early limit on engine-power output. This fact is particularly pertinent to engines with small cylinders because a greater portion of the cylinder's initial convertible energy must be extracted to run the turbine.

It is the writer's belief that a thorough examination of factors relevant to the design of high-speed turbosupercharged diesel engines would disclose the following facts:

1 For any given combination of supercharge and compression pressures, the effective compression-ratio requirement of small-cylinder engines is substantially greater than that of large-cylinder engines.

2 At each particular combination of manifold pressure and piston speed, there is a unique optimum air/fuel ratio. Moreover, the air/fuel ratio at fixed speed must be decreased with increase of manifold pressure in order safely to raise the power/displacement ratio of the engine.

3 To realize the promising performance capabilities of the turbocompounded opposed-piston engine, the phase lag of the inlet-port control piston must be continuously variable as a function of engine load and speed. Furthermore, the supercharge pressure will be critically related to the phase lag and thereby introduce a complicated control relationship.

4 For any given peak continuous-power requirement, there probably is a unique optimum combination of cylinder arrangement, cylinder size, and crankshaft speed. Thus it is conceivable that multicylinder opposed-piston engines with moderate cylinder dimensions could be optimum over a given narrow power and speed regime, but it would be a gross error to say that the opposed-piston configuration is ideally suited to all high-speed two-cycle diesel-engine applications.

RALPH MILLER.⁶ The author shows the potential output per cubic inch of two and four-cycle engines much to the disadvantage of the latter (Figs. 13, 14, and 15 of the paper). In actual practice the most advanced designs of high-output two and four-cycle engines, such as we see operating in diesel locomotives in great numbers, show 0.193 and 0.194 hp per cu in. for uniflow and opposed-piston two-cycle engines, respectively, and 0.225 hp per cu in. for four cycle. A high-output four-cycle engine recently developed for the United States Navy rated at 4500 hp does 0.253 hp per cu in. It is operating on the Miller supercharging system.

This condition is the result of three factors which adversely affect the output of the two-cycle engines.

1 The necessary practice of operating two-cycle engines at about 75 per cent of four-cycle piston speed.

⁶ Consulting Engineer, Nordberg Manufacturing Company, Milwaukee, Wis. Mem. ASME.

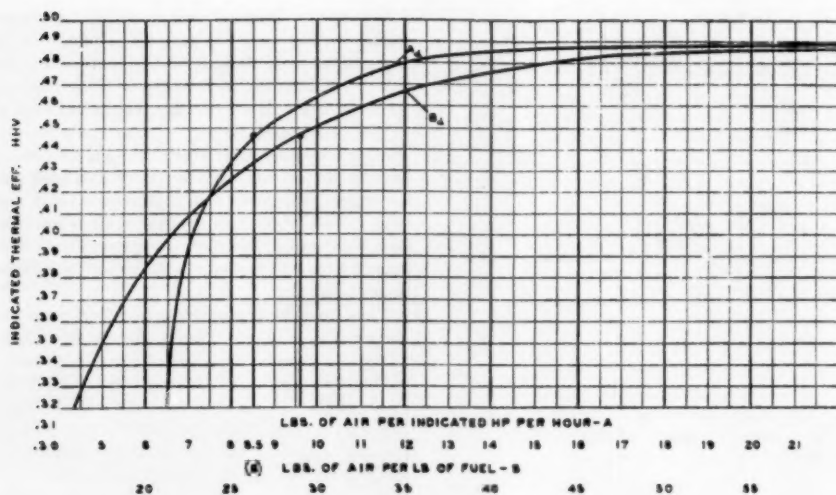


FIG. 18

2 The loss of effective stroke in the two-cycle engine corresponding to the height of the scavenging port.

3 The scavenging efficiency being only about 85 per cent or less compared with 100 per cent for the supercharged four-cycle engine.

The effect of lower piston speed is seen in the equation

$$HP = \frac{PLAN}{33,000}$$

The effect of loss of effective stroke and low scavenging efficiency is seen in the equation

$$P_i = \frac{37,150 \times P_2^{0.73} P_{mf}^{0.28} E_{sc}}{(R-1) T_{mf} W} \dots \dots \dots [31]^*$$

where

- P_i = mean indicated pressure, psia
- P_2 = compression pressure, psia
- P_{mf} = air-manifold pressure (four-cycle), psia
- P_{mf} = pressure at beginning of compression (two-cycle), psia
- E_{sc} = scavenging efficiency, per cent
- R = compression ratio (piston displacement + clearance volume/clearance volume)
- T_{mf} = temperature scavenging or supercharging air, deg R
- W = pound of air per ihp per hr

The Deltic engine operating at 2000 rpm and 2500 bhp develops 0.465 bhp per cu in. The bmep is 92.5 psi with a probable imep of 120.

With the compression pressure limited to 690 psia, as stated, and an effective compression ratio of 14, the pressure at beginning of the compression will be about 15 psia. This is obtained with an air-manifold pressure of about 5 psig (see Fig. 4).

With an assumed scavenging efficiency of 0.90 and a compression ratio of 16 based on the full piston stroke, we have

$$\begin{aligned} \text{Pounds of air per ihp/hr} &= W \\ &= \frac{37,150 \times 690^{0.73} \times 15^{0.28} \times 0.9}{120 \times 16 \times 590} = 6.9 \end{aligned}$$

Fig. 18 of this discussion shows 42 per cent thermal efficiency

* See Appendix for development of Equation [31].

at this air quantity per ihp/hr corresponding to an air-fuel ratio of 22.5. The resulting fuel consumption should then be about 0.4 lb per bhp/hr.

Will the author tell us how close these calculations come to actual engine performance?

While compounding promises a very great increase in power output, it is nevertheless interesting to see what could be done by operating the engine on the Atkinson cycle, pressure-charged by an exhaust-gas-driven turbocharger to 30 lb gage pressure (the Miller supercharging system).

By intercooling to 100 F, maintaining the compression pressure at 690 psia and retaining the same clearance volume, we have

$$P_i = \frac{37,150 \times 690^{0.73} \times 45^{0.28} \times 0.9}{16 \times 560 \times 6.9} = 172 \text{ psi}$$

and

$$BHP = 4000$$

It will be noted that the effective compression ratio is 7.25.

The Atkinson cycle is accomplished in the opposed-piston engine by phasing the exhaust and scavenging-piston cranks to reduce effective compression ratio but maintaining normal expansion ratio. Starting and light-load operation requires progressively increasing compression ratio with decreasing load. The mechanism needed to carry out these functions of variable compression and expansion ratios is difficult in the opposed-piston engines, but quite simple in the types A and B shown in Fig. 3.

APPENDIX

Development of Equation [31]

Pounds of air per hour in cylinder charge = W_c

$$W_c = \frac{(V_c N) 60 (P_2 \times 144)}{53.3 T_2}$$

where

V_c = clearance volume, cu ft

$$= \frac{AL}{R-1}$$

where

A = piston area, sq ft

L = stroke, ft

R = compression volume ratio (piston displacement + clearance volume/clearance volume)

N = number of power strokes/min

P_2 = compression pressure, psia

T_2 = compression temperature, deg R = $T_{mf} \left(\frac{P_2}{P_{mf}} \right)^{\frac{n-1}{n}}$

where

T_{mf} = manifold temperature, deg R (temperature of scavenging or supercharging air)

P_{mf} = air-manifold pressure, psia

n = compression exponent (assume 1.39)

Then

$$W_c = \frac{(ALN) 60 (P_2^{0.73} P_{mf}^{0.28}) 144}{53.3 (R - 1) T_{mf}}$$

$$\text{Lb of air/ihphr} = W = \frac{W_c}{\text{IHP}}$$

Hence

$$\text{IHP} = \frac{(ALN) 60 (P_2^{0.73} P_{mf}^{0.28}) 144}{53.3 (R - 1) T_{mf} W}$$

Also

$$\text{IHP} = \frac{P_i LAN}{33,000}$$

Therefore

$$\begin{aligned} P_i &= \frac{(ALN) 60 (P_2^{0.73} P_{mf}^{0.28}) 144 \times 33,000}{(LAN) 144 \times 53.3 (R - 1) T_{mf} W} \\ &= \frac{37,150 P_2^{0.73} P_{mf}^{0.28}}{(R - 1) T_{mf} W} \text{ for 100 per cent scavenging} \\ &= \frac{37,150 P_2^{0.73} P_{mf}^{0.28} E_{sc}}{(R - 1) T_{mf} W} \end{aligned}$$

where E_{sc} = scavenging efficiency.

AUTHOR'S CLOSURE

Before attempting to comment on the individual contributions to the discussion the author would like to make a general statement which he feels has a bearing on practically the whole discussion.

Any diesel engineer will readily appreciate the difficulty which confronts an author in attempting to make comparisons between basic performance possibilities of engines of different types. It is necessary to make assumptions which are reasonably valid for each type considered and which make no allowances for the individual characteristics demonstrated by particular engines which must reflect the skill of their designers and their ability to interpret, in practical form, the inherent potentialities. Some oversimplification is therefore unavoidable, but the author was careful to ensure that, as far as possible, the assumptions made were valid and that the conclusions drawn in the paper would not be affected in substance, even if in degree, by any errors in the assumptions made. For example, Mr. Holvenstot and Mr. Ralph Miller are obviously of the opinion that the performance possibilities of the 4-cycle engine, as demonstrated in the paper, are lower than they should be and that for various reasons such engines can approach more closely to those

obtainable from the 2-cycle opposed-piston engine. This may well be so, but it is a fact that the Deltic compound cylinder is operating at a brake mean effective pressure of 190 psi and piston speed of 2,416 ft per min with a cylinder bore of 5 1/4 in. To obtain equal power per cubic inch of swept volume it would be necessary for the 4-cycle engine to operate at 380 psi and, as far as is known, no 4-cycle engine has so far obtained such an output. It is felt, therefore, that the author's claim for the superiority of the opposed-piston 2-cycle design from this particular point of view is substantiated even if the gap between the 2-cycle and the 4-cycle engines is not so great as indicated in the paper. In short, the author considers that his conclusions are valid even if the relative orders of merit are not exactly those which have been derived.

Turning now to individual contributions, the following comments are offered:

C. E. Holvenstot disagrees with two points of my analysis—the potential power of the 4-cycle cylinder and, second, the thermal load comparator.

Dealing with the first point, I feel it would be possible to question some of Mr. Holvenstot's premises. For example, if the valve overlap is increased to provide scavenging of the order suggested surely there will be some loss of stroke, just as in the 2-cycle engine. For this, and other reasons, I do not feel that the figure of 71 per cent of the 2-cycle output shown in Table 1 will be achieved, but even if it were, the validity of the conclusions reached in the paper is not affected.

With regard to the "thermal load comparator," I cannot agree that this should be different for 2-cycle and 4-cycle engines. In any given period of time the total duration of exposure of the piston to hot and cool gas will be essentially the same in both cases, and the cooling due to gas scrubbing occurs just as much in the uniflow or opposed piston 2-cycle as in the 4-cycle engine. I would probably agree that for "the same gas temperature at peak and release" the 4-cycle piston might run cooler, but for equal power outputs the heat release in the 4-cycle must be double that of the 2-cycle and under these conditions the 4-cycle would show no advantage.

It would seem that what Mr. Holvenstot is suggesting is that the mean temperature of the whole operating cycle would provide a better comparator. This sounds logical enough and is indeed the comparator which I first used when compiling the paper. Unfortunately however, results worked out on the basis of this did not prove to bear any relation to piston temperatures obtained in practice, either on 2-cycle engines or such 4-cycle engines for which data were available. The only comparator explored which gave reasonable correlation with practical results was that used in the paper.

A. W. Hussman's remarks are interesting. He agrees with the conclusions arrived at but clearly doubts the quantitative orders of merit of the various types of engines considered. He asks the question whether there is practical evidence to support the conclusion that a 5-in. \times 7-in. cylinder with a manifold pressure of 80 psi(g) can produce as much power as an 8-in. \times 7-in. cylinder with a manifold pressure of 20 psi(g) for the same limiting piston temperature.

I should say there is some evidence to support this. Piston temperature tests as between a 6-in. piston (Nomad) and the 5 1/4-in. piston of the Deltic show a relationship between piston diameter and temperature agreeing with that derived by the method shown in the paper, and while there is considerable extrapolation from a 6-in. piston to one of 8 in. there can be little doubt that the 8-in. piston will be more difficult to cool than the 5-in. and will therefore reach its limiting temperature at a lower cylinder output. In the absence of any better method of predicting the piston temperature reached under various operating

conditions I am prepared to stand by the method given in the paper which, though admittedly not based on sound theoretical reasoning, does appear to agree with a large number of practical tests.

Israel Katz understandably enquires why no reference was made in the paper to the "loop-scavenged" engine. There is a very good reason for this; the 4-cycle, uniflow 2-cycle, and opposed-piston designs referred to in the paper are well defined basic types which can be discussed without much fear of misunderstanding. The term loop-scavenge on the other hand covers a large variety of porting arrangements and its inclusion in the paper would have led to a great increase in its complexity. Furthermore, the paper is concerned mainly with a study of potential cylinder performances, and while the loop-scavenged engine may possess the merit of mechanical simplicity it is difficult to see that any improved performance can be claimed for it relative to the uniflow arrangement.

It is quite true, as Mr. Katz points out, that in the Nomad engine, described at the SAE Summer Meeting in June, 1954, some very high cylinder performances are obtained but this resulted from several years of research and development devoted mainly to porting and scavenging problems. There is no doubt that these problems, at least at high manifold pressures, are much more difficult in the loop-scavenged cylinder than in the uniflow or opposed piston types.

The reason why the loop-scavenge system was used in the Nomad was that it was designed as an engine for aircraft propulsion and low specific weight was an essential and primary requirement. An opposed-piston engine with two crankshafts would have been heavier and bulkier and clearly the triangular arrangement of the Deltic would not have been applicable. The uniflow arrangement would also have compared unfavorably on the grounds of weight and space occupied.

The second major question raised by Mr. Katz refers to the phase difference between exhaust and inlet crankshafts in the Deltic engine. This point was not dealt with in detail in the paper as fairly complete technical information on this matter had been given in a previous paper to the SAE (The Napier Deltic Diesel Engine, November, 1955). Let me again assure Mr. Katz that the phase difference in the Deltic is indeed 20 deg. Furthermore, because each crankpin carries one inlet and one exhaust piston the torques at each crankpin are identical, this being one of the important advantages of the triangular cylinder arrangement, which makes his fears on crankshaft loadings and vibrations quite unfounded. The problem here therefore is not to prove the demonstrated fact that the Deltic has a phase difference of 20 deg but to explore where Mr. Katz has gone astray in his geometrical analysis. It is not necessary to look very far. If he will reverse the rotation of the two top

crankshafts in his "Case 1" diagram leaving everything else unaltered or, alternatively, if he will interchange the labels of all the inlet and exhaust pistons in his "Case 2" diagram he will easily satisfy himself that the phase difference is 20 deg.

It is agreed that Equation [16], for the ideal air standard efficiency, does not strictly apply to a highly supercharged diesel engine in which some combustion will occur slightly after the dead center position. In the paper however, this equation has been taken as an indicator of the ideal possible achievement and it is difficult to see how its use in this manner can be criticised.

Mr. Katz' later remarks appear to be related to a turbocharged engine in which the turbocharger is not coupled to the engine, in which case his arguments may apply. If the turbocharger is mechanically coupled to form a compound engine the power requirements of the turbine place no limit on the power output of the engine; economy may suffer but it is still possible to obtain enhanced power.

Ralph Miller attempts to develop a general case that the 4-cycle engine is capable of developing more power than the 2-cycle for various reasons. After referring to a high output 4-cycle engine operating on the Miller system which develops 0.253 horsepower per cubic inch he then proceeds to demonstrate that the mechanically blown Deltic (without turbocharging) produces 0.465 horsepower per cubic inch, which makes his argument rather difficult to follow. The compound Deltic cylinder has already demonstrated over 1.00 bhp per cubic inch.

Referring to the numbered paragraphs used in the development of his argument I would say first that it is difficult to find evidence based on published data that it is the practice to run 2-cycle engines at 75 per cent the piston speed of 4-cycle engines. It is difficult to see any reason for this.

Secondly, the loss in effective stroke of the 2-cycle engine is admitted and is an inherent factor in the cycle. It applies also to the 4-cycle engine when extended valve overlaps are used.

Thirdly, the scavenging efficiency of 85 per cent is far too low for any respectable 2-cycle engine. We normally assume 90 per cent for calculation purposes but know from experimental data that up to 95 per cent is obtainable in practice.

With reference to Mr. Miller's calculations relative to the Deltic, there are errors in his figures and these do not relate to the curves of Fig. 18, but he has arrived at a reasonable answer. The actual designed air/fuel ratio (trapped) is 25/1 and the fuel consumption at full power is 0.40 lb/bhp/hr.

The performance of an opposed-piston engine at 30 psi(g) supercharging pressure at 40/1 over-all air/fuel ratio from Fig. 15 is 4,500 hp from 18 cylinders, which compares with the 4,000 hp for the Atkinson cycle calculated by Mr. Miller. It is not possible to check his calculations due to the differences between his equations and the curves of Fig. 18.

Analysis of a Process-Fluid-Flow Network by Electrical Analogy

By C. F. KAYAN¹ AND J. A. BALMFORD,² NEW YORK, N. Y.

In a process-fluid-flow network of numerous interconnected branches of different proportions, the determination of the flow distribution by calculation is difficult because of the pressure-drop versus flow-rate characteristics of each individual component of the complex. Not only does the pressure drop vary with the effective pipe dimensions and surface condition, for a given fluid, but also markedly with the flow rate, and usually, in turbulent flow, with flow rate modified by some exponent with value on the order of 2.0. The concept of flow "resistance," to represent opposition to fluid flow, is a useful tool. The pressure drop in any process branch line may be considered as proportional to the product of the flow rate and the pipeline resistance, and for turbulent flow the resistance itself may be considered a function of the flow rate. Thus the flow characteristics of a network may be simulated by electrical analogy, with the electrical resistance in each branch simultaneously adjusted to some desired function of the electrical current. Voltage and current determinations at given points are representative of the corresponding fluid pressure and flow rates. An illustrative process-plant network with numerous branches and discharge points is analyzed, with predictions of flow distributions and pressures.

INTRODUCTION

PREDICTION of flow distribution in a multibranched process-fluid-flow network proves difficult because of the non-linear character of the flow process when its nature is, as generally, turbulent in character. Especially disturbing is the determination of pressure distribution when fluid discharges at various remote points in the system are to be accounted for. Mathematical, graphical, and other procedures are fraught with many discouraging difficulties.

The identification, in a network, of a fluid-flow "bottleneck" with large restrictive pressure drops, may prove rather laborious in usual orthodox procedures so that improvement in computing techniques offers a welcome prospect. Going beyond fluid flow as such, the electrical analogy computer procedures subsequently discussed are applicable equally well to other "flow-network" problems, such as heat transfer in its different ramifications. It is of course recognized that the method of electrical analog analysis has hitherto been applied to a variety of heat-flow problems; reference may be made to some different steady-state studies on variegated problems in this field by one of the authors (1-7).³ It

is, however, to be pointed out that in these prior studies by electrical analogy, the flow processes in general were represented by linear relationships, with flow rate varying directly with the strength of the motivating forces. Other solutions of fluid-flow networks also have been undertaken hitherto, among the most noteworthy being that of Camp and Hazen (8) using an electric-network analyzer with resistances adjusted stepwise to an ultimate solution; next the "relaxation" method of Cross (9) involving extended and laborious iteration; and then that of Mellroy (10) employing network resistances having some selected characteristics depending on current flow, in this way tending to simulate line behavior.

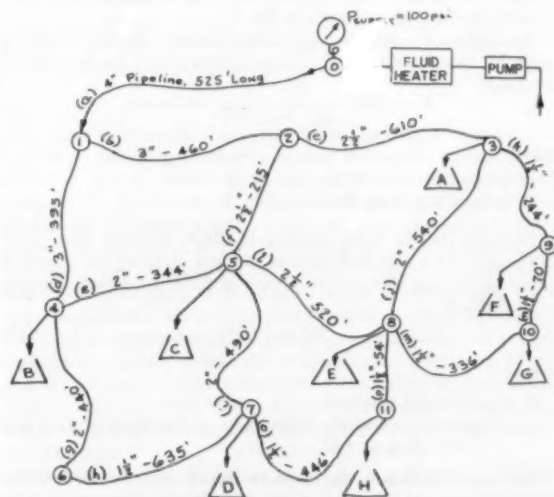


FIG. 1

The present problem is best understood in terms of a steady-state process-plant fluid-flow network of many branches and different sizes, Fig. 1. Here hot water is supplied from a central source under specified initial supply pressure for simultaneous distribution of requisite quantities to a number of remotely located process operations.

FLOW OF FLUID IN PIPES AND FITTINGS

In turbulent flow, identified by a characteristic Reynolds number above 2500-3000, the pressure difference across a given length of pipe varies exponentially with the flow rate; for laminar flow at low Reynolds number, the pressure difference varies linearly with the flow rate. Many factors enter into the variation of pressure drop with flow rate, and many investigations have been carried out in this realm not only for liquids, but also for gases and vapors; for practical purposes, reference is made only to several typical studies (11-15), which present general design data. (The choice of appropriate performance data for a given flow channel is not particularly at issue here, since the performance predictions

¹ Professor of Mechanical Engineering, Columbia University; Consulting Engineer, New York. Mem. ASME.

² Professor of Electrical Engineering, Columbia University; Consulting Engineer, New York.

³ Numbers in parentheses refer to the Bibliography at the end of the paper.

Contributed by the Process Industries Division and presented at the Annual Meeting, New York, N. Y., November 25-30, 1956, of THE AMERICAN SOCIETY OF MECHANICAL ENGINEERS.

NOTE: Statements and opinions advanced in papers are to be understood as individual expressions of their authors and not those of the Society. Manuscript received at ASME Headquarters, September 14, 1956. Paper No. 56-A-187.

for a network complex must necessarily depend on the acceptance of the original assumptions of flow characteristics.)

The pressure drop for turbulent pipe flow depends on a number of factors. Foremost is the variation, for a given length, with the flow velocity v , i.e., the flow-rate Q , exponentially

$$\Delta P = f(\rho/144)(v^3/2g)(L/D) \dots \dots \dots [1]$$

where

ΔP = pressure drop, psi

f = friction factor for pipe, depending on Reynolds number Re (i.e., flow rate), size, and surface characteristics of pipe

Re = Reynolds number, dimensionless, $= Dvp/\mu$

D = internal pipe diameter, ft

v = flow velocity, fps

ρ = fluid density, pcf

μ = absolute viscosity of fluid, lb/ft-sec

g = acceleration of gravity, ft/sec²

L = length of pipe, ft

The friction factor f is shown typically as a function of Reynolds number Re in Fig. 2, and the variation of μ with temperature for a typical fluid, such as water, in Fig. 3.

For a given size and length of pipe, Equation [1] may be shown with ΔP as a function of the friction factor f and the flow rate Q squared

$$\Delta P = c(fQ^2) \dots \dots \dots [2]$$

where

c = const

Q = fluid-flow rate, lb/min

With the friction factor varying, in effect, with flow rate, use is often made of a modified form of the flow equation for practical purposes, in connection with a pipe of fixed dimensions passing a given fluid

$$\Delta P = C(Q^x) \dots \dots \dots [3]$$

where

C = specialized constant

x = exponent, variously taken as a value between 1.80 and 1.90, often as 1.85

As noted previously, the pressure drop is quite sensitive to the realized value of the friction factor f , itself so much influenced by the flow rate and surface condition of the duct.

For a given composite pipeline consisting of straight pipe lengths, along with fittings such as couplings, unions, elbows, and tees, plus necessary additions of control valves, there are, consequently, other supplemental causes of pressure drop which are in

addition to the flow through the straight pipe. These are (a) pressure losses owing to entering and leaving conditions on a run, (b) setting up of the effective fluid velocity, and (c) the rather important pressure-drop effects occasioned by the various fittings and other accessories. The last is the most important for any extended pipe runs such as considered here, and therefore deserves primary treatment.

Various approaches are used in evaluating the valve and fitting losses; perhaps the most practical one in use is to consider the

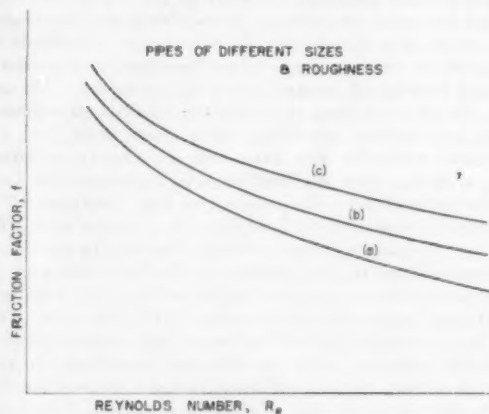


FIG. 2

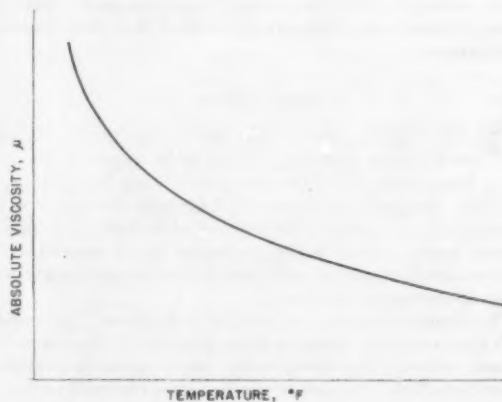


FIG. 3

TABLE 1 L_f FEET FOR STANDARD NOMINAL PIPE SIZES (IPS), IN.

Type of Fitting, etc.	1 1/2	2	2 1/2	3	3 1/2	4
Standard 90° elbow	4.5	5.5	6.2	8.0	10.0	11.0
Standard 45° elbow	2.0	2.5	3.0	3.8	4.5	5.0
Close return bend	10	13	15	18	22	24
Globe valve, open	43	55	67	85	97	110
Gate valve						
3/4 closed	110	135	165	200	250	275
1/2 closed	25	34	40	50	58	68
1/4 closed	5.5	7	8	10	12	14
Fully open	1.0	1.2	1.4	1.8	2.0	2.3
Swing check valve						
fully open	10	14	16	20	22	25

loss equivalent to that occasioned by a given length of straight pipe. Table 1, adapted from Crane (15), shows the typical length values L_f for fittings, and so on, in different pipe sizes (nominal Iron Pipe Size IPS). Thus, equivalent total pipe lengths L_e may be set up, comprised of pipe length L_p and the L_f for the fittings, etc.

$$L_e = L_p + L_f \dots \dots \dots [4]$$

Thus, if a pipe branch of 4-in. standard pipe consists of six 90-deg elbows, 250 ft of straight pipe, and a gate valve $1/4$ closed, the equivalent length L_e would be $L_e = 250 + 6 \times 11 + 14 = 330$ ft of straight pipe, as a good representation of the effective straight-pipe equivalent.

Basing the pressure drop for a given pipeline component on a standard effective length L_e (such as 100 ft), the variation of pressure drop with flow rate will be proportional for other lengths, as shown typically in Fig. 4 as based on Equation [3]

$$\Delta P_{L_e} = \Delta P_{100}(L_e/100) \dots \dots \dots [5]$$

Finally, it should be noted that for a given pipeline exposed to an over-all pressure difference across its extremes, the flow rate Q is the result. Accordingly, the following equation expresses the relationship

$$Q = (\Delta P/C)^{1/2} \dots \dots \dots [6]$$

RESISTANCE CONCEPT OF FLUID FLOW

In terms of Equation [3], $\Delta P = CQ^2$, for a pipe of given dimensions, the pressure drop ΔP as a motivating force may be con-

sidered to overcome a fluid-flow resistance in transporting the fluid at a given rate Q through the flow channel. Thus the equation may be rewritten

$$\Delta P = QR \dots \dots \dots [7]$$

and

$$R = \Delta P/Q = CQ^2/Q = CQ^{-1} \dots \dots \dots [8]$$

It is to be noted, as indicated previously, for liquids such as water, x for turbulent flow usually entails a value between 1.80 and 1.90. Thus, from a curve chosen to represent the ΔP - Q relationship such as depicted in Fig. 4, a corresponding value for resistance R may be developed as a function of Q . Typically the related values are shown in Fig. 5. In this manner use may be made of the concept of resistance in establishing the motivating force for fluid flow in a given channel. This is similar to the application of Ohm's law for electrical circuits, and, correspondingly, for thermal circuits (1-6), and for energy-transport circuits (7). There is, however, one outstanding distinction here: The flow resistance R is not constant, but is variable and specifically a function of the flow rate Q . In fact, it may or may not be a linear function of the flow rate.

As previously indicated, analysis of pipe-network problems has been carried out with the use of resistance, in various manners, by other investigators (8, 10); of particular concern, in the present analysis, has been the recognition of the continuous variation of resistance with flow rate, regularly or irregularly.

SOLUTION BY ELECTRICAL ANALOGY

In general, with the setting up of the "resistance concept" for fluid flow, assuming constant values of resistance, the use of the electrical analogy would be an obvious development; electrical voltage, the equivalent of pressure, and electrical current, the equivalent of fluid-flow rate. However, with dependency of resistance on the flow rate, that is, varying as some function of the flow rate, the problem becomes more complex. Nonetheless, herein it is resolved, in terms of an accepted ΔP - Q curve, through a servo-controlled variable electrical resistance which follows the desired R - Q relationship through an appropriate cam. R is thus varied with the rate of electrical current flow. Utilization of the cam introduces flexibility to cover the particularly required variation of resistance with flow rate, whether regular or irregular, under command of a current-detecting instrument in series with the resistance.

The utilization of the resistance-controlling elements will best be understood by considering their application to the solution of the hydraulic circuit represented in Fig. 1.

ILLUSTRATIVE EXAMPLE

The process-plant hydraulic circuit shown in Fig. 1 is supplied with hot water at 180 F from a pump-and-heater installation at a pressure, at point 0, of 100 psi. The flow-distribution system consists of 16 different interconnected branches (from a to p) of different lengths plus accessory fittings, and pipe sizes (nominal), as indicated in the diagram. At eight locations, points 3, 4, 5, 7, 8, 9, 10, and 11, required discharge rates to process vats A, B, C, D, E, F, G , and H , are to be maintained simultaneously at a minimum pressure of 25 psi. The required discharge rates are listed in Table 2.

Representative ΔP_{100} - Q relationships for 100 ft effective length, conforming to the general evaluation shown in Equation [3], are shown in a logarithmic plot in Fig. 6. These are for pipes in good condition and of different sizes. The relationships are

TABLE 2 REQUIRED DISCHARGES TO PROCESS VATS

Point.....	3	4	5	7	8	9	10	11
Vat.....	A	B	C	D	E	F	G	H
Q, lb/min.....	250	625	800	500	500	300	250	175

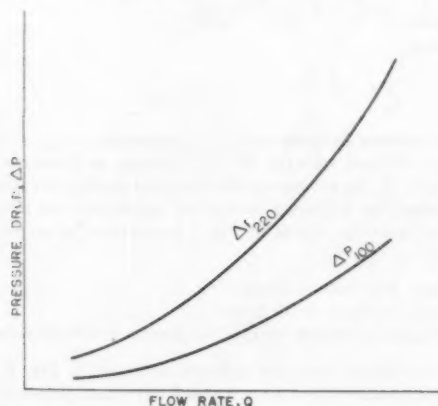


FIG. 4

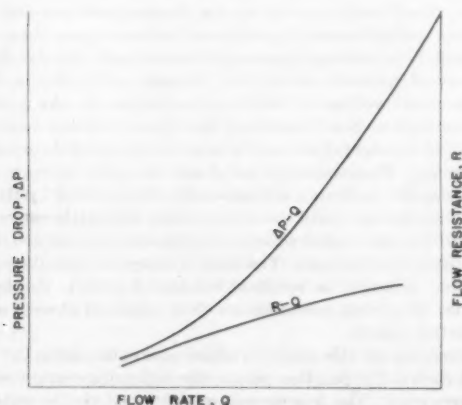


FIG. 5

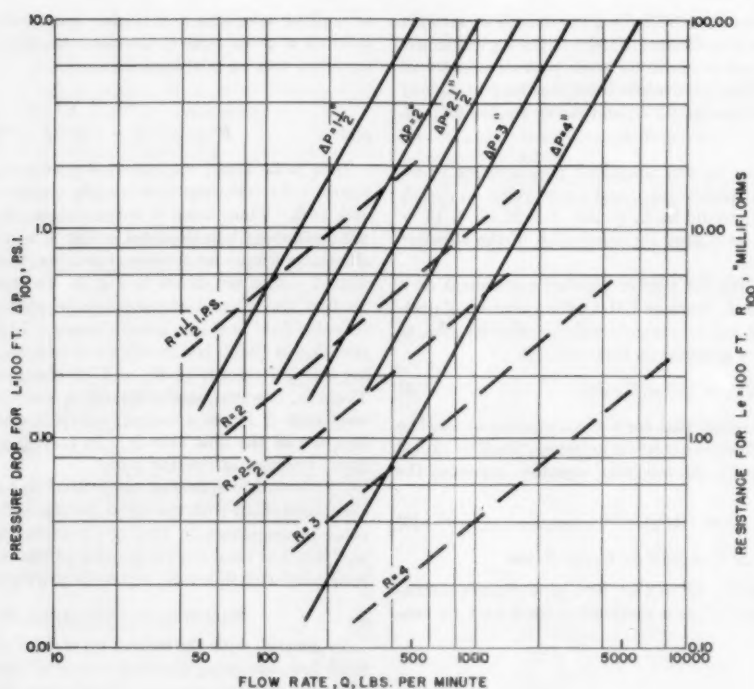


Fig. 6

assumed, for the purposes of the problem, to represent fairly the friction circumstances of the process network. Pressure drop ΔP_{100} is shown in pounds per square inch for a 100-ft length, and flow rate Q in lb/min. In the same figure, equivalent resistance curves $R-Q$ are shown. (In the absence of a standard designation for the unit of flow resistance, for convenience here, as suggested by electrical practice, the term "flohms" is used, where 1 flohm = 1 psi per 100 ft per unit flow rate of 1 lb/min.)

The hydraulic circuit of Fig. 1 is simulated in electrical analogy with each of the 16 branches represented by an automatic control current-measuring instrument, cammed to self-adjust the value of a variable electrical resistance in series with it, in accordance with the desired $R-Q$ relationship. The instrument is equipped

with an ammeter shunt to extend the instrument range and make it directly conform with the $R-I$ requirement, as illustrated typically in Fig. 7. In setting up the electrical analogy for this computer circuit, the following conversion equivalents are employed with the hydraulic circuit of Fig. 1 reproduced as an electrical network:

Voltage: 1.00 volt = 10 psi

Current: 1.00 ma = 50 lb/min

Resistance: 1.00 ohm = 0.000200 flohms = 200 microflohms

The equivalent computer network is shown in Fig. 8. The eight drain points called for in Table 2 have been included. The required drains, representing in effect the output flows of the entire system, are served by adjustable constant-current instruments. Each instrument is set for the requisite amount, and serves to control a variable resistance to the common "low" side or "ground" in meeting its constant-current requirements. Across the over-all network circuit, i.e., between points 0 and 12, a direct-current voltage of 10.00 volts is imposed. As a result, currents tend to flow through all the sixteen different branches, and out of the eight drain outlets to meet the imposed current requirements. Progressively throughout the entire network, each "pipe-branch" resistance is continually self-adjusted by its corresponding current, until the entire system ultimately comes into balance; i.e., the branch resistances adjusted as a function of the resultant branch current. The drain instruments simultaneously maintain, as nearly as resultant conditions permit, the desired outputs. Electrical potentials are then measured at each of the 12 junction points.

In carrying out this study, in addition to determining the voltage at each of the junction points, the indicating current meters also were read. The true current was obtained via the meter indication and the instrument shunt meter calibration. Potential

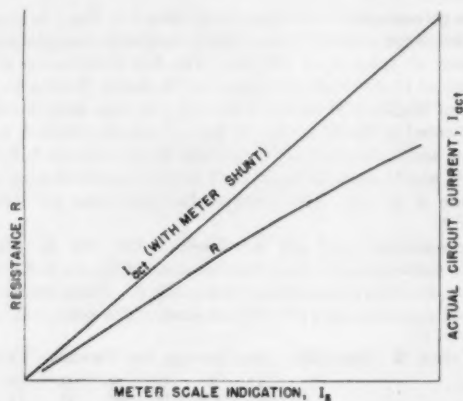


Fig. 7

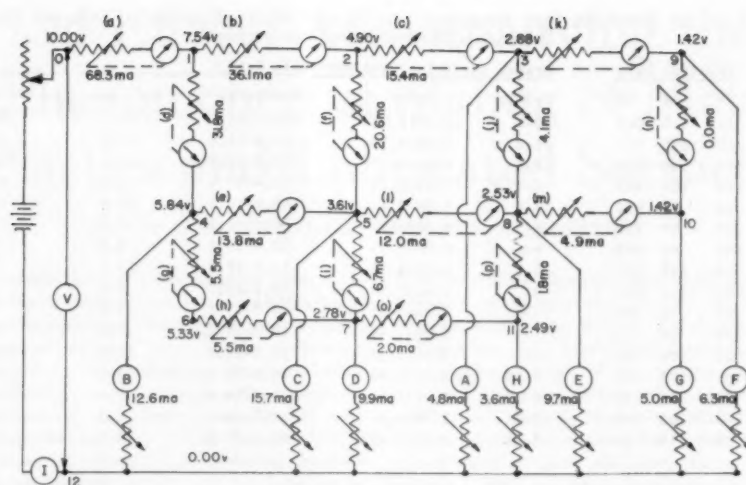


Fig. 8

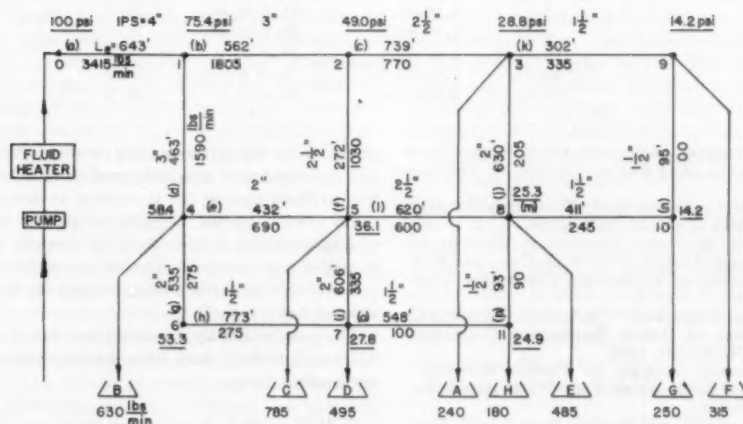


Fig. 9

differences across the ends of each branch line were determined by difference. Equivalent hydraulic data, to cover the resultant performance prediction of the network under the imposed conditions, followed from the electrical data, and are shown, with pertinent branch-line information, in Table 3.

Fig. 9 shows the network hydraulic results, with the pertinent values from Table 3 entered upon it. The indicated drain flows total up to 3380 lb/min versus a total setting value of 3400 lb/min, with small plus and minus discrepancies in the various drain values. It is interesting to note that branch *n*, between points 9 and 10, was useless, passing no flow. The requirement of a minimum of 25 psi at the different drain points was not satisfied completely; whereas point 11, with 24.9 psi for vat *H* is just acceptable; points 9 and 10, for vats *F* and *G*, with 14.2 psi are not acceptable, and network branch sizing must be scrutinized further.

In conclusion, it may be said that the development provides a method for studying the flow and pressure distribution in complex nonlinear systems; its over-all accuracy appears well within the limits of error of fundamental data; and it is readily and eco-

nomically adapted to a wide range of resistance versus current requirements.

ACKNOWLEDGMENT

The authors wish to acknowledge, with grateful appreciation, the support of The Research Corporation, through a grant-in-aid to Columbia University, in making this project possible.

BIBLIOGRAPHY

- 1 "An Electrical Geometrical Analog for Complex Heat Flow," by C. F. Kayan, *Trans. ASME*, vol. 67, 1945, pp. 713-718.
- 2 "Heat Flow and Temperature Analysis of Complex Structures Through Application of Electrical Resistance Concept," by C. F. Kayan, Sixth International Congress for Applied Mechanics, Paris, France, September, 1946.
- 3 "Temperature and Heat Flow for a Concrete Slab With Imbedded Pipes," by C. F. Kayan, *Refrigerating Engineering*, vol. 54, August, 1947, p. 143.
- 4 "Heat Transfer Temperature Patterns of a Multicomponent Structure by Comparative Methods," by C. F. Kayan, *Trans. ASME*, vol. 71, 1949, pp. 9-16.
- 5 "Fin Heat Transfer Analysis by Electrical Analogy," by C. F. Kayan, *Industrial and Engineering Chemistry*, vol. 40, 1948, p. 1040.

TABLE 3 PHYSICAL DATA ON NETWORK PIPE BRANCHES AND DRAIN POINTS; ELECTRICAL ANALOGY DATA, AND ULTIMATE HYDRAULIC PERFORMANCE PREDICTIONS

Pipeline		Physical Data			Branch Electrical and Hydraulic Data					
Branch	Size, in.	L_p	L_r	L_e	Points	Volts	Pressures	ΔP psi	Current, ma	Flow Q
a	4	525	118	643	0-1	10.00-7.54	100.0-75.4	24.6	68.3	3415
b	3	460	102	562	1-2	7.54-4.90	75.4-49.0	26.4	36.1	1805
c	2 1/2	610	129	739	2-3	4.90-2.88	49.0-28.8	20.2	15.4	770
d	3	395	168	463	1-4	7.54-5.84	75.4-58.4	17.0	31.8	1590
e	2	344	88	432	4-5	5.84-3.61	58.4-36.1	22.3	13.8	690
f	2 1/2	215	57	272	2-5	4.90-3.61	49.0-36.1	12.9	20.6	1030
g	2	440	95	535	4-6	5.84-5.33	58.4-53.3	5.1	5.5	275
h	1 1/2	635	138	773	6-7	5.33-2.78	53.3-27.8	25.5	5.5	275
i	2	490	116	606	5-7	3.61-2.78	36.1-27.8	8.3	6.7	335
j	2	540	90	630	3-8	2.88-2.53	28.8-25.3	3.5	4.1	205
k	1 1/2	244	58	302	3-9	2.88-1.42	28.8-14.2	14.6	6.7	335
l	2 1/2	520	100	620	5-8	3.61-2.53	36.1-25.3	10.8	12.0	600
m	1 1/2	336	75	411	8-10	2.53-1.42	25.3-14.2	11.1	4.9	245
n	1 1/2	70	25	95	9-10	1.42-1.42	14.2-14.2	0.0	0.0	00
o	1 1/2	446	102	548	7-11	2.78-2.49	27.8-24.9	2.9	2.0	100
p	1 1/2	54	39	93	8-11	2.53-2.49	25.3-24.9	0.4	1.8	90
Drains										
A					3-12	2.88-0.00	28.8-00.0	28.8	4.8	240
B					4-12	5.84-0.00	58.4-00.0	58.4	12.6	630
C					5-12	3.61-0.00	36.1-00.0	36.1	15.7	785
D					7-12	2.78-00.0	27.8-00.0	27.8	9.9	495
E					8-12	2.53-00.0	25.3-00.0	25.3	9.7	485
F					9-12	1.42-00.0	14.2-00.0	14.2	6.3	315
G					10-12	1.42-00.0	14.2-00.0	14.2	5.0	250
H					11-12	2.49-00.0	24.9-00.0	24.9	3.6	180

6 "Heat Transfer Equipment Analysis by the Resistance Concept," by C. F. Kayan, *Refrigerating Engineering*, vol. 59, 1951, pp. 1195-1199, 1240.

7 "Electrical Analogger Application to the Heat Pump Process," by C. F. Kayan, *Trans. ASHVE*, vol. 59, 1953, p. 361.

8 "Hydraulic Analysis of Water Distribution Systems by Means of an Electric Network Analyzer," by T. R. Camp and H. L. Hazen, Massachusetts Institute of Technology, Cambridge, Mass., Serial No. 110, June, 1935.

9 "Analysis of Flow in Networks of Conduits or Conductors," by Hardy Cross, University of Illinois Engineering Experiment Station, Bulletin No. 286, November, 1936.

10 "Direct-Reading Electric Analyzer for Pipeline Networks," by M. S. McIlroy, *Journal of the American Water Works Association*, vol. 42, April, 1950, pp. 347-366.

11 "A Study of Data on the Flow of Fluids in Pipes," by E. Kemler, *Trans. ASME*, vol. 55, 1933, HYD-55-2, pp. 7-22.

12 "The Flow of Fluids in Closed Conduits," by R. J. S. Pigott, *Mechanical Engineering*, vol. 55, 1933, p. 497.

13 "Piping Design," by William Goodman, *Heating, Piping and Air Conditioning*, vol. 13, March, 1941, p. 145.

14 "Hot Water Heating System Design," by F. E. Giesecke, *Heating, Piping and Air Conditioning*, vol. 13, August, 1941, p. 485.

15 "Flow of Fluids Through Valves, Fittings and Pipe," Engineering and Research Division, Crane Company, May, 1942, Paper No. 409.

Discussion

JOHN EVERETTS, JR.⁴ The authors have presented to industry a valuable tool which greatly reduces the risk inherent in the design of multiterminal fluid-flow systems.

The electrical analog described in this paper handles a difficult design problem with unbelievable simplicity and picks up the inadequacy of conventional design methods as shown by the results of low pressure at points 9 and 10.

In reviewing this paper, it appears that the authors neglected to point out possible important uses for this analog, other than in

design. Can this type of analog be used to take terminal pressures and measured flow quantities and determine actual resistance to flow to check against the theoretical or design values? This also could predict partial clogging of piping and, with preventive maintenance the system could be cleaned, thus eliminating the hazard of a major shutdown due to complete stoppage.

Could this electrical analog be used for low-density fluids such as air or natural gas?

The possibilities appear unlimited and it is hoped the authors will continue their work with this important aid to industry and engineering design.

C. F. HOLSKE.⁵ It is interesting to note that the authors proceeded from heat-flow to fluid-flow problems in this electrical analogy series.

There are many applications for this approach to complex fluid-flow problems in refrigeration, one of the more obvious being the study of brine flow in skating-rink piping networks. These are not customarily supplied with valves for regulation of individual pipeline flow, although uniformity of flow in the many individual circuits, which comprise a fair-size ice skating-rink installation, is of utmost importance. Perhaps through electrical analogy it will be convenient to make some studies, particularly concerning the changes in uniformity of flow when total fluid flow is varied to conform with load conditions.

AUTHORS' CLOSURE

The authors wish to express their grateful appreciation to Messrs. Everetts and Holske for their thought-provoking discussions and wish to report that work is now under way on low-density fluids, namely, on the problem of flow distribution in a multi-branched distribution system of an air-conditioning installation. It is also contemplated to study not only ice-rink brine systems, but also hot-water heating systems.

⁴ Professional Engineer, The Vilter Manufacturing Company, New York, N. Y.

⁵ Engineering, Office of C. S. Leopold, Engineer, Philadelphia, Pa.

Electrical Effects Accompanying the Stick-Slip Phenomenon of Sliding of Metals on Plastics and Lubricated Surfaces¹

By G. W. SOHL,² J. GAYNOR,³ AND S. M. SKINNER⁴

The electrical transients which accompany the stick-slip phenomenon in boundary lubrication have been investigated by an apparatus which permits simultaneous oscillographic measurement of any two of the following: The instantaneous load, the instantaneous frictional drag, the electrical transient potentials during the stick-slip motion. The phenomenon has been investigated with unlubricated metal-metal contact using four metals in various combinations, lubricated metal-metal contact using various combinations of metals and five lubricants, and metal-plastic contact; in all cases, the contact was a sliding contact at low speed, since this accentuates the stick-slip phenomenon. Definite time correlation between the mechanical stick-slip and the electrical transients has been found. The characteristics of the electrical discharge appear to favor a charge-discharge mechanism rather than a thermoelectric potential or a dielectric breakdown mechanism, although further experiments are necessary to provide unambiguous proof of such a conclusion. Certain related frictional experiments were performed which, however, also favor such a mechanism.

INTRODUCTION

IT IS well known that as the thickness of the lubricant film decreases, the smooth, low-friction behavior encountered in thick-film or hydrodynamic lubrication changes into a very different type of behavior characteristic of boundary lubrication. In addition to the greater frictional forces then encountered, the behavior is not dependent on the properties of the lubricant alone, and the nature of the solid surface, as well as the "oiliness" of the lubricant must be taken into account. Oiliness is a quantity difficult to define,^{5,6,7} but qualitatively may be regarded as an in-

dication of those characteristics which cause two oils of the same viscosity, at the same temperature, and otherwise under identical conditions, to exhibit differences in observed friction.

Under boundary lubrication, the frictional force depends upon the relative velocity of the moving surfaces. When this dependence produces a periodic effect on the relative motion, "stick-slip" exists. Initially the surfaces stick together. As the moving surface commences motion, the stationary one moves with it for a very small distance, and elastic forces build up to oppose this motion. When the elastic forces are great enough, the two break free and the stationary surface rebounds, slipping past the other surface. At some point in the rebound, possibly in the initial rebound, possibly when the first swing has been completed and the stationary surface is traveling again in the same direction as the moving surface, the relative velocity becomes small enough so that sticking again occurs. The repetition of such periodic motion may introduce undesirable vibration into shafts, resulting in earlier fatigue, unsymmetrical and increased wear in bearings, and deviations from computed loads.

Stick-slip behavior is characteristic of solid-solid friction and the friction between insufficiently lubricated surfaces, and therefore of boundary lubrication. It is not observed when the fluid film is thick enough so that true hydrodynamic lubrication is attained. Since it is often desirable to apply the maximum possible load to a given size bearing, boundary-lubrication conditions are encountered under conditions of actual use. In the category of stick-slip phenomena may be included also such diverse phenomena as the squeaking of a wagon axle, or the motion of a violin string during bowing.

It is generally accepted that stick-slip occurs when the kinetic

¹ The work described in the text which follows was performed with the support of the Office of Ordnance Research, U. S. Army. This presentation includes primarily work done by G. W. S. in partial fulfillment of the requirements for the degree of Master of Science in Chemical Engineering at Case Institute of Technology. It is the initial portion of a more extensive project.

² B. F. Goodrich Chemical Company, Avon Lake, Ohio.

³ Chemical Engineer, General Engineering Laboratory, General Electric Company, Schenectady, N. Y.

⁴ Associate Professor of Chemistry, Department of Chemistry and Chemical Engineering, Case Institute of Technology, Cleveland, Ohio.

⁵ (a) "Properties of Lubricating Oil and Engine Deposits," by C. A. Bouman, The Macmillan Company, New York, N. Y., London, England, 1950.

(b) "Lubrication," by A. E. Norton, McGraw-Hill Book Company, Inc., New York, N. Y., 1942.

(c) "Performance of Lubricating Oils," by H. H. Zuidema, American Chemical Society Monographs, Reinhold Publishing Corporation, New York, N. Y., 1952.

⁶ "Studies in Lubrication, K. Friction Phenomena and the Stick-Slip Process," by F. Morgan, M. Muskat, and D. W. Reed, *Journal of Applied Physics*, vol. 12, 1941, p. 743.

⁷ "Oiliness in Relation to Viscosity," by A. W. Burwell and J. A. Camelford, General Discussion on Lubrication and Lubricants, Proceedings of The Institution of Mechanical Engineers, London, England, vol. 2, 1938, pp. 261-273.

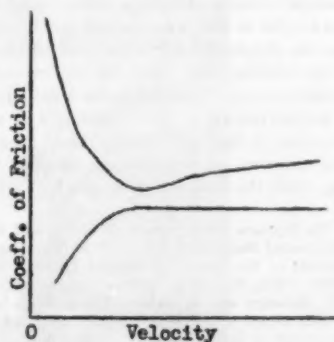


FIG. 1

Contributed by the Rubber and Plastics Division and presented at the Annual Meeting, New York, N. Y., November 25-30, 1956, of THE AMERICAN SOCIETY OF MECHANICAL ENGINEERS.

NOTE: Statements and opinions advanced in papers are to be understood as individual expressions of their authors and not those of the Society. Manuscript received at ASME Headquarters, August 28, 1956. Paper No. 56-A-163.

friction between surfaces in relative motion depends upon the relative velocity in the manner shown in the upper curve in Fig. 1. Since the friction increases as the velocity decreases, any accidental decrease in the rate of relative motion causes an increase of friction and therefore more decrease of relative velocity, until eventually adhesion (or what amounts to adhesion) occurs. This adhesion continues only until elastic forces are built up great enough to break the two surfaces apart, but the stressed condition of the surfaces then causes rapid slip.

Just as the fundamental factors in boundary lubrication are not understood completely, so are the particular mechanisms responsible for the stick-slip phenomenon and its quantitative behavior neither completely understood nor identified. Identification and study of particular mechanisms involved is of value in a fuller understanding, but any one mechanism cannot be accepted as the complete explanation of observed behavior, since the eventual explanations must be applied to the practical conditions under which lubricated surfaces operate in the factory or on the vehicle.

THE SCHNURMANN EFFECT

That electrical potentials may be observed during stick-slip phenomena was shown by Bowden⁸ and co-workers, who describe them as thermal emf, and by Morgan, Muskat, and Reed.⁹ In 1942 Schnurmann¹⁰ published similar investigations in which the electrical behavior was investigated in detail, and a dielectric breakdown mechanism was proposed; this was followed by a more extensive investigation reported in 1950.⁹ Schnurmann's explanation of the stick-slip relaxation oscillations is that the force of friction has an electrostatic component of a suitable order of magnitude; the cycle of slow electrical charging of the lubricant (by frictional means) and rapid discharge by dielectric breakdown when the electrical field in the lubricant or oxide becomes large is responsible for a periodically varying electrostatic component of friction, and therefore for stick-slip.

The work here reported is an initial investigation of the Schnurmann effect including a study of factors which might permit a choice between the two different points of view with respect to the electrical transient potentials.

APPARATUS

General Description. The frictional apparatus is shown in Fig. 2. It consists basically of a flat rotating metal disk against which is placed a slider in the form of a half sphere. The boundary conditions are obtained by the pressure of the stationary slider against the rotating plate. An electrical contact was made to the slider, which was insulated from the remainder of the apparatus by a polystyrene rod. The slider picked up electrical discharges occurring in the course of frictional runs. The frictional drag was measured by a strain gage attached to the vertical steel spring, while the load was measured by a strain gage on

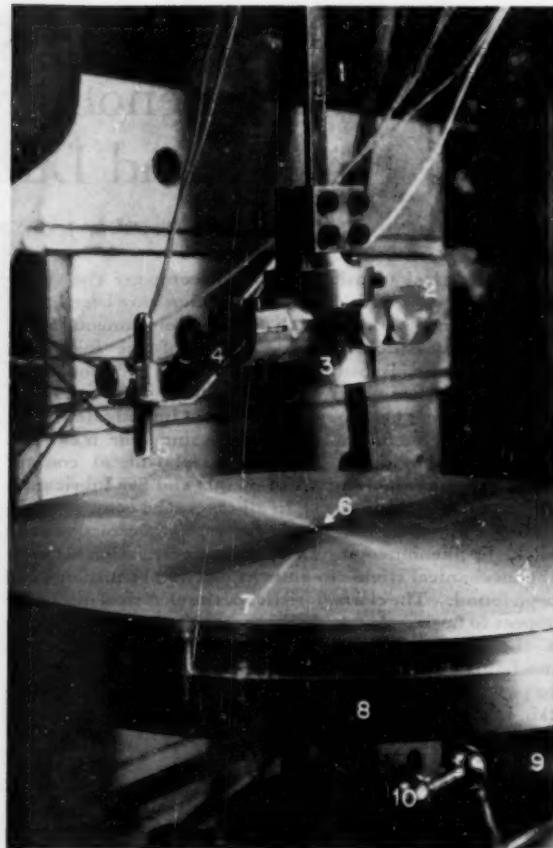


FIG. 2 SLIDER AND TEST PLATE

- | | |
|--------------------------|---------------------------|
| 1 Steel spring | 6 Mercury well |
| 2 Styrene rod | 7 Aluminum test plate |
| 3 Brass holder | 8 Brass backing plates |
| 4 Phosphor-bronze spring | 9 Graham speed dial |
| 5 Copper slider | 10 Lever for Graham speed |

the horizontal phosphor-bronze spring, holding the slider. The metal test plates were made of $1/4$ -in-thick stock cut to 12 in. diam with the center portion removed for installation of a mercury well. The sliders were $1/4 \times 2$ -in. rods which were rounded on each end in the form of a half sphere.

Mechanical Friction Apparatus. The friction apparatus was built on the frame of a Cincinnati 18 Royal drill press. The drive mechanism for the rotating plate was a Graham variable-speed motor and transmission. It can operate between speeds of 1 and 28 rpm. An aluminum base plate was designed which was bolted to the movable table of the drill press and on it were mounted the Graham transmission and motor. This permits the apparatus to be raised or lowered as needed.

On the drive shaft of the transmission, which is equipped for a thrust bearing, is mounted the rotating disk, by a flanged coupling topped by a 4-in.-diam plate to which the upper bearing plates are bolted. This flanged coupling is joined by set screws to the output drive shaft from the Graham transmission. To the assembly is bolted an upper plate of brass, 12 in. diam and $3/4$ in. thick; to the latter plate is fastened an 11 $3/4$ -in.-diam plate by three countersunk screws which permit adjustment of the plane of rotation. In the center of each of the two plates is a 1-

⁸ See, e.g., "The Surface Temperature of Solids and Metals, Temperature of Lubricated Surfaces," by F. P. Bowden and K. E. W. Ridler, *Proceedings of the Royal Society of London, series A*, vol. 154, 1938, p. 640; "The Nature of Sliding and the Analysis of Friction," by F. P. Bowden and L. Shen, *Proceedings of the Royal Society of London, series A*, vol. 169, 1939, p. 371; and "The Friction and Lubrication of Solids," by F. P. Bowden and D. Tabor, The Clarendon Press, Oxford, England, 1950; footnote 6.

⁹ "The Electrostatic Component of the Force of Sliding Friction," by R. Schnurmann and E. Warlow-Davies, *Proceedings of the Physical Society, London, England*, vol. 54, 1942, p. 14.

¹⁰ "Thermoelectric Experiments With Extreme Pressure Lubricants," by R. Schnurmann, *Journal of Applied Physics*, vol. 20, 1949, p. 376.

"The Electrostatic Component of the Force of Friction," by R. Schnurmann, a paper in the 1950 Symposium on the Physics of Lubrication, published as Supplement No. 1 to the *British Journal of Applied Physics*, 1951.

in-diam hole in which a mercury well is situated for electrical contact; the hole accommodates the slip ring which holds the test plate in place. The test plates were 12 in. diam and $\frac{1}{4}$ in. thick, made, respectively, of copper 99.9 per cent, tin 99 per cent, aluminum 96 per cent, and nickel 99.6 per cent pure. The center of each test plate is tapped with a $\frac{7}{8}$ -in. tap and a slip ring is screwed in. When applied to the test machine, the plate is placed on the $11\frac{3}{4}$ -in. disk with the slip ring fitting in the hole of the mounting plates; static friction between mounting and test plates keeps the test plate rotating at the same speed as the mounting table.

The spindle of the drill press is anchored in place by set screws and to it is attached the slider arrangement and holder. The piece of spring steel is heavy enough to resist twisting motions that might occur during stick-slip but flexible enough to allow stick-slip operation. The actual slider attachment is shown in Fig. 2. The styrene rod insulates the slider from the rest of the apparatus and permits lateral motion of the slider to obtain a fresh sliding surface.

The sliders are made from the same purity and type of metal as are the test plates, usually from the same stock. Thus the metals may be used interchangeably as like metal with like metal, or one metal as test plate and another metal as slider.

The slider is brought into contact with the rotating test plate by turning down the drill spindle. A microswitch was placed under the stop, which automatically turned on the oscillograph camera. At any pressure or moment of contact, the strain gages indicate the vertical and horizontal loads; a separate compensating gage is mounted on the post of the drill press for each strain gage.

Electrical Apparatus. Four oscillographs were used: One measured the horizontal component (instantaneous frictional force) and one the vertical component (load) of the mechanical force. Another measured the electrical transients, and the fourth was a dual-beam slave which permitted simultaneous presentation of the deflections on any two of the other oscillographs. Figs. 3, 4, 5 show the circuits and actual apparatus.

The electrical transients produced from the stick-slip were measured on a Dumont Type 323 oscilloscope by connection from the insulated slider. Between ground and the Y-input of the 323 oscillograph, there was the input impedance (2 megohm) of the 323. Since the table and test plate of the apparatus were connected to ground by the mercury well, the charge transferred during friction decayed to ground through this input impedance. Photographs were taken initially using the sweep of the oscillograph, but more successful results were obtained by using the driven no-gate setting so that only a dot appears on the screen, which is moved vertically by the input voltage, and moving the film past the dot. By means of the dual-beam oscillograph, it was possible to show simultaneously the electrical transients and the instantaneous drag or load on the slider.

MATERIALS

The metal plates and sliders used were, as mentioned, from the same stock. Tin, copper, aluminum, and nickel were used. The plate to be used was removed from the mineral-oil bath in which it was stored, the mineral oil was removed by solvent, and the surface dried until no evidence of oil was present. The slider and metal plate were cleaned with the same solvent; when necessary, cleaning was repeated during a run, and cleaning was

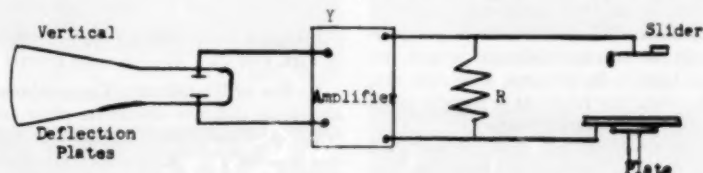


FIG. 3 ELECTRICAL CONNECTION TO 323 OSCILLOGRAPH



FIG. 4 VIEW OF FRICTION APPARATUS SETUP

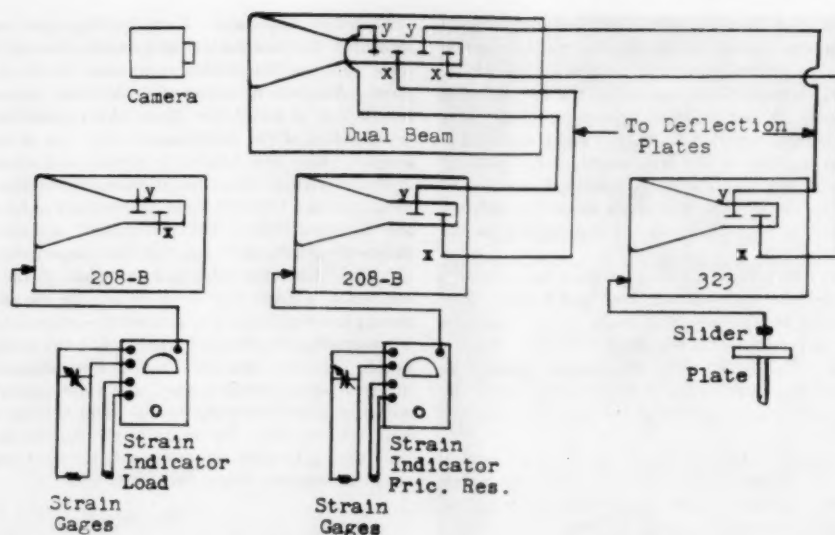


FIG. 5 SCHEMATIC OF CIRCUITS USED IN FRICTION MEASUREMENT

repeated before each contact, so that the conditions were as nearly reproducible as possible.

In the case of the lubricated metals, the procedure was the same, except that the cleaning was followed by spreading the fresh lubricant on the metal plate. The lubricants used were mineral oil grade A, Sohio, or the various molecular-weight polybutenes, B-24, B-64, B-128, of average molecular weight, respectively, 840, 1370, and 1500.¹⁰ In all cases, after each run, there was removed from the slider any lubricant or possible metal which may have been transferred to it during contact.

Runs also were made in which the metal slider contacted various polymeric materials instead of metal. These were especially helpful in the interpretation of the results. The following plastics were used: Saran, Mylar, polyvinyl chloride, polyester, methylmethacrylate, and Teflon. They may be regarded as a thicker dielectric film than would be obtained from a surface coating or lubricant on a metal.

THE STICK-SLIP LOAD AND DRAG

In Fig. 6 are shown two representative pictures of the simultaneous load and drag measurements during stick-slip. It had been thought that load would vary during stick-slip, and the apparatus was designed with the load-measuring gage more responsive than the drag-measuring gage. The figures show that this is not the case. Although the elastic strain varied considerably during a violent stick-slip operation, corresponding to a change of over 500 grams frictional resistance, the load curve changed very little. The large broad trace is the drag-stress curve, while the smaller underlying band is the trace from the load-strain gage. The load remains constant at 1000 grams while the drag varies from 600 grams (in stick portions) to only 50 grams in slip portions. Measurements were made with a simulated frictional resistance of 500 grams, and it was found that the displacement of the slider was less than 10 deg; since the cosine of 10 deg is 0.986, the measured vertical component on the slider is for all practical purposes equal to the load.

The lighter lubricants, B-24, B-64, and mineral oil, as well as the dry frictional contact, and the contact between metal and

plastic gave good indications of the drag fluctuations. The B-128 (which is sometimes used as a pressure adhesive) was quite thick and sticky, and tended to mask the drag fluctuations.

ELECTRICAL EFFECTS

Electrical Transients. Typical electrical transients are shown in Figs. 7 to 16. The following general results were obtained:

- 1 Size of Transients: The combination of nickel plate and aluminum slider or aluminum plate and nickel slider, and the nickel on nickel showed many small and rapidly recurring transients, especially during slip. The remainder of the metals and lubricants showed transients which were fairly large. These effects are shown in Figs. 7 and 8.

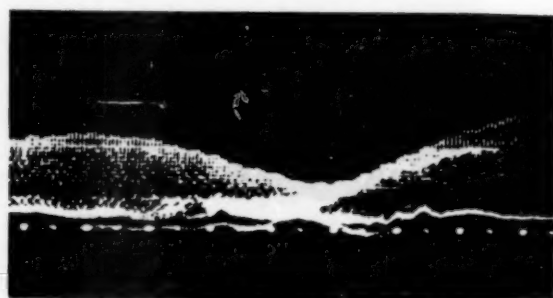
- 2 Transients With Like Metals: All combinations of like-metal plate and slider gave transients. The nickel and the tin frictional contact transients in Figs. 9 and 10 are samples.

- 3 Time of Occurrence: In general the transients were accompanied by visible variations in drag, although these drag variations lasted longer than the transients, because of the larger time constant of the measuring apparatus. The electrical transients were over within $1/100$ sec, but the slip lasted from $1/20$ to $1/10$ sec. The stick (build-up to peak) occupied of the order of 1 sec. The electrical transients generally would occur just at the peak drag or immediately thereafter. Fig. 11 shows transients occurring during the decrease in drag, and Fig. 12 shows rapid stick-slip with the transient at maximum drag. However, in some, but few cases, there were transients at minimum drag or while the drag was rising again to a maximum. In metal-plastic friction, the electrical transients consistently occurred at the time the slip started.

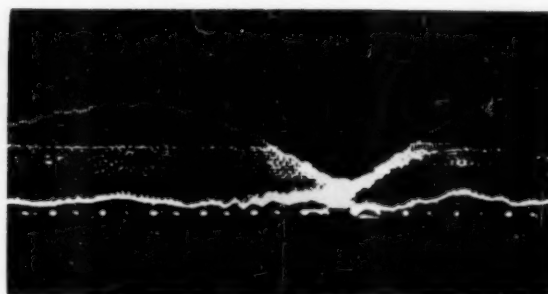
- 4 Number of Transients: Where the transients were quite small, they were numerous and fairly close together. Usually the transient would occur singly, with an accompanying drag variation, but with large discharges two or more transients would occur in the same general time period, Fig. 11.

- 5 Nature of Frictional Contact: The same general types of transients were obtained with metal-plastic contact as with metal-metal, lubricated or unlubricated. This is shown in Figs. 13 to 16. The relationship between the drag fluctuations and the

¹⁰ Supplied by the Enjay Chemical Company.



←Increasing time
Load versus drag
Tin plate, tin
Slider, mineral oil
Load = 1000 grams
Drag (max) = 600 grams
Drag (min) = 50 grams



←Increasing time
Load versus drag
Tin plate, tin
Slider, mineral oil
Load = 1000 grams
Drag (max) = 500 grams
Drag (min) = 30 grams

FIG. 6 REPRESENTATIVE VIEWS OF SIMULTANEOUS LOAD AND DRAG MEASUREMENTS DURING STICK-SLIP

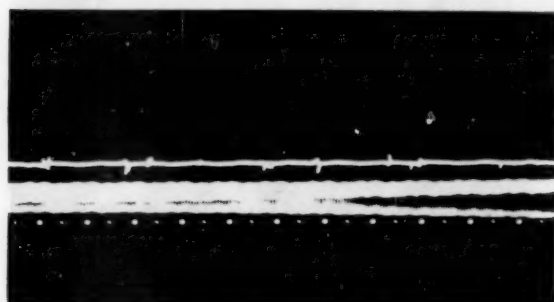


FIG. 7 NICKEL PLATE, ALUMINUM SLIDER, LUBRICANT B-128
←Increasing time

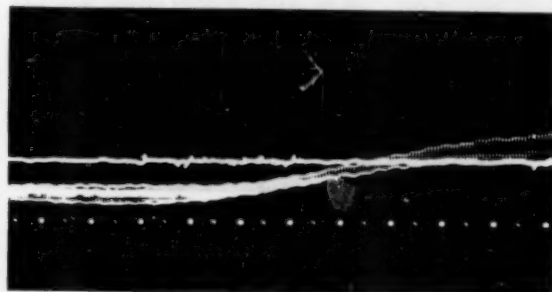


FIG. 8 NICKEL PLATE, NICKEL SLIDER, LUBRICANT B-64
←Increasing time

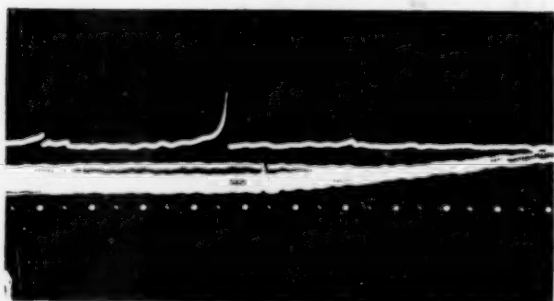


FIG. 9 NICKEL PLATE, NICKEL SLIDER, DRY
←Increasing time

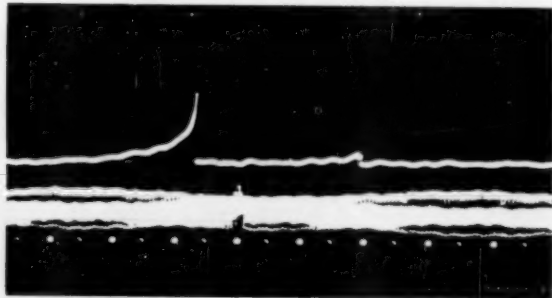


FIG. 10 TIN PLATE, TIN SLIDER, DRY
←Increasing time

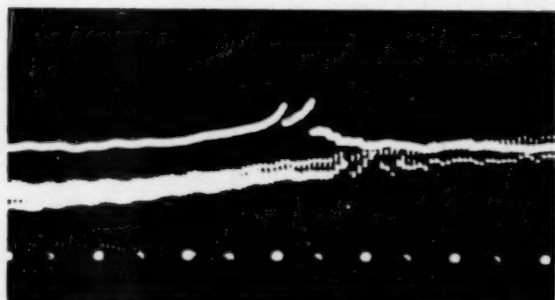


FIG. 11 TIN PLATE, NICKEL SLIDER, MINERAL OIL
←Increasing time

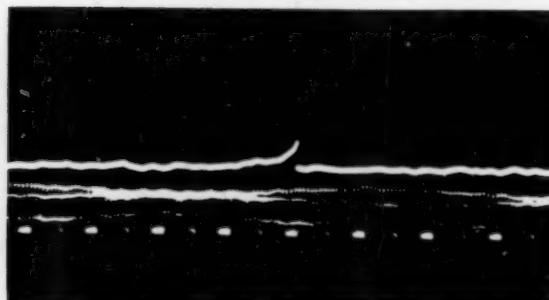


FIG. 12 COPPER PLATE, ALUMINUM SLIDER, B-64 RAPID STICK-SLIP
←Increasing time

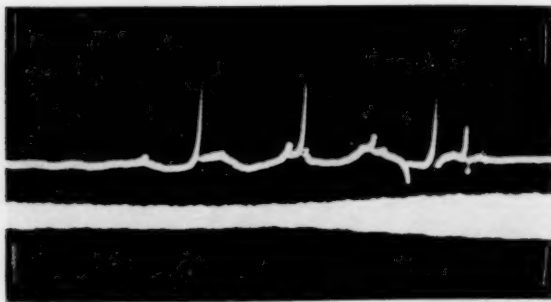


FIG. 13 SARAN AND COPPER SLIDER
←Increasing time

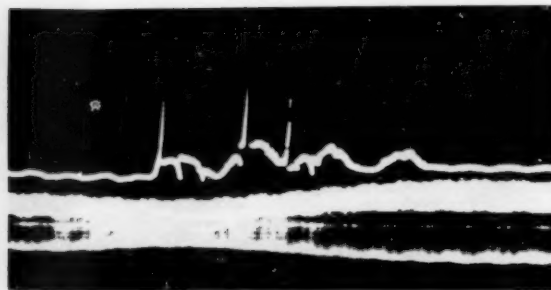


FIG. 14 SARAN AND COPPER SLIDER
←Increasing time

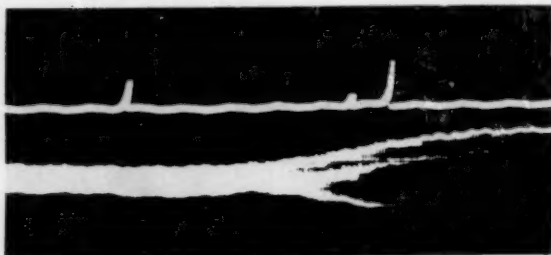


FIG. 15 POLYMETHYLMETHACRYLATE AND COPPER SLIDER
←Increasing time

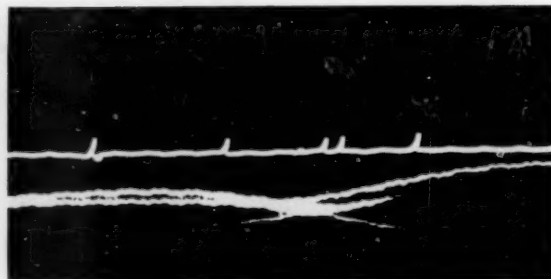


FIG. 16 POLYMETHYLMETHACRYLATE AND COPPER SLIDER

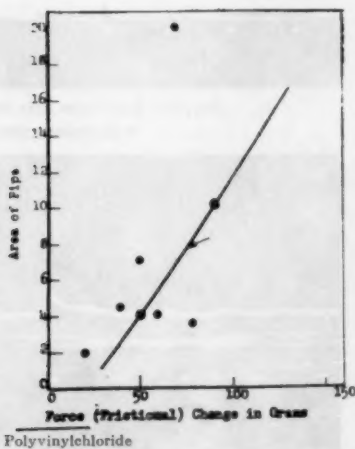
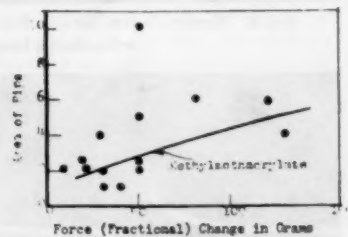
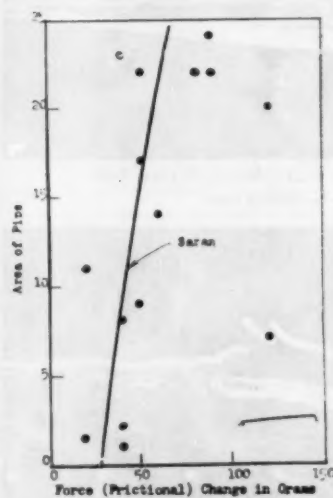
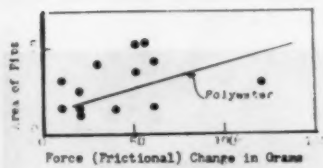


FIG. 17 FRICTIONAL RESISTANCE CHANGE VERSUS ELECTRICAL DISCHARGES FOR VARIOUS PLASTICS



electrical transients can be analyzed better with the plastics, since the plastic surfaces used were more uniform than those with the metals. The electrical discharges in these cases consistently came just as the slip started and their size depended upon the plastic under test. Saran showed the greatest area under the transients per unit change in drag and Teflon and Mylar showed large transients in relation to the accompanying stick-slip.

6 Drag Change Versus Quantity of Charge Transferred: Within the degree of accuracy possible, the potential in the oscillograph represents the current flow times the resistance of the

external circuit. Therefore the area under the transients is very nearly proportional to the charge transferred. In Figs. 17 and 18 are plotted the change in drag (frictional resistance change) against the area under the voltage transient in the case of metal sliders in frictional contact with various plastic materials. Less consistent results were obtained in lubricated metal-metal sliding, as would be expected, e.g., Fig. 19.

7 Sign of Charge in Metal-Plastic Frictional Contact: The discharge was in the direction leaving the slider positive after contact; i.e., leaving the plastic negative. This also was checked by the use of colored, charged fluorescent powders dusted onto

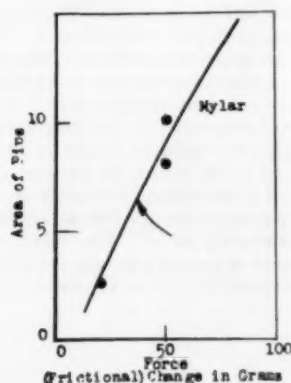


FIG. 18 FRICTIONAL RESISTANCE CHANGE VERSUS ELECTRICAL DISCHARGES FOR VARIOUS PLASTICS

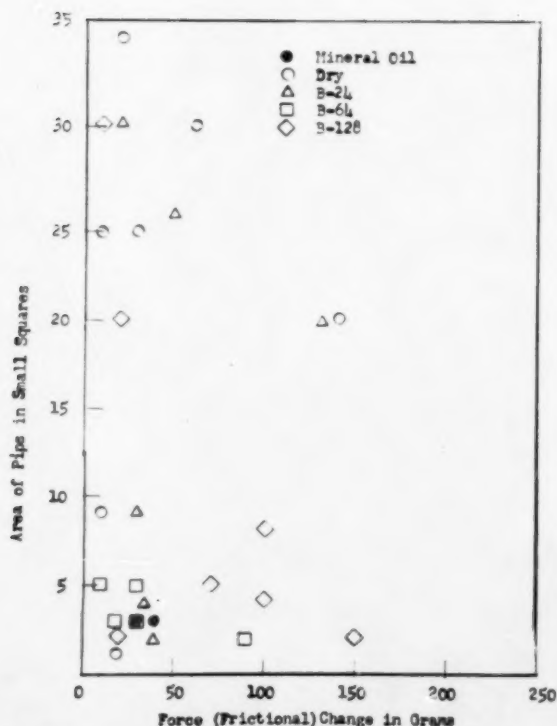
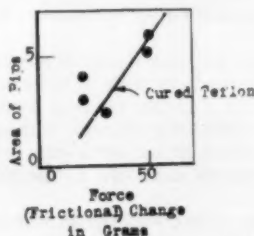


FIG. 19 ELECTRICAL DISCHARGES VERSUS FRICTIONAL RESISTANCE CHANGE FOR ALUMINUM PLATE WITH VARIOUS SLIDERS

the plastics after frictional contact. The sliding track was easily outlined by the powder charged positively.

8 Confirmatory Experiments on Charging of Plastics by Frictional Contact: In view of the charge transfer, additional experiments were performed on the sliding of polymer powders down metal slides to measure the charge transfer. These have been reported¹¹ already and confirm the qualitative conclusions drawn from the foregoing.

CONCLUSIONS

1 The stick-slip phenomenon in boundary lubrication is accompanied by an electrical transient of the nature of a discharge. Since such discharges were observed in metal-plastic contact, quite similar to those in metal-metal contact, lubricated or unlubricated, and since (a) conduction in the usual sense is not possible through thick plastic sheets, and (b) no evidence was observed of dielectric breakdown, the nature of the transient is quite possibly a charging mechanism, followed by a mechanical breaking away of charged surfaces from each other and subsequent decay.

2 The mechanical stick-slip and the accompanying electrical transients are observed in the dry friction between metals, both if they are different or from the same stock. They also are observed in lubricated frictional contact between the metals and in contact between metals and various plastics which were thick enough so that electrical breakdown was unlikely to have occurred.

3 The electrical transients are accompanied by a change in the frictional drag. The period of time during which the change in drag takes place is long compared to the duration of the transients, but is still small; the transients usually occur almost at,

¹¹ "Electrostatic Charges in Plastics," by S. M. Skinner, J. Gaynor, and G. W. Sohl, *Modern Plastics*, vol. 33, February, 1956, pp. 127-130, 132-134, 136, and 246.

or exactly at, the beginning of the slip, but a few occur at other times. In some few cases, electrical transients were obtained without observable change in the drag; these may be due to changes in the chemical surface conditions which produced localized electrochemical potentials. However, change in the measured drag does not occur without the presence of electrical transients.

4 During stick-slip the large changes in the measured drag are not accompanied by noticeable changes in the measured vertical load. Since Amonton's law is usually valid, the time average of the stick-slip drag must be proportional to the load; however, the variation of friction with relative velocity of the moving surfaces can be accounted for by variations in the time average with velocity.

5 The electrical discharge and drag change in metal-plastic frictional contact show more regularity than do those in metal-metal contact. The quantity of charge involved depends directly upon the change in frictional resistance. Although the points are scattered, they show sufficient consistency so that a straight line can be drawn through them, with a slope which depends upon the plastic used.

6 The transfer of charge during stick-slip in metal-plastic contact has been confirmed in two additional ways; namely, by dusting charged powders on the plastic and by sliding polymer powders down metal sliders.

It is too early to discuss the mechanism and more experimental work is under way to investigate this further. Other possible causes for the charge transfer could include the Faraday effect, i.e., the cutting of the earth's magnetic field by the slider in its rapid recovery, and the making and breaking of a circuit containing a resistor and a condenser with a source of external potential from a thermocouple. However, the former would not be involved in the sliding of polymer powders over metals nor in a magnetically shielded region, and in so far as the latter is concerned, the metal-plastic contact includes no thermocouple source of potential in the usual sense, although temperature effects at the interface may be involved. Experiments on the breaking of metal-adhesion samples with polymer adhesive also show electrical potentials and charge transfer at equilibrium. It appears, therefore, that although no precise conclusion can be drawn as yet, the evidence favors a charging mechanism during the stick portion of the stick-slip, and a mechanical breaking away of the slider from the moving surface during which charged surfaces are rapidly separated, thus producing increasing potentials on the slider. These potentials build up as the separation increases (aided by the mechanical rebound of the surfaces previously in contact). Since a path to ground exists in the experimental arrangement, the build-up ends in a typical RC decay. When the moving plate is a plastic, the resistance to ground is so high that the charges can be measured after the frictional contact has ended.



